



# Recurrences in past climates

Novel concepts & tools for the study of Palaeoseasonality  
and beyond

**Tobias Braun**  
September, 2022

A cumulative dissertation for the degree  
doctor rerum naturalium (Dr. rer. nat.) in  
Theoretical Physics

submitted to  
The Faculty of Mathematics and Natural Sciences at the  
University of Potsdam – Institute of Physics and Astronomy  
and the  
Potsdam Institute for Climate Impact Research (RD4)  
Germany

Date of disputation: 23.03.2023

This work is protected by copyright and/or related rights. You are free to use this work in any way that is permitted by the copyright and related rights legislation that applies to your use. For other uses you need to obtain permission from the rights-holder(s).  
<https://rightsstatements.org/page/InC/1.0/?language=en>

### **Supervisors:**

Prof. Dr. Dr. h.c. mult. Jürgen Kurths  
University of Potsdam, Institute of Physics and Astronomy.  
Research Domain Complexity Science, Potsdam Institute for Climate Impact Research (PIK),  
Member of the Leibniz Association, Telegrafenberg, Potsdam, Germany.  
Institute of Physics, Humboldt Universität zu Berlin, Germany.

Dr. habil. Norbert Marwan  
Research Domain Complexity Science, Potsdam Institute for Climate Impact Research (PIK),  
Member of the Leibniz Association, Telegrafenberg, Potsdam, Germany.  
University of Potsdam, Institute of Earth and Environmental Science.

**Submission date:** 28th September 2022

### **Referees:**

Dr. habil. Norbert Marwan  
Research Domain Complexity Science, Potsdam Institute for Climate Impact Research (PIK),  
Member of the Leibniz Association, Telegrafenberg, Potsdam, Germany.  
University of Potsdam, Institute of Earth and Environmental Science.

Prof. Dr. Andrej Spiridonov  
Department of Geology and Mineralogy  
Faculty of Chemistry and Geosciences  
Vilnius University  
M. K. Ciurlionio g. 21/27, Vilnius 03101, Lithuania

Prof. Dr. Karoline Wiesner  
Institute of Physics and Astronomy  
University of Potsdam  
Karl-Liebknecht-Straße 24/25, 14476 Potsdam-Golm, Germany

### **Copyright**

Recurrences in past climates –  
Novel concepts & tools for the study of Palaeoseasonality and beyond  
©Tobias Braun, University of Potsdam, Potsdam, Germany

Published online on the  
Publication Server of the University of Potsdam:  
<https://doi.org/10.25932/publishup-58690>  
<https://nbn-resolving.org/urn:nbn:de:kobv:517-opus4-586900>

*To my grandmother*

"Dripping water hollows out stone,  
not through force  
but through persistence."  
**Ovid**



## Abstract

Our ability to predict the state of a system relies on its tendency to recur to states it has visited before. Recurrence also pervades common intuitions about the systems we are most familiar with: daily routines, social rituals and the return of the seasons are just a few relatable examples. To this end, recurrence plots (RP) provide a systematic framework to quantify the recurrence of states. Despite their conceptual simplicity, they are a versatile tool in the study of observational data. The global climate is a complex system for which an understanding based on observational data is not only of academical relevance, but vital for the predurance of human societies within the planetary boundaries. Contextualizing current global climate change, however, requires observational data far beyond the instrumental period. The palaeoclimate record offers a valuable archive of proxy data but demands methodological approaches that adequately address its complexities. In this regard, the following dissertation aims at devising novel and further developing existing methods in the framework of recurrence analysis (RA). The proposed research questions focus on using RA to capture scale-dependent properties in nonlinear time series and tailoring recurrence quantification analysis (RQA) to characterize seasonal variability in palaeoclimate records ('Palaeoseasonality').

In the first part of this thesis, we focus on the methodological development of novel approaches in RA. The predictability of nonlinear (palaeo)climate time series is limited by abrupt transitions between regimes that exhibit entirely different dynamical complexity (e.g. crossing of 'tipping points'). These possibly depend on characteristic time scales. RPs are well-established for detecting transitions and capture scale-dependencies, yet few approaches have combined both aspects. We apply existing concepts from the study of self-similar textures to RPs to detect abrupt transitions, considering the most relevant time scales. This combination of methods further results in the definition of a novel recurrence based nonlinear dependence measure. Quantifying lagged interactions between multiple variables is a common problem, especially in the characterization of high-dimensional complex systems. The proposed 'recurrence flow' measure of nonlinear dependence offers an elegant way to characterize such couplings. For spatially extended complex systems, the coupled dynamics of local variables result in the emergence of spatial patterns. These patterns tend to recur in time. Based on this observation, we propose a novel method that entails dynamically distinct regimes of atmospheric circulation based on their recurrent spatial patterns. Bridging the two parts of this dissertation, we next turn to methodological advances of RA for the study of Palaeoseasonality. Observational series of palaeoclimate 'proxy' records involve inherent limitations, such as irregular temporal sampling. We reveal biases in the RQA of time series with a non-stationary sampling rate and propose a correction scheme.

In the second part of this thesis, we proceed with applications in Palaeoseasonality. A review of common and promising time series analysis methods shows that numerous valuable tools exist, but their sound application requires adaptations to archive-specific limitations and consolidating transdisciplinary knowledge. Next, we study stalagmite proxy records from the Central Pacific as sensitive recorders of mid-Holocene El Niño-Southern Oscillation (ENSO) dynamics. The records' remarkably high temporal resolution allows to draw links between ENSO and seasonal dynamics, quantified by RA. The final study presented here examines how seasonal predictability could play a role for the stability of agricultural societies. The Classic Maya underwent a period of sociopolitical disintegration that has been linked to drought events. Based on seasonally resolved stable isotope records from Yok Balum cave in Belize, we propose a measure of seasonal predictability. It unveils the potential role declining seasonal predictability could have played in destabilizing agricultural and sociopolitical systems of Classic Maya populations.

The methodological approaches and applications presented in this work reveal multiple exciting future research avenues, both for RA and the study of Palaeoseasonality.

## Zusammenfassung

Unsere Fähigkeit, den Zustand eines Systems vorherzusagen, hängt grundlegend von der Tendenz des Systems ab, zu früheren Zuständen zurückzukehren. Solche "Rekurrenzen" sind sogar Bestandteil unserer Intuition und alltäglichen Erfahrungswelt: regelmäßige Routinen, soziale Zusammentreffen und die Wiederkehr der Jahreszeiten sind hierfür nur vereinzelte Beispiele. Rekurrenzplots (RPs) stellen uns in diesem Kontext eine systematische Methode zur Verfügung, um die Wiederkehreigenschaften von Systemzuständen quantitativ zu untersuchen. Obwohl RPs konzeptionell vergleichsweise simpel sind, stellen sie eine vielseitige Methode zur Analyse von gemessenen Beobachtungsdaten dar. Das globale Klimasystem ist ein komplexes System, bei dem ein datenbasiertes Verständnis nicht lediglich von rein akademischen Wert ist – es ist viel mehr relevant für das Fortbestehen der Gesellschaft innerhalb der natürlichen planetaren Grenzen. Um die heute beobachteten Klimaveränderungen allerdings in einen langfristigen Kontext einzuordnen, benötigen wir empirische Daten, die weit über die Periode hinaus gehen, für die instrumentelle Daten verfügbar sind. Paläoklimatologische Datenreihen repräsentieren hier ein wertvolles Archiv, dessen Auswertung jedoch Analysemethoden erfordert, die an die Komplexitäten von paläoklimatologischen 'Proxydaten' angepasst sind. Um einen wissenschaftlichen Beitrag zu dieser Problemstellung zu leisten, befasst sich diese Doktorarbeit mit der Konzeptionierung neuer Methoden und der problemstellungsbezogenen Anpassung bewährter Methoden in der Rekurrenzanalyse (RA). Die hier formulierten zentralen Forschungsfragen konzentrieren sich auf den Nachweis zeitskalen-abhängiger Eigenschaften in nichtlinearen Zeitreihen und, insbesondere, der Anpassung von quantitativen Maßen in der RA, um paläosaisonale Proxydaten zu charakterisieren ('Paläosaisonalität').

Im ersten Teil dieser Arbeit liegt der Schwerpunkt auf der Entwicklung neuer methodischer Ansätze in der RA. Die Vorhersagbarkeit nichtlinearer (paläo)klimatologischer Zeitreihen ist durch abrupte Übergänge zwischen dynamisch grundlegend verschiedenen Zuständen erschwert (so zum Beispiel das Übertreten sogenannter 'Kippunkte'). Solche Zustandsübergänge zeigen oft charakteristische Zeitskalen-Abhängigkeiten. RPs haben sich als Methode zum Nachweis von Zustandsübergängen bewährt und sind darüber hinaus geeignet, Skalenabhängigkeiten zu identifizieren. Dennoch wurden beide Aspekte bislang selten methodisch zusammengeführt. Wir kombinieren hier bestehende Konzepte aus der Analyse selbstähnlicher Strukturen und RPs, um abrupte Zustandsübergänge unter Einbezug der relevantesten Zeitskalen zu identifizieren. Diese Kombination von Konzepten führt uns ferner dazu, ein neues rekurrenzbasiertes, nichtlineares Abhängigkeitsmaß einzuführen. Die quantitative Untersuchung zeitversetzter Abhängigkeiten zwischen zahlreichen Variablen ist ein zentrales Problem, das insbesondere in der Analyse hochdimensionaler komplexer Systeme auftritt. Das hier definierte 'Rekurrenzfluß'-Abhängigkeitsmaß ermöglicht es auf elegante Weise, derartige Abhängigkeiten zu charakterisieren. Bei räumlich ausgedehnten komplexen Systemen führen Interaktionen zwischen lokalen Variablen zu der Entstehung räumlicher Muster. Diese räumlichen Muster zeigen zeitliche Rekurrenzen. In einer auf dieser Beobachtung aufbauenden Publikation stellen wir eine neue Methode vor, mit deren Hilfe differenzierbare, makroskopische Zustände untersucht werden können, die zu zentralen, zeitlich wiederkehrenden räumlichen Mustern korrespondieren. Folgend leiten wir über zum zweiten Teil dieser Arbeit, indem wir uns Anpassungen von Methoden zur Untersuchung von Paläosaisonalität zuwenden. Messreihen paläoklimatologischer Proxydaten geben uns nur indirekt Informationen über die ihnen zugrunde liegenden Klimavariablen und weisen inhärente Limitationen auf, wie zum Beispiel unregelmäßige Zeitabstände zwischen Datenpunkten. Wir zeigen statistische Verzerrungseffekte auf, die in der quantitativen RA auftreten, wenn Signale mit nichtstationärer Abtaststrategie untersucht werden. Eine Methode zur Korrektur wird vorgestellt und anhand von Messdaten validiert.

Der zweite Teil dieser Dissertation befasst sich mit angewandten Analysen von paläo-

saisonalen Zeitreihen. Eine Literaturlauswertung verbreiteter und potentiell vielversprechender Zeitreihenanalysemethoden zeigt auf, dass es eine Vielzahl solcher Methoden gibt, deren adäquate Anwendung aber Anpassungen an Klimaarchiv-spezifische Grenzen und Probleme sowie eine Zusammenführung interdisziplinärer Fähigkeiten erfordert. Daraufhin untersuchen wir an einem Stalagmiten gemessene Proxydaten aus der zentralen Pazifikregion als ein natürliches Archiv für potentielle Veränderungen der El Niño-Southern Oscillation (ENSO) während des mittleren Holozäns. Die bemerkenswert hohe zeitliche Auflösung der Proxy-Zeitreihen erlaubt es uns, Verbindungen zwischen der Ausprägung der ENSO und saisonalen Zyklen herzustellen, wobei wir erneut Gebrauch von der RA machen. Die letzte Publikation in dieser Arbeit untersucht, in wie fern die Vorhersagbarkeit saisonaler Veränderungen eine Rolle für die Stabilität von Gesellschaften spielen könnte, deren Nahrungsversorgung auf Landwirtschaft beruht. Die klassische Maya-Zivilisation erlitt zwischen 750-950 CE eine drastische Fragmentierung urbaner Zentren, die mit regionalen Dürren in Verbindung gebracht werden. Auf Grundlage von saisonal-aufgelösten Proxydaten aus der Yok Balum Höhle in Belize, definieren wir ein quantitatives Maß für saisonale Vorhersagbarkeit. Dies erlaubt Schlussfolgerungen über die potentielle Rolle, die ein Verlust saisonaler Vorhersagbarkeit für die sich destabilisierenden agrarwirtschaftlichen und soziopolitischen Systeme der Maya gehabt haben könnte.

Die methodischen Ansätze und Anwendungen in dieser Arbeit zeigen vielseitige, spannende Forschungsfragen für zukünftige Untersuchungen in der RA und Paläosaisonalität auf.





## List of Publications

This dissertation is based on the following publications:

### Main publications

- (P1) **Braun, T.**, Unni, V. R., Sujith, R. I., Kurths, J., & Marwan, N. (2021). Detection of dynamical regime transitions with lacunarity as a multiscale recurrence quantification measure. *Nonlinear Dynamics*, 104(4), 3955-3973. [1]
- (P2) **Braun, T.**, Kraemer, K. H., & Marwan, N. (2022). Recurrence flow measure of non-linear dependence. **accepted for EPJ ST**
- (P3) Mukhin, D., Hannachi, A., **Braun, T.**, & Marwan, N. (2022). Revealing recurrent regimes of mid-latitude atmospheric variability using novel machine learning method. **under review for Chaos**
- (P4) **Braun, T.**, Fernandez, C. N., Eroglu, D., Hartland, A., Breitenbach, S. F., & Marwan, N. (2022). Sampling rate-corrected analysis of irregularly sampled time series. *Physical Review E*, 105(2), 024206. [2]
- (P5) Kwiecien, O., **Braun, T.**, Brunello, C. F., Faulkner, P., Hausmann, N., Helle, G., Hoggarth, J. A., Ionita, M., Jazwa, C., Kelmelis, S., Marwan, N., Fernandez, C. N., Nehme, C., Opel, T., Oster J. L., Perşoiu, A., Petrie, C., Prufer, K., Saarni, S. M., Wolf, A., Breitenbach, S. F. M. (2022). What we talk about when we talk about seasonality—A transdisciplinary review. *Earth-Science Reviews*, 225, 103843. [3]
- (P6) Fernandez, C. N., **Braun, T.**, Fox, B., Hartland, A., Kwiecien, O., Pederson, C. L., Hoepker, S., Bernasconi, S., Hellstrom, J., Gázquez, F., French, A., Marwan, N., Immenhauser, A., Breitenbach, S. F. M. (2022). Mid-Holocene rainfall changes in the southwestern Pacific. [4] **in prep**
- (P7) **Braun, T.**, Breitenbach, S. F. M., Skiba, V., Lechleitner, F., Ray, E., Baldini, L. M., Polyak, V. J., Baldini, J. U. L., Kennett, D. J., Prufer, K. M., & Marwan, N. (2022). Decline in seasonal predictability potentially destabilized Classic Maya societies. **under review for Communications Earth & Environment**

The following publications haven also been written in the process of this dissertation but will not be considered in the following:

### Other publications

- (P8) Wolf, A., Ersek, V., **Braun, T.**, French, A., McGee, D., Bernasconi, S., Skiba, V., Griffiths, M. L., Johnson, K. R., Fohlmeister, J., Breitenbach, S. F. M., Pausata, F. S. R., Tabor, C., Longman, J., Roberts, W. H. G., Chandan, D., Peltier, W. R., Salzmann, U., Limbert, D., Trinh, D. A. (2022). Drivers of Holocene Southeast Asian monsoon variability. **submitted to Nature Communications**
- (P9) Haselhoff, T., **Braun, T.**, Hornberg, J., Lawrence, B., Ahmed, S., Gruehn, D., Moebus, S. (2022). Analysing interlinked frequency dynamics of the urban acoustic environment. **under review for Journal of Sound and Vibration**
- (P10) Haselhoff, T., Hornberg, J., Lawrence, B., Ahmed, S., Gruehn, D., Marwan, N., Moebus, S., **Braun, T.** (2022). Complex frequency networks of the urban acoustic environment. **in prep**

## Author contributions

In the following, I will list the contributions of all authors for each work discussed in this thesis. Whenever an author has contributed to the writing of the original draft ('Writing (original draft)'), this automatically implies that the respective author has contributed to the revisions of the manuscript, too. For co-authored publications, I add a short explicit summary of my contribution.

- (P1) **T. Braun:** Conceptualization, Method Development, Software, Analysis, Visualizations, Writing (original draft); V. R. Unni: Experiments and Data Retrieval, Visualizations, Writing (revision); R. I. Sujith: Experiments and Data Retrieval, Supervision, Writing (revision); J. Kurths: Supervision, Writing (revision); N. Marwan: Conceptualization, Method Development, Funding, Supervision, Writing (revision)
- (P2) **T. Braun:** Conceptualization, Method Development, Software, Analysis, Visualizations, Writing (original draft); K. H. Kraemer: Conceptualization, Writing (revision); N. Marwan: Conceptualization, Method Development, Funding, Supervision, Writing (revision)
- (P3) D. Mukhin: Conceptualization, Method Development, Software, Analysis, Funding, Visualizations, Writing (original draft); A. Hannachi: Conceptualization, Method Development, Analysis, Visualizations, Writing (original draft); **T. Braun:** Analysis, Visualizations, Writing (original draft); N. Marwan: Funding, Visualizations, Supervision, Writing (revision)

### *Explicit author contribution:*

I have conducted the recurrence quantification analysis to obtain a well-interpretable distinction of the atmospheric regimes based on their dynamical properties and designed the corresponding hypothesis tests. I have generated the respective figures and written the respective parts of the manuscript in the original draft. I have contributed to the discussion and interpretation of results and revision of all versions of the manuscript.

- (P4) **T. Braun:** Conceptualization, Method Development, Software, Analysis, Visualizations, Writing (original draft); C. N. Fernandez: Fieldwork and Data Retrieval, Analysis, Visualizations, Writing (revision); D. Eroglu: Conceptualization, Analysis, Writing (revision); A. Hartland: Fieldwork and Data Retrieval, Writing (revision); S. F. M. Breitenbach: Fieldwork and Data Retrieval, Writing (revision), Supervision; N. Marwan: Conceptualization, Method Development, Funding, Writing (revision), Supervision
- (P5) *Authors worked chapter-wise and revision/synthesis of the full manuscript was carried out in plenum. I have written chapter 9 (Numerical tools for extracting seasonality changes from palaeoenvironmental time series) and contributed ideas to the Introduction and Discussion. Here, all authors are listed that contributed in particular to chapter 9 with their contributions to this chapter alone:*  
O. Kwiecien: Supervision, Writing (revision); **T. Braun:** Review of articles, Conceptualization, Software, Visualizations, Writing (original draft); N. Marwan: Conceptualization, Funding, Supervision, Writing (revision); S. F. M. Breitenbach: Supervision, Writing (original draft);

### *Explicit author contribution:*

I have carried out an extensive literature review of methods and tools for extracting seasonality from all archives covered in the review and wrote the corresponding chapter 9, including figures and computations. Ideas from this process were also partly introduced in the introduction and discussion.

- (P6) C. N. Fernandez: Fieldwork and Data Retrieval, Conceptualization, Analysis, Visualizations, Writing (original draft); **T. Braun**: Method Development, Analysis, Visualizations, Writing (original draft); B. Fox: Conceptualization, Analysis, Writing (revision); A. Hartland: Fieldwork and Data Retrieval, Writing (revision); O. Kwiecien: Fieldwork and Data Retrieval, Supervision, Writing (original draft); C. Pederson: Writing (revision); S. Bernasconi: Fieldwork, Experiments and Data Retrieval, Writing (revision); J. Hellstrom: Experiments and Data Retrieval, Writing (revision); F. Gázquez: Experiments and Data Retrieval, Writing (revision); A. French: Experiments and Data Retrieval, Writing (revision); N. Marwan: Method Development, Writing (revision); A. Immenhauser: Writing (revision); S. F. M. Breitenbach: Fieldwork and Data Retrieval, Conceptualization, Analysis, Supervision, Writing (original draft);

*Explicit author contribution:*

I have conceptualized and computed the (re-calibrated) seasonality proxy from the greyscale record, performed the corresponding RA, generated the respective figures and written the respective parts of the manuscript in the original draft. Furthermore, I have actively contributed to the wavelet analysis and PCA. In particular, I modified the hypothesis test for the wavelet analysis to account for irregular sampling. I have contributed to the discussion and interpretation of results and revision of all versions of the manuscript.

- (P7) T. Braun: Conceptualization, Method Development, Software, Analysis, Visualizations, Writing (original draft); S. F. M. Breitenbach: Conceptualization, Analysis, Visualizations, Supervision, Writing (revision); V. Skiba: Conceptualization, Analysis, Writing (revision); F. Lechleitner: Conceptualization, Analysis, Writing (revision) E. Ray: Writing (revision) L. M. Baldini: Writing (revision) V. Polyak: Experiments and Data Retrieval, Writing (revision); J. U. L. Baldini: Analysis, Writing (revision); D. Kennett: Analysis, Writing (revision); K. M. Prufer: Conceptualization, Analysis, Writing (original draft); N. Marwan: Conceptualization, Method Development, Funding, Supervision, Writing (revision)

## Acknowledgements

No full justice can be done to this dissertation if it is regarded as the sole outcome of a lonesome physicist sitting in his barred room, plagued by pandemic boredom and isolation. Fortunately so! I need to pay credit to the great people – mentors, colleagues, friends, family – who I have met along the way or who have accompanied me far beyond the very challenging past three years. It was a time as turbulent and strenuous as it was exciting and enriching, and I would not have made it all the way without these people who kept me sane.

First and foremost, I am deeply grateful to my advisor Dr. Norbert Marwan who has not only helped me grow professionally but has always been supportive with his calm, compassionate words even when crises beyond academia came crashing in. With the faith he put in me, I learnt that scientific creativity does thrive on freedom, even under difficult circumstances. I will not forget the caves in Sägistal and hope to return with you! I would further like to thank Prof. Jürgen Kurths both for his long-sighted suggestions and the casual chats over a cup of coffee. Thank you for welcoming me as a part of your multifaceted and fascinating research group.

It is not an overstatement to say that if I had not met Dr. Seb Breitenbach, my doctoral work would have neither been as insightful nor as fun. He became both a mentor and a friend over the past three years and I would like to thank him for introducing me to the world of speleothems, persuading me to join for the expedition to Siberia and countless other opportunities and inspiring ideas. I also owe gratitude to him and Dr. Ola Kwiecien for inviting me to the seasonality work shop in Bochum when I just started with my thesis. I would not have met so many great new friends and colleagues if it were not for you!

Meeting new people (or, as the scientists call it, ‘networking’) and keeping in touch was generally rather difficult in these troubled pandemic years. Thus, I am deeply grateful for all those regular (semi-scientific) video calls that truly were silver linings in the pandemic routine. In this context, I would like to thank Dr. Annabel Wolf, Dr. Cinthya Nava-Fernandez and Vanessa Skiba for the fun and insightful, sometimes even paper-related, discussions. Another thank you goes to my fellow Duisburger physicists, Dr. Tim Vranken, Henrik Bette and Lukas Martinez, for the many virtual cups of coffee we shared. Here, I undoubtedly owe a special thanks to Tim, since if it were not for you teaming up with me in our studies, I would probably still be stuck solving obscure analytical math exercises today instead of submitting this thesis.

Luckily, there were even some terrific people I met along the way outside the virtual world. I would like to thank Dr. Abhirup Banerjee, both a lab mate and a friend, for countless intriguing and fun conversations. Many thanks to my office neighbour Shraddha Gupta for always helping out with her great expertise – be it complex network or paperwork-related – and many witty in-between-doors chats. At a time when the offices and hallways of PIK felt particularly empty and inanimate, Vanessa Skiba suddenly showed up and somehow made working a lot of fun again! Thank you very much for the engaging scientific discussions and being the outspoken and fun colleague and friend you are.

Visiting different fascinating places should be a central part of anyone’s PhD experience. I was blessed with some opportunities to do so, thanks to the people who invited me. I would like to thank Prof. Alexander Feigin for welcoming me in his research group in Nizhny Novgorod for two very enjoyable visits. These stays would not have been as insightful and enriching if I had not met Dr. Dmitry Mukhin, Dr. Evgeny Loskutov, Dr. Andrey Gavrillov and Aleksei Seleznev. Thank you for your hospitality, scientific discussions and shared beers. The field trip to Botovskaya cave in Siberia was truly a highlight of my doctoral work. However, it was the *мощность* of Dr. Stuart Umbo, Jade Robinson and Julia Homann that made this experience so special. Thank you for flipping those logs with me.

I am deeply indebted to the Deutsche Forschungsgesellschaft (German Research Founda-

tion) that founded my research (MA4759/11-1). I would also like to express my gratitude to the Potsdam Institute for Climate Impact Research (PIK) for providing a motivating and scientifically excellent working environment with its lush campus that has inspired many of my research ideas. Not to be forgotten are Till Hollmann, Sophia Kostial and Gabriele Pilz for always helping out with sometimes arduous administrative obstacles.

For the challenging task of proofreading this thesis, I have gathered a group of exceptionally smart people, who I would like to thank here for their helpful suggestions: a big thanks to Timo Haselhoff, Dr. Tim Vranken, Matheus Palmero, Dr. Stuart Umbo, Vanessa Skiba, Max Brüggemann and Henrik Bette.

Mentioned last, but only to give special emphasis, I would like to express my deepest gratitude to my friends and family. I will not go through all of your names, but having an old and fantastic group of friends like you I share so much with has supported me far beyond finishing this dissertation. Some of you who were exposed to an exceptional amount of my scientific gibberish should, however, not go unmentioned: thank you Timo, Tjark, Camilla and Max for listening to my countless drivels on recurrence plots. The importance of having a relaxed chat and sometimes just letting work be work must not be overlooked: thanks a lot to Malte for always being up for that. It is hard to tell if I would have made it to this point without Ines. You have accompanied and supported me on my journeys beyond measure and for that, I am deeply grateful. Even though she will not be able to read this, I would like to thank my grandmother. She showed me that curiosity is something that goes beyond age. At last, my parents are the ones who always believe in me and have never ceased to encourage me to surpass myself. Thank you.



# Contents

List of Publications . . . . .	ix
List of Acronyms . . . . .	xix
List of Symbols . . . . .	xxi
List of Figures . . . . .	xxiii
List of Tables . . . . .	xxvii
<b>I Introduction</b>	<b>1</b>
1 Motivation	2
2 Main concepts	7
3 Research objectives	14
4 Organization of thesis	15
<b>II Novel approaches in recurrence analysis</b>	<b>19</b>
<b>5 Detection of dynamical regime transitions with lacunarity as a multiscale recurrence quantification measure</b>	<b>23</b>
Tobias Braun, Vishnu R. Unni, R. I. Sujith, Norbert Marwan, Juergen Kurths	
5.1 Introduction . . . . .	24
5.2 Methodology . . . . .	25
5.2.1 Recurrence Analysis . . . . .	25
5.2.2 Recurrence Lacunarity . . . . .	27
5.3 Dynamical Transitions in Synthetic Data . . . . .	31
5.3.1 Logistic Map . . . . .	32
5.3.2 Roessler System . . . . .	33
5.3.3 Bistable Noise-Driven System . . . . .	34
5.4 Application to Thermoacoustic Instability Time Series . . . . .	36
5.4.1 Experimental Setup and Data Acquisition . . . . .	37
5.4.2 Results . . . . .	38
5.5 Conclusion . . . . .	39
<b>6 Recurrence flow measure of nonlinear dependence</b>	<b>43</b>
Tobias Braun, K. Hauke Kraemer, Norbert Marwan	
6.1 Introduction . . . . .	43
6.2 Recurrence Flow . . . . .	44
6.3 Application to Model Examples . . . . .	47
6.3.1 Nonlinear Dependence . . . . .	47
6.3.2 Uniform Time Delay Embedding . . . . .	47

6.3.3	Non-uniform Time Delay Embedding . . . . .	52
6.4	Conclusion . . . . .	53
<b>7</b>	<b>Revealing recurrent regimes of mid-latitude atmospheric variability using novel machine learning method</b>	<b>55</b>
	Dmitry Mukhin, Abdel Hannachi, Tobias Braun, Norbert Marwan	
7.1	Methods . . . . .	57
7.1.1	Kernel principal component analysis . . . . .	57
7.1.2	Recurrence network partitioning . . . . .	59
7.1.3	Studying dynamical properties of the regimes . . . . .	61
7.1.4	Method summary . . . . .	62
7.2	Data and calculation setup . . . . .	63
7.2.1	QG3 model time series . . . . .	63
7.2.2	Reanalysis data . . . . .	63
7.2.3	Distance metric, kernel and recurrence matrices . . . . .	64
7.2.4	Data weighting . . . . .	65
7.3	Results . . . . .	66
7.3.1	QG3 model time series . . . . .	66
7.3.2	Reanalysis data . . . . .	70
7.4	Summary and conclusions . . . . .	73
<b>8</b>	<b>Sampling rate-corrected analysis of irregularly sampled time series</b>	<b>77</b>
	Tobias Braun, Cinthya N. Fernandez, Deniz Eroglu, Adam Hartland, Sebastian F. M. Breitenbach, Norbert Marwan	
8.1	Introduction . . . . .	78
8.2	Methodology . . . . .	80
8.2.1	The (m)Edit-distance measure . . . . .	80
8.2.2	Recurrence analysis . . . . .	81
8.3	Segment size dependence . . . . .	82
8.4	Sampling rate constrained surrogates . . . . .	85
8.4.1	Constrained randomization . . . . .	86
8.4.2	Recurrence analysis of an AR(1)-process . . . . .	88
8.5	Real-world application: rainfall seasonality in the central Pacific . . . . .	88
8.6	Conclusion . . . . .	91
<b>III</b>	<b>Palaeoseasonality</b>	<b>95</b>
<b>9</b>	<b>What we talk about when we talk about seasonality – A transdisciplinary review</b>	<b>99</b>
	Ola Kwiecien, Tobias Braun, Camilla Francesca Brunello, Patrick Faulkner, Niklas Hausmann, Gerd Helle, Julie A. Hoggarth, Monica Ionita, Chris Jazwa, Saige Kelmelis, Norbert Marwan, Cinthya Nava-Fernandez, Carole Nehme, Thomas Opel, Jessica L. Oster, Aurel Perşoiu, Cameron Petrie, Keith Prufer, Saija M. Saarni, Annabel Wolf, Sebastian F.M. Breitenbach	
9.1	Introduction . . . . .	100
9.1.1	What we talk about when we talk about seasonality? . . . . .	100
9.2	Numerical tools for extracting seasonality changes from palaeoenvironmental time series . . . . .	108
9.2.1	Statistical tools . . . . .	111
9.2.2	Spectral analysis . . . . .	116



9.2.3	Nonlinear time series analysis . . . . .	117
9.2.4	Methodological challenges and strategies . . . . .	119
9.3	Summary and outlook . . . . .	120
9.3.1	Compositional make-up of climate seasonality . . . . .	120
9.3.2	Relevance of trans- and multidisciplinary approaches . . . . .	121
9.3.3	Proposed framework . . . . .	121
<b>10</b>	<b>Mid-Holocene rainfall changes in the southwestern Pacific</b>	<b>123</b>
	Cinthya Nava-Fernandez, Tobias Braun, Bethany Fox, Adam Hartland, Ola Kwiecien, Chelsea L. Pederson, Sebastian Hoepker, Stefano Bernasconi, Madalina Jaggi, John Hellstrom, Fernando Gázquez, Amanda French, Norbert Marwan, Adrian Immenhauser, Sebastian F. M. Breitenbach	
10.1	Introduction . . . . .	124
10.2	Geographic and climatic setting . . . . .	125
10.3	Material and Methods . . . . .	126
10.3.1	Stalagmite C132 . . . . .	126
10.3.2	Sampling for geochemical analyses . . . . .	127
10.3.3	U-Th dating . . . . .	127
10.3.4	Greyscale analysis . . . . .	127
10.3.5	Age-depth modelling . . . . .	127
10.3.6	Speleothem oxygen and carbon isotope analyses . . . . .	127
10.3.7	Isotope analysis of rain and dripwater . . . . .	128
10.3.8	Trace element analysis . . . . .	128
10.4	Results . . . . .	129
10.4.1	U-Th dating and age modelling . . . . .	129
10.4.2	Greyscale record . . . . .	129
10.4.3	Oxygen and carbon isotopes record . . . . .	130
10.4.4	Trace elements records . . . . .	130
10.5	Statistical analysis . . . . .	132
10.5.1	Principal component analysis (PCA) . . . . .	132
10.5.2	Seasonality determination . . . . .	134
10.5.3	Spectral analysis . . . . .	134
10.5.4	Recurrence analysis . . . . .	135
10.6	Discussion . . . . .	136
10.6.1	Interpretation of environmental proxies . . . . .	136
10.6.2	Climatic interpretation of the proxy time series . . . . .	138
10.6.3	Climatic interpretation of the proxy time series . . . . .	138
10.7	Conclusion . . . . .	141
<b>11</b>	<b>Decline in seasonal predictability potentially destabilized Classic Maya societies</b>	<b>143</b>
	Tobias Braun, Sebastian F. M. Breitenbach, Vanessa Skiba, Fanziska Lechleitner, Erin Ray, Lisa M. Baldini, Victor J. Polyak, James U. L. Baldini, Douglas J. Kennett, Keith M. Prufer, Norbert Marwan	
11.1	Introduction . . . . .	144
11.2	Results . . . . .	146
11.2.1	Background climate and seasonal cycle . . . . .	146
11.2.2	Seasonal rainfall predictability . . . . .	147
11.2.3	Classic Collapse and rainfall seasonality . . . . .	147
11.2.4	Multidecadal rainfall variability, ITCZ dynamics and the tropical North Atlantic . . . . .	150

11.3 Discussion . . . . .	154
<b>IV Discussion</b>	<b>159</b>
12 Conclusion	161
13 Synthesis	164
14 Outlook	168
<b>Appendix</b>	<b>173</b>
A Code implementations	175
B Supplementary material for Chapter 7: Recurrence flow measure of non-linear dependence	177
C Supplementary material for Chapter 6: Revealing recurrent regimes of mid-latitude atmospheric variability using novel machine learning method	179
D Supplementary material for Chapter 11: Sampling rate-corrected analysis of irregularly sampled time series	185
E Supplementary material for Chapter 10: Mid-Holocene rainfall changes in the southwestern Pacific	191
F Supplementary material for Chapter 12: Decline in seasonal predictability as potential trigger of Terminal Classic Maya Collapse	197
<b>Bibliography</b>	<b>211</b>
References . . . . .	213

## List of Acronyms

<b>ACF</b>	autocorrelation function
<b>AO</b>	<b>A</b> rctic <b>o</b> scillation
<b>AR(1)</b>	autoregressive process of first order
<b>BP</b>	before <b>p</b> resent
<b>CE</b>	<b>C</b> ommon <b>E</b> ra
<b>CWS</b>	continuous <b>w</b> avelet spectrum
<b>COPRA</b>	<b>C</b> Onstructing <b>P</b> roxy <b>R</b> ecords from <b>A</b> ge models
<b>CRP</b>	<b>C</b> ross- <b>R</b> ecurrence <b>P</b> lot
<b>DLE</b>	<b>d</b> iagonal line <b>a</b> rtifacts
<b>ENSO</b>	<b>E</b> l Niño- <b>S</b> outhern <b>O</b> scillation
<b>EOF</b>	empirical orthogonal function
<b>FNN</b>	false <b>n</b> earest <b>n</b> eighbours
<b>HGT</b>	geopotential height
<b>IS</b>	<b>I</b> nitial <b>S</b> eries
<b>ITCZ</b>	<b>I</b> ntertropical <b>C</b> onvergence <b>Z</b> one
<b>JRRF</b>	joint recurrence rate fraction (accordance between two RPs)
<b>KDE</b>	<b>K</b> ernel <b>D</b> ensity <b>E</b> stimate
<b>LFV</b>	low frequency <b>v</b> ariability
<b>LIA</b>	<b>L</b> ittle <b>I</b> ce <b>A</b> ge
<b>LS</b>	<b>L</b> omb <b>S</b> cargle
<b>MHD</b>	<b>M</b> aya <b>H</b> ieroglyphic <b>D</b> atabase
<b>MC</b>	<b>M</b> onte <b>C</b> arlo
<b>MCR</b>	<b>m</b> ost central realization
<b>MI</b>	<b>m</b> utual information
<b>(m)edit</b>	<b>m</b> odified edit distance measure
<b>NAO</b>	<b>N</b> orth <b>A</b> tantic <b>o</b> scillation
<b>NUTDE</b>	<b>n</b> on- <b>u</b> niform <b>t</b> ime <b>d</b> elay <b>e</b> mbedding
<b>NTSA</b>	<b>n</b> onlinear <b>t</b> ime series <b>a</b> nalysis
<b>PCA</b>	<b>p</b> rincipal component <b>a</b> nalysis
<b>PC</b>	<b>p</b> rincipal component
<b>PCP</b>	<b>p</b> rior carbonate <b>p</b> recipitation
<b>PDF</b>	<b>p</b> robability <b>d</b> ensity function
<b>QG3</b>	three-level <b>Q</b> <b>G</b> atmospheric model
<b>RA</b>	<b>R</b> ecurrence <b>A</b> nalysis
<b>RL</b>	<b>R</b> ecurrence <b>L</b> acunarity
<b>RMSE</b>	root- <b>m</b> ean-square <b>e</b> rrors
<b>RP</b>	recurrence <b>p</b> lot
<b>RQA</b>	recurrence <b>q</b> uantification <b>a</b> nalysis
<b>SFA</b>	<b>s</b> tream <b>f</b> unction <b>a</b> nomalies
<b>SNR</b>	<b>S</b> ignal to <b>N</b> oise <b>R</b> atio
<b>SRC</b>	<b>s</b> ampling-rate <b>c</b> onstrained
<b>SSA</b>	<b>S</b> ingular <b>S</b> pectrum <b>A</b> analysis
<b>SST</b>	<b>s</b> ea surface <b>t</b> emperature
<b>TC</b>	<b>T</b> ropical <b>C</b> yclone

**TCC** . . . . . **T**erminal **C**lassic **C**ollapse  
**TDE** . . . . . **t**ime-**d**elay **e**mbedding  
**TSA** . . . . . **t**ime **s**eries **a**nalysis  
**UTDE** . . . . . **u**niform **t**ime **d**elay **e**mbedding  
**U/Th** . . . . . ratio between **t**horium-230 and its radioactive parent **u**ranium-234, used  
for dating

## List of Symbols

$\alpha$	significance level, <i>or</i> in the context of power laws, the scaling exponent
$\gamma$	threshold for binarization of kernel matrix
$\Gamma$	skewness of a distribution
$D$	(metric) distance
$d$	dimension
$\delta^{13}\text{C}$	isotopic signature, ratio between stable isotopes $^{13}\text{C}$ and $^{12}\text{C}$ , reported in parts per thousand [‰]
$\delta^{18}\text{O}$	isotopic signature, ratio between stable isotopes $^{18}\text{O}$ and $^{16}\text{O}$ , reported in parts per thousand [‰]
$\Delta, \Delta t$	sampling interval
DET	recurrence quantification measure: determinism
$\varepsilon$	vicinity threshold (used to generate a recurrence plot from a distance matrix)
$\langle \varepsilon^* \rangle(\tau)$	continuity statistic
$\zeta$	delay variable for delay differential ENSO model
$\eta(t, \sigma), \xi(t)$	white noise process
$n$	length of time series (as the number of samples)
$\theta$	recurrence flow measure of redundancy
$\Theta$	Heaviside function, or in the context of the sampling interval distribution, a scale parameter
$\Theta$	diagonal matrix containing eigenvalues of a decomposed matrix
$\mathbf{K}$	kernel matrix
$\kappa$	order parameter in delay differential ENSO model
$l_{\min}$	minimum (diagonal/vertical) line length
LAM	recurrence quantification measure: laminarity
$\lambda$	Lyapunov exponent, or in the context of irregular sampling, the sampling rate
$\lambda$	a weighting matrix
$\Lambda$	recurrence lacunarity, or in the context of the edit distance, a cost parameter
$m$	embedding dimension
$P(X)$	probability distribution of a random variable $X$
$\varphi$	high-dimensional multivariate mapping between original state space and a feature space
$\phi_{i,j}$	recurrence flow matrix
$\phi$	equivalence ratio
$\Phi$	recurrence flow
$Q$	Modularity of a network
$R_{i,j}$	recurrence matrix
$\rho$	probability density function
$\mathcal{S}$	time series segment
$\sigma$	standard deviation, or in the context of noise contamination, noise strength
$t$	time
$T$	length of a time period, e.g., covered by a time series
$T_{\text{pred}}$	seasonal predictability ( <i>not</i> corrected for sampling rate dependence)
$\tau$	time delay, or in the context of the modified edit distance, a location parameter of the logistic function
$\tau_{\text{pred}}$	seasonal predictability (corrected for sampling rate dependence)

$\vec{v}$	. . . . .	embedding vector
$w$	. . . . .	box (or window) size
$\mathcal{X}$	. . . . .	dynamical regime
$\omega$	. . . . .	frequency, or in the context of SRC-surrogate technique, $\beta$ -distributed weights

# List of Figures

1.1	Schematic overview of the links between observational data from complex systems, the theory of dynamical systems and nonlinear time series analysis. . . .	3
2.1	A sketch for the definition of recurrence plots. . . . .	8
2.2	A sketch of textures that resemble some degree of self-similarity. . . . .	9
2.3	Schematic illustration of alternative definitions of recurrences relevant to this dissertation. . . . .	10
2.4	Schematic illustration of the reconstruction problem in Palaeoclimatology. . .	12
4.1	Organization of this thesis. . . . .	15
5.1	Recurrence plots for time series of different deterministic and stochastic systems.	29
5.2	Recurrence lacunarity curves $\Lambda(w)$ in double-logarithmic plot. . . . .	30
5.3	Schematic illustration of the relation between box-counting on RPs and dynamics in phase space. . . . .	30
5.4	Bifurcation diagram of Logistic Map and corresponding RL curves. . . . .	32
5.5	Robustness of RL to varying noise intensity and time series length for the logistic map. . . . .	33
5.6	Bifurcations of the Roessler System and and corresponding RL curves. . . . .	34
5.7	Regime shift detection for bistable noise-driven system with RL. . . . .	36
5.8	Schematic illustration of the combustion chamber employed in the experimental setup. . . . .	37
5.9	Application of RL to acoustic pressure fluctuation time series from a thermoacoustic combustor. . . . .	40
6.1	Recurrence flow for a noisy sinusoidal. . . . .	46
6.2	Detection of lagged, nonlinear dependence between nonlinearly coupled sinusoidals. . . . .	48
6.3	Uniform delay selection for numerical insolation model. . . . .	50
6.4	Sensitivity of recurrence flow against measurement noise, compared to other dependence measures. . . . .	51
6.5	Non-uniform delay selection for delay-differential ENSO model with periodic dynamics. . . . .	53
6.6	Non-uniform delay selection for delay-differential ENSO model with irregular oscillations. . . . .	54
7.1	Schematic representation of the proposed procedure. . . . .	63
7.2	Representation of the distance defined by Eq. 7.8. . . . .	64
7.3	Modularity increment after first division of recurrence network into two communities vs. the threshold $\gamma$ . . . . .	65
7.4	Dependence of the weight given by Eq. (7.9) on latitude. . . . .	66
7.5	Regimes of the QG3 model behavior in the space of the leading two KPCs. . .	67

7.6	Composite patterns of the QG3 model SFA corresponding to the obtained regimes. . . . .	68
7.7	Recurrence plots of atmospheric patterns obtained from the QG3 model data for the three different time series. . . . .	69
7.8	Results of recurrence quantification analysis for the atmospheric regimes obtained in the QG3 model data set for one of the three time series. . . . .	70
7.9	Partitioning of HGT states into atmospheric regimes. . . . .	71
7.10	Composite patterns of HGT corresponding to the obtained regimes . . . . .	72
7.11	Composite patterns of surface air temperatures (SAT) corresponding to the obtained HGT regimes. . . . .	73
7.12	Results of recurrence quantification analysis for the atmospheric regimes obtained in the reanalysis data set. . . . .	74
8.1	Schematic illustration of how irregularly sampled segments of varying lengths are transformed with the (m)Edit-distance method. . . . .	84
8.2	Cost matrices $C(N_a, N_b)$ for the transformation of segments with different lengths. . . . .	85
8.3	Schematic illustration of the constrained randomization procedure that generates SRC-surrogates for an exemplary irregularly sampled time series with non-stationary sampling rate. . . . .	87
8.4	Application of SRC-surrogate correction method to an irregularly sampled AR(1)-process with non-stationary sampling rate and linearly increasing autocorrelation time. . . . .	89
8.5	Greyscale record extracted from a high resolution scan of the surface of the stalagmite C132 from Niue Island. . . . .	90
8.6	Application of SRC-surrogate correction method to an irregularly sampled greyscale proxy-record from the central Pacific. . . . .	92
9.1	Schematic illustration of different seasonal features based on Yok-G record. . . . .	112
9.2	Schematic illustration of how seasonality can be extracted from a palaeoenvironmental archive. . . . .	119
10.1	Austral summer daily precipitation across the Pacific with the position of the South Pacific Convergence Zone and Niue Island. . . . .	126
10.2	Age-depth model of the Holocene section of stalagmite C132. . . . .	129
10.3	Proxy time series obtained from stalagmite C132. . . . .	131
10.4	Detailed view of a 10 mm section of stalagmite C132 with proxy records superimposed on the stalagmite image. . . . .	132
10.5	Results of the principal component analyses for stalagmite C132. . . . .	134
10.6	Wavelet spectral analysis of C132 greyscale and seasonality records. . . . .	135
10.7	Analysis of different signals encoded in proxy records from C132, as well as seasonal and ENSO variability and seasonal predictability. . . . .	139
11.1	Long-term variability of YOK-G $\delta^{13}\text{C}$ record and indications of annual extreme hydroclimate conditions, along with regional drought events inferred from other regional records. . . . .	148
11.2	Seasonal predictability of YOK-G $\delta^{13}\text{C}$ record and archaeological indicators of population size in the Maya lowlands. . . . .	150
11.3	Relationship between long-term dry/wet states in background hydroclimate and seasonal predictability $\tau_{\text{pred}}$ . . . . .	152



11.4	Summer SST reconstruction from the Cariaco Basin, local rainfall coherency index (YOK-G) and deviations of seasonal predictability $\tau_{\text{pred}}$ from its long-term mean. . . . .	153
12.1	Overview of how the presented works contribute to answering the overarching research questions. . . . .	163
C.1	Analysis of time series of the three-well model based on the simple Euclidean distance between state vectors. . . . .	180
C.2	The same analysis as in Fig. C.1, but based on Euclidean distance between normalized vectors defined by Eq. 7.8. . . . .	180
C.3	Comparison of results of recurrence quantification analysis for the atmospheric regimes obtained in the QG3 model data set between the three different time series. . . . .	181
C.4	Time series of the leading three KPCs of the reanalysis data. . . . .	182
C.5	Recurrence plot of atmospheric patterns obtained from the reanalysis data. . . . .	183
D.1	Subcosts for adding/deleting and shifting operations for exponentially distributed sampling intervals. . . . .	188
D.2	Zoomed section of synthetic AR(1)-time series (black) and five exemplar SRC-surrogate realizations (gray). . . . .	189
D.3	Zoomed section of grayscale anomaly time series (black) and five exemplar SRC-surrogate realizations (gray). . . . .	190
E.1	Stalagmite C132 oxygen and carbon isotope ratios correlate in both, high and low resolution data sets. . . . .	191
E.2	Results of principal component analyses of stalagmite C132. . . . .	192
E.3	Seasonality derived from the difference between the wet and dry season averages of stalagmite C132 greyscale time series. . . . .	192
E.4	Wavelet analysis of the principal components extracted from PCA-2 of the annually resolved C132 proxy records. . . . .	193
E.5	Two exemplary recurrence plots of the C132 greyscale time series that yield distinct determinism parameter DET values for the respective time periods. . . . .	194
E.6	Relationship between $\delta^{18}\text{O}$ and $\delta\text{D}$ of Niue rain and dripwater collected in February 2020. . . . .	195
F.1	Evolution of $2\sigma$ age uncertainty after application of COPRA age model (50 U/Th-dated depths). . . . .	197
F.2	Long-term variability of YOK-G proxy records. . . . .	198
F.3	Detrending of YOK-G age model medians and most central realizations using Singular Spectrum analysis (SSA). . . . .	199
F.4	Most central realizations of YOK-G $\delta^{13}\text{C}$ and $\delta^{18}\text{O}$ for the full covered time period (after detrending). . . . .	200
F.5	Sliding window correlation between YOK-G stable isotope seasonal variations. . . . .	201
F.6	Sliding window correlation between YOK-G stable isotope multidecadal variations. . . . .	201
F.7	Optimization of sampling interval $\Delta t$ for linear interpolation, used in YOK-G wavelet analysis. . . . .	203
F.8	Time-frequency analysis of YOK-G stable isotope records. . . . .	204
F.9	Continuous wavelet spectra for most central realizations of YOK-G $\delta^{13}\text{C}$ age model ensembles. . . . .	205

F.10	Continuous wavelet spectra for most central realizations of YOK-G $\delta^{18}\text{O}$ age model ensembles. . . . .	205
F.11	Illustration of aliasing effect that occurs when sampling resolution falls below the Nyquist frequency of 2 samples/year based on a synthetic sinusoidal model.	205
F.12	Exemplary recurrence plots from the sliding window recurrence analysis of YOK-G proxy records. . . . .	207
F.13	Predictability of sub-annual rainfall distribution, given by relative mean predictability times $\tau_{\text{pred}}$ of 20 detrended YOK-G proxy realizations for each stable isotope record. . . . .	208

# List of Tables

5.1	Overview of studied systems for detecting dynamical regime shifts. . . . .	31
7.1	Parameters of the communities extracted from three analyzed time series of the QG3 model. . . . .	70
7.2	The same as in Table 7.1, but for the regimes obtained from the reanalysis HGT data set. . . . .	71
10.1	Results of the $^{230}\text{Th}/\text{U}$ dating. . . . .	128
10.2	Descriptive statistics for the trace element ratios determined along the growth axis of stalagmite C132. . . . .	130
10.3	Resolution and time span of the C132 proxy records. . . . .	133
10.4	PCA groups and time span for stalagmite C132. . . . .	133



---

# Introduction

# 1 | Motivation

The so called ‘collapse’ of the Classic Maya civilization around 1200 years ago is among the most popular and intensively researched societal responses to changing climate conditions. It is thus an example for what can be termed the study of the ‘history of climate and society’ [5], a subject that is expected to have significant implications for the rapid transformation processes we experience today due to anthropogenic climate change [6]. To gain an understanding of how a society adapts (or fails to adapt) to its changing environment, we must accept the interwoven nature of these systems. Neither society nor climate are closed systems. Neither of them, by itself, offers reliable predictability of its dynamics by knowing only the dynamics of its subcomponents. For the analysis of such complex systems, we have to surpass the confined perspective offered by reductionist, Newtonian physics and instead accept the paradigm of complexity science: most real-world systems consist of an astounding variety of components that interact via nonlinear feedbacks and respond sensitively to perturbations that invoke abrupt shifts between fundamentally different dynamical states. Nonlinear time series analysis (NTSA) provides tools to transfer this paradigm into the analysis of empirical data, aiding us in the study of systems as complex as a society evolving in its changing environment, such as the disintegrating Maya civilization.

Complexity science examines the universal properties that govern a broad range of systems, such as ecology [7], socio-political systems [8], stock markets [9], epidemiology [10] and climate [11]. While it has originated from many different disciplines, the study of chaos and nonlinearity represents one of its most fundamental roots. Chaos theory, by some regarded as one of the three big ideas of the 20<sup>th</sup> century [12], provides a formal description of the rich and surprising results entailed by the observation that seemingly random, disordered processes do in fact follow a complex underlying order. A chaotic system is by definition deterministic and thus in principle predictable. However, an extreme sensitivity to initial conditions and exponential growth of perturbations renders any prediction beyond a certain *Lyapunov time* infeasible. This key feature of chaotic systems leaves us unable to, e.g. reliably forecast the weather more than a few days in advance. For finite-dimensional dynamical systems, chaotic motion results from nonlinearity in its underlying mechanics, i.e. cause and response are not proportional. Nonlinearity hurts the fundamental principle of superposition, challenging our common intuition: eating your two favorite foods at the same time will unlikely result in a taste experience twice as good [13]. Embodied in the insight that ‘more is different’ [14, 15], these ‘emergent’ properties are just one of the intriguing universal findings offered by the study of complex nonlinear systems. In fact, the phenomena implied by nonlinear characteristics of a system are plentiful and motivate us to explore tools to empirically study such features in the systems surrounding us.

When we study a complex system, we usually carry out measurements in such a way that we capture as many of the system’s independent variables as is technically feasible. However, instrumental as well as financial limitations constrain this procedure and inevitably result in a lower-dimensional representation of the system (Fig. 1.1). Time series, i.e. sequences of observations ordered in time, are of finite length and rarely recorded in a controlled ensemble fashion which could in principle offer realizations of the underlying process with varying

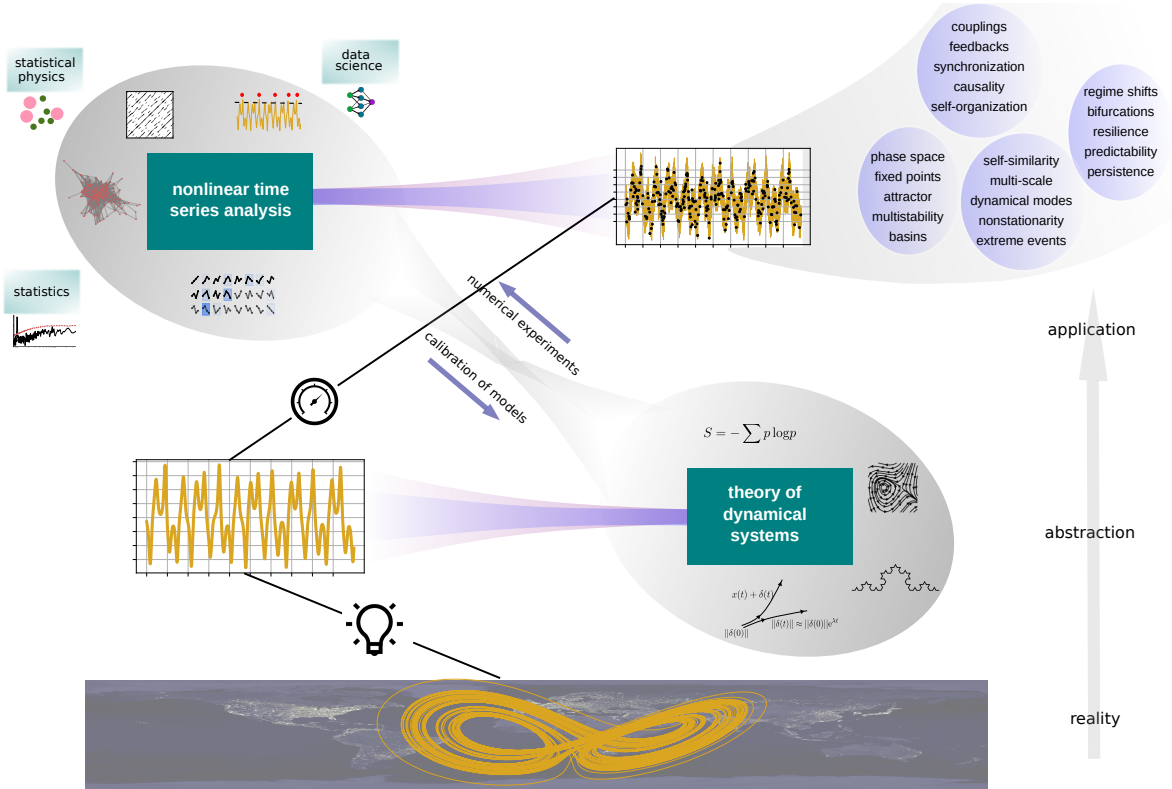


**Figure 1.1:** Schematic overview of the links between real-world complex systems, the theory of dynamical systems (abstract realm) and nonlinear time series analysis (applied realm). Many systems follow a high-dimensional state space trajectory (yellow). Since most of the observations we make are limited, the theory of dynamical systems tries to understand both the topology and stability of high-dimensional systems as well as their lower-dimensional projections based on paradigmatic models and mathematical concepts. Measurements introduce additional problems, e.g. noise, irregularly spaced measurements *et cetera*. Nonlinear time series analysis, supported by methods from statistics, statistical physics and newer disciplines like data science, attempts to provide tools for the study of empirical nonlinear time series, based on the concepts developed in the theory of dynamical systems. This enables us to study a plethora of nonlinear properties of complex systems (blue bubbles).

initial and boundary conditions. The theory of dynamical systems enables us to transfer the properties observed from recorded time series into an abstract representation of the system, giving rise to paradigmatic models and mathematical descriptions of the idealized dynamics of the system. We can use these models and concepts to conduct numerical experiments that evaluate the usefulness and validity of time series analysis (TSA) methods. Nonlinear time series analysis transfers ideas and insights from the abstract domain into practise. It requires a process of creative and parsimonious conceptualization to propose effective, problem-oriented and numerically tractable tools that uncover the most significant features of a nonlinear system (blue bubbles in Fig. 1.1). Modifications of existing methods tailor them to the specific time series at hand (see below). In this respect, Occam’s razor deprecates excessiveness in the process of conceptualization, suggesting method design to be as complex as necessary, yet, as simple as possible.

A particularly versatile framework in the analysis of nonlinear time series is recurrence analysis (RA). Systems that lose some fraction of their energy to their environment (‘dissipative systems’) tend to recur to states they have visited before after sufficiently long time. This

observation has been formalized by Poincaré for certain dynamical systems in 1890 [16] and is surprisingly compatible with our every day notion of recurrence. We as individuals comfort ourselves with routines that encompass the recurrence of, e.g. social interactions (meeting friends or colleagues) or rituals (celebrating anniversaries or attending music festivals) and, in turn, constitute patterns of recurrence for the larger complex systems we are embedded in (political elections, harvest of crops, fashion trends). Recurrence even affects our conception of aesthetics [17] and has inspired culturally distant schools of philosophy in their metaphysics [18]. For the systematic study of recurrences in nonlinear systems, the recurrence plot (RP) was first introduced by Eckman in 1987 [19]. An RP encodes recurrences between pairwise states of a system in a binary matrix: 1s denote states that have returned *close* to a state the system has visited before, 0s indicate the absence of recurrence. Any one- or high-dimensional time series representation of a system can be transformed into an RP without presuming any intricate mathematical conditions. The notion of *closeness* however requires a thoughtful idea of how it could be best defined for the individual system under study. RA further offers various ways to quantify the recurrence patterns encoded in an RP by means of recurrence quantification analysis (RQA) [20]. Over the course of the past 35 years, RA has pervaded the whole range of systems studied in complexity science, comprising studies in the Life Sciences [21] and Neuroscience [22] as well as applications in Finance [23] and Engineering [1] to the Earth Sciences [20], including Palaeoclimatology [24]. It provides methods to study a plethora of problems, including couplings between variables, classifying systems with respect to their dynamical complexity, detecting transitions and predicting a system’s future dynamics. Nevertheless, many questions remain unanswered as of now. They motivate future investigations, such as those I pursue in this thesis. In particular, three key properties of nonlinear observational time series that are within the scope of RA are of high relevance here: the self-similarity and multi-scale properties of a system, the analysis of couplings and the detection of regime shifts.

**Self-similarity** is a ubiquitous property found in many natural systems. Originally introduced by Benoît Mandelbrot in his groundbreaking work ‘The fractal geometry of nature’ [25], self-similarity has been defined based on mathematical objects that show similar patterns under different degrees of magnification, so called ‘fractals’. Since the scale-independence property of fractals results in non-integer dimensionality, they might be mistaken for a rather obscure, abstract concept. However, self-similar patterns can not only be found in nature (leaves, romanescos, coastlines) but have also attracted great interest in the study of complex systems, e.g. in the Geosciences [26]. This success derives from the fact that the complexity of many geoscientific systems can only be adequately captured if the multitude of their interacting spatio-temporal scales is considered.

**Couplings** generally comprise any sort of interaction or feedback between the components of a complex system, including time-delayed couplings to itself (‘serial dependence’). As illustrated above, couplings can entail counter-intuitive behaviour at the macroscopic level and give rise to complex behaviour of systems that are made up of supposedly simple microscopic entities, e.g. interacting agents that follow a simple set of rules. In the Earth Sciences, correlations between spatially displaced measurements of climate or environmental variables are of particular importance. This is complicated by the nonlinearity and multi-scale nature of many coupled systems we encounter in nature – for example, atmospheric pressure variations at locations thousands kilometres distant from each other are linked by *teleconnection patterns* and result in synchronized extreme weather events that can threaten the livelihood of millions of people around the globe.

**Regime shifts** (or critical transitions) epitomize a notoriously challenging characteristic of nonlinear systems as we currently learn in our ‘experiments’ with the natural limitations of the Earth system. Several components of the global climate system are believed to show



abrupt and interlinked ‘tipping’ behaviour [27] if certain threshold values of the climate’s order parameters are crossed, e.g. permafrost thawing or ‘Savannification’ of the Amazon rainforest [28]. Generally, regime shifts bear on the notion of bifurcations in dynamical systems, i.e. a change in stability of local or global attracting sets in the system’s state space. For the identification of dynamical transitions from time series data, recent research has focused on how different quantifications of a system’s predictability, resilience or stability can be used with a focus on detecting abrupt regime shifts and uncovering precursors.

A methodology that captures any of these specific nonlinear features may still not capture all the peculiarities and challenges associated with a particular observational time series (Fig. 1.1). Returning to the example raised at the beginning, we would need to tailor our method to the particular properties of a climate reconstruction that covers the period of the Maya civilization’s cultural disintegration and link it to demographic reconstructions. In fact, we would have to familiarize ourselves with the ways in which climate signals are recorded over the course of hundreds to thousands of years, that is, we need to study Palaeoclimatology. For most of the applications in this dissertation, the latter is the challenge we are faced with. The study of palaeoclimate records is based on different natural archives (for example, tree rings, ice cores, lake sediments, speleothems) that do not directly capture a climatological signal but provide ‘proxies’. A proxy mixes the desired signal (e.g. temperature) with other environmental (e.g. salinity) and/or archive-specific signals (e.g. smoothing in a sediment core due to bioturbation). For instance, speleothems are an archive of seasonal to orbital scale climate that are formed by mineral deposits accumulated in a cave. This accumulation process relies on infiltrating water (for instance, rainfall, snow, meltwater) that is transported along potentially complicated flow paths in the ground layers above the cave. The decay process of uranium-234, which is incorporated in these deposits, into thorium-230 allows for precise dating (U/Th-dating), far back into the Earth’s climates hundreds of thousands years ago. The incorporation of stable carbon and oxygen isotopes as well as trace elements in the stalagmite’s mineral layers act as the proxies, reflecting valuable information on climate parameters, such as rainfall. However, none of these geochemical processes are easily understood. While U/Th-dating indeed yields highly precise dates for measured isotopic concentrations, dating errors are not negligible and may alter or hinder interpretations of proxy time series variability. These uncertainties further impede direct application of common time series techniques as time intervals between consecutive measurements vary, resulting in irregular sampling. The time scales that are most informative for processes that shape and determine the existence of societies (e.g. the Maya) require seasonal to multi-annual resolution of records. Only at these scales can we really learn how potential changes may have affected human-environmental systems such as agriculture. Even if our method is adapted to consider these uncertainties, we need to tread carefully when interpreting the mixed signals encoded in proxy records as it is hard to estimate and disentangle the relative contributions of the desired and the undesired signals. Nonlinear time series analysis has established itself as a versatile framework into which these complexities can be integrated effectively [29].

Faced with these intriguing challenges, the study of the dynamical properties mentioned above, their links with recurrence analysis and their empirical detection raise a multitude of research questions that are as exciting as they are diverse, some of which are:

- How can we use RA to characterize multi-scale properties, quantify nonlinear couplings and detect regime shifts in nonlinear time series? How can we extend RA to deepen our understanding of these properties for the study of complex systems?
- Can we modify the tools provided by RA as well as other time series analysis techniques

such that they account for data-specific limitations, e.g. uncertainties and sampling-related issues?

- Combining RA with other suitable time series analysis techniques, can we carry out feasible analyses of past climates, in particular with respect to if and how seasonal variability has changed over the past hundreds to tens of thousands of years in different regional climates?

These questions guide the thematically broad research spectrum I am collating in this dissertation. A methodological inspection of the concepts (Chapter 2) that I use will enable us to refine these general questions (Chapter 3) and provide an overview of the research I have conducted (Chapter 4).

## 2 | Main concepts

### Recurrence analysis

Recurrence analysis provides a versatile framework for studying many central problems of nonlinear time series analysis<sup>1</sup> [20]. Recurrences between pairs of states  $\vec{x}_i$ ,  $\vec{x}_j$  are recorded in a recurrence plot:

$$R_{ij} = \Theta(\varepsilon - D(\vec{x}_i - \vec{x}_j)) = \begin{cases} 1 & \text{if } D(\vec{x}_i, \vec{x}_j) \leq \varepsilon \\ 0 & \text{if } D(\vec{x}_i, \vec{x}_j) > \varepsilon. \end{cases} \quad (2.1)$$

Any pair of states  $\vec{x}_i$ ,  $\vec{x}_j$  at times  $i$ ,  $j$  generates a 1 in the RP if they are *close* by means of their dissimilarity  $D(\vec{x}_i, \vec{x}_j)$  and the vicinity threshold  $\varepsilon$  (Fig. 2.1A). The notion of *closeness* between states is problem-dependent. In many applications, the states  $\vec{x}_i$  are time series of  $d$ -dimensional vectors,  $\vec{x}_i = \vec{x}(t_i)$ ,  $i = 1, \dots, N$ . We then measure dissimilarity by means of a standard metric distance measure, e.g. the Euclidean norm  $D(\vec{x}_i, \vec{x}_j) = \|\vec{x}_i - \vec{x}_j\|$ . In other applications, e.g. where the sequence of observed states is irregularly sampled, we need to define a different suitable metric distance. As we are interested in the similarity between all states of a system, we obtain a (symmetric) distance matrix  $\mathbf{D} = (D_{i,j})$ . We are now able to define which states are *close* by means of the vicinity threshold  $\varepsilon$ , the only parameter that needs to be selected for the computation of an RP. Depending on the data at hand, different criteria can be used to make an informed estimate on the ‘best’ value for  $\varepsilon$ . A robust method that entails a globally fixed fraction of recurrences (e.g. a recurrence rate (RR) of 10%) in the RP is to use a quantile of the distribution of distance values ( $D_{i,j}$ ) [30]. If  $\varepsilon$  is chosen too small, informative recurrence patterns might be missed. On the other hand, large values result in a merging of structures in the RP and might blur the most significant information. The Heaviside step function  $\Theta(\cdot)$  ensures that only those states are registered as recurrences whose metric distance falls below (or is equal to) the vicinity threshold  $\varepsilon$ . In many applications, the evolution of states of a system is actually given by a  $d$ -dimensional sequence of vectors but we may only be able to obtain lower-dimensional, perhaps univariate measurements. In such cases, we can use a method called *time-delay embedding* (TDE) to reconstruct the higher-dimensional characteristics of a system that are hidden from us [31]. A reconstructed version of the system’s phase space conserves some of the topological properties of the original phase space and can be used to identify recurrences between phase space vectors.

An RP is a square, symmetric and binary matrix. It contains a rich diversity of geometric recurrence patterns that can be exploited for quantification. Most recurrence quantification measures are computed based on the statistical distribution of line structures in an RP. The presence and absence of certain patterns will depend on the dynamical properties of the studied system:

- Long, uninterrupted diagonal lines encode periodic behaviour and occur if two closeby

---

<sup>1</sup>A comprehensive literature overview of studies that use or develop RA can be found here: <http://www.recurrence-plot.tk/bibliography.php>. Software implementations are collected here: <http://www.recurrence-plot.tk/programmes.php>

segments of a time series/trajectory evolve in parallel (Fig. 2.1B). Their separation in the RP ideally corresponds to the period of the periodic signal.

- Interrupted diagonal lines indicate chaotic dynamics. The average diagonal line length can be regarded as a proxy for the mean prediction time of a system.
- Isolated recurrences suggest random, uncorrelated dynamics ('recurrence by chance').
- Vertical line (or box-like) structures represent 'laminar' states, i.e. the system remains trapped close to a certain state.
- White vertical gaps can be interpreted as recurrence times and may relate to (quasi-)periodicities.

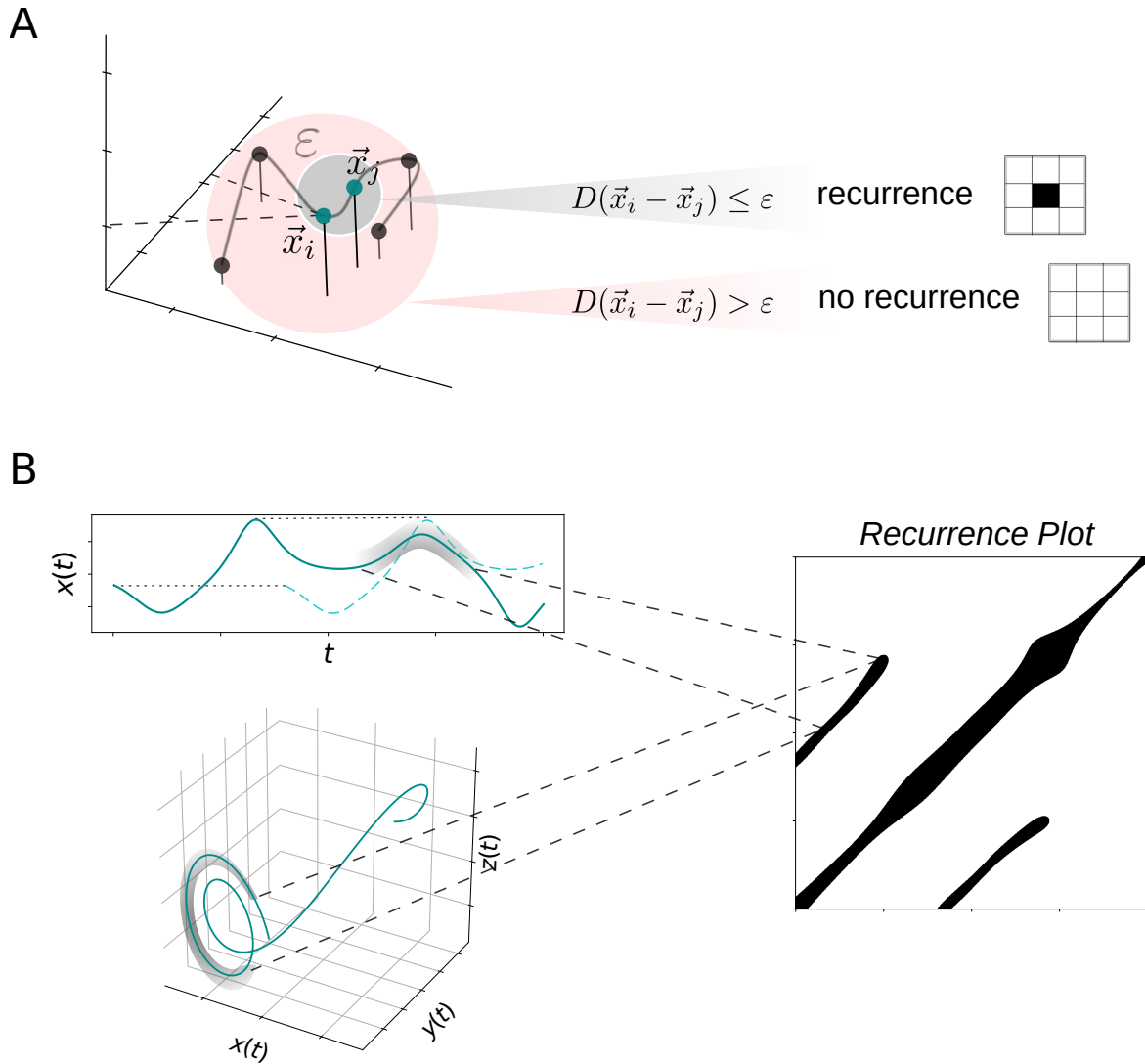


**Figure 2.1:** The sketch displays, A: the notion of a recurrence between two vectors  $\vec{x}_i$  and  $\vec{x}_j$  based on the vicinity threshold  $\epsilon$  and a distance metric  $D(\vec{x}_i, \vec{x}_j)$ , B: the emergence of diagonal lines in an RP from closely segments of a univariate time series or phase space trajectory evolving in parallel.

Diagonal line structures will be of particular importance in parts of this work as they imply a notion of predictability: as closely segments of a time series evolve in parallel, one could have in principle predicted one segment from the other. If the dynamics of a system

change significantly, this will often entail corresponding changes in the predictability of the system’s states.

Several effects can disturb recurrence patterns and entail biased estimators in RQA. For instance, perpendicular diagonal lines can arise from including an erroneous time scale or redundant information on the system’s state in the generation of an RP and an inadequate choice for  $\varepsilon$  will artificially conflate line structures.

## Self-similarity

The variability of many real-world complex systems is distributed among a broad band of time scales. With their ability to capture recurrence and prediction times, RPs are an effective method to detect and untangle scale-specific variability. More generally, patterns in nature that exhibit similar behaviour at any time scale  $s$  are usually well described by a power law  $p(s) \propto s^{-\alpha}$ . Put differently, the frequency  $p$  of how often a given scale  $s$  occurs is inversely proportional to some power  $\alpha$  of the scale. Systems for which a power law holds exhibit self-similarity [25]. While only mathematical objects called fractals (Fig. 2.2, left) exhibit perfect self-similarity, the general concept can be transferred to real textures (Fig. 2.2, center) using a box-counting procedure: we cover the texture with boxes of width  $s$  and count the number of boxes  $p$  required to fully cover the texture. By selecting a broad range of different scales  $s$  that cover several orders of magnitude, the exponent  $\alpha$  can be estimated and corresponds to the box-counting dimension, a common estimator for the fractal dimension (or Hausdorff dimension) of a texture. Interestingly,  $\alpha$  does not need to be an integer value. A fractal with  $\alpha = 1.8$  fills space more ‘roughly’ than a smooth 2-dimensional texture. If more than one suitable value of  $\alpha$  is required for a sufficient description of a texture, one usually refers to such textures as ‘multifractals’. Box-counting based statistics go beyond merely characterizing the dimensionality of patterns but for instance, also capture their scale-dependent heterogeneity (‘lacunarity’, see (P1)) and permeability (‘succolarity’, see (P2)). Generally, this can prove helpful for distinguishing between self-similar patterns of equal fractal dimension.



**Figure 2.2:** A sketch of textures that resemble some degree of self-similarity: the Koch curve, a section of the British coastline and line structures in an RP generated from a fractional Brownian Motion process (from left to right).

In practise, significant deviations from power law behaviour at some scales indicate that these scales might be of particular relevance to understand the underlying processes. Dimensionality estimators similar to the box-counting dimension can help to classify dynamically distinct complex systems, for example based on their attractors. In the analysis of climate time series (for instance, rainfall or temperature), understanding scale-dependent variability is arguably one of the most crucial challenges whereas tools like Fourier power spectra and

wavelet analysis are among the most popular methods. Even recurrence patterns can show self-similar properties (Fig. 2.2, right) which will inspire some of the methods introduced in this dissertation (see (P1) and (P2)).

## Couplings

For the detection of couplings between multiple variables, identifying the most relevant time scales is once more of great relevance: for some pairs of variables  $\mathcal{X} \leftrightarrow \mathcal{Y}$  that exert an influence on each other, the effect of variable  $\mathcal{X}$  on variable  $\mathcal{Y}$  is simultaneous. Other systems predominately exhibit delayed relationships with specific delays  $\tau_1, \dots, \tau_m$  between their  $m$  variables. A standard measure to capture such contemporaneous and delayed relationships between two time series  $x(t)$  and  $y(t)$  is the linear correlation coefficient (*Pearson's  $r$* ), given by the ratio between their covariance and their standard deviations. If the covariation between variables is, however, not limited to a linear relation,  $r$  will yield limited information and nonlinear dependence measures (e.g. mutual information) must be considered. Once more, RPs can be of great utility as they also capture nonlinear features. Cross-RPs (CRPs) are computed from a set of time series that can represent the variables of a system by regarding each time series as one time-dependent coordinate of a composite system. Relevant time delays between the variables are included here by shifting each time series against the others.

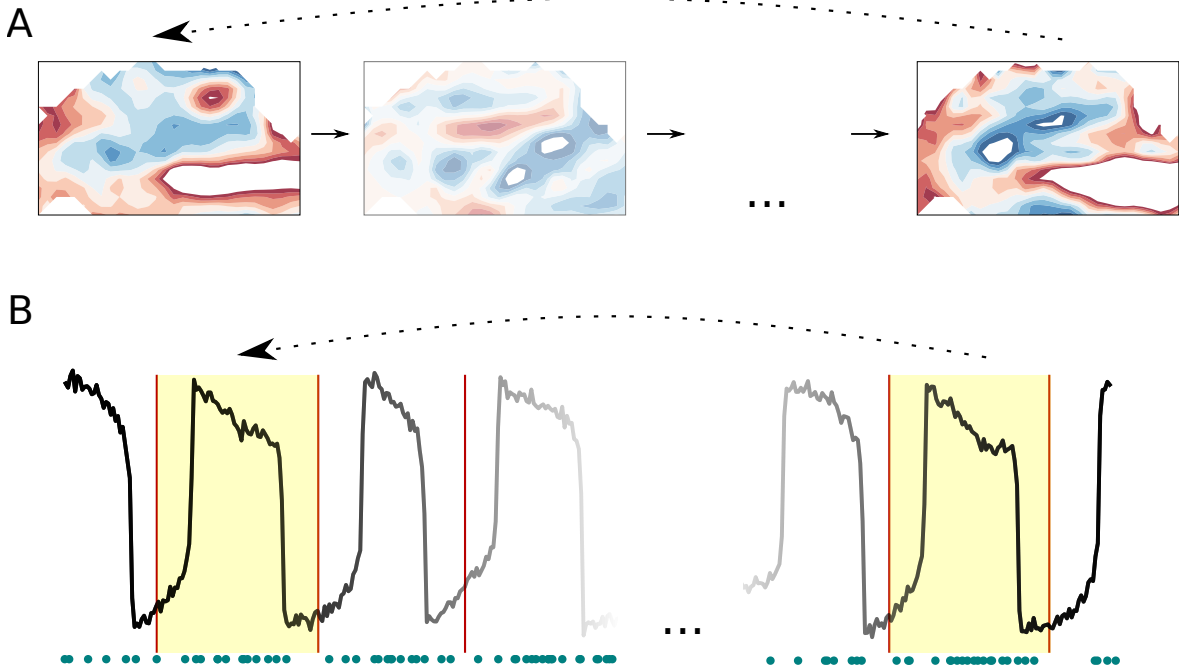


**Figure 2.3:** Schematic illustration of alternative definitions of recurrences relevant to this dissertation. A: recurrence between spatial patterns of a climate field, B: recurrence between segments of non-uniform size of an irregularly sampled cyclical time series. The dots represent a possible irregular sampling of the underlying signal (black).

We sometimes need to account for a high number of interlinked variables. In such cases, it is instructive to list all pairwise linear correlations in a correlation matrix and compute the most relevant modes of variability (in terms of explained variance) using a singular value decomposition of the correlation (or covariance) matrix. This yields a new set of variables, the principal components (PCs), and the corresponding eigenvectors (often called empirical orthogonal functions (EOFs)) that can be interpreted as the ‘loadings’ of the PCs onto the

original variables. The PCs are linear combinations of the original variables and can be regarded as a new, more informative coordinate system for the observed data. For normally distributed data, all EOFs will be uncorrelated. For spatial data, i.e. sequences of observations at different locations (for example, geopotential height or sea surface temperature), principal component analysis (PCA) can be used to inform on the most relevant spatial modes of a system. The EOFs are projected onto a map based on their geographical coordinates and give rise to often well-interpretable spatial patterns. If nonlinear relationships between the variables exist, modes will not be independent and extensions like kernel PCA (kPCA) should be employed. Often, the spatial patterns exhibited by spatially extended systems (for example, an evolving climate field like the one displayed in Fig. 2.3A), recur in time. While usually, the (univariate) recurrences of the single climate variables are studied, the recurrence of the emerging spatial patterns are not considered. For a complex system, however, we cannot expect that the recurrence properties of the sub-components will fully determine the recurrences of the emerging spatial patterns. This will motivate a novel definition of recurrence (Fig. 2.3A) discussed in (P3).

## Regime shifts

Couplings and the variability at distinct time scales can vary in time. Many parts of this work focus on detecting regime shifts in nonlinear time series, i.e. abrupt changes in the underlying system's dynamics. Regime shifts, or 'critical transitions' [32] can denote several different changes in the behaviour of a dynamical system, all of which are more or less based on the theory of bifurcations or ideas from multi-stability in chaotic systems. For instance, a time series can exhibit an abrupt shift in its amplitude or undergo transitions between regimes of different dynamical complexity, e.g. shift from a chaotic regime  $\mathcal{X}_1$  to a periodic regime  $\mathcal{X}_2$ . Irrespective of the transition's nature, the detection in practise often relies on some measure of complexity, resilience or predictability. For the detection of 'tipping points', increasing lag-1 autocorrelation and variance of a signal have recently gained popularity as precursors to record a critical slowing down (i.e. the system recurs to equilibrium more slowly) that precedes the actual transition. RA supplies a whole toolkit of measures to detect abrupt or continuous variations in a system's dynamical behaviour. In order to tell apart significant and non-significant transitions, we additionally need hypothesis tests specifically tailored to the nonlinear time series under study, deeming traditional hypothesis tests with their severe constraints insufficient. However, bootstrap procedures [33] and surrogate testing [34] can provide flexible testbeds for studying regime shifts without the above mentioned limitations. When the variability of a system is distributed among a multitude of time scales (as discussed above), transitions might only be detectable at certain time scales. This raises the need for scale-sensitive regime shift detection measures, as I will discuss in more detail in (P1).

## Methodological challenges in Palaeoclimate

Many of the described methods prove effective in the analysis of palaeoclimate proxy records [29], a goal I have pursued for most parts of this thesis. Reconstructions of past climates enable us to contextualize current climate changes but come along with a range of challenges. Here, a special focus lies on the analysis of proxy records derived from speleothems [35]. The 'reconstruction problem' results from limitations in the measurement procedure (Fig. 2.4) as well as from the complexity of cave-environmental processes that are notoriously difficult to unravel. To obtain a proxy time series with an 'error-free' time axis, we carry out two measurement procedures in concert: along the growth axis of a stalagmite, we take a uranium-series to obtain precise U/Th-dated samples, a method that is considerably more precise (and

expensive) than radiocarbon dating. Alongside these measurements, we take samples at each dated sample and many positions in between to examine ratios of stable isotopes deposited in the mineral layers of the stalagmite. Usually, rainfall feeds the karst systems above the cave and eventually forms drops that drip from the cave’s ceiling or a stalactite, growing the stalagmite in height and diameter. Here, we mostly study stable oxygen ( $\delta^{18}\text{O}$ ) and carbon ( $\delta^{13}\text{C}$ ) ratios. Drip-water  $\delta^{18}\text{O}$  in the cave predominately reflects rainfall  $\delta^{18}\text{O}$  but is also affected by a multitude of other complex processes, e.g. evaporative processes potentially far from the cave site.  $\delta^{13}\text{C}$  tracks local hydroclimate conditions that often include changes in effective infiltration above the cave and prior carbonate precipitation dynamics in the epikarst. However, additional cave-environmental processes can affect stable isotope records and need to be well investigated for each cave based on cave monitoring studies as well as comparison to other independent regional proxies and archives. To obtain a proxy time series from the U/Th dates and stable isotope ratios, the last missing piece of the puzzle is the construction of an age model: based on the U/Th-dating errors, some age models (e.g. COPRA [36]) sample different possible time axes from the error distribution in a Monte Carlo fashion. For the unknown dates of stable isotope ratios in between two U/Th dates, (linear) interpolation is used. This procedure yields an ensemble of time axis that aligns with the isotope series. Some age models now allow to transfer the dating uncertainty into uncertainty of the proxy magnitudes, finally resulting in an ensemble of proxy time series that can be used to propagate dating uncertainties.

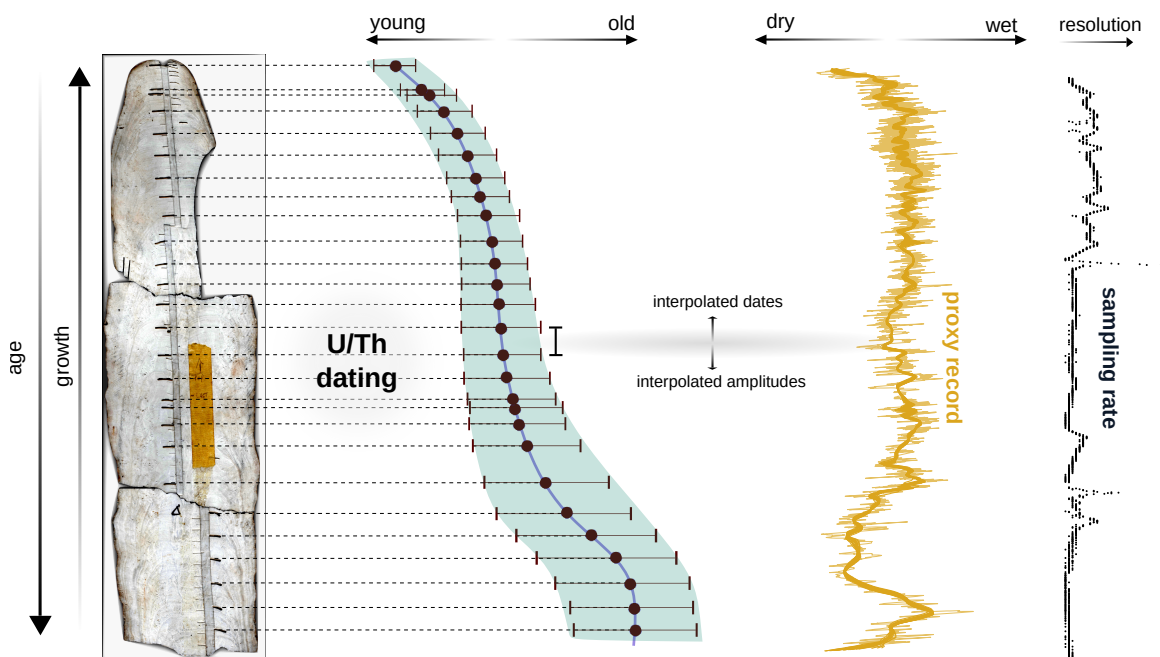


**Figure 2.4:** Schematic illustration of the reconstruction problem: a stalagmite is sampled at a limited number of depths (dashed lines). Each sample is precisely dated by evaluating U/Th concentrations, yet leaving a non-negligible dating error (shaded band/error bars). Dating errors increase with age. Construction of an age model yields a distribution of possible ages for each sample. At the same time, a high number of proxy values (e.g. stable isotope ratios, yellow) is sampled, at and in between the few dated samples. For these values, dates are the result of interpolation between available U/Th dates. The sampling rate of the resulting proxy time series generally varies, with episodes of low and high resolution (black).

For any of the above mentioned methods, application to palaeoclimate proxy records requires a propagation strategy of uncertainties. Otherwise, scale-dependent variability might be overestimated, some couplings could be detected spuriously or regime shifts could be



mislocated in time. Furthermore, the sampling procedure entails an irregularly sampled time axis, i.e. sampling intervals are not uniform (Fig. 2.4, black time series). For proxy records from stalagmites, the non-uniform sampling rate is related to the stalagmite’s growth rate and is thus rooted in a correlated, climate-related process. We have to ensure that the application of any nonlinear time series analysis tool does not entail significant biases for irregularly sampled data, both with respect to the *non-uniformity* of sampling intervals and potential drastic changes of sampling resolution arising from the *non-stationarity* of the underlying processes. If neglected, time-scale dependent variability (e.g. based on Fourier spectra) might be assigned to the wrong time scale, assessing correlations will fail due to lacking alignment of time series, and shifts in the sampling rate might be mistaken for real regime shifts.

For RA, this implies that we need to implement a different notion of dissimilarity as, e.g. the Euclidean metric fails to account for non-uniform sampling intervals and would mix time scales encoded in line structures. The edit distance measure [37] was proposed as a solution for this problem. An irregularly sampled time series is segmented into windows whereas each may cover a different number of values and two segments are found to be recurring if their *transformation cost* falls below  $\varepsilon$ . Four basic operations – shifting in time, shifting/scaling of amplitudes, deletion, adding – are defined and assigned with heuristic cost parameters. The minimum cost of transforming segment  $\mathcal{S}_A$  into segment  $\mathcal{S}_B$  is computed and represents the dissimilarity measure. For the study of Palaeoseasonality by means of RA, we will regard seasonal patterns as the segments (Fig. 2.3B). This will put additional emphasis on the *non-stationarity* problem of irregular sampling whereby we need to account for variations in the sampling rate of a proxy (P4).

## 3 | Research objectives

Based on the main concepts and methods outlined in Chapter 2, I formulate the following research questions to guide the investigations in this thesis:

- (Q1) Can we transfer concepts from the study of self-similar patterns to RA in order to define a *scale-sensitive* measure for the identification of regime shifts, exploiting multi-scale features in the recurrence patterns of a dynamical system? Can we use this measure to provide a recurrence based tool to characterize the time-frequency content of a (potentially high-dimensional) signal?
- (Q2) Are there any universal links between the self-similar properties of recurrence patterns of a signal and the self-similar properties of the signal itself, given by a time series or its phase space trajectory?
- (Q3) How could RA be used to characterize transitions between regimes of spatially-extended systems, e.g. spatial patterns in atmospheric circulation? Can we classify such regimes based on their dynamical properties as reflected by recurrence quantification measures?
- (Q4) Can we adopt tools from RA to reliably detect significant transitions in Palaeoseasonality over time periods of hundreds to thousands of years, based on palaeoclimate reconstructions from speleothems? How do these tools provide interpretable measures for specific applications, also considering societal repercussions?
- (Q5) In the context of this analysis, can we adequately account for data-specific challenges and limitations, most crucially irregular sampling and dating uncertainties? In particular, can we correct recurrence analysis for biasing effects imposed by growth rate variations of a stalagmite? Can other time series analysis methods be modified analogously?

## 4 | Organization of thesis

The formulated research questions give rise to a natural way to organize this dissertation into two parts (Fig. 4.1): the first part focuses on the development of novel and modification of existing methods in recurrence analysis (Q1-Q3). The second part deals with specific applications of recurrence based (and other) time series analysis methods to characterize Palaeoseasonality based on reconstructions of the hydroclimate at different regions and during different episodes of the Holocene (Q4 & Q5).

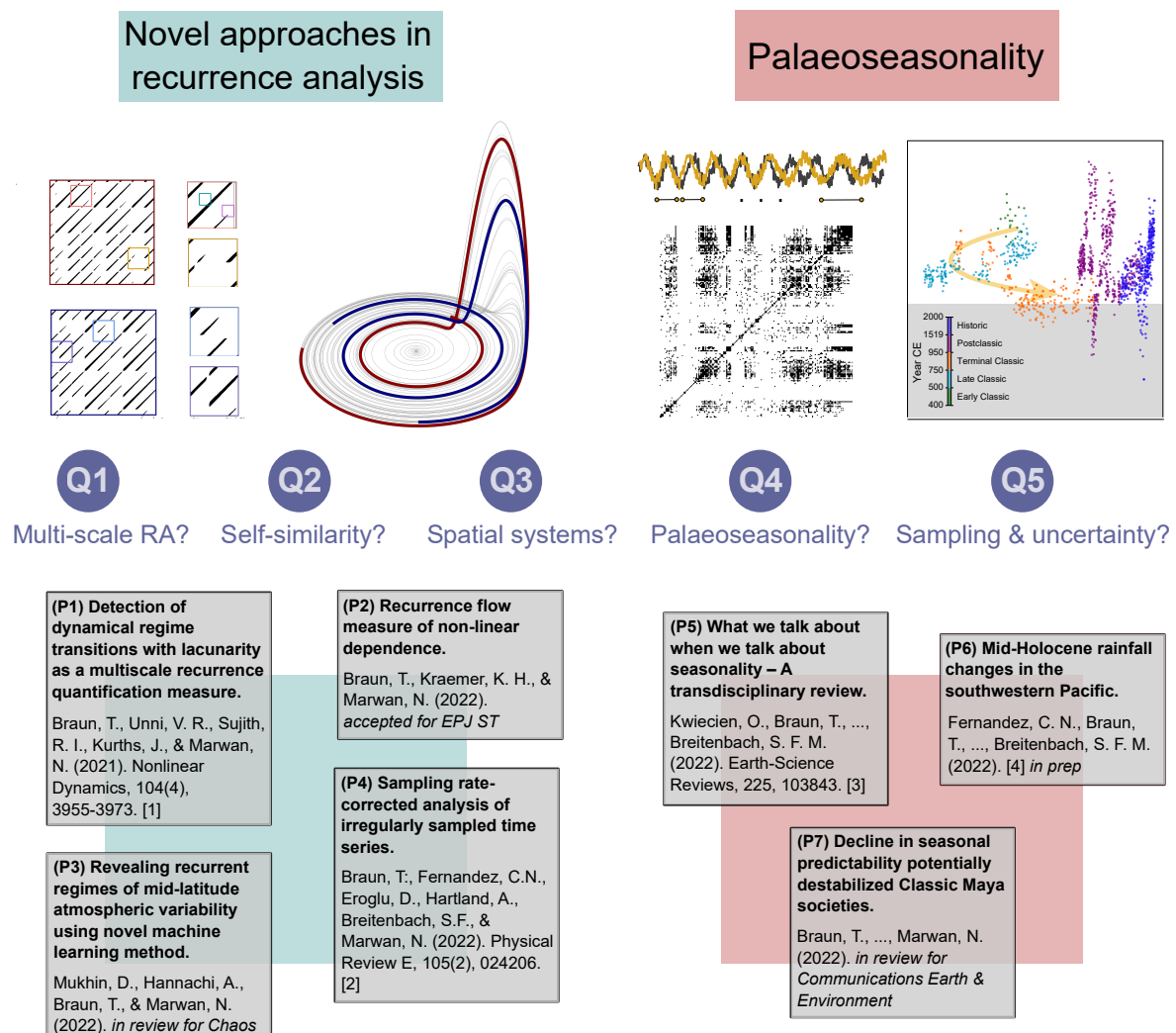


**Figure 4.1:** Organization of this thesis into two parts: first, conceptualization and validation of novel recurrence based methods ('Novel approaches in recurrence analysis') and second, applications to palaeoclimate time series with a focus on reconstructing seasonality from stalagmite proxy records ('Palaeoseasonality').

The first part is composed of four and the second part is composed of three research papers. Six research papers are articles and one is a review. Four articles are first author contributions. At the time of submission of this thesis, three works are published, one is accepted, two are in review and one will be re-submitted soon. Each research paper is presented in its original, independent form, including appendices and supplements. A single joint bibliography has been compiled. For the sake of brevity, the review paper (P5) is not fully included and I instead focus on my contribution. Research article (P6) has been reviewed as a discussion paper (*Climate of the Past Journal*) but not found suitable for publication. The respective preprint is included in this dissertation and a modified manuscript will be re-submitted to a different journal soon.

Part one is predominately devoted to the development of novel approaches in RA and is an attempt to find answers to questions (Q1-Q3). Inspired by the ideas of B. Mandelbrot for characterizing fractals and self-similar textures in nature, Chapter 5 and 6 transfer concepts from this domain into RA. Recurrence quantification analysis is more and more becoming an established framework for the detection of regime shifts. However, an ample amount of information so far remained unutilized as existing approaches concentrated on line-based measures and have not fully exploited the time scale-sensitivity of RPs. In Chapter 5, we propose a novel recurrence quantification measure based on B. Mandelbrot's 'lacunarity' measure. Applied to a binary texture, lacunarity quantifies its scale-dependent heterogeneity. This enables us to resolve the complexity of recurrence patterns at multiple time scales and put forward a tool that is both sensitive to the spectral content of a signal and detects transitions in empirical time series of acoustic pressure fluctuations from a turbulent combustor. In Chapter 6, yet another of B. Mandelbrot's fascinating concepts, called 'succolarity', inspires the definition of a novel recurrence based nonlinear dependence measure. Succolarity characterizes the permeability of a texture. We simplify this approach, transfer it to RA and show that the formation of diagonal line artifacts can be exploited to characterize delayed couplings in potentially high-dimensional systems. The 'recurrence flow' appears especially useful in the delay selection problem for state space reconstruction of a dynamical system. Chapter 7 tackles the problem of identifying recurrent dynamical regimes from atmospheric circulation patterns raised in (Q3). For future climate change, regionally heterogeneous and complex responses of large scale atmospheric teleconnection patterns are expected while their dynamics and implications for resulting extreme weather events are subject of current research [38]. I identify recurring regimes of atmospheric teleconnection patterns in the mid-latitudes based on model and empirical data. The identified regimes can be classified based on their dynamical complexity whereby 'recurrence lacunarity' and other recurrence quantification measures prove informative. Next, I turn to a methodological challenge that is encountered in RA of irregularly sampled palaeoclimate time series: in many cases, sampling intervals are not only non-uniform but undergo considerable variations in time, biasing recurrence quantifiers. Chapter 8 explores how this bias can be corrected based on a constrained randomization procedure. I generate synthetic ensembles of surrogate time axes that share the undesired property of variable sampling resolution to control for this effect and show that this approach helps to tell apart real from spurious regime shifts of palaeoseasonal variability, referring to (Q5).

In part two of this thesis, different palaeoclimate proxy records from different regions are studied with respect to a common question – how can we reconstruct and quantify changes in seasonality (Q4 & Q5)? I initiate the study of Palaeoseasonality with an overview of how seasonality can be defined in the context of Palaeoclimatology in Chapter 9. I review which numerical tools are most established and promising for the analysis of palaeoseasonal records.

Accounting for archive-specific challenges and limitations is of vital importance. This and other insights are highlighted and collated to express goals for future studies of palaeoseasonality.

Chapter 10 demonstrates a more specific application of how seasonal rainfall has been recorded in a stalagmite from Niue Island in the Central Pacific that covers a 1000-year period in the mid-Holocene. PCA reveals how different geochemical proxies encode seasonal variations. Scans of annual stalagmite layers allow a high-resolution reconstruction of seasonal amplitude from greyscale values of deposited calcite laminae. With its strategic location in the central Pacific, links between seasonal variations and El-Niño-Southern-Oscillation (ENSO) dynamics can be explored using wavelet analysis and RA, contributing to the answer of (Q4 & Q5).

Finally, Chapter 11 is dedicated to the intriguing question raised in the very beginning of this thesis: could changes in seasonal rainfall predictability have adversely affected Maya agricultural yield and, in turn, contributed to the abandonment of population centers? While most works agree on the role that drought events have played, seasonal rainfall variability undoubtedly constituted the most vital factor in securing reliable surplus crop yield for Maya farmers. In the context of research objectives (Q4 & Q5), I define a robust recurrence based measure of seasonal rainfall predictability and apply it to a precisely dated speleothem record from the Maya lowlands. A decline in seasonal rainfall predictability that aligns with the period of sociopolitical disintegration suggests that adverse changes in year-to-year rainfall availability might have played a so far underestimated role in the ‘collapse’ of Classic Maya civilization.

In the end, a discussion with emphasis on the synthesis of the presented works and conceivable future research avenues is given. Appendix A presents an overview of the software that I have implemented in this thesis and links to the respective online resources where it can be downloaded (open access). Appendices B-F contain appendices and supplements to the research papers (in order of appearance).



---

# Novel approaches in recurrence analysis







*A glimpse of the Great Barrier Reef, the largest coral reef on the planet. After several devastating bleaching events, the reef has recently been recurring to a more healthy state, showing resilience in spite of incessantly increasing ocean temperatures. A full recovery under prevailing stress, however, remains questionable. (Australia, 2018)*



## 5 | Detection of dynamical regime transitions with lacunarity as a multiscale recurrence quantification measure

Tobias Braun<sup>1</sup>, Vishnu R. Unni<sup>3</sup>, R. I. Sujith<sup>4</sup>, Norbert Marwan<sup>1,2</sup>, Juergen Kurths<sup>1</sup>

1 – Potsdam Institute for Climate Impact Research, 14473 Potsdam, Germany

2 – University of Potsdam, Institute of Geosciences, Potsdam, Germany

3 – Department of Mechanical and Aerospace Engineering, Princeton University, NJ, USA

4 – Indian Institute of Technology Madras, Chennai 600036, India

*Braun, T., Unni, V. R., Sujith, R. I., Kurths, J., & Marwan, N. (2021). Detection of dynamical regime transitions with lacunarity as a multiscale recurrence quantification measure. *Nonlinear Dynamics*, 104(4), 3955-3973. doi: 10.1007/s11071-021-06457-5 [1]*

### Abstract

We propose lacunarity as a novel recurrence quantification measure and illustrate its efficacy to detect dynamical regime transitions which are exhibited by many complex real-world systems. We carry out a recurrence plot based analysis for different paradigmatic systems and nonlinear empirical data in order to demonstrate the ability of our method to detect dynamical transitions ranging across different temporal scales. It succeeds to distinguish states of varying dynamical complexity in the presence of noise and non-stationarity, even when the time series is of short length. In contrast to traditional recurrence quantifiers, no specification of minimal line lengths is required and rather geometric features beyond linear structures in the recurrence plot can be accounted for. This makes lacunarity more broadly applicable as a recurrence quantification measure. Lacunarity is usually interpreted as a measure of heterogeneity or translational invariance of an arbitrary spatial pattern. In application to recurrence plots, it quantifies the degree of heterogeneity in the temporal recurrence patterns at all relevant time scales. We demonstrate the potential of the proposed method when applied to empirical data, namely time series of acoustic pressure fluctuations from a turbulent combustor. Recurrence lacunarity captures both the rich variability in dynamical complexity of acoustic pressure fluctuations and shifting time scales encoded in the recurrence plots. Furthermore, it contributes to a better distinction between stable operation and near blowout states of combustors.

## 5.1 Introduction

Many efforts in nonlinear time series analysis have been dedicated to the challenge of detecting transitions between different dynamical states of a system [39, 40, 41]. A broad range of real-world systems undergo such shifts between distinct regimes and their identification provides a better understanding of the complex dynamics under study [42, 43, 44, 45, 46, 45, 47, 48, 49]. The universality of transitions between different dynamical states for a broad spectrum of different systems elucidates why applications have been widely dispersed among many disciplines. For instance, time series in earth sciences usually require sophisticated approaches to determine abrupt changes in the complex dynamics [43, 50, 51]. Regime shift detection has also gained popularity in analysis of EEG data [52], neuroscientific time series [53, 54] and other medical research fields [55] where the identification of pathological regimes is crucial. Due to their complexity, financial and social time series offer interesting applications as well [56, 57, 58].

Major challenges in detecting regime shifts in real-world data are often data related, e.g. by means of unevenly sampled [50], nonstationarity, noisy or short time series. In convenient cases, transitions are visible to the eye but usually, the exact localization of the occurring dynamic transition and, in particular, the identification of precursors poses a challenge. Segments of a time series may appear qualitatively similar at first glance but could turn out to show significantly different dynamical features. With respect to climate systems, multiple spatial and temporal scales can also hamper clear distinctions between variations in complexity of a time series. Even though regime transitions occur in a broad class of systems, data related peculiarities raise the need of a comprehensive box of tools rather than a single universal method.

In contrast to linear methods such as autocorrelation or power spectrum analysis, nonlinear techniques are able to uncover more subtle transitions in complex time series data. Multiple different approaches constitute the state-of-the-arts toolbox, ranging from complex networks [59], entropies [40], detrended fluctuation analysis [60] or symbolic dynamics [61]. Since many empirical time series are univariate and no prior knowledge is accessible about the true dimensionality of the system, phase space reconstruction is a powerful approach to study the system's dynamics [40]. Approaches based on the phase space trajectory are closely related to the well-known Lyapunov exponents and have proven to be effective in classifying different dynamical states [45, 58].

Another technique with relatively low numerical effort is the analysis of nonlinear time series by *recurrence plots* (RPs) [19]. The basic idea behind this method relates back to the perspective that dynamical systems recur to states they have visited before [16]. As a representation of such recurrences, the binary recurrence matrix  $\mathbf{R}_{ij}$  of a phase space trajectory  $\mathbf{x}_i \in \mathbb{R}^d$  indicates times where the system recurs to formerly visited states by 1s and all other times by 0s. It is widely used as a graphical tool but also allows for quantification of various dynamical aspects of the system under study. Since its first conception the method was successfully extended and applied to various real-world systems [62]. The detection of regime transitions has become a prototypical field of application for RPs since it enables us to analyse complex temporal patterns of nonlinear time series in a simplified fashion [20]. The majority of measures in recurrence quantification analysis (RQA) are based on black or white line structures in an RP. For instance, diagonal lines resemble parallel segments of the phase space trajectory and thus entail a degree of predictability. Approaches to capture more complex features in RPs beyond the reductionist approach of measuring line lengths have been conceived [63, 47], e.g. by allowing for the entirety of possible permutations of recurrences in small submatrices. This leads to the observation that the variety of distinct microstates in deterministic and stochastic systems occupies only a fraction of the possible permutations,

yielding lower entropy values. Even though this technique generally shows good robustness and does not require specification of minimum line lengths, such an approach is limited to the information captured by small submatrices on a restricted local level. We propose a method where recurrences are also evaluated regardless of their exact orientation in the recurrence matrix, but with a surplus quantification of the scaling from the smallest to the largest possible submatrices. This can be achieved by not analysing the permutations of recurrences but by the statistics of their locally determined count.

To this extent, we make use of a measure called *lacunarity* [25, 64]. Traditionally, it has been applied to quantify complex spatial patterns. Perhaps, the clearest interpretation of lacunarity is that it quantifies the degree of heterogeneity of the studied pattern. Often, it is applied in the context of distinguishing fractal patterns [65] because objects of same fractal dimensionality can still exhibit different degrees of heterogeneity. As a rule of thumb, patterns with larger gaps yield higher values of lacunarity. Beyond this straight-forward interpretation, it classifies patterns with respect to their deviation from translational invariance [65]. This highlights its applicability as a measure of heterogeneity. Characterizing the heterogeneity of RPs on different temporal scales using lacunarity yields meaningful information about the complexity of the underlying time series. Besides, heterogeneity has already been considered as a quantifier to analyse recurrence networks [66]. Lacunarity has successfully been applied to various systems ranging from characterizations of the scaling properties of the Amazon rainforest [67] and urban areas [68] to heterogenous patterns in bone structures [69] and stellar mass distributions [70]. It is also a popular tool in Neuroscience [71]. To our best knowledge, it has not yet been applied to RPs. Combining both approaches as a powerful tool to detect dynamical regime shifts is the main contribution of this work. In order to demonstrate the scope of the developed methodology, we showcase applications to both paradigmatic systems and nonlinear empirical time series.

This work is organized as follows: in Sect. 5.2 we introduce our methodology by briefly summarizing the RP technique and describing the computation of lacunarity by a box-counting algorithm. In this context, we give a brief dynamical interpretation of our method. Subsequently, we study results for synthetic data from three paradigmatic systems in Sect. 5.3, namely the Logistic Map, the Roessler system and a bistable noise-driven system. The robustness of our method against noise and short time series length is examined. Finally, we provide first evidence that the proposed method is capable of detecting regime transitions in complex empirical time series. In Sect. 5.4, we identify known dynamical states in time series of acoustic pressure in a turbulent combustor [72] and attempt to illustrate the distinction between two dynamically similar but practically contrary regimes. We conclude our findings in Sect. 5.5.

## 5.2 Methodology

First, we introduce recurrence plots in Sect. 5.2.1 and briefly revise traditional recurrence quantification analysis. Afterwards, we define lacunarity and present detailed information for its application to RPs in Sect. 5.2.2. To gain a more profound understanding of the proposed method, we discuss its dynamical interpretation for the phase space trajectory.

### 5.2.1 Recurrence Analysis

Many real-world systems show a tendency to recur to states they have visited before. Such information can be captured by a two-dimensional visualization that may yield striking patterns which resemble the recurrences at all time instances of the time series. By studying regularities in such recurrence patterns, rich information can be obtained on the dynamics of

the underlying system that go beyond the scope of linear statistical methods of time series analysis such as autocorrelation functions. In particular, different quantification measures of the visual representation prove powerful in classifying differing systems, detecting non-linear correlations and identifying dynamical regime transitions. The basic concept can be outlined by defining the recurrence matrix

$$\mathbf{R}_{ij} = \begin{cases} 1 & \text{if } \|\mathbf{x}_i - \mathbf{x}_j\| \leq \varepsilon \\ 0 & \text{if } \|\mathbf{x}_i - \mathbf{x}_j\| > \varepsilon \end{cases} \quad (5.1)$$

with a time series  $\mathbf{x}$  at two arbitrary times  $i$  and  $j$  and a suitable norm  $\|\cdot\|$ . The vicinity threshold  $\varepsilon$  needs to be fixed with respect to the distances of time series values such that a meaningful expression of recurrences is obtained. A popular approach to do so is, for example, to choose a value which entails a fixed recurrence rate for the RP [20]. The resulting visual representation of a recurrence matrix is a binary image of black and white dots from which temporal patterns can be inspected. For higher dimensional systems, recurrence analysis needs to be based on a phase space representation of the time series as a trajectory in  $d$ -dimensional space. Despite the fact that the dimension of the regarded system is often unknown, Takens' theorem [73] ensures that a time-delay embedding can be found that gives an appropriate phase space reconstruction. To this extent, an embedding delay is often specified prior to fixing the optimal embedding dimension for the system. We will apply the broadly used mutual information criterion and the False Nearest Neighbours (FNN) method [74, 75] to estimate both parameters.

For many systems, RPs have been successfully applied to reveal a high degree of complexity both in terms of nonlinear dynamics and stochastic fluctuations [20]. In the detection of regime transitions, a reliable quantifier that yields an unambiguous distinction of dynamical regimes is generally required. Traditional complexity indicators such as Lyapunov Exponents [76] are not always robust against noise and require rather long time series. They are also often not able to capture the relevant time scales of the system's shifting dynamics which is particularly important for systems with multiple characteristic time scales. Yet, such information is contained in RPs and can be uncovered using recurrence quantification measures [77]. Most of them are based on the statistical distribution of line structures in RPs. For instance, diagonal lines of certain length indicate a similar evolution of different segments of a time series. A popular quantification of an RP based on diagonal lines is defined as the fraction of lines that exceed some specified minimal line length. As it quantifies the degree of determinism in a time series, it is referred to as DET. Vertical lines indicate that the system is trapped in a certain phase space region for subsequent times. White vertical gaps indicate transitions between different phase space regions while black square-like structures point at time intervals in which the system remains confined in a small region of the phase space. If such patterns reoccur with statistical significance, they uncover regularities of the time series and may yield characteristic recurrence time scales. Line-based recurrence measures have been applied to a diversity of complex real-world systems as complexity measures to uncover transitions [20]. Yet, different embedding parameters can yield varying results and edge effects as well as high sampling rates might result in spurious quantifications [78], thus requiring corrections [79]. On top of that, the application of line-based RQA measures is limited to systems that do not show more complex recurring patterns which are referred to as microstates of an RP [63]. Related complexity measures that go beyond this scope have shown that they can have superior performance [58, 47]. In this work, will put forward a novel RQA measure that characterizes the heterogeneity of an RP and is not based on certain microstructures.

### 5.2.2 Recurrence Lacunarity

Lacunarity is often illustrated as a measure of ‘gappiness’ or as a property that can characterize the heterogeneity of a spatial pattern. It was introduced to distinguish between different fractal patterns of equivalent fractal dimensionality. However, its scope goes beyond the distinction of fractal structures. More formally, we can regard it as a measure of deviance of a pattern from translational homogeneity [64, 80]. As lacunarity is usually derived for different spatial scales, it is possible to identify a certain scale above which a pattern is translational invariant and below which it is too heterogenous to be regarded as such.

Even though box-counting algorithms can also be modified so that an analysis of grayscale-[81] or RGB-encoded [82] patterns is possible, in application to RPs a basic algorithm for binary patterns suffices. The quantity that enables us to analyse scaling properties of a complex pattern is the size of boxes on the applied grid. Given an RP as a  $T \times T$ -matrix and a fixed box size  $w$ , the mass  $M$  of each box is obtained by counting the black pixels inside the box. This results in a mass distribution  $P_w(M)$  for all  $N$  boxes. From this distribution, we compute the moments

$$Z^{(q)}(w) = \sum_M M^q P_w(M) . \quad (5.2)$$

In the definition of lacunarity  $\Lambda$ , only the first and the second moments  $Z^{(1,2)}$  are considered:

$$\tilde{\Lambda}(w) = \frac{Z^{(2)}(w)}{[Z^{(1)}(w)]^2} = 1 + \frac{\sigma^2(w)}{\mu^2(w)} \quad (5.3)$$

with mean  $\mu$  and standard deviation  $\sigma$ . To have a measure in  $[0, 1]$ , we normalize lacunarity by also computing the lacunarity  $\tilde{\Lambda}^\dagger$  of the complement of the set (1s replaced by 0s and *vice versa*). Consequently, we define it as

$$\Lambda(w) = 2 - \left( \frac{1}{\tilde{\Lambda}(w)} + \frac{1}{\tilde{\Lambda}^\dagger(w)} \right) . \quad (5.4)$$

This refined definition of lacunarity also enhances the detection of significant gap sizes compared to eq. (3) and is thus preferred [69]. Various box-counting methods beyond the basic approach employed in this work are known (e.g. gliding box-counting [83]) and generalized versions exist (e.g. for multifractal data [84]). The often used standard gliding box approach results in a higher number of boxes but is also known to cause biased values due to edge effects [85]. Note that in any case, minimum and maximum box size have to be chosen based on the time series length.

In view of RPs, black pixels are equivalent to recurrences of a trajectory in reconstructed phase space. Thus, we are effectively carrying out an analysis of local (in a temporal sense) recurrence statistics and quantification of local variations. This is essentially implemented via the computation of variance of recurrence points contained in boxes which are located at different positions in the RP. An extension to higher statistical moments is also conceivable [86]. Our approach circumvents the necessity of defining any sort of microstate and is not restricted to the usual statistical analysis of line structures in the RP. The scaling (successive increasing of time intervals) is expected to pinpoint relevant temporal scales related to average recurrence times and quasi-periodicities. This is confirmed by the displayed recurrence lacunarity curves in Fig. 5.2 from which some will be studied in more detail in Sect. 5.3. Figure 5.1 shows examples of RPs of systems that show fundamentally different dynamics. While a white noise process entails an RP with randomly distributed black dots, a Logistic Map in the chaotic regime ( $r = 3.9$ ) still results in some local structures such that RL is

---

**Algorithm 1** Recurrence Lacunarity

---

```
1: if embedding required then
2:   Choose  $d, \tau$  and embedd time series
3: end if
4: Compute RP  $\underline{R}$  with specified vicinity threshold  $\varepsilon$ 
5: for box width  $w = 2, 3 \dots \ll T$  do
6:   Split  $(T \times T)$ -matrix  $\underline{R}$  into  $N = \lfloor T/w \rfloor \times \lfloor T/w \rfloor$  disjunct boxes
7:   for each box  $b_w^{(i,j)}$  do
8:     Count recurrences:  $M = \sum_{i',j'}^{i,j} \delta(\underline{R}_{i',j'} - 1)$ 
9:   end for
10:  Compute normalized lacunarity  $\Lambda$  for fixed  $w$  from eq. (2-4)
11:  Apply bootstrap by randomly drawing sufficient number of boxes  $b_w^{(i,j)}$  for significance testing
12:  if  $T \% w \neq 0$  then
13:    repeat iteration with varied grid position
14:    until robustness ensured
15:  end if
16: end for
```

---

higher for almost all  $w$ , resembling higher complexity. A Roessler system in the periodic regime generates well pronounced lines corresponding to deterministic periodic dynamics. As expected, the characteristic width between the lines is captured in the variation of RL as a local minimum (left dotted circle) since for boxes of the same size, homogeneity is enhanced. The second visible minimum (right dotted circle) is located at twice the period of the time series. Stochastic signals such as an AR(2)-process and Multifractal Gaussian Noise (MFGN) [87] yield a higher degree of complexity in terms of low translational invariance of the corresponding RPs. Both the MFGN and the bistable noise-driven system (see Sect. 5.3.3) time series have a visible periodic modulation which is resembled by the distinct gap sizes in the respective RPs. For the former time series, RL sharply drops when  $w$  reaches the gap size. For the latter, the stochastic component results in slight variations of the gap size but still, RL captures them as a local minimum at  $w \approx 10^2$ .

## Dynamical Interpretation

As standard RQA measures are based on line structures in the RP, they have clear interpretations in terms of the phase space trajectory and their relationships to dynamical invariants (such as Lyapunov exponents and Renyi entropy) are well established [20]. These questions also arise for RL. Picking a box within an RP and deriving some related statistics can be interpreted as sampling two segments of a phase space trajectory. If we denote the starting point of the first trajectory by  $i$  and the second by  $j$ , the lower left corner of the box is located at  $(i, j)$  and its upper right corner at  $(i + w, j + w)$ . The number  $M_{i,j}$  of recurrences contained in the box characterizes the similarity between the two trajectory segments by means of their recurrences. For fixed  $\varepsilon$ , these are equivalent to the number of contained phase space vectors that are nearest neighbours by means of a low distance in phase space. Figure 5.3 illustrates the relation between box-counting of recurrences and the phase space trajectory based on the Roessler attractor as a paradigmatic example (see Sect. 5.3.2). RL quantifies the heterogeneity of recurrent temporal patterns representing different segments of the phase space trajectory. For increasing length of trajectory segments (from right to left in Fig. 5.3), their recurrence as well as their divergence can be captured by means of recurrence patterns



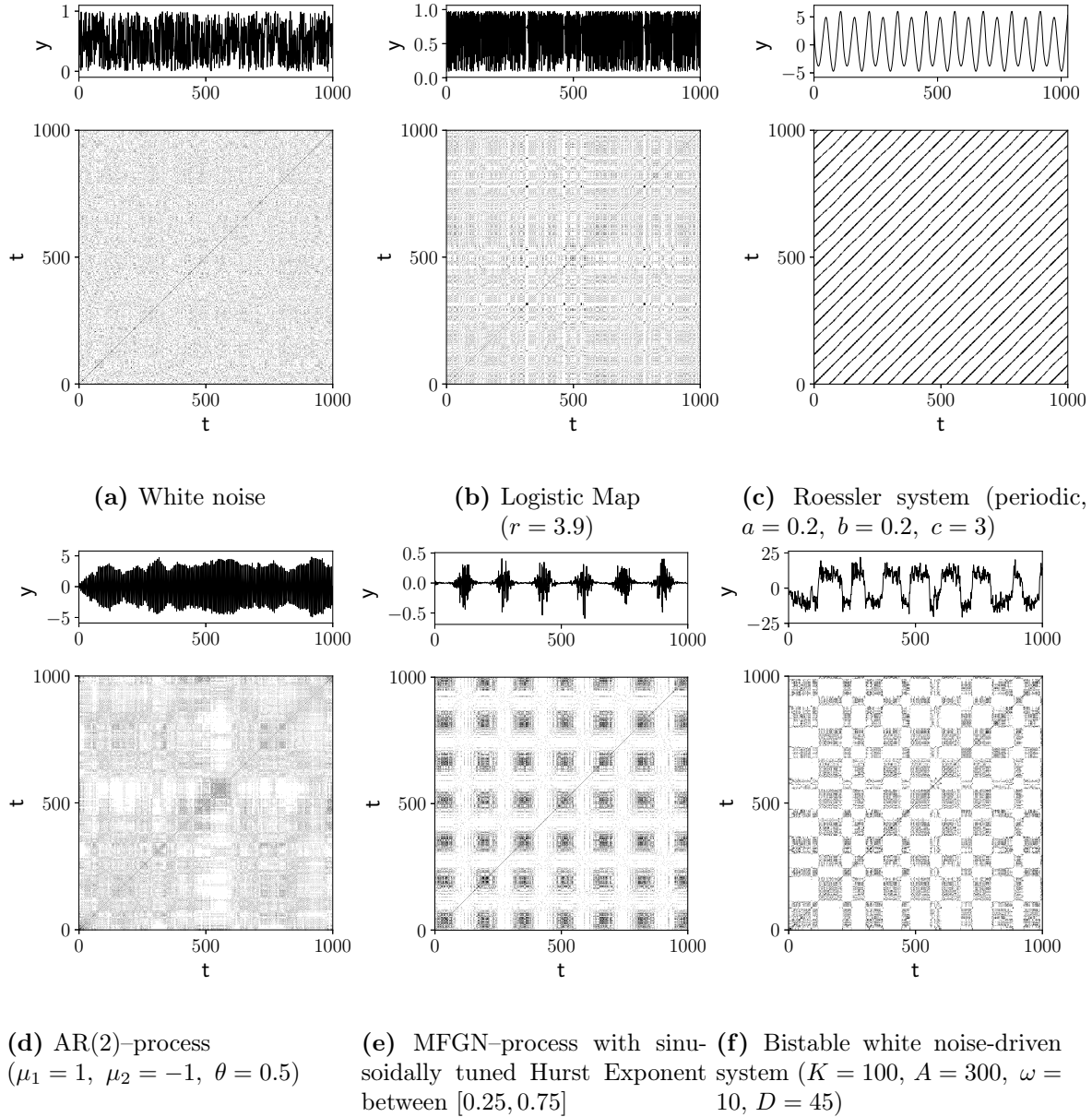


**Figure 5.1:** Recurrence plots for time series of different deterministic and stochastic systems.

encoded in the RP. Apart from the dynamical interpretation, it is an open question how fractality of RPs is related to self-similarity in the underlying time series or the attractor [88]. As a general conception, the very basic structures of RPs such as diagonal lines, vertical lines and blocks show some resemblance to typical 1- and 2-dimensional fractals like the Cantor set or the Sierpinski carpet [89]. Self-similarity by definition arises from the spatial recurrence of patterns [90]. Even though ideal monofractal patterns can not be expected to occur in a pure fashion in RPs, some degree of self-similarity appears intuitive: small-scale recurring patterns often constitute the correlations on longer time scales which resembles what is displayed in an RP. Self-similarity over some range of box sizes applied to an RP could thus be interpreted as a similar tendency to recur to formerly visited states regardless of the respective time scale. On top of that, it is known that geometrical quantities computed from recurrence networks show relations to the phase space dimension and exhibit fractal scaling properties [91]. This ultimately raises the question whether there is a direct relation of RPs fractality to the degree of fractality of the time series and the attractor. This should be explored in more detail in a

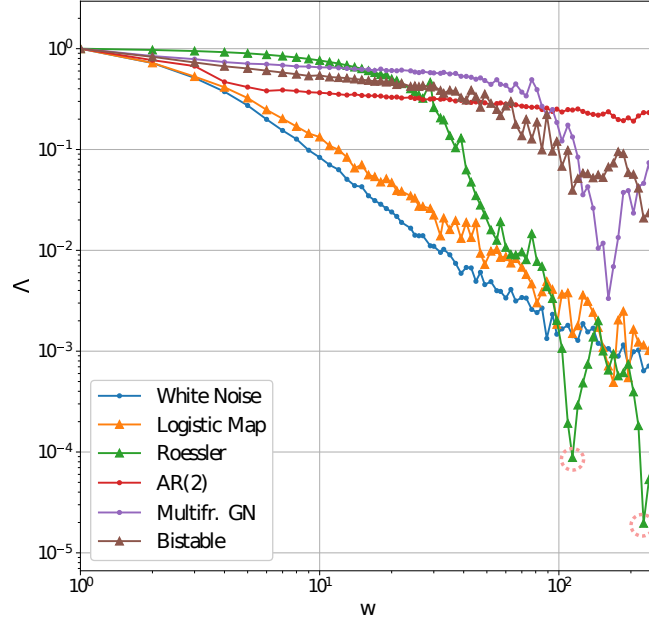


**Figure 5.2:** Recurrence lacunarity curves  $\Lambda(w)$  in double-logarithmic plot, corresponding to displayed RPs in Fig. 5.1.

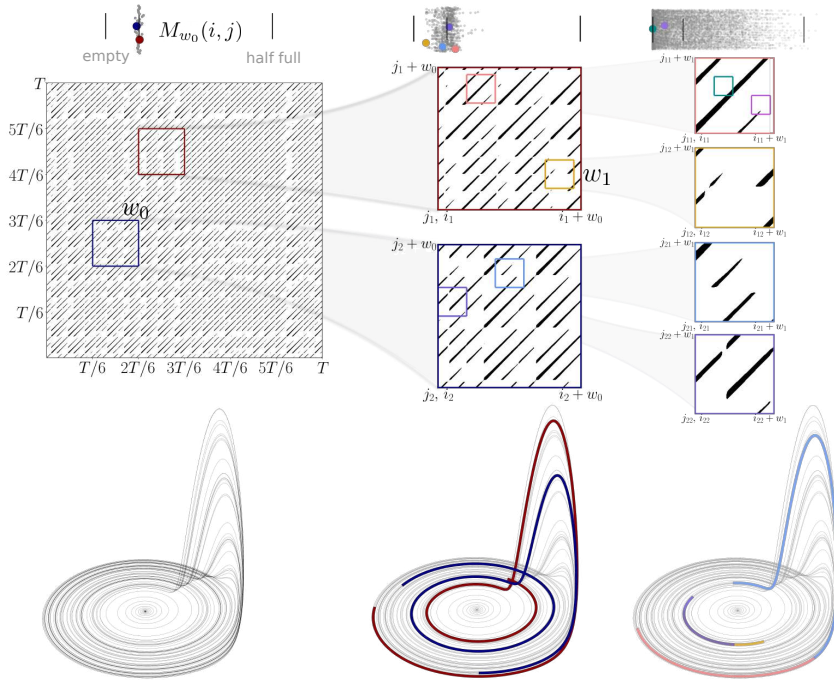


**Figure 5.3:** Schematic illustration of the relation between box-counting on RPs and the underlying phase space trajectory for the Roessler attractor ( $a = 0.1$ ,  $b = 0.1$ ,  $c = 14$ ). The full RP is displayed on the left with two exemplary boxes (blue and red). Above, the box counts  $M_{w_0}(i, j)$  of all boxes (although not indicated) located at grid positions  $(i, j)$  are shown with the average box count (vertical line) whereas their index is chosen as a y-coordinate for better visibility. From left to right, boxes of decreasing width  $w$  are zoomed in and additional boxes are indicated. The segments of the phase space trajectory that correspond to the boxes are color coded respectively. The scatter plots illustrate that for decreasing box widths, heterogeneity by means of dispersion of the box counts increases.

future study and is beyond the scope of this work.

### 5.3 Dynamical Transitions in Synthetic Data

We demonstrate the ability of RL to capture different kinds of regime shifts by its application to model data from different dynamical systems (Table 5.1). These systems cover some of the important aspects that need to be accounted for if transitions in real data should be identified. In Sect. 5.3.1, we study transitions between chaotic and periodic dynamics for the Logistic Map. In Sect. 5.3.2, transitions in the Roessler System as a three-dimensional continuous system are analysed. A bistable noise-driven stochastic process is examined in Sect. 5.3.3 in order to demonstrate the ability of our approach to uncover rather subtle transitions. Finally, we examine an experimental dynamical systems in Sect. 5.4.

System	Dynamical regimes	Equations	Param.	Embedding
Logistic Map	deterministic/chaotic	$x_{n+1} = rx_n(1 - x_n)$ , $r \in [3.5, 3.95]$	$r$	/
Roessler	deterministic/chaotic	$\dot{x}(t) = -(y(t) + z(t))$ , $a = 0.2$ $\dot{y}(t) = x(t) + ay(t)$ , $b = 0.2$ $\dot{z}(t) = b + (x(t) - c)z(t)$ , $c \in [2, 10]$	$c$	$d = 3,$ $\tau/\Delta t = 18$
Bistable noise-driven	determ./stochastic	$\dot{x}(t) = [K(x(t) - x^3(t)) + A \cos \omega t] + D\xi(t)$ $(K = 100, A = 320)$	$\omega, D$	/
Thermoacoustic combustor	experimental	/	equiv. ratio $\phi$	$d = 5,$ $\tau = 23$

**Table 5.1:** Overview of studied systems for detecting dynamical regime shifts. The systems are distinguished based on their exhibited dynamical regimes, underlying equations, transition parameters and delay-embedding parameters.

Moreover, we characterize the scaling of RL curves by computing the slope  $\alpha$  of  $\log \Lambda$  against  $\log w$  by linear regression. Note that if multiple scaling regions coexist for one RP, a single slope will yield ambiguous results and other indicators should be chosen (e.g. the regression error).

Complexity measures indicate transitions by changing to significantly high or low values. In order to assess significance, we apply the following bootstrapping method that entails confidence intervals: we draw a random sample (with repetitions) from all boxes the RP was divided into and derive RL only from this sample (see Algorithm 1). This resampling procedure is repeated  $N$  times to obtain a distribution of RL values that jitter around the true value. The 5%/95%–quantiles characterize the width of this distribution and are used as confidence bounds. Similar approaches are usually employed with other complexity measures [92, 34, 93]. In most applications, confidence bounds should reflect significance equally sufficient for all values obtained for the respective complexity measure (i.e. for each configuration of the parameters that control regime transitions). In our case, this consequently raises the question whether to sample from the global or local distribution of box counts. In the local

case, box counts for a single window are used to compute confidence bounds whereas in the global case, box counts from all windows are joined. In both cases, the calculation of quantiles is performed such that only a single parameter-independent value is obtained, yielding horizontal lines that indicate the separation between ‘regular’ dynamics and dynamical transitions. Extensive comparative analysis of the resulting confidence bounds indicates that the latter approach yields more convincing results for the studied systems. Bootstrapping from the global box-count distribution generally yields more narrow bounds that seem to overestimate the true number of regime shifts. Consequently, for an underlying series of length  $T$ , we obtain  $T$  locally bootstrapped RL distributions of size  $N$  from which we compute 95% – confidence bounds.

### 5.3.1 Logistic Map

As a first paradigmatic example, we employ the Logistic Map [94] as a system that is well-known to produce pronounced transitions between periodic, chaotic and laminar behaviour. The variation of the parameter  $r$  introduces bifurcations between regimes of different complexity as displayed in Fig. 5.3. While increasing  $r$  entails a tendency of less predictability, windows of periodic dynamics arise in between. For each parameter value  $r \in [3.5, 3.95]$  with  $\delta r = 0.00045$  we generate a time series of suitable length such that after discarding transients, we have  $T = 1000$  points in time. For each such time series  $x_r(t)$ , we calculate an RP. We choose the threshold  $\varepsilon = 0.1\sigma_{ts}$  with  $\sigma_{ts}$  being the standard deviation of  $x_r(t)$ . From each RP, we compute RL for a number of  $k = 70$  different box sizes  $w \in [2, T/4]$ . This results in a single RL curve like in Fig. 5.2. A standard measure to detect regime transitions for such paradigmatic systems is the largest Lyapunov exponent  $\lambda_1$  [40]. We use it as a reference for our results to evaluate the detection of transitions.

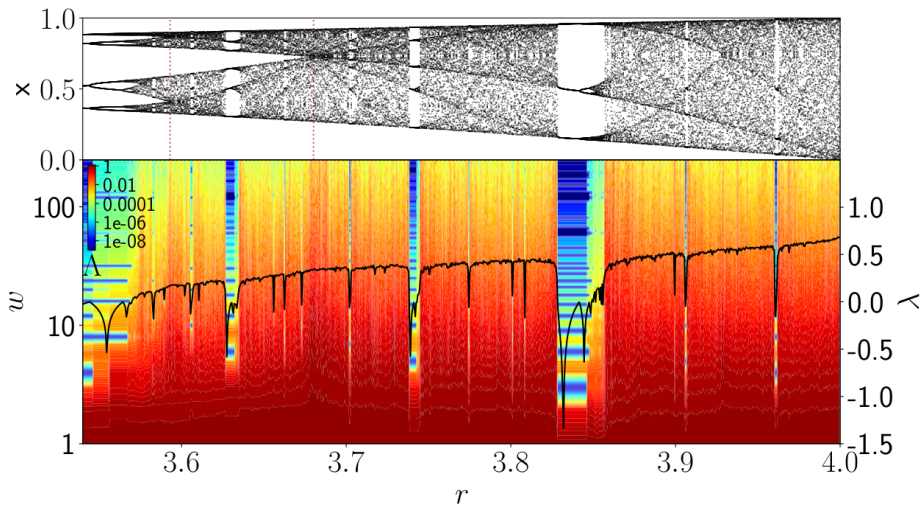
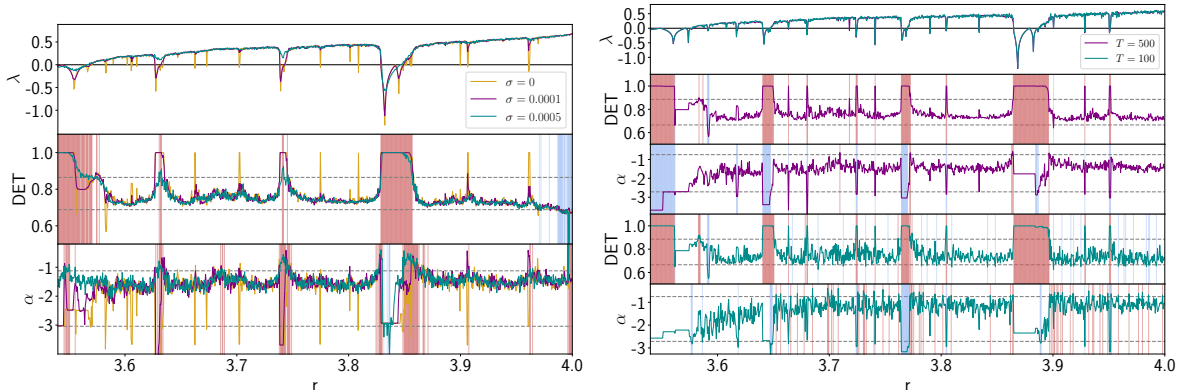


**Figure 5.4:** Bifurcation diagram of Logistic Map and RL curves for varying  $r \in [3.5, 3.95]$  with  $n = 2000$ . Dashed vertical lines indicate chaos-chaos transitions. Each time series has  $T = 1000$  values after discarding transients. For the RL curves,  $w$ -axis and color coding are scaled logarithmically. The black curve illustrates the variation of  $\lambda_1$ .

Below the bifurcation diagram in Fig. 5.4, RL is displayed using color coding. Each RL curve is plotted in double-logarithmic coordinates. Periodic windows are clearly detected as the corresponding RPs are homogenous at all time scales. Furthermore, it appears that e.g. around  $r \approx 3.68$  (red vertical line) it identifies a transition to a regime not well captured by  $\lambda_1$  which is known to arise from the intersection of the *supertrack functions* [52]. At these, an unstable singularity results in laminar behaviour i.e. the time series becoming ‘trapped’



(a)  $\lambda_1$ , DET and the slope  $\alpha$  of the RL curve for varying  $r \in [3.5, 3.95]$  with  $n = 1000$ . Different curves correspond to different noise intensities. Each time series has  $T = 1000$  values after discarding transients. 95% – confidence bounds (gray dashed lines) for both RQA measures are obtained via bootstrapping and refer to the noise-free case. Significant transitions outside of these are indicated by blue/red rectangles for noise with  $\sigma = 0.0005$ .

**Figure 5.5:** Robustness of RL to varying noise intensity and time series length for the logistic map.

in a certain range of values for some time intervals. RL is able to detect such chaos–chaos transitions.

Figure 5.5a shows bifurcations for varying noise strength. We plot both DET and the slope  $\alpha$  of the RL curve for  $r \in [3.5, 3.95]$ . RPs are generated as described above but for time series that are contaminated by uncorrelated white noise of different strength. The largest Lyapunov exponent  $\lambda_1$  shows that for  $\sigma_n = 0.0005$ , only few of the chaos–periodic transitions are detected. For  $\sigma_n = 0.0001$ , some transitions are still well depicted by both measures while others become less prominent already. We evaluate the performance of detecting transitions for  $\sigma_n = 0.0005$  by calculating confidence intervals for the noise-free case as a rather strict bound. Both measures perform with similar success. Yet we point out that RL seems to resolve transitions close to strongly periodic dynamics more clearly in presence of noise, e.g. at around  $r \approx 3.55$  and  $r \approx 3.83$ . Analogously to this analysis, we plot results for different time series lengths in Fig. 5.5a. As expected, it appears that the number of false detections increases for both measures for shorter time series. However, both still succeed to pinpoint chaos–order transitions even for very short time series with  $T = 100$ . Beyond that, the laminar parameter range is also still identified. Anyway,  $\alpha$  indicates more false shifts than DET which may be due to the rather basic box-counting approach that limits the computation of RL to a few boxes in case of very short time series.

### 5.3.2 Roessler System

We further explore the ability of RL to detect regime transitions for continuous dynamical systems with the Roessler system as a standard example (see Tab. 5.1). We vary  $c \in [2, 10]$  with  $n = 2000$  different values. Increasingly dominant chaotic behaviour is expected whereas the average distance between unstable periodic orbits decreases for increasing  $c$ . The nonlinearly coupled  $x$ –component is embedded with parameters given in Tab. 5.1. The vicinity threshold is fixed as  $\varepsilon = 0.5\sigma_{ts}$ .

Instead of  $\alpha$ , we analyse single scale-specific values of  $\Lambda(w)$  since in general, multiple

scaling regions can be identified that are not well represented by a single scaling exponent (see Fig. 5.2).

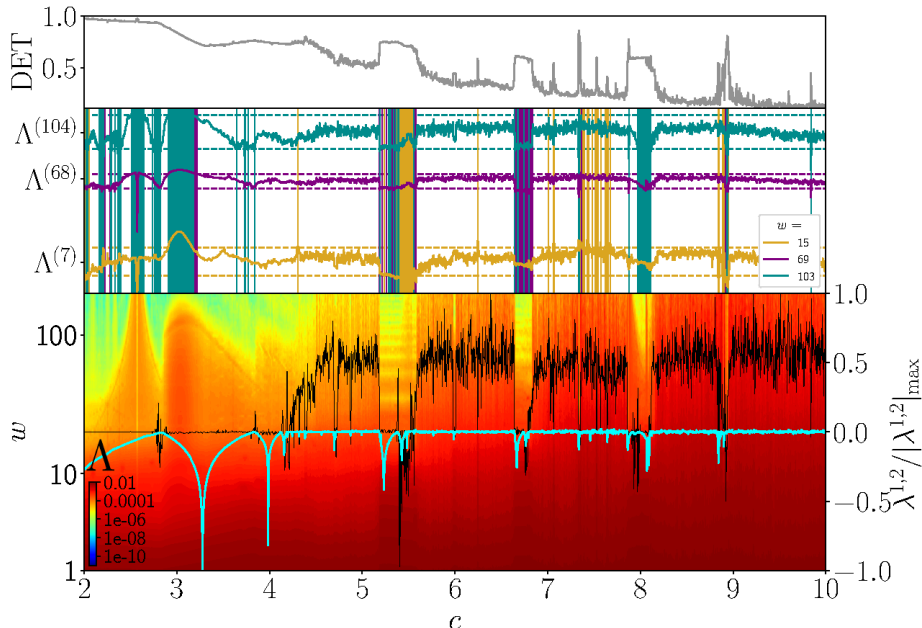


**Figure 5.6:** DET, single scale-specific lacunarities  $\Lambda^{(w)}$  and RL curves for varying  $c \in [2, 10]$  with  $n = 2000$  for the Roessler system. 95%– confidence bounds are obtained via bootstrapping and excursions outside the indicated horizontals are indicated. Each time series has  $T = 1000$  values after discarding transients. In the lower panel,  $w$ -axis and color coding are scaled logarithmically. Black (cyan) curves display the first (second) Lyapunov exponent normalized to their maximum absolute values for better visibility.

In the lower panel of Fig. 5.6  $\lambda_1$  (black) and the second Lyapunov exponent  $\lambda_2$  (white) serve as a reference and enable us to localize periodic windows in the regarded parameter range. The color coded RL curves display rich information on various characteristic scales underlying the chaotic and periodic dynamics. Note that RL detects bifurcations only captured by both of the displayed Lyapunov exponents. For instance, this can be seen in the range  $c \in [2, 4]$  where RL corresponds well to  $\lambda_2$  for larger box sizes whereas pronounced variations are neither captured by  $\lambda_1$  nor by determinism. Above  $c = 5$ , the transitions captured by RL match those indicated by DET. Particularly for the smaller box sizes, a trend in overall complexity for increasing  $c$  is present. We subtract this quadratic trend from three lacunarities for fixed box sizes  $w$  in the upper panel of Fig. 5.6 and compute confidence bounds via the introduced bootstrapping procedure. Almost all of the occurring transitions are detected as indicated by the colored vertical lines. Interestingly, certain periodic windows are most prominently captured by distinct box sizes such as at  $c \approx 3.7$  or  $c \approx 6.4$ . This is due to the fact that as soon as a box size that corresponds to a characteristic scale is reached, the RP becomes more homogenous on this scale and entails low RL. From this perspective, RL may additionally provide similar spectral information on the time series as usually obtained from Wavelet analysis [95] in some cases.

### 5.3.3 Bistable Noise-Driven System

Finally, we demonstrate that RL can also uncover subtle transitions in the time evolution of a nonstationary, stochastic system. To this extent, we study a bistable system which is driven by uncorrelated noise  $\xi(t)$  and a periodic component. Such a system is often illustrated as

a Brownian particle trapped in a double-well potential with a periodic driving force [96]. It can be described by the Langevin equation given in Tab. 5.1 where  $K$  controls the shape of the deterministic potential function,  $A$  yields the strength of the periodic component with its frequency  $\omega$  and  $D$  controls the noise strength.  $\xi(t)$  is chosen as Gaussian white noise. Equation 5.2.2 is solved using the Euler–Maruyama method with a sampling interval of  $\Delta t = 0.002$  and subsequent downsampling to  $\Delta t = 0.006$ . The interplay of the noise strength and the periodic force determines the transition dynamics between the two stable fixed points as described by the general phenomenon of stochastic resonance [97]. For fixed  $A$ , an optimal  $D$  exists such that the signal-to-noise ratio (SNR) is maximized.

There are several notions of how different regime shifts can be classified [98]. A basic differentiation may be made between transitions which are induced by a stochastic or a deterministic component of the respective system. We vary both the frequency  $\omega$  of the driving force and noise strength  $D$  to test whether RL is able to detect these two different types of transitions. Both increasing  $\omega$  and decreasing  $D$  result in a lower SNR since it triggers more high-frequency variability and impedes regular switching. We generate time series of total length  $T = 1.5 \cdot 10^4$  whereas the frequency  $\omega$  is first abruptly decreased from  $\omega = 20$  to  $\omega = 8$  at  $t_1 = T/3$  while noise strength remains constant at  $D = 36$ . At  $t_2 = 2T/3$ , noise strength  $\sigma$  is decreased from  $D = 36$  to  $D = 28$  while retaining  $\omega = 8$ . 100 realizations  $x_i(t)$  with random initial conditions are generated. The height of the potential barrier is  $h = K^2/4 = 2500 \gg A$ , therefore jumps between the potential minima can not be solely caused by the periodic forcing. However, both noise strengths can result in purely noise-driven jumps. RL is computed for RPs with a fixed recurrence rate of 10% on sliding windows of width 2000 with a 90% overlap for each sample. In total, the following two shifts are studied:

$$\mathcal{X}_1 \rightarrow \mathcal{X}_2 \rightarrow \mathcal{X}_3|_{K=100, A=320} : \\ (\omega = 20, D = 36) \xrightarrow{t_1} (\omega = 8, D = 36) \xrightarrow{t_2} (\omega = 8, D = 28)$$

between states  $\mathcal{X}_1$ ,  $\mathcal{X}_2$  and  $\mathcal{X}_3$ . The upper panel of Fig. 5.7 shows an example of a sampled time series. We can observe the subtlety of the two parameter shifts which can not be solely localized through visual inspection. In the lower panel, the variation of color-coded RL curves is displayed whereas the average over all generated samples is shown. As expected, the transitions are most striking for the largest considered box sizes  $w$  since these have the same order of magnitude as the switching time scales between the two fixed points. Such switches are encoded as gaps in the RPs and can thus be well identified by RL. The decrease of  $\omega$  after  $\mathcal{X}_1 \rightarrow \mathcal{X}_2$  results in more homogenous RPs on these time scales since the system on average resides for shorter time periods within one potential minimum. Within the  $\mathcal{X}_2$  regime, SNR is enhanced yielding a more regular switching behaviour. This regularity further stands out as an almost stable switching period as indicated by RL at  $w \approx 100$ . Recurrences within this regime can consequently be regarded as less complex for time periods exceeding this switching cycle. A similar increase in large-scale RL can be observed for the decrease in noise intensity  $\mathcal{X}_2 \rightarrow \mathcal{X}_3$ : as noise-driven transitions are less likely, the RPs are more ‘gappy’ on longer time scales.

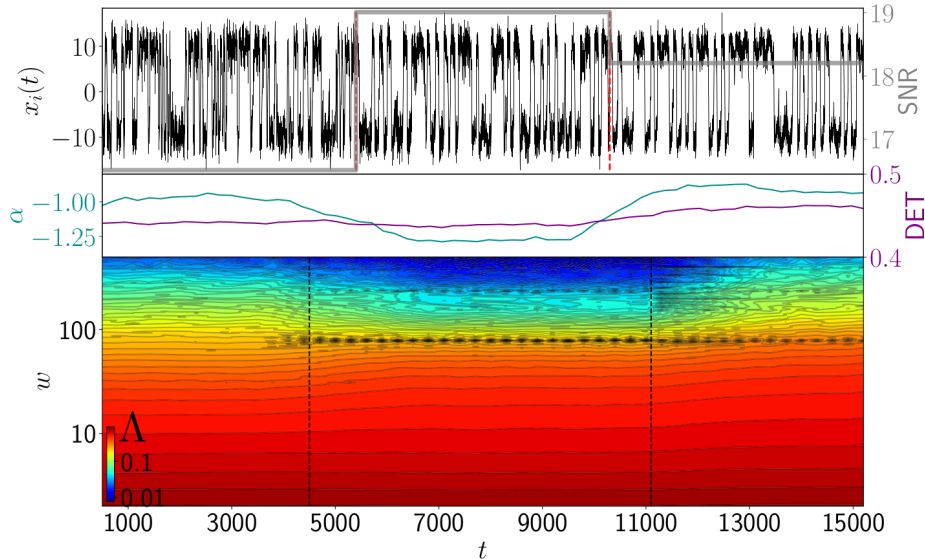


**Figure 5.7:** Single time series realization and averaged RL curves on sliding windows for bistable noise-driven system. Sample averaged SNR (gray) is indicated in the upper panel, sample averaged DET (purple) and  $\alpha$  (cyan) are compared in the center panel. Vertical dashed lines mark the two transitions  $\mathcal{X}_1 \rightarrow \mathcal{X}_2$  and  $\mathcal{X}_2 \rightarrow \mathcal{X}_3$ . For the RL curves,  $w$ -axis and color coding are scaled logarithmically.

Both states  $\mathcal{X}_1$  and  $\mathcal{X}_3$  thus share the feature that lower frequency variability is more complex in terms of more diverse recurrent patterns. Anyway, they differ with respect to their high-frequency variability. For small box sizes (mostly reflecting intra-well dynamics), RL is higher in the  $\mathcal{X}_3$  regime as indicated by the gray contours.

When both the driving frequency and noise intensity are low, recurrences are less erratically clustered, yielding more coherent, variable recurrent periods for short durations. The semi-stable period is preserved in  $\mathcal{X}_3$  but less pronounced than in  $\mathcal{X}_2$  since lower noise strength results in a weakened SNR through the mechanism of stochastic resonance. Finally, we compute three regime-specific RL curves for each of the 100 samples and calculate the sample averaged slopes  $\alpha$  for the different regimes. With  $\alpha_{\mathcal{X}_1} = -1.09 \pm 0.17$ ,  $\alpha_{\mathcal{X}_2} = -1.38 \pm 0.18$  and  $\alpha_{\mathcal{X}_3} = -1.00 \pm 0.18$ , the two regimes  $\mathcal{X}_1$  and  $\mathcal{X}_3$  can be well distinguished from  $\mathcal{X}_2$  but are similar to each other in the range of their respective standard errors. Anyway, the middle panel in Fig. 5.7 shows that  $\alpha$  still captures both transitions more clearly compared to DET. While DET performed superior for short time series (see 5.5b), RL gives more convincing results for these rather subtle shifts.

## 5.4 Application to Thermoacoustic Instability Time Series

In order to evaluate the performance of RL as a complexity indicator for empirical data, we apply it to acoustic pressure time series from a laboratory combustor with turbulent flow, operating at atmospheric pressure. The univariate time series was measured with a 10kHz resolution and is known to undergo a rich variety of transitions between chaotic, intermittent and periodic dynamics [49]. Practical relevance arises e.g. from the use of gas turbine engines for propulsion and power generation. The two main acting subsystems are the unsteady heat release and the acoustic field. Positive feedbacks between both may lead into a state called thermoacoustic instability, enhancing heat transfer to the walls of the combustion chamber and resulting in increased mechanical stress. This can cause severe damages to an aircraft's



engine or shutdown in the case of a power plant [99]. The parameter which can drive the turbulent system into an unstable state is the fuel/air ratio. If it falls below a critical threshold, flame blowout can be the result which leads to an abrupt drop of thrust for an aircraft. This raises the need of effective monitoring to detect impending instabilities and thermoacoustic transitions such including thermoacoustic instability and blowout. In the following, we will apply RL analysis to RPs of the system in order to identify the different regimes and localize the shifts between them. Several studies have been carried out in this context, classifying dynamical states with fractal measures [48], employing complex networks [100, 59] and RPs [101, 102, 49, 103]. Special emphasis will be given to the distinction of normal operating conditions (combustion noise) and an impending blowout situation. We first introduce the experimental setup in Sect. 5.4.1. In Sect. 5.4.2, we investigate regime shifts in the system in terms of varying RL of acoustic pressure time series.

### 5.4.1 Experimental Setup and Data Acquisition

The acoustic pressure ( $p'$ ) data used for the study was obtained from a turbulent combustor with a bluff body stabilized flame. The combustor consists of a rectangular chamber (length = 140 cm, cross section = 9 cm × 9 cm) that houses a circular disk (bluff body, diameter = 4.7 cm, thickness = 1 cm) aligned along the axis of the combustion chamber. The bluff body produces stagnation points and recirculation zone in the flow where the flame can be stabilized. The flame is unsteady due to the turbulent fluctuations in the flow. The unsteady fluctuations of the flame and the fluctuations in the acoustic field of the combustion chamber is in feedback with each other. At certain conditions, the feed back is positive causing growth of amplitude of periodic acoustic pressure oscillations inside the combustion. The amplitude of oscillations eventually saturates as the losses (damping) due to the nonlinearities in the system increase with the increase in the amplitude of acoustic pressure oscillations. Such pressure oscillations are known as thermoacoustic instability.

The acoustic pressure fluctuations in the combustion chamber is measured using a pressure transducer (PCB103B02) at  $1 \times 10^4$  samples per second. The fuel used is LPG (40% Butane, 60% Propane). The flow rate of partially premixed air-fuel mixture is varied in a quasi steady manner by increasing the air flow rate for a fixed fuel flow rate (1.04 g/s). This also reduces the equivalence ratio,  $\phi$ , of the fuel-air mixture defined as the ratio of actual fuel-air mass flow rate ratio to the stoichiometric fuel-air mass flow rate ratio. As  $\phi$  reduces by increasing the airflow rate, initially the pressure fluctuations change from aperiodic oscillations to thermoacoustic instability via intermittency. On further reduction of  $\phi$ , the pressure oscillations exhibits intermittency post thermoacoustic instability. When  $\phi$  is reduced further, we approach flame blowout. Flame blowout is a phenomena where the flame loses its ability to stabilize inside a combustion chamber and hence undergoes extinction. Prior to flame blowout, the pressure oscillations have low amplitude and are aperiodic. Further details of the experimental setup (Fig. 5.8) and different dynamic regimes are detailed in [48].

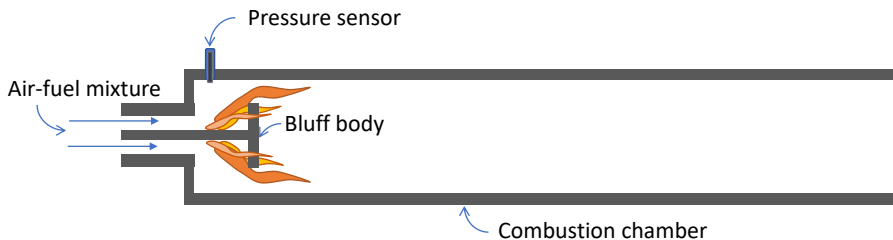


**Figure 5.8:** Schematic illustration of the combustion chamber employed in the experimental setup.

### 5.4.2 Results

The different operating conditions of a thermoacoustic combustor have been extensively studied in the literature both in laboratory conditions and model system data [99]. Measures based both on RPs and recurrence networks have been successfully applied to detect dynamical transitions between different regimes [102, 49]. Prior to our analysis, we can already give a brief classification of the different dynamical states based on these insights. Figure 5.9 shows the full time series in the bottom panel and enlarged segments with normalized amplitude of it in the top panel. The first segment shows combustion noise ( $\mathcal{X}_1$ ) which is the general term for stable operating conditions. It is comprised of low amplitude aperiodic pressure fluctuations which can be classified as chaotic dynamics. Every dotted gray line in the lower panel marks a decrease in  $\phi$ . In this sense, each three second sub-time series should be regarded as a separate experiment with constant parameters and will be evaluated as such in the following. As  $\phi$  is discontinuously increased along the time axis, we observe a dynamical state characterized by aperiodic oscillations interrupted by large amplitude harmonic oscillations. This state is generally referred to as intermittency ( $\mathcal{X}_2$ ) and is observed as a transition state between aperiodic oscillations and thermoacoustic instability. The third zoomed segment shows thermoacoustic instability ( $\mathcal{X}_3$ ) which is constituted by periodic large amplitude pressure fluctuations. As  $\phi$  is increased further, the periodic oscillations subside and a different state of intermittency ( $\mathcal{X}_4$ ) is observed which we will refer to as intermittency after instability (in contrast to intermittency prior to instability). The last segment again shows aperiodic oscillations of low amplitude which are a precursor of an impending blowout situation where the flame can not longer be sustained ( $\mathcal{X}_5$ ).

In order to carry out our analysis, an adequate phase space embedding is required for the measured time series as the underlying system should be regarded as high-dimensional. We apply the mentioned standard methods to fix a suitable embedding delay and dimension. Since we aim at analysing the dynamics of the combustor for a range of parameters, we estimate common embedding parameters appropriate for all different dynamical states. To also evaluate significance of our results for RL, we apply a sliding window analysis to the time series. We choose a window size of 900 ms with 95% overlap between consecutive windows while no overlap is allowed between the different sub-time series with fixed  $\phi$ . We ensured that all of the following results are robust in a reasonable range of window and overlap widths. A sufficient tradeoff for all time series segments is obtained by analysing how strongly both embedding parameters fluctuate for the different regimes in time. Embedding delay is maximum for combustion noise and it decreases towards enhanced periodic oscillations. Highest average embedding dimensions are estimated for intermittency prior to instability. We conclude that our global parameter choice of  $d = 5$ ,  $\tau = 23$  is suitable for further analysis.

Based on this choice, we compute RPs on sliding windows based on the delay-embedded phase space trajectory of the system. We choose a threshold  $\varepsilon$  such that it yields constant recurrence rate of 10% for all RPs. All results are qualitatively sustained for reasonable variations of  $\varepsilon$ . For a visual impression of RPs of a similar system, the reader is pointed to [101, 102]. The procedure is now carried out as follows: we first calculate a RL curve for each obtained RP which refers to a certain time instance for fixed  $\phi$ . We concatenate the entire set of RL curves to illustrate them in the same fashion as for the synthetic data examples to display variations of complexity on all time scales. Additionally, we classify the different dynamical regimes by scale-averages of the RL curves. In order to estimate scale averages of RL, we first average all RL curves for fixed  $\phi$  obtained from the sliding window analysis. Next, we average RL values for time scales  $w \leq 1$  ms,  $1 \text{ ms} < w < 100$  ms and  $w \geq 100$  ms separately. Note that these groups cover different numbers of RL values. The results are shown in Fig. 5.9.

In the lower panel, we observe a gradual descent of RL at all time scales  $w$  from combustion

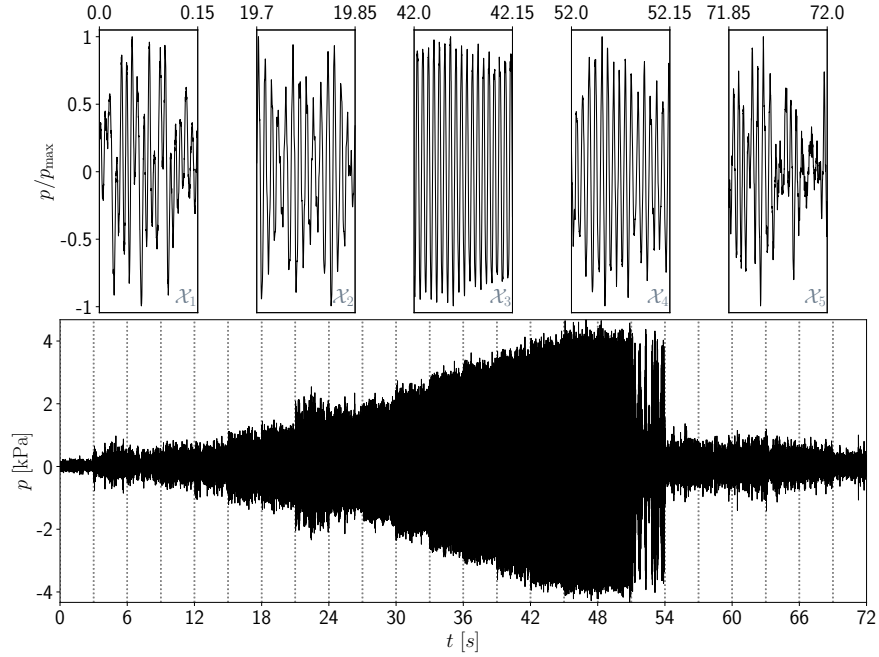
noise into the impending instability, interrupted by spikes of varying amplitude. The overarching trend until about 51s shows a reduction in dynamic complexity from the aperiodic, chaotic oscillations during stable operation into periodic oscillations during thermoacoustic instability. By means of RL, we can interpret this decrease as weakened heterogeneity of recurrences, entailing that the system shows temporal patterns with less strong variability as it approaches the instability regime. The intermittency route into instability becomes well visible by the shape of the RL curves: the cut-off value of the truncated power law decay is continuously reduced, displaying a significant shift of characteristic time scales in the pressure fluctuations of the combustor. Cut-off values can be inferred approximately from the graph by tracking sudden color switches. In the range between 24 – 38s, intermittency manifests itself in the episodic reduction of large scale heterogeneity in the RPs. The system jumps between harmonic and aperiodic oscillations and thus shifts its characteristic time scale discontinuously until multiple coexisting periods (horizontal yellow lines) are reduced to a single dominant period. A sharp rise of RL at all scales marks the slow intermittency regime prior to the near blowout situation. The average level of complexity during this lean blowout state appears close to that observed for combustion noise at the beginning of the measurement series. In the upper panel, the scale-averages yet uncover a difference in sub-ms RL between combustion noise and lean blowout state: the aperiodic oscillations in the former regime seemingly occur in a more heterogeneous fashion than for the latter. The two other scales-averages do not indicate a remarkable difference between these two regimes. Note that the scale averages are rescaled to  $[0, 1]$  for better comparison. Consequently, RL enables us to detect five distinct regimes and to track respective variations in the characteristic time scale of the system. These findings generally corroborate those from earlier studies. Furthermore, it detects a subtle difference in the complexity between the dynamically similar combustion noise state and the near blow out situation.

## 5.5 Conclusion

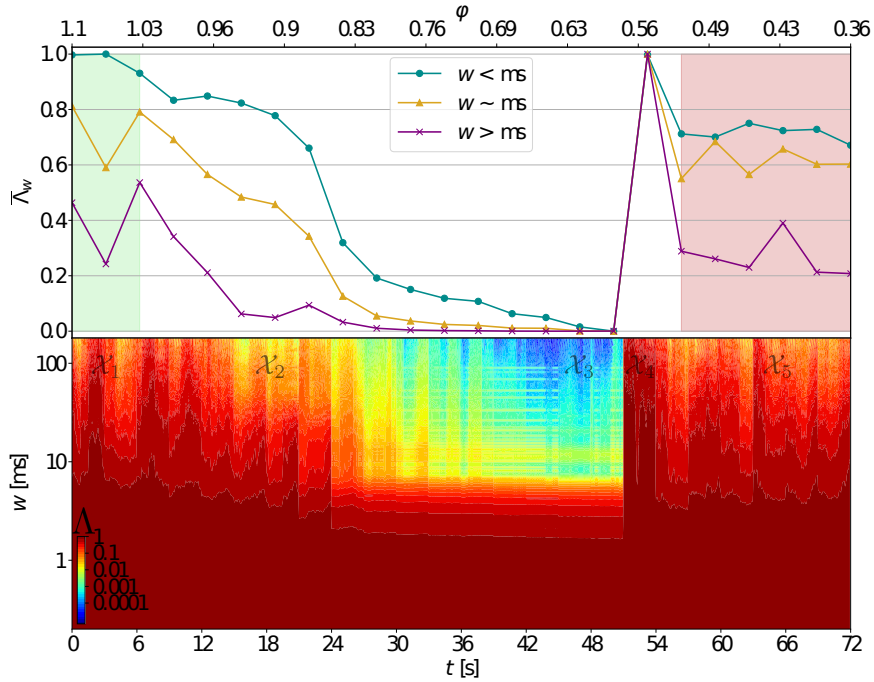
We have put forward a novel recurrence quantification measure to quantify the degree of complexity of nonlinear time series, namely recurrence lacunarity. The identification of different dynamical regimes in multiple real-world applications has attracted a lot of interest in the literature. The method we propose contributes to this toolbox of complexity indicators by representing a time series as a recurrence plot and characterizing its heterogeneity on all time scales relevant to the system. Even though both recurrence plots and lacunarity are broadly acknowledged as powerful stand-alone tools, we have demonstrated that their combination can yield valuable insights in the context of regime shift detection.

The method’s main advantage is that it is able to capture multiscale features of the recurrence plot while traditional measures are based on line structures which can always only encode a certain aspect of the dynamics. Our approach does not require specification of minimum line lengths. It naturally yields information both on the heterogeneity of recurrence plots and their scaling properties, opening up a new perspective of analysing point statistics in partitioned RPs rather than constricted structures. We have shown that the applicability of lacunarity to general nonlinear dynamical systems by means of the well established recurrence plot approach can be fruitful.

As this work’s main focus was on the identification of dynamical regime shifts, we have studied three different paradigmatic systems in detail to showcase the potentials of the method. We have found that the proposed method is able to uncover transitions of different origin even in presence of noise and for short time series which makes it broadly applicable to many real-world phenomena. We have further demonstrated that recurrence lacunarity may also be useful in characterizing subtle transitions of different nature.



(a) Enlarged, normalized time series segments of different dynamical regimes and the entire measurement time series of acoustic pressure in kPa. Each fixed parameter window covers a duration of three seconds. The displayed dynamical states are referred to as combustion noise ( $\mathcal{X}_1$ ), intermittency prior to instability ( $\mathcal{X}_2$ ), thermoacoustic instability ( $\mathcal{X}_3$ ), intermittency after instability ( $\mathcal{X}_4$ ) and near-blowout oscillations ( $\mathcal{X}_5$ ) respectively.



(b) Scale-averaged lacunarities  $\bar{\Lambda}_w$  and RL curves for full time series computed on sliding windows of 900 ms width. In the upper panel, green and red shading indicate combustion noise ( $\mathcal{X}_1$ ) and near blowout oscillations ( $\mathcal{X}_5$ ) respectively. Air flow rate is increased in a quasi-static manner after maintaining it steady for a duration of 3 seconds. In the lower panel,  $w$ -axis and color coding are scaled logarithmically.

**Figure 5.9:** Application of RL to acoustic pressure fluctuation time series from a thermoacoustic combustor.

In comparison to DET as a traditional recurrence quantifier, it showed comparable well performance for noisy time series. Even though the results were less convincing for a short time series, RL performed superior for subtle transitions in the bistable system.

Finally, we have employed a system exhibiting thermoacoustic instability to study whether our approach enables us to detect regime shifts in an (experimental) real world system. Our method has enabled us to identify the different dynamical transitions that the system undergoes. We found that the intermittency route from stable operation into thermoacoustic instability manifests itself as a continuous transition from aperiodic to harmonic oscillations. We have ultimately addressed the challenge of differentiating between the dynamically similar but practically different states of stable operation and a near blowout situation. It appeared that short-term acoustic pressure fluctuations show less variable temporal recurrent patterns during a near-blowout situation than during regular operating mode. How this can be interpreted and whether it can also be captured in terms of (nonlinear) serial dependence should be addressed in future work.

Furthermore, it appears as a promising direction for future work to investigate in more detail the relations between the fractal scaling of RPs and fractality of the underlying time series and the attractor dimension. Including RL in feature selection approaches may also improve the performance of machine learning techniques that classify nonlinear data [104]. Another line of research should be concerned with the robustness of the proposed method against spurious effects introduced by erroneous embedding and RP related pitfalls when compared to traditional RQA measures [78, 79].

## Acknowledgements

This research was supported by the Deutsche Forschungsgemeinschaft in the context of the DFG project MA4759/11-1 ‘Nonlinear empirical mode analysis of complex systems: Development of general approach and application in climate’, the DFG project MA4759/9-1 ‘Recurrence plot analysis of regime changes in dynamical systems’ and it has received funding from the European Union’s Horizon 2020 research and innovation programme under grant agreement No 820970 as a TiPES contribution. RIS acknowledges the Science and Engineering Research Board (SERB) of the Department of Science and Technology, Government of India for the funding under the grant Nos.: DST/SF/1(EC)/2006 (Swarnajayanti Fellowship) and JCB/2018/000034/SSC (JC Bose Fellowship). VRU thanks University of California San Diego for the postdoctoral fellowship.

## Conflict of interest

The authors declare that they have no conflict of interest.



# 6 | Recurrence flow measure of nonlinear dependence

Tobias Braun<sup>1</sup>, K. Hauke Kraemer<sup>1</sup>, Norbert Marwan<sup>1,2</sup>

1 – Potsdam Institute for Climate Impact Research, 14473 Potsdam, Germany

2 – University of Potsdam, Institute of Geosciences, Potsdam, Germany

*Braun, T., Kraemer, K. H., & Marwan, N. (2022). Recurrence flow measure of non-linear dependence. accepted for EPJ ST*

## Abstract

Couplings in complex real-world systems are often nonlinear and scale-dependent. In many cases, it is crucial to consider a multitude of interlinked variables and the strengths of their correlations to adequately fathom the dynamics of a high-dimensional nonlinear system. We propose a recurrence based dependence measure that quantifies the relationship between multiple time series based on the predictability of their joint evolution. The statistical analysis of recurrence plots (RPs) is a powerful framework in nonlinear time series analysis that has proven to be effective in addressing many fundamental problems, e.g., regime shift detection and identification of couplings. The *recurrence flow* through an RP exploits artifacts in the formation of diagonal lines, a structure in RPs that reflects periods of predictable dynamics. By using time-delayed variables of a deterministic uni-/multivariate system, lagged dependencies with potentially many time scales can be captured by the recurrence flow measure. Given an RP, no parameters are required for its computation. We showcase the scope of the method for quantifying lagged nonlinear correlations and put a focus on the delay selection problem in time-delay embedding which is often used for attractor reconstruction. The recurrence flow measure of dependence helps to identify non-uniform delays and appears as a promising foundation for a recurrence based state space reconstruction algorithm.

## 6.1 Introduction

Measures of statistical dependence represent one of the cornerstones in the analysis of empirical data. The study of time series measured from complex real-world systems poses a broad variety of challenges in quantifying uni- and multivariate data sets, e.g., lagged dependencies, non-stationarity, noise contamination, uncertainties and the limited length of time series. The set of tools to detect and quantify statistical dependencies ranges from standard correlation analysis techniques [105] over graph theoretical approaches, such as complex

networks [106, 107], towards causal discovery algorithms [108, 109, 110], and detecting critical transitions [111, 112, 113]. A notoriously challenging problem is to adequately quantify non-monotonous and nonlinear relationships in stochastic and deterministic systems. In this context, information theoretic measures have established as an effective framework [114, 115, 116]. However, popular methods, such as the mutual information (MI), are not designed to treat higher-dimensional data appropriately (even though extensions have been suggested [117, 118]). The nature and strength of links in complex systems additionally often exhibits scale-dependence, i.e., multi-scale behaviour [119]. This motivates the need of methods that are capable of unravelling dependencies at a broad range of scales, e.g., wavelet based methods [120, 121, 1]. Few methods succeed to combine both capabilities of capturing nonlinear dependencies at multiple time scales [122, 75].

A powerful method that captures both nonlinear and multi-scale properties of a high-dimensional dynamical system is the recurrence plot (RP) [19]. An RP is a mathematically simple yet effective tool that encodes the tendency of a time series to recur to formerly visited states [20]. An RP is based on a binary recurrence matrix in which recurrences are marked by value one, giving rise to intriguing and well-interpretable structures in the RP. Various quantification measures can be applied to a recurrence matrix and prove powerful in classifying differing systems [123, 124, 125, 126], identifying dynamical regime transitions [21, 29], and detecting non-linear correlations as well as synchronization [110, 127, 22]. Recurrence quantification analysis (RQA) based on diagonal lines in the RP not only allows identification of periodic behaviour [128, 1], but also helps to identify unstable periodic orbits in high-dimensional chaotic systems [129]. The conceptual simplicity of RPs allows for a broad range of real-world applications, also for challenging data that is event-like or unevenly sampled in time [130, 131]. Recurrence measures of dependence have not only facilitated the study of synchronization in dynamical systems [132, 133, 134, 22] but have also been extended to account for lagged and conditional dependencies [127, 135, 136, 110]. Further concepts, including symbolic analyses of relationships, have been conceived more recently [137]. Recurrence based quantification of statistical dependencies, thus, bares high potential to meet the combination of above mentioned challenges. Here, we propose a novel recurrence based measure of dependence that uses delay coordinates from a given observational time series. Since the measure is based on RPs, nonlinear dependencies with multiple time lags can be quantified which makes the measure applicable to the problem of non-uniform delay selection [122, 75]. The proposed dependence measure, thus, contributes to the challenge of characterizing complex real-world interactions using RPs.

This work is structured as follows: in Sect. 6.2, we introduce the recurrence flow as a measure of dependence along with a brief review of the RP method. We showcase its scope in different numerical experiments in Sect. 6.3, covering the characterization of lagged nonlinear dependence and delay selection for uniform and non-uniform TDE. We conclude our findings in Sect. 6.4.

## 6.2 Recurrence Flow

We are interested in characterizing nonlinear dependencies in a deterministic, high-dimensional system that is represented by  $M$  observational time series  $\{s_n(t) \mid n = 1, \dots, M\}$ . In general, the relationships between the different time series  $s_n(t)$  and their coordinates do not need to be instantaneous but are often associated with time delays  $\tau_1, \tau_2, \dots, \tau_m$ . Consequently, we define the recurrence flow measure of redundance to capture such lagged dependencies.

The key idea of the proposed measure is based on the existence of diagonal lines in RPs. An RP is a two-dimensional matrix that encodes how a system recurs to formerly visited



states  $\vec{v}_i$ ,  $i = 1, \dots, N$ . In general, this representation can be computed for systems of any dimension  $d$  and is formally given by

$$R_{i,j}(\tau) = \Theta(\varepsilon - \|\vec{v}_i(\tau) - \vec{v}_j(\tau)\|) = \begin{cases} 1 & \text{if } \|\vec{v}_i(\tau) - \vec{v}_j(\tau)\| \leq \varepsilon \\ 0 & \text{if } \|\vec{v}_i(\tau) - \vec{v}_j(\tau)\| > \varepsilon \end{cases}. \quad (6.1)$$

with two arbitrary times  $i$  and  $j$ , the vicinity threshold  $\varepsilon$  and a suitable norm  $\|\cdot\|$ . The states denoted by  $\vec{v}$  are either given by the available components (state variables) of the system or, in case of only limited access to the state variables, by delayed copies of the one (or multiple) observational time series  $s_n(t)$  of the studied system. In particular,  $\vec{v}$  is then obtained by stacking these copies on top of each other as it is common practise in time delay embedding (TDE).

Diagonal lines of length  $L_d$  in an RP resemble periods of enhanced predictability as two trajectory segments at times  $i$  and  $j$  evolve in parallel in an  $\varepsilon$ -tube for  $L_d$  time instances. For a given system, this may reveal time periods of continuously high determinism or uncover abrupt regime shifts [24]. Properties of the diagonal line length distribution of an RP are linked to dynamical invariants of paradigmatic dynamical systems [138]. However, spurious artifacts are known to disrupt, lengthen or thicken diagonal lines due to erroneous computation of an RP [78]. An inadequate choice of the vicinity threshold  $\varepsilon$  will disrupt diagonal lines, thus, underestimating the system's predictability. On the other hand, too high values will artificially merge fundamentally distinct regions of phase space. Sampling can also alter diagonal line structures: if the system is undersampled, diagonal lines might not emerge continuously as deterministic time intervals are not resolved sufficiently. On the other hand, oversampling results in artificially thickened diagonal lines (*tangential motion*) [79]. Erroneous time delay embedding of uni-/multivariate time series can have several undesired effects on the formation of diagonal lines; if the embedding dimension is chosen too high, diagonal lines are artificially lengthened and can even emerge in absence of determinism for an uncorrelated stochastic process due to correlations in the underlying distance matrix [139]. A non-optimal choice for the embedding delay will result in diagonal lines that are perpendicular to the line of identity ( $i = j$ , LOI). This indicates inclusion of erroneous time scales [78]. The formation of perpendicular lines is caused by the ambiguity in the reconstruction that is introduced by not eliminating the full serial dependence; this results in close evolution of states both forward and backward in time:  $\|\vec{v}_i - \vec{v}_j\| < \varepsilon$ ,  $\|\vec{v}_{i+1} - \vec{v}_{j-1}\| < \varepsilon$ , i.e., the trajectory segments closely evolve in parallel, but with opposite time directions. On top of that, additional deformations to a diagonal line can occur, e.g., in form of bowed diagonal lines indicating that the evolution of states at different time intervals is similar but occurs with different velocity or temporal resolution [140].

We utilize the formation of such diagonal line artifacts (DLA) to identify time scales of the system that result in well-expressed diagonal lines. The proposed method is, thus, based on the assumption that the studied system exhibits (at least to some degree) deterministic dynamics which will result in meaningful diagonal lines in an RP. An effective way of retrieving information on the formation of DLA is given by scanning an RP diagonal-wise. We can identify an index for each diagonal at which the first recurrence pixel is located. It appears intuitive to regard these pixels as 'obstacles' to an imaginary fluid that flows along each diagonal into the RP and is not allowed to turn (Fig. 6.1C/E). The formation of DLA blocks the flow. As a basic example, we consider a noisy sinusoidal time series (Fig. 6.1A) with  $n = 5,000$  and a period of  $T = 100$ . Formation of perpendicular diagonal lines for  $\tau = \mu T$ ,  $\mu \in \mathbb{N}$  (Fig. 6.1B) reduces the flow through the RP compared to  $\tau = T/4$  (Fig. 6.1D). We use the symmetry of the RP by only flooding the upper triangular matrix to save computation time. The recurrence flow  $\Phi(\tau)$  can be computed for varying delays  $\tau$  and encodes similar information as an inverse autocorrelation function, yielding a continuous representation of

the redundancy between the time series and its delayed version (Fig. 6.1F). For continuous variations of  $\tau$  from  $\tau = 0$  to  $\tau = T/4$ , the perpendicular diagonal lines are progressively eliminated. This reproduces the well-known result that a sinusoidal signal needs to be shifted by (odd multiples of) a quarter of its period against itself to minimize redundancy.

To quantify the flow through the RP, we define the recurrence flow matrix  $\phi$  (Fig. 6.1C/E)

$$\phi_{i,j}(\tau) = \left(1 - \Theta(\varepsilon - \|\vec{v}_i(\tau) - \vec{v}_j(\tau)\|)\right) \Theta(\ell_j - i), \quad i, j = 1, \dots, N \quad (6.2)$$

with the time delay  $\tau$  and the length  $\ell_j$  of the  $j^{\text{th}}$  flooded diagonal, i.e., the number of subsequent zeros up to the first one. A flooded diagonal  $\ell_j$  has to be distinguished from a diagonal line  $L_d$ : it denotes a diagonal of the RP (parallel to the LOI) starting at time instance  $j$  that is flooded with a fictive fluid, regardless of whether any diagonal lines exist on this diagonal. Accordingly, the factor  $\Theta(\ell_j - i)$  in eq. (6.2) ensures that the flooding of the  $j^{\text{th}}$  diagonal stops at the first recurrence on this diagonal.  $\phi_{i,j}$  depends on the vicinity threshold  $\varepsilon$ , i.e., the fraction of recurrences. We fix  $\varepsilon$  at some reasonable value that corresponds to a fixed recurrence rate (RR).

We study the dependence on the time delay  $\tau$  contained in the vector  $\vec{v}(\tau)$  similar as it is done in TDE where the delays  $\tau_1, \tau_2, \dots, \tau_m$  for the different coordinates are free parameters and need to be chosen with respect to some notion of optimality [141]. The recurrence flow  $\Phi(\tau)$  is computed by summing over the recurrence flow matrix  $\phi_{i,j}$  at given  $\tau$  and dividing by the number of non-recurrences (i.e., zeros in the RP):

$$\Phi(\tau) = \frac{\sum_{i,j=1}^N \phi_{i,j}(\tau)}{\sum_{i,j=1}^N (1 - R_{i,j}(\tau))}. \quad (6.3)$$

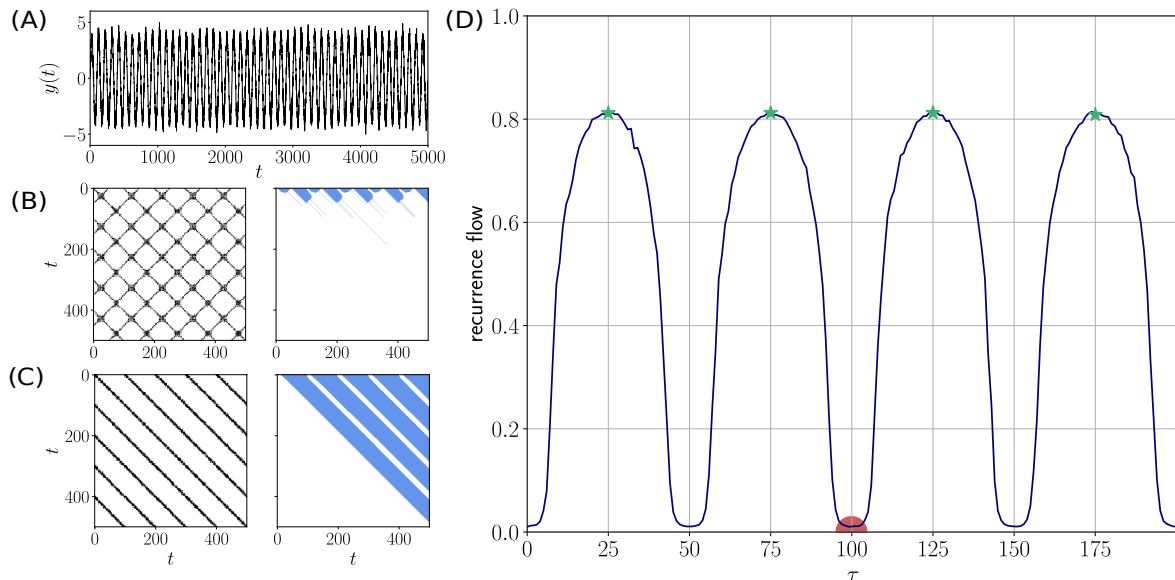


**Figure 6.1:** Recurrence flow for a noisy sinusoidal. (A) Time series of the noisy sinusoidal and (B/C) RPs for two different embedding vectors  $\vec{v}(t)$ :  $\vec{v}(t) = [y(t), y(t+T)]$  and  $\vec{v}(t) = [y(t), y(t+\frac{T}{4})]$  (left) and flooded RPs/recurrence flow matrices (right). (D) Recurrence flow  $\Phi(\tau)$  through the RP for varying delay  $\tau$ . The red dot marks the period  $T$ .  $\Phi(\tau)$  is maximized for delays that are odd multiples of  $T/4$ .

In a multivariate application,  $\vec{v}$  can encompass time series from different systems to study their cross-dependencies. In such a scenario, it is more instructive to define the recurrence flow

as a direct measure of correlation/redundance. We, thus, define the recurrence flow measure of redundancy (RFMR)  $\theta(\tau)$  as

$$\theta(\tau) = 1 - \Phi(\tau). \quad (6.4)$$

The significance of recurrence flow values can be tested against a random null model based on uncorrelated white noise (App. B). Finally, it needs to be noted that the idea of using RPs to identify optimal embedding parameters has been considered before, but to our best knowledge has not been performed systematically [142, 143].

### 6.3 Application to Model Examples

We now demonstrate the scope of the proposed method by highlighting two different potential applications: the quantification of nonlinear correlations (Sect. 6.3.1) and the identification of uniform embedding delays for TDE of nonlinear signals (Sect. 6.3.2).

#### 6.3.1 Nonlinear Dependence

We exemplify the efficacy of  $\theta(\tau)$  as a nonlinear dependence measure for deterministic systems with a simple bivariate system:

$$\begin{aligned} x(t) &= \sin(2\pi t/\omega) + \eta(t, \sigma_1) \\ y(t) &= ax(t - \tilde{\tau})^2 + \eta(t, \sigma_2) \end{aligned} \quad (6.5)$$

with frequency  $\omega = 2\pi/T$ , period  $T$ , time lag  $\tilde{\tau} = 20$ , and normal-distributed white noise processes  $\eta(t, \sigma)$  with standard deviations  $\sigma_1$  and  $\sigma_2$ . This system exhibits a sinusoidal cycle with frequency  $\omega$  in its  $x$ -component. The  $y$ -component is nonlinearly coupled to  $x(t)$  and exhibits a cycle with half of the period of  $x(t)$ .  $y(t)$  follows  $x(t)$  with a fixed time lag  $\tilde{\tau}$ . Both components are superimposed by measurement noise  $\eta(t)$ . We consider time series with  $n = 5,000$  samples (Fig. 6.2A). Due to the specific coupling, the relationship between  $x$  and  $y$  is nonlinear (Fig. 6.2B).

We test whether we can detect the coupling and the corresponding time lag  $\tilde{\tau}$  by computing  $\theta(\tau)$  for delays in the range  $\tau \in [-200, 200]$  (Fig. 6.2C). In fact, we find that  $\theta(\tau)$  reaches local maxima at integer multiples of  $\tilde{\tau}$ , including  $\tau = \tilde{\tau}$  (red dashed line). Similar results are obtained if the mutual information is used (Fig. 6.2C, black curve), confirming that nonlinear relationships between deterministic time series can be captured by recurrence flow in presence of measurement noise. In this case, the MI yields sharper peaks than the recurrence flow. However, the suggested recurrence flow measure provides advantages for high-dimensional data as discussed below.

#### 6.3.2 Uniform Time Delay Embedding

The ability of the recurrence flow to detect delayed dependencies between multiple variables motivates its use in the delay selection problem faced in TDE. Proficient delay selection must be based on a measure that captures the redundancy in a (potentially large) set of correlated time series.

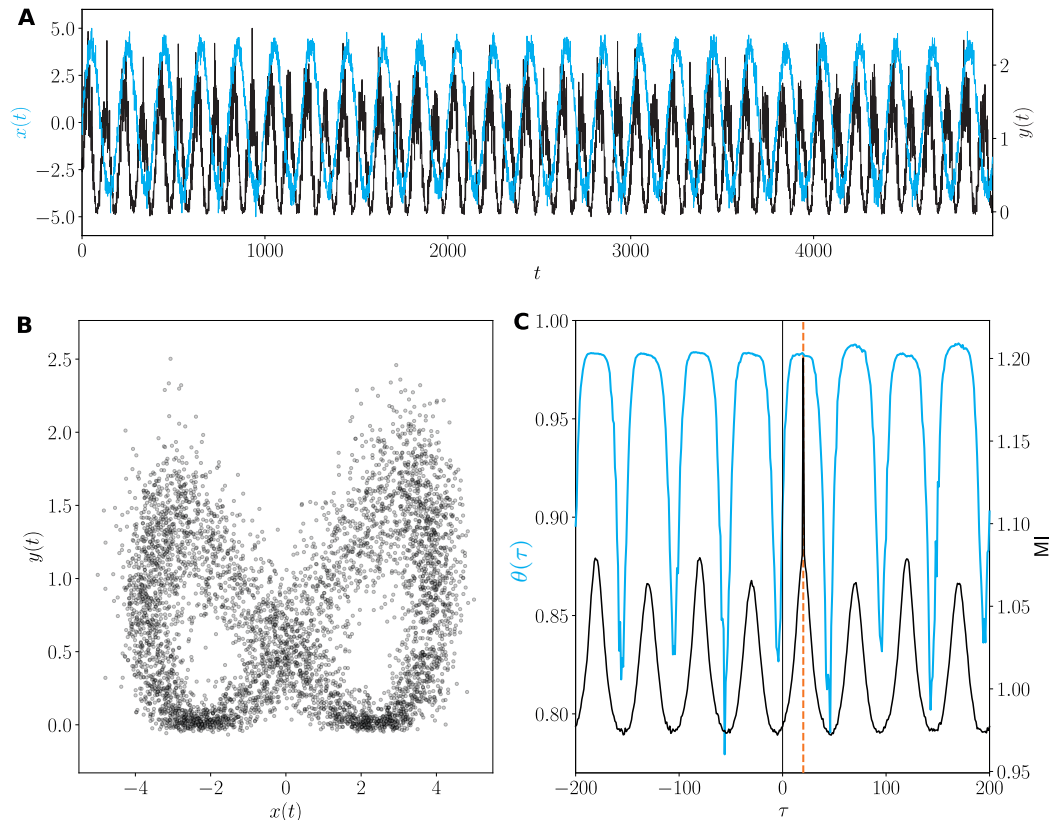


**Figure 6.2:** Detection of lagged, nonlinear dependence between nonlinearly coupled sinusoids. (A) The  $y(t)$  time series (black) results from squaring  $x(t)$  (blue) and shifting it by a fixed time delay. (B) Nonlinear relationship between  $x(t)$  and  $y(t)$ . (C) Recurrence flow measure of redundance  $\theta(\tau)$  (blue) detecting the time delay between  $x(t)$  and  $y(t)$  (red dashed line), confirmed by the cross-mutual information (black).

A popular solution is to use mutual information (MI). However, characterizing the required joint probability density function  $p(s_1, s_2, \dots, s_m)$  becomes cumbersome for a large number of variables  $m$  and is rendered infeasible for many high-dimensional real-world systems. Compared to nonlinear correlation measures like standard MI that are based on binning, recurrence flow offers the advantage that computation times increase less rapidly: given  $k_m$  bins, an increase in dimensionality  $m \rightarrow m + 1$  results in  $(k_m - 1)k_m$  additional bins while in the computation of  $\Phi$ , a  $k$ - $d$ -tree nearest neighbour search based RP computation increases only linearly with the dimensionality of the system. It has yet to be noted that more sophisticated nearest neighbour based approaches for MI computation do not suffer from this drawback [118].

Due to the popularity of this problem, other nonlinear correlation measures that do not suffer from the curse of dimensionality have been conceived [144, 75]. In order to validate the effectiveness of the measure proposed here for selecting embedding delays, we do not only compare it to the linear autocorrelation function (ACF) and the auto-mutual information (MI), but also to the delay selection method proposed in [75]: the *continuity statistic* is based on a hypothesis test of whether a component, added to an existing  $m$ -dimensional reconstruction vector, is functionally independent of all existing  $m$  components. This is tested by first defining a set of fiducial points and their  $k$ -nearest neighbours from the  $m$ -dimensional reconstruction vector. These are mapped onto the one-dimensional number line. The continuity statistic  $\langle \varepsilon^* \rangle(\tau)$  denotes the smallest scale at which the number of observed neighbours mapped onto this line is larger than the number expected from a binomial distribution, im-

plying a functional relationship. For further details the reader is referred to [75, 145]. For the estimation of the optimal embedding dimension, we employ Cao’s method with a threshold of  $\Delta_{\text{afn}} = 0.2$  for the change of the number of averaged false neighbors from  $m \rightarrow m + 1$  [74]. For the selection of embedding delays using the proposed recurrence flow measure, we identify all peaks of  $\Phi(\tau)$  at different delays  $\tau$  and choose the highest of these to obtain the corresponding embedding delay  $\tau^{(\Phi)}$ . In case there is several peaks of identical height, we choose the one for the smallest  $\tau$  (i.e., the first one).

To illustrate the procedure, we consider a time series of the past 1 million years of insolation on Earth at  $52.39^\circ$  latitude (see App. B) [146]. The insolation depends on the Earth orbit and the Earth axis tilt and precession, thus, varies in specific cycles (Milankovich cycles). Cao’s method suggests an embedding dimension  $m = 4$ . We present results for the second and third component of the embedding vector. By using first-crossing of ACF and first minimum of MI, both measures suggest a delay of  $\tau_1^{(\text{ACF})} = \tau_1^{(\text{MI})} = 6 \text{ ka}$  (Fig. 6.3A). Since none of both measures is capable of selecting different embedding delays for higher components of the embedding vector, this yields the three-dimensional embedding vector  $\vec{v}(t) = [y(t), y(t - 6 \text{ ka}), y(t - 12 \text{ ka})]$ . Next, we compute  $\Phi(\tau)$  to check if the estimate of  $\vec{v}(t)$  based on the traditional TDE metrics is confirmed: we find  $\tau_1^{(\Phi)} = 5 \text{ ka}$  in close agreement with the ACF and MI-criteria (Fig. 6.3C). Moreover, the continuity statistic  $\langle \varepsilon^* \rangle(\tau)$  suggests the same embedding delay for the first component as the auto-correlation and MI (first local maximum). It does not indicate a global maximum at this delay, yielding a more ambiguous choice of the optimal embedding delay than  $\Phi(\tau)$ . Finally, we examine if both multi-dimensional measures suggest  $\tau_2 = 2\tau_1$  for the second embedding delay as expected for a traditional uniform time delay embedding (UTDE). Interestingly,  $\langle \varepsilon^* \rangle(\tau)$  offers only limited information on an optimal embedding delay for the third component of  $\vec{v}(t)$  (Fig. 6.3D). Multiple local maxima offer a variety of choices with no clear optimal value. We choose the global maximum (marked by star). Conversely,  $\Phi(\tau)$  once more provides a clear choice for the second embedding delay with globally maximized flow for  $\tau_2^{(\Phi)} = 2\tau_1^{(\Phi)}$ .

We visually evaluate the quality of the resulting embeddings by comparing the line structures in the corresponding RPs (Fig. 6.3E). The enlarged details of the RPs illustrate how well deterministic intervals in the evolution of insolation are resolved based on the phase space reconstructions yielded by the ACF, continuity statistic, and recurrence flow. While the uniform embedding vectors obtained from the ACF and  $\Phi(\tau)$  result in well-separated, undisturbed diagonal lines, multiple diagonal lines and the related cycles are poorly expressed in the phase space suggested by  $\langle \varepsilon^* \rangle(\tau)$ . The reconstructed phase space based on the embedding vector obtained from the recurrence flow criterion reveals several unstable periodic orbits (Fig. 6.3F), constituting a concentric spiral-like phase space trajectory in three dimensions.

Many real-world systems allow taking only a relatively short series of measurements for a single variable with high levels of superimposed measurement noise. We study how well a known phase space of a paradigmatic system can be reconstructed based on the four different measures considered above with increasing noise strength. In particular, we generate  $n = 2,000$  samples of a Rössler system (see App. B) such that the resulting trajectory only covers relatively few unstable periodic orbits. We reconstruct the known three-dimensional phase space from the  $y(t)$ -component (Fig. 6.4A) with superimposed uncorrelated white noise realizations (Fig. 6.4B).

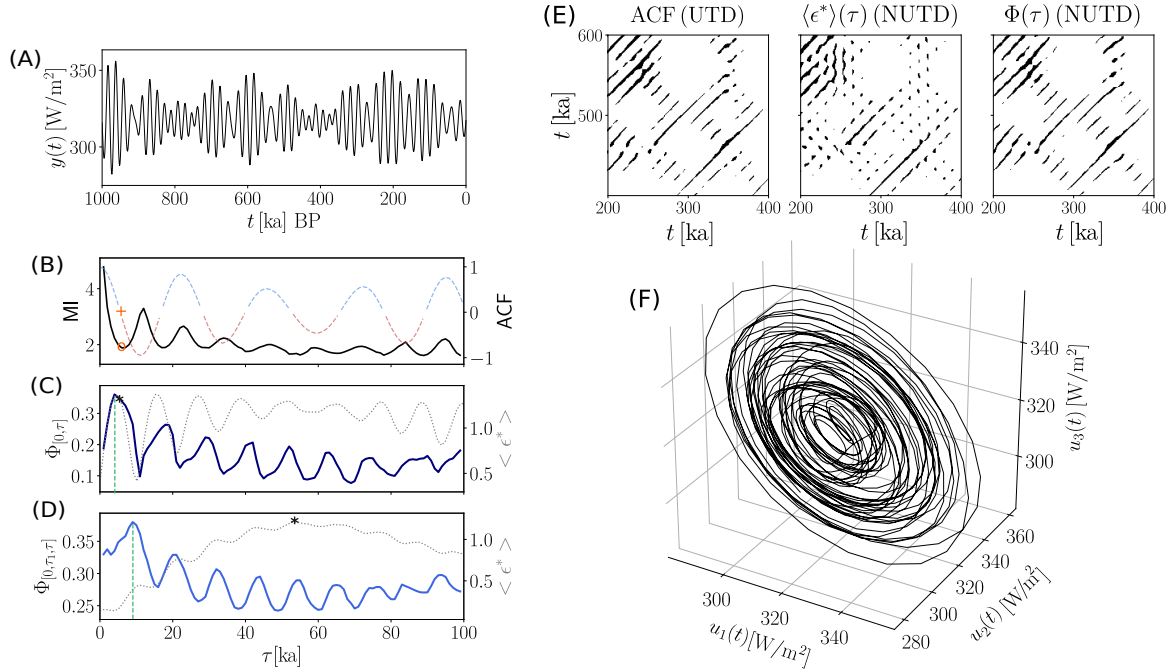


**Figure 6.3:** Uniform delay selection for numerical insolation model. (A) Insolation time series  $y(t)$  in  $\text{W m}^{-2}$ . (B) Serial dependence of  $y(t)$ , measured in terms of ACF (red/blue) and auto-MI (black) for the univariate time series, (C/D) as well as by the continuity statistic  $\langle \epsilon^* \rangle(\tau)$  (gray) and the recurrence flow  $\Phi(\tau)$  (dark blue) for (C) two- and (D) three-dimensional embedding vectors  $\vec{v}(t)$ . The optimal delay is marked by a circle/cross/star/vertical green line) for the ACF(/MI/continuity statistic/recurrence flow), respectively. (E) Zoomed RPs for the ACF,  $\langle \epsilon^* \rangle(\tau)$  and  $\Phi(\tau)$  (from left to right). (F) Three-dimensional phase space reconstruction based on recurrence flow shows a spiral-like trajectory.

The noise strength (standard deviation of the noise) is varied in multiples of the standard deviation  $\sigma_{\text{Roe}}$  of the undisturbed  $y(t)$ . Even with only 10% measurement noise, the original attractor is already significantly less smooth (Fig. 6.4B). We compare the ACF, MI, continuity statistic, and recurrence flow as delay selection measures while only uniform time delays are considered, i.e., the optimal embedding delay is selected only once for the step from a one- to a two-dimensional embedding. This ensures that the two high-dimensional measures ( $\Phi(\tau)$  and  $\langle \epsilon^* \rangle(\tau)$ ) can be compared adequately to the traditional measures.

To quantitatively evaluate the dependence of the reconstruction on noise strength, we generate an RP for each reconstruction and for each of the four delay selection methods. For each RP, we compute the joint recurrence rate fraction (JRRF):

$$JRRF = \frac{\sum_{i,j}^N JR_{i,j}}{\sum_{i,j=1}^N R_{i,j}^{\text{ref}}}, \quad JRRF \in [0, 1]$$

with

$$\mathbf{JR} = \mathbf{R}^{\text{ref}} \circ \mathbf{R}^{\text{rec}}$$

from the RP of the (real) reference system  $\mathbf{R}^{\text{ref}}$  and the RP of the respective reconstruction  $\mathbf{R}^{\text{rec}}$ . We use it to quantify the accordance of the real RP of the corresponding noisy Rössler system to the reconstructions with respect to its recurrence structure (the higher JRRF, the better the reconstruction).

We generate 50 individual noise realizations for each noise strength between 0% and 100% of the original standard deviation  $\sigma_{\text{Roe}}$  and average the corresponding JRRF values

(Fig. 6.4C). As expected, with increasing noise level, the quality of the reconstruction decreases.

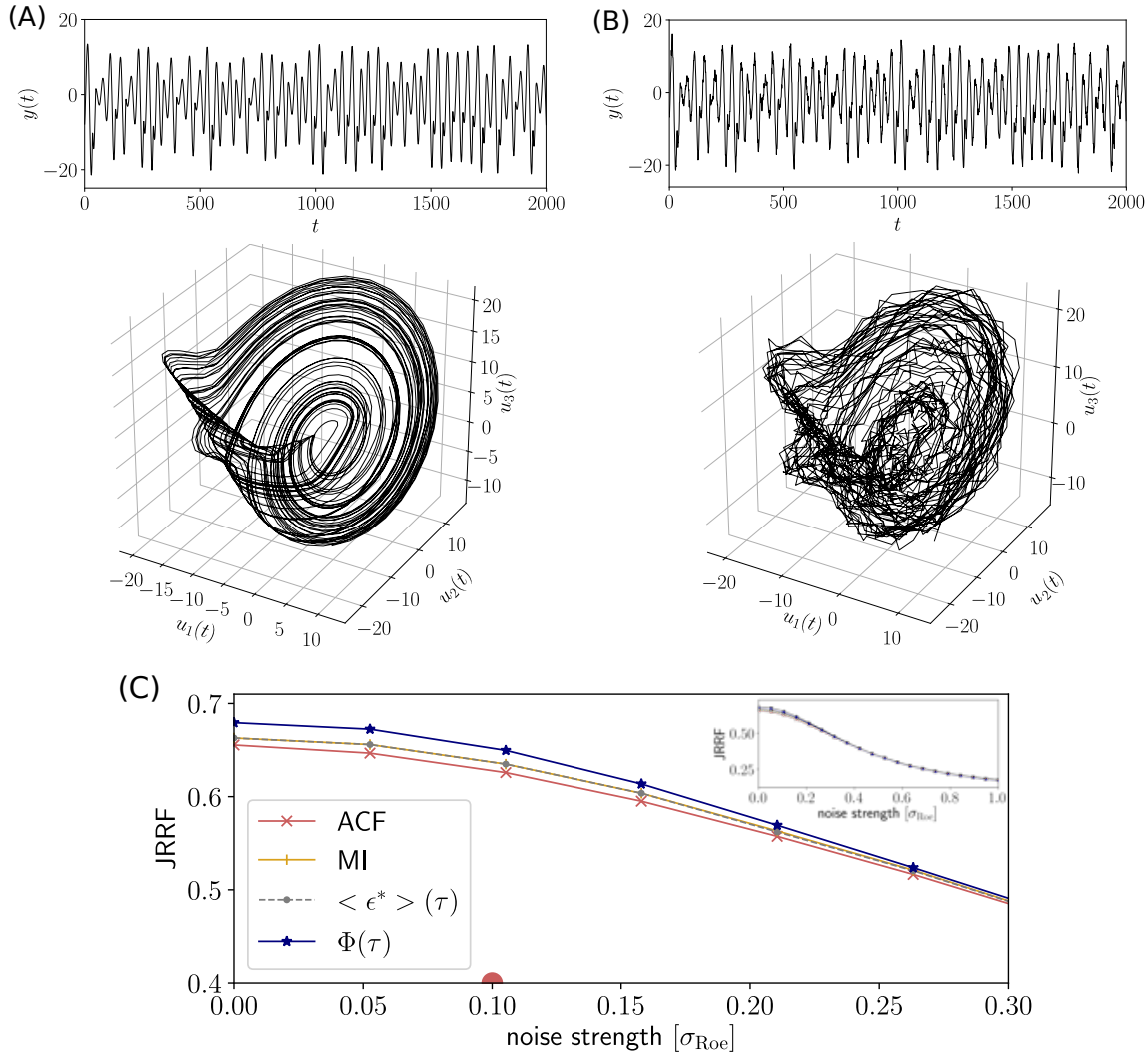


**Figure 6.4:** Sensitivity of recurrence flow against measurement noise, compared to other dependence measures. (A)  $y(t)$ -component and reference phase space of Rössler system without noise contamination; (B) the same, but with 10% measurement noise. (C) Performance of ACF, auto-MI, continuity statistic  $\langle \epsilon^* \rangle (\tau)$  and recurrence flow  $\Phi(\tau)$  in terms of JRRF for noise strengths from 0% to 30% (and 100% inset).

For noise strengths between 10% and 30%, the linear ACF performs worst in terms of JRRF while the MI and continuity statistic perform equally well. The almost perfect alignment of both might seem surprising but is due to the discreteness immanent in the delay selection. While their agreement might be interpreted in the way that this has to be the optimal delay (i.e., the reconstructed system preserves most of the recurrence structure), the recurrence flow  $\Phi(\tau)$  shows superior performance with noise strengths up to 30%, i.e., three times the noise level illustrated in Fig. 6.4B. Beyond 30%, all four measures yield approximately the same performance (Fig. 6.4C inset), as for  $\text{JRRF} < 0.5$ , the alignment could be explained by random joint recurrences.

### 6.3.3 Non-uniform Time Delay Embedding

For many real-world dynamical systems, it is not sufficient to consider only a single characteristic time scale. Instead, multi-scale systems are governed by a multitude of processes that imprint (quasi)-periodic cycles of various lengths onto the measured time series. The selection of delays must account for this complexity by considering non-uniform embedding delays (non-uniform time delay embedding, NUTD). One of the most studied systems that exhibits multi-scale dynamics is the El Niño-Southern Oscillation (ENSO). ENSO represents a quasi-periodic climate pattern that is associated with spatio-temporal variations of sea surface temperatures in the central and eastern Pacific Ocean, oscillating between El Niño and La Niña events. We use the delay differential ENSO model proposed in [147] to examine if the recurrence flow can unveil distinct delays for a three-dimensional state space reconstruction of model time series. The model is based on a nonlinear delay differential equation and reproduces an abundance of key features of ENSO (see App. B). We study two different solution types that are associated with distinct dynamical regimes, i.e., a seasonal oscillation with superimposed faster low-amplitude oscillations prior to a period-doubling and irregular oscillations that are reminiscent of El Niño and La Niña events of random magnitudes. A more detailed discussion of these solution types can be found in [147].

The first solution type exhibits well-pronounced seasonal cycle and fast, amplitude-modulated wiggles on top (Fig. 6.5A). Cao’s method suggests that this solution type can be embedded in a  $m = 3$ -dimensional embedding space. We find that MI does not yield an unambiguous choice for an embedding delay while the ACF suggests  $\tau_1^{(\text{ACF})} = 0.25$  years, i.e., the expected value of a quarter of the seasonal cycle (Fig. 6.5B). The same delay is identified with  $\Phi(\tau)$  whereby  $\langle \varepsilon^* \rangle(\tau)$  yields a slightly higher optimal embedding delay (Fig. 6.5C). While traditional UTDE now suggests  $\tau_2^{(\text{ACF})} = 2\tau_1^{(\text{ACF})}$  for a three-dimensional embedding, both  $\Phi(\tau)$  and  $\langle \varepsilon^* \rangle(\tau)$  instead show that a different choice yields a superior phase space reconstruction in terms of minimized redundancy (Fig. 6.5C/D). Both  $\langle \varepsilon^* \rangle(\tau)$  and  $\Phi(\tau)$  effectively uncover the faster cycle by means of local maxima. However, both also detect a delay that is the sum of the seasonal and the fast cycle as a promising candidate. The fact that the estimate of this conjoint cycle differs for both measures can be explained by the different estimates on  $\tau_1$ . Since for  $\Phi(\tau)$  both local maxima have the same height, we pick the first. The zoomed RPs clearly express that both NUTD selection methods entail more coherent diagonal lines with less perpendicular distortions (Fig. 6.5E). Despite the different embedding vectors  $\vec{v}^{(\Phi)}$  and  $\vec{v}^{(\varepsilon^*)}$ , both reconstructions give a convincing representation of the seasonal cycle in the RP, respectively. The reconstructed phase space based on the delays selected from the recurrence flow yields a clear visualization of the system’s periodic oscillations (Fig. 6.5F).

In the same manner, we study the second solution type of irregular ENSO-like oscillations (Fig. 6.6). Cao’s method yields a 4-dimensional TDE. Both the ACF and MI identify different but similar delays slightly larger than  $\tau_1 = 0.35$  years (Fig. 6.6B).  $\langle \varepsilon^* \rangle(\tau)$  and  $\Phi(\tau)$  agree on an embedding delay of  $\tau_1^{(\Phi)} = \tau_1^{(\varepsilon^*)} = 0.33$  years which is slightly smaller than both  $\tau_1^{(\text{ACF})}$  and  $\tau_1^{(\text{MI})}$  (Fig. 6.6C). Again, the estimates  $\tau_2^{(\Phi)}$  and  $\tau_2^{(\varepsilon^*)}$  differ from the choice that would result from UTDE and indicate that describing the dominant variability in the observed irregular oscillations requires a multi-scale approach (Fig. 6.6D). Slight deviations in both estimates give rise to minor discrepancies between the emerging diagonal lines in the respective RPs (Fig. 6.6E). For none of the three reconstructions, DLA are entirely removed which hints at an optimal embedding dimension  $m > 3$  as identified by Cao’s method. This is supported by the displayed attractor reconstruction that has a two-winged structure reminiscent of the famous Lorenz attractor but potentially be unfolded further (Fig. 6.6F). However, both NUTD selection measures once more provide a more convincing result in terms of sparse, continuous diagonal lines than the ACF and, thus, capture the system’s predictability more adequately.



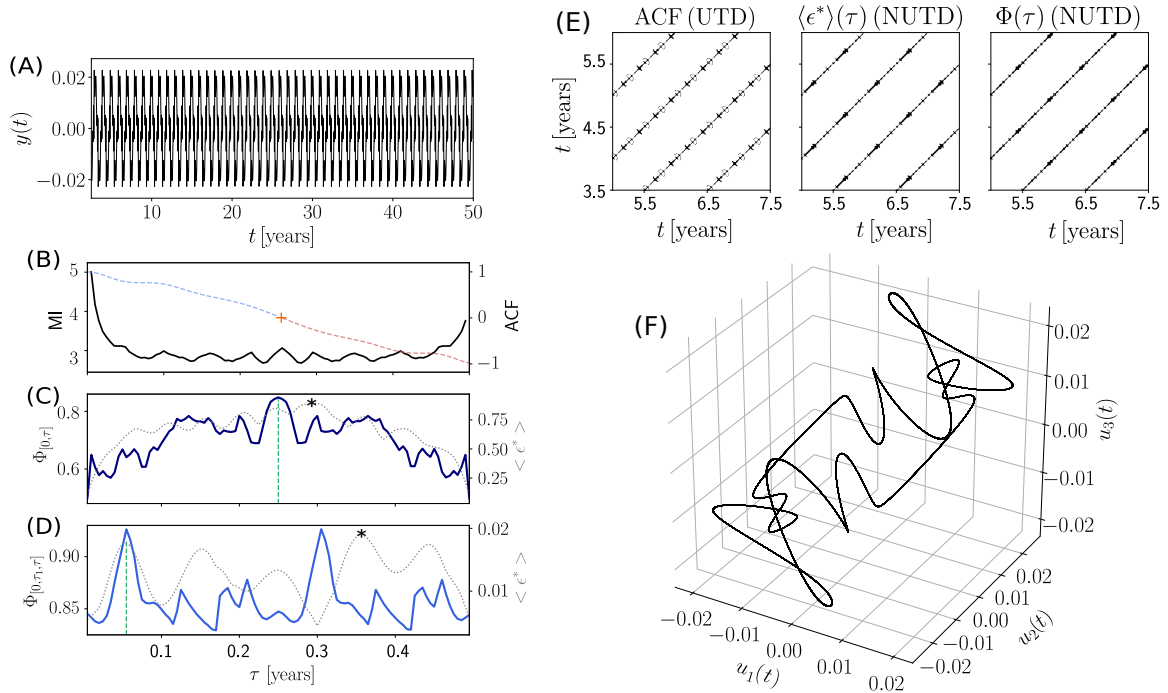


**Figure 6.5:** Non-uniform delay selection for delay-differential ENSO model with (A) periodic dynamics, analogously to Fig. 6.3. Serial dependence of  $y(t)$ , measured in terms of (B) ACF (red/blue) and auto-MI (black) for the univariate time series, as well as by (C/D) the continuity statistic  $\langle \varepsilon^* \rangle(\tau)$  (gray) and the recurrence flow  $\Phi(\tau)$  (dark blue) for (C) two- and (D) three-dimensional embedding vectors  $\vec{v}(t)$ . The optimal delay is marked by a circle(/cross/star/vertical green line) for the ACF(/MI/continuity statistic/recurrence flow), respectively. (E) Zoomed RPs for the ACF,  $\langle \varepsilon^* \rangle(\tau)$  and  $\Phi(\tau)$  (from left to right). (F) Three-dimensional phase space reconstruction based on recurrence flow.

## 6.4 Conclusion

The nonlinearity and scale-dependence of relationships observed in high-dimensional empirical data calls for appropriate and easily applicable methods. Recurrence plots offer a mathematically simple yet effective framework for the study of dependencies in high-dimensional dynamical systems and are an established tool in applied nonlinear time series analysis. For deterministic systems, diagonal lines in an RP yield valuable information on the evolution of a system's trajectory. We propose a novel recurrence based dependence measure, called recurrence flow. It builds on the fact that an RP can be computed from delayed copies of one (or multiple) time series that are stacked on top of each other as it is common practise in time delay embedding. The absence of spurious structures perpendicular to diagonal lines hints at a correct choice of (embedding) delays between the embedding vector's coordinates. We exploit the emergence of these structures to characterize the serial dependence in uni- and cross-dependence of multi-variate, high-dimensional systems. We demonstrated that the recurrence flow  $\Phi(\tau)$  captures nonlinear, lagged dependencies in presence of observational noise. Due to its conceptual proximity to time delay embedding, we put a focus on the delay selection problem that underlies attractor reconstruction.

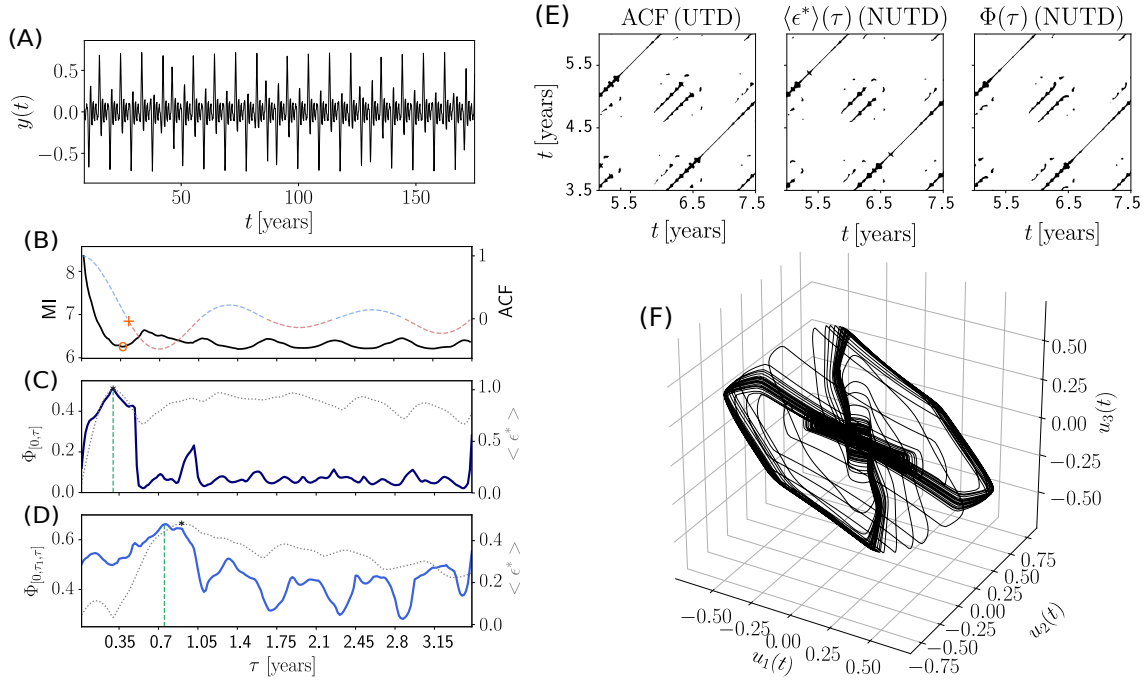


**Figure 6.6:** Non-uniform delay selection for delay-differential ENSO model with (A) irregular oscillations, analogously to Fig. 6.3. Serial dependence of  $y(t)$ , measured in terms of (B) ACF (red/blue) and auto-MI (black) for the univariate time series, as well as by (C/D) the continuity statistic  $\langle \epsilon^* \rangle(\tau)$  (gray) and the recurrence flow  $\Phi(\tau)$  (dark blue) for (C) two- and (D) three-dimensional embedding vectors  $\vec{v}(t)$ . The optimal delay is marked by a circle/cross/star/vertical green line) for the ACF(/MI/continuity statistic/recurrence flow), respectively. (E) Zoomed RPs for the ACF,  $\langle \epsilon^* \rangle(\tau)$  and  $\Phi(\tau)$  (from left to right). (F) Three-dimensional phase space reconstruction based on recurrence flow.

## Code availability

Scripts and data used to perform this study are available via Zenodo ([doi:10.5281/zenodo.6631137](https://doi.org/10.5281/zenodo.6631137)).

## Acknowledgements

This research was supported by the Deutsche Forschungsgemeinschaft in the context of the DFG project MA4759/11-1 “Nonlinear empirical mode analysis of complex systems: Development of general approach and application in climate”.

## Conflict of interest

The authors declare that they have no conflict of interest.

# 7 | Revealing recurrent regimes of mid-latitude atmospheric variability using novel machine learning method

Dmitry Mukhin<sup>1</sup>, Abdel Hannachi<sup>2</sup>, Tobias Braun<sup>3</sup>, Norbert Marwan<sup>3,4</sup>

1 – Institute of Applied Physics of the Russian Academy of Science, Nizhny Novgorod, Russia

2 – Department of Meteorology, Stockholm University, Stockholm, Sweden

3 – Potsdam Institute for Climate Impact Research (PIK), Member of the Leibniz Association, 14473 Potsdam, Germany

4 – University of Potsdam, Institute of Geosciences 14473 Potsdam, Germany

*Mukhin, D., Hannachi, A., Braun, T., & Marwan, N. (2022). Revealing recurrent regimes of mid-latitude atmospheric variability using novel machine learning method. under review for Chaos*

## Abstract

The low frequency variability of the extratropical atmosphere involves hemispheric-scale recurring, often persistent, states known as teleconnection patterns or regimes, which can have profound impact on predictability on intra-seasonal and longer timescales. However, reliable data-driven identification and dynamical representation of such states are still challenging problems in modeling dynamics of the atmosphere. We present a new method, which allows both to detect recurring regimes of atmospheric variability, and to obtain dynamical variables serving as an embedding for these regimes. The method combines two approaches from nonlinear data analysis: partitioning a network of recurrent states with studying its properties by the recurrence quantification analysis and the kernel principal component analysis. We apply the method to study teleconnection patterns in a quasi-geostrophical model of atmospheric circulation over the extratropical hemisphere as well as to reanalysis data of geopotential height anomalies in the mid-latitudes of the Northern Hemisphere atmosphere in the winter seasons from 1981 to the present. It is shown that the detected regimes as well as the obtained set of dynamical variables explain large-scale weather patterns, which are associated, in particular, with severe winters over Eurasia and North America. The method presented opens prospects for improving empirical modeling and long-term forecasting of large-scale atmospheric circulation regimes.

**Behavior of weather systems over the mid-latitudes is well-known as strongly chaotic and having a very limited horizon of reliable forecasting. While movements of synoptic-scale structures like cyclones and**

anticyclones are predicted well within 1-2 weeks, larger structures of atmospheric circulation with longer time scales are still poorly investigated. As it is shown by models and data analysis, dynamics on these time scales, also called the low-frequency variability, is characterized by recurrent global patterns, or regimes, which can strongly impact long-term weather conditions in different regions. However, both identification and dynamical representation of such regimes based on data is a controversial problem due to the lack of robust and reliable methods of data analysis/data analysis methods. Here we suggest a method which allows to detect the regimes and, simultaneously, to obtain dynamical variables representing their dynamics. The method involves and join together/combines several approaches from nonlinear data analysis: partitioning a network of recurrent states, recurrence quantification analysis and nonlinear principal component analysis. Studying winter low frequency variability (LFV) in the Northern Hemisphere mid-latitudes by the suggested method allows us to reveal and investigate dynamical properties of large-scale weather patterns, which are associated, in particular, with severe winters over Eurasia and North America. The results presented open prospects for improving data-driven modeling and long-term forecasting of large-scale atmosphere circulation regimes.

Many non-linear multidimensional systems exhibit chaotic behavior with a continuum of time scales, are poorly predictable, and are generally difficult to distinguish from a random process. However, in the state space of the system there may be sets of states in which the system is found more often than others. Such intermittently recurrent states can have varying lifetimes (or persistence) and regularity of occurrence. Their study is important from a practical point of view, because in the space of observables they correspond to the most typical regimes of the system dynamics. However, both the identification and analysis of their dynamical properties based on the observations are still challenging, especially when the observations live in a high-dimensional space, such as our weather and climate system [148].

Studies of atmospheric variability often distinguish between synoptic scales which embed day-to-day variability steered by baroclinic instability in the storm track region, and low-frequency variability with longer time scales. Compared to baroclinic processes, low-frequency variability is still not entirely well understood and is known to be challenging to model and predict [149]. Low-frequency variability embeds, in particular, tropospheric planetary waves and coherent large-scale structures including blocking and different phases of teleconnections, such as the North Atlantic Oscillation (NAO). A proper understanding of low-frequency variability proves invaluable in improving weather/climate prediction on intraseasonal and/or seasonal timescales, in addition to many other applications not least subgrid parametrization, climate change feedback, downscaling etc, see, e.g., the review [150] and references therein.

The atmospheric system is a highly nonlinear dynamical system per excellence with complex interactions between very many degrees-of-freedom involving different temporal and spatial scales. As far as large scale flow is concerned there is evidence of the existence of preferred recurrent and persistent circulation patterns [150]. For example, it is well known that northern hemisphere (NH) low-frequency variability is partly manifested by several teleconnection patterns [151, 152, 153, 154, 155], which can have profound impact in improving predictability on intra-seasonal and longer, such as subseasonal to seasonal timescales [156].

Compared to the tropics, extratropical dynamics involves a great variety of wave-wave and wave-mean flow interactions, highlighting, hence, more involved nonlinearity, in particular, preferred intra-seasonal large scale structures of nonlinear flow regimes. The persistence

timescale of these patterns is normally much longer than synoptic baroclinic timescales but smaller than typical intra-seasonal variability timescales of radiative fluxes and bottom boundary conditions, such as sea surface temperature anomalies [152, 157, 158].

The extratropical persistent and quasi-stationary states are associated with teleconnection patterns and states/positions of the jet stream [159, 160]. An extensive number of studies has analysed and identified these nonlinear flow regimes ranging from various cluster analysis methods, bump hunting of the probability density function (pdf) to hidden Markov models and self-organizing maps. The number of these structures, however, is a matter of debate between researchers, and depends on the location and extension of the geographical region and season. An extensive discussion with more details can be found in the review [150], and references therein.

One of the challenging issues in the identification of the above extratropical nonlinear structures is the choice of the low-dimensional space, which allows appropriate reduction of weather-related noise and efficient separation of these states. The space spanned by the leading empirical orthogonal functions (EOF) is conventionally used as reduced space. EOFs have, however, a number of weaknesses putting limits on what can be achieved [161, 162]. To overcome those weaknesses and, in consistency with the nonlinear nature of the dynamics, these authors applied kernel EOFs as a low-order state space to identify the nonlinear flow structures. In particular, those structures are interpreted as quasi-stationary states based on the flow tendency within the same space. This flow tendency can only be applied with very long time series, as is possible with the quasi-geostrophic model of potential vorticity on the sphere but is not appropriate for data from reanalysis.

Many problems in the real world, such as physical, computer, and social sciences, can be formulated and solved using the concept of networks or graph theory. A network is a collection of objects or nodes that are connected by edges. These connections can be defined based on a chosen metric in the system state space [163]. An example of such graphs can be found in the Isomap method [164] and an application to the Asian monsoon can be found in [165]. Many networks allow a natural splitting of the system into groups or communities/modules [166]. To complement the analysis of the low frequency variability system within the low-dimensional kernel EOF space, we adopt and apply here for the first time the concept of network modularity to study the nonlinear dynamical feature of the mid-latitude atmosphere.

In this manuscript we revisit and extend the analysis of Hannachi and Iqbal [161] by using kernel EOFs combined with a recurrence network partitioning method [166, 167]. The recurrence network analysis allows an elegant and easy partitioning of the state space into communities in a natural way, providing an efficient way to identify the nonlinear flow structure within the low-dimensional kernel EOF space. Moreover, this makes it possible to use the tools of recurrence quantification analysis (RQA) [20] to study important dynamical features of the detected structures.

The manuscript is organised as follows. Sect. 7.1 describes the methodology, the data and calculation procedure are given in Sect. 7.2, Sect. 7.3 presents the results, and a summary and conclusion are provided in the last section.

## 7.1 Methods

### 7.1.1 Kernel principal component analysis

Detecting the regimes of a given (dynamical) system's variability can be formulated as the problem of separating structures of related states in the phase space. Typically, when studying the atmospheric dynamics, we have at our disposal multivariate time series of some physical variables, such as temperature, pressure, geopotential height, etc., on a spatial grid,  $\mathbf{x}_t, t =$

$1, \dots, N$ , and hence, the structures of interest are embedded in a high-dimensional space. The nonlinearity of the system makes traditional linear data decomposition methods, such as empirical orthogonal function (EOF) analysis, inefficient and sometimes inadequate in disentangling these structures. The reason is that they are not necessarily oriented along linear directions, but are possibly lying on complex manifolds, and may be embedded in a very large number of principal components (PCs). A suitable approach to overcome this complexity is to construct a nonlinear embedding of the state space, through a high-dimensional multivariate mapping  $\varphi(\cdot)$ , from the original state space into a new *feature* space, so that the structures would be captured and could be well-separated by a few PCs in the new feature space. In this setting, the problem is reduced to linear PCA applied to the transformed time series  $\varphi(\mathbf{x}_t)$  of the original multivariate  $d$ -dimensional time series  $\mathbf{x}_t$  with  $t = 1, \dots, N$ . A straightforward way to solve this problem – via explicit assignment of the functions  $\varphi$  – is in most cases impractical, because it is difficult to guess both the functional form and its dimension, which are optimal for detecting the regimes. The *kernel trick* can solve this problem in an elegant way. The kernel function  $K(\cdot, \cdot)$  can be defined as a scalar product in such a way that  $K(\mathbf{x}, \mathbf{y}) = \varphi(\mathbf{x})^T \varphi(\mathbf{y})$ , and can be chosen from a large family such as polynomials or Gaussian functions. The choice of  $K(\cdot, \cdot)$  then defines implicitly the mapping  $\varphi$ , i.e., without an explicit expression of it, which is generally very high (and may be even infinite) dimensional. Then, all we need to know for calculating PCs in the new feature space is the matrix of inner products  $K_{ij} = \varphi(\mathbf{x}_i)^T \varphi(\mathbf{x}_j) := \sum_l \varphi_l(\mathbf{x}_i) \varphi_l(\mathbf{x}_j)$ . Hence specifying the mapping  $\varphi(\cdot)$  is not needed to perform PCA; we can just introduce the kernel function  $K(\cdot, \cdot)$  that defines the dot products  $K_{ij} = K(\mathbf{x}_i, \mathbf{x}_j)$ ,  $i, j = 1, \dots, N$ . Such an implicit kernel-based nonlinear transformation of the original space is the core idea of the kernel PCA (KPCA) approach [168, 169, 148], which was shown to be effective, e.g., in identifying the LFV regimes in the extratropical atmosphere [162]. The kernel function can be selected based on some general assumptions reflecting the similarity of states within the state space. According to the spectral decomposition theorem, the kernel function may be decomposed into an infinite series as  $K(\mathbf{x}, \mathbf{y}) = \sum_l \lambda_l f_l(\mathbf{x}) f_l(\mathbf{y})$ , where  $f_l(\cdot)$ ,  $l = 1, 2, \dots$ , are the eigenfunctions of the integral operator with kernel  $K(\cdot, \cdot)$ . Accordingly, the mapping  $\varphi_l(\cdot)$ ,  $l = 1, 2, \dots$ , are then given by  $\varphi_l(\mathbf{x}) := \sqrt{\lambda_l} f_l(\mathbf{x})$ , as mentioned in Ref. [162]. Thus, the approach makes it possible to consider infinite-dimensional embedding to achieve optimal separation of distinct states. Technically, in kernel PCA, the  $N \times N$  matrix  $\mathbf{K}$  is decomposed as follows

$$\mathbf{K} = \bar{\mathbf{K}} + \mathbf{K}_c = \bar{\mathbf{K}} + \sum_{i=1}^{N-1} \mathbf{u}_i \cdot \mathbf{u}_i^T. \quad (7.1)$$

where the mutually orthogonal vectors  $\mathbf{u}_i$ ,  $i = 1, \dots, N-1$ , are the kernel principal components (KPCs), and  $\bar{\mathbf{K}}$  is

$$\bar{\mathbf{K}} = \mathbf{K} - \mathbf{K}_c = \frac{1}{N}(\mathbf{1} \cdot \mathbf{K} + \mathbf{K} \cdot \mathbf{1}) - \frac{1}{N^2} \mathbf{1} \cdot \mathbf{K} \cdot \mathbf{1}, \quad (7.2)$$

representing the deviation of  $\mathbf{K}$  from the centered matrix  $\mathbf{K}_c = \mathbf{C} \cdot \mathbf{K} \cdot \mathbf{C}$ , with  $\mathbf{C}$  being the  $N \times N$  centering matrix  $\mathbf{C} = \mathbf{I} - \frac{1}{N} \mathbf{1}$ , and  $\mathbf{I}$  and  $\mathbf{1}$  are respectively the identity matrix and the matrix of the same size filled with ones. The centering of the kernel matrix excludes the temporal mean of the features (or states) in the feature space from the decomposition, which could result in a distortion of the decomposition as the leading KPC gets attracted towards the main diagonal. This allows us to treat  $\mathbf{K}_c$  as the matrix of covariances between the states at different times (temporal covariances) yielding, in particular, zero-mean of the KPCs. Thus, the KPC vectors  $\mathbf{u}_i$ ,  $i = 1, \dots, N-1$ , can be obtained from the eigendecomposition of the

centered array  $\mathbf{K}_c$ :

$$\begin{aligned}\mathbf{K}_c &= \mathbf{V} \cdot \mathbf{D} \cdot \mathbf{V}^T, \\ \mathbf{u}_i &= D_{ii}^{1/2} \mathbf{v}_i, i = 1, \dots, N - 1\end{aligned}\tag{7.3}$$

where  $\mathbf{v}_i$  is the  $i^{\text{th}}$  eigenvector, forming the matrix  $\mathbf{V}$ , and  $D_{ii}$  is the corresponding eigenvalue – the variance of the  $i^{\text{th}}$  KPC.

Following the work [162], here we use kernels that are Gaussian function of a distance  $d(\cdot, \cdot)$  between state vectors at different times, i.e.,

$$K_{ij} = K(\mathbf{x}_i, \mathbf{x}_j) = \exp(-d^2(\mathbf{x}_i, \mathbf{x}_j)/2\sigma^2).\tag{7.4}$$

Such a distance-based Gaussian kernel accounts for local similarity between the states, which is a useful property for capturing nonlinear manifolds in the phase space. The only generalization allowed in Eq. (7.4), compared to the kernels used in Ref. [162], is the use of an arbitrary metric (not necessarily Euclidean) determined by the specific problem. However, using some metric  $d(\cdot, \cdot)$ , we should ensure that the kernel function Eq. (7.4), and, hence, the matrix  $\mathbf{K}$ , are positive semi definite, since they are designed to define an inner product. This requirement is fulfilled with those metrics for which the metric space can be embedded in the Euclidean space [170]. In case of other metrics, when negative eigenvalues of the kernel matrix are possible<sup>1</sup>, we may consider using an *approximation* of  $\mathbf{K}$  by a positive semi definite matrix instead.

By applying KPCA to multidimensional time series we can expect clustering of the states in a space with low- to moderate number of KPCs, so that each cluster can be associated with certain circulation regime of variability. The problem here is that neither the number of clusters, nor the dimension of the subspace in which the clusters are embedded, are *a priori* known. This means that these parameters should be optimized for obtaining statistically justified clustering. However, reliable optimization of the clustering procedure is difficult in real climate applications, due to insufficient statistics from the limited observed time series. Moreover, the clusters can have substantially non-Gaussian shapes, thus making such robust methods as, e.g., Gaussian mixture models [171] or kernel density estimate [172], inefficient. Below we describe a method providing the detection of significant regimes that avoids such difficulties.

### 7.1.2 Recurrence network partitioning

Conventional recurrence networks are based on neighborhood thresholding using a Euclidean metric between pairs of states [163]. Given a set of multivariate states  $\mathbf{x}_t$ ,  $t = 1, \dots, N$ , and a recurrence threshold  $\varepsilon$ , the recurrence matrix  $\mathbf{R} = (R_{ij})$  is defined by  $R_{ij} = 1_{\|\mathbf{x}_i - \mathbf{x}_j\| < \varepsilon}$ , that is 1 if  $\|\mathbf{x}_i - \mathbf{x}_j\| < \varepsilon$ , and zero otherwise [20]. In this regard the kernel matrix  $\mathbf{K}$  can be used to produce a recurrence matrix through binarization using the metric  $d(\cdot, \cdot)$  and threshold  $\gamma$  as:

$$R_{ij}(\gamma) = \begin{cases} 1, & K(\mathbf{x}_i, \mathbf{x}_j) > \gamma \\ 0, & \text{otherwise.} \end{cases}\tag{7.5}$$

This matrix can be visualized as a recurrence plot (RP), by plotting  $R_{ij} = 1$  as a black pixel (and blank elsewhere). A line is then defined as a sequence of successive black pixels. A recurrence network is a graph using  $\mathbf{R}$  as the adjacency matrix. The nodes of the graph correspond to the observed states  $\mathbf{x}_t$ , and if two states  $\mathbf{x}_i$  and  $\mathbf{x}_j$  are neighbors with respect to the metric  $d(\cdot, \cdot)$ , then the corresponding nodes are connected by an edge, i.e.,  $R_{ij} = 1$ . The

<sup>1</sup> This situation is out of scope in this article.

number  $k_i = \sum_{j=1}^N R_{ij}$  is the degree of node  $i$  and represents the number of nodes connected to it (i.e., the number of recurrences of the state at time  $i$ ). With this conceptual framework, the problem of regime detection can be formulated as recognizing communities of nodes, such that there are significantly more connections within communities than between them – a situation akin to  $k$ -means clustering concerning between- and within-variances. Actually, each community joins the related states of the system based on the similarity measure Eq. (7.4). Therefore, dividing the network into communities allows matching each state to a certain type of behavior.

To detect the communities we use an approach suggested by Newman [173], in which the best division of the network maximizes a special cost-function called modularity. For a given division, the modularity measures the difference between the fraction of edges falling within the communities and the same fraction expected from a network with randomly distributed connections, regardless of the division. This random network is assumed to have the same number and degrees of nodes as in the analyzed network. Since elements of the matrix  $R$  can only take 0 or 1, the expected value of  $R_{ij}$  in a network with random connections equals to the probability to find an edge between nodes  $i$  and  $j$ . This probability is estimated as  $k_i k_j / 2m$ , where  $m = \frac{1}{2} \sum_{i=1}^N k_i$ , and represents the total number of edges in the network. The modularity is then expressed as

$$Q = \frac{1}{2m} \sum_{i,j} \left( R_{ij} - \frac{k_i k_j}{2m} \right) g_{ij} = \frac{1}{2m} \sum_{i,j} \bar{R}_{ij} g_{ij}, \quad (7.6)$$

with  $g_{ij} = 1$  if nodes  $i$  and  $j$  belong to the same community and 0 otherwise. Here the matrix  $\bar{R}_{ij}$  represents the deviation of  $R$  from the expected adjacency matrix of a random network.

An elegant way to find the communities maximizing Eq. (7.6) was proposed in Ref. [166]. The approach is based on iteratively splitting each community into two communities so that each split must provide the maximal positive increment of the whole network modularity, until indivisible communities are obtained. Let us consider a particular community  $\mathbf{H}$  – a subset of nodes of our network – which we wish to split. If we are, for example, at the starting point of the algorithm, then  $\mathbf{H}$  is the whole set of nodes indexed by  $i = 1, \dots, N$ . Splitting  $\mathbf{H}$  into two groups can be represented by a vector  $\mathbf{s}$  (classifier or indicator), whose elements  $s_i = -1$  for the first group and  $s_i = 1$  for the second. Note that the dimension of  $\mathbf{s}$  is the size  $i_H$  of  $\mathbf{H}$ . It can be shown that the increment  $\Delta Q$  of the whole network modularity, after this split, takes the form:

$$\Delta Q = \frac{1}{4m} \mathbf{s}^T \mathbf{B} \mathbf{s} = \frac{1}{4m} \mathbf{s}^T \mathbf{W} \Theta \mathbf{W}^T \mathbf{s}, \quad (7.7)$$

$$\mathbf{B} = (B_{ij}), \text{ with } B_{ij} = \bar{R}_{ij}^{(H)} - \delta_{ij} \sum_{k \in \mathbf{H}} \bar{R}_{ik}^{(H)},$$

where  $\bar{\mathbf{R}}^{(H)}$  is the submatrix of  $\bar{\mathbf{R}} = (\bar{R}_{ij})$  obtained by selecting the elements of  $\bar{\mathbf{R}}$  with the indices  $i, j \in \mathbf{H}$ ,  $\delta_{ij}$  is the Kronecker delta, and  $\mathbf{W} \Theta \mathbf{W}^T$  is the eigendecomposition of the matrix  $\mathbf{B}$ , with  $\Theta = \text{diag}(\theta_0, \dots, \theta_{i_{\mathbf{H}}-1})$ . Accordingly, the problem of splitting  $\mathbf{H}$  boils down to finding the classifier (or indicator) vector  $\mathbf{s}$  consisting of numbers 1 and  $-1$  that maximizes the quadratic form, Eq. (7.7), which is equivalent to maximizing the dot product of  $\mathbf{s}$  with the eigenvector  $\mathbf{w}_0$  of the matrix  $\mathbf{B}$  corresponding to its largest eigenvalue  $\theta_0$ . The exact solution is the vector  $\mathbf{s}$  with components  $s_i$  having the same sign as the corresponding components  $w_{0i}$  of the leading eigenvector  $\mathbf{w}_0$  of  $\mathbf{B}$ . If the matrix  $\mathbf{B}$  has positive eigenvalues, two new communities defined by the vector  $\mathbf{s}$  will emerge, provided that  $\Delta Q > 0$ . Otherwise, if there are no positive eigenvalues in  $\mathbf{B}$ , its largest eigenvalue is always zero, since one of the



properties of this matrix is the zero sum over each row or column. In this case, all components of the leading eigenvector have the same value, which means that all  $s_i$  are also the same, i.e.  $\mathbf{H}$  is no longer divisible. The described splitting process of the network communities can continue until the  $\Delta Q > 0$  condition is violated for each current community<sup>2</sup>.

Besides the indicator or classifier vector  $\mathbf{s}$ , useful information about the structure of the resulting communities is also provided by the leading eigenvector  $\mathbf{w}_0$ . As it can be seen from Eq. (7.7), the absolute value of  $w_{0i}$  measures the contribution of the  $i^{\text{th}}$  element to the modularity of the network, i.e., the gain in modularity from the inclusion of the corresponding node in the community. The number  $|w_{0i}|$  is referred to as the *centrality* of the corresponding node in the resulting community, and therefore for each community we get a vector of centralities. In terms of interpretation in connection to the atmospheric circulation regime detection, large centrality of some node  $k$  of the network indicates that the corresponding spatial pattern  $\mathbf{x}_k$  is similar to a large number of other patterns belonging to the same community, and represents therefore a typical pattern for the regime associated with this community.

The main advantage of Newman’s method described above is that it provides an efficient and elegant way to cluster the network into communities without any prior information on their size and number using simple matrix calculations. This is particularly convenient in climate data analysis where the set of regimes is not known in advance and the problem of the data-driven identification comes to the forefront. The suggested method of decomposing the analyzed time series allows us to label the states of the system in the space of the leading kernel PCs in accordance with the detected communities. As a result, looking at the labelled/marked states in the KPC space, we can easily select a number of leading KPCs that provides clear separation of the communities (see the results below). Further, the selected KPCs can play the role of dynamical variables that describe the sporadic switching of the system trajectory between the dynamical circulation regimes.

### 7.1.3 Studying dynamical properties of the regimes

The adjacency (recurrence) matrices of the partitioned recurrence networks can be analysed using RQA [20]. Each regime-specific recurrence plot (RP) can be regarded as a particular subset of the full RP constrained by the community labels. In order to compare the dynamical properties of the different regimes, RQA is carried out separately for each regime-specific RP.

A simple quantifier for the overall intrinsic *similarity* of an atmospheric regime can be defined by the ratio of total recurrences in the regime-specific RP relative to the (squared) time that is spent in the respective regime, i.e., recurrence rate RR,  $RR = \sum_{i,j} R_{ij}/N^2$ . In traditional RQA, the statistics of diagonal and vertical line structures are studied to characterize the predictability and intermittency of a system. Diagonal lines in an RP reflect time periods during which two segments of the phase space trajectory evolve in parallel, indicating deterministic and well-predictable dynamics. By counting the number of diagonal lines that exceed a specific length for the regime-specific RPs, we study if the evolution of spatial patterns during different time periods is similar. *Predictability* of atmospheric patterns in each regime is quantified by the determinism DET of the RP which is given as the fraction of diagonal lines that exceed a minimum line length of  $l_{\min} = 5$  days to all diagonal lines, i.e.  $DET = \sum_{l \geq l_{\min}} lP(l) / \sum lP(l)$ , where  $P(l)$  is the distribution of diagonal line lengths  $l$ . Vertical lines in an RP identify periods in which the dynamics are ‘slowed down’. Consequently, we interpret them as corresponding to quasi-stationary patterns potentially associated with atmospheric blocking and possibly zonal flow. *Persistence* of atmospheric patterns in each regime is quantified by laminarity LAM which is computed as the fraction of the total vertical

---

<sup>2</sup>In practice, however, we may consider using a threshold slightly above zero to avoid “too thin” separation, if, for example, further splitting gives much less modularity increment as compared with the previous splits

lines with  $l_{\min} = 5$  days to all vertical lines:  $LAM = \sum_{v \geq v_{\min}} vP(v) / \sum vP(v)$ , where  $P(v)$  is the distribution of vertical line lengths  $v$ . Recently, an approach using recurrence lacunarity (RL) was proposed to characterize features of an RP that are distributed among multiple time scales and are not necessarily expressed in line structures [1]. RL generally reflects the heterogeneity of an RP. Thus, we interpret it as the *diversity* of the regime behaviour. While regular RL informs about the general heterogeneity of recurrences, its extension to diagonal/vertical line structures is straight-forward and is introduced here. For the computation of diagonal/vertical line RL (dRL/vRL), the number of diagonal/vertical lines exceeding  $l_{\min} = 5$  days in each box is counted and reflects how strongly predictability/persistence of atmospheric patterns varies throughout different time periods. The box width is fixed to one year, highlighting interannual variability. High values indicate that, e.g., high persistence during one time period only has limited implications for other time periods. Thus, we always show these three different RL-based measures of diversity.

Significance testing allows to test the dynamical properties of atmospheric regimes against different null hypotheses. We test for two different hypothesis: (i) we check whether the recurrence network partitioning yields regimes that are significantly different from random regimes with respect to above mentioned recurrence quantifiers and (ii) we test which regime yields significantly high values for a given recurrence quantifier.

The first test is done by random deletion of recurrences from the full RP. In particular, for the  $i^{\text{th}}$  regime-specific RP with  $n_i$  recurrences, we randomly delete  $m = N - n_i$  recurrences from the full RP that contains  $N > n_i$  recurrences while also reproducing the column-wise recurrence rate of the  $i^{\text{th}}$  regime-specific RP. We generate 200 random samples for each RP and compute the 99%-quantile for each RQA measure from this ensemble as an upper confidence level to test for significance.

For the second test, we apply a bootstrapping procedure with  $n_B = 2,000$  runs [93]: we first collect all diagonal lines(/vertical lines/counts) from the distributions obtained from each regime-specific RP separately. In a single bootstrap run, we draw  $M$  times (with replacement) from the unification of these length(/count) distributions and compute the measure of interest, yielding a single value.  $M$  is given by the number of lines/the total count in the  $i^{\text{th}}$  regime-specific RP. By repeating this procedure  $n_B$  times, an empirical test distribution for this measure is obtained from which we compute the upper 99%-confidence level. This method is applied for all measures except the recurrence rate; in this case, we test against the hypothesis that recurrences are distributed among the regimes with respect to the time spent in each regime. Consequently, we obtain each regime-specific significance level by dividing the total number of recurrences (from all regimes) by the individual (squared) time spent in a regime.

#### 7.1.4 Method summary

The whole procedure described in the above subsections 7.1.1-7.1.3 is represented schematically in Fig. 7.1. The main goal of the KPCA is to obtain a few number of variables (leading KPCs) which are suitable for differentiating the obtained regimes. The same kernel matrix as in KPCA is used for building the recurrence network which is partitioned to yield a set of regimes. As a result, we obtain a state space in which the regimes are well separated as well as a representation of the regimes in physical space via composites. This enables us to study properties of the regimes by the RQA methodology.

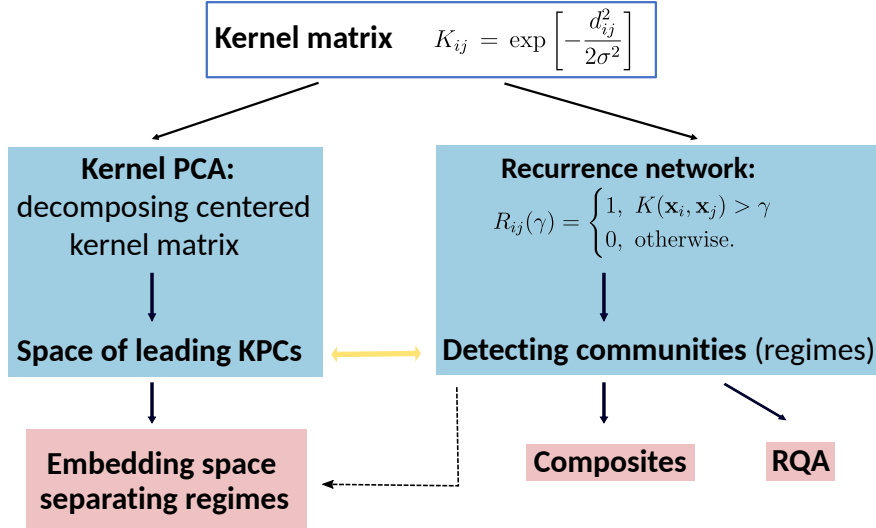


Figure 7.1: Schematic representation of the proposed procedure.

## 7.2 Data and calculation setup

### 7.2.1 QG3 model time series

Quasi-geostrophic (QG) models of the atmosphere are popular polygons for testing algorithms concerning weather/climate dynamics. Being simplified representations of atmospheric dynamics, QG models demonstrate a rich spectrum of variability at different time scales and are competitive to intermediate and full general circulation models regarding complexity and dynamical features/processes. Here we use time series generated by a three-level QG model (QG3) on the sphere [174] with realistic orography and surface boundary condition. Based on the potential vorticity equations at three (200, 500, and 800 hPa) pressure levels [174, 175, 176], the model is tuned to simulate winter atmospheric circulation over the extratropical hemisphere. The model exhibits highly nonlinear behavior with a chaotic attractor in its phase space with more than 100 positive Lyapunov exponents [175]. The LFV behaviour of the model regimes was studied in a number of works, based on different kinds of clustering in a truncated phase space. In particular, the authors of the work [177] identified four clusters in the space of three leading PCs calculated from a very long (54,000 days) time series of the mid-level stream function anomalies (SFA). These clusters are associated with the well-documented atmospheric modes or teleconnections, namely, Arctic oscillations (AO) and North Atlantic oscillation (NAO). Similar results were obtained in Ref. [178] based on reduced data-driven models, but using a much shorter sample of 5,000 days. Hannachi and Iqbal [162] used KPCs as a space for a PDF-based cluster detection; however, only two clusters related to the AO were detected. Here we present results of our analysis applied to three 10,000-day time series of the mid-level stream function anomalies, distributed over latitudes 36°N to 90°N with approximately  $5.5 \times 5.5$  degree resolution. These non-overlapping time series are randomly taken from a very long (300,000 days) QG3-model run. Then the analysis is performed to each time series independently.

### 7.2.2 Reanalysis data

To study the circulation regimes of the real atmosphere, we use daily geopotential height (HGT) time series at the 500 hPa pressure level from the NCEP/NCAR reanalysis dataset [179]. The time series is provided on a  $2.5 \times 2.5$  degree latitude-longitude resolution, north

of 30°N covering the period 1980 to 2020. The data are de-seasonalized by removing the daily seasonal mean signal over the whole period smoothed in time with a Gaussian window with the standard deviation of 15 days. Such smoothing suppresses the day-to-day noise in the resulting annual cycle, while re-taining the intra-annual seasonal structure. Only winter (December-January-February) values are taken from the obtained time series of daily HGT anomalies, yielding a sample of 3,579 days.

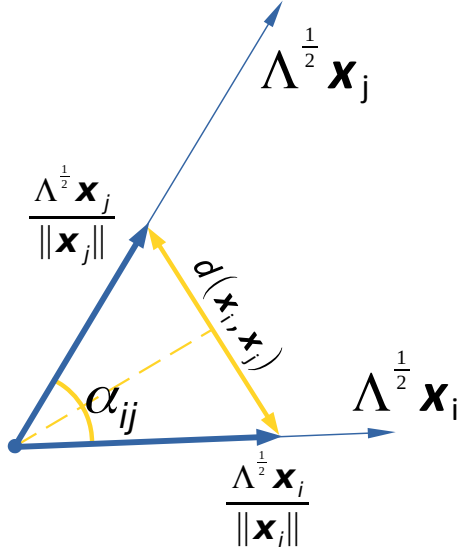


**Figure 7.2:** Representation of the distance defined by Eq. 7.8.

### 7.2.3 Distance metric, kernel and recurrence matrices

Since our goal is to separate sets of states, each of which joins spatial patterns yielding similar atmospheric conditions, we focus on the pattern’s structure/shape rather than their amplitudes. Accordingly, we define a distance given by the sine of the angle  $\alpha_{ij}$  between pairs of patterns:

$$d(\mathbf{x}_i, \mathbf{x}_j) = \left\| \frac{\mathbf{x}_i}{\|\mathbf{x}_i\|} - \frac{\mathbf{x}_j}{\|\mathbf{x}_j\|} \right\| = 2 \left| \sin \frac{\alpha_{ij}}{2} \right|, \quad (7.8)$$

where  $\|\mathbf{x}\| = (\mathbf{x}^T \Lambda \mathbf{x})^{\frac{1}{2}}$  is the metric using a  $d \times d$  diagonal weighting matrix  $\Lambda$  reflecting the non-uniformity of the spatial grid (see below). Clearly, this metric inherits all properties of the Euclidean metric, as it is nothing more than the Euclidean distance between the weighted vectors  $\Lambda^{\frac{1}{2}} \mathbf{x}$  normalized to unit norm (see Fig. 7.2). This always yields a positive semi-definite kernel matrix Eq. (7.4). A very important parameter that determines the recurrence network structure and strongly impacts the splitting of the network into communities is the threshold  $\gamma$  in the definition of the recurrence matrix, Eq. (7.5) [78]. If it is too large (remember that here the thresholding is opposite to the classical recurrence definition), the network degenerates into many communities yielding high modularity. Such a network may eventually not help to reveal any connections between patterns except those close in time.

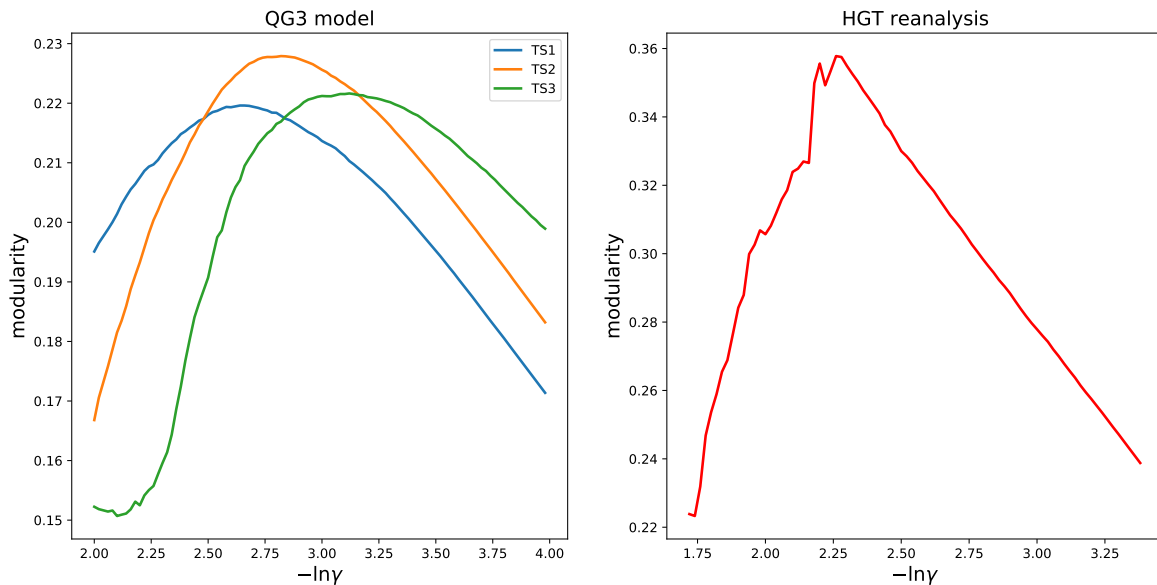


**Figure 7.3:** Modularity increment after first division of the network into two communities vs. the threshold  $\gamma$ . Curves obtained from the three time series of the QG3 model and the HGT reanalysis time series are plotted in the left and right panels, respectively.

If, on the contrary,  $\gamma$  is too small, we end up with a poorly divisible network, in which each node is connected to most of the remaining nodes. Hence, this calls for the need to optimize the threshold parameter. Here we select  $\gamma$  to provide the best division of the network into two basic communities at the initial splitting of the whole network. Under this requirement, the resulting value of  $\gamma$  maximizes the modularity increment  $\Delta Q(\gamma)$  at the first iteration of the algorithm. Such a choice is justified in the case of mid-latitude atmospheric dynamics, since two opposite types of circulation associated with the strength of the polar vortex are known to be the dominant modes in this region [180], and the network should distinguish them well at the most basic level. It is obtained (see Fig. 7.3) that there are pronounced maxima of this dependence for both datasets considered here. By adjusting  $\gamma$  we do not need to care too much about the precise value of  $\sigma$  in the kernel function, Eq. (7.4). We find that setting  $\sigma = 2 \min_{i,j} d(\mathbf{x}_i, \mathbf{x}_j)$  in all examples below provides quite robust results, which is close to assumptions from the work [162].

#### 7.2.4 Data weighting

The data considered here is defined on a grid that is uniform in polar coordinates, so its cells cover unequal areas. In line with the traditional approach, we had to distribute the weights of the grid nodes in the distances  $d(\mathbf{x}_i, \mathbf{x}_j)$ , Eq. (7.8), according to the area fractions around each grid node. This corresponds to weights  $\Lambda_{mm} \propto \cos \theta_m$ , where  $\theta_m$  is the latitude (in radians) of the  $m^{\text{th}}$  component  $x_m$  (or  $m^{\text{th}}$  grid point)  $m = 1, \dots, d$ , of the state vector  $\mathbf{x}$ . A main problem with such weighting in our case is related to the resulting larger magnitude of anomalies at the southern bound of the considered latitude band. This moves the focus of analysis from the mid-latitudes – the region of interest – to the subtropics. No weighting, on the other hand, yields dramatic increase of polar latitudes contribution, thus shifting focus on the Polar vortex region rather than the mid-latitude circulation. The problem of proper weighting was stated, e.g., in the works [181, 182]. Here, we take into account the latitudinal dependence of the characteristic spatial scale of atmospheric anomalies responsible for planetary-scale circulation regimes.

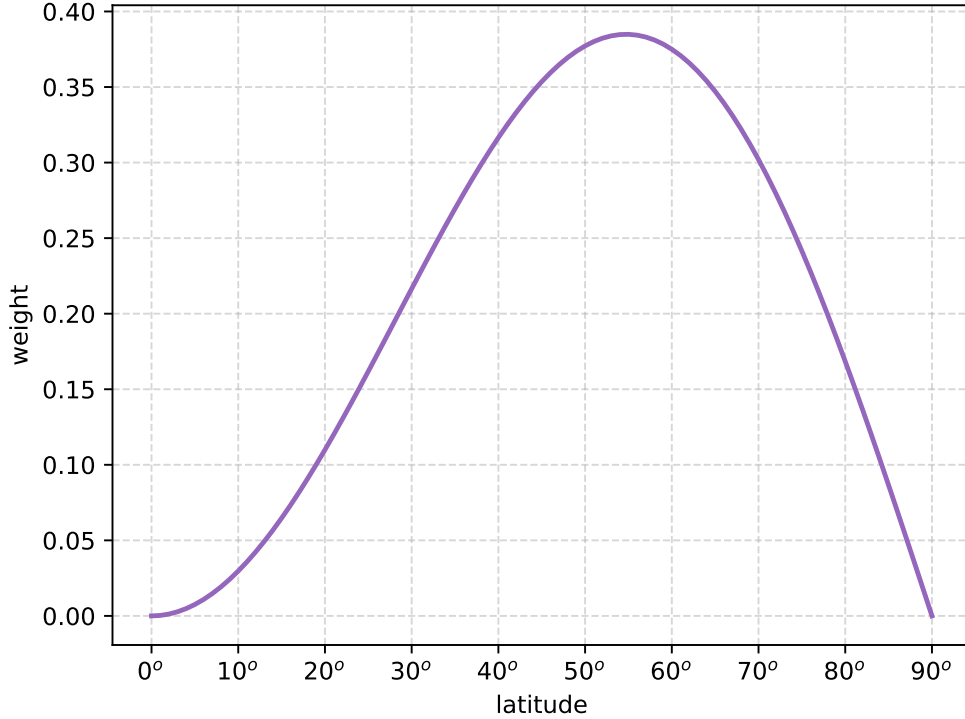


**Figure 7.4:** Dependence of the weight given by Eq. (7.9) on latitude.

In the extratropics, this scale is proportional to the Rossby deformation radius [183], which depends on the latitude as  $\frac{1}{\sin \theta}$ . Therefore, normalization of the grid cell areas through scaling by the characteristic areas of anomalies ( $\propto \frac{1}{\sin^2 \theta}$ ) allows us to better capture the peculiarities and typical features of the atmospheric circulation using a given spatial grid. As a result, we use weights in the distance measure that focus on the midlatitudes expressed as

$$\Lambda_{mm} = \cos \theta_m \sin^2 \theta_m, \quad (7.9)$$

or, equivalently, multiply the signal at each grid point by  $\sin \theta_m \sqrt{\cos \theta_m}$ . Such weighting distinguishes mid-latitudinal and subpolar nodes of the grid, reaching the maximum at approximately 55°N (Fig. 7.4).

## 7.3 Results

### 7.3.1 QG3 model time series

We apply the methodology described above to each of the three SFA time series separately. For all time series the recurrence network division method gives the same number of communities, or regimes, equal to three. To illustrate clustering of the communities in the KPC-space, we plot elements of each community in the plane of the two leading KPCs (see Fig. 7.5). The most typical (i.e., having large centralities in their communities) states from different communities are well-separated in this plane, and hence, these two variables can serve well as an embedding for the three identified regimes.

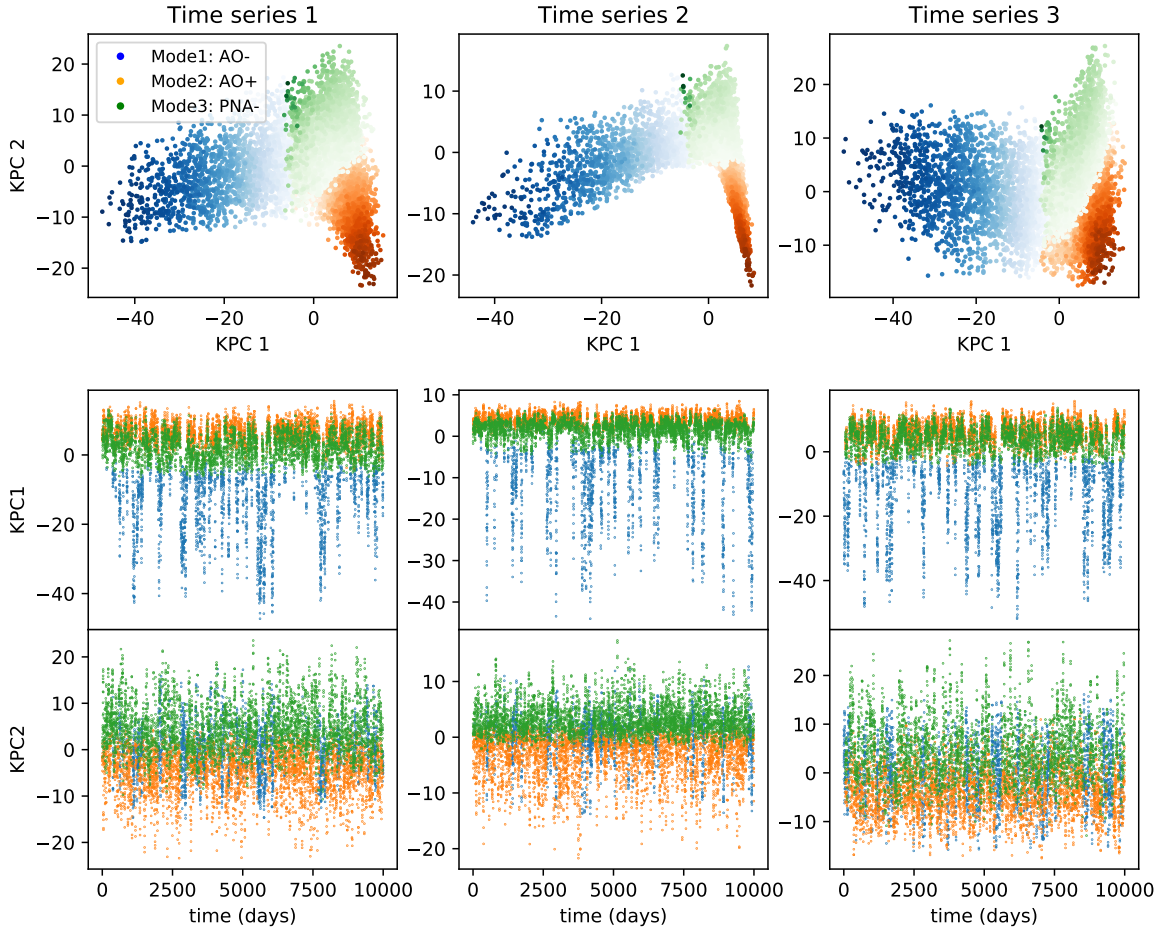


**Figure 7.5:** Regimes of the QG3 model behavior in the space of the leading two KPCs. The three columns correspond to the three analyzed time series. In upper panels states of each regime (mode) are shown in the KPC1-KPC2 plane (see the text). States belonging to different regimes are marked by different colors; color saturation corresponds to the centrality of a state in its community. Time series of the KPC1 and KPC2 variables are plotted in the lower panels.

Unlike in EOF decomposition or some of its nonlinear generalizations (see, e.g., Refs. [184, 185]), there is no explicit mapping of the KPCs to the data space. A coarse geographical structure of SFA relating to a specified regime can be obtained via composite analysis, i.e., the spatial field of SFA averaged over the most central states of the regime (as shown in Fig. 7.5, top). The resulting composites are clearly related to the three well-known atmospheric teleconnection patterns (Fig. 7.6). The first two are the positive and negative phases of AO, connected with an anomalous pressure difference between the polar region and the mid-latitude belt, and, respectively, stronger or weaker (zonal) westerly flow. The third one resembles the negative Pacific North American (PNA) pattern characterized in winter seasons by dominating tripol structure with positive anomalies over the North Pacific and near southeastern United States and negative anomalies over central Canada. We note that we have not obtained a separate regime corresponding to NAO, but NAO-related anomalies are captured by mode 1, which encompasses the negative NAO phase, whereas modes 2 and 3 feature of the positive NAO phase. Studying the nature of, and the relation between the various teleconnection patterns, including PNA, NAO and AO/NAM (Northern Hemisphere Annular Mode), has a long history (e.g. Refs. [151] and [152]). The nonlinearity and/or non-distinguishability between the NAO and AO teleconnection has been discussed thoroughly

in the literature (e.g. Refs. [180] and [186]).

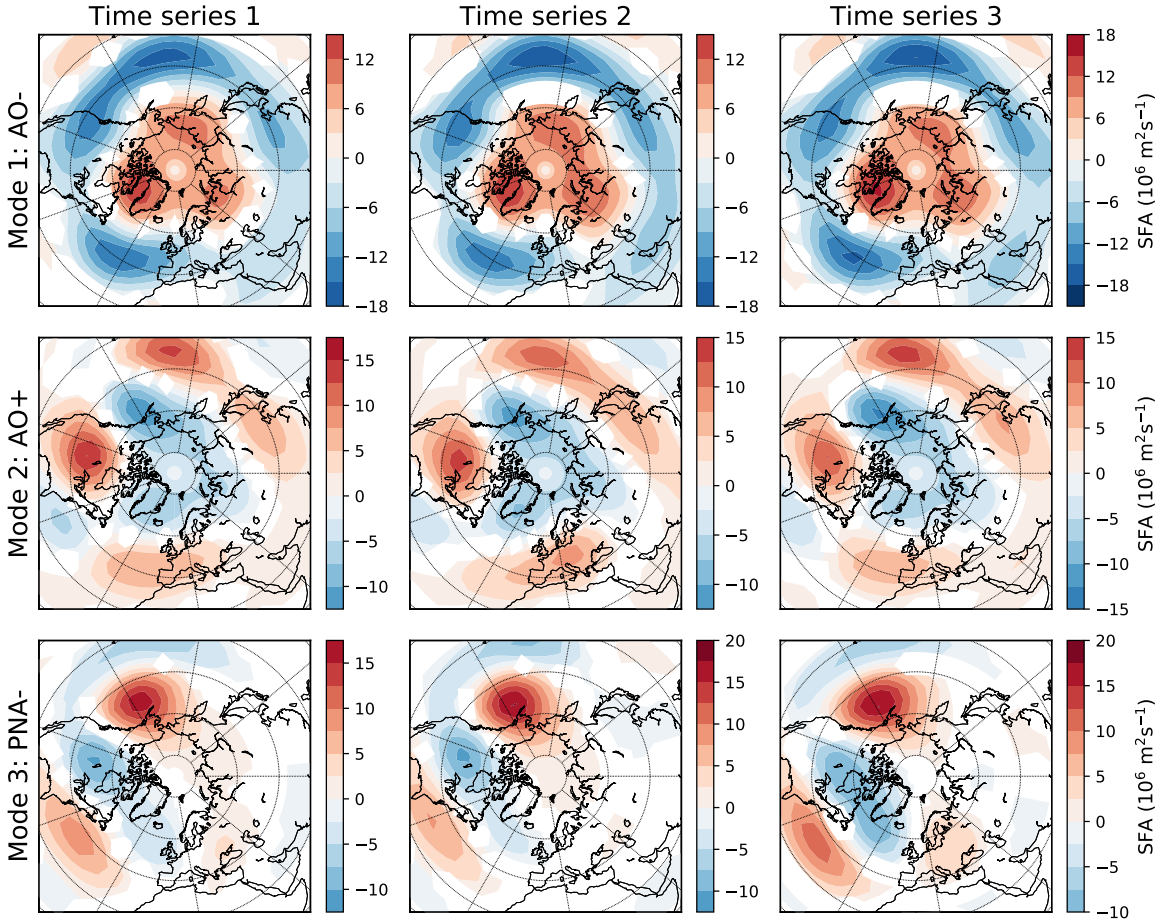


**Figure 7.6:** Composite patterns of the QG3 model SFA corresponding to the obtained regimes. Columns correspond to different time series, rows to different regimes. The composites are calculated as SFA averaged over 20% most typical states of each of the obtained regimes (see the text). Only values that are significantly different from zero by Student’s t-test with a critical value of 0.01 are shown.

Linear EOF analysis, and even nonlinear cluster analysis cannot categorically distinguish between NAO and AO. For example, [187] examined, based on composite analysis, the null hypothesis that the NAO and AO/NAM persistent events are not distinguishable. They found that the null hypothesis cannot be rejected even at 20% significance level. In another analysis, [188] examined the nature of AO through SOM (Self Organizing Map) analysis. They found that AO, derived from the 250-hPa geopotential height anomalies, can be interpreted in terms of a continuum that can be approximated by five discrete AO-like patterns, which overlap with the discrete NAO-like pattern. These findings explain why no separate NAO and AO regimes are identified in this analysis.

The negative AO regime is the most distinguishable mode of the QG3 model dynamics (Tab. 7.1): its contribution to the network modularity is substantially greater than the contribution of the other two modes, although with a small frequency of occurrence. For this reason, the most central states of this mode are separated stronger from other states, moving into the area of large negative values of the first leading KPC. Consequently, the transitions to this regime look like rare irregular outliers in the time series of the first leading KPC (see Fig. 7.5, bottom). Indeed, this KPC1 can be considered as an index describing joint AO and NAO dynamics. At the same time, the second variable (KPC2) helps differentiate between



the positive AO and negative PNA states (Fig. 7.5 top), both of which contribute to the positive NAO.

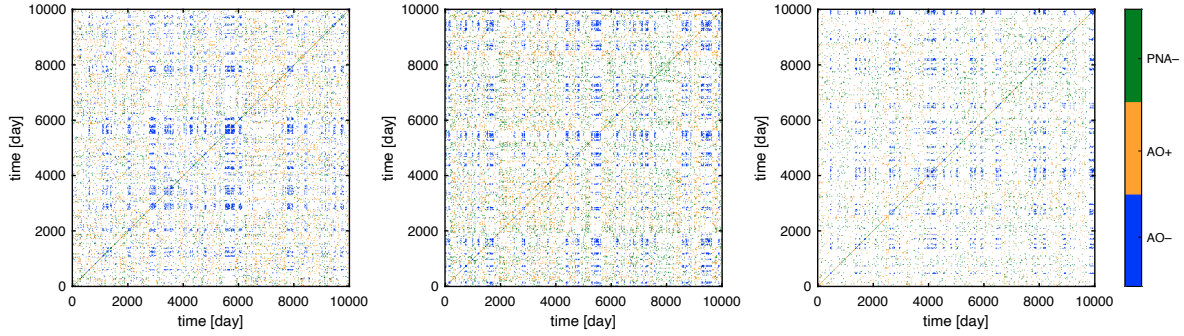


**Figure 7.7:** Recurrence plots of atmospheric patterns obtained from the QG3 model data for the three different time series. Recurrences within a given regime are color coded accordingly. A specific rendering is used to make the RP appear less sparse.

Let us now turn to the dynamical properties by considering the RPs separately for each regime (Fig. 7.7, see. also Sect. 7.1.3), along with the RQA (Fig. 7.8). The RQA reveals distinct dynamical properties of the identified regimes (Fig. 7.8 and supplementary Fig. C.3). The negative AO regime stands out as the most similar, persistent and predictable regime. This suggests that it encompasses periods of atmospheric blocking as these are characterized by atmospheric patterns that persistently reside for relatively long time periods without significant spatial variations. During a blocking event, atmospheric conditions are consequently more similar and predictable. On the other hand, the negative AO regime is characterised by a high degree of intermittency, reflecting the low predictability of blocking events on interannual and decadal time scales. These findings are fostered by the corresponding regime-specific RP (Fig. 7.7); on longer time scales, the RP appears heterogeneous while block-structures reflect periods of atmospheric blocking. The positive AO regime is associated with stronger westerly zonal flow which appears to result in transient, short-lived atmospheric patterns that do neither exhibit a significant degree of persistence nor allow for reliable short-term predictions. Low-frequency variability of atmospheric patterns in this regime is relatively low as indicated by low values in the different RL measures. Time periods, during which atmospheric conditions are characterized best by the negative PNA regime are identified with moderately predictable and persistent dynamics. Given the total time this regime is detected, the number of recurrences is relatively low, representing low similarity. Both diagonal and vertical line structures in the regime-specific RP exhibit strong heterogeneity, suggesting that the temporal variations in this regime run through both well-predictable, persistent and stochastic, volatile periods. This could be interpreted as a high degree of non-stationarity of the dynamical properties of this regime. Finally, results between the three different time series show good general correspondence (supplementary Fig. C.4), supporting the given interpretation of regimes. The most significant deviation is found for the first time series compared to the second and the third with respect to the similarity of all three regimes.

Overall, the results (Figs. 7.5, 7.6, Tab. 7.1 and supplementary Fig. C.4) confirm that the suggested methodology gives a fairly stable solution: the number of regimes, their spatial and temporal structures, the embedding spaces, as well as the modularity rates, show coherency between the three different, independently analyzed time series.

	Community 1 (AO-)	Community 2 (AO+)	Community 3 (PNA-)
Modularity (TS1; TS2; TS3)	0.219; 0.222; 0.228	0.169; 0.174; 0.155	0.107; 0.118; 0.103
Number of states (TS1; TS2; TS3)	2235; 1861; 2484	3746; 3863; 4058	4019; 4275; 3458
Modularity per state (TS1, TS2, TS3), ( $\times 10^{-5}$ )	9.8; 11.9; 9.18	4.51; 4.5; 3.82	2.66; 2.76; 2.98

**Table 7.1:** Parameters of the communities extracted from three analyzed time series of the QG3 model (the time series are referred to as TS1, TS2 and TS3). First row: contribution of a community to the network modularity. Second row: the number of SFA states (number of days) belonging to a community. Third row: mean contribution of a state to the modularity of its community.

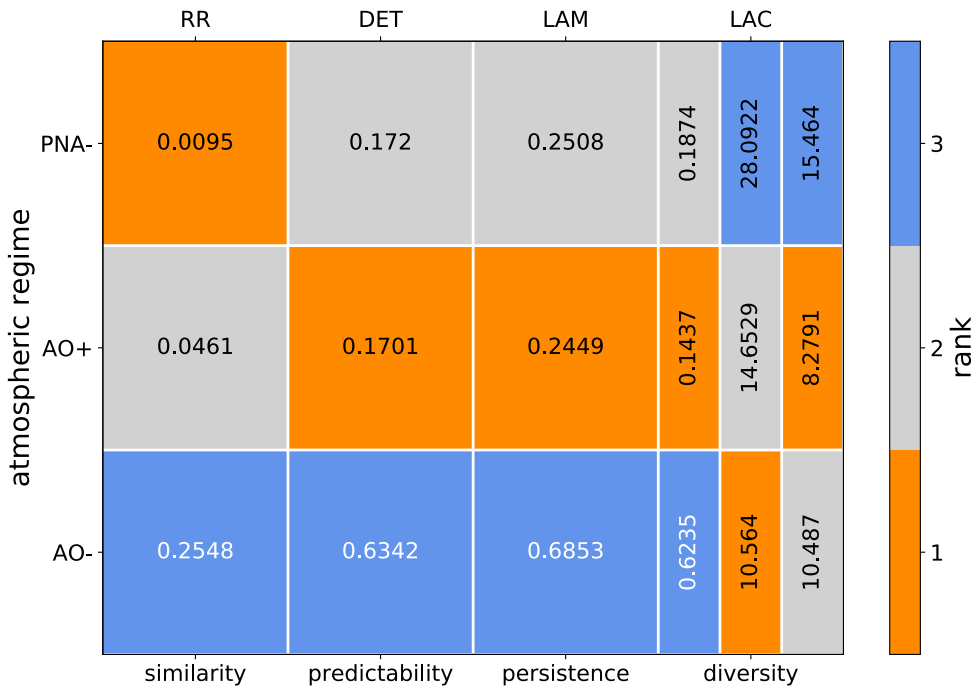


**Figure 7.8:** Results of recurrence quantification analysis for the atmospheric regimes obtained in the QG3 model data set for one of the three time series. The four different RQA measures are labelled with their respective interpretation. Significant (insignificant) values are printed in white (black) numbers. Color coding illustrates the ordering of the RQA values (ascending column-ranking) for better comparability.

### 7.3.2 Reanalysis data

For the HGT reanalysis data we detect four regimes (Fig. 7.9, Tab. 7.2). These communities are embedded well in the space of three leading KPCs, organized into a loop/ring (Fig. 7.9). The composites form typical HGT patterns in each community (Fig. 7.10). Additionally, in order to study weather impacts of the detected circulation regimes, we take the same dates as used for the HGT composites to calculate the composites of near-surface air temperature anomalies<sup>3</sup> (Fig. 7.11).

The composites (Fig. 7.10) demonstrate qualitatively different structures of atmospheric anomalies related to the detected regimes. The first regime is characterized by anticyclonic anomalies south of Greenland, projecting onto negative AO and NAO. This pattern blocks the transport of warm air from the Atlantic to Europe, while increasing the advection of subtropical air to the northeast of North America, and advecting warm/humid air into North Africa (Fig. 7.11). The second regime features a positive NAO and PNA, manifested by a

<sup>3</sup>We use air temperature data at 0.995 sigma level taken from the NCEP/NCAR reanalysis [179]. The anomalies were produced by deseasonalizing in the same way as with the HGT data (see Sec. 7.2, 7.2.2).

lowering pressure over the North Atlantic and increasing pressure in the northeastern Pacific Ocean. Anticyclonic anomalies in the Pacific Ocean block zonal airflow and lead to cooling in northern USA and Canada and warming in eastern Russia and Arctic. The third regime with a high pressure center over northwest Russia and Scandinavia slows down zonal air transport in the Euro-Atlantic region, leading to extremely cold winters in Europe and heating the Arctic Ocean area north of central Russia. Simultaneously, stable zonal flow over the north Pacific induces warm conditions in Canada (Fig. 7.11). Finally, the fourth flow pattern relates to positive AO and NAO; it is characterized by increased zonal airflow in the north Atlantic, providing warmer than normal winters in Europe and Russia (Fig. 7.11).

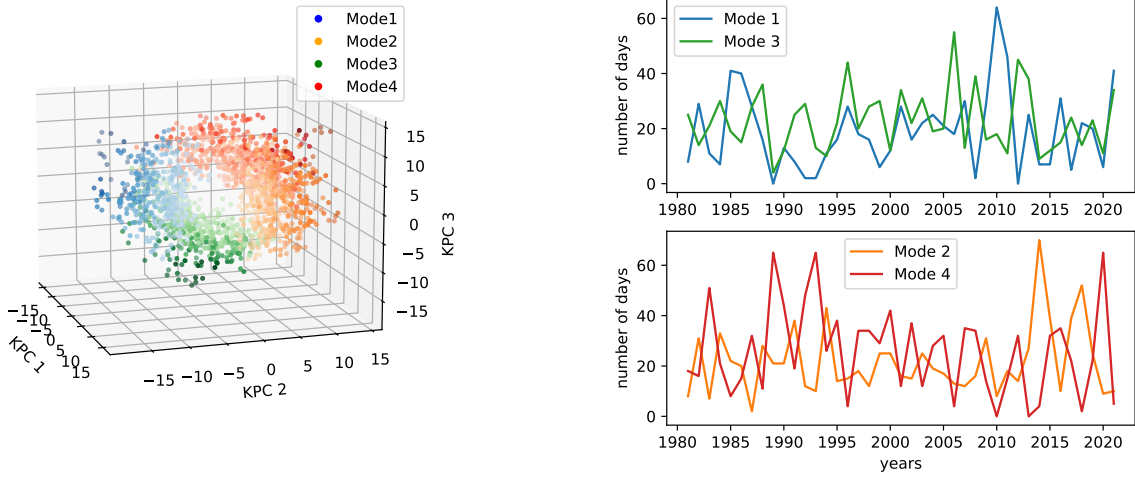


**Figure 7.9:** Partitioning of HGT states into regimes. Left panel: 50% of the most typical states of each regime (mode) in the space of three leading KPCs. Color saturation corresponds to the centrality value of a state in its community. Right panel: number of days per winter related to different regimes. The years of January of each winter are shown (e.g., 2001 corresponds to the winter 2000-2001).

The number of days in each winter corresponding to a given flow regime (Fig. 7.9), as well as in the KPC time series (not shown), we observe pronounced strong inter-annual variability of dominating types of behavior of the winter atmospheric circulation. In particular, we see that regimes 1 and 3, leading to cold weather in Europe, can be correlated on a large scale. The amplitude of the inter-annual variability is not regular; e.g., there are sets of extreme winters with strong domination of a single regime (see, for example, the abnormal winters 2009-10 and 2019-20 showing domination of regimes 1 and 4, respectively). Regimes 1 and 2 occur less often than 3 and 4 (Fig. 7.9, Tab. 7.2), although they have larger modularity per state, i.e., the HGT states belonging to them are more distinguishable. Atmospheric patterns

	Community 1	Community 2	Community 3	Community 4
Modularity	0.109	0.122	0.115	0.13
Number of states	777	890	940	1062
Modularity per state, ( $\cdot 10^{-4}$ )	1.4	1.37	1.22	1.22

**Table 7.2:** The same as in Table 7.1, but for the regimes obtained from the reanalysis HGT data set.

characteristic for the first regime are rendered persistent and predictable at intra-seasonal time scales (Fig. 7.12). However, this regime exhibits high diversity, indicating strong variability at longer (inter-annual and decadal) time scales. This corroborates the general finding that atmospheric blocking structures entail stationary winter atmospheric circulation while their

prediction at inter-annual to decadal time scales is cumbersome. We find significantly high similarity for the second regime, implying that the spatial anticyclonic anomaly patterns characteristic for this regime are comparable between different years. Note that high similarity obtained for the first and second regimes is likely the source of large values of the modularity per state within these regimes (see Tab. 7.2). Conversely, we find that atmospheric conditions as identified in the third regime which, e.g., often result in extremely cold European winters are poorly predictable at inter-annual time scales. Finally, positive AO and NAO phases as represented by the fourth regime are dynamically opposite to the atmospheric blocking structures (negative AO and NAO) captured by the first regime.

This is in agreement with Ref. [159], and references therein, who investigated characteristic NAO time scales. They found that the two phases of the NAO have intrinsically different decay characteristics, with the negative NAO events showing enhanced persistence associated with blocking, see als [189]. Ref. [159] investigate the jet positions over the North Atlantic region. They found that the southern jet position, associated with the negative NAO phase (and Greenland blocking) has smaller tendency, and therefore more persistent (see [150]) than the northern position, associated with the positive NAO phase.

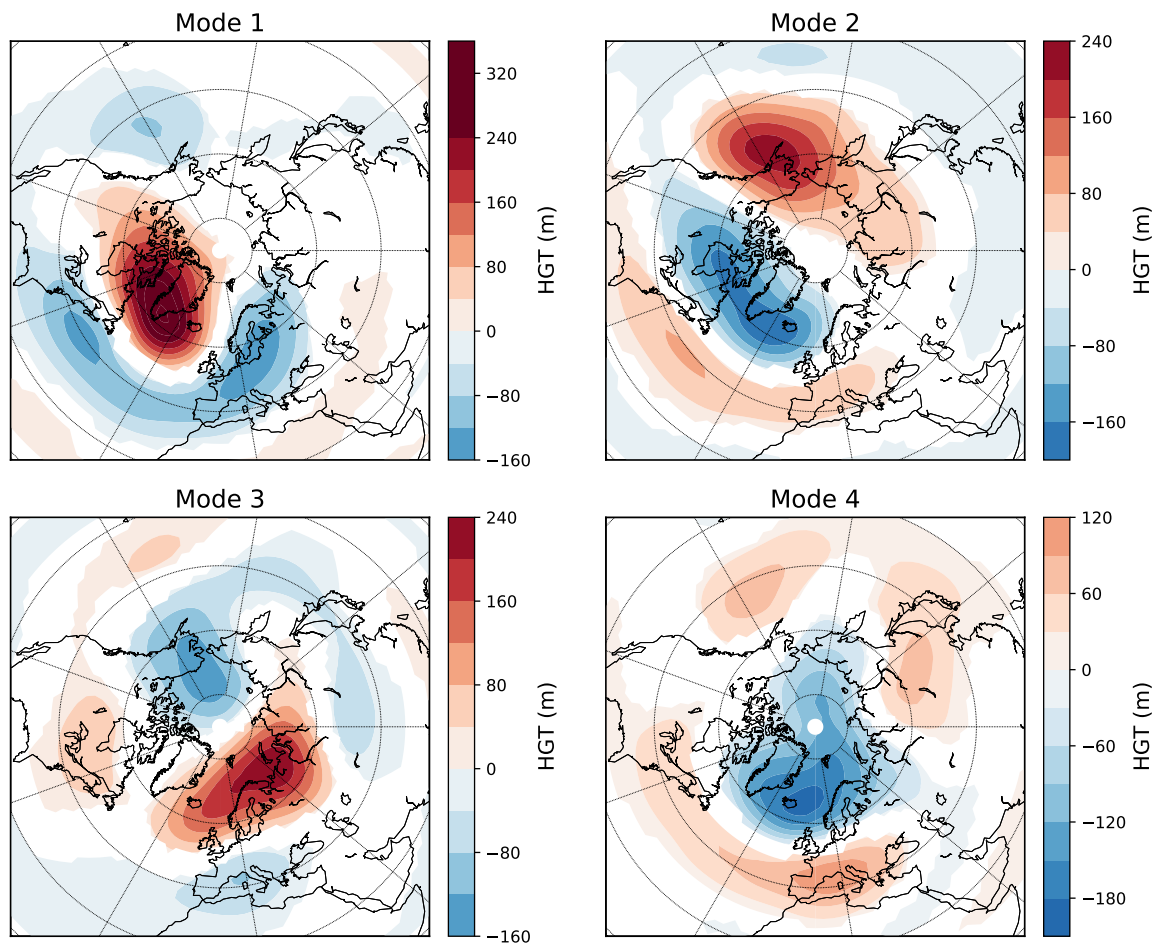


**Figure 7.10:** Composite patterns of HGT corresponding to the obtained regimes. The composites are calculated as HGT averaged over 20% most typical states of each of the regimes. Only values that are significantly different from zero by Student’s t-test with a critical value of 0.01 are shown.

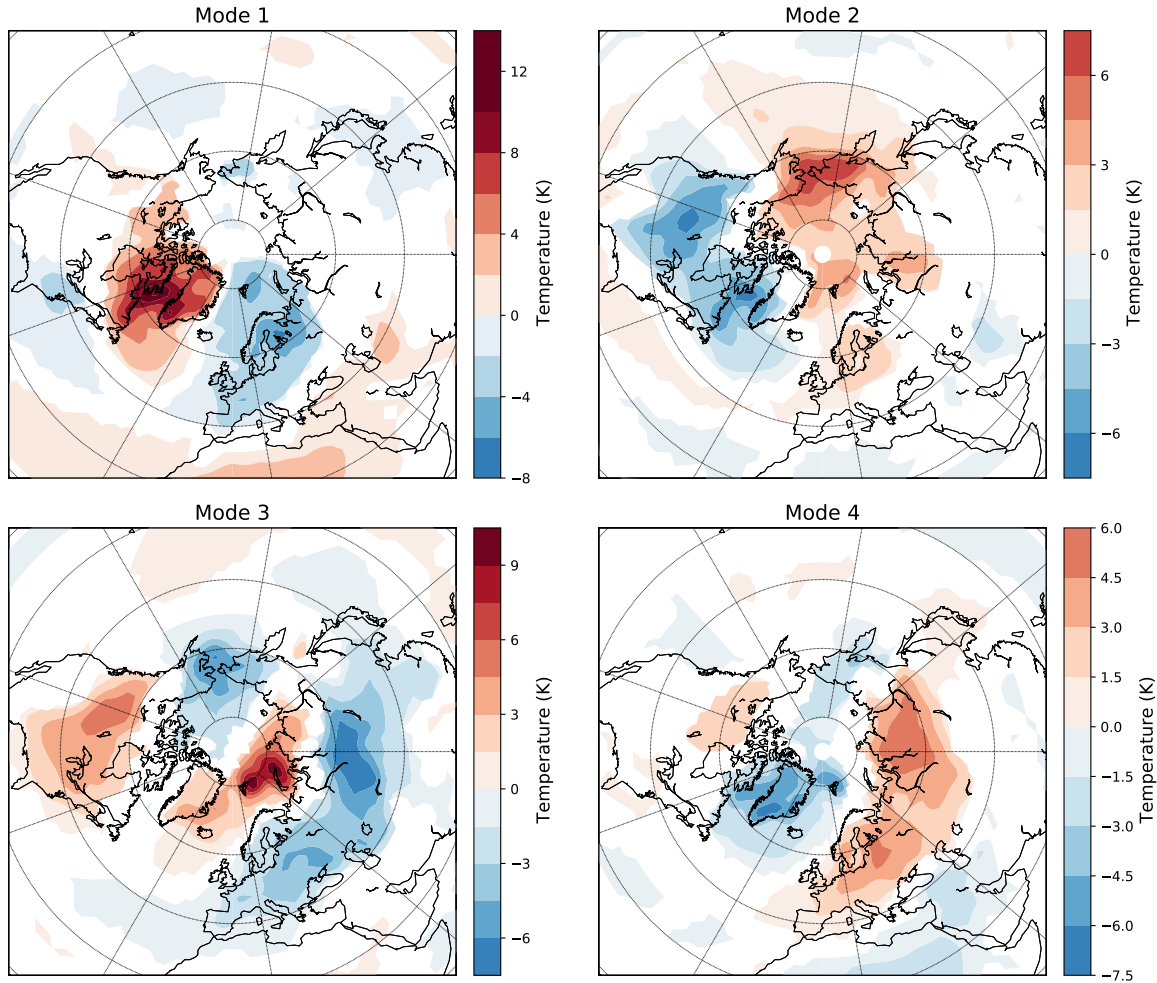


**Figure 7.11:** Composite patterns of surface air temperatures (SAT) corresponding to the obtained HGT regimes. The composites are calculated as SAT averaged over 20% most typical states of each of the regimes. Only values that are significantly different from zero by Student’s t-test with a critical value of 0.01 are shown.

## 7.4 Summary and conclusions

The proposed method allows us to (1) reveal recurrent regimes of atmospheric circulation from spatially distributed observations, and, simultaneously, (2) obtain a set of dynamical variables serving as an embedding for the regimes. A combination of the two nonlinear data-driven approaches – KPCA and recurrence analysis – provides comprehensive investigation of the mode content of the observed dynamics, including the regime identification, their dynamical representation and characteristics, and analyzing the dynamical properties of inter-regime evolution. Both parts of the method are based on constructing the same kernel matrix that consists of pairwise similarities between atmospheric states at different dates. In the first part this matrix produces the recurrence network, which when partitioned yields separation of all observed states into the regimes. RQA applied to the obtained submatrices relating to different regimes (or communities), helps to study important properties of temporal evolution of the regimes, e.g., predictability, persistence, similarity, and intermittency. In the second part, the principal components of the kernel matrix (KPCs) are used to construct a space in which the states belonging to different regimes are well-separated.

It is worth noting that the KPCA with Gaussian kernels is very close to the diffusion map

method [190], based on decomposition of a diffusion operator reconstructed from the data. More precisely, the 1-step diffusion maps should give the same, up to a transformation, basis of principal components as Gaussian KPCA. Thus, we can expect a clear separation of the regimes in the diffusion space too. Moreover, the use of an n-step diffusion map space as an embedding for the regimes may be more effective, since many paths between network's nodes render it more robust against noise. In this work, we demonstrate that even the basic Gaussian KPCA represents the recurrence network communities well due to the same distance matrix used in both the RP definition and Gaussian kernels. In future, diffusion maps could be adopted for this purpose.

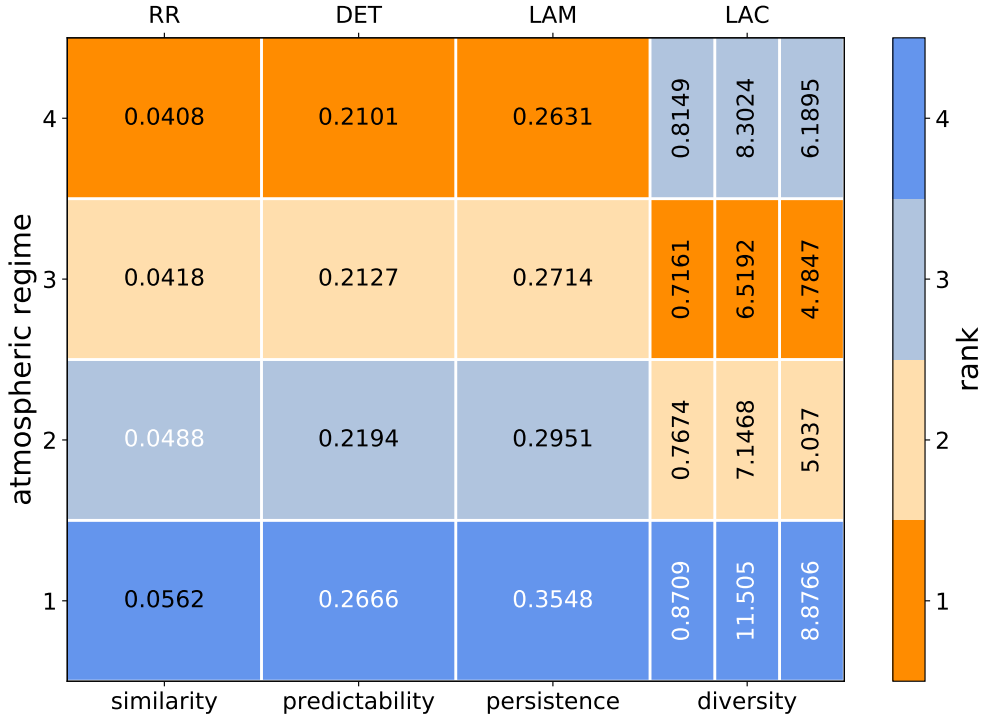


**Figure 7.12:** Results of recurrence quantification analysis for the atmospheric regimes obtained in the reanalysis data set. The four different RQA measures are labelled with their respective interpretation. Values that significantly exceed the values corresponding to randomly obtained partitions (see the text) are printed in white; other values are printed in black. Color coding illustrates the ordering of the RQA values (ascending column-ranking) for better comparability.

We demonstrate, using both model and observation data, that the detected regimes of the Northern Hemisphere mid-latitude winter atmosphere correspond to qualitatively different states, which cover the well-known modes NAO, AO, and PNA. We show that typically only a few leading KPCs are sufficient for the embedding of the regimes. Thus, these KPCs can be used as dynamical variables describing the alternation of the obtained regimes, and future works can aim at predictive data-driven models of their dynamics (see, e.g., Refs. [191, 192]). Moreover, having the dynamical variables representing the atmospheric modes, we can state a problem of finding long-term climatic predictors (e.g., ENSO, QBO, solar cycle, etc.) making it possible to elaborate a scheme for inter-annual forecast of dominating weather patterns.

The kernels Eq. (7.4), based on the distance Eq. (7.8), reflect similarity between two short-term patterns, each realized within one day. This leads to extracting the recurrent but not necessary persistent patterns (the persistence is separately studied by the RQA), which are distributed over the whole mid-latitude belt. However, we can change the distance definition, adapting it to the desired properties of regimes to extract. For example, we can

target the method to long-living (persistent) regimes via time-lag extension of states, or use other weightings, Eq. (7.9), to emphasize some geographical regions. Those topics are left for future research.

## Acknowledgments

The authors are grateful to the two anonymous reviewers for fruitful suggestions and comments. They helped to improve the article significantly. The QG3 model code is provided by the courtesy of Dmitri Kondrashov (UCLA) and Fabio d'Andrea (ENS). This work was supported by the grant #22-12-00388 of the Russian Science Foundation (D. Mukhin) and Deutsche Forschungsgemeinschaft in the context of the DFG project MA4759/11-1 'Nonlinear empirical mode analysis of complex systems: Development of general approach and application in climate' (T. Braun).

## Author Declaration

### Conflict of Interest

The authors have no conflicts to disclose.

### Author Contributions

DM and AH developed the method for detecting regimes, TB and NM analyzed the regimes by the RQA approach. All the authors analyzed results and contributed to writing the manuscript.

## Data Availability Statement

The data that support the findings of this study are openly available in NCEP/NCAR reanalysis [179] archive at <https://ps1.noaa.gov/data/gridded/data.ncep.reanalysis.html>. The time series of the QG3 model are available upon request.





## 8 | Sampling rate-corrected analysis of irregularly sampled time series

Tobias Braun<sup>1</sup>, Cinthya N. Fernandez<sup>2</sup>, Deniz Eroglu<sup>3</sup>, Adam Hartland<sup>4</sup>, Sebastian F. M. Breitenbach<sup>5</sup>, Norbert Marwan<sup>1,6</sup>

- 1 – Potsdam Institute for Climate Impact Research (PIK), Member of the Leibniz Association, 14473 Potsdam, Germany, Tel.: +49-331-28820744
- 2 – Institute for Geology, Mineralogy and Geophysics, Ruhr-Universität Bochum, 44801 Bochum, Germany
- 3 – Faculty of Engineering and Natural Sciences, Kadir Has University, 34083 Istanbul, Turkey
- 4 – Environmental Research Institute, School of Science, University of Waikato, Hamilton, Waikato 3240, New Zealand
- 5 – Department of Geography and Environmental Sciences, Northumbria University, Newcastle upon Tyne, NE1 8ST, UK
- 6 – University of Potsdam, Institute of Geosciences 14473 Potsdam, Germany

**Braun, T.**, Fernandez, C. N., Eroglu, D., Hartland, A., Breitenbach, S. F., & Marwan, N. (2022). Sampling rate-corrected analysis of irregularly sampled time series. *Physical Review E*, 105(2), 024206. doi: 10.1103/PhysRevE.105.024206 [2]

### Abstract

The analysis of irregularly sampled time series remains a challenging task requiring methods that account for continuous and abrupt changes of sampling resolution without introducing additional biases. The edit-distance is an effective metric to quantitatively compare time series segments of unequal length by computing the cost of transforming one segment into the other. We show that transformation costs generally exhibit a non-trivial relationship with local sampling rate. If the sampling resolution undergoes strong variations, this effect impedes unbiased comparison between different time episodes. We study the impact of this effect on recurrence quantification analysis, a framework that is well-suited for identifying regime shifts in nonlinear time series. A constrained randomization approach is put forward to correct for the biased recurrence quantification measures. This strategy involves the generation of a novel type of time series and time axis surrogates which we call sampling rate constrained (SRC) surrogates. We demonstrate the effectiveness of the proposed approach with a synthetic example and an irregularly sampled speleothem proxy record from Niue island in the central tropical Pacific. Application of the proposed correction scheme identifies a spurious transition that is solely imposed by an abrupt shift in sampling rate and uncovers periods of reduced seasonal rainfall predictability associated with enhanced ENSO and tropical cyclone activity.

## 8.1 Introduction

The analysis of time series from complex systems calls for numerical methods that capture the most relevant features in the observed variability. At the same time, the impact of various frequently encountered data-related intricacies such as low signal-to-noise ratio, nonstationarity, and limited time series length must be accounted for. A major challenge is posed by irregular sampling, i.e., variations in the interval  $\Delta_i = t_i - t_{i-1}$  between consecutive measurement times  $t_{i-1}$  and  $t_i$ . Irregular sampling is observed in many complex real-world systems. The underlying mechanisms that render the temporal sampling irregular may differ: sampling can be inherently irregular due to an additional process that controls the sampling interval (e.g., financial or cardiac time series [193, 194]); a mixture of various external processes can result in ‘missing values’, i.e., multiple interacting processes result in the non-availability of measurements (e.g., sociological or psychological survey data [195]) or cause failures of the system (e.g., mechanical/electrical systems [196]); finally, the measurement process often results in irregularly sampled time series (e.g., astronomical [197] or geophysical systems [198]). Proxy time series obtained from palaeoclimate archives are a particularly challenging example since irregularity in the temporal sampling can itself contain valuable information on the processes of interest [199]. The growth rate of a stalagmite for example depends on variable environmental factors, including temperature in the cave and drip rate [200], among others. Since these factors and their variability are strongly coupled to the environmental conditions outside the cave, growth rate must be regarded as a dynamical indicator for example, hydrological conditions which in turn determine variations in the temporal sampling of the proxy time series.

Across many research communities, resampling based on interpolation techniques and imputation approaches are popular methods for making irregularly sampled time series compatible with standard time series analysis tools [201, 202]. Artefacts and statistical biases caused by interpolation techniques are well-known and may result in misinterpretation of the extracted time series properties, an issue further aggravated by the fact that biases introduced by interpolation may vary among different systems [203]. The robustness of results arising from different interpolation techniques for the same data set is rarely examined. For instance, linear interpolation will not compensate for the effect of lower variability during sparsely sampled episodes in a time series compared to more densely sampled periods. In fact, linear interpolation and mean imputation decrease variance to a hardly quantifiable, data-related degree [204]. Finally, more complex imputation models may account for such finite (sampling) size effects but may not represent the ‘natural’ variability of a time series adequately. For data *not-missing-at-random*, the assignment of a sufficient imputation model can be challenging and must account for nonstationarity in the underlying non-random effects (e.g., for the palaeoclimate example mentioned above). Similar biases are known from the problem of imbalanced data, i.e., given two populations that should be compared based on a statistical model, a majority class exists that contains significantly more samples than the minority class and thus, oversampling techniques are applied to compensate for the resulting bias [205, 206].

Geophysical time series frequently exhibit nonlinear features such as nonlinear oscillations and critical regime transitions, e.g., tipping points [207]. Dynamical system theory regards observations from such systems as embedded in a higher-dimensional phase space and offers a range of tools to quantify gradual or abrupt changes in these dynamics [40, 29]. The power of these methods relies on their ability to uncover features that regular techniques, such as autocorrelations or variance estimation, fail to uncover [41]. Aiming for higher applicability of nonlinear time series analysis methods in the Earth sciences, irregular sampling approaches have been proposed [208, 209, 210]. One of these approaches is based on the idea of transform-

ing sub-sequences of unequal lengths in a time series into each other and comparing the costs of these transformations for all sub-sequences [23]. More generally, the definition of a metric distance between states at different instances of time can entail dynamical information on the evolution of the phase space trajectory of the studied system. While standard metrics (such as Euclidean distance) fail to account for irregular sampling, the TrAnsformation-Cost Time-Series (TACTS) [211] includes the temporal information for distinct time series segments. The TACTS method is based on the edit distance measure, which was originally introduced to measure the similarity between marked point processes [23]. Similar approaches based on the edit or Levenshtein distance have been used in natural language processing [212] and metric analyses of point processes [130], among many others.

In this work, we focus on the application of the (m)Edit-distance [130], which is a modified edit distance measure using a nonlinear transformation function instead of a scaler factor for measuring a cost operation. The modification helps to evaluate temporal patterns in sparse datasets such as paleoclimate proxies or extreme events. The time sampling regularization by (m)Edit-distance preprocesses irregularly sampled time series for the computation of recurrence plots (RPs) [20]. The (m)Edit-distance approach can potentially be employed in any methodological framework that includes computation of a distance (or similarity) measure. The RP technique represents one particular application that has proven to be a powerful approach, tackling many of the fundamental problems in time series analysis, such as time series classification [213], the study of synchronization between multiple time series [214], and detection of regime transitions [93]. Recurrence quantification analysis (RQA) provides a means of quantifying the tendency of a time series to revisit previously visited states and has grown in its scope from basic predictability quantification towards more ambitious measures that, e.g., capture the multiscale nature of transitions [63, 215, 1]. The identification of shifts stands out as a particularly interesting application since critical transitions can often be linked to the vulnerability of the respective regional climate system towards external shocks or feedback mechanisms. The combination of the (m)Edit-distance approach and RPs offers a promising approach to identify regime transitions in irregularly sampled records, which may otherwise be impeded without an adequate technique designed to account for sampling variations [37, 50, 216]. In following this approach, special care must be taken if irregular sampling intervals undergo strong variations, i.e., where the process(es) that control the sampling rate are rendered non-stationary. In some applications, segments can be chosen such that they do not cover the same time period but the same number of values on average. Other applications require fixing a particular time period to be covered by each segment since this time period corresponds to the time scale under investigation, e.g., a year for seasonal time series. Even if such an approach is not motivated by the research question, splitting the time series into segments that correspond to non-equal time periods will result in mixing of time scales in the resulting distance matrix if the sampling rate is highly non-stationary. Here, we focus on segments that cover equal time periods but varying numbers of values, referred to as *segment size*. We will show that in such cases, the resulting strong variations in segment size entail a non-trivial sampling bias of the (m)Edit-distance.

We introduce the (m)Edit-distance methodology in Sect. 8.2.1 followed by a short summary of recurrence analysis in Sect. 8.2.2. Sect. 8.3 illustrates the problem of strong variations in the sampling rate whereas model time series are studied to elucidate the sample size effects. A correction scheme based on constrained randomization is proposed in Sect. 8.4. In Sect. 8.5, we demonstrate the importance to correct for the identified sample-size dependence in an application to a palaeoclimate record from Niue island in the central Pacific where we identify variations in seasonal predictability. We conclude our findings in Sect. 8.6.

## 8.2 Methodology

### 8.2.1 The (m)Edit-distance measure

Many approaches in nonlinear time series analysis are based on some notion of a (dis)similarity measure. For deterministic systems, embedding the univariate time series into an  $m$ -dimensional phase space offers a multitude of quantitative approaches to analyse the variability of its trajectory [145]. Yet appropriate techniques to extract the embedding dimension and delay from empirical data are needed. These approaches can be cumbersome. In this work we focus on univariate time series wherein the most widespread dissimilarity measure between distinct segments  $\mathcal{S}_a, \mathcal{S}_b$  is the Euclidean distance. It is a metric distance, i.e., its value is always positive  $D(\mathcal{S}_a, \mathcal{S}_b) \geq 0$ , it is symmetric  $D(\mathcal{S}_a, \mathcal{S}_b) = D(\mathcal{S}_b, \mathcal{S}_a)$ , and the triangle inequality holds  $D(\mathcal{S}_a, \mathcal{S}_c) \leq D(\mathcal{S}_a, \mathcal{S}_b) + D(\mathcal{S}_b, \mathcal{S}_c)$ . If the time series is characterized by missing values or the sampling interval  $\Delta_i$  is irregular (e.g., due to irregularities in the measurement process), no straight-forward application of Euclidean distance or comparable metrics is possible: dissimilarity of values at unequal time scales would be computed without accounting for their non-equality. Linear interpolation as a means of resampling the time series values onto a regular time axis is among the most popular approaches to regularize sampling [217]. Yet, hardly controllable artefacts arise from linear interpolation, ranging from difficulties related to altered absolute timing to underestimation of variance or overestimation of persistence [203, 33].

Originally proposed for natural language processing, the edit distance measure [218] is designed to compare sequences of variable length. Shifting and adding & deleting of strings were proposed as two elementary operations to quantify dissimilarities between words, an objective also pursued by other methods such as dynamic time warping [219]. The resulting costs are calculated by identifying a minimum cost path to transform one sequence into the other. Taking the next step towards an application to empirical time series, the edit distance was applied to point process data whereby cost parameters for the elementary operations remained arbitrary [23, 220]. By equipping the technique with data-driven cost parameter estimates, it was then applied to irregularly sampled palaeoclimate time series [211]. A further modification ((m)Edit distance) with an application to extreme events was proposed to consider the saturation of shifting costs when a certain time scale  $\tau$ , separating the two compared segments, is exceeded [130]. The main difference between applying the edit distance to series of events/spike trains and irregularly sampled time series is that for the latter, amplitudes of time series values must be considered. In the following, whenever no assumptions are made about the amplitudes of a signal, we refer to ‘events’. The edit distance between two segments  $\mathcal{S}_a, \mathcal{S}_b$  of an irregularly sampled time series is computed by minimizing the transformation costs by:

$$D(\mathcal{S}_a, \mathcal{S}_b) = \min \left\{ \sum_{\alpha, \beta \in \mathcal{C}} \left[ \underbrace{f_{\Lambda_0}(t(\alpha), t(\beta); \tau)}_{\text{shifting}} + \underbrace{\Lambda_k \|L_a(\alpha) - L_b(\beta)\|}_{\text{amplitude change}} \right] + \underbrace{\Lambda_S (|I| + |J| - 2|C|)}_{\text{adding and deleting}} \right\} \quad (8.1)$$

with a norm  $\|\cdot\|$  (e.g., the Euclidean norm), the  $\alpha$ -th/ $\beta$ -th amplitudes  $L_a(\alpha), L_b(\beta)$  of the segments  $\mathcal{S}_a, \mathcal{S}_b$  and the cardinalities  $|\cdot|$  of the sets  $I, J$  and  $\mathcal{C}$ . While the latter are a set of indices of the time series values,  $\mathcal{C}$  denotes the values that are shifted.  $D(\mathcal{S}_a, \mathcal{S}_b)$  is a metric distance. The cost parameters  $\Lambda_0, \Lambda_k$ , and  $\Lambda_S$  need to be fixed prior to cost optimization. We choose the cost parameter for amplitudes changes  $\Lambda_k$  as suggested in [211]:

$$\Lambda_k = \frac{M - 1}{\sum_{i=1}^{M-1} \|x_i - x_{i+1}\|} \quad (8.2)$$

The cost parameter  $\Lambda_S$  for deleting & adding has to be chosen such that deletions are neither ‘too cheap’ nor ‘too expensive’. For a set of time series values with a large temporal distance or very distinct amplitudes, a deletion and addition should be favorable while a too low value of  $\Lambda_S$  will result in a transformation of sequences solely by deletion and adding operations even for very close time series values. We follow the scheme proposed in [37] by assuming normality for the distance values between all segments of the time series and optimize  $\Lambda_S$  within a specified range using a Kolmogorov-Smirnov (KS)-test to ensure that the normality assumption holds as close as possible. Following the modification proposed in [130], costs associated with shifting of time instances between two time series values are controlled by the logistic function

$$f_{\Lambda_0}(t(\alpha), t(\beta); \tau) = \frac{\Lambda_0}{1 + e^{-(\|t_a(\alpha) - t_b(\beta)\| - \tau)}} \quad (8.3)$$

where  $\tau$  is the location parameter of the logistic function, reflecting a characteristic time scale that separates exponentially increasing from saturating/bounded exponentially increasing costs for shifting. We choose  $\tau$  as the average sampling interval of the time series;  $\tau = T/M$  with the total time period  $T$  and the number of samples  $M$ . Interpreting  $\tau$  as a ‘temporal tolerance’, this choice ensures that shifting exponentially fast becomes less favorable if time instances are separated by several standard deviations of the sampling interval distribution. Finally, a value for the maximum costs associated with shifting  $\Lambda_0$  needs to be set. The ratio  $\Lambda_K/\Lambda_0$  reflects the relative importance of temporal and magnitudinal separation; in the limiting case  $\Lambda_K/\Lambda_0 \gg 1$ , irregular sampling is no longer accounted for and the resulting distance between two segments solely reflects the norm  $\|L_a(\alpha) - L_b(\beta)\|$  for all amplitudes  $L_a(\alpha)$ ,  $L_b(\beta)$  of both segments  $\mathcal{S}_a$ ,  $\mathcal{S}_b$ . In the opposite case  $\Lambda_K/\Lambda_0 \ll 1$ , the time series can be regarded as a series of events since cost optimization is independent of their amplitudes. We choose  $\Lambda_K = \Lambda_0 = 1$ . It must be stressed that this rate depends on the research question and the data under study.

In the following, we discuss the finite-sample effects bias (m)Edit-distance values  $D(\mathcal{S}_a, \mathcal{S}_b)$  and give a summary of the RP methodology. This facilitates the presentation of finite-sample effects discussed in Sect. 8.3 alongside an illustration of the (m)Edit-distance methodology (Fig. 8.1).

### 8.2.2 Recurrence analysis

The tendency to recur to previously visited states is a ubiquitous feature shared by time series from many different complex systems. Recurrence plots encode this information in a 2-dimensional binary matrix, indicating a recurrence between two states  $\vec{x}_i$  and  $\vec{x}_j$  at times  $i$  and  $j$  if the respective states are similar with respect to a given norm  $D(\vec{x}_i, \vec{x}_j)$  [19]:

$$R_{ij} = \begin{cases} 1 & \text{if } D(\vec{x}_i, \vec{x}_j) \leq \varepsilon \\ 0 & \text{if } D(\vec{x}_i, \vec{x}_j) > \varepsilon. \end{cases} \quad (8.4)$$

The norm  $D(\vec{x}_i, \vec{x}_j)$  yields a symmetric, real-valued distance matrix  $\mathbf{D}$  between states at all time instances  $i, j$ . By thresholding  $\mathbf{D}$  with the vicinity threshold  $\varepsilon$ , a notion of similar and dissimilar states is implemented and defines the recurrence between each pair of states. The underlying idea is based on the Poincaré recurrence theorem that states the recurrence of a dynamical system’s trajectory  $\vec{x}(t)$  to an  $\varepsilon$ -neighborhood of any perviously visited state after sufficiently long time [16]. For the main diagonal of the RP, it always holds that  $R_{ij} \equiv 1$ . If no phase space reconstruction is applied, states  $\vec{x}_i$  and  $\vec{x}_j$  correspond to time series amplitudes  $x_i$  and  $x_j$ . The threshold  $\varepsilon$  can be chosen based on different data-dependent criteria. In many applications, the recurrence rate is fixed to a certain percentage (e.g., 10 % recurrences [30])

or set to a multiple of the standard deviation of the distance matrix  $\mathbf{D}$  [124]. The geometric recurrence patterns encoded in a RP can be exploited to distinguish between stochastic and deterministic systems [20]; while a purely random white noise process will result in isolated dots in the recurrence matrix, time series from deterministic systems are known to yield diagonal line structures [20]. Long diagonal lines are characteristic for periodic systems; interrupted diagonal lines indicate chaotic dynamics. Recurrence quantification analysis (RQA) which evaluates the statistical properties of a RP has proven a versatile tool for diverse real-world applications, such as time series classification [221], study of causal relations [110] or regime shift detection [24].

Recurrence analysis overcomes some of the flaws of other statistical analysis tools when applied to geophysical time series, such as the Lyapunov exponent or correlation dimension [76, 222]. It is less sensitive to noise and can be applied to short time series. In combination with the (m)Edit-distance approach, first applications demonstrated its ability to detect regime transitions in palaeoclimate proxy records [223, 211]. In order to compute a RP for irregularly sampled time series,  $D(\vec{x}_i, \vec{x}_j)$  in Eq. (8.4) is identified with the modified edit distance from Eq. (8.1). In contrast to regular computation of metric distances, segments of the time series are required to obtain a distance value between two states. Generally speaking, segment size should be chosen sufficiently small to ensure that no aliasing effects arise due to interference between the segment width and the characteristic time scale of a time series (e.g., characteristic period of a periodic time series). For some applications the segments can be chosen such that all are equally sized  $|\mathcal{S}_a| = |\mathcal{S}_b| = \dots = N$ . If this is not possible, the variance of segment widths can still be minimized and for each pair of segments with differing widths; deletion & adding operations will contribute to the resulting transformation cost. If time series are short, we can allow for an overlap between segments, although caution is advised since this introduces a serial dependence in the resulting edit distances of overlapping segments and violates the normality assumption used in the estimation of  $\Lambda_S$ . Here, we focus on the most general case of unequal segment sizes. Apart from cases where segment size deviations can hardly be minimized, this is relevant in some real-world applications where we are interested in the recurrences between segments that correspond to a particular time scale, or where sampling rate is highly non-stationary and selecting a constant segment size would result in mixing of distinct time scales. The application to palaeoclimate data (Sect. 8.5) will illustrate such a case. There, the focus lies on the comparison of seasonal sequences in an irregularly sampled proxy time series.

Predictability is a feature of time series that can help to identify and classify different dynamical regimes in the evolution of the studied system. Since the lengths of diagonal lines in a RP reflect the predictability of a system, the number of diagonal lines which exceed a specified minimum line length  $l_{\min}$  can be used as a predictability measure:

$$\text{DET} = \frac{\sum_{l=l_{\min}}^N P(l)}{\sum_{l=1}^N P(l)} \quad (8.5)$$

with the number  $P(l)$  lines of length  $l$ . Determinism (DET) can be linked to the correlation dimension of a dynamical system [224] and has successfully been used in diverse empirical analyses [37, 50, 24] to detect transitions between regimes of varying predictability. We use DET as a recurrence quantifier to test the impact of the sampling-based correction scheme introduced below.

### 8.3 Segment size dependence

Finite-sample effects are known to entail statistical biases in various time series analysis methods. Linear or spline interpolation is often employed as a pre-processing technique to

enable the application of standard time series analysis tools to irregularly sampled time series. Interpolation techniques do not account for basic finite-sample biases. For instance, statistical location and scale measures (such as the median or volatility indicators) are known to be biased for small sample sizes [225, 226]. Given two segments  $\mathcal{S}_a, \mathcal{S}_b$  with  $|\mathcal{S}_a| \gg |\mathcal{S}_b|$ , estimating their variance (e.g., as a volatility indicator or in order to compute a continuous wavelet spectrum) can result in underestimation of the variance for the shorter segment. Similarly, persistence estimators are generally biased due to finite-sample effects, even for Markovian stationary stochastic processes [227]. Whenever a sliding-window analysis for nonstationary, irregularly sampled time series is carried out, variations in the sampling rate will inevitably result in a mixture between the actual variability of the statistical indicator and purely sampling-related variations. As interpolation techniques are usually limited to resampling values such that sampling intervals are equal, this effect is not compensated. Similar intricacies need to be considered in short time series, e.g., when computing correlations between multiple time series (of varying length) [228].

While not designed to compensate such effects, the (m)Edit-distance methodology does not introduce any known additional biases. The computation of transformation costs is demonstrated with two exemplary pairs of segments  $\mathcal{S}_a, \mathcal{S}_b$  and  $\mathcal{S}_c, \mathcal{S}_d$  (Fig.8.1). The segments  $\mathcal{S}_a, \mathcal{S}_b$  all display distinct operations for transforming a segment into another: in the first step, a shift of amplitude and time are applied to transform the time instance  $t_a(1)$  and amplitude  $L_a(1)$  of the first segment into time instance  $t_b(2)$  and amplitude  $L_b(2)$  of the second segment. The cost  $C_1$  associated with this operation is the sum of shifting both time and amplitude. After shifting the third value of  $\mathcal{S}_a$  to match the third value of  $\mathcal{S}_b$ , both a deletion and an adding operation are performed in step 3 with twice the cost  $\Lambda_S$  for a adding/deleting operation. The same transformation could have been achieved with an additional shifting operation. The preferred operation is determined by the particular choice of cost parameters. As  $|\mathcal{S}_a| = 3$  and  $|\mathcal{S}_b| = 4$ , the first value of  $\mathcal{S}_b$  is added in step 4. The resulting cost is the sum of all costs for each step. While different transformation paths are possible, the algorithmic implementation ensures that  $C$  is minimized with respect to all possible combinations. Another example is displayed in the right column of Fig.8.1. The setup differs in that the indicated segments  $\mathcal{S}_c, \mathcal{S}_d$  are longer than  $\mathcal{S}_a, \mathcal{S}_b$  ( $|\mathcal{S}_c| = 8, |\mathcal{S}_d| = 7$ ). Despite a similar set of transformations, the resulting costs  $\tilde{C}$  are significantly higher for the exemplary choice of parameters.

A systematic derivation of transformation costs on segment size/sampling rate for exponentially distributed sampling intervals is given in appendix D. Note that the identified effect is not due to an immanent misconception in the edit distance computation. It solely arises from the fact that the edit distance is applied in a setting where the time axis is not only irrations in its sampling rate. In particular, abrupt transitions in the sampling rate between a time period  $T_1$  with low sampling rate  $\lambda_1$  and  $T_2$  with high sampling rate  $\lambda_2$  will imprint a non-trivial  $\lambda_1, \lambda_2$ -dependence on the transformation cost  $D(\mathcal{S}_a \mathcal{S}_b)$  between any two segments. In a recurrence analysis of time series, the focus lies on the similarity of states based on the amplitudes of the time series. Hence, we argue that the identified dependencies counteract the goal of recurrence analysis of irregularly sampled time series and thus need to be corrected such that recurrence quantification measures reflect the dynamical behaviour of the underlying system rather than mere shifts in the sampling rate.

We numerically examine the dependence of transformation costs between segments  $\mathcal{S}_a, \mathcal{S}_b$  on their sizes  $N_a, N_b$  for simple synthetic time series. We test irregularly sampled time series from three different model systems: uncorrelated uniform noise, an AR(1)-process ( $\tau = 5$ ), and a sinusoidal ( $\nu = 1/25$ ) with superimposed low-amplitude white noise. Segments of specified sizes from each of these systems are drawn to compute segment size-specific costs.

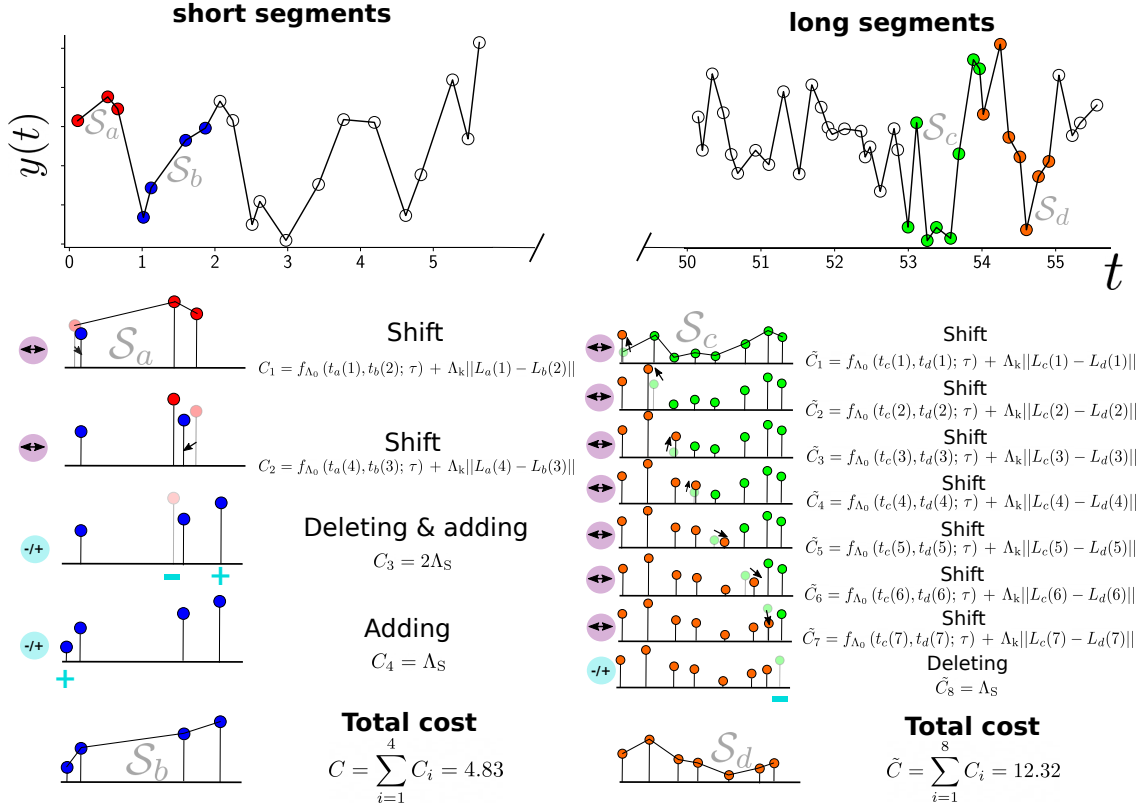


**Figure 8.1:** Schematic illustration of how irregularly sampled segments of varying lengths are transformed with the (m)Edit-distance method. Two exemplary pairs of segments  $S_a$ ,  $S_b$  (**A**: red, blue) and  $S_c$ ,  $S_d$  (**B**: green, orange) of an irregularly sampled synthetic AR(1)-time series are displayed. Each row shows an operation applied to the respective segment (shift: purple, deletion/adding: cyan). Final costs  $C$  and  $\tilde{C}$  result from a specific choice of cost parameters as described in Sect. 8.2.1. Please note that the higher total cost in **B** showcase the dependence on segment length.

Irregular time axes are generated from a  $\gamma(\Delta; k, \Theta)$ -distribution with scale  $\Theta$  and shape  $k = \sqrt{2/\Gamma}$ , where  $\Gamma$  denotes the skewness of the distribution. This choice is motivated by the observation that sampling intervals in palaeoclimate proxy time series are often  $\gamma$ - rather than exponentially-distributed. For each system, we generate a ‘superpopulation’ ( $K = 100$ ) of time series and time axes. Fixing a different skewness  $\Gamma$  of the  $\gamma$ -distribution of each of the time axes between  $\Gamma \in [1, 8]$  ensures that for  $T = 10,000$ , segment sizes range between  $N \in [1, 20]$ . The modified edit-distance is used, Eq. (8.1) and deletions are included as a competing operation to shifting. The optimal  $\Lambda_S$  is estimated for each system according to the procedure outlined in Sect. 8.2.1: the KS-statistic is minimized for each systems, yielding  $\Lambda_S^{(\text{unif})} = 1.5$ ,  $\Lambda_S^{(\text{AR1})} = 1.5$ ,  $\Lambda_S^{(\text{sin})} = 3.5$ .

Figure 8.2a displays the obtained transformation costs in the cost matrices  $C(N_a, N_b)$  and  $\tilde{C}_{\text{shift}}(N_a, N_b)$  after averaging over  $K = 100$  different realizations. Regardless of the irregularity of the time axis and the respective system, a tendency of increasing total costs for larger segment sizes is observed (upper row). For the AR(1)-system, this increase is slower for fixed  $N_b$  and increasing  $N_a$  composed to the uncorrelated noise and the sinusoidal examples. More generally, the rate of increase differs between the considered systems but follows the same trend. In total,  $|N_a - N_b|$  ‘basic deletions’ (or adding operations) need to be carried out for each pair of segments with  $N_a \neq N_b$ . If costs for these basic deletions are subtracted and computed per shifting step, a similar dependency on  $N_a, N_b$  as observed in Fig. D.1c for the more simple case can be observed in the cost matrices  $\tilde{C}_{\text{shift}}(N_a, N_b)$  in Fig. 8.2b :



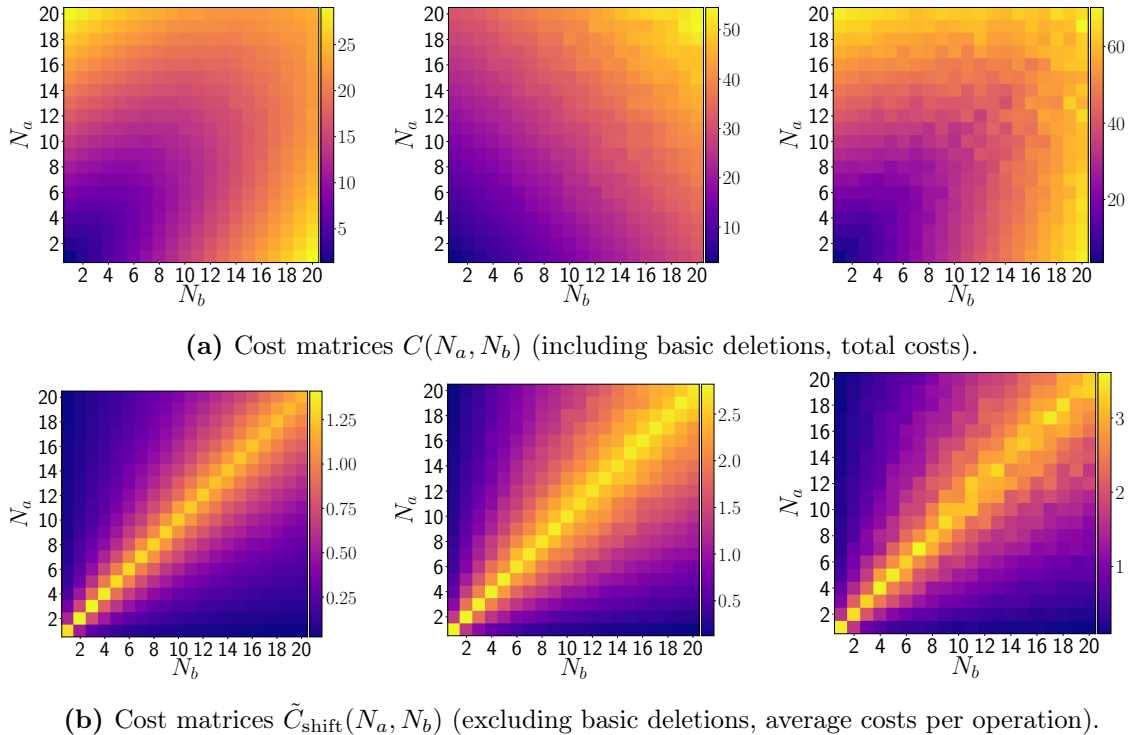


**Figure 8.2:** Cost matrices  $C(N_a, N_b)$  for the transformation of segments with different lengths, including basic deletions (a) and excluding basic deletions (b). Costs are shown for uncorrelated uniform-distributed noise (left), an AR(1)-process (center) and a sinusoidal with superimposed white noise (right). Sampling intervals are  $\gamma$ -distributed.

the cost of an average shift from a segment with  $N = N_a$  increases towards  $N_b = N_a$  and decays if segment size increases further. Consequently, the leading effect results from the basic deletions that are directly linked to the difference in segment sizes  $|N_b - N_a|$ . Yet, transformation costs still depend on segment size even after aligning both segment sizes by means of basic deletions; this effect likely results from having a higher probability of finding closely spaced values on the time axis as the sampling rate of one segment increases, yielding an increasing trend for average costs per operation (in fig. 8.2b).

## 8.4 Sampling rate constrained surrogates

Irregularly sampled time series with constant sampling rate can be studied with the (m)Edit-distance to obtain dissimilarity estimates between different time series segments. The resulting distance matrix can be used to perform a recurrence analysis. Moreover, other analysis techniques such as complex networks, clustering, or correlation analysis are based on (dis)similarity measures and could use the (m)Edit-distance as a metric to account for irregular sampling or to characterize event-like data. In section 8.3 we showed that in case of a non-constant sampling rate, an estimation of the (m)Edit-distance matrix is biased by significant differences in the segment sizes.

In the following, we propose a numerical correction-technique for recurrence analysis. We generate an ensemble of time series and time axis surrogates that reproduces the sampling properties of the real irregularly sampled time series. This surrogate ensemble is used for bias-correction of recurrence quantification measures, exemplified by the determinism DET.

### 8.4.1 Constrained randomization

When studying a system's dynamics with time series analysis tools, a null-hypothesis is formulated which can be tested. In case of recurrence analysis, this hypothesis could for example be non-stationarity of a dynamical property of the system (predictability, serial/cross-dependence, ...) expressed by a particular recurrence quantification measure. In the used example, the null-hypothesis tests whether the observed dynamics could be solely caused by variations in the sampling rate.

Parametric hypothesis testing for time series analysis often poses severe constraints on the statistical properties of the underlying probability distribution, e.g., normality. Surrogate tests represent a non-parametric and flexible method to test for a range of properties in a system, including nonlinearity or periodicity, among others [229, 230, 34]. Time series surrogates are altered copies of a real, underlying time series that only preserve a specified set of properties of the real time series. The general technique to generate surrogate realizations of a time series is constrained randomization [231]. After defining a set of constraints that state which properties of the real time series should be preserved, the time series is randomized such that these constraints are still fulfilled. Here, randomization will be carried out on the sampling interval  $\Delta_i$  with the constraint that for each segment  $\mathcal{S}_i$  of the real time series, segment size  $N_i$  is preserved. This is achieved by drawing sampling intervals  $\Delta_i$  (with replacement) from the empirical sampling interval distribution  $p(\Delta, \lambda(t))$ . For a given segment  $\mathcal{S}_i$  with size  $N_i$ ,  $N_i$  sampling intervals are drawn from  $p(\Delta, \lambda(t))$  and cumulated to generate a surrogate realization of the particular time axis segment:

$$\tilde{t}_{\mathcal{S}_i}^{(0)} = t_{\mathcal{S}_i}^{(0)}, \quad \tilde{t}_{\mathcal{S}_i}^{(j+1)} = \tilde{t}_{\mathcal{S}_i}^{(j)} + \sum_{m=0}^j \Delta_i^{(m)} \quad (8.6)$$

Let  $w$  be the time period covered by each segment. For any randomly sampled set of sampling intervals, the constraint of preserved segment size requires that

$$\tilde{t}_{\mathcal{S}_i}^{(N_i)} \stackrel{!}{\leq} w, \quad (8.7)$$

otherwise the random sampling of sampling intervals  $\Delta_i$  has to be repeated. If the distribution of segment sizes is short-tailed, i.e., no segments with size  $N \gg \mathbb{E}[k]$  exist, this simple randomization procedure converges rapidly for each segment. If segments of relatively large size are present – which is likely the case for non-stationary sampling rates – only a small subset of sampling intervals from the left tail of  $p(\Delta, \lambda(t))$  will fulfill the condition (8.7). In order to ensure convergence of the algorithm for large segments, a weight-function can be introduced for all sampling intervals to increase the likelihood of drawing short sampling intervals when a segment with large size is generated. We suggest the use of  $\beta$ -distributed weights  $\omega$ :

$$\omega(X; \alpha, \beta) = \frac{1}{B(\alpha, \beta)} x^{\alpha-1} (1-x)^{\beta-1} \quad (8.8)$$

with the  $\beta$ -function  $B(\alpha, \beta)$ . This choice is motivated by the fact that for  $\alpha = \beta = 1$ ,  $\omega(X; \alpha, \beta)$  becomes a uniform distribution. In our application, we choose  $\alpha = \beta = 1$  when the first iteration of sampling  $N_i$  sampling intervals  $\Delta_i$  is carried out. The population of sampling intervals is ordered from shortest to largest and each  $x_i \leftrightarrow \Delta_i$  is assigned a  $\beta$ -distributed weight  $\omega_i$ , i.e., for the first iteration, every sampling interval is drawn with equal probability. If the iteration fails ( $\tilde{t}_{\mathcal{S}_i}^{(N_i)} > w$ ),  $\alpha$  is increased by a small number  $\Delta\alpha$ , reshaping the beta-distribution and increasing the probability of drawing small sampling intervals. Thus, we perform a weighted sampling from the empirical distribution  $p(\Delta, \lambda(t))$  of sampling intervals with  $\beta$ -distributed weights. In the  $l$ -th iteration, we use  $\omega(X; \alpha_l, \beta = 1)$ ,  $\alpha_l = 1 + l\Delta\alpha$  as the

weight function for each segment. Finally, we can identify an amplitude difference  $\Delta y_i$  of the time series with each sampling interval  $\Delta_i$ . This correspondence is exploited by also drawing the respective amplitude difference for each drawn sampling interval. After the procedure is finalized and a surrogate has been generated, amplitude differences are cumulated, that yields both a time axis and time series surrogate. Both are denoted as sampling rate constrained surrogate (SRC-surrogates). The full randomization procedure thus preserves segment sizes in the correct temporal order and by definition approximately reproduces the distribution of amplitude differences and sampling intervals. It also preserves the correspondance between sampling intervals and amplitude differences, ensuring that if periods with high local sampling rate entail larger variance/strong amplitude changes in a real time series, this property is also included in the SRC-surrogates. The full procedure is outlined in Fig. 8.3 for an exemplary time series. Other randomization schemes are conceivable, e.g., varying the sampling weights after drawing each single sampling interval based on the size of the latter, or stratified randomization, i.e., performing the randomization differently for strata that correspond to the different segment sizes. However, the proposed scheme has proven to be effective within the scope of this work.

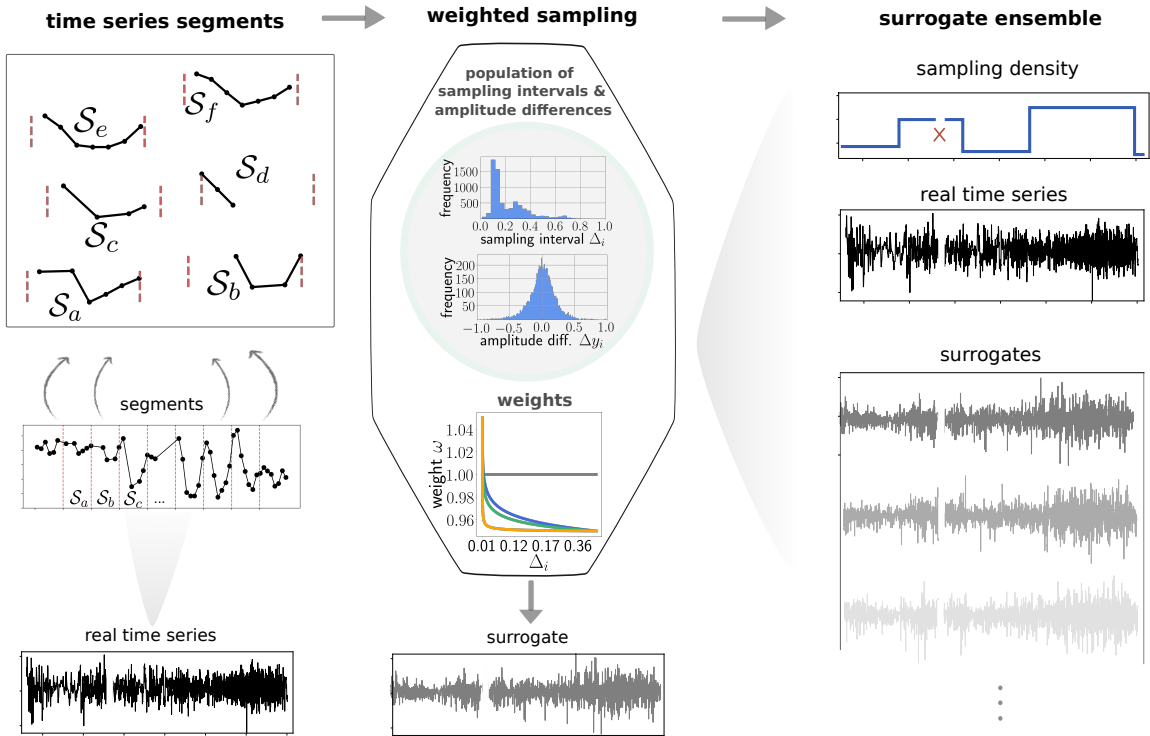


**Figure 8.3:** Schematic illustration of the constrained randomization procedure that generates SRC-surrogates for an exemplary irregularly sampled time series with non-stationary sampling rate. The left column shows the segmentation of the time series into segments of constant time period  $s$  but of variable size  $N_i$ . The center column illustrates the weighted sampling of sampling intervals and amplitude differences. Each sampling interval is assigned a  $\beta$ -distributed weight whereby the  $\alpha$ -parameter of the weight distribution is increased with each  $l$ -th failed iteration to favor short sampling intervals. The resulting surrogates preserve the empirical distributions and segment sizes. Since amplitude differences are sampled jointly with the respective sampling intervals, increased volatility simply due to a higher local sampling rate is reproduced by the SRC-surrogates.

With the presented scheme of generating SRC-surrogates, an ensemble of surrogates can be generated and (m)Edit-distance matrices  $\mathbf{D}$  computed for each SRC-surrogate. Any measure that is based on  $\mathbf{D}$  can consequently be computed for each surrogate separately, yielding a

distribution that can be used for testing the null-hypothesis formulated above based on the desired  $\alpha$ -confidence level.

### 8.4.2 Recurrence analysis of an AR(1)-process

In the example below, the proposed correction scheme is applied to an irregularly sampled AR(1)-process (Fig. 8.4a). We consider an autocorrelation increasing with time, visible by autocorrelation time  $\tau$  (Fig. 8.4b). A recurrence analysis is used to characterize the predictability of the time series in a sliding window analysis. Predictability is computed by means of determinism, DET, as defined in Eq. (8.5). In particular, we study how an abrupt shift of the sampling rate (represented by the skewness of  $\gamma$ -distributed sampling intervals) affects DET and if a continuous increase of predictability can be recovered despite this shift by using the proposed SRC-surrogate method. The shift appears at  $t = 1250$  (visible by variation of the segment size, Fig. 8.4b). We expect DET to reproduce the linear increase in autocorrelation time, because increased serial dependence implies longer and more diagonal lines in the RP. For the computation of the (m)Edit-distance measure, segments are picked such that each covers a constant time interval of  $w = 1$  which could correspond to a year in a real-world application. 200 SRC-surrogates are generated (see appendix D) with  $\alpha_0 = 1, \beta = 1$  and a step size for the shape parameter  $\alpha$  of the beta-distribution  $\Delta\alpha = 0.15$ . We set an upper limit of  $N_{\text{it}}^{(\text{max})} = 1000$  for the number of iterations in the generation of each segment which is never exceeded in the performed simulations. The deletion/adding cost parameter  $\Lambda_S$  is estimated separately for the real time series and the surrogate realizations, yielding  $\Lambda_S^{(\text{real})} = 5.3$  and  $\Lambda_S^{(\text{SRC})} = 2.6$ . Recurrence plots are computed on sliding windows of size  $s = 200\Delta$  with 75% overlap (time series length:  $T = 5000$ ). We fix a recurrence rate of 15% and do not apply any time-delay embedding. For each window, two DET values are obtained (Fig. 8.4c): the DET value of the real time series and the  $\alpha(= 95\%)$ -confidence level of DET values calculated from the SRC-surrogate ensemble. The DET measure indicates a spurious transition of predictability induced by the abrupt shift in sampling rate (Fig. 8.4c, grey shading). Both the real time series and the surrogate ensemble indicate this shift, demonstrating that the proposed SRC-surrogates effectively reproduce the sampling bias. The SRC-based correction is applied to DET values by dividing the real DET-series by the 95%-confidence level for each window (Fig. 8.4d). The resulting predictability estimates reproduce the expected linear increase in serial dependence whilst eliminating the spurious shift due to the jump of the sampling rate.

## 8.5 Real-world application: rainfall seasonality in the central Pacific

Many real-world proxy time series are characterized by irregular sampling or missing data and stationarity of the underlying process that controls the sampling rate cannot be guaranteed. This perspective even goes beyond uneven time axes as for some systems, it might be desirable to apply an adaptive windowing in order to obtain segments with segment sizes depending on specific parameters of the system. For instance, when analyzing cardiac time series it might be reasonable to choose the segment size adaptively to capture one heart-beat cycle within each segment. The length of every cycle is controlled by a variety of other physical, non-stationary parameters. Below, we focus on an irregularly sampled palaeoclimate proxy time series with a non-stationary temporal sampling rate. We demonstrate the effectiveness of the proposed approach by carrying out a sliding window recurrence analysis.

The palaeoclimate record analysed here is a seasonally resolved stalagmite proxy record from Niue Island in the southwestern Pacific (19°S, 169°W). It covers 1000 years in the mid-

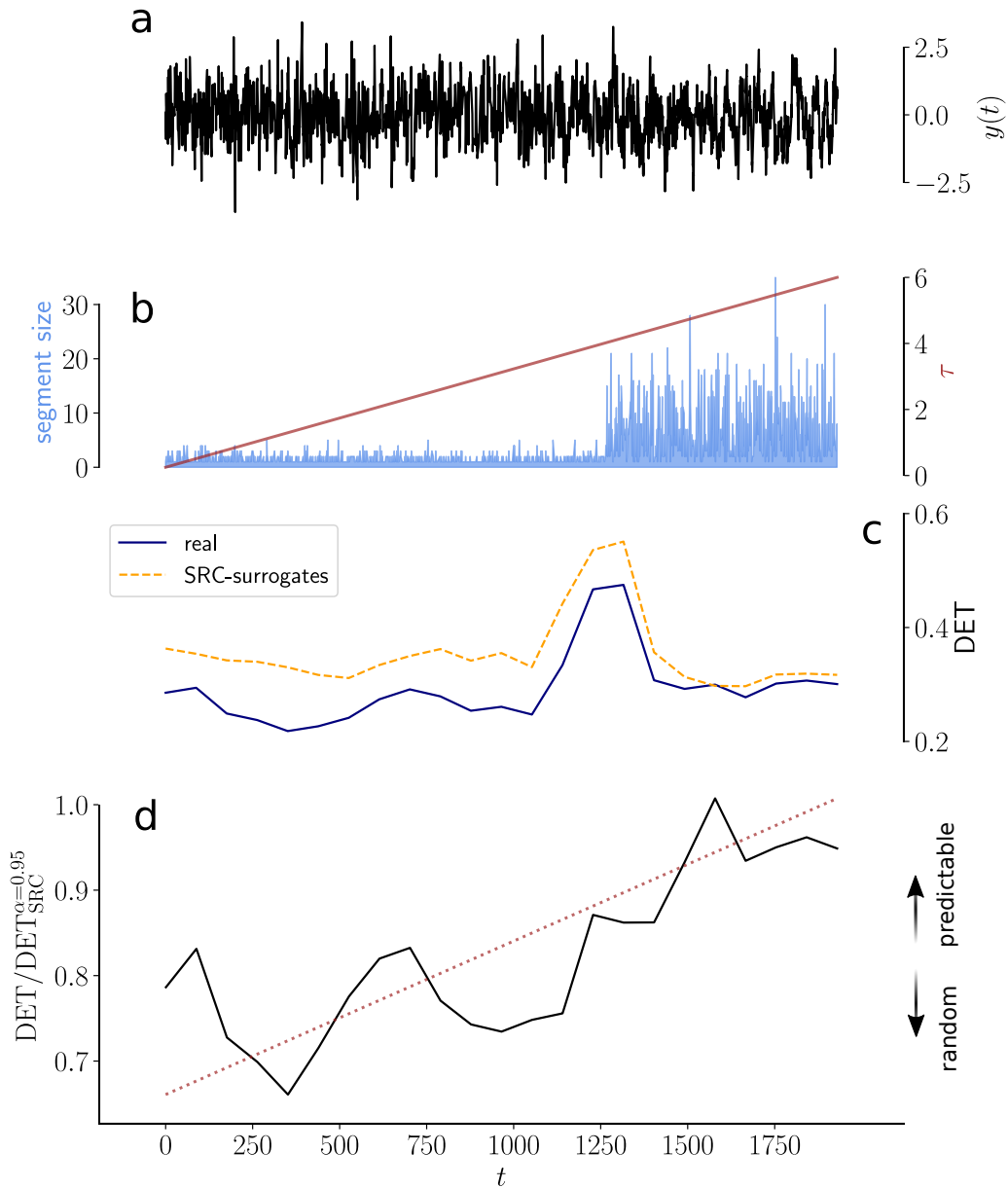


**Figure 8.4:** Application of SRC-surrogate correction method to (a) an irregularly sampled AR(1)-process with (b) non-stationary sampling rate (blue) and linearly increasing autocorrelation time (red). Gray shading indicates the abrupt shift in sampling rate. (c) A sliding window RQA using determinism (DET) as a predictability measure is carried out. Real DET values are displayed in dark blue, the 95%-confidence level computed from 200 SRC-surrogates is shown in yellow. (d) The ratio  $DET_{\text{real}}$  by  $DET_{\text{SURR}}$  provides a sampling-bias corrected predictability measure that reproduces the linear increase in serial dependence.

Holocene (6.4-5.4 thousand years before present (ka BP)). Niue island has a tropical climate, receiving an average of 2000 mm of precipitation annually with a pronounced wet season from November to April. Rainfall is most strongly controlled by seasonal displacement of the South Pacific Convergence Zone but also reacts sensitively to atmospheric circulation changes associated with the El Niño-Southern Oscillation. Here, we analyse seasonal rainfall variability on Niue recorded in greyscale changes that arise from crystallographic variations caused by changes in the stalagmite growth rate (Fig. 8.5). Greyscale values are obtained from high

resolution scans of the stalagmite surface along its growth axis subsequently extracted with ImageJ [232]. During the dry season, low drip rates promote the deposition of layers with compact and dark crystals, yielding low greyscale values. In the wet season, the drip rates are higher and crystal growth is enhanced as dissolved inorganic carbon is supplied to a greater extent. (see Fig. 8.5). The inferred link between dark layers and dry season is supported by earlier studies [233, 4].

Prior to the recurrence analysis of the greyscale time series, we subtracted a centennial-scale trend using a Gaussian kernel filter in order to focus on the high-frequency variability in the record (Fig. 8.6a, black line). Next, we downsampled the time series uniformly by only storing every 10<sup>th</sup> value due to computational constraints. This downsampling does not alter the relative changes in the sampling rate (Fig. 8.6b). The number of samples per year (i.e., the segment size) undergoes an abrupt shift at  $\approx 6.15$  ka BP. The period with the highest average segment size ( $\approx 6.4$  to  $6.15$  ka BP) coincides with the wettest period covered by the record, indicated by high greyscale values. This suggests that during this wet period, stalagmite growth was enhanced which resulted in thicker crystal laminae and a higher number of samples per layer. This observation reflects the complex nature of irregular sampling of palaeoclimate-proxy data. If spatial sampling on the stalagmite is performed such that the number of samples is as high as possible, it will inevitably be linked to its growth rate and thus to other environmental parameters and their non-stationary characteristics. Finally, we

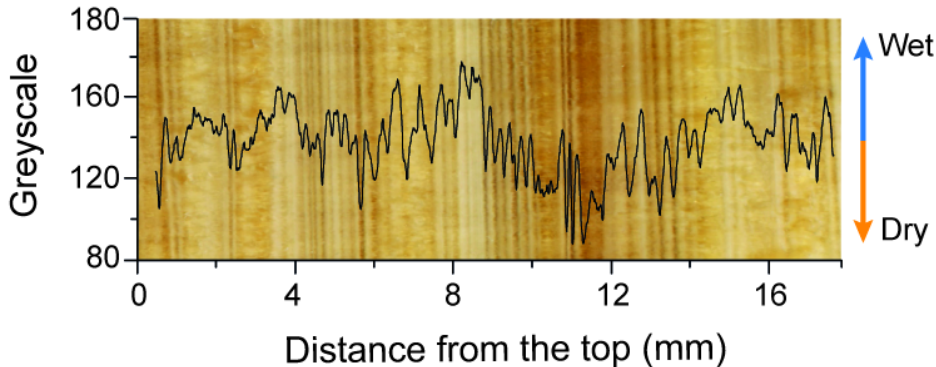


**Figure 8.5:** Greyscale record (in black) extracted from a high resolution scan of the surface of the stalagmite C132 from Niue island. Lower grey values are associated with dense microcrystalline calcite layers that form during drier periods.

perform the recurrence analysis (Fig. 8.6c). In order to characterize seasonal features, the period covered by one segment is fixed as one year. Optimization of deletion/adding costs yields  $\Lambda_s = 2$ . A window size of  $s = 200$  years is chosen with 90% overlap. A recurrence plot with fixed recurrence rate of 15% is obtained for each window and analyzed with DET. DET reveals variations in seasonal-scale predictability for the real greyscale record (Fig. 8.6c, blue line). The effect of the varying sampling size is obtained by the 95%-quantile of the DET distribution from 200 SRC-surrogates (Fig. 8.6c, yellow line). Five exemplar SRC-surrogate realizations are shown in appendix D. Both DET time series indicate an increase of seasonal-scale predictability during the wet period between 6.35 to 6.2 ka BP, potentially caused by the simultaneously increased sampling rate. The predictability estimate is corrected for the identified sampling bias by considering the ratio  $\text{DET}_r/\text{DET}_{\text{surr}}$  (Fig. 8.6d). Two periods (6.4 and 6.2 ka BP, and between 5.9 and 5.72 ka BP) show relatively low segment size-corrected seasonal predictability  $\text{DET}_r/\text{DET}_{\text{surr}} < 1$ . While the latter is not significantly affected by the correction, the former can only be identified as less predictable when the variations in sampling rate are taken into account. This result corroborates previous findings that suggested that both of these identified periods were more irregular, i.e. showing less steady

seasonal fluctuations [4]. However, it was not possible to characterize all sub-annual values as a proxy for sub-annual rainfall distribution rather extracting only the contrast between wet and dry season. The (m)Edit-distance approach employed here in combination with the proposed correction technique allows for a more reliable interpretation of mid-Holocene seasonal variations in the west Pacific.

In particular, an enhanced control of the seasonal cycle by ENSO-scale variability was found in [4] for the periods of reduced predictability (6.4 and 6.2 ka BP, and between 5.9 and 5.72 ka BP). High tropical cyclone activity between 6.4-6.2 ka BP could have been triggered by increased ENSO activity, yielding a more irregular sub-annual distribution of rainfall. Our results indicate that not only contrast between both seasons is rendered less predictable during this period but also the seasonal rainfall distribution appears less stable from one year to another. Reconstructing past climate variability at seasonal scale plays a critical role in the context of human adaption to continuous and abrupt climate variations and therefore our approach has direct relevance for teasing out the seasonal-scale signals.

## 8.6 Conclusion

The characterization of time series from complex nonlinear systems is a challenging task. Irregular sampling, i.e., variations in the sampling interval between consecutive values, additionally impedes typical research objectives such as spectral analysis, persistence estimation or quantifying the predictability of a system. Even though interpolation techniques offer a seemingly efficient way of pre-processing a time series to allow application of standard time series analysis tools, these entail various biases which are difficult to control. A different perspective is pursued by the (m)Edit-distance method. Many analysis methods are based on an estimate of (dis)similarity. With the (m)Edit-distance, a suitable distance measure between states of a system at different times  $i$  and  $j$  is defined by computing the transformation cost of segments centered at these time instances. First analyses demonstrated its scope in the context of recurrence analysis, enabling researchers to examine predictability variations of irregularly sampled palaeoclimate time series. Applications to other complex systems (also for time series with ‘missing values’) and other methodological frameworks (e.g., complex networks, clustering, correlation analysis, ...) are possible and should be attempted in the near future.

For some real-world systems, it is instructive to quantitatively compare sequences corresponding to a specific time scale in order to analyse the scale-specific variability. In such cases, segment sizes will vary in the presence of irregular sampling. Furthermore, splitting time series with a non-stationary sampling rate into segments that do not cover the same time period will result in a mixing of time scales. We have shown that (m)Edit-distance-based recurrence analyses are affected by variations in segment sizes, resulting in a non-trivial sampling bias if episodes with variable sampling rate are included in a single RP. The (m)Edit distance regards pairs of longer segments to be generally more dissimilar than shorter segments due to higher deletion costs. Shifting costs conversely decrease for increasing segment size, resulting in a non-trivial dependence of costs on local sampling rates. When including amplitudes of a signal into the (m)Edit-distance computation, similar general tendencies were observed but the strength of the segment size-dependencies varied for different systems. A more detailed examination of how dissimilar amplitude segments of different paradigmatic systems depend on their time scale will be investigated in a future study.

We introduced a numerical technique based on constrained randomization to address and correct the issue of segment-size dependence in recurrence analysis. This method involves generating an ensemble of sampling rate constrained surrogate realizations (SRC-surrogates). Each SRC-surrogate reproduces the real variations of sampling rate and its assignment to

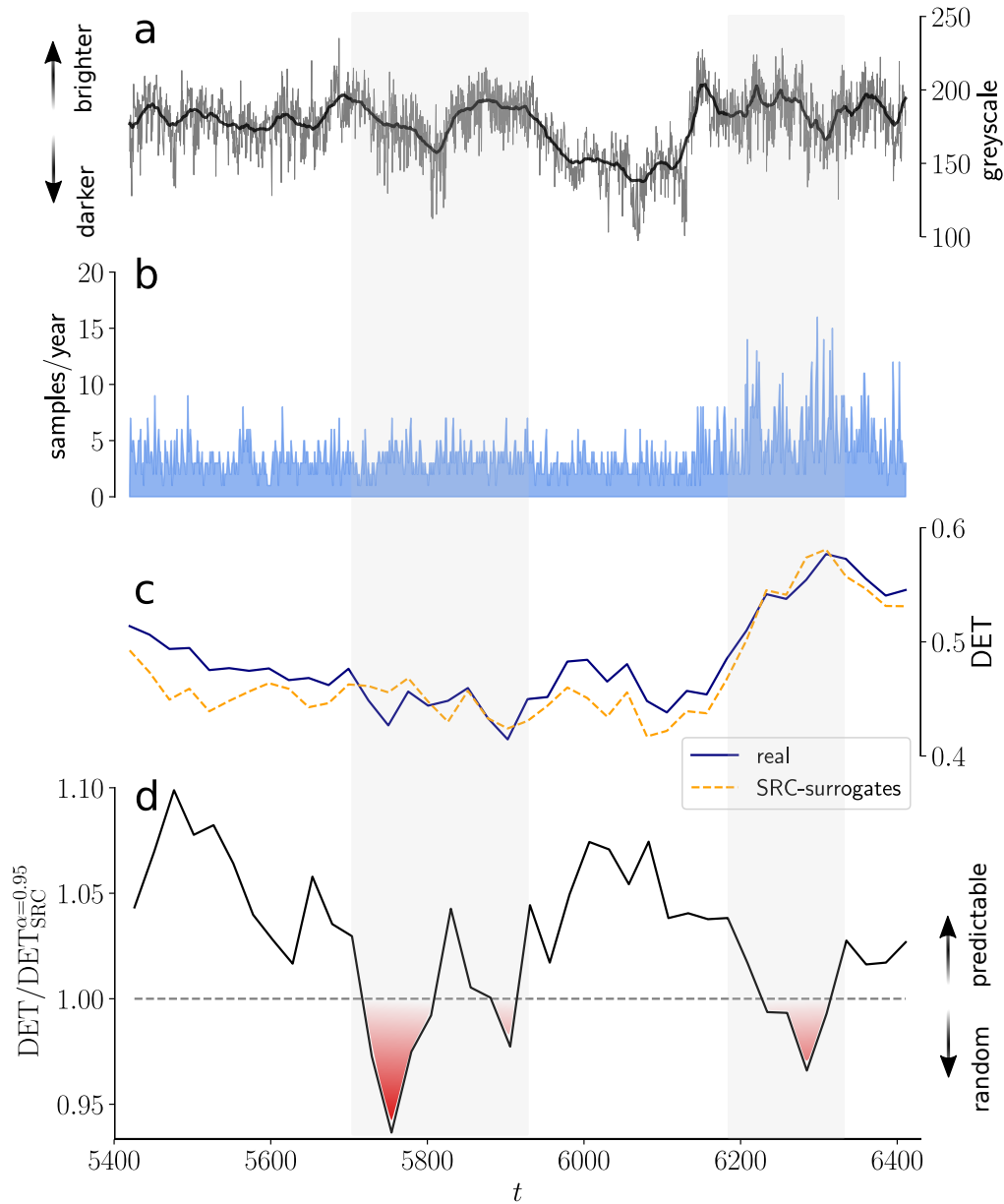


**Figure 8.6:** Application of SRC-surrogate correction method to an irregularly sampled greyscale proxy-record from the central Pacific (a) with non-stationary sampling rate (blue) (b). A sliding window RQA using determinism (DET) as a predictability measure is carried out (c). Real DET values are displayed in dark blue, the 95%-confidence level computed from 200 SRC-surrogates is shown in yellow. Dividing  $DET_{\text{real}}$  by  $DET_{\text{surr}}$  yields a sampling-bias corrected predictability series (d) that indicate mid-Holocene variations in seasonal-scale predictability. Gray shading indicates two periods with low seasonal predictability.



the corresponding amplitude differences, allowing the ensemble to be used for correcting the undesired segment size-dependence. The effectiveness of the proposed correction was applied to a synthetic AR(1)-time series and real palaeo-proxy data. In both applications, a recurrence analysis successfully recovered variations in the scale-specific predictability of the system whilst discarding spurious effects imprinted by sampling rate variations. We found that seasonal-scale predictability varied significantly during the mid-Holocene in the West Pacific, corroborating and extending the results from a recent study. The reasons for these changes in predictability warrant further investigation.

The identified sampling bias is a specific case of a more general problem in time series analysis; sliding window analyses (or the study of short time series) often suffer from finite-sampling biases which may introduce artificial variability into any statistical indicator that is computed. As pointed out in Section 8.5, finite-sampling biases are also not limited to irregular temporal sampling but are likely to also occur in settings where other parameter axes determine suitable window sizes or adaptive windowing is required. In future, the proposed method could also be applied in such settings to test its effectiveness beyond the examples considered in this study.

## Code availability

Python code for the generation of SRC-surrogates is available at <https://github.com/ToBraun/SRC-surrogates>.

## Acknowledgements

This research was supported by the Deutsche Forschungsgemeinschaft in the context of the DFG project MA4759/11-1 ‘Nonlinear empirical mode analysis of complex systems: Development of general approach and application in climate’. It also received financial support from the European Union’s Horizon 2020 Research and Innovation programme (Marie Skłodowska-Curie grant agreement No. 691037). Deniz Eroglu acknowledges funding by TÜBİTAK (Grant No. 118C236) and the BAGEP Award of the Science Academy. Cinthya Nava-Fernandez acknowledges financial support from the German Academic Exchange Service (DAAD). AH also acknowledges support from the Royal Society of New Zealand (grant no. RIS-UOW1501), and the Rutherford Discovery Fellowship programme (grant no. RDF-UOW1601).

## Conflict of interest

The authors declare that they have no conflict of interest.



---

# Palaeoseasonality





*An aspiring cave researcher crawls his way out of Botovskaya cave (eastern Siberia) with a bag full of samples, a head full of experiences and an impressive collection of bruises (photo by Seb Breitenbach, February 2022).*



## 9 | What we talk about when we talk about seasonality – A transdisciplinary review

Ola Kwiecien<sup>1,\*</sup>, Tobias Braun<sup>2</sup>, Camilla Francesca Brunello<sup>3,4</sup>, Patrick Faulkner<sup>5</sup>, Niklas Hausmann<sup>6</sup>, Gerd Helle<sup>3</sup>, Julie A. Hoggarth<sup>7</sup>, Monica Ionita<sup>4,8</sup>, Chris Jazwa<sup>9</sup>, Saige Kelmelis<sup>10</sup>, Norbert Marwan<sup>2</sup>, Cinthya Nava-Fernandez<sup>11</sup>, Carole Nehme<sup>12</sup>, Thomas Opel<sup>13</sup>, Jessica L. Oster<sup>14</sup>, Aurel Perşoiu<sup>8,15</sup>, Cameron Petrie<sup>16</sup>, Keith Prufer<sup>17</sup>, Saija M. Saarni<sup>18,19</sup>, Annabel Wolf<sup>1</sup>, Sebastian F.M. Breitenbach<sup>1</sup>

- 1 – Northumbria University, Newcastle upon Tyne, Department of Geography and Environmental Sciences, NE1 8ST, United Kingdom
- 2 – Potsdam Institute for Climate Impact Research, Member of the Leibniz Association, 14473 Potsdam, Germany
- 3 – GFZ-Potsdam, Section Climate Dynamics and Landscape Evolution, 14473 Potsdam, Germany
- 4 – Alfred Wegener Institute Helmholtz Centre for Polar and Marine Research, Climate Sciences - Paleoclimate Dynamics Division, 27570 Bremerhaven, Germany
- 5 – Department of Archaeology, The University of Sydney, Australia
- 6 – Römisch Germanisches Zentralmuseum (RGZM), Mainz, Germany
- 7 – Department of Anthropology and Institute of Archaeology at Baylor University, Waco, Texas 76798, USA
- 8 – Emil Racovita Institute of Speleology, Romanian Academy, Cluj-Napoca, 400006, Romania
- 9 – Department of Anthropology, University of Nevada, Reno, USA
- 10 – Department of Anthropology and Sociology, University of South Dakota, Vermillion, South Dakota, USA
- 11 – Sediment- and Isotope Geology, Institute for Geology, Mineralogy and Geophysics, Ruhr University Bochum, Universitätsstr. 150, 44801 Bochum, Germany
- 12 – University of Rouen Normandy, IDEES UMR 6266 CNRS, Mont Saint-Aignan, France
- 13 – Alfred Wegener Institute Helmholtz Centre for Polar and Marine Research, Helmholtz Young Investigator Group PALICE and Polar Terrestrial Environmental Systems, 14473 Potsdam, Germany
- 14 – Vanderbilt University, Department of Earth and Environmental Sciences, Nashville, TN, 37212, USA
- 15 – Stable Isotope Laboratory, Stefan cel Mare University, Suceava, Romania
- 16 – Department of Archaeology, Cambridge University, Downing Street, Cambridge, CB2 3DZ, UK
- 17 – Department of Anthropology, University of New Mexico, Albuquerque, NM 87106, USA
- 18 – Faculty of Biological and Environmental Sciences, Helsinki University, Finland
- 19 – now at: Geology Section, Department of Geography and Geology, University of Turku, Finland

*Kwiecien, O., Braun, T., ... , Breitenbach, S. F. M. (2022). What we talk about when we talk about seasonality – A transdisciplinary review. Earth-Science Reviews, 225, 103843. doi:*

This review paper has ten sections from which only the three sections (Introduction, Numerical tools for extracting seasonality changes from palaeoenvironmental time series, Summary and outlook) the author has actively contributed to, are included in the following.

## Abstract

The role of seasonality is indisputable in climate and ecosystem dynamics. Seasonal temperature and precipitation variability are of vital importance for the availability of food, water, shelter, migration routes, and raw materials. Thus, understanding past climatic and environmental changes at seasonal scale is equally important for unearthing the history and for predicting the future of human societies under global warming scenarios. Alas, in palaeoenvironmental research, the term ‘*seasonality change*’ is often used liberally without scrutiny or explanation as to which seasonal parameter has changed and how.

Here we provide fundamentals of climate seasonality and break it down into external (insolation changes) and internal (atmospheric CO<sub>2</sub> concentration) forcing, and regional and local and modulating factors (continentality, altitude, large-scale atmospheric circulation patterns). Further, we present a brief overview of the archives with potentially annual/seasonal resolution (historical and instrumental records, marine invertebrate growth increments, stalagmites, tree rings, lake sediments, permafrost, cave ice, and ice cores) and discuss archive-specific challenges and opportunities, and how these limit or foster the use of specific archives in archaeological research.

Next, we address the need for adequate data-quality checks, involving both archive-specific nature (e.g., limited sampling resolution or seasonal sampling bias) and analytical uncertainties. To this end, we present a broad spectrum of carefully selected statistical methods which can be applied to analyze annually- and seasonally-resolved time series. We close the manuscript by proposing a framework for transparent communication of seasonality-related research across different communities.

## 9.1 Introduction

### 9.1.1 What we talk about when we talk about seasonality?

Seasonality is a common denominator for several academic disciplines and its accurate reconstruction is highly relevant across both the natural and human sciences. At a basic level, climate seasonality is expressed intuitively as the cyclical changes in temperature and/or rainfall over the course of the year, which in turn determines both the composition and the dynamics of ecosystems. Overall, climate seasonality plays a critical role in influencing the persistence of all living organisms. For example, the seasonal changes in precipitation and temperature affect different components of the climate system (e.g., soil moisture, snow cover, evaporation rates, river flows and lake levels). The changes in these variables lead further to changes in vegetation and ecologic requirements of plants and animals, which in turn influence the type and amount of food available for humans and other organisms. For the majority of multicellular organisms, the diurnal and seasonal cycles are the most important pacemakers of biological functions. For humans, the influence of seasonality affects the biological



world they interact with and extends across the cultural domain, including construction of niches, subsistence, religious, and economic activities. Studying past changes in seasonality is of great interest and importance for palaeoclimatology, palaeoecology, anthropology and archaeology, and, last but not least, modern climate science, conservation and phenology, all of which face the uncertain future of global warming [234]. Palaeoclimatology aims at documenting how seasonal changes affect the climate system through time [235, 236], and *the amplitude of seasonal changes* [237, 238, 239, 240, 241]. Palaeoecology deals with *the effect of seasonality changes on the ecosystem* [242, 243], while anthropology and archaeology document *the effect of seasonality and changes in seasonality on human evolution, residency, subsistence strategies, and the adaptation of those strategies* (the latter two involving human-ecosystem interaction; [244], and references therein). Recent work by [245] emphasized pitfalls of integrating data and knowledge between academic disciplines with different practices and standards of evidence. Increasing scientific interest in what the authors termed 'history of climate and society' warrants proposing frameworks which facilitate interdisciplinary research. Thus, this review proposes a framework for addressing past climate seasonality changes.

An opinion piece by [246] echoes the seminal work by [247] and outlines the most important, but often overlooked, aspects of seasonality in palaeoenvironmental studies. Firstly, climate is defined not by annual means of temperature or precipitation, but by the annual cycles of these climate variables (see Box 1). Annual mean values, so often extracted from proxy records, while important, do not fully capture past climate variability. Secondly, relatively small changes in natural processes acting on a seasonal timescale are the drivers that foster large climate shifts. Not detailed by [246] are the often simplified or overlooked aspects of spatial heterogeneity of environments and human actions, including the seasonality and timing of subsistence activities, which further influence the rhythms of other cultural behavior(s).

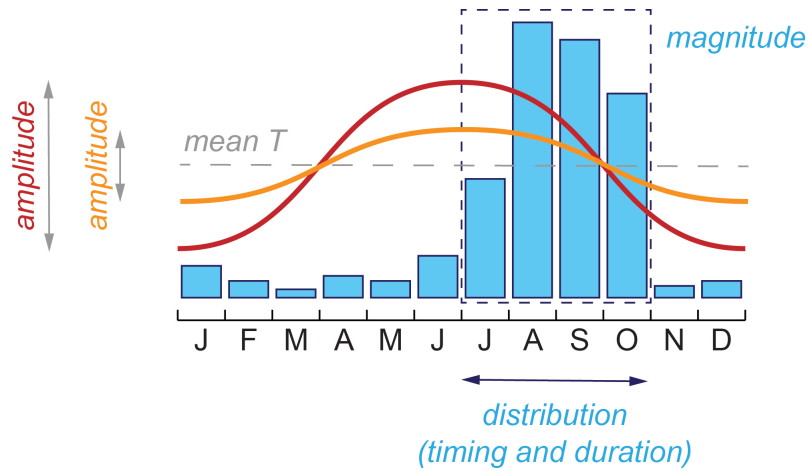
### Box 1 : Definitions

'Seasonality' is widely used in many disciplines of palaeo-research, yet it is lacking a clear definition. In the scientific literature, references to changes in seasonality are as frequent as they are ambiguous. A survey of this literature raises many questions: what does 'increased' or 'decreased seasonality' actually mean? Can we quantify this change? And is the amplitude all that matters? What about temporal distribution? Does temperature and precipitation always respond symmetrically and harmonically? [248] highlighted that one should refer to the annual cycle rather than the seasonal cycle since the period is one year, not one season, and we endorse this approach. Here we define key concepts related to seasonality and how they will be used throughout this review.

**Annual cycle of temperature** – can be symmetric, sinusoidal, and is defined by maxima and minima. **Seasonality of temperature** refers to an amplitude between maxima and minima. In theory, the annual budget reaches zero, meaning that colder winters are counterbalanced by warmer summers.

**Annual cycle of precipitation** – is defined by magnitude (amount) and temporal distribution (timing – when: duration – for how long). **Seasonality of rainfall** should take all three of these components into consideration, which, in case of palaeoenvironmental archives and their limitations in resolution, is rarely feasible. In modern climatology the beginning of the hydrological year differs from the beginning of the calendar year.

Seasonality of temperature and seasonality of rainfall together make **climate seasonality**.



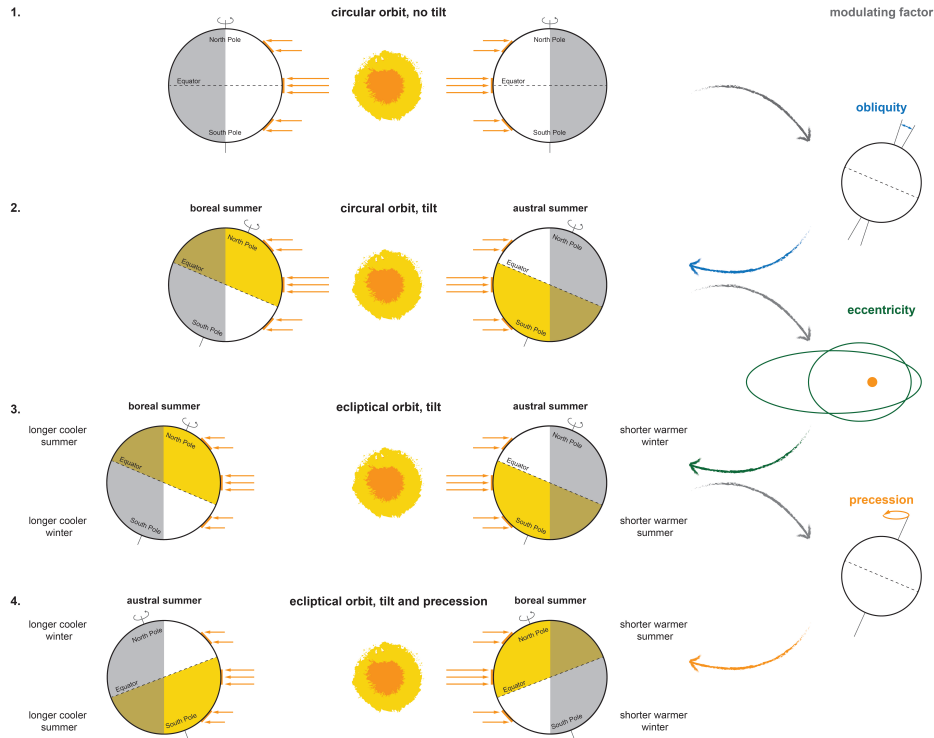
**Annual cycle of human activities** (e.g., foraging, farming, migration) – strongly related to natural temperature and precipitation cycles, which influence the growing season and availability of static resources and the movement patterns of mobile resources (see Box 5). The availability and sustainability of these resources influence human subsistence strategies, which in turn inform other types of cultural behavior. **Seasonality of an activity** refers to its timing and duration.

The two aspects of seasonality reiterated by [246], namely: 1) the fact that it defines climate and 2) that the small changes accumulate in large-scale oscillations (e.g., glacial/interglacial cycles), constituting a challenge for scientists working with archives that often lack seasonal resolution and/or are biased towards one season only. Alternatively, archives record seasonal changes but are discrete in nature and represent only snapshots of time rather than a continuous interval. Consequently, regional palaeoclimate syntheses frequently suggest different responses to seasonality changes to account for discrepancies between different archives and proxies covering the same time span, or between data-based reconstructions and climate model output. The classical example comes from the Mediterranean region where [249] reconciled glacial lake levels, where high levels suggested increased humidity, with contemporary pollen records that indicate drier conditions, by proposing an increased seasonality in precipitation with wetter winters and drier summers. Yet, the term ‘*seasonality*’, while so often used by the palaeo-community, lacks formal definition, and the phrase ‘*seasonality change*’ is often used to refer to a bundle of processes encompassing changes in both the external forcing and internal conditions modulating the local response. The external forcing is prescribed by the orbital parameters (see Box 2).

### Box 2 : Orbital influences on annual and diurnal cycles

The diurnal (Earth rotation around its axis, 24 h) and annual (Earth rotation around the Sun, 1 year) cycles can be observed and experienced during a human lifetime. On longer, multi-millennial time scales, these cycles are influenced by changes in Earth’s orbital parameters, obliquity, eccentricity, and precession. Changes in orbital parameters have been calculated theoretically [250] and their persistence on Earth climate has been documented in geological record ([251] and more). Fundamentally, seasonal vari-

ability is controlled by the amount of incoming solar radiation (**insolation**), arriving at different latitudes at different angles as Earth orbits the sun. Below we consider four different scenarios to illustrate how changes in orbital parameters influence the annual insolation distribution and the length of day.



1. If the Earth's rotational axis was perpendicular to the orbital plane, the insolation angle for each latitude would be constant throughout the year. Insolation gradients would exist between the latitudes, but there would be no seasonal changes. Daytime would have the same length at each latitude.

2. Increasing the tilt (**obliquity**) changes the insolation angle during Earth's rotation around the sun. The hemisphere tilted towards the sun experiences warmer temperatures (summer), and longer days. The amplitude of seasonal differences increases with the tilt. The length of the obliquity cycle is ca 42 ka. At the equator, the length of the daytime is roughly constant throughout the year, it gets longer (24 h) towards the 'summer' pole and shorter (0 h) towards 'winter' pole. Summer and winter are of equal length in both hemispheres.

3. Changing the shape of the orbit (**eccentricity**) influences the distance of the Earth to the sun and the length of the seasons. **Eccentricity of the orbit modulates the effect of the obliquity.** The seasons at aphelion are colder (the Earth is further away from the sun) and longer (further away from the sun it's gravitational pull is weaker, so the Earth moves slower) than at perihelion. Eccentricity has two cycles, a short one, ca. 100 ka, and a long one, ca. 400 ka. In the presented scenario (corresponding to modern day conditions) the gradient between summer and winter insolation (here, translated into temperature) is steeper in the southern hemisphere (SH) compared to the northern hemisphere (NH).

4. The wobble of Earth's rotational axis (**precession**) changes the direction of the tilt and determines which hemisphere is tilted towards the sun at perihelion (summer). The same hemisphere will be tilted away from the sun at aphelion (winter). **Precession thus determines on which hemisphere the amplitude of annual change in insolation is larger.** The overall length of the precessional cycle is ca 23 ka.

While systematic changes in insolation are, next to atmospheric CO<sub>2</sub> concentration, the most important driver for seasonal temperature variations, other factors can modify temperature variations (see Box 3).

The amount of insolation received at any point on the planet is a function of season and latitude. It can be theoretically calculated for the past and the future and broadly translated into relative temperature changes, with flat seasonal gradients in the tropics and steep gradients at the poles (see Box 3).

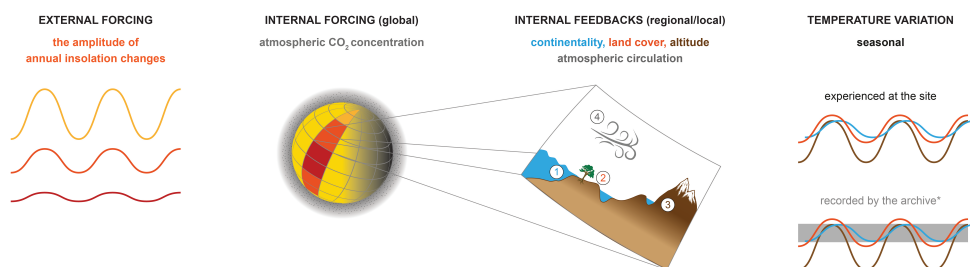
### Box 3 : External and internal forcing, and internal feedbacks

The energy received from the sun per unit area (insolation) is kept in check by Earth's atmospheric CO<sub>2</sub> concentration. Insolation changes (**external forcing**) are periodic and fixed for a given season and latitude (see Box 2) and as such are predictable. In pre-industrial times CO<sub>2</sub> concentration (internal forcing) varied little between the hemispheres, following the respective vegetation season, and large variations in CO<sub>2</sub> level were global [252, 253].

At the low latitudes the total amount of the insolation received is larger than that received at the high latitudes and the poles, but the amplitude of annual change is very small. Hence in low latitudes annual cycle is expressed in precipitation changes (wet and dry season). The amplitude of annual insolation change increases with distance from the equator and manifests itself in temperature and daylight duration changes.

Still, the Earth unit area receiving insolation is rarely homogeneous and the surface properties can modulate (dampen, amplify, or delay) the local response. **Internal feedbacks** are semi-stochastic.

A novel (in a geological sense) element of internal feedback, referred to as anthropogenic climate variability, combines greenhouse gas emission, deforestation and land use change. The sensitivity of a given archive can further influence the palaeoenvironmental record.



- **Continentality:** a measure of the difference in the annual temperature maxima

and minima that occurs over land compared to water. The oceans capacity for storing heat (thermal inertia) is greater than that of the continents which means it warms slower but also cools slower than land masses. Further, the upper ocean layer can distribute heat both, vertically and horizontally. By storing heat in summer and releasing it in winter oceans considerably dampen the annual cycle of temperature. In contrast, the continental interiors experience much larger annual temperature differences. The large thermal inertia of the oceans shifts the annual temperature maxima and minima of surface water and coastal regions in relation to temperature over continental interiors. The land-ocean distribution is also important in moderating the insolation-prescribed hemispheric seasonality contrast: under modern day conditions the gradient between summer and winter insolation is steeper in the SH compared to the NH; however, the SH ocean/land ratio counteracts the large temperature gradients. Size and distribution of the continents have also impact on the seasonal precipitation patterns, with continental interior receiving less rainfall than coastal regions.

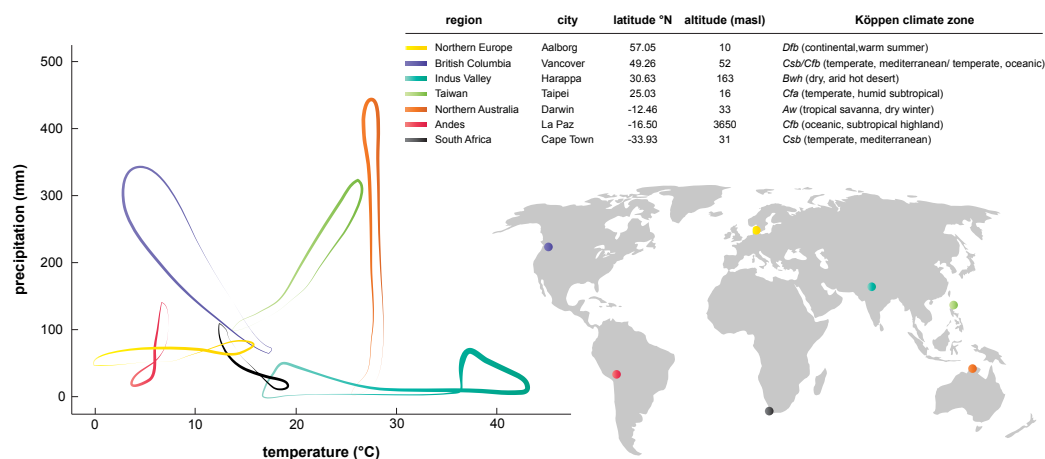
- **Land cover:** differences in surface properties represented by vegetation changes (e.g.: forest vs steppe vs bare rock), snow cover, or surface water distribution affect the albedo and the heat capacity of the surface. The effect of these differences on the overlying atmosphere is analogous to the ocean surface temperature anomalies, but on a much smaller spatial scale.
- **Altitude:** temperature in the troposphere (lowest layer of atmosphere) decreases with increasing altitude. The rate (lapse rate) is approximately 1°C for every 100 m.
- **Atmospheric circulation patterns:** seasonal variability of precipitation and temperature is modulated by the large-scale atmospheric circulation patterns and by the ocean circulation, operating on interannual to multidecadal time scales (e.g., El Niño-Southern Oscillation (ENSO), the North Atlantic Oscillation (NAO), the Pacific North American pattern (PNA), the Pacific Decadal Oscillation (PDO) and the Atlantic Multidecadal Oscillation (AMO), among others). These atmospheric and ocean modes of variability can influence the precipitation and temperature in different ways. For example, NAO exerts a strong influence on the hydroclimate variability of Europe, while the PNA strongly influences the hydroclimate of the U.S.
- **Volcanic activity:** volcanic eruptions inject large quantities of aerosols into the atmosphere, and stratospheric circulation distributes them across the planet. In general, aerosols have a cooling effect. However, the scale of this effect depends on where (hemisphere and latitude), when (season), how much (the volume), and for how long (single or multiple eruption events) the material was injected.

The internal forcing – atmospheric CO<sub>2</sub> concentration – is a global feature, and its changes are relatively well documented for the course of the Pleistocene and Holocene [254, 253]. The local conditions, however, are inherently heterogenic, and factors like continentality (land-mass and ocean distribution), altitude, land cover, and atmospheric circulation patterns and volcanic activity play an important role in modulating insolation- and CO<sub>2</sub>-prescribed local temperature (see Box 3). Thus, the resulting local expression of climate seasonality varies between sites along the same or similar latitude (see Box 4). Further, the natural archives exposed to seasonal changes might display a bias or an offset in recording the local signal

(see Box 4). Last but not least, if the natural archives might be influenced by, or are the direct outcomes of human activity, considering anthropogenic aspects is essential. Depending on the nature of their adaptations, resilience and sustainability, humans developed different strategies to cope with and/or take advantage of seasonal changes (e.g., choosing migratory or stationary lifestyles, hunting and foraging or farming). Importantly, the degrees to which particular strategies are successful are likely to change through time, based on environmental circumstances, population size, and technology (see Box 6 in the original manuscript). Consequently, the archaeological archives related to human occupation sites constitute a special case, i.e., a confluence of natural changes and developing human adaptations (e.g., [255]).

#### Box 4 : Combined influence of latitude, continentality, and altitude

Köppen's [256] classification of climate divides climate zones into 5 main groups (tropical - A, dry - B, temperate - C, continental - D and polar - E), based on seasonal temperature and precipitation patterns. This grouping takes into consideration not only latitude but also continentality and altitude. Köppen's climate zones are the best example of differences in amplitude of seasonal change along the same latitude (the theoretical line subjected to the same insolation forcing). We have chosen 7 examples of archaeologically relevant sites from around the globe to illustrate the possible range of local seasonal temperature and precipitation (modern data from <https://en.climate-data.org>). Tropical and temperate climates are characterized by larger amplitude of precipitation changes, dry and continental climate by larger amplitude of temperature. In case of tropical site in the Andes, the altitude is responsible for low temperature values. Note that the plot does not account for potential evapotranspiration.

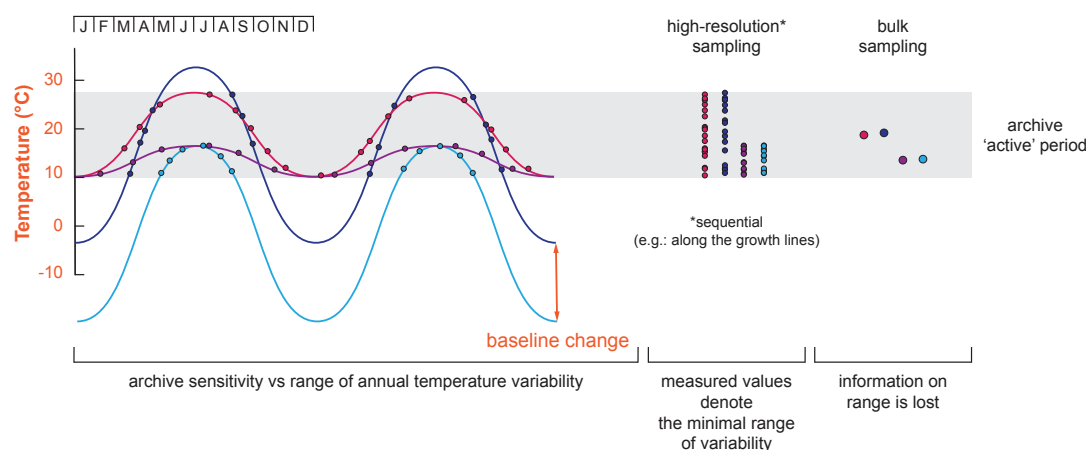


This review answers the call by [246] for a reevaluation of the scientific focus and methodological habits of the scientific community. It is time to scrutinize 'seasonality changes' and address individually different components which together produce the climate- and human history records we work with. Considering the breadth of the audience, first we take a step back and take up the issue of climate seasonality (see Box 1) at a fundamental level of external forcing (see Box 2) internal, regional and local changes (see boxes 3 and 4). Further, we summarize how seasonality is reflected in different archives and explore advantages and potential limitations of each archive. The next chapter demonstrates statistical methods useful in extracting and analyzing seasonal information from high-resolution but often irregularly sampled archives. Finally, we suggest a framework for discussing scientific observations in

order to avoid confusion and promote transparency in multi- and transdisciplinary research.

### Box 5 : Relevance of seasonal bias recognition and adapting sampling strategy

Treating seasonally biased records as representing annual means might lead to flawed interpretations. The opposite is also true: records reflecting annual means should be treated with caution when interpreting seasonal changes in temperature or rainfall. In our conceptual example here, some archives record the full range of annual temperatures, while others only a portion. The correct recognition of the recorded interval is crucial for further interpretation, regional or global synthesis, and comparison [257, 258]. Adequate sampling is an additional challenge, in particular when the sedimentation/growth rate of the archive is low. [259] discuss in depth how sampling strategy might influence obtained results and propose a schematic guide for choosing the optimal approach. Depending on archive sensitivity and sampling strategy, the shift of the baseline without change in the amplitude might be inaccurately perceived as an increase or decrease in seasonality of respective parameter. Further, comparing the same proxies (e.g.,  $\delta^{18}\text{O}$ ) from different archives, or the same, but geographically distant, archive does not guarantee that they record the same season.



The beauty of seasonally-resolved archives, whether continuous or discrete, lays in their capacity of recording the baseline of seasonal variation. Deviation from this baseline can inform on frequency and magnitude of events (e.g., floods or droughts), while stepwise change suggests the reorganization of the large-scale atmospheric and/or oceanic circulation (e.g., glacial termination). Anchoring seasonal changes in a wider palaeoenvironmental narrative allows for insight into the complex dynamics of Earth's system's and human response to external climate forcing.

Not all palaeoenvironmental archives have the potential of recording seasonal variability. Of those which can, not all can be dated with annual resolution. Here, we first focus on instrumental and historical data as these have natural and direct connection to the Present. Next, we move to archaeological records as an overarching subject discussing relevance of seasonal changes for humanity's past, beyond instrumental and historical reach. This chapter alludes to natural archives which are often found either directly at sites of human occupation or in close vicinity and have the potential to record seasonal changes. The different archives (i.e., marine biogenic carbonates, stalagmites, tree rings, laminated lake sediments, glacier ice, cave ice, and permafrost ground ice) are highlighted in the following chapters.

The element conspicuous by its absence is pollen. When calibrated, pollen records indis-

putably provide information on temperature and precipitation ranges in physical units ( $^{\circ}\text{C}$  and ml) and as such can be related to specific seasons [260]. Applying transfer functions to pollen assemblages is a powerful tool for quantifying past environmental change. Alas, the temporal resolution of this proxy is inherently coupled with the sedimentation rate of the media it resides in and this review addresses seasonally resolved archives rather than proxies.

## 9.2 Numerical tools for extracting seasonality changes from palaeoenvironmental time series

As the previous chapters show, seasonality expresses itself in different fashions in each environmental archive, and is accompanied with individual challenges and limitations. Seasonality reconstruction is concerned with the extraction of prominent features which closely link to the respective notion of seasonality, such as periodicity, seasonal amplitude, timing/duration or complexity (see Box 7) of seasonal patterns (Fig. 9.1). In order to characterize seasonal variability, quantitative time series analysis methods allow extraction of various features related to seasonality and to gain confidence in their statistical significance. Here we give an overview of how systematic application of numerical tools can help to extract and substantiate the reconstruction of seasonality in presence of data-related obstacles.

While well-dated proxy records allow for direct assessment of subannual or seasonal variations [261, 262], lower resolved time series may contain valuable information on variability that is linked to seasonal variability. Some records reflect information related to different seasons, others only yield a specific response to a single season ([263], see Chapters 5 and 8 in the original manuscript) (see Box 7). In some records, the most prominent and valuable information on seasonality might be found in extreme excursions from the baseline [264, 265]. In all these cases, nonstationarity (see Box 7) in the underlying geophysical and geochemical processes can render the recorded seasonal features highly variable over time. Numerically extractable information goes beyond detecting changes in an annual cycle; even in the presence of a stable annual cycle throughout a time series. Not only can the ‘seasonal amplitude’ vary significantly, but also timing and duration of seasons are distinct features that become detectable (see Box 1), e.g., as phase shifts (Fig. 9.1). Where the underlying forcing mechanisms are well understood, proxy data can be linked to a specific season even in lower resolved time series [263].

Obstacles for retrieving seasonality include (among others) limited temporal resolution and lacking reproducibility [259]. Frequently, standard methods (e.g., periodograms) must be adapted before they can be used to extract seasonality from irregularly sampled time series [266]. Further, the sampling integration (i.e., the time integrated in each discrete sample) is vitally important when assessing the suitability of a time series for seasonality analysis. Unambiguous differentiation between an actual seasonal cycle and noise can be challenging even in well-dated records, with remaining age uncertainty obscuring the significance of a present seasonal fingerprint. Archives with lower-than-annual resolution can only yield seasonality-related information when a clear mechanism links proxies to environmental parameters, and/or to a specific season (see chapter 8 in the original manuscript) (see Box 5). Therefore, the mechanism that embeds seasonal signals in an archive decides upon which method is ultimately best suited to extract them.

This chapter is intended as overview of statistical methods to extract information on seasonality from palaeoenvironmental archives. We first summarize methods frequently used in palaeoclimatology, then we briefly discuss recently developed tools that help scrutinizing diverse seasonality archives across disciplines.



## Box 7 : Glossary for statistical terms

- **Boostrapping** is a nonparametric statistical technique that allows to estimate confidence bounds or prediction errors for a signal through resampling. Based on an empirical estimate of a system's probability distribution,  $n$  values from this distribution are randomly drawn with replacement in each of  $N_b$  bootstrap runs.
- **Complexity** of a signal comprises a range of features that are typically encountered in the study of nonlinear and nonstationary systems. Measuring the complexity of a signal complements and exceeds characterization of strictly linear signals, e.g. by reflecting their tendency to exponentially deviate from a given value or the degree of irregularity in their variability. Even systems which predominately exhibit regular, periodic behaviour may show episodic bursts of irregular, chaotic dynamics that can be best captured by complexity measures. In seasonal climate signals, this can be expressed as a superposition of variations in periodicity, amplitude, and timing as well as in abrupt shifts from predictable to stochastic or intermittent dynamics (e.g., caused by a changing influence of semi-stochastic large scale atmospheric patterns).
- **Continuous Wavelet Transform (CWT)** is a signal decomposition into small oscillations with specific frequency. Each oscillation is represented by a shifted and scaled version of a *Mother Wavelet*. CWT is a powerful tool to track signal cycle changes through time (e.g., the annual cycle). They are similar to a time series power spectrum but allow for better reconstruction of the signal in time.
- **Dynamic Time Warping** allows matching signals of varying length and with distinct sampling. Its application to proxy records can be interesting for comparing signals with very different temporal resolution. It can inform on optimal signal alignment and provides a (dis)similarity measure.
- **Entropy** is a universal concept in thermodynamics that can be interpreted as the amount of information that is associated with state of a system. In applications to (nonlinear) time series, it is commonly utilized as a complexity measure. Many different definitions are possible (Shannon entropy, permutation entropy, ...) while each of them requires the empirical estimation of a probability distribution. It is often also loosely interpreted as an indicator of how 'disordered' a system behaves.
- **Exceedence times** are time instances at which a time series  $x(t)$  has a larger than pre-specified value  $a$ :  $x(t) > a$ . For palaeoseasonality, a characteristic value (e.g., mean wet season rainfall, see fig. 15 in main text) can be computed in order to study at which time  $t_i$  this value is first exceeded in an given year. Decreasing exceedance times would then indicate a trend towards an earlier wet season onset.
- **Granger causality** is a prediction-based concept of statistical causality. If a signal  $X_1$  causes a signal  $X_2$ , then past values of  $X_1$  should allow to predict future  $X_2$  values beyond the information contained in past  $X_2$  values alone. The mathematical formulation of Granger causality is based on linear regression modelling of stochastic processes [267].
- **Hilbert-Huang analysis, Empirical mode decomposition and Singular Spectrum Analysis** are distinct methods that are used to decompose a signal into *intrinsic modes*. If a signal contains significant variability at multiple

timescales, each mode may represent this scale-specific variability. In contrast to CWT, decomposition does not rely on a specific type of function.

- **Hilbert-transformation (HT)** is a mathematical transformation of a signal that allows to extract its *instantaneous frequency and phase*. It is related to the Fourier transform. When studying an annual cycle, the instantaneous phase of a signal reflects *how much is cycle is shifted forwards and backwards for different episodes in time*.
- **Independence** of a signal is a common prerequisite for applying statistical analyses and means that the studied signal does not exhibit any serial dependence, implying an absence of trends, cycles or stochastic long-range dependence.
- **Kolmogorov-Smirnov distance** measures similarity between probability distribution functions (PDF). It is used to test whether an empirical PDF is compatible with a known reference distribution (e.g. a normal distribution) or if two empirically estimated PDFs could be generated from the same reference distribution. It may yield spurious results if many extreme values are included in the empirical sample.
- **Least-squares based wavelet approach** allows extraction of cycles through time. Least-squares optimization aims at minimizing the squared deviation between a result and the optimal result. When applied to wavelets, this approach can obtain a near-optimal wavelet representation of a cycle through time, despite uneven sampling.
- **Nonstationarity** in a signal can indicate that an external process affects the studied system such that it, e.g., results in a continuous change of the mean in a time series. Other nonstationary signal variations include shifts in variance, extreme events, or continuous variations in dominant cycles.
- **Non-rectangular, smooth kernel function** apply weights to neighboring observed data in a time series. Often used in sliding-window analyses, e.g. moving averages. A window function is chosen that decays smoothly towards the edges of the time window of specified width  $h$ . Smooth kernel windows allow better temporal localization of the covered time series segment, thereby limiting spurious artefacts in spectral analysis compared to sliding window analyses. A popular example are normal-weighted Gaussian kernel windows.
- **Normality** refers to the notion that the empirical estimate of a signal's probability density function can be well approximated by a normal distribution.
- **Quantiles** are statistical values that characterize a PD. For empirical data a quantile is a specific value that splits the sample of all values into one fraction  $p$  that is smaller and one fraction  $1 - p$  that is larger than the quantile. This value is referred to as the (empirical)  $p$ -quantile of the sample. Quantiles are often used to report confidence intervals.
- **Return periods** are periods in which a time series returns to a similar or equivalent magnitude it has visited before. In extreme value analysis, a certain extremely high (low) magnitude is specified as *return level*. The return time corresponding to this return level denotes the time interval typically passed between

two events above (below) this return level. It is estimated from a model description of the time series called *generalized extreme value distribution*.

- **Seasonality indicators** are standardized, quantified characterizations of one or more seasonal features. They allow to enhance comparability between different expressions of seasonality in distinct archives and help multi-proxy palaeoseasonality studies. Often focussed on quantifying a single feature of seasonal change.

### 9.2.1 Statistical tools

The broad spectrum of methods that can be subsumed under the term *statistical tools* ranges from simple seasonal averaging to extreme value analysis and linear correlations. A suitable combination of these tools can help to tackle some of the challenges related to seasonality detection and move towards quantitative analysis.

**Descriptive statistics.** A first step towards quantifying seasonality is related to estimating statistical properties of a record's frequency distribution. The frequencies can be found by binning histograms or by estimating kernel density representations. For sufficiently long records, histograms for distinct episodes or (non)overlapping time windows can give a statistical estimate of temporal seasonality evolution [268]. Empirical distributions may then be compared, e.g., between different study sites or time periods by means of suitable similarity measure, such as Kolmogorov-Smirnov distance [269].

The estimation of statistical properties, like sample average, variance or quantiles, reveal tendencies (trends) if computed for time periods that characterize distinct seasons. For instance, analyzing the  $\delta^{18}\text{O}$  signal of limpet shells, [270] detected a cooling trend in the seasonal temperature for the Late Holocene from 3300–2500 BP to the Roman Warm Period (2500–1600 BP) by means of varying seasonal averages. Computing statistical properties on sliding windows can help tracking seasonality changes [271], and the use of basic statistics can substantiate the interpretation of seasonality dynamics beyond qualitative analysis [272]. Testing seasonal amplitude or seasonal vs. non-seasonal patterns can also be carried out with more sophisticated measures like conditional entropy. Entropy generally quantifies the 'informativeness' of a distribution (e.g., a subannual rainfall distribution), resulting in higher values in case of more complex and more contrasted distributions [273]. Although specifically designed statistical tests can characterize a record's seasonality [274, 275, 276, 277], they remain rarely applied because they often do not account for the full complexity in proxy time series. Restrictions like independence or normality often pose significant limitations to the scope of basic hypothesis tests. Yet, meaningful seasonality-related properties can be extracted by combining multiple suitable tests and careful, case-specific definition of the null-hypothesis. Bootstrapping techniques [278, 33] offer a parameter-free approach to compute confidence limits by resampling a time series, without the need to make assumptions with respect to the data.

**Seasonality indicators** are often based on basic statistical measures to make specific statements about seasonality, e.g., to compare seasonality at different geographical locations [279] or between modeled and empirical proxy data [280]. A popular definition is established by the contrast of temperature or rainfall between seasons, expressed by differences or ratios [268, 262] ('seasonal amplitude', Fig. 9.1C). For example, rainfall seasonality has been characterised by dividing values for strong by such for low rainfall season [281], whereas — for instance — the difference between maximum and minimum monthly coral Sr/Ca and  $\delta^{18}\text{O}$

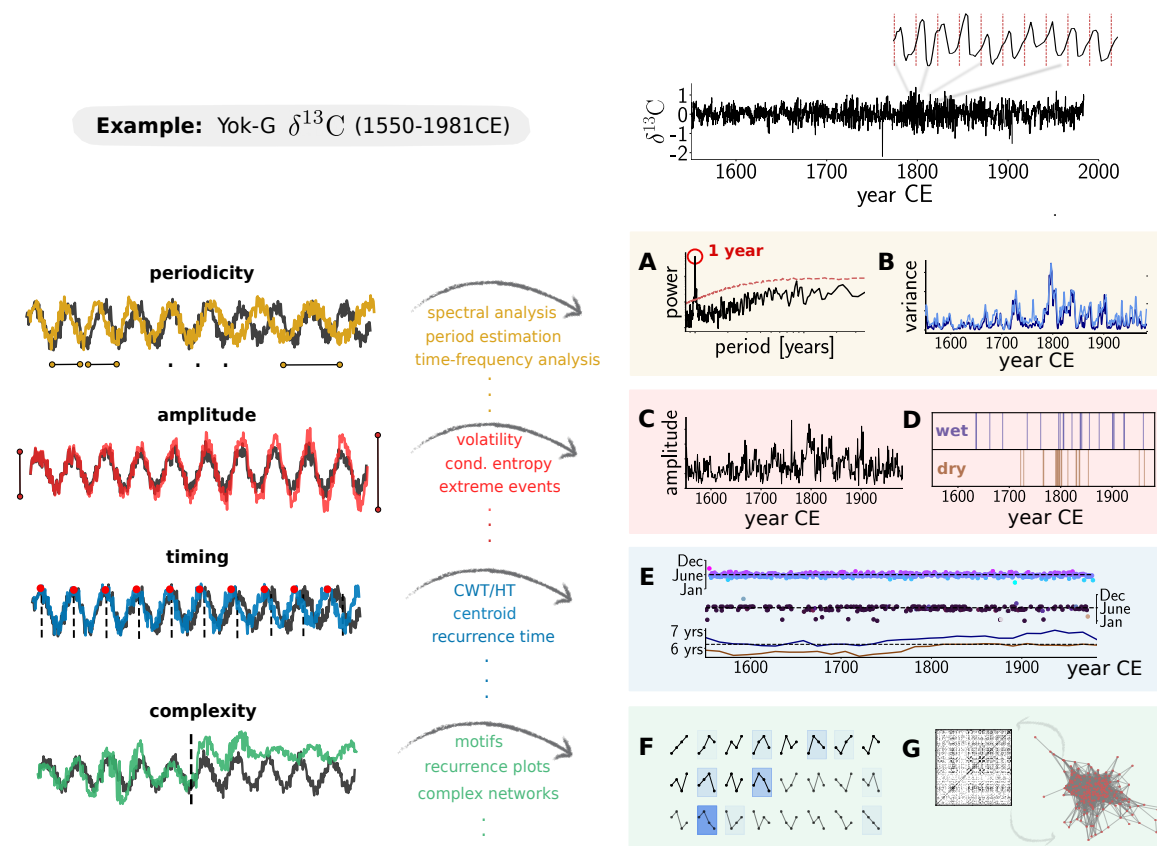


**Figure 9.1:** Four features of seasonal variations with schematic illustrations on the left and examples for their analysis on the right, i.e. periodicity, amplitude, timing and complexity. The  $\delta^{13}\text{C}$  variability measured on stalagmite Yok-G from Yok Balum cave, Belize, offers very high resolution and a layer-counted chronology [261]. The detrended record (using a Gaussian kernel filter) confines the analysis to seasonal-scale changes (upper right panel). Annual periodicity is extracted via a Lomb-Scargle periodogram (A) and studied over time by means of a continuous wavelet scale average around the annual period (dark blue) and sliding Gaussian kernel window variance analysis (bright blue) (B). Seasonal amplitude is computed as difference between annual maxima and minima (C) and an event series of extreme dry/wet seasons is obtained by a peaks-over-threshold approach with a 99%-quantile threshold (D). Timing of the wet season is extracted as the centroid of subannual patterns (upper panel) and exceedance times of the average wet season  $\delta^{13}\text{C}$  value for each individual year (center panel). Average recurrence times between  $\delta^{13}\text{C}$  values of distinct wet (dry) seasons are shown in the bottom panel in blue (brown) (E). Seasonal patterns are encoded as ordinal patterns ( $l = 4$ ). The blue shading indicates their frequency in the (linear interpolated) record (F). Complexity of irregularly sampled seasonal patterns are characterized by a recurrence plot/recurrence network, based on a computation of the edit distance measure.

values has been used to quantify seasonality in temperature the Caribbean at the end of the last interglacial [262]. Figure 9.1C shows an example of variations in the seasonal amplitude derived from  $\delta^{13}\text{C}$  variations measured at very high resolution on annually laminated stalagmite Yok-G over the last 400 years. In this case, it is defined as the difference between maximum and minimum proxy values for a given year and reflects seasonality of local rainfall. Such a characterization is yet not able to define the timing of seasons, e.g., how the subannual rainfall distribution changes from year to year (see Fig. 9.1E). If subannual resolution can be assessed, seasonality indicators should always account for the different manifestations of seasonality in the data and not be limited to a single seasonal property. For example, variable approaches have been considered to quantify variability of seasonal timing [282]. Annually laminated archives are particularly useful to extract information on seasonal timing, e.g., as shown in Fig. 9.1E: here, timing of the wet season was extracted by deriving centroids ('center of mass') from the subannual rainfall distributions and computing exceedance times of a pre-defined value for each year (upper and center panel). Recurrence times between dry/wet seasons of distinct years can also unveil intriguing information on the seasonal cycle (lower panel).

The definition of a seasonality indicator benefits from such diverse approaches. [283] define a seasonality index using multiple regression on fossil records and distinguish summer and winter rainfall regimes in South Africa. [273] give a spatial characterization of distinct seasonal rainfall regimes across the tropics based on how complex subannual rainfall distributions are rendered in terms of their seasonal amplitude, timing and duration. Also indicators of extreme weather have been used to characterize seasonality dynamics [265, 284, 264] (see below). Consequent application of seasonality indicators across disciplines could improve inter-comparability of independent proxy archives. Combining multiple methods enhances the interpretational value of seasonality reconstructions.

**Nonstationary extreme value analysis** can characterize events found in palaeoclimate proxy records, like floods, droughts, extreme precipitation, which can be season-specific [285, 286]. Extreme events have significant repercussions for agricultural, social and ecological dynamics [287], making their analysis particularly worthwhile when studied along with historical proxy archives (see also chapter 3 in the original manuscript). As climate is inherently nonstationary, suitable methods and implementations are employed [288], whereby two basic approaches can be distinguished, i.e., the computation of block maxima/minima, and the so called peak-over-threshold approach [285].

The *block maxima/minima* approach splits time series into consecutive blocks and computes maxima and minima, e.g., seasonal maxima in proxy data. For instance, an extensive analysis of 26 bivalve shell surfaces from the North Atlantic revealed that seasonal climatic extremes had an impact on the evolution of Norse colonies during warm and cold periods [289]. Time series with lower than seasonal resolution may be split into larger blocks. Since droughts for example occur within a specific season, some trends regarding the intensity (i.e., number of extreme events) of that season can be estimated. Using estimates of extreme value distribution (or their parameters) in a multi-proxy framework can give insights into spatio-temporal recurrence of extreme climate conditions [287].

The *peak-over-threshold* approach analyses the frequency of amplitudes above or below a threshold (often a quantile of the dataset). The frequency of threshold exceedances and return periods are useful to understand the temporal variability in the occurrence of season-related extreme conditions [290]. Fig. 9.1D shows series of season-specific extreme events extracted from  $\delta^{13}\text{C}$  values based on the 99%-quantile of the full time series. The same approach also helped to identify phases of stationary and nonstationary hydroclimatic changes in the Western Mediterranean in a 2800 year long seasonally-resolved lake record [291]. Evaluating

exceedance and recurrence probabilities of extreme precipitation events, this study found that the modern frequency of heavy rainfall events is normal in a historical perspective, but likely to increase under future warming conditions. If an event time series is suspected to contain periodicities, these can be identified, e.g., by computing the Rayleigh measure: for example, [292] test a time series characterized by Dansgaard–Oeschger cycles for periodicity in a Bayesian framework which also helps evaluation of seasonal-scale dynamics. Individual proxy time series can be embedded in larger proxy ensembles from different locations and the co-occurrence of extreme events can be studied using synchronization measures between events [293, 37] while accounting for proxy-specific uncertainties. Some proxy time series may entail immediate implications linked to seasonal extreme weather, like droughts in Spain since 1506 C.E. that are identified in accounts of religious ceremonies [294].

**Detrending and frequency filtering** is a standard pre-processing step when focusing on variability on single timescales in a proxy record [295]. After subtracting a trend from the original time series, the effectiveness of this decomposition should be evaluated, e.g., using spectral analysis and signal-to-noise ratio. As a basic approach, moving averages yield trends of intrinsic variability of time series. However, the degree of smoothing is only controlled by the applied window width. Importantly, moving averages can result in spurious trend characterizations and their frequency response makes them vulnerable to erroneous high-frequency variations [296]. Non-rectangular, smooth kernel functions are more appropriate for sliding window statistics and have been used in an uncertainty-aware regression approach to estimate trends in proxy time series. Local or global polynomial and spline regression can be employed to extract trends of varying complexity and can also be combined with kernel functions.

Another widely used technique is band-pass filtering, or applying a filter-bank to a time series. For example, [297] low-pass filtered a stalagmite-based isotope record and extracted seasonal strength that they were able to link to multi-decadal summer NAO variability. These approaches should be used carefully, since band-pass filters are neither designed for irregularly spaced or chronologically ‘uncertain’ data, nor accounting for above-mentioned intricacies surrounding moving averages. Seasonal and Trend decomposition using LOESS (STL decomposition) extracts smooth components of a time series by using local regression [298] which has, for example, been applied to extract smooth long-term trends from palaeoclimate records [24].

Mode decomposition approaches such as Singular Spectrum Analysis (SSA) and Empirical Mode Decomposition (EMD) capture nonlinear oscillatory modes and trends [299, 300, 301]. Modifications for time series with missing data exist [302, 266] and some applications to palaeoclimate data have been carried out [303]. These approaches offer the advantage that they capture the intrinsic variability of the time series, can yield higher modes of variability, and account for nonlinear oscillations. In summary, every detrending approach involves the risk of eliminating variability so that the remainder is spuriously interpreted as a seasonal component despite of its actual insignificance or that seasonal variability is unintentionally eliminated.

**Linear correlations** are a popular tool in time series analysis to characterize relations between multiple time series or the serial dependence of a time series when the data is normally distributed. Being limited to detecting linear relations, linear correlations do not account for more complex or causal relationships often found in (palaeo)climate data. (Non-)linear correlations can greatly improve significance of statements compared to simple visual inspection (‘wobble-matching’), which is still popular [304]. With regard to seasonality extraction, correlations are applied to confirm seasonal proxy interpretation [305, 306, 307], to test model

validity between empirical and simulated seasonal signals [308], or studying lead-lag effects. Multiple approaches allow the computation of correlations for irregularly sampled proxy time series [198, 309]. Statistical testing for significant correlations can also be designed such that it includes the dating uncertainties of a record [310]. Each of these is preferable against aggregating or interpolating the time series on a regular time axis without accounting for uncertainty since this introduces statistical biases that can hardly be controlled [204]. A kernel-based approach [198] together with an estimate for confidence limits [311] can be considered a robust method to detect linear correlations in irregularly sampled records. Finally, causality (directionality) between irregularly sampled, age uncertain proxy records can also be tested based on measures that are conceptually inspired by Granger causality [267, 312]. These methods might help identify drivers of seasonally variable strength.

With multiple and spatially distributed proxies that are known to record the same climatological parameter, seasonality can generally be detected beyond a regional scale and be compared between single proxies [313]. In this context, spatio-temporal mode decomposition approaches allow for extraction of a limited number of dominant modes that encompass a certain part of the variability from such spatial data. The most popular approach in this range is the Empirical Orthogonal Functions technique which is also frequently employed in climate field reconstructions [314] and is effectively applied to instrumental climate data [315] and proxy data with uncertainties [316]. Some applications show that the climate field perspective unveiled by mode decomposition approaches allows for detection of season-specific reconstructions on (pan-)regional scales [317, 318, 319]. [320] reconstruct the May–September precipitation field of China for the past 500 years using a dataset comprising 479 proxy records and identify three dominant modes with different spatio-temporal dynamics by means of ensemble empirical mode decomposition.

**Regression techniques** help to determine how multiple proxies or spatially distinct archives depend on each other by regarding them as a set of a dependent and multiple independent variables. They can be flexibly adapted to many problems and can help to detect seasonality. If a suitable measure for seasonality can be established, a linear regression can be computed to quantify the dependence of seasonality on the variability at other timescales or links to other proxy records. For example, [268] employed a linear regression on a multi-proxy, multi-site coral and mollusc dataset while accounting for uncertainties. Contrasting standard assumptions presumed in PMIP3 models, they uncover a positive relation between ENSO variance and seasonality. Linear regression is also used to validate proxy interpretation. For example, [321] use uncertainty-aware linear regression against instrumental data to support their interpretation of the chlorophyll content in a sediment core as proxy for regional summer temperature.

**Uncertainty propagation** in statistical analysis significantly enhances confidence in extracted (seasonal) characteristics. Accounting for dating uncertainties is particularly important when the significance of an annual period (see Sect. 9.2.2) or seasonal timing is evaluated. Many frameworks allow for such a characterization of age uncertainty that can be propagated through period estimation techniques for stalagmite proxy records, ranging from Bayesian approaches [322, 323, 324, 325] to Monte Carlo sampling-based techniques [326, 36, 327]. Whenever seasonality in high resolution records is to be aligned with records from other locations that are characterised by different climatic conditions, integrating multiple proxies with variable temporal resolution in presence of uncertainties arises as significant issue. [328] combined multiple proxies to reconstruct temperature using a Bayesian hierarchical model, accounting for uncertainty and coherently integrating multiple proxies despite distinct temporal resolutions.

### 9.2.2 Spectral analysis

Spectral analysis is a powerful tool to find seasonal cycles in temporally sufficiently resolved proxy records, and to test their significance. Even if a record does not allow the detection of annual or subannual cyclicities due to sparse temporal sampling, spectral analysis can provide valuable insights into the modulation of signals related to seasons or longer periods that can affect seasonal patterns, e.g., ENSO. Periodogram approaches are probably the most popular technique to study which periods are present [329, 330, 331, 332, 333, 334]. Based on the Fourier transform of the studied time series, regular periodogram-based methods are somewhat limited: straight-forward application is only viable for constantly sampled records without related uncertainty since irregular sampling intervals result in a loss of structure in Fourier peaks [335, 336]. Intricacies like high-frequency noise, dating uncertainties, limited record length, and measurement artefacts need to be considered when interpreting identified periods (see below). In the following, methods that are designed to estimate periods in such records are discussed. Subsequently, we give an overview of how this can be achieved in presence of nonstationarity.

**Period estimation** techniques are of increasing interest in seasonality studies. Unfortunately, no automated or optimal strategy for estimating periods in proxy records exists and each method requires a systematic evaluation of significance.

A prominent method to estimate periods in unevenly sampled records with dating uncertainties is the Lomb–Scargle (LS) periodogram [197, 337]. Similar to the classical periodogram, it can be understood as a least squares fit of sinusoids at each frequency which uses a  $\chi^2$ -expression to minimize the residuals. It can account for dating uncertainties by including Gaussian errors around each proxy value [337]. Often the LS periodogram is applied together with the estimation of AR(1)-spectra to assess significance (REDFIT, [338, 339]), although the robustness of this approach has recently been questioned [340]. Figure 9.1A shows a LS periodogram for the Yok-G  $\delta^{13}\text{C}$  record using the REDFIT algorithm to evaluate the significance of the identified annual spectral peak. In order to integrate uncertainties, periodograms can be computed for different realizations of an age-modelled proxy whereas each realization is compatible with the dating uncertainties [341]. When tasked with detecting seasonal periods, potential aliasing must be considered: if the sampling frequency of an irregularly sampled record episodically falls below half the annual frequency, seasonality can no longer be reliably extracted (Nyquist theorem). Specifying a frequency grid to prevent aliasing may thus be impeded [33].

Although still relatively rare, spectral estimates are used in seasonality studies. For example, [342] have reconstructed late Cretaceous annual cycles using high resolution isotope and trace element records from fossil shells. Others studies have used LS periodograms to relate wet/dry cycles in varved lake sediments to Indian summer monsoon changes even in the absence of sub-annual resolution of the proxy record [331]. LS periodograms have also helped to identify the influence of orbital forcing on seasonal strength [343]. To generalize classical LS periodograms and improve frequency detection or significance testing, spectral density can be combined with other methods [344, 345]. For highly resolved records, Welch overlapping segment averaging [346] might be particularly useful, as smoother periodograms can be estimated. Another approach that is based on a windowed representation of a time series is the Multitaper method [347, 348]. Methods specifically designed to estimate periods in irregularly sampled records furthermore include Gaussian kernel-based spectra [198], phase-folding techniques and Bayesian approaches [349, 350, 351, 335]; depending on the specific application, these are sometimes superior to classic methods.

In multiple proxy records, cross-spectral analysis allows identification of shared spectral power within the same frequency band, similar to LS periodograms [352] or Gaussian kernel



approaches [198]. Cross-power spectra have successfully been used to test the influence of solar forcing on droughts [353], or to study Holocene rainfall seasonality [354].

**Time-frequency (TF) analysis** extends classic period estimation techniques and evaluates the presence of periodicities through time [355]. As an arbitrarily accurate determination of both frequency and time is impossible, respective methods need to offer a compromise. Continuous Wavelet Transform (CWT) [356] does so while yielding a clear graphical output and standardized significance testing [357]. It is efficient in retrieving low and high frequencies as well as nonstationary features of a time series (such as frequency variations). Instantaneous phase estimates can be made by the Hilbert-transformation (HT) of a time series. By tracking the mutual spectral power between multiple time series through time via cross-wavelet or wavelet coherence analysis [358], significant periods of different intertwined processes can also be extracted (e.g., from instrumental records [301, 359, 360]). The increasingly frequent application of CWT on bivalves, speleothems, and tree rings highlights the popularity of this method for seasonality studies [361, 362, 363, 364]. For instance, the authors of [364] support their hypothesis that a strategically located speleothem reflects dry rather than monsoon season infiltration as an often overlooked interpretation by applying CWT to the proxy record. Still, irregular sampling remains rarely addressed. Often, spline or polynomial interpolation methods are used that are known to introduce artefacts, especially in the high-frequency bands. Figure 9.1B displays variance in the annual band of a CWT (Wavelet scale average) for the Yok-G stable isotope record (dark blue), whereby linear interpolation was used to regularize the time axis. In comparison, a Gaussian kernel variance estimate [198] with suitable bandwidth that naturally accounts for irregular sampling is shown (bright blue), showcasing how distinctiveness of the seasonal cycle can be tracked through time.

Several approaches have addressed a solution to account for irregular sampling in CWT: Foster's Morlet Weighted Wavelet Z-Transform method [365] has contributed to the definition of Wavelets for irregularly sampled astronomical time series. It has also found some application in the palaeoclimate literature [366] whereas some studies take uncertainty into account as well [367]. Using this method, [368] found evidence for seasonality changes in varved sediments from Lake Holzmaar, including winter cooling, summer rainfall intensity, and changes in season onsets/offsets during the 8.2 ka event. An extension to cross wavelet analysis is available and was, e.g., employed to capture how spatial coherence of periodic components in proxy time series is restructured throughout the Holocene by analysis of a global multiproxy data set [369]. Inspired by the LS periodogram, a least-squares based wavelet approach has also been put forward [370]. Another direction has been approached using projection methods where first applications remain to be carried out as of now [371]. Work on related TF-analysis techniques has also partially been directed towards treatment of irregular sampling [372]. Significance testing (see Sect. 9.2.3) can be applied by randomization of wavelet coefficients, retaining wavelet-related properties of the underlying time series [373]. Finally, alternative techniques like Hilbert-Huang and Singular Spectrum Analysis remain less frequently used in palaeoclimatological contexts, likely due to a more intricate mathematical background [299, 374, 301]. Effectiveness in application to both seasonal climate data [375, 376] and palaeoclimate records [377] has been demonstrated, yielding performance comparable to CWT analysis [377].

### 9.2.3 Nonlinear time series analysis

The fundamental processes that constitute seasonal proxy signals are often highly nonlinear, comprising nonlinear feedbacks, non-Gaussian distributions and nonlinear interrelations. For instance, abrupt transitions result from nonlinear threshold responses of interconnected

climate subsystems [378]. Rather than representing simple sinusoidal signals, seasonal variability and cycles with higher periods in broadband records consist of nonlinear oscillations. A comprehensive description of such systems requires application of well-established nonlinear time series analysis methods. Several techniques allow to test time series for nonlinear features [379]. If the seasonal signal in a proxy record is modulated by a range of frequencies, we can test if nonlinear oscillations can adequately describe these dynamics [380]. Surrogate testing is a powerful, non-parametric approach where ‘surrogate’ realizations of a time series are generated to test for certain features, e.g., nonlinearity. An ensemble of random realizations mimics the scrutinized signal with respect to some of its specific features by preserving them in a constrained randomization procedure [229]. For instance, simple random shuffling can be performed with the goal of significance testing, either on the time series itself (with the null-hypothesis of absent serial dependence) or on estimated phases to preserve power spectral density (e.g. with the null-hypothesis of different TF characteristics) [381].

**Nonlinear correlation measures** are often better suited to study interdependencies between multiple records, like mutual information or event synchronization [198, 382, 110, 383], rather than relying on linear correlations. Dynamic Time Warping (DTW) [384] helps in estimating similarities between records of different length. For example, [385] use DTW to demonstrate a significant correlation between the Mg/Ca record and water temperatures in molluscs and highlight their importance as archives of seasonality. [386] employ a recurrence plot based technique with the similar goal of matching unaligned rock magnetic data of two different sediment cores.

**Recurrence analysis** is a very flexible technique and can be applied to irregularly sampled and age-uncertain records [37, 50, 51]. Where seasonal changes can be linked to abrupt transitions, their detection is often based on some measure of complexity or anomaly detection [201, 387]. Recurrence plots stand out as a simple-to-implement albeit powerful tool [20], as they cannot only detect rapid shifts, but can also estimate periods, provide information on the underlying dynamics, and identify nonlinear relationships in multivariate data sets [388, 389, 128, 110]. Figure 9.1G shows a recurrence plot based on the edit distance approach proposed in [37] and illustrates the possibility to transform it into a complex (recurrence) network.

**Symbolic dynamics** represents an additional means to detect abrupt shifts and characterize recurring patterns in nonlinear time series. By encoding a time series as a sequence of symbols (motifs or ‘words’), it is well applicable to data with relatively high levels of noise and can deal with irregular or low sampled nonlinear time series [210, 209]. A possible choice for such symbols are ordinal patterns as displayed in Fig. 9.1F: given a pattern length of 4, 24 distinct patterns can be distinguished and the computation of their frequency in the (linearly interpolated) Yok-G  $\delta^{13}\text{C}$  record allows for statements on the seasonal-scale complexity.

**Information theoretical methods** exhibit yet another perspective on seasonality extraction, often facilitating estimation of periods in nonlinear time series that are noisy and irregularly sampled [390, 387]. While many applications to irregularly sampled astronomical records exist [391], palaeoclimate studies that often address similar objectives remain to be carried out with such methods.

**Complex time series networks** (Fig. 9.1G) and (palaeo-)climate spatial networks [392] can finally provide quantitative frameworks that improve confidence in the fidelity of proxy records as reflectors of regional seasonality and its teleconnectivity [393, 223].

## 9.2.4 Methodological challenges and strategies

Despite the availability of a range of tools, sole visual inspection of proxy records is still a common strategy. It appears that many studies focus on the challenging task of reconstructing climate variability from proxy evidence, thereby limiting their efforts of additional, more complex, analyses.

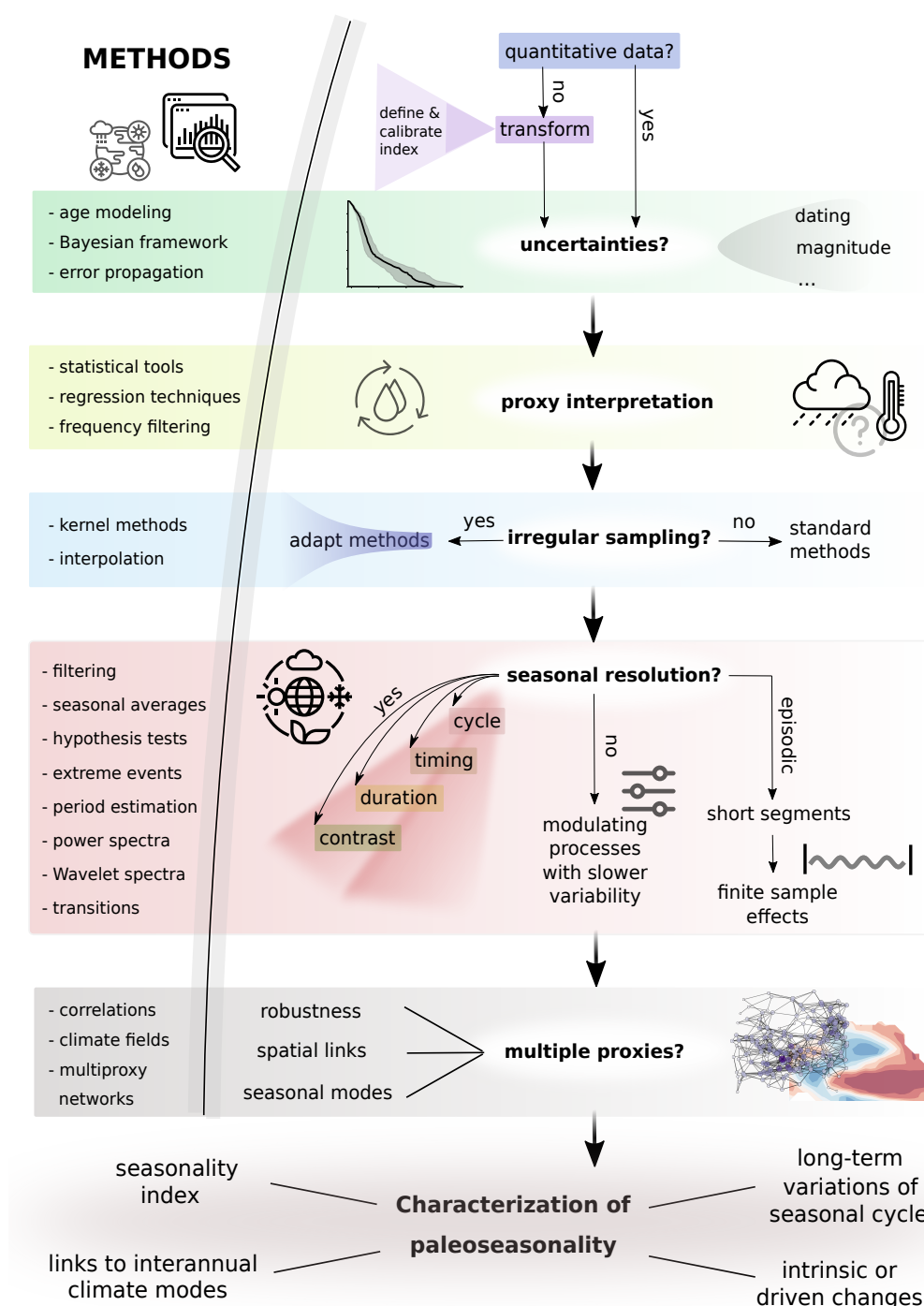


**Figure 9.2:** Schematic illustration of how seasonality can be extracted from a palaeoenvironmental archive. Each box represents a typical proxy-specific challenge that may need to be accounted for. Numerical methods that are well-suited to extract and quantify seasonality are displayed in the left part of the flow chart.

Many recent studies highlight the great potential of effective collaboration between researchers from both the proxy and methodological domains. Innovation on both fronts - proxy development and calibration, and statistical approaches to high-resolution irregularly sampled data - is essential for accurate reconstruction of seasonal dynamics. We highlight several challenges in this endeavor: (a) **Shortness of records** limits the applicability of most standard time series analysis methods. (b) **Uncertainties** – both related to proxy values and dating – need to be propagated in thorough statistical analyses; accounting for uncertainties is vital for palaeoseasonality studies as they are often on the same order of magnitude as the proxy value or sampling frequency. (c) **Irregular sampling** poses a major challenge for extracting seasonal information. Only a few methods beyond spectral analysis account for non-uniform sampling intervals. Statistical biases may dominate records resolved at sub-annual timescale, especially when the number of samples per year undergoes significant variations. (d) **Signal-to-noise ratios** are critical for highly-resolved proxy data as very few archives record an unambiguous climate signal. Figure 9.2 summarizes how these challenges can be approached when palaeoseasonality is targeted using numerical methods.

One suggestion which might facilitate methodological soundness of analyses and transdisciplinary collaboration, is supplementing innovative methods with well-documented and easily accessible open-source software.

Including local seasonal records from different, and spatially dispersed, archives will improve the understanding of regional climate dynamics, but only under the premise that uncertainties at both, the data/results and the interpretational level are taken into consideration [394]. Such scrutiny is feasible only if adequate assumptions and statistical methods are in place. On the other hand, the application of transdisciplinary multi-archive and multi-proxy approaches harbors enormous potential to refine seasonality detection across archives and environments; related phenomena often encompass a broad range of semi-stochastic phenomena (see Box 3) [313].

Consequently, combining different archives in palaeoseasonality studies will encourage more universal definitions of seasonality indicators that account for a broader set of ubiquitous seasonal features (see Fig. 9.1). Variations in palaeoseasonality are best represented by standardized indicators which consider more than one seasonal feature, are designed to compare seasonality across archives, and are based on a mathematically sound definition that effectively tackles above listed technical challenges.

## 9.3 Summary and outlook

### 9.3.1 Compositional make-up of climate seasonality

Seasonal changes in our environment are periodic and global, happening at the temporal scale of human behavior. This, and the fact that seasonal dynamics are perceptible over human live spans, makes the reconstruction of past changes in seasonality of paramount importance for the study of past human-environment interactions.

The concept of seasonality is rooted in the annual march of the Earth around the Sun, and the nonlinear response of the physical climate system (and human adaptation) to regular changes in solar forcing. The regional and local expression of seasonal changes is always a consequence of (semi-)stochastic internal feedbacks that are superimposed on predictable external solar forcing. Accordingly, the range of annual temperature and precipitation changes varies notably even along the same latitude. The most important factors modulating the seasonal signal are continentality and altitude, both (relatively) constant over longer time scales, and large-scale atmospheric circulation patterns that vary periodically but not regularly (semi-stochastically). Further, archive-specific sensitivity and sampling approaches have the

potential to modulate proxy signals.

### 9.3.2 Relevance of trans- and multidisciplinary approaches

Recent years revealed the importance of close collaboration between disciplines, including (palaeo-)climatology, (palaeo-)ecology, history, physics, archaeology, and anthropology, when tackling pressing questions in Earth Sciences. Finding a common language in such trans-disciplinary studies is a vital, but often challenging, prerequisite for communicating results and ideas across scientific communities, and the public. Similarly, acknowledging archive- and proxy-specific limitations and analytical uncertainties allows for assessing data quality and provides robust input for statistical approaches, which often reveal and quantify hidden information better than the naked eye. Choosing adequate statistical method(s) is challenging, and providing scrupulous interpretations and relevant outcomes calls for informed, close collaboration between palaeoenvironmental scientists and statisticians.

Recurring, archive-independent challenges relate to a) precise high-resolution sampling of often fragile, not linearly-grown or -accumulated, and size-limited material to capture the full range of seasonal variability, b) establishing the environment-proxy relationship that is constant over time and related to only one variable (e.g., only temperature, or only precipitation), c) quantifying seasonal change in terms of physical units ( $^{\circ}\text{C}$ , mm, number of days, etc.).

Continuous instrumental developments, and detailed monitoring and calibration efforts allow for addressing these challenges at least at a local scale. At regional or global scales, the most inconvenient issue is a deficiency of long, radiometrically-dated and seasonally-resolved records whose spatial and temporal coverage permits broader-scale inferences. The compilation and compare & contrast approach across different archives is essential in overcoming this inconvenience. At the same time a stringent quality assessment of each individual archive in its own merit and with its own limitations – age uncertainty, recorded season, qualitative or quantitative information and analytical error propagation – is critical. Simple, or more sophisticated statistical methods help in extracting the seasonal signal, assuring data quality, and juxtaposing seasonally resolved data in their own domain(s).

### 9.3.3 Proposed framework

Misconceptions and challenges in interpreting true or purported seasonal signals often originate from integrating data that were not/poorly quality-checked, or produced using different scientific practices and uncertainty propagation strategies. Below, we propose a framework that might be beneficial when targeting seasonal signals in palaeoenvironmental archives:

- examine the archive(s) critically, including sampling resolution, age control (both layer-counted and, if available, radiometric), proxy sensitivity or bias towards a certain season, and adapt the most adequate sampling strategy.
- try to identify climate variable (temperature, precipitation) that has changed, and the direction of this change (increase or decrease in annual amplitude) rather than refer to ‘change in seasonality’. Note that if the sampling is not continuous or sequential, but ‘bulk’, a change in baseline might appear as a ‘change in amplitude’.
- keep in mind that environmental archives only rarely can inform on the timing and duration of seasonal precipitation. Over longer timescales, the amount of precipitation might stay constant but its distribution may change.
- compare the direction of the documented change(s) with the one predicted by insolation forcing. Discrepancies in the expected direction of change might reveal more details and

a deeper insight into environmental evolution and response to insolation forcing than a simple admission that such a change has happened.

- in some cases, particularly when talking about rainfall or the combination of temperature and rainfall changes, several scenarios might be possible. Clearly articulating and justifying these (often contradictory) scenarios provides an explicit step in disentangling external forcing factors and internal feedbacks, and help completing the mosaic of past environments and human societies.
- while comparing seasonal signals from different archives keep in mind individual archive-specific limitations.

The transparency of communicating results gains in importance in trans-disciplinary projects. Different environments, and human societies within them, might react differently to the same forcing, the former depending on their natural architecture, the latter on their societal structure, vulnerability, conditioning, and resilience. Yet, admitting the heterogeneity of possible responses is as important as identifying the factors dictating this heterogeneity. A careful approach involving quality-controlled data and in-depth consideration of internal feedbacks operating in a given natural or anthropogenic environment will provide profound insights into how regional and local conditions adjusted to external forcing. Such insights are of critical importance as they inform the predictions of the effects of anthropogenic climate change on local to regional environments.

# 10 | Mid-Holocene rainfall changes in the southwestern Pacific

Cinthya Nava-Fernandez<sup>1</sup>, Tobias Braun<sup>2</sup>, Bethany Fox<sup>3</sup>, Adam Hartland<sup>4</sup>, Ola Kwiecien<sup>5</sup>, Chelsea L. Pederson<sup>1</sup>, Sebastian Hoepker<sup>4</sup>, Stefano Bernasconi<sup>6</sup>, Madalina Jaggi<sup>6</sup>, John Hellstrom<sup>7</sup>, Fernando Gázquez<sup>8,9</sup>, Amanda French<sup>4</sup>, Norbert Marwan<sup>2</sup>, Adrian Immenhauser<sup>1,10</sup>, Sebastian F. M. Breitenbach<sup>5</sup>

1 – Sediment- and Isotope Geology, Institute for Geology, Mineralogy and Geophysics, Ruhr-Universität Bochum, Universitätsstrasse 150, 44801 Bochum, Germany

2 – Potsdam Institute for Climate Impact Research, 14473 Potsdam, Germany

3 – Department of Biological and Geographical Sciences, School of Applied Sciences, University of Huddersfield, Queensgate, Huddersfield, UK

4 – Environmental Research Institute, School of Science, Faculty of Science and Engineering, University of Waikato, Hamilton, Waikato, New Zealand

5 – Department of Geography and Environmental Sciences, Northumbria University, Newcastle upon Tyne NE1 8ST, UK

6 – Department of Earth Sciences, ETH Zurich, Sonneggstrasse 5, 8092 Zurich, Switzerland

7 – School of Earth Sciences, The University of Melbourne, Australia

8 – Department of Biology and Geology, Universidad de Almería, Almería, 04120, Spain

9 – Andalusian Centre for the Monitoring and Assessment of Global Change (CAESCG), University of Almería, Spain

10 – Fraunhofer Research Institution for Energy Infrastructures and Geothermal Systems IEG, Am Hochschulcampus 1, 44801 Bochum, Germany

*Nava Fernandez, C., Braun, T., Fox, B., Hartland, A., Kwiecien, O., Pederson, C. L., Hoepker, S., Bernasconi, S., Jaggi, M., Hellstrom, J., Gázquez, F., French, A., Marwan, N., Immenhauser, A., Breitenbach, S. F. M. (2022). Mid-Holocene rainfall changes in the southwestern Pacific. *Climate of the Past Discussions: 1-29*. doi: 10.5194/cp-2021-172 [4]*

This discussion paper is a preprint. It has been under review for the journal *Climate of the Past* (CP). The manuscript was not accepted for further review after discussion. A revised manuscript is currently under preparation for submission to a different journal.

## Abstract

A better understanding of ENSO dynamics is essential for modelling future climate change and its impacts on the ecosystems and lives of the inhabitants of the tropical Pacific islands, which face considerable environmental risk in the coming decades. This study reconstructs past ENSO dynamics using a multi-proxy approach applied to a stalagmite from Niue Island that covers the period

6.4-5.4 ka BP.  $\delta^{18}\text{O}$  and  $\delta^{13}\text{C}$ , trace-element concentrations and image analysis are linked to an age-depth model constrained by eight U/Th dates and a complete lamina count. Principal component analysis of the proxy time series reveals hydrological changes at seasonal scale that are expressed in differential stalagmite lamina growth and geochemical characteristics. Increased concentrations of host-rock derived elements (Mg/Ca and U/Ca) and higher  $\delta^{18}\text{O}$  and  $\delta^{13}\text{C}$  values are observed in the dark, dense calcite laminae that are deposited during the dry season, whereas during the wet season higher concentrations of soil derived elements (Zn/Ca, Mn/Ca) and higher  $\delta^{18}\text{O}$  and  $\delta^{13}\text{C}$  values are found in pale, porous calcite laminae. Greyscale intensity values measured along the stalagmite growth axis are used here as an indicator of colour and density changes of the alternating laminae, allowing for the construction of a further seasonality record which expresses the contrast between wet and dry seasons. The multi-proxy record from Niue shows seasonal cycles associated with hydrological changes controlled by the South Pacific convergence zone. Wavelet analysis of the greyscale record reveals that ENSO was continuously active during the depositional period, with two weaker intervals at 6-5.9 and 5.6-5.5 ka BP. ENSO activity is also observed in the seasonality record, but muted periods are more prolonged, and intervals of significant ENSO-band power are more episodic. Recurrence analysis of nonlinear behaviour shows the influence that ENSO activity exerts on seasonality patterns and allows us to quantify the predictability of the climate system. Our results suggest that recurrence in the seasonal cycle of rainfall was reduced during periods when ENSO activity was stronger, pushing the system towards stochastic conditions. The tipping points from stochastic to predictable conditions may represent transitions in the Tropical Pacific mean state.

## 10.1 Introduction

Tropical Pacific dynamics play a key role in global climate. The South Pacific Convergence Zone (SPCZ) is the major climate feature that channels convective rainfall in the south Pacific at a seasonal scale [395]. At interannual scales, the coupled ocean-atmosphere phenomenon El Niño-Southern Oscillation (ENSO) controls climate variability [396]. These climate features modulate rainfall amount as well as the frequency and intensity of extreme climate events (e.g., tropical cyclones and droughts), and therefore these modes of climate variability greatly impact the ecosystems and the lives of the inhabitants of Pacific islands and the east and west coasts of the Pacific basin [397]. A range of projections resulting from climate models have forecasted the high vulnerability of the tropical Pacific islands to the impacts of anthropogenically driven warming [397]. Accurately dated, high-resolution and long-term records of climate and ENSO variability are essential for evaluating the robustness of climate models and of forecasts of regional and global climate changes [398, 399, 268]

Diverse studies across the Pacific have reconstructed ENSO during the Holocene using climatic archives such as marine sediments [400], corals [401, 402], clastic lake sediments [403, 404], and speleothems [405]. The resolution of these records ranges from multi-decadal to monthly, but they often represent discrete points in time rather than continuous intervals. Several studies from the Pacific have concluded that ENSO variability was reduced in terms of intensity and frequency during the mid-Holocene. These include eastern Pacific records such as lake sediments from Ecuador and the Galapagos [403, 406] and foraminifera from deep-sea sediments [407], as well as western Pacific records such as pollen from Australasia [408] and corals from Papua New Guinea [402]. According to a numerical model [409], this reduction



in ENSO strength during the mid-Holocene (3-5 ka) was a response to orbitally driven seasonality changes. Other authors whose records showed a reduction in ENSO variance during the mid-Holocene suggested that the driver was a change in the equatorial Pacific mean state [405, 401, 410].

Speleothems (secondary cave carbonates) offer a variety of environmentally sensitive proxy records and accurate age control. They have near-global distribution [411] and temporal resolution ranging from intra-seasonal [261] to orbital [412]. Stable oxygen isotope ratios ( $\delta^{18}\text{O}$ ) of speleothems can provide information about regional moisture (e.g., rainfall amount and water vapor source) [413, 414], whereas the interaction of soil  $\text{CO}_2$  and local infiltration processes inherent to the karst system are reflected by variations in stable carbon isotopes ( $\delta^{13}\text{C}$ ) [415, 416] and trace-element ratios (e.g., Mg/Ca and Sr/Ca) [411]. Less-used indicators of environmental conditions include the variations in physical features of speleothems such as density, colour, and lamina thickness, which are a function of hydrology, karst conditions, drip rate, and drip water chemistry [417]. These processes are reflected in the speleothem lamina growth rate and seasonal depositional changes (dry/wet) and can be observed by using high resolution imaging [418]. Accounting for these features can improve the interpretation of geochemical data.

Here we present a seasonally resolved mid-Holocene multi-proxy stalagmite record from Niue Island in the southwestern Pacific. This multi-proxy approach integrates an array of stable isotopes, trace elements, and physical properties measurements. The research objectives of this study include a) characterization of the nature of the speleothem laminae; b) identification of the environmental controls on the physical and geochemical proxies; c) establishing a chronology for the proxy records; d) extraction the fundamental periodicities from the observed proxy variability; and e) exploration of interactions between and possible controls on the main modes of climate variability in the region. We used traditional statistical analysis such as principal component analysis and wavelet analysis to extract the governing mechanisms of the climatic variability and advanced statistical tools such as recurrence plots to identify predictable, recurring features within the time series and detect transitions in climate system dynamics.

We present the first continuous, sub-annually resolved record of past hydrological changes associated with the south/north movements of the SPCZ between 6.4 ka and 5.4 ka BP and show that ENSO was active during this period. In addition, these findings provide evidence on the interaction of ENSO and rainfall seasonality in the tropical Pacific and insights into the effect of El Niño and La Niña events on the predictability of the climate system.

## 10.2 Geographic and climatic setting

Niue Island is a carbonate edifice located in the southwestern tropical Pacific ( $19^\circ 03\text{ S} / 169^\circ 55\text{ W}$ ) (Fig. 10.1). The island reaches a maximum altitude of ca. 60 m a.s.l. and hosts numerous caves, particularly in the Mutulau reefal limestone and the coastal cliffs [419]. The natural vegetation cover is characterized by dense tropical forest. Located ca. 490 km north of the Tropic of Capricorn, Niue is characterised by a tropical (Af) climate [420], with a mean annual air temperature of  $24^\circ\text{C}$  ( $T_{\min} = 20^\circ\text{C}$  in July,  $T_{\min} = 29^\circ\text{C}$  in January). Niue receives ca. 2000 mm of rainfall per year, mostly from November to April, while the period from May to October is cooler and relatively dry [397]. Rainfall variability is controlled by the seasonal movement of the South Pacific Convergence Zone (SPCZ) (Fig. 10.1). The southward-positioned SPCZ brings convective rainfall during the warm wet season, while

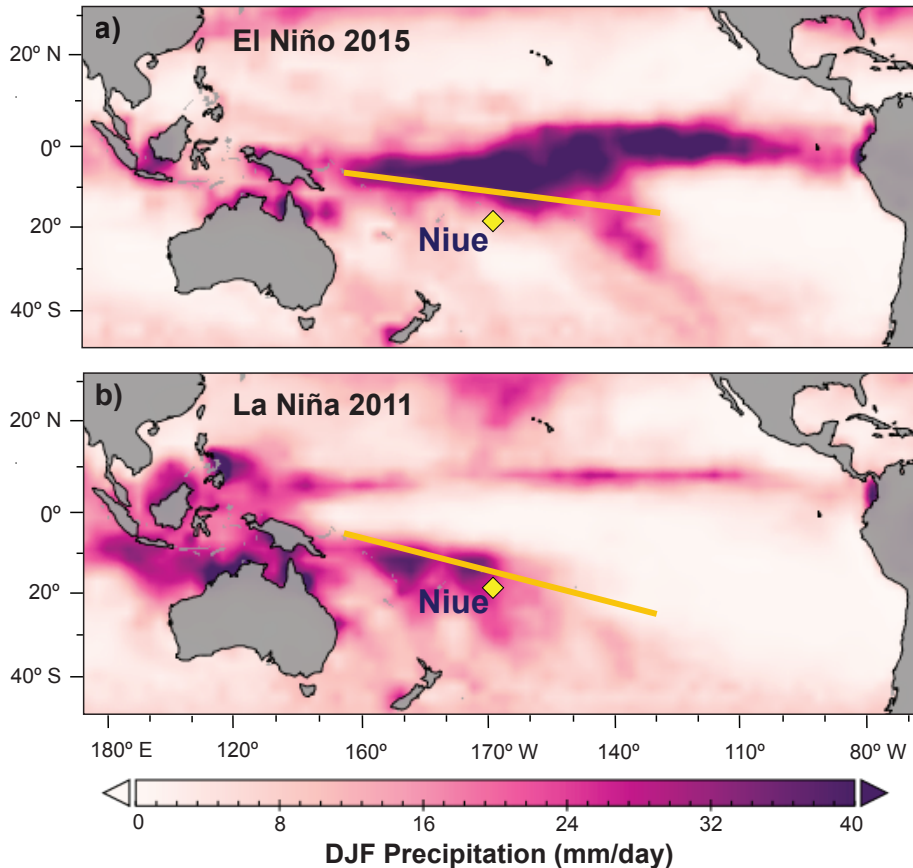


**Figure 10.1:** Austral summer (December-February) daily precipitation across the Pacific. Position of the South Pacific Convergence Zone (yellow lines) during two strong ENSO events: a) El Niño 1998; and b) La Niña 2011. The yellow diamond indicates the location of Niue Island. NOAA Climate Data Record (CDR) of GPCP Satellite-Gauge Combined Precipitation.

the northward shift of the SPCZ results in cool and drier conditions. Due to its location near the southwestern margin of the SPCZ, Niue is sensitive to sea surface temperature and atmospheric circulation changes linked to interannual El Niño-Southern Oscillation (ENSO) dynamics [421]. El Niño events are associated with a northeastward displacement of the SPCZ and hence drier conditions in Niue, particularly during the normally wet austral summer season (Fig. 10.1a). During La Niña events, the SPCZ inclination shifts ca. 1-3° towards the south-east resulting in increased rainfall in Niue (Fig. 10.1b) [395, 422]. Between 1969 and 2010, at least one or two TCs have hit Niue each wet season [397]. During El Niño years, above-average sea surface temperatures (SSTs) in the central and western equatorial Pacific enforce positive cyclonic vorticity [423], resulting in an increase of frequency of TCs [397].

## 10.3 Material and Methods

### 10.3.1 Stalagmite C132

Stalagmite C132 was collected from Mataga Cave, between the villages of Tuapa and Hio on the West coast of Niue Island. The stalagmite was found broken, with the top segment of the stalagmite missing, in a small grotto at the end of the cave. The collected segment is 43.4 cm long (Fig. 10.2) with visible layers of milky-white/pale porous calcite (PPC) and dark dense calcite (DDC) [424].

### 10.3.2 Sampling for geochemical analyses

Powder samples were obtained for geochemical analyses using a Sherline microdrill with a 1 mm diameter tungsten-carbide drill and a digital read-out. Eleven powder samples of  $\sim 200$  mg were collected for U/Th dating. Stable isotope samples were drilled every 3 mm (low-resolution,  $n = 144$ ), and milled every  $50 \mu\text{m}$  (high-resolution,  $n = 5102$ ) following the procedure outlined in [199]. Fig. 10.2 shows the sampling tracks.

### 10.3.3 U-Th dating

The U-Th ages were determined using a Nu Instruments Plasma MC-ICP-MS at the University of Melbourne. Sample powders were dissolved and equilibrated with a  $^{229}\text{Th}/^{233}\text{U}$  mixed spike solution before U and Th were separated from the matrix using Eichrom TRU-Spec resin. The purified U/Th fraction was introduced to the MC-ICP-MS via a Cetac Aridus membrane desolvator, giving total system efficiencies of ca. 0.3% for both elements. See [425] for detailed description of the protocol.

### 10.3.4 Greyscale analysis

Greyscale values were extracted from high resolution (2400 dpi) scans of the stalagmite surface along the growth axis using the image analysis software IMAGEJ version 1.51k (<https://imagej.nih.gov/ij/index.html>) [426]. This analysis provides a record of intensity values between zero (black) and 255 (white), with a spatial resolution of  $10.6 \mu\text{m}$ .

### 10.3.5 Age-depth modelling

The age-depth model of stalagmite C132 was initially constrained using eight U-Th ages as input to the COPRA age-modelling software [36]. This U-series-based age-depth model was then further constrained by comparison with the layer counting chronology. The series of counted layers vs. stalagmite depth was anchored to the depth of the topmost U/Th date. This layer chronology fell within the  $2\sigma$ -uncertainties of the older U/Th dates. This procedure leaves an overall error margin of  $\pm 20$  years. The final age model is the median record based on ensembles of 2000 Monte Carlo age-depth realisations derived using the COPRA routine [36].

### 10.3.6 Speleothem oxygen and carbon isotope analyses

Every fourth high-resolution sample was analysed, resulting in an actual resolution of  $200 \mu\text{m}$ . First set ( $n = 607$ ) of samples covering the depth ranges 4-16.25 mm and 46.85-92.26 mm was measured at Ruhr University Bochum. Between 90 and 110  $\mu\text{g}$  of sample powder was acidified with orthophosphoric acid at  $70^\circ\text{C}$  and reacted for 60 min before analysis. The released  $\text{CO}_2$  gas was dried and measured in continuous flow mode on a ThermoFisher MAT253 gas source isotope ratio mass spectrometer coupled to a GasBench II (ThermoScientific, Bremen, Germany). Results are presented in delta notation with  $\delta$ -values reported as parts per thousand (‰) relative to the international Vienna PeeDee Belemnite (VPDB) standard. Results are corrected using a two-point calibration using the international standards IAEA-603 and NBS18. The long-term  $1\sigma$  reproducibility of the internal standard is 0.06 ‰ for  $\delta^{13}\text{C}$  and 0.09 ‰ for  $\delta^{18}\text{O}$ . A second set ( $n = 740$ ) of isotope measurements, covering the depth ranges of 92.35-205.26 mm and 16.84-47.16 mm, was performed at ETH Zurich using a ThermoFinnigan Delta V Plus isotope ratio mass spectrometer coupled to a ThermoScientific Gasbench II. See technical details in the supplementary material E.

### 10.3.7 Isotope analysis of rain and dripwater

Rain and drip water samples from four Niue caves were collected in a fieldwork campaign in February 2020. The oxygen and hydrogen isotope ( $\delta^{18}\text{O}$  and  $\delta\text{D}$ ) composition of samples was measured using cavity ring-down spectroscopy (CRDS; [427]) at the Universidad de Almería, Spain. The CRDS device was interfaced with an A0211 high-precision vaporiser. The internal standards were JRW, BOTTY and SPIT. The results were normalised to the VSMOW (Vienna Standard Mean Ocean Water). Typical long-term instrumental precisions ( $\pm 1\sigma$ ) were  $\pm 0.06\text{‰}$  for  $\delta^{18}\text{O}$  and  $\pm 0.06\text{‰}$  for  $\delta\text{D}$ , based on the repeated analysis of an internal standard every 6 samples.

Sample ID	Depth [mm]	U [ngg <sup>-1</sup> ]	[ <sup>230</sup> Th/ <sup>238</sup> U] <sup>a</sup>	[ <sup>234</sup> U/ <sup>238</sup> U] <sup>a</sup>	[ <sup>232</sup> Th/ <sup>238</sup> U]	[ <sup>230</sup> Th/ <sup>232</sup> Th]	Age (ka BP) <sup>b</sup>	[ <sup>234</sup> U/ <sup>238</sup> U] <sub>i</sub> <sup>c</sup>
C132-1	3.5 ± 0.5	269	0.0533 ±0.0004	1.0767 ±0.006	0.000174 ±0.000002	306	5.439 ±0.059	1.0779 ±0.0061
C132-2	29.7 ± 0.5	370	0.0537 ±0.0007	1.075 ±0.0027	0.000044 ±0.000001	1225.7	5.514 ±0.077	1.0762 ±0.0028
C132-3	78.7 ± 0.5	311	0.0549 ±0.0005	1.0733 ±0.002	0.000026 ±0.000001	2115.2	5.653 ±0.055	1.0745 ±0.0020
C132-4	136.3 ± 0.5	592	0.0568 ±0.0005	1.0793 ±0.002	0.000010 ±0.000001	5768.5	5.825 ±0.059	1.0806 ±0.0020
C132-5	161.2 ± 0.5	396	0.0571 ±0.0003	1.0738 ±0.0059	0.000057 ±0.000001	1002.2	5.879 ±0.047	1.0751 ±0.0060
C132-6	185.4 ± 0.5	507	0.0572 ±0.0004	1.075 ±0.0024	0.000011 ±0.000001	5165.7	5.892 ±0.045	1.0763 ±0.0024
*C132-7	213.4 ± 0.5	492	0.0621 ±0.0006	1.0769 ±0.0024	0.000013 ±0.000001	4948.9	6.406 ±0.066	1.0814 ±0.0018
C132-8	290.7 ± 0.5	n. a.	0.0604 ±0.0004	1.0799 ±0.0017	0.000105 ±0.000002	575.4	6.195 ±0.044	1.0814 ±0.0018
C132-9	365.8 ± 0.5	693	0.0619 ±0.0007	1.0747 ±0.0027	0.000068 ±0.000001	n. a.	6.39 ±0.079	1.0761 ±0.0027
*C132-10	394.9 ± 0.5	n. a.	0.0607 ±0.0004	1.0761 ±0.0011	0.000068 ±0.000001	n. a.	6.256 ±0.041	1.0774 ±0.0011
C132-11	401.4 ± 0.5	200	0.5210 ±0.0025	1.0981 ±0.0061	0.000091 ±0.000001	5754.3	69.264 ±0.73	1.1193 ±0.0072

<sup>a</sup> Activity ratios determined at the University of Melbourne after Hellstrom (2003).

<sup>b</sup> Age in kyr before 1950 AD corrected for initial <sup>230</sup>Th using eqn. 1 of Hellstrom (2006), the decay constants of Cheng et al. (2013) and [<sup>230</sup>Th/<sup>232</sup>Th]<sub>i</sub> of 0.43 ± 0.043

<sup>c</sup> Initial [<sup>234</sup>U/<sup>238</sup>U] calculated using corrected age

\* Outlier not used in age-depth model

2σ uncertainties in brackets are of the last two significant figures presented.

**Table 10.1:** Results of the <sup>230</sup>Th/U dating.

### 10.3.8 Trace element analysis

Concentrations of a suite of 15 elements were measured along the growth axis of C132, following the greyscale track. Measurements were performed at the University of Waikato (New Zealand) by laser ablation-inductively coupled mass spectrometry (LA-ICP-MS) using a RESOLUTION SE 193 nm excimer laser ablation system equipped with a Laurin Technic S155 laser ablation cell coupled to an Agilent 8900 QQQ-ICP-MS. See technical specifications at the supplementary material E.

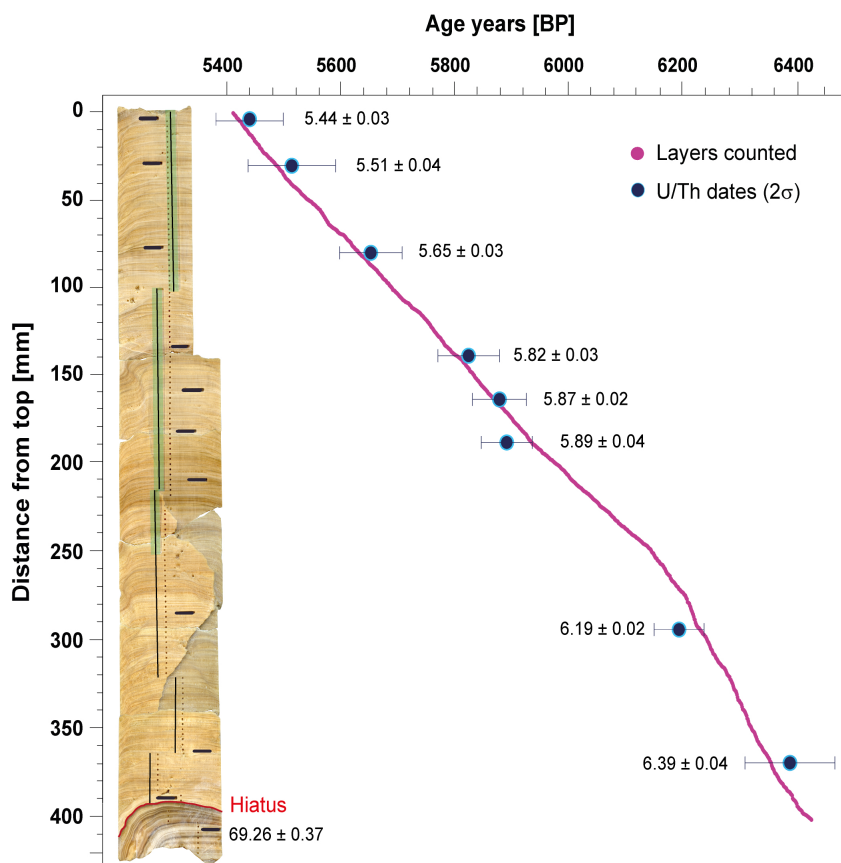


**Figure 10.2:** Age-depth model of the Holocene section of stalagmite C132. Blue circles indicate  $^{230}\text{Th}/\text{U}$ -ages with their  $\pm 2\sigma$  errors. The purple line indicates the layer counting profile. The image of sample C132 shows the U-Th sampling locations (black bars), LA-ICP-MS tracks and greyscale (black lines), the sampling trench for high-resolution stable isotopes (green shading), and low-resolution stable isotope sample locations (dots).

## 10.4 Results

### 10.4.1 U-Th dating and age modelling

The age model of stalagmite C132 is confined by eight U/Th ages. Two out of the eleven U/Th measurements were discarded due to large uncertainties, one due to likely hiatus (Table 10.1). The latter (69.3 ka) in the lowermost part of the stalagmite, was measured on a sample taken below a visible crystal fabric change (Fig. 10.2). Radiometric dating indicates that the stalagmite grew continuously from 6.428 to 5.411 ka BP (with present referring to 1950 CE). The Holocene portion of the record is the focus here. The Holocene U-series chronology is further refined by layer-counting based on greyscale data. The layer count indicates that the Holocene part of the record spans 1019 years.

### 10.4.2 Greyscale record

The greyscale intensity values vary between 93.5 and 273.3 (Fig. 10.3a), with a mean of 179.4. Pale porous calcite (PPC) laminae have higher values than adjacent dark dense calcite (DDC) laminae. The greyscale record has the highest resolution of all C132 proxy records and exhibits variability from seasonal to multi-decadal time scales. The growth rate record reveals a notable change in average growth rate at 6.1 ka BP, with faster growth prior to 6.1 ka BP

(0.57 mm/yr), and slower growth (0.34 mm/yr) between 6.1 ka and 5.4 ka BP (Fig. 10.3f).

### 10.4.3 Oxygen and carbon isotopes record

In total, 144 samples were measured at interannual resolution (6.39-6.002 ka BP), and 1347 samples were measured at sub-annual resolution (6.002-5.422 ka BP). Over the analysed interval,  $\delta^{18}\text{O}$  varied between -7.19‰ and -3.47‰, with a mean of -5.5‰ (Fig. 10.3d). The  $\delta^{13}\text{C}$  values ranged from -13.74‰ to -6.5‰, with a mean of -9.62‰ (Fig. 10.3e). The  $\delta^{18}\text{O}$  and  $\delta^{13}\text{C}$  time series record sub-annual to centennial-scale changes. The  $\delta^{18}\text{O}$  and  $\delta^{13}\text{C}$  values are positively correlated ( $r = 0.58$ ,  $p < 0.001$ ), with both isotope systems varying synchronously throughout the record (suppl. Fig. E.1). The stable isotope values fluctuate within  $\pm 1.5\sigma$  of the mean. The highest  $\delta^{18}\text{O}$  values of the record occur between 5.50 and 5.46 ka BP, where a decadal-scale positive excursion of ca. 1.3‰ is followed by a rapid decrease towards the mean (Fig. 10.5e). A similar trend is observed in  $\delta^{13}\text{C}$ , although in this case the values are much closer to the mean.

### 10.4.4 Trace elements records

High-resolution LA-ICP-MS analysis showed distinct variations in a suite of 14 elements. The results are reported as metal/Ca ratios and summarised in Table 10.2. This section focuses on variations of Mg and Zn, which represent contributions from the host rock and the soil, respectively (Fig. 10.3b and c) [419, 428]. The resolution of the LA-ICP-MS analyses allows the detection of sub-annual variability in the trace element record (Tables 3 and 4). Mg/Ca concentrations vary between 2.95 and 36.07 mmol/mol with a mean value of 11.92 mmol/mol (Fig. 10.3b). The Zn/Ca ratios ranges from 0.1 to 420  $\mu\text{mol/mol}$  with a mean value of 17.95  $\mu\text{mol/mol}$  (Fig. 10.3c). Higher Zn/Ca values generally coincide with PPC laminae (Fig. 10.4e). Technical difficulties resulted in a gap in the trace element data at 276.225-281.662 mm (6.219-6.213 ka BP).

Metal/Ca ratio	Mean value	SD	Maximum value	Minimum value	Units
Mg/Ca	11.92	4.95	36.07	2.95	mmol/mol
Sr/Ca	0.81	0.11	1.32	0.46	mmol/mol
P/Ca	1.32	0.39	3.18	0.16	mmol/mol
Al/Ca	0.04	0.11	2.49	0.00	mmol/mol
Na/Ca	1.13	1.19	16.85	0.13	mmol/mol
Br/Ca	1.33	0.48	3.27	0.26	mmol/mol
U/Ca	0.20	0.06	0.42	0.00	$\mu\text{mol/mol}$
Pb/Ca	0.23	0.24	2.76	0.00	$\mu\text{mol/mol}$
Fe/Ca	22.6	51.5	1151.18	0.00	$\mu\text{mol/mol}$
Mn/Ca	0.96	1.9	65.70	0.00	$\mu\text{mol/mol}$
Ba/Ca	1.17	0.41	4.12	0.27	$\mu\text{mol/mol}$
Cu/Ca	9.7	21	393.67	0.36	$\mu\text{mol/mol}$
Ni/Ca	3.3	3.5	31.33	0.07	$\mu\text{mol/mol}$
Zn/Ca	17.95	25	420.45	0.10	$\mu\text{mol/mol}$

**Table 10.2:** Descriptive statistics for the trace element ratios determined along the growth axis of stalagmite C132.

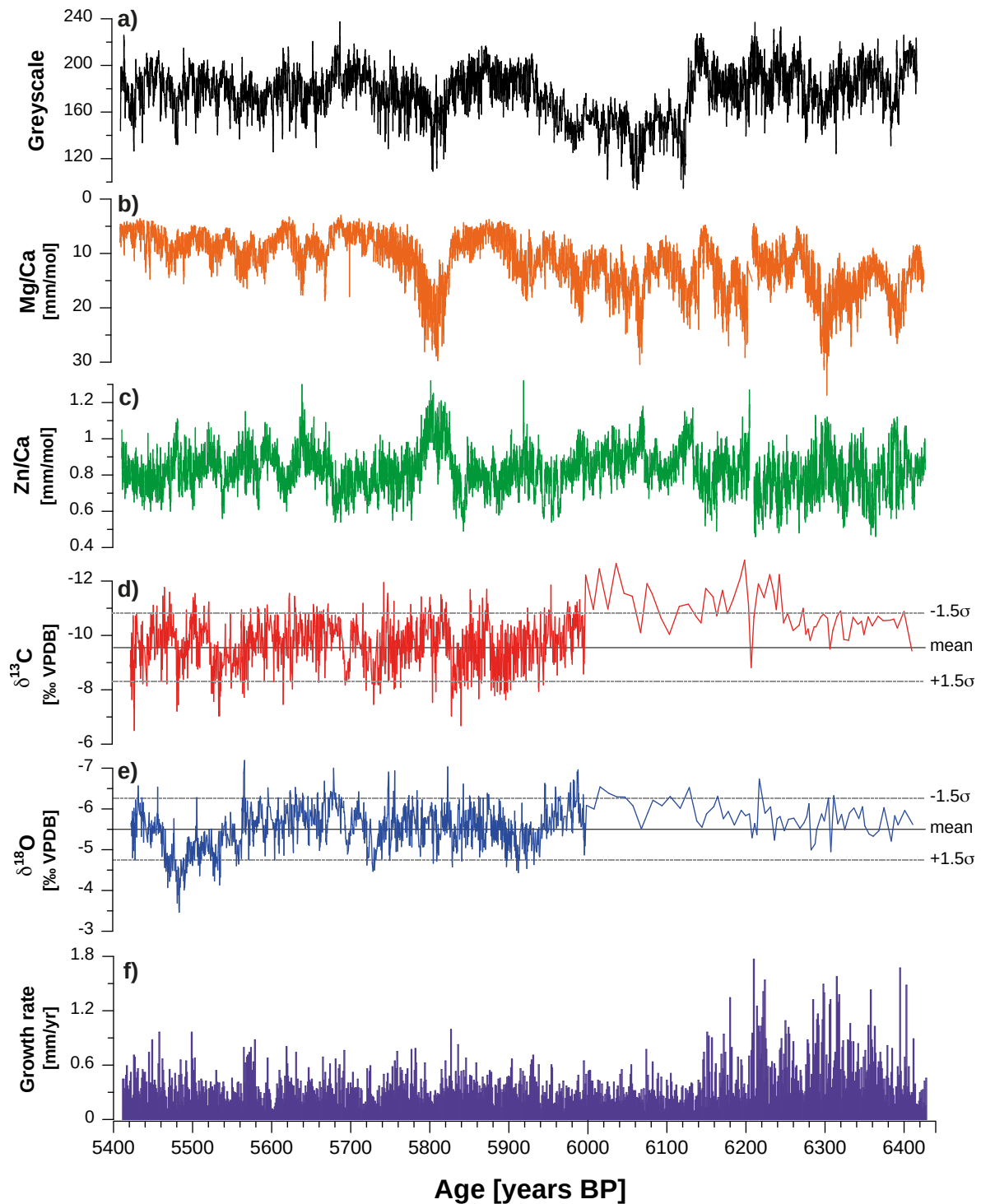


**Figure 10.3:** Proxy time series obtained from stalagmite C132. Note the different temporal resolutions achieved for carbon (d) and oxygen (e) isotope analyses for the periods 6.002-5.422 ka BP (high-resolution) and 6.39-6.002 ka BP (low-resolution).

## 10.5 Statistical analysis

### 10.5.1 Principal component analysis (PCA)

Principal component analysis (PCA) allows the identification of associations which might be interpreted as common forcing in the proxy time series.

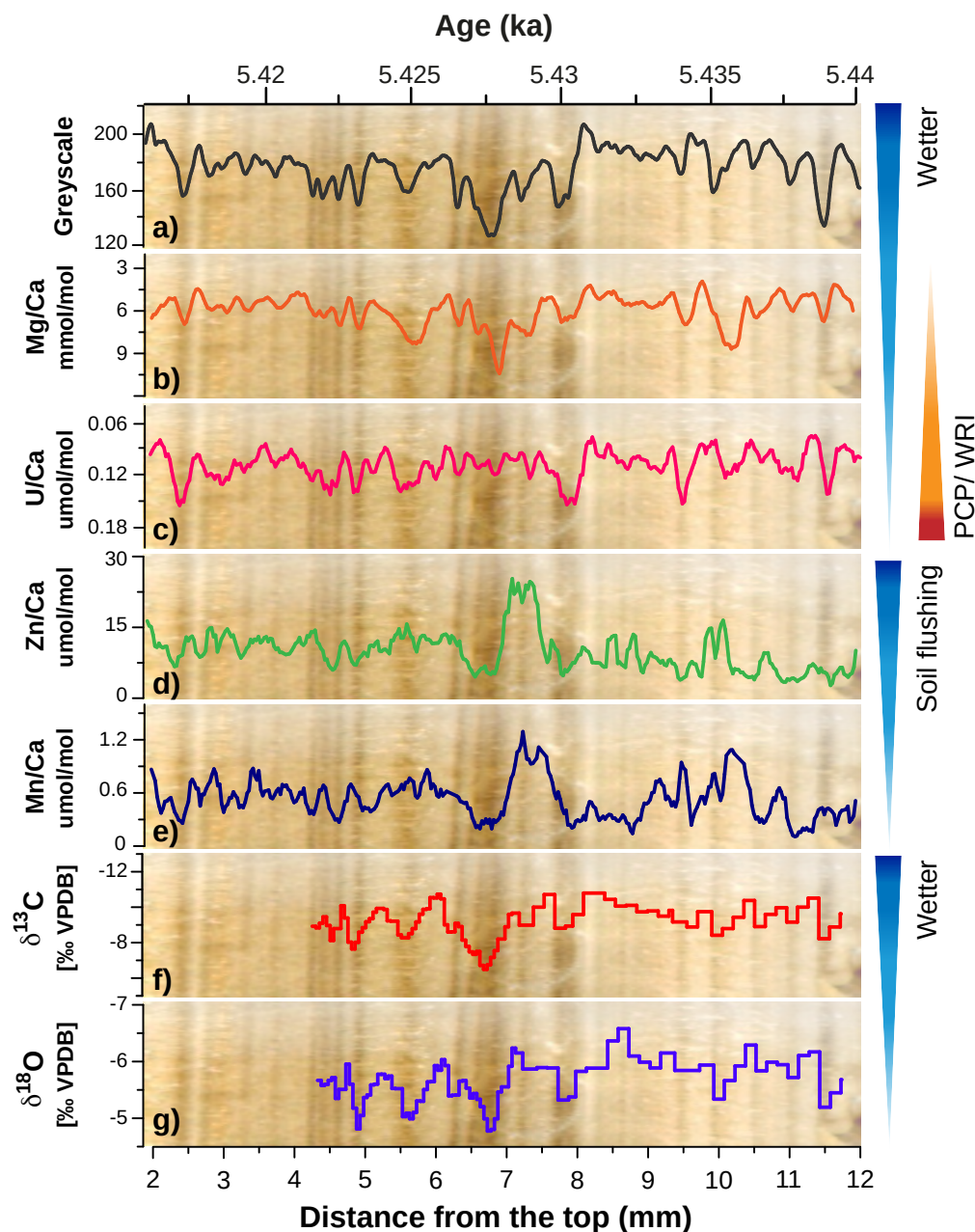


**Figure 10.4:** Detailed view of a 10 mm section of stalagmite C132 with proxy records superimposed on the stalagmite image, showing the relationship of the proxies with the alternation between pale porous calcite (PPC) and dark dense calcite (DDC) laminae. For the explanation of the arrows on the right-hand side, see the discussion section.

We carried out several PCAs on different groupings of datasets derived from stalagmite C132. All records included in each PCA were standardised to the lowest resolution in the group by averaging the data corresponding to each lowest-resolution time interval to accommodate the differences in temporal resolution (Table 10.3). Table 10.4 summarises the different PCA



groupings and temporal resolution. Data preparation prior to principal component analyses included imputing missing values using the iterative PCA algorithm from the MISSMDA library in the software R and log transformation of the data series. PCAs were performed in R software using the PCASHINY algorithm from the FACTORSHINY (v.2.2) package.

Three PCAs were performed: PCA-1, PCA-2, and PCA-3 (Table 10.4). Technical difficulties resulted in a gap in the trace element data at 276.225-281.662 mm (6.219-6.213 kaBP). Below this gap, several of the trace element series have a substantially higher variance compared to those above the gap. To avoid potential instrumental biasing, the trace element time series data was split into two sets and PCAs were performed separately on the uppermost and lowermost sections (PCA-1a and PCA-1b). PCA-3, including only trace elements, is presented in suppl. Fig. E.2. Fig. 10.5 displays the PCA results, where each dot signifies the loading of the respective record onto principal components (PCs) 1 and 2. For PCA-1a, the first two principal components (PCs) explain 56.48% of the variance in the original data (Fig. 10.5a). Zn, Mn, Fe, Pb, and Al show a strong positive correlation with PC1 (loadings > 0.7) and a moderately positive correlation with PC2 (loadings < 0.6). Mg, U, Sr, and P define a group which is moderately negatively correlated with PC2 (loadings < 0.6) and weakly to moderately positively correlated with PC1 (loadings < 0.5).

<b>Proxy</b>	<b>Resolution (points/year)</b>	<b>Time interval (years BP)</b>
Greyscale (GS)	30-60	5411 – 6428
Trace elements	8-36	5411 – 6428
Stable isotopes high resolution	2-4	5422 – 6002
Growth rate (GR)	1	5412 – 6428

**Table 10.3:** Resolution and time span of the C132 proxy records.

<b>PCA</b>	<b>Groups of proxy records</b>	<b>Resolution of PCA</b>	<b>Time interval (years BP)</b>
PCA- 1a	GS, GR, Trace elements	Annual	5411 – 6213
PCA- 1b	GS, GR, Trace elements	Annual	6219 – 6428
PCA- 2	GS, GR, Trace elements, Isotopes	Annual	5422 – 6002
PCA- 3a	Trace elements (see Supplement)	Sub-annual	5411 – 6213
PCA- 3b	Trace elements (see Supplement)	Sub-annual	6219 – 6428

**Table 10.4:** PCA groups and time span. GS = greyscale, GR = growth rate.

The first two components of PCA-1b explain 61.64% of the total variance and show similar associations of elements (with Br added to the second group) and similar correlations to the two PCs as in PCA-1a. PCA-2 produces similar groupings to PCAs 1a and 1b but also indicates a third group that includes Ba, Na, and Br (green circle, Fig. 10.5c) and is moderately positively correlated to both PC1 and PC2 (loadings < 0.6). The stable isotopes do not contribute to PC1 and PC2; instead, they present high loadings for PC4. In both PCA-1 and PCA-2 the greyscale record is projected onto the lower left quadrant of the coordinate system spanned by the PCs, indicating an inverse relationship to the group of elements Sr, Mg, U, and P. Full-resolution PCAs of trace element data (PCA-3a and b) were also performed with similar results (suppl. Fig. E.2).

## 10.5.2 Seasonality determination

For the study of mid-Holocene rainfall seasonality, we performed a minor recalibration on the monthly-scale dating of the greyscale record. Based on the fact that mean rainfall is higher during the wet season (November to April) than in the dry season (May to October), the greyscale record was anchored on its time axis such that wet season averages are higher than dry season averages in the maximum possible number of years. This yielded a (constant) shift of +5 months. Rainfall seasonality was afterwards calculated for each year as the difference between average greyscale values in the wet and the dry season (Fig. 10.7a/b and suppl. Fig. E.3).

## 10.5.3 Spectral analysis

To investigate which processes drive the variability recorded in the C132 dataset, we applied the BIWAVELET package in R to perform wavelet power spectrum analyses using Morlet wavelets [356] on the suite of annually resolved proxy data, the seasonality record and the two first principal components (PCs) derived from PCA-2.

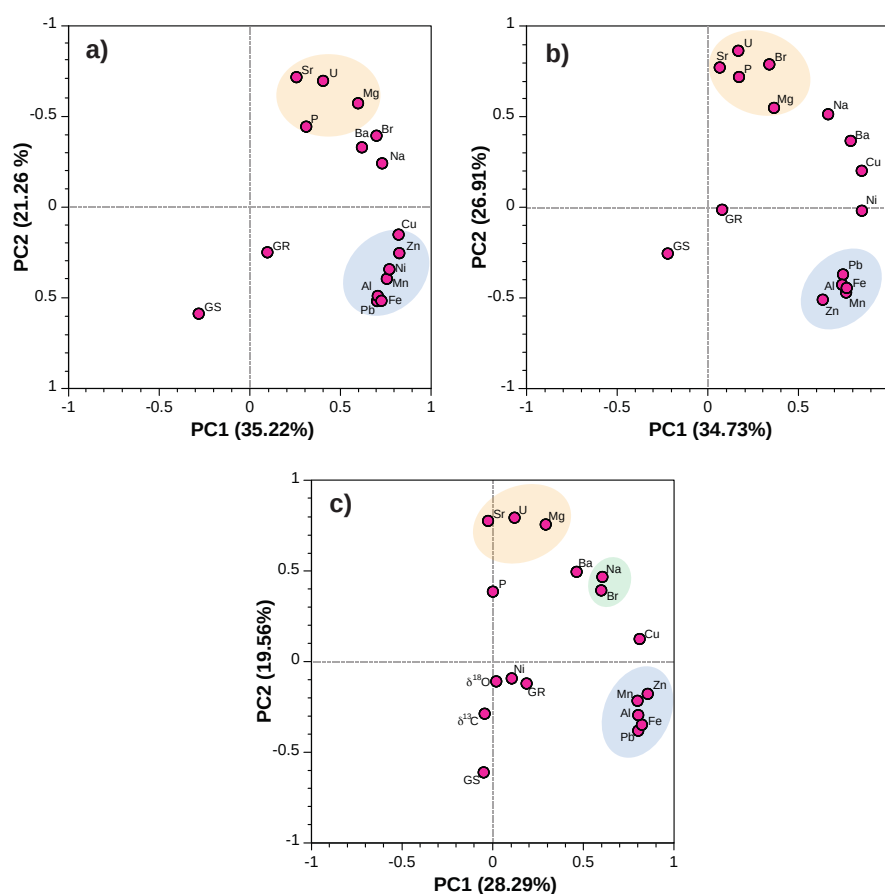


**Figure 10.5:** Results of the principal component analyses. a) PCA-1a, b) PCA-1b, c) PCA-2. All PCAs reveal two prominent groups: group 1 (blue shaded area) is formed by Zn, Mn, Fe, Pb, and Al, and group 2 (orange shaded area) that includes Sr, Mg, U, and P (except for PCA-2 where P is not included in this group). For all PCAs the data were pre-treated assuming normal distributions after a log-transformation (see Section 10.5.1). For details of the interval and resolution of the datasets for each PCA, see Table 10.4. Note that in PCA-1a (a), the algorithm assigned the opposite sign to the PC2 axis compared to PCA-1b and PCA-2. This axis is thus reversed for easier comparison.

The wavelet spectrum of the greyscale record displays significant power (>95% confidence

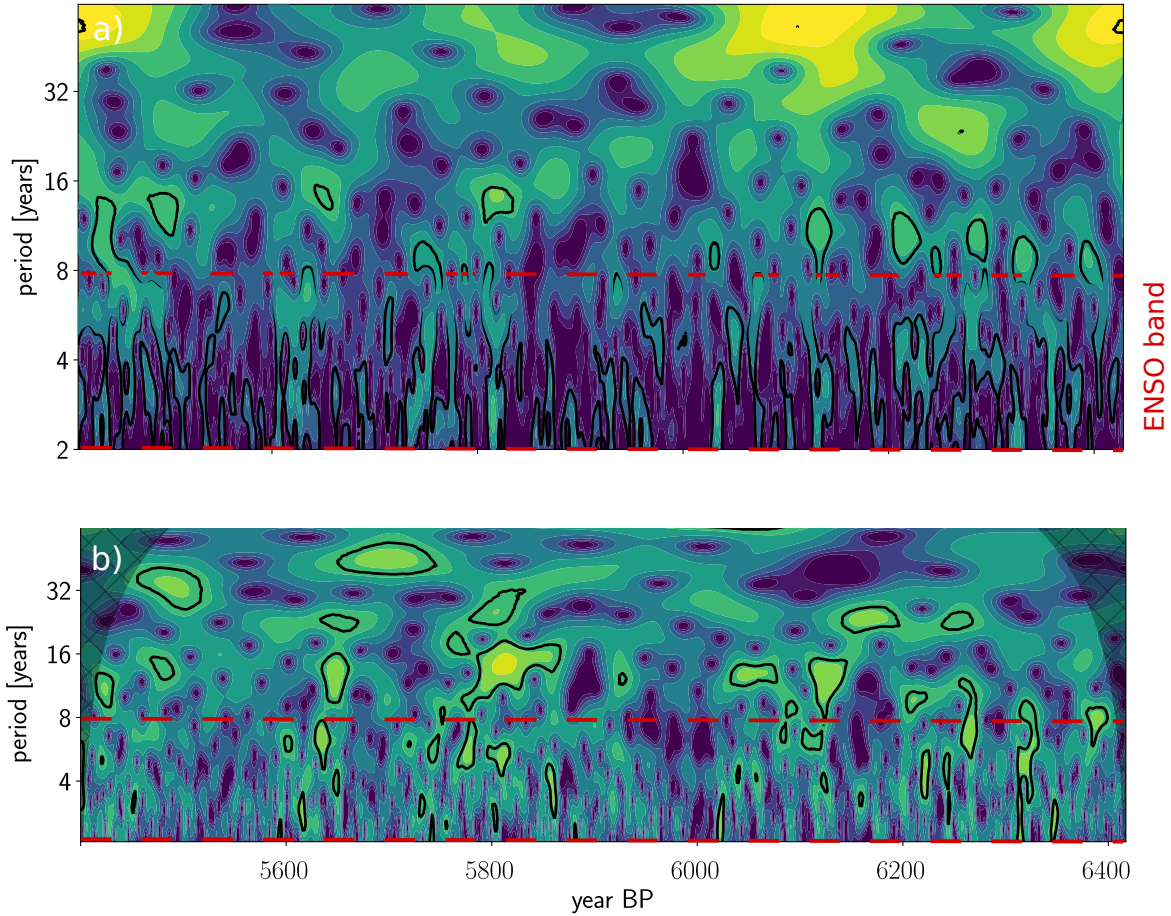


**Figure 10.6:** Wavelet spectral analysis of C132. a) Annually resolved greyscale record and b) Constructed seasonality record. Significant ( $> 95\%$ ) power is delineated by black contours. The ENSO band (2-8 years) is outlined in red.

level) in the ENSO band (2 to 8 years) continuously through the recorded period (Fig. 10.7a). The seasonality record exhibits episodic ENSO-scale variability with two periods of muted ENSO activity, the first from 6030 to 5900 y BP and the second from 5600 to 5500 (Fig. 10.7b). The wavelet spectra of PC1 and PC2 of PCA-2 show irregular patches of significant periodicities associated with ENSO-band variability at 6000-5950, 5700-5650, and 5500-5400 years BP (suppl. Fig. E.4).

#### 10.5.4 Recurrence analysis

Recurrence analysis is used to test if a time series revisits formerly visited states in a regular or erratic fashion. The predictability of rainfall seasonality was computed based on a recurrence plot (RP) analysis [20, 24]. RPs with a fixed recurrence rate of 15% were computed on 200-year sliding windows after embedding each time series segment with an embedding dimension of 3 and an embedding delay of 2; the selection of these parameters is explained in suppl. Fig. E.5.

## 10.6 Discussion

### 10.6.1 Interpretation of environmental proxies

#### Greyscale values

The greyscale variability of stalagmite C132 is a measure of the alternation between PPC and DDC laminae, which are related to crystal growth and matrix-density variations. Higher greyscale values represent porous crystal growth arrangements, whereas lower greyscale values reflect denser calcite crystal patterns (Fig. 10.4a). Factors such as drip water saturation, drip water pH, drip rate, and CO<sub>2</sub> degassing promoted by cave ventilation govern the formation of distinctive crystal fabrics depending on the seasonal environment [429, 430]. We interpret the variation in crystal growth style (and thus greyscale values) as a function of the dissolved carbonate supply. During the wet season, the supply of drip water (and with it dissolved inorganic carbon, DIC) is high, allowing for rapid CaCO<sub>3</sub> deposition. In the dry season, water supply is more restricted, drip rates are lower, and thinner, denser, and darker carbonate laminae form. Consequently, as previously observed in other coastal Niuean caves [419, 421], long crystals form in the wet season and micritic carbonate (i.e., micro-crystalline, nearly glassy) layers form during the dry season. We suggest that the mechanism that promotes the preservation of seasonal signals in the C132 proxy records is the seasonal cycle in drip water supersaturation, leading to sub-annual changes in stalagmite growth rate. These factors produce seasonal variation in geochemical proxyrecords in fast-growing speleothems [431, 424].

#### Oxygen isotope values of rain, drip water and speleothem calcite

We attribute the sub-annual  $\delta^{18}\text{O}$  variability observed in the C132 record to changes in amount of rainfall delivered to Niue Island over the depositional period. Due to the small size of the island and its geographical location, the source of Niue's rainfall is entirely oceanic. The summerly southward movement of the SPCZ and tropical cyclones bring strong vertical convective rainfall with a depleted  $\delta^{18}\text{O}$  signature (see for example suppl. Fig. E.6). Rain and drip water from Niue Island fall on the South Pacific Meteoric Water Line (SPMWL:  $\delta D = 7.7 \cdot \delta^{18}\text{O} + 9.3$ ,  $r^2 = 0.96$ ) derived from Samoa and Rarotonga rainfall databases [432], as well as on the GMWL (suppl. Fig. E.5). These results are consistent with monitoring studies of two other Niuean caves that suggest seasonal variability in the isotopic composition of drip waters, with higher  $\delta^{18}\text{O}$  values in the dry season and lower  $\delta^{18}\text{O}$  values during the wet season [428, 421, 433]. Changes in stalagmite  $\delta^{18}\text{O}$  thus provide information about the location of the SPCZ and/or the prevalence of tropical cyclones in the Central Pacific during the mid-Holocene. Lower stalagmite  $\delta^{18}\text{O}$  values are found in the PPC laminae indicating the intensity of the wet season and higher  $\delta^{18}\text{O}$  values found in the DDC that represent the dry season.

#### Carbon isotopes of speleothem calcite

The  $\delta^{13}\text{C}$  values of stalagmite C132 have a similar range to those of a stalagmite record from the nearby Avaiki Cave [428]. In both records, the  $\delta^{13}\text{C}$  values are lower in PPC laminae deposited during the wet season and higher in the DDC laminae formed during the dry season (Fig. 10.4f). As with the greyscale changes discussed above, the variations in the isotopic composition of the alternating laminae can be explained by seasonal changes in water and dissolved inorganic carbon (DIC) supply. It has been shown that  $\delta^{13}\text{C}$  values in drip waters in Niue caves represent a mixed signal from both soil CO<sub>2</sub> ( $-29.4 \pm 0.09\text{‰}$ ; 91%) and carbonate bedrock ( $-0.4 \pm 0.09\text{‰}$ ; 9 %) [419]. The  $\delta^{13}\text{C}$  variations in C132 are likely caused by changes in the proportions of these two carbon sources. Lower drip rates during

the dry season allow for prolonged CO<sub>2</sub> degassing from the dripping water, enhancing kinetic fractionation and resulting in higher speleothem  $\delta^{13}\text{C}$  values. During the wet season, increased moisture supply promotes microbial and vegetation activity in the soil [434, 416], decreasing the pH of the infiltrating water and intensifies water-rock interaction [435] while reducing prior calcite precipitation (PCP), resulting in lower speleothem  $\delta^{13}\text{C}$  values.

### Trace elements

A series of PCAs were used to investigate the processes controlling trace element variations in stalagmite C132 at annual and sub-annual scale. All PCAs consistently reveal two main groups based on their loadings on PC1 and PC2: Zn, Fe, Cu, Pb, Al, and Mn (Group 1) and U, Sr, Mg, and P (Group 2) (Fig. 10.5). Group 1 includes the soil-derived elements which are transported into the epikarst via high infiltration events [436, 437, 438]. Group 2 comprises elements that are derived from the host-rock as well as variable inputs of marine aerosol. This includes Mg and Sr, which are incorporated into the speleothem calcite by water-rock interaction (WRI) and/or modified by prior calcite precipitation (PCP) and are often interpreted as a proxy for local hydrology, with high Mg and Sr indicating drier conditions [417]. It is likely that in this cave system, the incorporation of U and P into the calcite follows a similar mechanism as observed for Mg, i.e., substitution for CO<sub>3</sub><sup>2-</sup> in the crystal lattice. Dry periods induce less host-rock dissolution, leading to lower CO<sub>3</sub><sup>2-</sup> activity and increased U and P partitioning [439], allowing higher incorporation of U and P in the slower-growing DDC laminae. In contrast, supersaturation in the wet season promotes a higher growth rate through enhanced degassing and increased competition for U and P ions to replace carbonate in the lattice of the PPC laminae [440]. Group 2 (host-rock) elements are strongly positively correlated with PC2, which explains ca. 26% of the total variance. Importantly, the greyscale record is moderately to strongly negatively correlated with PC2, while Group 1 (soil-derived) elements are weakly to moderately negatively correlated with PC2. Since greyscale values are primarily controlled by drip water (and thus rainfall) amount, PC2 likely represents the variation between wetter and drier years, with the positive direction indicating dry and the negative direction indicating wet (see note to Fig. 10.5). Wetter conditions would result in more soil-derived elements being transferred to the cave, leading to the negative correlation with PC2, while host-rock elements are concentrated in the calcite during drier conditions due to lower drip rates. The same control (i.e., drier conditions) would also serve to concentrate Mg derived from marine aerosols within the epikarst water store, leading to higher Mg/Ca and other element/Ca ratios that are highly concentrated in seawater (e.g., Na, Sr, Ba). It is notable that these elements are separated from the soil-derived elements by PC2 and distributed toward the host-rock-derived elements. Thus, while increases in host-rock-derived elements (e.g., U, Mg) support an interpretation of drier climate states, the similar result would be found if a small contribution of marine aerosol were present. Although this study does not draw on drip water monitoring, it is highly probable that marine aerosol also contributed to the elemental composition of C132, similar to earlier findings [433]. This reasoning does not affect the general interpretation of the elemental data. PC1 explains 28-35% of the variance in the datasets. Soil-derived elements are strongly positively correlated with this axis, while host-rock/marine elements show a weakly positive to no correlation, and greyscale shows weakly negative to no correlation. Soil-derived elements are transferred to the cave by the flow of water through the epikarst. However, overall wet/dry conditions would affect greyscale and host-rock derived elements to a greater and more predictable extent, as discussed above. A major transfer of soil-derived elements may occur through flushing of the epikarst during extreme rainfall events [437], such as tropical cyclones. These events are short-lived and would be unlikely to have a major effect on the style or rate of (longer-term) calcite crystallisation, thus having a limited effect on greyscale and host-rock elements. We

thus interpret PC1 as controlled by the prevalence of extreme rainfall events in the tropical Pacific. With loadings of comparable magnitude on both PC1 and PC2, Na and Br are located between the host-rock and the soil-derived trace metal groups. As previously noted, Na and Br are concentrated in sea water, and previous studies estimated a sea water contribution of 89% for Na and Br in the drip water of Niuean coastal caves [433]. Following this finding, we interpret these elements as being mostly derived from marine aerosols.

### 10.6.2 Climatic interpretation of the proxy time series

The term ‘rainfall seasonality’ is used here to refer only to the difference in the amount of rain between the wet and dry seasons within one annual cycle, as measured by the difference in the greyscale values between a PPC lamina and the adjacent DDC lamina. We developed a seasonality time series based on the difference between the PPC lamina peaks (wet season maximum) and the DDC lamina troughs (dry season maximum) from the greyscale record (suppl. Fig. E.3). Low rainfall seasonality values refer to low contrast between the wet and dry seasons, while high rainfall seasonality values represent higher contrast between wet and dry seasons. Changes in the consistency of seasonal oscillations are defined by the DET parameter, which allows us to quantify seasonal predictability in the system and to identify transition points from predictable to random conditions and vice versa (Fig. 10.7g). Periods of more predictable seasonality are distinguishable from those with irregular seasonal variations based on the 95%-confidence level obtained from a bootstrapping procedure (dotted grey line, Fig. 10.7g). Whenever this confidence level is exceeded, seasonal rainfall variations have significantly shifted towards a regime of greater or lower predictability.

### 10.6.3 Climatic interpretation of the proxy time series

Our 1019-year hydrological reconstruction from Niue Island reveals five main stages delineated by multi-centennial (200-300 yrs) oscillations between generally increased and decreased predictability of rainfall seasonality during the mid-Holocene. Phase 1, from 6.4 ka to 6.2 ka BP, is characterized by wetter conditions as indicated by a high mean growth rate and greyscale (Fig. 10.3a,f). PC2 (background rainfall) is relatively high during this period, while PC1 (indicating extreme events, possibly driven by strong ENSO) is moderate to low, though with some high peaks. During this period the wavelet spectrum of the greyscale record (overall rainfall) shows significant continued ENSO band variability, and the wavelet spectrum of the seasonality record present also periods of significant ENSO band variability but sparse on time (Figs. 10.6 and 10.7f). In Phase 2 (6.2-5.9 ka BP), the variability in background rainfall is reduced below the mean, and heavy rainfall/high infiltration events increased in frequency (Fig. 10.7a, b). During most of this period seasonality values are moderate to low, with increased predictability of rainfall seasonality (Fig. 10.7e,g). This suggests that during Phase 2 rainfall more evenly spread out over the year, presumably due to high infiltration events in the dry season linked to TCs. Phase 3 (5.9 to 5.72 ka BP) starts with the lowest PC2 values (background rainfall), occurring after a notable decrease at 5.85 ka BP. After ca. 5.8 ka BP the PC2 returns to higher values again, suggestive of "normal" background rainfall. Concurrently, the low PC1 signal suggests few high infiltration events. Two peaks in  $\delta^{18}\text{O}$  and  $\delta^{13}\text{C}$  records coincide to the "normal" background rainfall conditions reveal two decadal-scale maxima. It seems that Phase 3 was generally wet, with superimposed decadal-scale dry episodes. We interpret these signals as indication for pronounced seasonality and low rainfall predictability due to significant influence of ENSO on atmospheric conditions over Niue. Phase 4 (5.72 to 5.5 ka BP) is characterised by multi-decadal oscillations between wet/dry periods, represented by background rainfall (PC2), the high infiltration events record (PC1), as well as the  $\delta^{18}\text{O}$  and  $\delta^{13}\text{C}$  records. The most pronounced drying signal in the  $\delta^{18}\text{O}$  record

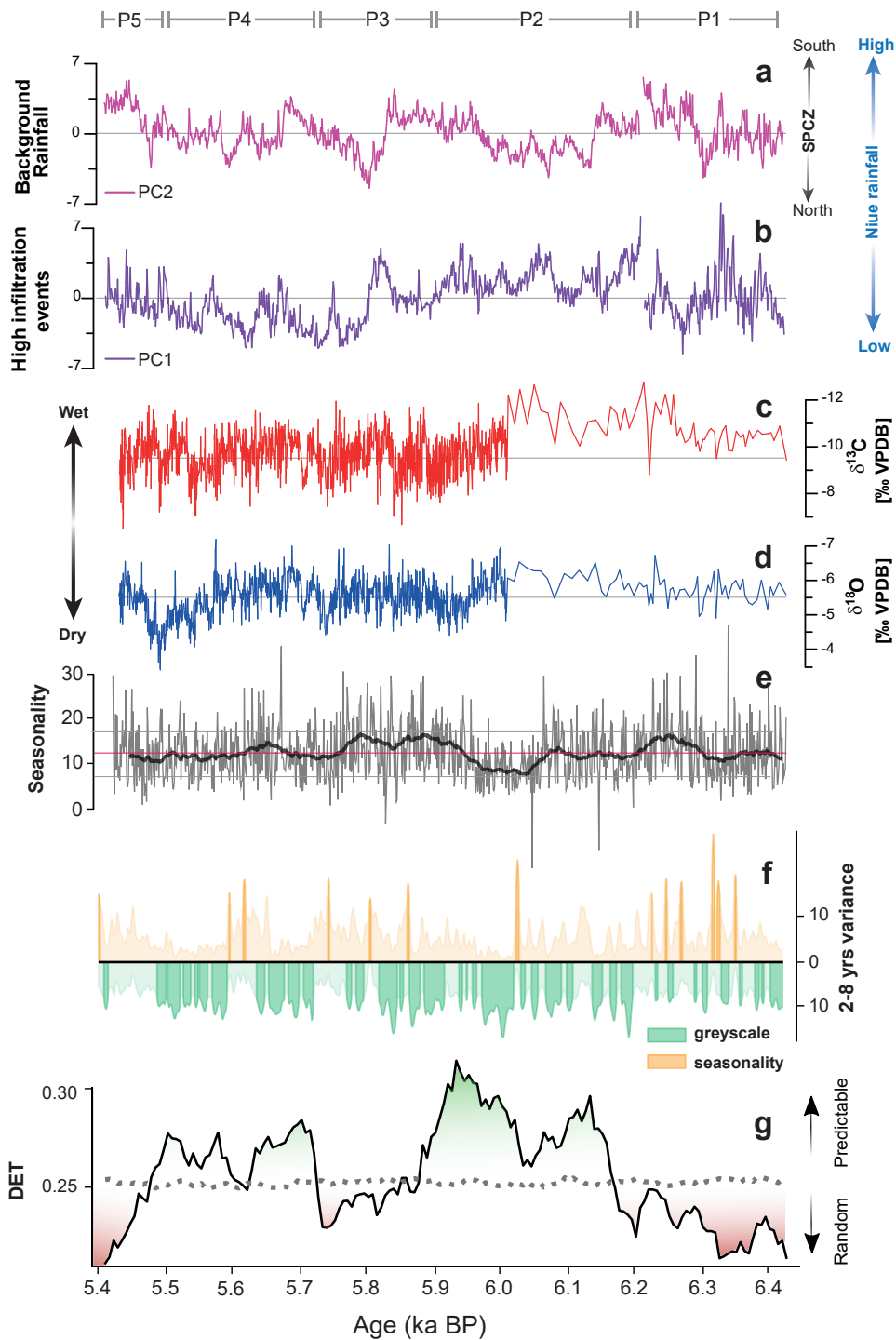


**Figure 10.7:** a) Background rainfall (PC2). b) High infiltration events (PC1). c)  $\delta^{13}\text{C}$  record. d)  $\delta^{18}\text{O}$  record. e) Seasonality record extracted from the greyscale record. f) ENSO-scale variance computed as 2–8-year wavelet scale average (see Fig. 10.6) from greyscale record (green) and seasonality index (yellow); darker-shaded peaks are above 95% significance. g) Seasonal predictability computed as DET from sliding recurrence plots; green shading indicates more predictable/regular seasonality and red shading indicates less predictable/random seasonality. See Sections 10.5.2 and 10.5.4 for calculation of (e)-(g). P1-P5 indicate different predictability phases.

occurs around 5.5 ka BP at the same time there is a low in background rainfall, this could be indicating a northward displacement of the SPCZ. Seasonality is quite stable except for a decades-long maximum at ca. 5.65 ka that coincides with a decrease in the background rainfall and high infiltration events. This peak also corresponds to a shift from consistently significant ENSO power in the greyscale record to ENSO-band peaks in the seasonality record. Phase 4 thus was characterized by predictable seasonal rainfall, except for the short interlude at 5.65 ka BP. In the final Phase 5 of our record (5.5 to 5.4 ka), the background rainfall rapidly increases while the high infiltration events record shows a more subdued and gradual rise. This increase toward wetter conditions is supported by low  $\delta^{18}\text{O}$  values. During this period, ENSO variance is only marginally significant in the greyscale record, while it is muted in the seasonality record. Predictability of rainfall seasonality is low and decreasing. Significant ENSO-band variability in the greyscale record occurs at different times than in the seasonality record (green and yellow peaks, respectively, in Fig. 10.7f), which suggests different controls. Since the seasonality record reflects the wet/dry season contrast, whereas the greyscale record reflects mostly the wet season, we suggest that the ENSO-band variability in seasonality is controlled by changes in the amount of rain during the dry season, which would increase or reduce the contrast between seasons. El Niño conditions are characterised by drier conditions than normal; however, TCs are more frequent in El Niño years [441]. Given that dry season rainfall is generally relatively low, overall background reduction in dry season rainfall during El Niño years may be counter balanced by an increase in TC occurrence. This would lead to a reduced seasonality (drier wet season and wetter dry season) during El Niño years and decrease predictability. In Niue Island the most important controls on rainfall seasonal variability are the location of the SPCZ, followed by ENSO. During El Niño events, the wet season is drier, thereby reducing the contrast between the wet and dry seasons (i.e., reduced rainfall seasonality). La Niña events bring wetter rainy seasons, thus increasing the seasonal contrast (i.e., amplified rainfall seasonality). On a visual basis, the C132 record shows a consistent positive correlation between greyscale/seasonality ENSO band variability and rainfall seasonality predictability. In general, when ENSO band variance is significant, there is a decrease in the predictability of seasonality, i.e., the system turns into a more stochastic conditions, whereas when ENSO band variance is reduced/muted the seasonality predictability is increased, and particular dips in predictability often correlate with significant ENSO band power in seasonality (e.g., at 6.3, 6.03, 5.88, 5.75, and 5.6 ka BP). Assuming that La Niña events bring wetter conditions only during the wet season, because December typically aligns with the peak of La Niña events [396], this stretches the seasonal cycle above normal. It would be very unlikely that La Niña events result in wetter dry season because usually dry season months (June-August) correspond to either El Niño to La Niña transition or early growth El Niño stages; hence the relationship between ENSO activity and rainfall seasonality in Niue can be confirmed. A similar positive relationship between the seasonal cycle amplitude of near-equatorial sea surface temperatures (SSTs) and ENSO band variance was observed in Holocene coral records from the central Pacific [442]. The initial oceanic conditions for the development of a La Niña events depend of multiple factors such as spatial-temporal heat dynamics in the equator, the precedent El Niño flavour (East Pacific or Central Pacific El Niño events) [443]. These changing conditions reduce the predictability of La Niña events, although this conclusion is based in an analysis that assesses the forecasting skills of La Niña events and not the seasonal cycle [396]. It is similar to our findings in the way that La Niña events result from destabilization of the atmosphere-climate system and therefore less predictable conditions. Our findings suggest that ENSO variability modulates the amplitude of the seasonal rainfall cycle not only at an inter-annual scale, but also multi-decadal and centennial scales. These lower-frequency oscillations could in turn be modulated by long-term stationary states of the location of the SPCZ as well as its spatial



configuration, which is controlled by the feedback of internal variability factors [395]. This ENSO and tropical Pacific mean state connection at decadal and centennial scales has been detected in other highly resolved mid-Holocene ENSO records from the central Pacific [401] and Borneo [405]. Niue record contribute with new evidence of the interaction between SPCZ, ENSO and the mean state of the tropical Pacific throughout the identification of predictable and non-predictable stages in the climate system.

## 10.7 Conclusion

Investigated stalagmite from Niue Island in the southwestern Pacific offers a seasonally resolved multi-proxy reconstruction of mid-Holocene (6.4 to 5.4 ka BP) rainfall changes associated with dynamics of the South Pacific Convergence Zone (SPCZ). The combination of U-Th dating and layer counting allows for constructing an accurate chronology for the multi-proxy record, while the use of the non-destructive greyscale analysis supports and strengthens the interpretation of the geochemical proxies. Wet/dry conditions controlled by seasonal shifts of the SPCZ are recorded in the petrography, trace element distribution, and isotopic composition ( $\delta^{13}\text{C}$  and  $\delta^{18}\text{O}$ ) of the calcite laminae couplets of stalagmite C132. The wet season is reflected in pale porous calcite (PPC) laminae which are characterised by lower Mg/Ca, Sr/Ca, and U/Ca ratios as well as lower  $\delta^{13}\text{C}$  and  $\delta^{18}\text{O}$  values. In contrast, the dry season is reflected by higher Mg/Ca, Sr/Ca, and U/Ca ratios and higher  $\delta^{13}\text{C}$  and  $\delta^{18}\text{O}$  values in dark dense calcite (DDC) laminae. We suggest that the physicochemical variations in the stalagmite laminae are modulated by kinetic fractionation forced by differences in drip rate and thus stalagmite growth rate between the wet and dry seasons, which in turn depend on local climatic dynamics. Within the range of elements studied in sample C132, we have identified two groups due to their source and mechanism of incorporation into calcite show high climatic sensitivity. Group 1 comprises soil-derived elements (Zn, Mn, Fe, Al, and Pb) indicative of high infiltration events resulting from extreme but short-lived rainfall events (e.g., from tropical cyclones) that lead to significant soil flushing. The second group includes host-rock derived elements (Mg, Sr, U, and P) that are incorporated into the speleothem via water-rock interaction, with further contributions by marine aerosols. These elements are also sensitive to prior calcite precipitation during periods of reduced infiltration and record hydrological changes at a seasonal scale. This group also records lower baseline rainfall during El Niño events and higher baseline rainfall during La Niña events. In-depth time series and wavelet analyses of our 1000-year record not only reveals SPCZ changes but provides important insights into ENSO activity during the mid-Holocene. The wavelet analysis suggests that ENSO was continuously active over the covered period from 6.4 to 5.4 ka BP. However, ENSO affects dry season background rainfall and seasonal rainfall contrast in different ways. We suggest the main effect to be changes in the overall background rainfall, with La Niña years leading to wetter conditions and El Niño years to drier. A secondary effect, related to increased tropical cyclone activity in the dry season during El Niño years, is superimposed on these general dynamics and results in reduced seasonality (wetter dry season and drier wet season). Importantly, tropical cyclone activity linked to El Niño links seasonal predictability with ENSO-band variability in overall background rainfall, with increased ENSO-band variability corresponding to lower seasonal predictability.



# 11 | Decline in seasonal predictability potentially destabilized Classic Maya societies

Tobias Braun<sup>1,\*</sup>, Sebastian F. M. Breitenbach<sup>2</sup>, Vanessa Skiba<sup>1</sup>, Fanziska Lechleitner<sup>3</sup>, Erin Ray<sup>4</sup>, Lisa M. Baldini<sup>5</sup>, Victor J. Polyak<sup>6</sup>, James U. L. Baldini<sup>7</sup>, Douglas J. Kennett<sup>8</sup>, Keith M. Prufer<sup>9</sup>, Norbert Marwan<sup>1,10</sup>

1 – Potsdam Institute for Climate Impact Research, 14473 Potsdam, Germany

2 – Department of Geography and Environmental Sciences, Northumbria University, Newcastle upon Tyne NE1 8ST, UK

3 – Department of Chemistry, Biochemistry and Pharmaceutical Sciences and Oeschger Centre for Climate Change Research, University of Bern, Freiestrasse 3, 3012 Bern, Switzerland

4 – Department of Anthropology, University of New Mexico, Albuquerque 87131, New Mexico, USA

5 – School of Health & Life Sciences, Tesside University, Middlesbrough TS1 3BX, UK

6 – Radiogenic Isotope Laboratory, Earth and Planetary Sciences, University of New Mexico, Albuquerque NM 97131, USA

7 – Department of Earth Sciences, Durham University, Durham DH1 3LE, UK

8 – Department of Anthropology, University of California, Santa Barbara CA 93106, USA

9 – Department of Earth and Planetary Sciences, University of New Mexico, Albuquerque NM 87131, USA

10 – University of Potsdam, Institute of Geosciences, Potsdam, Germany

*Braun, T., Breitenbach, S. F. M., Skiba, V., Lechleitner, F., Ray, E., Baldini, L. M., Polyak, V., Baldini, J., Kennett, J. U. L., Prufer, D. J., Marwan, N. (2022). Decline in seasonal predictability potentially destabilized Classic Maya societies. under review for Communications Earth & Environment*

## Abstract

Despite intense study of the potential impact of decadal to centennial-scale climatic changes on the demise of Terminal Classic Maya sociopolitical institutions (750-950 CE), its direct importance remains debated. Classic Maya populations living in peri-urban states were highly dependent on seasonally distributed rainfall for reliable surplus crop yields. We provide a detailed analysis of a precisely dated speleothem record from Yok Balum cave, Belize, that reflects local hydroclimatic changes at seasonal scale over the past 1600 years. We find a pronounced decline in the predictability of seasonal rainfall starting prior to the onset of previously documented protracted drought conditions in the neotropical Maya lowlands. The

failure of Classic Maya societies to successfully adapt to volatile seasonal rainfall dynamics likely contributed to gradual but widespread processes of sociopolitical disintegration. We propose that the complex abandonment of Classic Maya population centers was not solely driven by protracted drought but also aggravated by year-to-year rainfall predictability decreases, potentially caused by a reduction in coherent Intertropical Convergence Zone-driven rainfall in the region.

## 11.1 Introduction

Seasonal hydroclimate variability has defined the environmental context for tropical agricultural societies for at least seven millennia [444]. The success or failure of Late Holocene urban societies reliant on rainfed agriculture was contingent on their ability to anticipate and adapt to the seasonal distribution of rainfall from one year to the next [445]. Today, shifting rainfall seasonality due to anthropogenic climate change poses a threat to both traditional agricultural practices and food security in regions practicing rainfall dependent agriculture [446]. Studying the predictability of seasonal rainfall beyond the instrumental period using exceptionally well-dated long-term palaeoclimate archives allows us to contextualize scenarios of future dynamics due to anthropogenic climate change [3, 273, 447].

In Central America, Maya urban states emerged by 900 BCE [448] following the adoption of maize as a staple grain [449] and the development of surplus agricultural production. After Maya societies underwent 1650 years of cyclical expansion and fragmentation, the period of largest demographic expansion (600-750 CE) was followed by dramatic contractions between 750-950 CE [450, 451] and the abandonment of large population centers led by despotically oriented dynastic lineages [452]. Maya leaders were heavily invested in wealth accumulation, kin selection, and costly ceremonial signaling that inhibited flexible and resilient responses to environmental change [453]. The inability of complex Maya societies that formed the Classic Period social and political systems to successfully respond to changing climate contributed to the geopolitical disintegration of dozens of urban centers [454] and a return to more decentralized low density agrarian villages [455]. The 200-year Terminal Classic Collapse (TCC) was a cultural process driven by increased warfare, population pressures and landscape degradation [456]. Whereas political centers in the southern Maya lowlands underwent an inexorable process of fragmentation that was not followed by emergence of new urban settlements, populations in the northern lowlands recovered and ultimately built the Maya capital of Mayapan [457, 458].

During the periods of population decline, conflicts between competing factions correlate with decadal scale episodes of reduced rainfall [459, 460, 305, 451, 306]. However, the general palaeoclimate record suggests that the worst of these droughts occurred after 850 CE when collapse processes were well underway [454]. Previous palaeoclimate studies in the Maya lowlands lacked temporal controls or sampling resolution to quantitatively assess variability in rainfall seasonality. Today, the seasonal distribution and rainfall onset date are among the most critical controls for Maya farmers, who are generally small land holders producing seed and root crops for home use, animal feed and limited cash-crop surplus [461]. Modern subsistence farmers face considerable uncertainty caused by a global warming-induced decline in predictability of seasonal rainfall in recent decades. These changes are forcing adaptations in traditional agricultural practices to maximize soil moisture and hedge against increasing uncertainty in the timing of the summer monsoons [462]. Many of the staple seed and tree crops consumed by both modern and Classic Maya populations are highly vulnerable to drought conditions. Additional vulnerability may arise from specialization of diets, impairing resilience of food systems against unpredictable year-to-year hydroclimatic conditions [463]. This suggests that instability in the seasonal distribution of rainfall, including recurring severe

drought events, significantly decreases productivity in growing most staple crops consumed by pre- and post-colonial Maya populations [464], considering the severe constraints in long-term grain storage [465]. In contrast to these modern analogs for small scale communities, the consequences of unpredictable seasonal rainfall distributions on large geopolitical formations, with high degrees of social inequity, economic specialization, and dependence on surplus food production to feed large non-producer segments of society have not previously been addressed for the Classic Maya. Our data support the proposition that declining ability to predict the seasonal distribution of rainfall may have had profound impacts on agricultural production and, in turn, geopolitical stability of Maya population centers [445]. Most crops grown in the Maya Lowlands, including maize, are not drought resistant and even short duration droughts are sufficient to disrupt agricultural production causing food shortages. During a moderate drought of one year without seasonal summer rainfall the number of edible plant parts available would decline by 69% including maize, beans, and squash, while in a severe multiyear period without normal summer rainfall the number of available crop foods would decline by 87% [464].

Here, we investigate rainfall seasonality in Central America over the past 1600 years using statistical analysis on a previously published, precisely dated and sub-annually resolved speleothem record from Yok Balum Cave, southern Belize (16° 12' 0 30.780" N, 89° 4' 24.420" W; 336 metres above sea level) [362]. Southern Belize has some of the highest rainfall and seasonality contrasts in the Neotropics [261, 199]. Due to its location near several Classic Maya centers in the southern Lowlands, Yok Balum Cave is strategically placed to explore linkages between local climate variability and cultural response. Stalagmite YOK-G has a high growth rate, low age uncertainty (based on U-Th dating) and is fed by an exceptionally steady and rapid drip, allowing us to examine hydroclimate conditions during the TCC and their potential impacts on Classic Maya agricultural practises at seasonal time scales [440, 199]. The speleothem stable carbon isotope ratio ( $\delta^{13}\text{C}$ ) from Yok Balum Cave reflects local hydroclimate conditions, encompassing changes in effective infiltration above the cave and prior carbonate precipitation dynamics in the epikarst [466, 467]. Additionally, stalagmite  $\delta^{13}\text{C}$  is affected by soil  $p\text{CO}_2$ , water residence time and host rock dissolution, and  $\text{CO}_2$  degassing from dripwater in the cave [468]. At our study site, all factors impacting  $\delta^{13}\text{C}$  follow local hydroclimate in the same direction, thereby enhancing the link between hydrology and  $\delta^{13}\text{C}$  in the stalagmite. We focus on speleothem  $\delta^{13}\text{C}$  as a proxy for local hydroclimate at seasonal scale near Maya sociopolitical centers whereas the oxygen isotope signal integrates more distal dynamics, reflecting convective activity strength, source moisture location, moisture path length, and local rainfall amount.

Modern seasonal rainfall variability in the region is primarily controlled by the dynamics of the Intertropical Convergence Zone (ITCZ) [469, 470]. Sub-annual rainfall distribution is distinctly seasonal, with 480-1120 mm in the wet season (June-September) due to the northward displacement of the ITCZ during boreal summer, and 120-280 mm in the dry season (February-April) when the ITCZ shifts southward. The spatio-temporal variability of the ITCZ is not limited to latitudinal migrations but can exhibit contractions/expansions and changes in seasonal residence times at its boundaries [471, 362]. Changes in the position and latitudinal extent of the ITCZ are coupled to large-scale patterns of sea-surface temperature variability in the tropical North Atlantic [472, 473, 474] and the tropical Pacific [475]. The seasonal amplitude of rainfall in the Maya lowlands is additionally affected by tropical cyclones (TCs, July-October) and northerly winter storms (Nov-Feb) [476, 477]. Several hypotheses for the climatological origins of the Terminal Classic drought have been proposed [478], including the latitudinal migration of the ITCZ [479, 454], significant changes of tropical Northern Atlantic sea-surface temperatures [472, 480, 473, 474], persistent El Niño conditions and potential interactions with TCs [476] as well as an interplay of some of these processes [473].

It has also been suggested that the ITCZ was entirely absent from the region across the Classic Maya interval, opening the door to alternative interpretations [362]. Regardless, Classic Period Maya farming systems would have been dependent on rainfall to support populations that may have grown to as large as 11 million people across the lowlands by 700 CE [481] and changes in the predictability of rainfall patterns may have negatively impacted surplus agricultural production.

The expression of such changes in climatological conditions at seasonal time scales and its repercussions on Classic Maya agriculture, however, have not yet been unraveled. Here we expand on the dynamics of local rainfall, and characterise its seasonality, year-to-year predictability of subannual rainfall distribution, and climate volatility due to extreme events. This allows unprecedented insights on potential links between rainfall seasonality and the TCC.

## 11.2 Results

### 11.2.1 Background climate and seasonal cycle

We use advanced statistical analysis to evaluate if and how the seasonal distribution of rainfall changed over the past 1600 years in southern Belize. Dating uncertainties ( $2\sigma \approx 5$  years, see suppl. Fig. F.1) are propagated through the entire analysis by studying a full ensemble of COPRA age model realizations that are compatible with dating errors [36] (see methods).

The YOK-G  $\delta^{13}\text{C}$  record suggests a pronounced dry period between ca. 550-900 CE, with the wettest conditions occurring during the Little Ice Age (LIA: 1400-1800 CE) (Fig. 11.1A), consistent with our previous study [362]. These multi-centennial trends are generally corroborated by both stable oxygen isotope ( $\delta^{18}\text{O}$ ) and trace element records from the same stalagmite (see suppl. Fig. F.2). Other regional records [454, 473] that indicate pronounced multi-annual droughts exhibit heterogeneity in the timing of Terminal Classic Drought (TCD) events (Fig. 11.1A), but predominately indicate that the most severe drought events occurred between 700-900 CE.

Fluctuations around the long-term trends of the YOK-G  $\delta^{13}\text{C}$  record (Fig. 11.1A, suppl. Fig. F.3/F.4) allow for the identification of volatile periods with strong (multi-)annual deviations from the mean climate state in contrast to periods of low variability. We use a Monte Carlo-based framework to extract indications of hydrological extreme events, i.e., exceptionally wet or dry years that reflect enhanced volatility, from the YOK-G  $\delta^{13}\text{C}$  record (Fig. 11.1B) (see methods). A period with fewer extreme events between 550-700 CE was followed by an episode of more frequent extreme events between 700 and 900 CE, aligning with the period of most severe drought events recorded in other proxy reconstructions from the Neotropics, and tracking demographic contraction across the Maya Lowlands starting around 700 CE (Fig. 11.2B-D) [456]. Enhanced extreme event frequency suggests more volatile, and thus less predictable, seasonal variations on interannual timescales, beginning at a time of maximal population, increasing warfare, and high levels of social inequality [450, 454]. We find two additional periods of relatively high extreme event frequency, one partly intersecting with the Medieval Climate anomaly (1100-1300 CE) and the other during the second half of the LIA (1600-1900 CE). Some indications of drought events after 1500 CE align with known historical multi-annual droughts (e.g., 1535 CE and 1765 CE [482]).

A significant positive correlation at seasonal time scales between  $\delta^{13}\text{C}$  and  $\delta^{18}\text{O}$  is indicative of prior calcite precipitation and/or kinetic fractionation dominating these proxies (suppl. Fig. F.5). We examine whether a seasonal cycle in the YOK-G record can be detected over the last 1600 years when dating uncertainties, irregular sampling intervals and potential aliasing are taken into account, using Lomb-Scargle periodograms and continuous Wavelet analysis

(suppl. Fig. F.7-F.11). Averaging wavelet spectral power within the 0.5-1.5 year band for each  $\delta^{13}\text{C}$  age model realisation we identify age model realisations with a significant expression of seasonality (Fig. 11.1C). Age model realisations that indicate a significant seasonal cycle for both  $\delta^{13}\text{C}$  and  $\delta^{18}\text{O}$  increase markedly post-1400 CE, whereas before 1400 CE, only a muted seasonal signal is detected (further supported by Lomb-Scargle periodograms, see Fig. S8A/C), corroborating the results in [362].

### 11.2.2 Seasonal rainfall predictability

From the perspective of Maya farmers, a regular and well-pronounced seasonal rainfall cycle allows for reliable projections of crop yield on a year-to-year basis. This entails several sets of decision making on the part of farmers. First, they need to know when to clear and prepare fields for planting. Today, this coincides with the end of the annual dry season when vegetation can be burned [458]. In much of the Maya lowlands preparation for the wet season involves clearing of vegetation, burning biomass for nutrients, and planting crops in anticipation of the arrival of the summer monsoons [461]. Delayed or failed arrival of the summer rains significantly increases the risk for crop failures. Classic Period farmers developed methods for continuous surplus agricultural production that was locally adapted for the diversity of environmental zones found in the lowlands [483]. This was accomplished through modifications of landscapes and the use of fire to clear land, with increasing productivity accomplished through intensification involving terracing of slopes, management of wetlands, and creation of raised beds [484, 485]. However, all of these strategies relied on seasonally distributed rainfall, a dependency that increased with population size [456].

We use recurrence plots (RPs) on annually split, detrended segments of the  $\delta^{13}\text{C}$  realisations to characterize the predictability of the seasonal rainfall cycle [20]. Recurrences between two annual stalagmite  $\delta^{13}\text{C}$  segments signify that seasonal distribution of rainfall was similar in the respective years, indicating enhanced predictability. The recurrence-based indicator of seasonal predictability  $\tau_{\text{pred}}$  employed here can be interpreted as a mean prediction time of seasonal rainfall distribution: it encodes the predictability of a year's seasonal rainfall profile based on information from the previous year's hydrological cycle. Low average  $\tau_{\text{pred}}$  values indicate a more erratic seasonal hydroclimate, requiring farmers to adapt their strategies from year to year. Sudden occurrence of a hydrological extreme event (be it drought or flood) represents one potential cause of a less predictable seasonal cycle. Most periods of low stalagmite growth also entail a less pronounced seasonal cycle in stalagmite  $\delta^{13}\text{C}$  (see Fig. 11.1C). The used recurrence-based approach partly eliminates biasing effects on seasonal predictability imposed by non-constant stalagmite growth, using the method proposed in [2] (see methods).

### 11.2.3 Classic Collapse and rainfall seasonality

The potential changes in local and regional hydroclimate discussed above may have had significant societal repercussions over the period covering the Early, Late and Terminal Classic. We find that seasonal predictability  $\tau_{\text{pred}}$  declines below the significance value of  $\tau_{\text{pred}} = 1$  between 800-1000 CE (Fig. 11.2A). Such low prediction times could be generated by a random null model that simply replicates the growth rate of the stalagmite with random seasonal variation. Thus, irregularities at seasonal time scale are so large during this period that accounting for past seasonal rainfall does not significantly enhance the forecast for upcoming years.

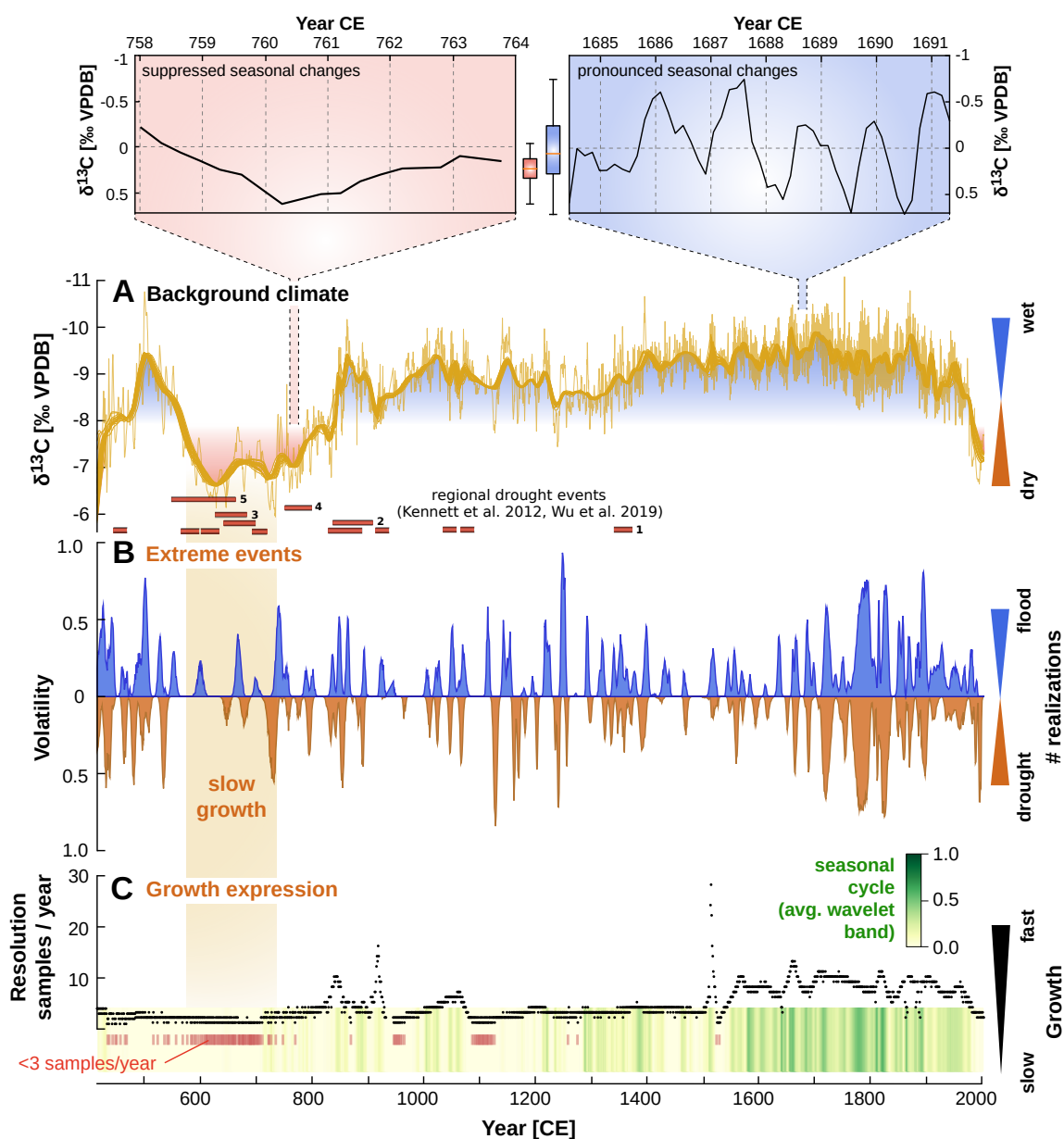


**Figure 11.1:** (A) Long-term variability of YOK-G  $\delta^{13}\text{C}$  record, highlighting wet (blue) and dry (red) periods in the Maya lowlands. Two insets show examples of seasonal variability. All age model realizations are detrended individually (Singular Spectrum Analysis with  $w \approx 10\text{yr}$ , trends for 50 realizations displayed as thick lines). The shown age model realization is the most central realization. Regional drought events from other regional records (1: Yok-I (Yok Balum cave) [454], 2: Punta Laguna, 3: Tecoh cave, 4: Juxtlahuaca Cave, 5: Chilibrillo Cave) are indicated by red bars. Drought indications of records 2-5 are displayed according to intense dry intervals as given in [473]. (B) Indications of annual extreme hydroclimate conditions. From the full ensemble of detrended  $\delta^{13}\text{C}$  time series, the fraction that indicates an annual drought/flood event is computed by counting how many realizations exceed the 95% quantile in each year, divided by the total number of realizations. (C) The number of samples per year represents changes in the stalagmite's growth rate. An indicator of seasonal cyclicity based on the seasonal band-average of continuous Wavelet spectra for all proxy realizations (suppl. Fig. F.8) shows that episodic cyclicity is given for most segments of the record. Years with less than three samples are marked by red lines. A period of slow growth is indicated by brown shading.



Societal processes of disintegration (increased warfare and site abandonments) were already underway between 750-830 CE in the heartland of Peten, Guatemala and Belize (Fig. 11.2B-C) prior to the most severe drought events after 830 CE, culminating in regional depopulation by 950 CE (Fig. 11.2C).

Our results reveal a highly complex, nonlinear dependency structure between background hydroclimate and seasonal predictability (Fig. 11.3). This relationship is also clearly different from the relationship returned from the null-model and is thus not caused by variations in temporal sampling (suppl. Fig. F.13C/D, gray dots). The most favorable conditions (i.e., highest predictable seasonal rainfall) are identified at moderately wet conditions ( $\delta^{13}\text{C} \simeq 8\text{‰}$ , Fig. 11.3), but no monotonous relation (e.g., ‘the drier, the more stable’) exists between average proxy values and seasonal predictability. Whenever the local or regional hydroclimate is shifting towards progressively wet conditions, either less or more seasonally predictable conditions may occur. When relating seasonal predictability, mean hydroclimate and Maya TCC, we find that, although moderately dry, the Early and Late Classic (400-750 CE) were characterized by persistently high predictability, and that predictability significantly decreased after 700 CE (Fig. 11.2a).

We hypothesize that climate volatility reduced the ability of farmers to predict the onset of rainfall, leading to reduced crop yields and surpluses. This in turn would have impacted the ability of urban dwelling non-farmers to engage in economic activities and ensuing declines in food security may have intensified stress on political and economic institutions that ultimately led to their destabilization. Quantitative proxies for Maya population change during Early to Terminal Classic and dated stone monuments, a proxy for Classic Period governing institutions, support this interpretation (Fig. 11.2D). At Uxbenká region, an urban center close to Yok Balum cave, this decline began around 680 CE when seasonal predictability had already deteriorated for several decades, while the final dated stone monument was erected in 780 CE, just 30 years before the site was abandoned [456]. This depopulation event aligns with demographic decline across the entire Maya lowlands starting after 700 CE and corresponds with the sharpest decline of seasonal predictability initiated shortly before 800 CE (Fig. 11.2B).

Our results suggest that a loss in seasonal predictability of rainfall may have destabilized Maya society even before the onset of severe drought conditions as indicated by the majority of palaeoclimate records from the Yucatán [473]. Moreover, due to the continuously low predictability after 800 CE, any recovery or adaptation to new climatic states were muted. This scenario is compatible with an observed increase in the number of dated urban monuments between 700 and 800 CE as a likely response to volatile seasonal conditions. Elites, confronted with reduced surplus to finance capital projects and prestige goods likely sought to enhance their status and legitimacy as divine rulers by increasing production of carved monuments. These attested to their roles as intermediaries with important ancestors and deities deemed responsible for rainfall, social well-being, and general health [486] and were demonstrated through public ceremony, likely in lieu of more effective adaptive strategies.

Reduced food security led to subordinate populations losing faith in those rulers as war-related events increased between 700-800 CE (Fig. 11.2B), reducing investment in urban and agricultural infrastructure. We suggest that the impacts of a sustained decline in seasonal predictability combined with multiple annual to decadal length droughts led to further emigration from urban areas, and an overall population decline, as well as the disintegration of more than 63% of urban polities with dated monuments by 835 CE [450].

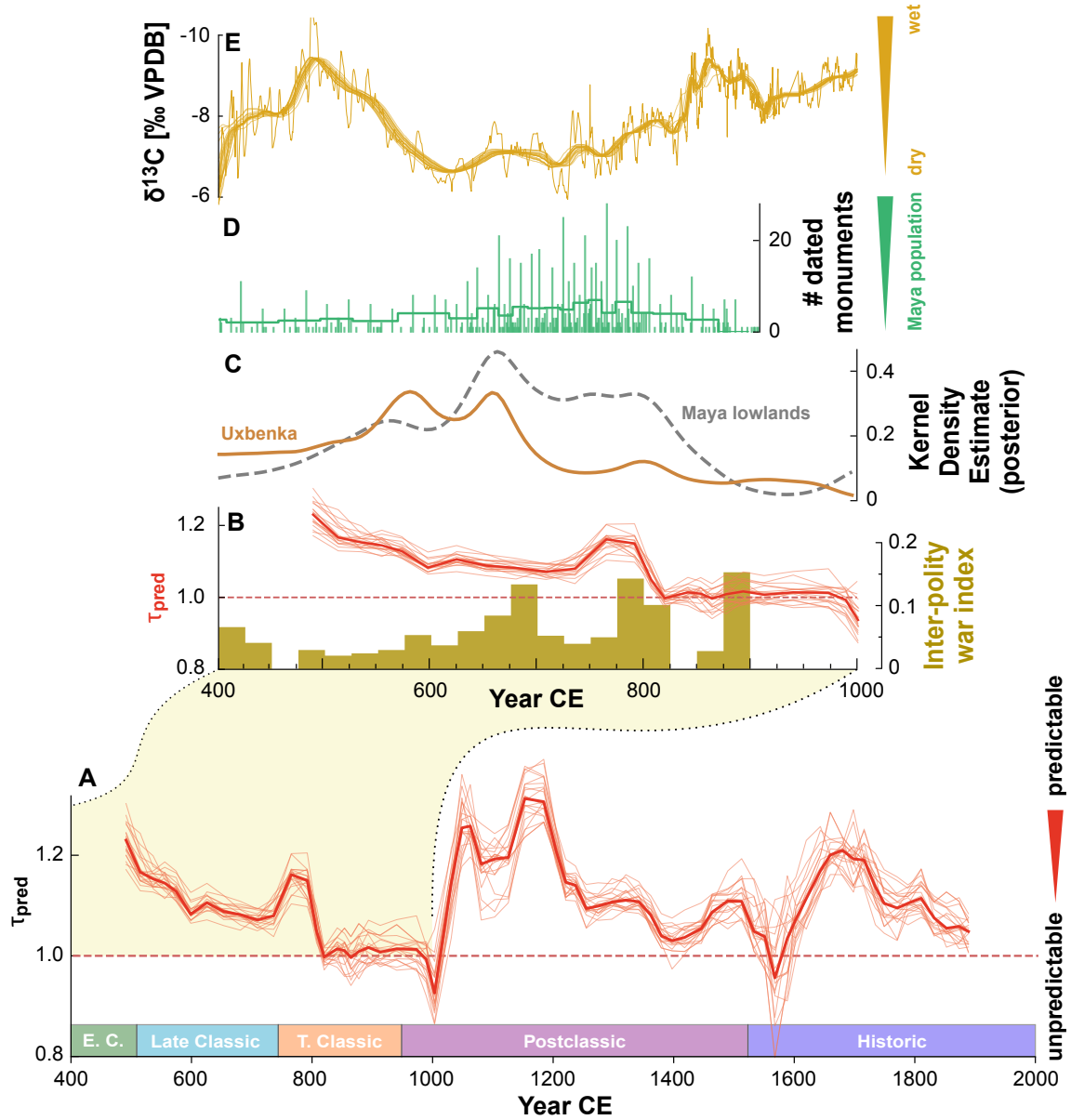


**Figure 11.2:** (A) Predictability of seasonal rainfall distribution, given by relative mean predictability times  $\tau_{\text{pred}}$  of 20 detrended proxy realizations for each isotope. The reference value of  $\tau_{\text{pred}}^{(\text{ref})} = 1$  (dashed line) indicates transitions between predictable states and states with a predictability that is not larger than expected from a random proxy-surrogate with the same sampling resolution. (B) A zoomed segment shows  $\tau_{\text{pred}}$ , indications of inter-polity war events and the evolution of Maya population size during the TCC, represented by (C) summed probability distributions of dated material in the Maya lowlands (gray) and the Uxbenká region (yellow) as well as (D) the total count of dated urban monuments. (E) Long-term drying is indicated by higher  $\delta^{13}\text{C}$  values between ca. 600 and 800 CE.

### 11.2.4 Multidecadal rainfall variability, ITCZ dynamics and the tropical North Atlantic

What are the potential climatic drivers that modulate seasonal rainfall predictability and the frequency of droughts or floods at multidecadal time scales in the Maya region? – The multidecadal variability of Atlantic Sea surface temperatures (SST) plays a major regulatory role on seasonal rainfall variability in the Neotropics. SST changes that result in signifi-

cant interhemispheric thermal disparities shift the ITCZ’s mean position towards the warmer hemisphere [487]. Lower SSTs across the (sub)tropical North Atlantic are less conducive to large-scale evaporation and the building of convective clouds along the ITCZ, resulting in a less coherent formation and reduced migration of the ITCZ into the northern hemisphere (NH), whereas higher SSTs have been found to increase summer precipitation in the northern Neotropics [488].

In order to assess the influence of tropical Atlantic multidecadal variability on rainfall frequency and intensity at Yok Balum Cave, we compare our seasonal rainfall predictability record with foraminifera Mg/Ca-based summer SST reconstruction from a sediment core drilled in the Cariaco basin [489] (Fig. 11.4A). The Cariaco basin is a very sensitive location for recording expansion/contraction or latitudinal shifts in the ITCZ as it is located in the North Atlantic beneath its northward extent [490].

We compute correlations between both YOK-G stable isotope records ( $\delta^{13}\text{C}$  and  $\delta^{18}\text{O}$ ) at seasonal (based on the most central realization (MCR) of the age model, suppl. Fig. F.5) and multi-decadal time scales (based on age model medians, suppl. Fig. F.6) by extraction of suitable trends (Singular Spectrum analysis, suppl. Fig. F.3). At seasonal time scales, YOK-G  $\delta^{13}\text{C}$  and  $\delta^{18}\text{O}$  remain significantly positively correlated throughout most of the Common Era, whereas at multidecadal timescales both periods of significantly positive, as well as periods with no relationship or significantly negative correlation exist (Fig. 11.4B). Periods of enhanced summer SSTs in the Cariaco basin align well with significantly positive proxy correlation in the YOK-G record and vice versa for lower SSTs, indicating a link between North Atlantic conditions and the nature of the isotope response in the stalagmite. The Medieval Climate Anomaly is marked by above average tropical Atlantic SSTs and significant proxy correlations in YOK-G. Periods of low SST and YOK-G proxy correlation occur episodically during the LIA and dominate between 1800-2000 CE. During the initial decline of the Terminal Classic Maya population (700-900 CE), insignificant/negative proxy correlations coincide with a period of low summer SSTs.

Previously, YOK-G  $\delta^{13}\text{C}$  (reflecting rainfall amount) and YOK-G  $\delta^{18}\text{O}$  (reflecting the combined influence of rainfall amount and characteristically low  $\delta^{18}\text{O}$  of tropical cyclone rainfall) have been combined to isolate the tropical cyclone signal since 1550 CE [477]. Both isotope records are therefore responding to hydroclimate variability, but  $\delta^{18}\text{O}$  is arguably more directly linked to North Atlantic SSTs and regional circulation patterns. Consequently, positive correlation between  $\delta^{18}\text{O}$  and  $\delta^{13}\text{C}$  at multidecadal time scales suggests that local hydrological conditions are in line with (pan)regional dynamics, i.e., the ITCZ and tropical Atlantic SSTs. Conversely, absence of correlation or a negative relation between both stable isotope ratios implies a control on  $\delta^{18}\text{O}$  which supersedes rainfall amount, revealing the dominant influence of different (non-local) control mechanisms. Modified moisture source, trajectory, or intensity of convection along the moisture mass trajectory are likely influencing factors. Correlations between YOK-G  $\delta^{18}\text{O}$  and  $\delta^{13}\text{C}$  can thus be interpreted as an index for local rainfall coherency.

The ITCZ sensitively tracks changes in the interhemispheric temperature gradient. At multi-decadal time scales, changes in the ITCZ’s mean position, its meridional range and its strength are all possible but remain debated for the Common Era, as argued by Asmerom *et al.* using the YOK-G record [362, 491, 492]. Most rainfall reconstructions from the Maya lowlands suggest considerable ITCZ-induced regional drying during the LIA [473]. Records from the NH do not provide convincing evidence of a large-scale latitudinal shift of the ITCZ during the Terminal Classic period [487, 493, 494, 479, 491]. A sound attribution of regional rainfall changes to latitudinal shifts of the ITCZ requires proxy records that cover its entire basin of influence, a spatially vast region that extends from South America to the northern Neotropics [495, 492]. Compiling a sufficient number of well-dated, highly resolved records

from this spatial range renders reconstructing the TCC interval challenging. However, ambiguity in TCC ITCZ reconstructions may also suggest more complexity exists above and beyond the popular hypothesis that drying is solely driven by latitudinal shifts of the ITCZ. In fact, recent studies favor scenarios of regionally heterogeneous ITCZ responses and challenge prevailing latitudinal shift hypotheses. A compilation of regionally disparate records suggests that it is crucial to take into account additional modes of ITCZ dynamics, including expansion/contraction and region-specific weakening/intensification [492]. In particular, correlations between additional records from the Neotropics and the YOK-G  $\delta^{13}\text{C}$  record studied here indicate that the ITCZ's control on the study region was considerably less dominant before 1400 CE than it is today due to ITCZ expansion/contraction [362]. Thus, whereas a cooling of North Atlantic SSTs may have triggered a southward shift of the ITCZ during the TCC, evidence for such a shift remains ambiguous.

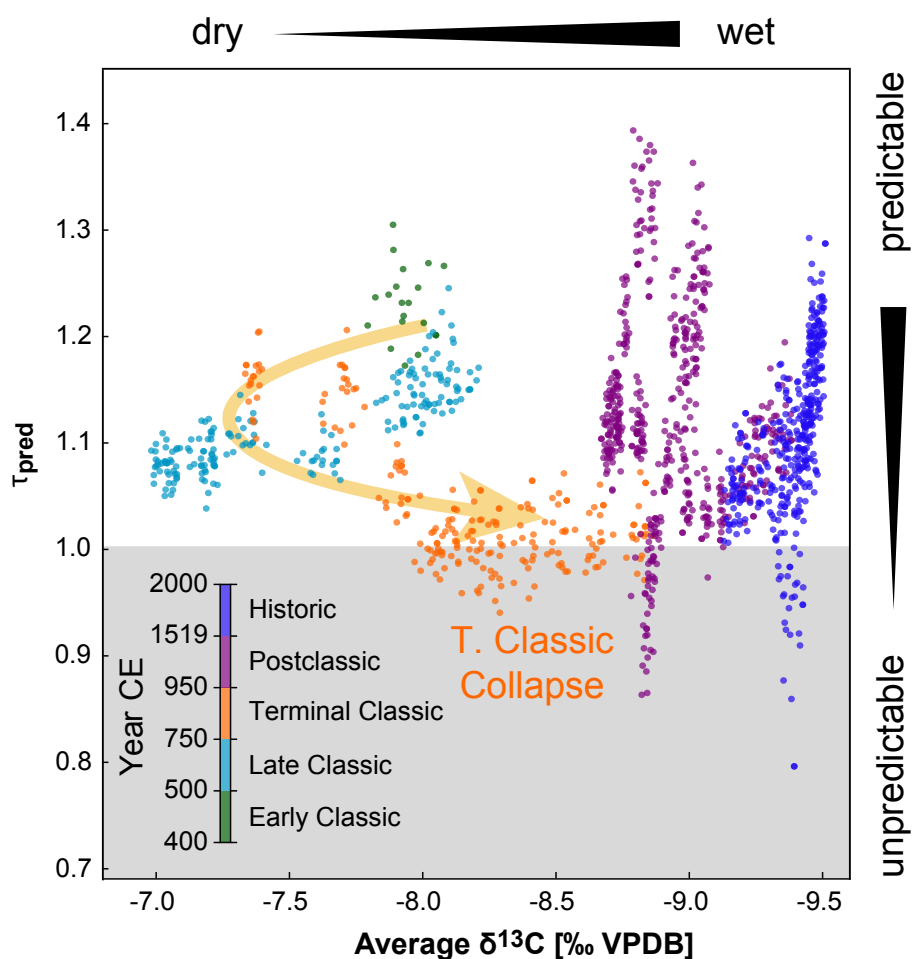


**Figure 11.3:** Relationship between long-term dry/wet states in background hydroclimate and seasonal predictability  $\tau_{\text{pred}}$ . Color coding indicates different time periods. The reference value of  $\tau_{\text{pred}}^{(\text{ref})} = 1$  (gray shading) indicates transitions between predictable states and states with a predictability that is not larger than expected from a random proxy-surrogate with the same sampling resolution. The Terminal Classic period shows the lowest predictability prior to Postclassic times. The arrow highlights the transition from more predictable and wetter conditions to a drier and less predictable state during the late Classic, to wetter, but poorly predictable hydroclimate during the Terminal Classic.

Based on the alignments between tropical North Atlantic SSTs, YOK-G proxy correlations, and seasonal predictability, (particularly for the TCC period (Fig. 11.4)), we argue that low

tropical Atlantic SSTs between 700-900 CE resulted in declining seasonal rainfall predictability due to less coherent formation of the ITCZ over the study region. A more ‘patchy’ emergence of rain-producing convective activity, enhanced year-to-year variability in ITCZ residence time over the region (e.g., shortening of wet season), and stronger fluctuations in ITCZ strength would render local hydroclimate more sensitive to transient perturbations such as Caribbean TCs [477, 496].

Due to extensive fractionation of uplifted water vapor, YOK-G  $\delta^{18}\text{O}$  exhibits strongly depleted values during a TC [477] which could explain the observed periods of negative proxy correlations: whereas local lack of rainfall during a period of low SSTs increases both  $\delta^{13}\text{C}$  and  $\delta^{18}\text{O}$  values, low rainfall combined with a larger proportion of TC rainfall would result in an anticorrelation. The strength of this anticorrelation could be further accentuated by wildfires that are more likely during drier episodes and following hurricane-induced deforestation leaving dead biomass behind as fuel. The resulting reduced biomass and soil bioproductivity above the cave would increase  $\delta^{13}\text{C}$ , whilst TC rainfall would drive  $\delta^{18}\text{O}$  strongly negative. The scenario described here would also explain an overall higher degree of volatility, reflected not only by reduced seasonal predictability  $\tau_{\text{pred}}$  but also increased frequencies in annual dry/wet extremes as observed in Fig. 11.1B.

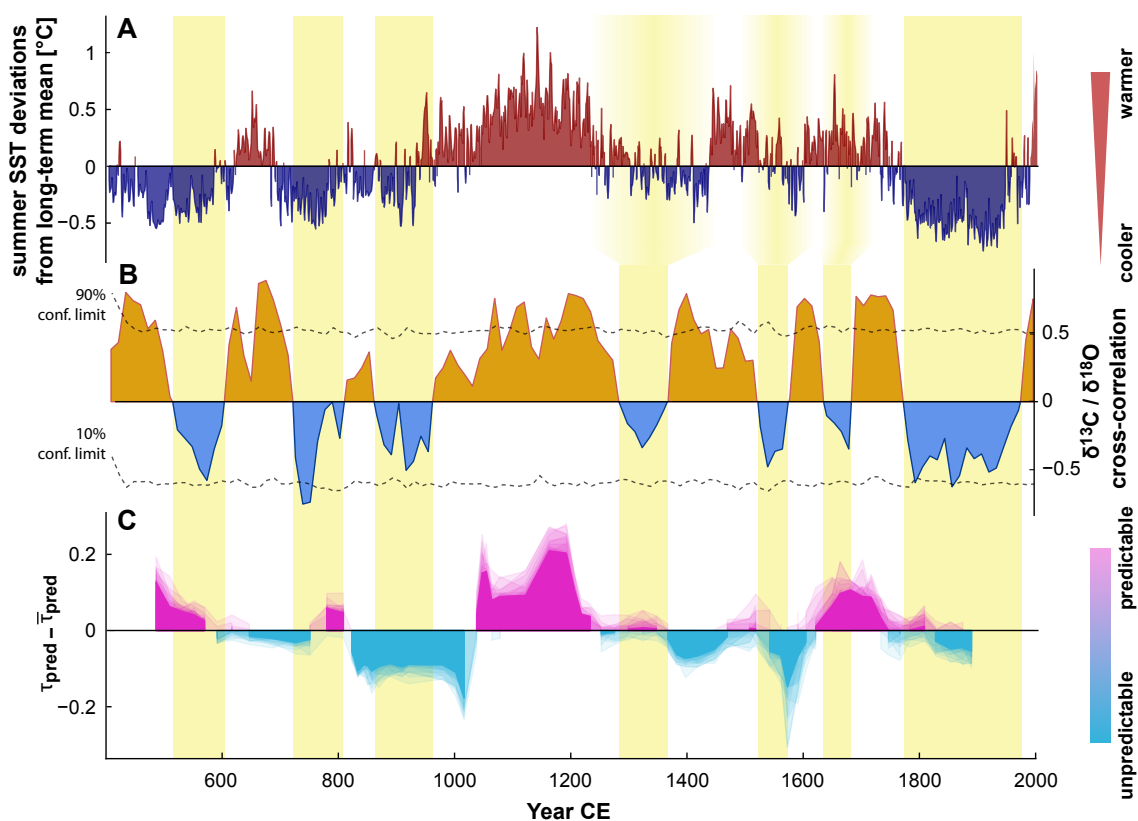


**Figure 11.4:** (A) Summer SST reconstruction from the Cariaco Basin with above (below) average temperatures indicated in red (blue) [489]. (B) Local rainfall coherency index, i.e., multidecadal correlations between detrended carbon and oxygen stable isotope records which exhibit periods of significant positive and insignificant/weakly negative correlation when tested against 1000 AR(1)-realizations with a 90%-confidence level. Periods of negative correlation align well with lower SSTs (yellow shading). Lags in the alignment between summer SST and proxy correlation might be due to chronological uncertainties. (C) Deviations of seasonal predictability  $\tau_{\text{pred}}$  from its long-term mean indicate predictability of local climatic conditions.

## 11.3 Discussion

After the establishment of densely populated urban centers, the Maya population grew to a point where economic inequality, population growth, and increasing conflict would have created vulnerabilities to efforts mitigating the effects of climate change, including significant changes in the seasonal distribution of precipitation. It has long been argued that early in the Classic peak (700 CE), the population began to push the environment towards its carrying capacity [479, 460]. Multiple dry events have been identified as triggers for the cultural disintegration that followed the peak Classic populations as lowland Maya societies failed to produce enough food. Our results suggest that the loss of seasonal rainfall predictability was initiated before the onset of drought conditions. Complex societies are able to thrive despite aridity, provided that the climate is predictable, and it is possible to put successful mitigation measures in place [445, 497]. We argue that the disintegration of Classic Maya was partially catalysed by reduced predictability in climate; the institution of divine kingship simply did not have measures in place to deal with irregular year-on-year changes in rainfall, sparking social unrest and inflicting societal conflicts. Based on our results, we suggest that the TCC was a period of destabilized regional climate control with reduced coherence of ITCZ-driven rainfall, giving rise to high hydroclimate volatility and reduced seasonal predictability. Today, conditions for smallholder farmers in Central America have already deteriorated significantly [498] while current projections suggest that climate change will further increase seasonal climate volatility [499]. The climate-induced disintegration of lowland Classic Maya civilization underscores the sensitivity of human-environment systems to climatological changes, stressing the severity of drastic current global climatic changes and the urgent need to implement effective strategies that maintain food security in societies with low adaptive capacity.

## Methods

### YOK-G record

The ca. 94 cm long stalagmite YOK-G from Yok Balum Cave in southern Belize (see [466]) is composed of aragonite. The YOK-G stalagmite proxy record is based on 7151  $\delta^{13}\text{C}$  and  $\delta^{18}\text{O}$  analyses, covering the last ca. 1600 years, as previously reported in [362]. The chronology of the YOK-G record is based on 52 U/Th dates (ca. 0.54 per cm of growth). Although the carbon isotope record is affected by several factors (including prior carbonate precipitation (PCP) in the epikarst,  $\text{CO}_2$  degassing from incoming dripwater, vegetation composition and activity, soil microbial dynamics, and temperature-induced isotope fractionation) it can be interpreted as a proxy for local effective rainfall [362, 466]. The various influencing factors generally act in concert such that higher  $\delta^{13}\text{C}$  values indicate drier conditions above the cave. The interpretation of the  $\delta^{13}\text{C}$  profile was confirmed by uranium concentration measurements [362]. Similar to the carbon isotope ratios, the YOK-G  $\delta^{18}\text{O}$  are influenced by multiple environmental processes, including moisture source and transport dynamics, rainfall amount, PCP, tropical cyclone activity, and (potentially) temperature changes [477]. However, previous studies [362, 261] indicate that YOK-G  $\delta^{18}\text{O}$  does reflect longer-term hydroclimate conditions above Yok Balum Cave. YOK-G  $\delta^{18}\text{O}$  thus acts as proxy for (pan-)regional hydroclimate variability, with lower  $\delta^{18}\text{O}$  values indicating generally wetter conditions.

### Summed probability distributions

Summed distributions of radiocarbon dates are powerful techniques widely used on large datasets that cover long time periods to assess the impacts of climate on cultural data [500]. While some archaeologists have suggested minimum sample size for these estimates [501], others suggest that sample size thresholds should be dependent on the scale, granularity, and magnitude of specific variations of concern [502]. These distributions can be used to reconstruct relative changes in population sizes, generally under the assumptions that (1) changes in past populations were proportional to the amount of anthropogenic carbon accumulated and (2) the dates are distributed randomly. In this study, we employ a Kernel Density Estimate (KDE) using the KDE\_model function in OxCal4.3 for both the Uxbenká [452] and Maya Lowland [503] radiocarbon datasets using methods outlined in [504] which also employ the Intcal20 calibration curve [505]. This Bayesian method uses a uniform prior for the bandwidth size,  $h$ , with an upper limit based on Silverman's rule, which provides a criterion for identifying  $h$  when the underlying distribution is Gaussian [504]. This is a reasonable way to deal with densities of events for which there is little or no prior knowledge [506]. We use the KDE visualization

as a simple proxy both for population changes and investment in the built environment at Uxbenká, and, by comparison, for the Maya Lowlands (Fig. 11.2).

### Historical Maya Texts

From the Early to the Terminal Classic periods Maya rulers recorded specific types of historical information, including elite political alliances, and wars, on stone monuments (stela, altar stones, and other types of dedicatory objects). Long count calendrical dates contemporaneous with the carving have been deciphered and these stone monuments can be correlated with the Gregorian calendar. Events recorded on monuments are also associated with specific long count dates. Taken together, historical records and precise dates inscribed on monuments provide an empirical foundation upon which to examine patterns of social change [507].

Following [454] we use data originally generated from the Maya Hieroglyphic Database (MHD) [508] to estimate the frequency of monument production during the Classic Period ca. 400-1000 CE. The MHD, collates monuments recording long count dates. Initial Series (IS) long count dates and calendar round dates that could be confidently correlated with the long count were only considered since they are believed to be concurrent with the original time of dedication. Focusing on the Classic Period, 882 dedicatory monuments and objects record dedicatory long count dates concurrent with time of erection from 115 sites throughout the Maya Lowlands (Fig. 11.2D). These monuments document more than 1900 events over the course of the Classic Period.

Our assessment of the frequency of warfare-related events during the Classic Period was based on keywords that relate directly to war or were commonly used by the ancient Maya describing instances of warfare, for example explicit references to captives, warriors, destructive burning events, polity collapses; and subordinate vassalage after a defeat (terms summarized in [509]).

Some mentions of war-related words that did not relate specifically to a specific warfare event that took place during the Classic Period were removed from the dataset. These included names (e.g., “He of 12 captives”), mythical events, and war-related glyphs without context. The final war-related event dataset (Fig. 11.2b) contained only those events involving warfare between two Maya sites or rulers, occurrences of vassalage, and other events that could be temporally grounded [454]. An index of number of warfare events to number of total events was then calculated. These datasets are plotted in Fig. 11.2B.

### Monte Carlo-based time series analysis

A prerequisite to extracting seasonality from a proxy record is that it exhibits significant variability at sub- and interannual time scales. This is affected by both sampling resolution and age uncertainty; whereas the former must be high enough to assess seasonal variations (with respect to the corresponding Nyquist frequency of 2 samples/year), the latter can obscure this variability. In this work, COPRA (COnstructing Proxy Records from Age models) is used to obtain a reconstruction of  $\delta^{13}\text{C}$  and  $\delta^{18}\text{O}$  time series. It uses a Monte Carlo simulation scheme to generate distinct realizations of proxy values for each given value on an error-free time axis. These realizations are compatible with the limits imposed by age uncertainty and can be thought of as squeezed, stretched and translated versions of the underlying ‘true’ proxy time series which cannot be assessed.

COPRA transfers dating uncertainties into uncertainties in the time series magnitude [36]. The age model median time series represents a central estimate of proxy values with age uncertainty included, but much of the variability at time scales below the dating uncertainties is averaged out. We employ a simple yet effective framework to assess such time scales whereas age uncertainty is still propagated. To this extent, each of the  $N$  single MC-realizations returned by the COPRA algorithm is analyzed separately by means of the statistics of interest. This technique yields  $N$  values for the respective statistics which subsequently can be averaged and tested for significance with a suitable hypothesis test. In particular, we pursue this framework for identification of extreme hydroclimate conditions (Fig. 11.1B) and the spectral/time-frequency analysis (see Fig 11.1C and suppl. Fig. F.7- F.11), all discussed in detail below. Whenever a single MC-realization is needed as a reference, we use the realization that has the highest average correlation to all other realizations and refer to it as the most central realization (MCR). Both (detrended) stable isotope MCRs are shown in suppl. Fig. F.4, providing an overview of the seasonal- and decadal-scale variability.

Similar ensemble-based procedures for propagating dating uncertainties in palaeoclimate proxy time series have been carried out in other works and it is argued that this approach can reveal more information than the usual ‘average age-model approach’ [510]. With the focus on intra- and interannual-scale variability in this work, the individual multi-centennial trend is first extracted from each realization (see Fig. 11.1A) using Singular Spectrum Analysis [300] with  $w = 50$  ( $\approx 10\text{yr}$ ). At this time scale, impact by irregular sampling is small. For each of the detrended realizations, the respective statistics are computed and a null-hypothesis is defined. Significance testing is carried out to test whether the obtained values are significantly different from the null model for each MC-realization.

### Identification of annual extreme events

For the identification of extreme hydroclimate conditions (Fig. 11.1B), we define an upper and lower threshold based on the 95% (5%)-quantile of all detrended proxy amplitudes. Next, we check for each year how

many proxy realizations exceed/fall below this threshold, indicating extreme hydroclimate conditions. As this is carried out separately for the 2000 MC-realizations of both stable isotope records, this extreme event indicator ranges between  $[0, 2000]$  and is normalized to  $[0, 1]$  by dividing by  $N = 2000$ . It has to be noted that in this analysis, no correction is applied for controlling for the variations in sampling resolution (see below).

### Time-frequency analysis

We carry out a time-frequency analysis to examine whether a seasonal cycle can be reliably detected throughout the full stable isotope records in presence of dating uncertainties, irregular sampling and aliasing effects. Despite the very high resolution of YOK-G proxy records, age uncertainty in the range of 2-12 years (see suppl. Fig. F.1) obscures spectral peaks for both  $\delta^{13}\text{C}$  and  $\delta^{18}\text{O}$  time series. Hence, we apply time-frequency analysis for each age model realization separately first and then tested for significance jointly to ensure that the identified cycles do not depend on a specific age model realization.

A continuous Wavelet analysis is applied to study the significance of different cycles continuously throughout the Common Era (using the PyCWT package) [356]. Since continuous Wavelet spectra (CWS) cannot deal with irregularly sampled data, linear interpolation is applied to the proxy time series with an optimized interpolation sampling time of  $\Delta t = 0.30$  years that still allows for extracting a seasonal cycle. Optimization is carried out based on Lomb-Scargle (LS) periodograms (suppl Fig. F.8A/C). Significance testing is based on irregularly sampled AR(1)-surrogates (estimated from non-interpolated data) and consequently includes the variations in spectral power due to changes in the sampling resolution that are expected from an AR(1)-process. A total of 2000 CWS are computed based on each proxy realization. This yields a single 'Monte-Carlo Wavelet Spectrum' (MC-Wavelet Spectrum, suppl. Fig. F.8B/D) that displays the number of proxy realizations indicating significant spectral power for a given time and frequency. Potential aliasing effects during time periods where sampling resolution in the original records falls below the Nyquist frequency (red crosses, Fig. 11.1C) is tested for with a simple sinusoidal model (see suppl. Fig. F.11). The seasonal cycle indicator in Fig. 11.1C is computed from the spectral band averages (0.5-1.5 years) of all Wavelet spectra obtained from the ensemble of  $\delta^{13}\text{C}$  realizations. It ranges between 0 (no proxy realization indicates significant Wavelet power around the annual band) and 1 (all 2000 proxy realizations indicate significant Wavelet power around the annual band). We test how adequately the CW-analysis – despite its limitations for irregularly sampled time series – captures the relevant cycles in the record using LS periodograms [335] (suppl. Fig. F.8A/C) with a Welch-overlapping sequences approach for more robust spectral estimates. We assess the significance of spectral peaks by an implementation of the REDFIT algorithm in Python 3.7 [338].

### Recurrence analysis

We perform recurrence analyses to characterize the varying degree of predictability of the sub-annual rainfall distribution. Recurrence analysis is based on the computation of a (binary) recurrence matrix  $\mathbf{R}$  that indicates the recurrence between two states at times  $i$  and  $j$  by a value of 1 while 0 represents no recurrence between those values. Recurrence plots are a powerful tool in the analysis of nonlinear time series that, for example, provide quantitative measures to detect regime shifts or identify couplings [20, 29].

Two time series values are regarded as 'recurrent' if their distance  $D_{ij}$  falls below a certain threshold  $\epsilon$ . In this work,  $\epsilon$  was chosen such that  $\mathbf{R}$  is always filled with 15% of recurrences. Diagonal lines in an RP signify periods in which two segments of the time series show similar variations, i.e., one segment is predictable from the other. We choose the mean diagonal line length of an RP as a quantifier of seasonal predictability. It can be interpreted as a mean predictability time, quantifying for how many subsequent years (on average) a sub-annual rainfall distribution could be predicted from other years.

The major obstacle of comparing the sub-annual distribution of different years is imposed by irregular sampling. Standard procedures to compute the distance matrix  $\mathbf{D}$  (e.g., Euclidean distance) cannot be utilized. Moreover, the number of samples per year is correlated to the growth rate of the stalagmite and thus represents additional meaningful information on the hydrological conditions. We employ the edit-distance method to compute distances between sub-annual segments to account for the irregular sampling [211]. The fundamental idea of this method is to estimate the distance between two segments by means of a transformation cost, i.e., a sum of basic operations that need to be applied to the one segment to transform it into the other. Time series values can only be shifted (both in time and amplitude), deleted or added whereas a certain cost needs to be specified for each of these operations. The costs associated with shifting must both include a cost related to the magnitudes and the time instances. In [130], a modification was introduced to account for the fact that the costs of shifting in time should saturate beyond a certain time scale  $\tau_e$ . The (m)edit distance between two segments  $S_a$  and  $S_b$  resulting from these added costs should be minimized over all possible combinations of operations and is given by

$$D(S_a, S_b) = \min_C \left\{ \sum_{\alpha, \beta \in C} \left[ \underbrace{f_{\Lambda_0}(t(\alpha), t(\beta); \tau_e)}_{\text{shifting}} + \underbrace{\Lambda_k \|L_a(\alpha) - L_b(\beta)\|}_{\text{amplitude change}} \right] + \underbrace{\Lambda_S (|I| + |J| - 2|C|)}_{\text{adding and deleting}} \right\}$$

with the  $\alpha$ -th/ $\beta$ -th amplitudes  $L_a(\alpha)$ ,  $L_b(\beta)$  of the segments  $S_a$ ,  $S_b$  and the cardinalities  $|\cdot|$  of the sets  $I$ ,  $J$



and  $C$ .  $D(S_a, S_b)$  is a metric distance. The cost parameters  $\Lambda_0$ ,  $\Lambda_k$  and  $\Lambda_S$  need to be fixed prior to cost optimization. The sigmoid function  $f_{\Lambda_0}(t(\alpha), t(\beta); \tau_e)$  introduced in [130] controls the costs of time shifting. We follow the empirical estimation procedures proposed in [211] to fix all parameters.

The (m)edit-distance method is applied to annual time series segments ( $w_{(m)\text{edit}} = 1$  year) on 200 years-sliding windows (25% overlap). Due to irregular sampling, the length of sub-annual segments (i.e., values per year) changes (see Fig. 11.1C). In [2], a systematic effect of such variations on the resulting (m)edit-distance was identified and examined. In context of a recurrence analysis, this effect needs to be corrected which is carried out following the proposed correction scheme: we generate 20 sampling rate-constrained surrogates (SRC-surrogates) for each proxy realization and the time axis returned from the COPRA age model. Each SRC-surrogate reproduces the numbers of samples per year while sampling intervals and proxy amplitude differences are drawn randomly, yielding a new set of synthetic time axis and time series. This way, the systematic sampling rate bias and its relation to variance in the amplitudes are conserved. A recurrence plot is computed for each SRC-surrogate following the procedure outlined above (examples: suppl. Fig. F.12). For each RP, we compute a mean diagonal line length  $T_{\text{pred}}$  that represents the mean prediction time of the given time window (in years). We account for the effect of nonstationary sampling rate by defining the relative prediction time:

$$\tau_{\text{pred}} = \frac{T_{\text{pred}}}{T_{\text{pred}}^{(\text{surr})}}$$

with  $T_{\text{pred}}^{(\text{surr})}$  as the 95%-quantile of the mean prediction time distribution obtained from the SRC-surrogate distribution. Whenever  $\tau_{\text{pred}} > 1$ , sub-annual proxy variations can be interpreted as predictable for longer time periods than expected solely from variations of the sampling resolution. Age uncertainty is partly included by repeating the analysis for 20 randomly selected, distinct proxy realizations due to computational constraints. Additional effects that result from stalagmite growth rate variations but are untreated by this method are conceivable, such as a wet season bias.

## Acknowledgments

This research was supported by the Deutsche Forschungsgemeinschaft in the context of the DFG project MA4759/11-1 ‘Nonlinear empirical mode analysis of complex systems: Development of general approach and application in climate’. VS is supported by DFG grant FO 809/6-1. FL acknowledges support from the Swiss National Science Foundation (SNSF) grant PZ00P2\_186135. Funding for the archaeological research at Uxbenká, the initial production of the Yok G and Yok I climate records, and ongoing research related to these records came from the US National Science Foundation (BCS BCS-0620445, Prufer, HSD 0827305 Prufer, Kennett, and Polyak), the Alphawood Foundation (2010-2016 Prufer).

## Author contributions

T.B. designed the study, performed the analysis, led the writing, and prepared the manuscript. K.M.P. initiated the joint work. S.F.M.B., F.L., J.U.L.B., D.J.K. and K.M.P. coordinated the synthesis. V.S., K.M.P. and N.M. contributed data and/or analysis. T.B. and N. M. developed the methods. V.J.P. carried out the measurements. S.F.M.B., T.B., N.M. and V.S. contributed to preparation of figures. S.F.M.B. and N.M. supervised the study. All authors provided critical feedback and helped shape the research, analysis and manuscript.

## Code availability

A collection of Python functions and scripts is provided via Zenodo. These can be used to replicate the manuscript’s main figures: [10.5281/zenodo.7104976](https://doi.org/10.5281/zenodo.7104976)

## Data availability

The YOK-G record has been published in [362]. We provide the studied YOK-G records and, specifically, the age model ensembles used here in the following Zenodo repository: [10.5281/zenodo.7104976](https://doi.org/10.5281/zenodo.7104976)

## Competing financial interests

The authors declare no competing financial interests.

---

## Discussion



## 12 | Conclusion

In this dissertation, I worked towards advancing several approaches in RA with a focus on their applicability, in particular in the context of palaeoseasonal records. With research questions (Q1) & (Q2), I wondered whether concepts from the analysis of self-similar textures can be effectively applied to RPs and if conceptual links between both concepts can be revealed. (Q3) links RA and recurring spatial patterns. (Q4) & (Q5) focus on Palaeoseasonality and the related technical challenges. We can now recapitulate to which extent these initially raised research questions were answered. Following, I will draw links between the broad range of research presented in this dissertation and compile a synthesis. Finally, open questions and limitations provide opportunities for future research which I will outline briefly.

The evaluation of how each work presented in this dissertation contributes to answering the overarching research questions is best summarized in a point-by-point manner, supported by a visual summary (Fig. 12.1):

- (P1) In this work, I proposed RL as a multiscale recurrence quantification measure. Its most obvious advantage is that it does not rely on the presence of line structures in an RP, avoiding many of the related pitfalls [78, 79]. RL opens new perspectives on the analysis of RPs based on recurrence statistics in partitioned RPs rather than constricted structures. Moreover, its sensitivity to transitions at different time scales offers a promising recurrence based approach for one of the most frequent and vital problems in time series analysis: the characterization of a signal's time-frequency content. Its definition and applications were a first step to answer (Q1). RL captures features similar to, and perhaps beyond, e.g. a continuous wavelet transform, as RPs also recover nonlinear oscillations, unstable periodic orbits and can be computed from high-dimensional systems.
- (P2) The recurrence flow measure defined in this work draws its strengths from the same generality of RPs: it provides a nonlinear dependence measure even for high-dimensional systems. It is thus more versatile and readily applicable to such systems than conventional measures, such as mutual information. It captures non-uniform delays in the dependence structure between several variables that are linked at multiple time scales (Q1) and is thus well-suited as a measure for selecting non-uniform delays in the state space reconstruction problem. It appears to be promising and worthy further development, as I will discuss in chapter 14.
- (P3) Spatially-extended systems, such as large-scale atmospheric circulation, constitute recurring macroscopic regimes that can only be sufficiently understood from their full spatial representation. To define recurrences in such systems, new formalisms need to be considered (Q3). I undertook first efforts to define recurring regimes in mid-latitude atmospheric circulation patterns based on partitioned recurrence networks. The identified regimes prove meaningful, a) in terms of their dynamical properties (reflected by the considered RQA measures), b) in the state space constructed by kPCA, and c) by means of their climatic origins (e.g. identification with known climate patterns like the AO by composite patterns). Thus, the desired classification of regimes was successful, but a better understanding of transitions (as desired in (Q3)) will need further investigations.

- (P4) This work represents the strongest progress in answering (Q5). When I was working on proxy records derived from speleothems in (P6) & (P7), I encountered a common problem: sampling rates of, e.g. stable isotope time series are not only *non-uniform* but also are also *non-stationary*. This non-stationarity is by itself often the result of a complex process, for example, growth of a stalagmite. To reliably detect regime shifts in the magnitudes of the records, i.e. the time series, I designed a constrained randomization scheme with a novel kind of surrogate ('SRC-surrogates') to control for the effect of shifts in the sampling, i.e. the time axis. While the edit distance method provides an effective framework to carry out RA with irregularly sampled time series with respect to the *non-uniformity* problem, this contribution explored the specific biases in RQA that result from systematic dependencies of transformation costs on the local sampling rate. Specifically for detecting shifts in seasonal-scale predictability – as exemplified with the Niue record – this method helps to gain confidence in the identified transitions, undoubtedly building a supporting case for (Q5).
- (P5) This work provides a foundation for the applied studies on Palaeoseasonality carried out in this thesis, and hopefully beyond. Concerning (Q4) & (Q5), it informs on the methodological challenges not only for speleothem proxy records but for a broad range of palaeoclimate archives. A reliable quantitative analysis of changes in seasonality requires a profound understanding of the information encoded in a proxy, low dating uncertainties and very high sampling resolution. While I believe that technological advances will spawn more such records in the near future, I found that still a majority of palaeoclimate studies limit investigations to a qualitative level ('wobble matching') and do not adequately propagate uncertainties. I collated tools to elevate future studies of palaeoseasonality beyond a qualitative understanding and encourage stronger cross-disciplinary collaborations between the 'palaeo-experts' and 'method-experts'.
- (P6) In a first application of RA to a palaeoseasonal record that fulfills the requirements stated above, I focused on the 'seasonal amplitude' of the record and potential links with ENSO dynamics. The 1000-year, mid-Holocene record from Niue Island in the Central Pacific offers remarkable temporal resolution, especially for the greyscale time series compiled from scans of the stalagmite surface along its growth axis. After gaining a general understanding of how we can interpret this and other proxy time series using PCA, I conducted continuous wavelet and recurrence analysis. In the wavelet analysis, I used a modified version of the standard AR(1)-hypothesis test to assess significance in the presence of the non-stationary sampling rate. Significant variability in the 2-8 yrs.-band throughout the record indicates that ENSO was active over the whole observation period (contributing to (Q4)). RA of the seasonal amplitude corroborates the findings from (P4), even though I used different approaches in both analyses. The identified phases of low and high seasonal-scale predictability yield interpretable insights beyond variations in the stalagmite's growth rate, responding to (Q5).
- (P7) This final transdisciplinary work encompasses four fascinating scientific disciplines altogether: Climate Research, Palaeoclimate, Archaeology and nonlinear time series analysis. After a period of demographic expansion (600-750 CE), the urban states formed by Classic Maya underwent dramatic contractions between 750-950 CE. The YOK-G record offers the three conditions outlined above for seasonality reconstruction: interpretable proxy variability, low dating uncertainties and very high sampling resolution. Methodologically, I implemented a notion of recurrence that considers the research question (Q4) and technical challenges (Q5) alike. This notion is based on splitting stable isotope time series into annual segments and comparing pairs of segments by means of their transformation costs. Two annual segments with sufficiently low transformation costs give

a recurrence. The mean diagonal line length  $T_{\text{pred}}$  in the resulting sliding RPs informs on the average prediction time of seasonal rainfall conditions. By correcting  $T_{\text{pred}}$  for biases due to non-stationary sampling (based on SRC-surrogates as proposed in (P4)), I detect significant shifts in seasonal predictability potentially relevant to Maya farmers and, in turn, societal stability. I identified a continuous decline in seasonal predictability that aligns well with the period of strongest population decline. My coauthors and I argue that the complex disintegration of Classic Maya was at least partially triggered or amplified by this reduced predictability and provide a potential climatological scenario that aligns with the observed dynamics, providing a multi-faceted contribution to (Q4 & Q5).

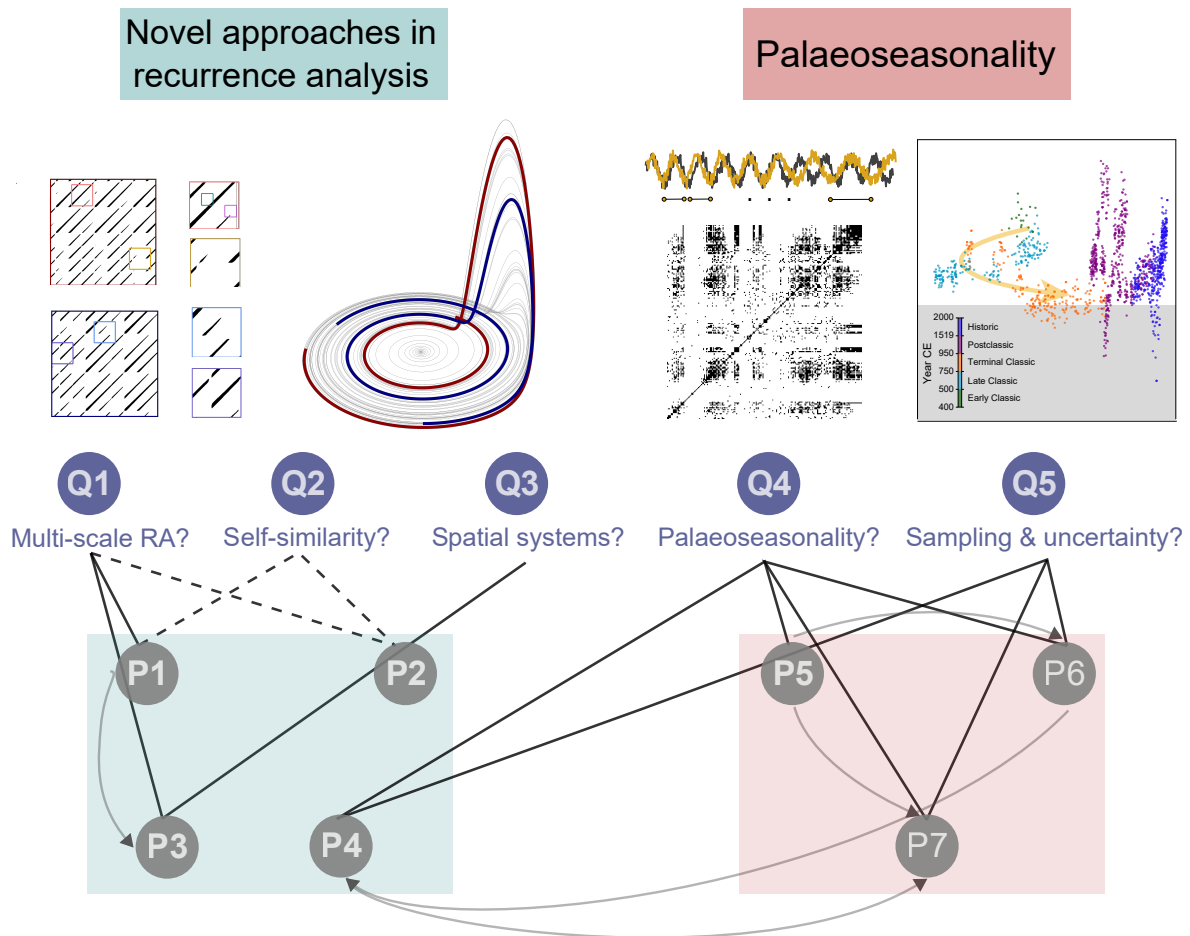


**Figure 12.1:** Overview of how the presented works contribute to answering the overarching research questions. Links between questions (Q) and papers (P) signify that the corresponding works have contributed to answer the respective question. Dashed lines indicate that question and paper are linked, but that the work did not help to answer the research question considerably. Arrows mark works that use concepts from other works.

## 13 | Synthesis

In this chapter I aim to reconcile all findings. I have started this dissertation by introducing nonlinear time series analysis as a research discipline that assembles concepts from the theory of dynamical systems and puts them into practise. This procedure entails methodologies that need to be tailored to the studied data with its individual complexities and technical challenges. The main focus of this thesis was the conceptualization and progression of such (nonlinear) TSA methods, especially in RA. Several applications have substantiated this process of conceptualization and enabled us to validate the efficacy of the proposed approaches. Altogether, this has helped to answer some of the overarching research questions, as will be shown now, and has left some partly unanswered.

Research questions (Q1) and (Q2) are tightly interwoven as both resulted from a curious intuition I expressed during the beginning of my doctoral research: does the apparent resemblance of patterns in an RP to self-similar textures bear any deeper implications and, if so, can we utilize this? Fractals – the mathematically pure instantiation of self-similarity – are generated by recurrent procedures, as I was not the first one to notice [90]. While I found that in fact, RPs yield non-integer box-counting dimensions in most interesting cases (supported by [88]), this does not by itself entail any conceptual link to, for example, the self-similarity in other properties of the system. The attractors of many chaotic systems are known to exhibit *strangeness*, meaning that their box-counting dimension is fractional. This results from the ‘stretching & folding’ of phase space vectors, a transformation that, after some number of iterations, will recur to its original state (an experience everyone who has ever baked a pizza from scratch has had before). As expressed in (Q2), one would expect that given the interwoven nature of recurrence and self-similarity, this would entail immediate links between both concepts. For instance, I briefly tested if Multiplicative Binomial Cascades [511], a class of iterative random processes, could serve as a potential generator of simplified, ‘surrogate’ RPs (another open problem of RA). These cascade processes in essence reverse the conventional box-counting approach to generate (multi)fractal patterns and depend on a few parameters which could in turn imply links to phase space dynamics. However, I did not find any formal correspondence between the two instances of self-similarity over the course of my doctoral work. Nor were any informative and robust links between self-similar properties of time series (e.g. Hurst exponent) and self-similar properties in their RP identified. Consequently, (Q2) remains an open question and will likely require a more rigorous, mathematical examination.

I have focused my efforts on defining and understanding utilizable tools based on ideas from the characterization of self-similar patterns that would be valuable additions to the already broad toolbox of recurrence quantification measures. This resulted in (P1) and (P2). RL proved to be of great utility in detecting transitions of different origins with a easily interpretable scale-sensitivity [1], and is a straight-forward application of the original concept to RPs. Furthermore, RL also enabled us to reveal a difference between the dynamically similar but practically opposing regimes of ‘combustion noise’ and ‘near blowout oscillations’ in pressure time series from a thermoacoustic combustor for the first time. Succolarity, originally proposed by B. Mandelbrot and formally defined for 2D binary textures afterwards [512], did not turn out to be of great additional utility for the detection of regime shifts beyond what is



already provided by RL. Succolarity is known not to exhibit any noteworthy scale-sensitivity [512]. However, additional contemplations resulted in the definition of the recurrence flow in (P2) with a different methodological focus: the characterization of nonlinear dependencies for high-dimensional time series data. Even though it is merely a by-product of the efforts undertaken based on (Q1 & Q2), it proved a multifaceted tool, for example, in the reconstruction of a system’s state space. A recent work [141] on this problem has regarded the ‘optimal’ state space reconstruction problem less traditionally (i.e. as it was originally proposed by Whitney, Mañé and Takens) but more problem-oriented: from a practitioner’s point of view, optimality depends on the research question. The recurrence flow selects optimal, non-redundant embedding delays based on the clear expression of diagonal line structures in an RP. The resulting notion of optimality is ubiquitous in TSA, that is, enhancing the system’s predictability. The recurrence flow consequently suggests a (potentially non-uniform) TDE that a) is based on non-redundant TDE vector components and b) yields an overall high-dimensional dynamics of the system that is predictable from the cross-dynamics of its subcomponents. Compared to other generalized dependence measures such as the continuity statistic by Pecora [75], the recurrence flow offers a more accentuated representation of the global maximum, that is, the optimal delay value. In applications where TDE is followed up by RA, the recurrence flow appears a natural choice as it has clearer implications for the obtained RPs than all other conventional methods for selecting embedding delays.

Only (P3) addresses how we can use RA to identify recurrent regimes in spatially extended data (Q3). Here, the novel idea is to investigate recurrences between evolving ‘spatial patterns’ of a physical property, in this case given by geopotential height anomalies. The atmospheric teleconnection patterns that emerge from spatially distant, albeit synchronized atmospheric pressure variations are known to result in recurring, often persistent regimes. The use of recurrence networks, a graph representation of a recurrence matrix, gives rise to a generalizable way to capture these regimes as communities in the network. The resulting regimes are well-separated in the space spanned by kernel principal components. The RA of these regimes not only substantiated the interpretation of how these regimes can be understood – it also offered another opportunity to test the scope of RL as a classifier of dynamical complexity. In this context, I have interpreted RL as a measure of diversity of recurrence patterns at decadal time scales. It was shown that RL provides additional information beyond the traditional recurrence quantifiers. Moreover, I extended RL to diagonal and vertical lines, showcasing its versatility. Other measures such as DET confirmed the persistence of atmospheric patterns associated with blocking events – the root cause of synchronized extreme weather events that are expressed more and more severely lately.

While all these works focus on developing or transferring novel methods to broaden the scope of RA, (Q5) calls for the modification of existing tools to render them suitable for data-specific challenges. This has been tackled in (P4). After reviewing a broad body of palaeoclimate literature with a focus on extracting seasonality from various archives (see (P5) [3]), I tried to introduce my insights into applications (P6 & P7). In the analysis of stable isotope time series from speleothems, two technical challenges stand out: the propagation of uncertainties and consideration of irregular sampling. While the first problem gained particular relevance in (P7), the latter is usually treated in RA by using the edit distance as the metric distance. My research question (Q4) however suggested a rather specific notion of a recurrence as implemented in (P4 & P7): a system recurs to its ‘seasonal state’ if two seasonal cycles align closely enough. Several ways to define a cycle are possible (e.g. based on local maxima [513]) but I decided to limit its definition to whatever evolution of the system is covered within one year. This, in turn, implies that temporal windows are equally sized but, given a non-stationary sampling rate, the number of values is strongly non-uniform. For proxy records, this is a common problem as non-stationarity is imposed by the stalagmite’s growth

rate (reflecting cave-environmental parameters) and sampling strategies of the experimentalist in the laboratory. Similar problems yet arise with different data if the evolution of a system (for example, pressure in a combustion engine or a stock price) is partitioned/stratified into segments according to a relevant order parameter (for example, air flow or traded order volume). While now we control for the order parameter and thus only compare pressure/price changes for the same unit of air flow/order volume, the segment size becomes a free parameter that needs to be corrected for. Biases are expected to arise not only for the dissimilarity between segments but also for some other statistical properties, for example variance. It needs to be stressed that this was found to be of considerable relevance only in cases when segment sizes are *small*, covering less than about 50 values, as it is the case for the problems studied here. The larger segments get, the less pronounced the finite-size bias becomes. The proposed correction approach, based on generation of SRC-surrogates, offers a remedy without the need to understand the exact statistical law of how the property of interest (edit distance, variance, etc.) scales with segment size. Attempts to do so did not turn out to be fruitful. I expect this relationship to differ significantly between different systems, depending on their serial dependence, the strength of stochastic components in the signal, and higher order properties. With respect to (Q5), the proposed method represents an expedient step towards equipping RA with adequate tools to study Palaeoseasonality, but it does not yet provide the solution to the more general problem (discussed in Chapter 14). It did, however, enable me to study regime shifts in the records from Mataga Cave (P6) and Yok Balum Cave (P7).

In the extraction of seasonality from stalagmite C132 (Mataga Cave, Niue Island), I was able to explore two different approaches to assess seasonal predictability at the same phase in my doctoral research: in (P6), I limited the definition of seasonality to the expression of seasonal amplitude, i.e. contrast between wet and dry season. Based on the assumptions that a) calcite layers were deposited annually, b) dark (bright) layers represent denser (more porous) calcite crystal patterns and thus drier (wetter) conditions, and c) the wet season is on average wetter than the dry season, I recalibrated the greyscale record to (pseudo-)monthly precision. The RA of this highly-resolved record revealed a period of low predictability (quantified by DET) prior to 6.2 ka BP and another one between 5.9 - 5.7 ka BP. Similar periods of low seasonal predictability were identified with the more comprehensive framework in (P4) where I used the edit distance to account for the full seasonal rainfall proxy profiles and applied the proposed sampling rate correction, demonstrating a satisfactory robustness of the identified shifts. Potential links between seasonality and ENSO dynamics in this understudied region were another interesting outcome of this study, contributing to both research question (Q4 & Q5).

A similar RA framework was used in (P7). The study of Palaeoseasonality and its potential links to the disintegration of Classic Maya urban centers was undoubtedly one of the most intriguing, yet challenging research problems that accompanied me over the entire course of my doctoral research. Methodological advancements, especially the sampling rate correction in (P4) and modifications of existing TSA methods to propagate uncertainties in (P7), were motivated by this exciting application. I have already discussed how the irregular sampling problem was considered here. The propagation of uncertainties must be regarded as an equally vital consideration for studying Palaeoseasonality. Measurements of isotope ratios on stalagmites yield negligible errors, and thus dating errors are the main source of uncertainty. Most state-of-the-art age models (e.g. OXCAL or BChron) offer the opportunity to study a time series in an ensemble fashion where each realization of the ensemble represents one possible candidate for the ‘real’ series of observations. COPRA, the age modelling software used here, does so too. However, COPRA users (as well as users of other comparable age modelling products) have rarely exploited this option. In spite of more sophisticated approaches to

uncertainty propagation for time series [51], I have explored the potential of COPRA age model ensembles for a MC-based uncertainty propagation for several TSA methods (continuous wavelet analysis, LS periodograms, extreme event analysis, RA, etc.). This decision was mainly a result from the striking simplicity of the approach. Put briefly, a TSA method of choice just needs to be repeated for each MC-realization, with each one exhibiting variability at the highest assessable time scales without any variability being ‘canceled-out’ as it is the case for the common age model medians/averages. From (P7), the MCR, as an alternative representative realization of an age model ensemble, appears to be a solid solution whenever only a single realization is needed. Hypothesis testing (e.g. as carried out for the MC-wavelets in (P7)) is straight-forward and entails intuitive visual representations that incorporate uncertainties. Over the past three years, I have noticed that more and more researchers use comparable schemes which I believe to be a promising development.

For the study of seasonal properties and regime shifts in the YOK-G proxy records, I assembled a plethora of TSA methods. This exploration of how changes in seasonality can generally be expressed (partly reflected in (Q5), see Fig. 9.1), and which of these expressions can be identified in speleothem records revealed a) different sensitivities of methods that quantify *seasonal amplitude* (e.g. variance, interquartile range, median absolute deviation, extreme events) against irregular sampling, b) pitfalls of standard methods to quantify *seasonal periodicity* (in particular, wavelets) in presence of varying sampling rates, c) severe limitations for quantifications of *seasonal timing* (e.g. centroid of seasonal cycle) with respect to dating uncertainties, and d) variable robustness of NTSA methods that characterize *seasonal complexity* (e.g. RA, permutation entropy, visibility graphs). The characterization of seasonal predictability based on the sampling rate corrected mean diagonal line length  $\tau_{\text{pred}}$  of an (edit distance-based) RP that was finally employed in manuscript (P7) is the outcome of this selection process. One could wonder why I did not take the opportunity to use the recurrence quantification measure proposed by myself here, namely RL (P1). As mentioned in Chapter 1, TSA requires parsimony (Occam’s infamous razor). In this sense, the already established mean diagonal line length sufficed and revealed valuable insights on the predictability of seasonal rainfall. The method development sparked by (P7) and the findings that resulted from application of these methods probably represent the most consequential contribution to (Q4 & Q5). Moreover, it gave rise to numerous additional questions and challenges for future research that will be discussed in the following chapter.

## 14 | Outlook

According to Friedrich Nietzsche, "Every philosophy is the philosophy of some stage of life". I believe that this also touches on the progression of scientific knowledge. In the near future, many of the insights in this dissertation may be rapidly progressed into different directions or surpassed, either by myself or others (which I genuinely hope for). I will summarize some of these prospects and research avenues here.

### Novel approaches in recurrence analysis

The works that deal with (Q1) suggest several potential pathways for future research. The introduction of RL as novel recurrence quantification measure in (P1) for instance reveals several straight-forward modifications and further applications. Firstly, computation of lacunarity by the proposed static grid approach offers lower sensitivity to significant structures than a gliding box approach. The latter, however, requires higher computational costs. Implementation of efficient gliding box algorithms for RL could enhance its scale-sensitivity to more subtle structures with low expenses in computational complexity [514, 515]. Generally, the idea of a box-counting based RQA could prove beneficial for some systems that encode their complexity not in regular line structures. A transfer of the RL concept to recurrence networks is also straight-forward and could reveal the relation of scale-dependent heterogeneity in recurrence patterns to other properties of the topology of recurrences. Furthermore, application of RL to palaeoclimate records could unveil additional advantages of the method. Potential use of non-uniform boxes could account for irregular sampling in proxy records. Lacunarity is in general also definable for ‘colored’ textures, i.e. grayscale matrices. Hence, an application to weighted or unthresholded RPs is conceivable and could be useful in application to RPs that involve uncertain recurrences. This is not straight-forward using traditional recurrence quantifiers. From the studied examples, the identified difference between combustion noise and near blowout states in a laboratory thermoacoustic combustor was a satisfactory validation of the method and should be studied further. If fast-scale oscillations in acoustic pressure fluctuations robustly distinguish between both regimes, this should be also detectable in additional similar experiments with potential utility for industry use. On a different note, it has recently been showcased that RPs bear great potential for the analysis of a signal’s spectral properties [516]. A strongly related problem is the analysis of signals with non-stationary spectral properties, e.g. transient cycles. Here, RL represents a vantage point for a first approach of a recurrence based time-frequency analysis method. This could particularly shed light on cases where traditional methods cannot yield robust results, such as cycles in high-dimensional dynamical systems, identification of transient quasi-periodic oscillations and unstable periodic orbits. A suitable approach for ‘RP-surrogates’ would be of great value here to equip this approach with a hypothesis test, as it has already been pointed out elsewhere in more detail [145].

While (Q2) remains an open question for now, it should nevertheless motivate further studies on the links between self-similarity and recurrence. This work has shown that from an applied perspective, their synthesis can be prolific. First ideas on how one could instead

explore conceptual links between self-similarity and recurrence more effectively using Hamiltonian systems were discussed towards the end of my doctoral work and will hopefully bear fruit in future works.

The idea that the rich information on dynamical properties of a system encoded in an RP appears useful for selecting parameters of an ‘optimal’ state space reconstruction is now 30 years old [142]. Yet, a systematic recurrence based TDE framework is still missing. The recurrence flow approach proposed in (P2) seems promising as a foundation for such a framework and I have undertaken considerable efforts in this direction in the final phase of my doctoral work. In particular, defining a both effective and parsimonious measure of *irrelevance* based on RPs would be the logical next step. Classical methods, such as the FNN approach, are effective but come along with some shortcomings, for example, when analysing map-like time series as they are often found in the Geosciences [517]. Here, RPs prove generally effective which could render a recurrence based estimator for the optimal embedding dimension more robust in such cases. State spaces reconstructions obtained with this approach could prove effective in predicting the dynamics of high-dimensional systems since the notion of optimality aims towards well-expressed diagonal lines in the RP. The resulting approach could also be transferred to closely related problems, for instance the selection of a sub-set of informative (non-redundant) explanatory variables for the prediction of a response variable from a large dataset that comprises potential confounders. What is more, I have briefly tested the utility of the recurrence flow measure of dependence in identifying regime shifts and found it to be potentially helpful for systems in which a critical transition is preceded by an increase in serial dependence.

In (P4), I proposed an approach tackling the problem of irregular sampling as outlined in (Q5). In RA, the introduction of the edit distance method was arguably a very fruitful development. From my experience, it yet requires heuristic calibration of several parameters (e.g. various cost parameters and the window size) which sensitively affect the validity of the transformation costs and, in turn, alter the representation of recurrences. Here, a sufficient understanding of the method and some experience is required. In the palaeoclimate community, sophisticated methods like edit distance-based RA are not very widespread yet, raising the need for cross-disciplinary collaboration if such methods are to be applied adequately. In an attempt to come up with a more simple approach for defining recurrences in irregularly sampled time series, I became convinced that, indeed, the edit distance is a very effective choice compared to other similar measures (e.g. Dynamic Time Warping, Fréchet distance, Nearest neighbour distance) which are used in other disciplines that face comparable problems (e.g. astrophysics or ecology [518]). One conceptually intuitive approach that could potentially be used as an alternative *ansatz* are kernel based (dis)similarity measures, underlined by their effectiveness in assessing correlations for irregularly sampled proxy time series [217]. Nevertheless, the edit distance itself should be further developed, applied to different settings (e.g. similarity of time series that are naturally ‘short’) and rethought, for instance as a possible measure for characterizing scale-dependent variability in time series (as initiated here: [131]).

## Palaeoseasonality

The problems associated with irregularly sampled proxy records (partly raised in (Q5)) are plentiful and have been discussed several times in this dissertation. After working on this challenge for the past three years, novel definitions and modifications of existing TSA tools still appear as the most obvious and immediate way to tackle this problem, yet they do not necessarily represent the only relevant way forward. A research avenue that deserves additional attention is the systematic investigation of sensitivities of existing methods to irregular sam-

pling and other sampling-related intricacies (e.g. signal smoothing). This should be based on simple proxy toy models, more sophisticated process-based (e.g. cave-environmental processes for speleothems) proxy system models and finally, large data sets of real palaeoclimate records (e.g. PAGES2k or SISAL). A natural focus should be put on the most frequently used methods for palaeoclimate archives, for instance correlations, power spectra and PCA from which each will exhibit time-scale dependent biases due to irregular sampling [217, 519, 520, 521]. Effects of common data treatment strategies such as linear interpolation need to be accounted for. While most studies in this direction currently focus on stationary sampling rates, the relevance of non-stationarity in the sampling rate has been emphasized here (see P4) and should motivate more realistic modelling of irregular time axes for proxy records. Determining the relevance of identified biases for the discrepancies observed in some systematic model-proxy comparisons would likely improve utilisation for data-model comparison. All of this applies in particular to the study of highly resolved proxy records, e.g. for studying Palaeoseasonality.

In the review process of (P6), one reviewer raised the problem that in the provided RA, the notion of predictability is difficult to understand and deviates from the notion of most climate scientists, i.e. predictable dynamics from some underlying model. While I am convinced that the notion of predictability based on diagonal lines in RPs is in fact very informative and more versatile than most metrics that are based on models (these usually come with a set of preliminary assumptions), the concern is valid and could motivate a comparative study of model-based predictability metrics and the ones provided by RQA.

Finally, no other study presented here has probably inspired as many prospects on possible future research as (P7) and the associated research question (Q4). While some of them have already been mentioned, I will list the remaining ones here for brevity:

- Some highly resolved proxy records that reflect hydroclimate allow for extracting ‘short-lived’ extreme events (Fig. 11.1), going beyond the notion of ‘droughts’ and ‘floods’ as continuous longer intervals of anomalous hydroclimate conditions common in Palaeoclimate. However, associated uncertainties with such short-lived extreme events due to proxy-specific issues (e.g. the ones mentioned above related to irregular sampling) need to be studied in more detail.
- Another highly resolved record from Yok Balum cave (YOK-I) is available and has been extensively studied before [454]. In the analysis of Yok-G stable isotope records, a range of discrepancies in  $\delta^{13}\text{C}$  and  $\delta^{18}\text{O}$  measured on YOK-G and YOK-I stood out that are expressed in unaligned prominent dry/wet periods. These different expressions need to be examined in detail and can hopefully be resolved based on cave-environmental considerations (e.g. different drip rates and flow paths) and statistical analysis (e.g. correlations and mode decomposition).
- Sensitivity of Classic Maya populations to regional droughts has been explored using conceptual modelling [478]. Our results on their potential vulnerability to variations in seasonal predictability could be incorporated in a conceptual modelling approach to potentially reveal additional socio-hydrological feedbacks and reflect on agricultural responses.
- The hypothesis on less coherent ITCZ dynamics during the TCC put forward in (P7) will require further investigations. These would benefit from both adequate proxy reconstructions of ITCZ dynamics for the past approx. 2000 years (comparable to the comprehensive 1000 year-reconstruction and methodological approach in [492]) and supplementing this analysis with atmospheric model results (e.g. ECHAM5 [522]) to test for different scenarios. While this is undoubtedly a challenging enterprise, it would likely provide further insights in the ongoing debate of Common Era ITCZ dynamics.

## Summary

Let us finally summarize the key findings once more, responding to all research questions and including some future prospects:

- (Q1) Yes, concepts from the study of self-similar patterns bear great potential for the use in RA. In particular, RL allows for the identification of regime shifts in different nonlinear time series and provides a first potential approach for a recurrence based time-frequency analysis. Moreover, the recurrence flow of an RP offers a recurrence based framework to study couplings in high-dimensional systems where multiple time delays play a role and could be used for a recurrence based state space reconstruction approach as well as related problems, for example for variable selection.
- (Q2) No robust and meaningful universal links between the self-similar properties of recurrence patterns of a signal and the self-similar properties of the signal itself could be identified in this dissertation. While there is a striking intrinsic link between recurrence and self-similarity in general, I believe that a more conceptual, mathematical exploration with suitable paradigmatic systems needs to be undertaken to reveal new insights on this fascinating problem.
- (Q3) One way RA can be used to characterize transitions between regimes of spatially-extended systems is to identify communities in the recurrence network associated with RPs. Conceptually, recurrence relations are established between spatial patterns of a climate field. This was shown for patterns of geopotential height that characterize atmospheric circulation. A classification of their dynamical properties was achieved based on traditional and novel recurrence quantification measures. Additional applications to other climate fields or complex systems that exhibit distinct spatial patterns and studying transitions between regimes will help to further develop this approach.
- (Q4) Yes, RA provides effective tools to reliably detect significant transitions in Palaeoseasonality for different palaeoclimate reconstructions from speleothems. I explored different ways in which seasonality and seasonal predictability can (and cannot) be quantified in different settings. Diagonal line based measures are well-established and implement a notion of ‘predictability’ that is easily transferable to applications in Palaeoseasonality. In particular, using the (sampling rate corrected) mean diagonal line length as a proxy for seasonal prediction times offered valuable insights on how changing seasonal rainfall conditions could have affected Maya agriculture, implying a chain of events that potentially contributed to the observed fragmentation of Classic Maya urban centers.
- (Q5) Accounting for data-specific challenges and limitations in the study of Palaeoseasonality using TSA tools in general still has a long path ahead. While many recent contributions in this field are very promising, their widespread use needs to be promoted by easy-to-use software and cross-disciplinary collaborations. The particular problem studied here, i.e. biasing effects imposed by growth rate variations of a stalagmite, could be treated by a novel constrained randomization procedure. However, a more general treatment of sampling effects and uncertainty propagation call for more general methodological frameworks and numerical experiments on pseudo-proxies, universally enclosing several prominent (N)TSA methods.





---

# Appendix



# A | Code implementations

For all first-authored works, comprehensively commented scripts and brief examples on how to use them were generated and uploaded to Github or public repositories. I provide a short summary of these online repositories here as an overview to facilitate the download. Every code was implemented in Python (Version 3.7). Package requirements are specified in the respective repositories.

I distinguish between three different ways the source code is provided: **(A)** ‘loosely’ composed scripts and examples that should enable a researcher to reproduce figures and results from the corresponding manuscripts with some additional effort and are readily applicable to other data as well, **(AA)** scripts that have been implemented in a way that allows straightforward replication of all main figures of the respective manuscript and are readily applicable to other data as well, and **(AAA)** code that is given as an extensively documented Python package in an object-oriented fashion, including illustrated examples and tutorials.

(Q1) Recurrence Lacunarity (RECLAC):

The RECLAC Python package provides functions to compute recurrence lacunarity as described in [1] (Open Source). Its functionality is basic at the current stage and will probably be extended in the near future. It also offers a basic implementation of traditional recurrence quantification measures and computation of box-counting dimensions. **(AAA)** <https://github.com/ToBraun/RECLAC>

(Q2) Recurrence Flow (RECFLOW):

Code accompanying the paper T. Braun et al: ‘Recurrence flow measure of nonlinear dependence’, 2022 (EPJ ST). A collection of functions is provided that enable the researcher to compute the recurrence flow from time series or an RP, use it for TDE (with known embedding dimension) or quantify lagged nonlinear relationships between two variables. A short tutorial is provided as a Jupyter Notebook.

**(A)** <https://github.com/ToBraun/RECFLOW>

(Q4) SRC-surrogates:

Code accompanying the paper T. Braun et al: ‘Sampling rate-corrected analysis of irregularly sampled time series’, 2022 (Physical Review E). A collection of functions is provided that enable the researcher to generate SRC-surrogates for a given time series and time axis. A short tutorial is provided as a Jupyter Notebook. No implementation for the edit distance is provided. However, a comprehensive implementation has been put forward by Celik Ozdes and coauthors, based on the paper [131]<sup>1</sup>.

**(A)** <https://github.com/ToBraun/SRC-surrogates>

(Q7) YOK-G:

Code accompanying the paper T. Braun et al: ‘Decline in seasonal predictability potentially destabilized Classic Maya societies’, 2022 (under review for Communications Earth & Environment). A collection of functions and scripts is provided that enable the

---

<sup>1</sup><https://zenodo.org/record/6038896#.YyHYy0qxVhE>

researcher to replicate the manuscript's main figures. However, some computations were originally performed on a high performance cluster and will require high computational times. Extensive documentation is provided in a readme file.  
(AA) [10.5281/zenodo.7104976](https://doi.org/10.5281/zenodo.7104976)

# B | Supplementary material for Chapter 7: Recurrence flow measure of nonlinear dependence

## Appendix A: Example Systems

To assess the performance of  $\Phi(\tau)$  as a measure to select embedding delays, the following systems are considered:

### Numerical Insolation Model

The complex superposition of gravitational forces between the earth and the other planetary bodies in the solar system perturbs the earth's rotation on an elliptic orbit around the sun and its axial rotation. The cycles that manifest due to these variations control the earth's climate at time scales of millions of years and are called Milankovich cycles. The nature of the underlying perturbation renders the variations in insolation chaotic. The model proposed in [146] considers all nine planets in the solar system and describes the orbit of the moon separately. A Hamiltonian, consisting of an integrable and perturbation component, is numerically integrated with a symplectic integrator scheme (SABAC<sup>4</sup>). Several dissipative effects (tides, core-mantle friction, climate friction) are included. The model returns time series for the earth's orbit's eccentricity, climatic precession, obliquity, and insolation, from which we study only the latter with  $n = 1,000$  samples. For the computation of RPs, we fix the recurrence rate to 5%.

### Rössler System

The Rössler system is a three-dimensional, continuous dynamical system that generates a strange attractor:

$$\begin{aligned}\dot{x} &= -y - z, \\ \dot{y} &= x + ay, \\ \dot{z} &= b + z(x - c).\end{aligned}$$

The time series only covers a few unstable periodic orbits with 3,000 samples from which we discard 1,000 as transients, resulting in  $N = 2,000$ . Uniform sampling intervals are fixed as  $\Delta t = 0.10$ . We set  $a = 0.02925$ ,  $b = 0.1$  and  $c = 8.5$ , ensuring chaotic dynamics. Independent realizations of uncorrelated white noise with different noise strengths between 0% and 100% are superimposed on the  $y(t)$ -component to mimic measurement noise. For the computation of RPs, we fix the recurrence rate to 8% regardless of the noise strength.

### Delay Differential ENSO Model

As an example for a system with multiple characteristic time scales, we examine a delay differential model of ENSO. On top of the seasonal mode, ENSO represents the predomi-

nant mode of sea surface temperature (SST) variability in the tropical Pacific. The SSTs exhibit recurring variations with time scales between 2 and 7 years between two regimes of well-distinguishable SST anomalies: El Niño (warming phase) and La Niña (cooling phase). These variations disturb large-scale air transport in the tropics and induce a multitude of global climatic impacts, e.g., droughts and floods in Australia or South America. Several conceptual models have reproduced key features of this oscillation by including hypotheses on the mechanistic origins of ENSO, including negative and positive feedbacks of temperature anomalies and atmospheric circulation and potential resonance phenomena with the seasonal forcing. The model studied here is taken from [147] and mimics ENSO dynamics based on two key mechanisms, i.e., delayed negative feedback and seasonal forcing

$$\frac{dy(t)}{dt} = -\tanh(\kappa y(t - \zeta)) + b \cos(2\pi\omega t).$$

We set the frequency of the periodic forcing to seasonal forcing ( $\omega = 1$ ) and fix  $b = 1$ . Variations in the delay  $\zeta$  and the parameter  $\kappa$  give rise to dynamically distinct time series. We study two solution types: a regular solution with a seasonal cycle and fast, amplitude-modulated wiggles ( $\kappa = 100$ ,  $\zeta = 0.025$ ) and a solution of irregular ENSO-like oscillations with stochastic amplitude variations ( $\kappa = 50$ ,  $\zeta = 0.42$ ). For both solution types, we generate  $n = 10,000$  values. For the computation of RPs, we fix the recurrence rate to 5%.

## Appendix B: Statistical Significance

For an uncorrelated white noise time series of infinite length, the presence of recurrences along a diagonal can be described by a binomial distribution. The flow along each diagonal can consequently be regarded as an idealized sequence of Bernoulli trials for which a success is equivalent to a recurrence, i.e., a black pixel. The probability of having  $X$  unsuccessful Bernoulli trials (no recurrences) until a trial succeeds is given by the geometric distribution

$$P(X = n) = (1 - p)^{n-1} p \tag{B.1}$$

with expectation value  $1/p$ . The probability of success  $p$  for each Bernoulli trial is given by the recurrence rate and depends on  $\varepsilon$ . It follows that we can derive the recurrence flow for an idealized uncorrelated white noise time series of length  $n$  as

$$\theta(\varepsilon) = 1 - \frac{n}{p(\varepsilon)}. \tag{B.2}$$

Given an observational time series of length  $n$  and a suitable choice for the vicinity threshold  $\varepsilon$ ,  $p(\varepsilon)$  can be identified with the recurrence rate and eq. (7) can be used to test whether the recurrence flow of the real signal can be distinguished from an uncorrelated random process.

## C | Supplementary material for Chapter 6: Revealing recurrent regimes of mid-latitude atmospheric variability using novel ma- chine learning method

This section demonstrates the ability of the proposed method to detect and separate recurrent states in a simple situation, when the true solution is known. To this end, we use a toy two-dimensional stochastic model with three-well potential, which was suggested in the work [523] for testing clustering methods and then also used in the work [524]:

$$d\mathbf{X} = -\nabla V(\mathbf{X}) + \epsilon dW_t$$

$$V(\mathbf{X}) = u(\mathbf{X} - \mathbf{A}_1) + u(\mathbf{X} - \mathbf{A}_2) + u(\mathbf{X} - \mathbf{A}_3) + b|\mathbf{X} - \mathbf{A}_c|^2, \quad (\text{C.1})$$

where  $W_t$  is the Wiener process, points  $A_1 = (0, 0)$ ,  $A_2 = (2a, 0)$  and  $A_3 = (a, a\sqrt{3})$  are the centers of profiles  $u(\cdot)$  which takes the form

$$u(\mathbf{X}) = -\alpha \exp\left[\frac{1}{|\mathbf{X}|^2 - a^2}\right]. \quad (\text{C.2})$$

The potential function  $V(\mathbf{X})$  has three minima placed in the vertices of a isosceles triangle centered in  $A_c = \left(a, \frac{a}{\sqrt{3}}\right)$ . Here we use the same values of parameters as in Ref. [523]:  $\alpha = 21$ ,  $a = 0,87$ ,  $b = 0,12$  and  $\epsilon = 0.05$ . This model produces random walks around the local minima of the potential function, provided that the phase trajectory spends more time near the centers of the potential than anywhere else. Thereby, the model simulates the situation with three regimes, or recurrent states in the phase space.

We integrate this model by Euler method with the time step 0.01. To exclude from consideration the points which are close to each other due to the temporal ordering, we take only each 100th point during the integration. For analysis we use 10,000-point time series (Fig. C.1 and C.2) taken after 20,000-step spin-up period.

We applied the presented method to this data, based on two different distances: (i) simple Euclidean distance  $d_{ij} = |\mathbf{X}_i - \mathbf{X}_j|$  and (ii) Euclidean distance between normalized vectors given by Eq. 7.8. In both cases we detect three regimes, central points of which are separated well in the plane of leading two KPCs (see Fig. C.1 and C.2). In the projections of the phase trajectory to this plane, states that belong to different regimes fall on different linear manifolds. At the same time, the time series of KPCs describe transitions between areas of the regimes. However, distribution of the centralities substantially depends on the distance choice: if in the first case it emphasizes the maxima of the probability density in 2d-space, in the second case it captures rather the density of angles of centered states vectors, because the normalization in Eq. 7.8 attaches all vectors to the unit sphere. The latter is especially

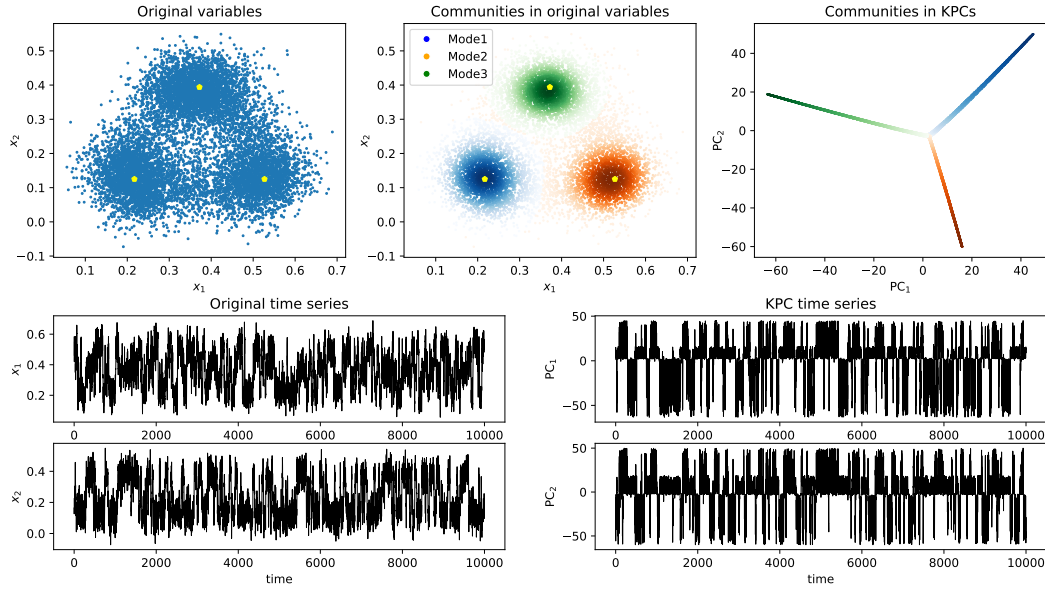


**Figure C.1:** Analysis of time series of the three-well model (Eq. C.1-C.2) based on the simple Euclidean distance between state vectors. Upper panels (from left to right): analyzed time series presented in original variables; the same, but with states marked according with the regimes they belong to; analyzed time series presented on the plain of leading two KPCs. Yellow dots mark “theoretical” centers of the potential function  $V(\cdot)$ . Color intensity corresponds to centrality of a state in its community. Low panels: time series of original variables (left) and leading two KPCs (right).

important in climate applications above, where we are interested in capturing the shapes of spatial patterns rather than their amplitudes.

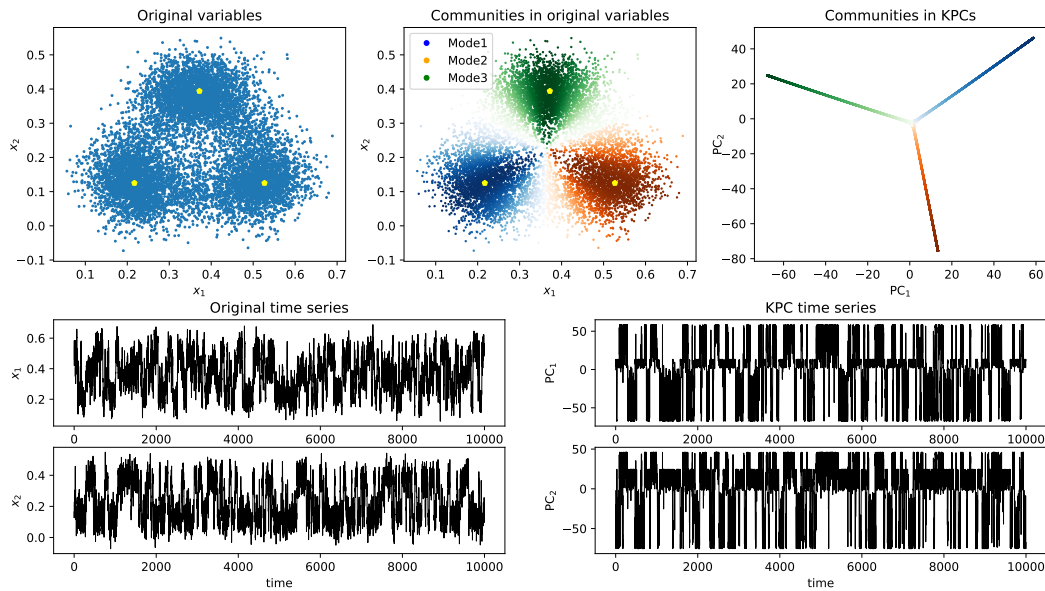


**Figure C.2:** The same analysis as in Fig. C.1, but based on Euclidean distance between normalized vectors defined by Eq. 7.8.



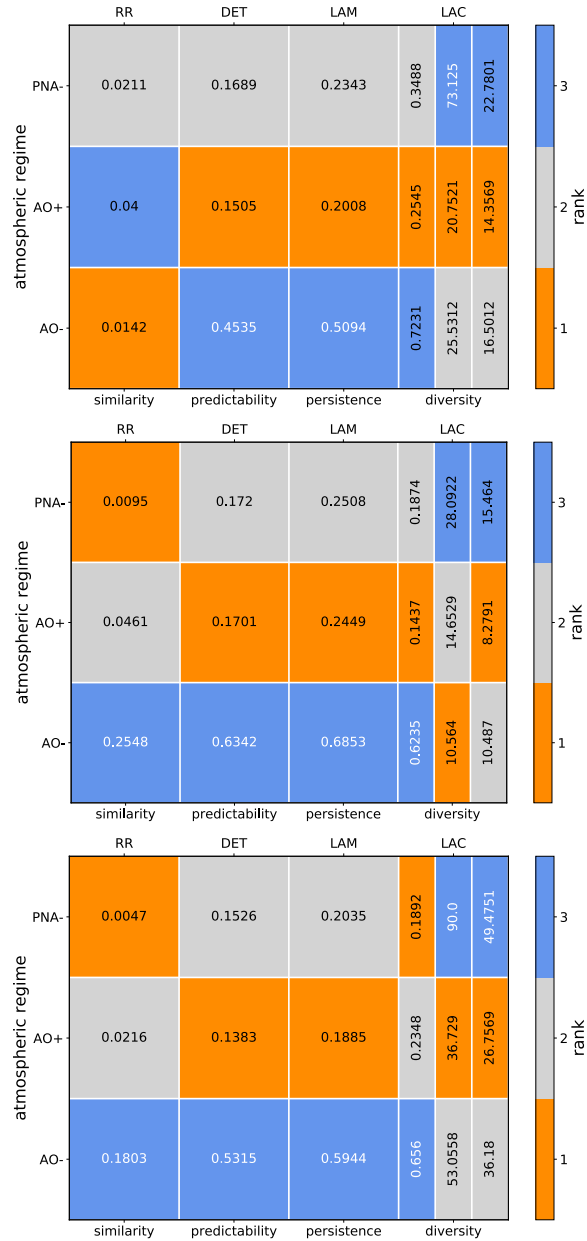


**Figure C.3:** Comparison of results of recurrence quantification analysis for the atmospheric regimes obtained in the QG3 model data set between the three different time series. The four different RQA measures are labelled with their respective interpretation. Significant (insignificant) values are printed in white (black). Color coding illustrates the ordering of the RQA values (ascending column-ranking) for better comparability.

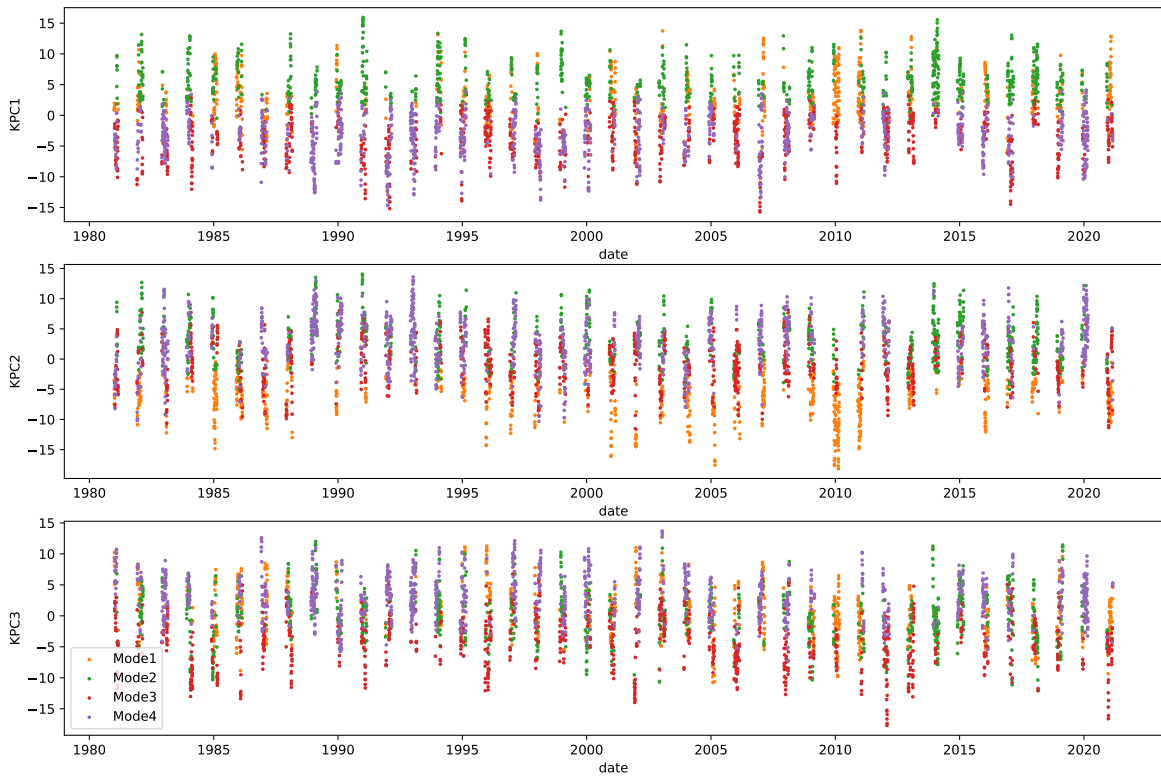


**Figure C.4:** Time series of the leading three KPCs of the reanalysis data. Different colors correspond to the obtained regimes. Since only the winter months are considered, the time series are split into segments separated by equidistant gaps.

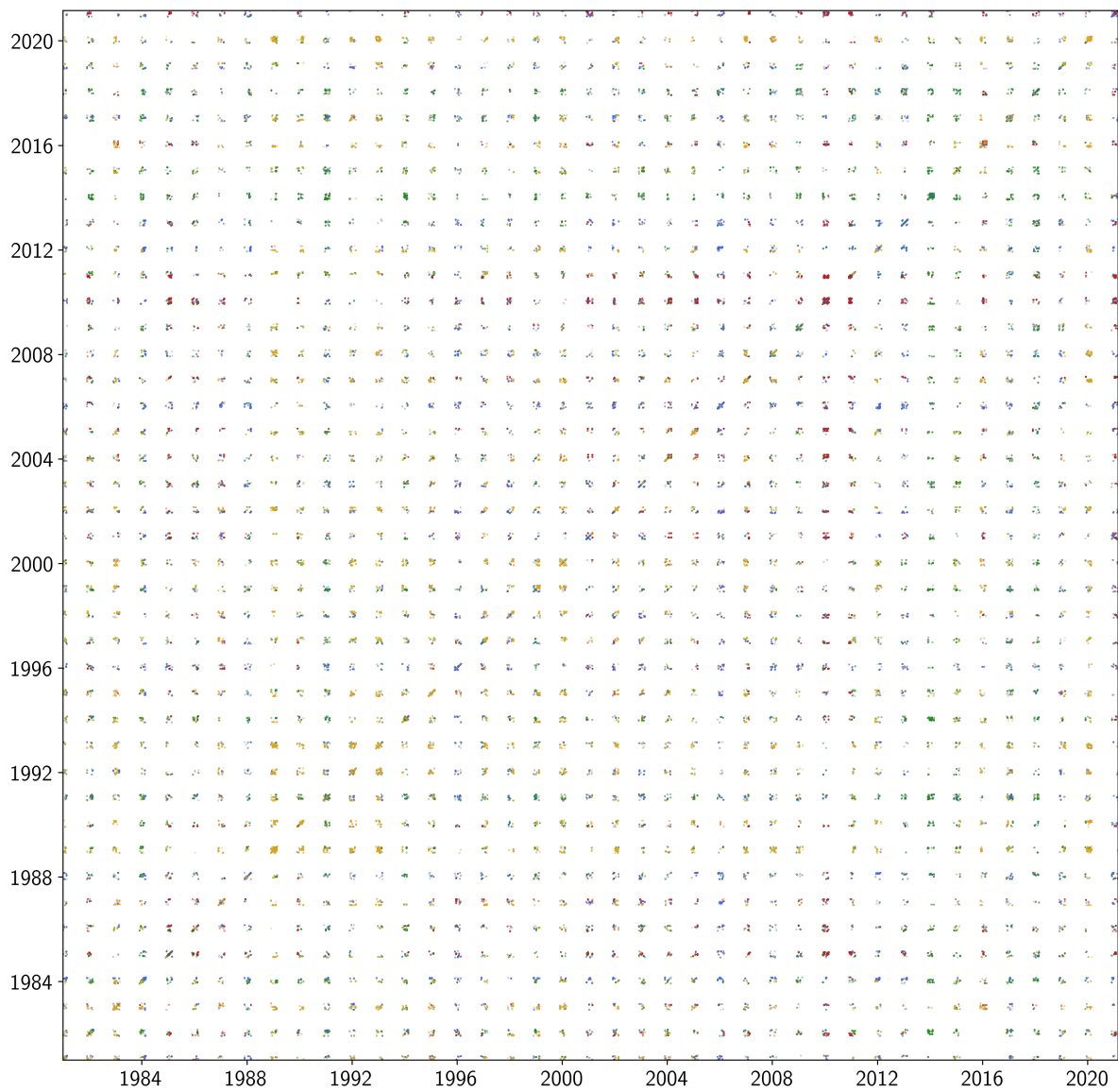


**Figure C.5:** Recurrence plot of atmospheric patterns obtained from the reanalysis data. Recurrences within a given regime are color coded accordingly. Since only the winter months are considered, the RP is split into sub-RPs separated by equidistant gaps.



# D | Supplementary material for Chapter 11: Sampling rate-corrected analysis of ir- regularly sampled time series

## Appendix A: analytical and numerical segment size relations

In the following, we elaborate on the systematic dependence of the (m)Edit distance on segment lengths  $N_a = |\mathcal{S}_a|$ ,  $N_b = |\mathcal{S}_b|$  in the most simple application: we study events (i.e., no assumptions about the amplitude of the signal) which are unevenly spaced by exponentially distributed sampling intervals  $\Delta$  with a sampling rate  $\lambda$ :

$$p(\Delta, \lambda) = \lambda e^{-\lambda\Delta} \quad (\text{D.1})$$

Consequently, the number of samples per unit interval  $k$  is Poisson-distributed

$$\rho(k, \lambda) = \frac{\lambda^k e^{-k}}{k!} \quad (\text{D.2})$$

with  $\lambda$  being equivalent to the expected number of samples per unit interval;  $\mathbb{E}(X) = \lambda$ . Furthermore, the  $n$ -th time step is Erlang-distributed with the rate parameter  $\lambda$ :

$$f(t; n, \lambda) = \frac{\lambda^n t^{n-1} e^{-\lambda t}}{(n-1)!} \quad (\text{D.3})$$

which is a general result for a sum of  $n$  independent exponential random variables with equivalent rate parameters  $\lambda$  [525].

We are interested in the segment size-dependence of deletion(/adding) and shifting costs for the edit distance. This can be evaluated by considering  $M$  exponential random variables where each is drawn from a distribution  $p(\Delta, \lambda_m)$  with distinct  $\lambda_m$ ,  $m = 1, 2, \dots, M$ . When applied, this setting can be considered equivalent to a scenario where a time axis changes its local sampling rate  $\lambda_m$  at  $M$  points and segments from these should be compared via the edit-distance. For a specific pair of segments with sizes  $N_a, N_b$ , the minimum deletion cost (no deletions as competing to shifts included) for their transformation is

$$C_{\text{del}}(N_a, N_b) = \Lambda_S |N_a - N_b| \quad (\text{D.4})$$

Consequently, for two segments of average sizes  $\mathbb{E}[N_a] = \lambda_1$ ,  $\mathbb{E}[N_b] = \lambda_2$  we obtain a minimum deletion cost of  $C_{\text{del}}(\mathbb{E}(N_a), \mathbb{E}(N_b)) = \Lambda_S |\lambda_1 - \lambda_2|$ . A cost matrix  $C_{\text{del}}(\lambda_1, \lambda_2)$  is exemplified in Fig. D.1a. The expected minimum deletion cost for two randomly selected segments from time periods with different rates  $\lambda_1, \lambda_2$  can be computed by using the the Skellam distribution

$$\rho_s(k = |z|; \lambda_1, \lambda_2) = \begin{cases} e^{-\lambda_1 - \lambda_2} \left( \left(\frac{\lambda_1}{\lambda_2}\right)^{\frac{k}{2}} I_k(2\sqrt{\lambda_1 \lambda_2}) + \left(\frac{\lambda_2}{\lambda_1}\right)^{\frac{k}{2}} I_{-k}(2\sqrt{\lambda_1 \lambda_2}) \right) & \text{if } k > 0 \\ e^{-\lambda_1 - \lambda_2} I_0(2\sqrt{\lambda_1 \lambda_2}) & \text{if } k = 0 \end{cases} \quad (\text{D.5})$$

for the difference  $Z = X - Y$  where  $X, Y$  are Poisson-distributed random variables with rates  $\lambda_1, \lambda_2$ , Eq. (D.2).  $I_k(a)$  denotes the modified Bessel function of the first kind. For  $k > 0$ , the moment-generating function is consequently given by

$$M(t; \lambda_1, \lambda_2) = e^{-\lambda_1 - \lambda_2} \left( \sum_{k=0}^{\infty} e^{tk} I_k(2\sqrt{\lambda_1 \lambda_2}) \left[ \left( \frac{\lambda_1}{\lambda_2} \right)^{k/2} + \left( \frac{\lambda_2}{\lambda_1} \right)^{k/2} \right] - I_0(2\sqrt{\lambda_1 \lambda_2}) \right) \quad (\text{D.6})$$

With ‘Marcum’s Q’

$$Q(\sqrt{2\lambda_1}, \sqrt{2\lambda_2}) = e^{-\lambda_1 - \lambda_2} \sum_{k=0}^{\infty} \left( \frac{\lambda_1}{\lambda_2} \right)^{k/2} I_k(2\sqrt{\lambda_1 \lambda_2}) \quad (\text{D.7})$$

and its derivative

$$\frac{d}{dt} Q(\sqrt{2\lambda_1}, \sqrt{2\lambda_2}) = e^{-\lambda_1 e^t - \lambda_2 e^{-t}} \left( \lambda_2 e^{-t} I_0(2\sqrt{\lambda_1 \lambda_2}) + \sqrt{\lambda_1 \lambda_2} I_1(2\sqrt{\lambda_1 \lambda_2}) \right) \quad (\text{D.8})$$

this can be written as

$$M(t; \lambda_1, \lambda_2) = e^{-\lambda_1 - \lambda_2} \left[ Q\left(\sqrt{2\lambda_2 e^{-t}}, \sqrt{2\lambda_1 e^t}\right) e^{\lambda_1 e^t + \lambda_2 e^{-t}} Q\left(\sqrt{2\lambda_1 e^{-t}}, \sqrt{2\lambda_2 e^t}\right) e^{\lambda_2 e^t + \lambda_1 e^{-t}} I_0(2\sqrt{\lambda_1 \lambda_2}) \right] \quad (\text{D.9})$$

Differentiating this moment-generating function (using eq. D.8) around  $t = 0$  with Leibniz rule yields the expected value:

$$\mathbb{E}[k; \lambda_1, \lambda_2] = 2e^{-\lambda_1 - \lambda_2} \left( \lambda_2 I_0(2\sqrt{\lambda_1 \lambda_2}) + \sqrt{\lambda_1 \lambda_2} I_1(2\sqrt{\lambda_1 \lambda_2}) \right) + (\lambda_2 - \lambda_1)(1 - 2Q(\sqrt{2\lambda_1}, \sqrt{2\lambda_2})) \quad (\text{D.10})$$

Hence,  $\mathbb{E}[C_{\text{del}}(\lambda_1, \lambda_2)] = \Lambda_S \mathbb{E}[k; \lambda_1, \lambda_2]$  (Fig. D.1a (middle)). In the right line plot of Fig. D.1a, two columns with  $\lambda_1$  fixed at 3.1 are shown to illustrate the scaling of deletion costs with the rate  $\lambda$  more clearly. While  $C_{\text{del}}(\mathbb{E}(N_a), \mathbb{E}(N_b))$  shows a sharp minimum at the rate  $\lambda_2 = \lambda_1$ ,  $\mathbb{E}[k; \lambda_1, \lambda_2]$  decreases more smoothly with increasing  $\lambda_2$ , and increases afterwards. The latter becomes minimal for a value  $\lambda < \lambda_2$  instead of  $\lambda = \lambda_2$  since Poisson-distributions  $\rho(k, \lambda)$  are right-skewed, having higher cumulated probability mass for all values  $k > \lambda$ . Note that all said above holds in the same way for adding operations.

For the analysis of shifting costs, we focus on the simple case of linear shifting costs

$$\tilde{f}_{\Lambda_0}(t(\alpha), t(\beta)) = |t(\alpha) - t(\beta)| \quad (\text{D.11})$$

between the  $\alpha$ -th event in segment  $\mathcal{S}_a$  and the  $\beta$ -th event in segment  $\mathcal{S}_b$  as proposed in the original, unmodified edit-distance measure. To exclude effects caused by absolute timing of events, timing of events within each segment is always transformed into the interval  $I = [0, 1]$ . The sum of all shifting costs for a pair of segments is denoted as  $d_{ab} = \Lambda_0 \sum_{\alpha, \beta} f_{\Lambda_0}(t(\alpha), t(\beta))$  with  $\Lambda_0 = 1$ . Note that  $N_a = N_b$  as  $|N_a - N_b|$  deletions/addings have already been carried out. A closed-form solution for the shifting costs between two time instances drawn randomly from

the distributions  $f(x; m_1, \lambda_1)$ ,  $f(y; m_2, \lambda_2)$  most likely exists, at least for the case  $m_1 = m_2$  but its computation is beyond this study. We examine shifting costs for this case numerically, while we explicitly exclude any deletions as an alternative operation to shifting after the necessary  $|N_a - N_b|$  deletions ('basic deletions') (Fig. D.1b). We fix  $w = 1$  as the unit interval (arbitrary units). The numerical estimate of the average cost for transforming a segment sampled with rate  $\lambda_1$  into a segment sampled with rate  $\lambda_2$  is based on generating time axes for a fixed time period  $T = 10,000$  (but varying number of events). Given a fixed combination of  $\lambda_1, \lambda_2$ , a total of  $K = 10,000$  segment pairs are randomly sampled (with replacement) from both corresponding time axes. The edit-distance is computed for each pair of segments and averaged over all pairs to obtain a single value  $\bar{d}(\lambda_1, \lambda_2)$  that is characteristic for the combination of rates  $\lambda_1, \lambda_2$ . This is shown as a cost matrix  $C_{\text{shift}}(\lambda_1, \lambda_2)$  of averaged total shifting costs between randomly drawn segments (Fig. D.1b, left). The total number of shifts performed after deleting  $|N_a - N_b|$  events generally differs for distinct pairs of segments  $\mathcal{S}_a, \mathcal{S}_b$  at fixed  $\lambda_1, \lambda_2$ . However, when averaged over all randomly drawn segment pairs, an increasing trend along the diagonals is observed. Furthermore, average total shifting costs  $\bar{d}(\lambda_1, \lambda_2)$  increase for fixed  $\lambda_1$  and increasing  $\lambda_2$  (Fig. D.1b, right) which is to be expected as a higher number of shifts will entail higher summed costs. On the other hand, no monotonous relation between the average shifting costs per shifting operation

$$\tilde{C}_{\text{shift}}(\lambda_1, \lambda_2) = \sum_{k=1}^K d(\mathcal{S}_{a,k}^{(\lambda_1)}, \mathcal{S}_{b,k}^{(\lambda_2)}) / \max\{N_a, N_b\} \quad (\text{D.12})$$

and sampling rate is observed (Fig. D.1b, center and bold black line on the right). With increasing sampling rates, the cost of an average single shifting operation decreases (diagonals of the matrix). For fixed  $\lambda_1$ , it is maximized at a value  $\lambda_2 < \lambda_1$  for the same reason as above, i.e. the Erlang distribution being right-skewed.

If we instead examine the dependence of shifting costs on the actual segment size  $\tilde{C}_{\text{shift}}(N_a, N_b)$  rather than the rates (Fig. D.1c), a sharp maximum at  $N_b = \lambda_1$  is found (black line, right plot). Total shifting costs increase for  $N_b < \lambda_1$  and continue to increase more slowly for  $N_b > \lambda_1$ . For fixed  $N_a$ , an increasing number  $N_b$  of events per unit interval increases the likelihood that some events are placed close to the events in segment  $\mathcal{S}_a$ , resulting in lower distances  $d_{ab}(N_a, N_b)$ .

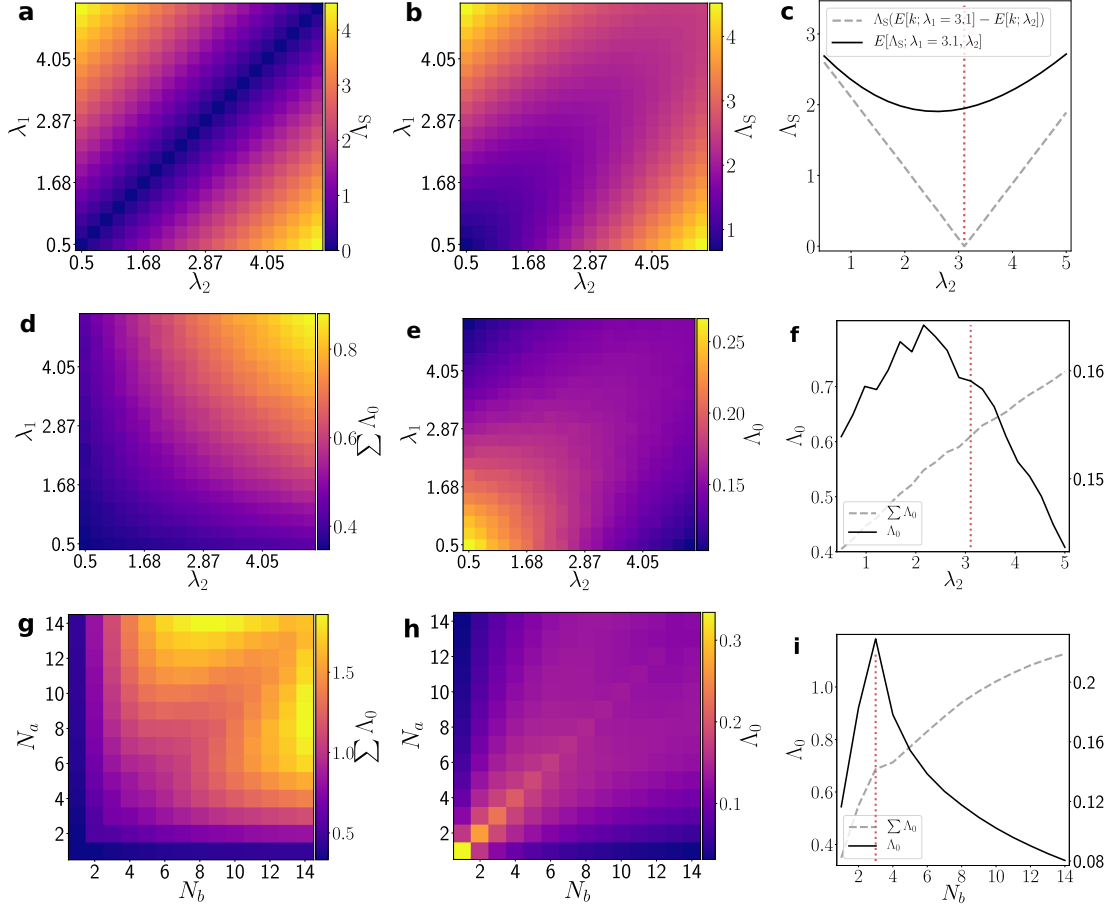


**Figure D.1:** Subcosts for adding/deleting (a-c) and shifting (d-i) operations for exponentially distributed sampling intervals. Only necessary deleting/adding operations are regarded (‘no competing operations’). The sampling rate-dependence of deletion costs is given as difference between expected number of samples per unit interval (left matrix and grey dashed line) and as expected costs given two rates  $\lambda_1, \lambda_2$  (right matrix and black line, eq. (D.10)). Shifting costs are studied (b) numerically with respect to their dependence on the sampling rates  $\lambda_1, \lambda_2$  and (c) on the actual number of samples per unit interval  $N_a, N_b$ . The left matrices shows shifting costs for the full transformation of segments, the center matrices show shifting costs per operation. Exemplary columns are displayed in the line plots whereas the red dashed line marks the respective rate  $\lambda_1$ /segment size  $N_b$ .



## Appendix B: sampling rate-constrained surrogates

The proposed sampling-rate correction approach involves a constrained randomization procedure, in which sampling rate-constrained surrogates (SRC-surrogates) are generated. To illustrate the resulting time series, we show five SRC-surrogate realizations of the irregularly sampled AR(1)-process from Sect. 8.4.2 in Fig. D.2. The transition in sampling rate (dotted red line) is well visible from the different surrogate realizations.

We can also identify the rapid increase in sampling rate for the grayscale proxy time series in the real-world example from Sect. 8.5 (Fig. D.3). Visually, it is expressed as an increase of variance which is reproduced by the SRC-surrogate realizations.

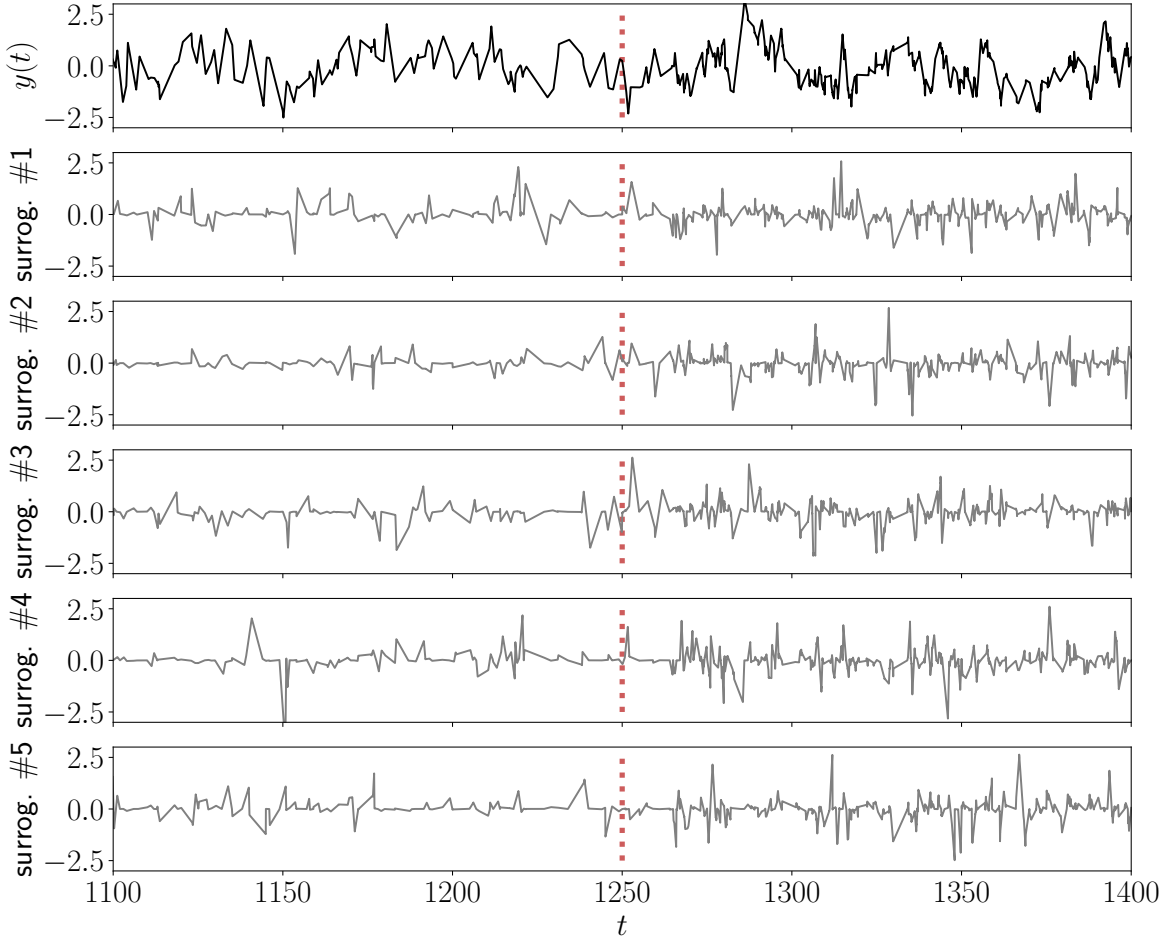


**Figure D.2:** Zoomed section of synthetic AR(1)-time series (black) and five exemplar SRC-surrogate realizations (gray). The red dotted line indicates the transition of the sampling rate towards more dense sampling. Sampling intervals are  $\gamma$ -distributed.

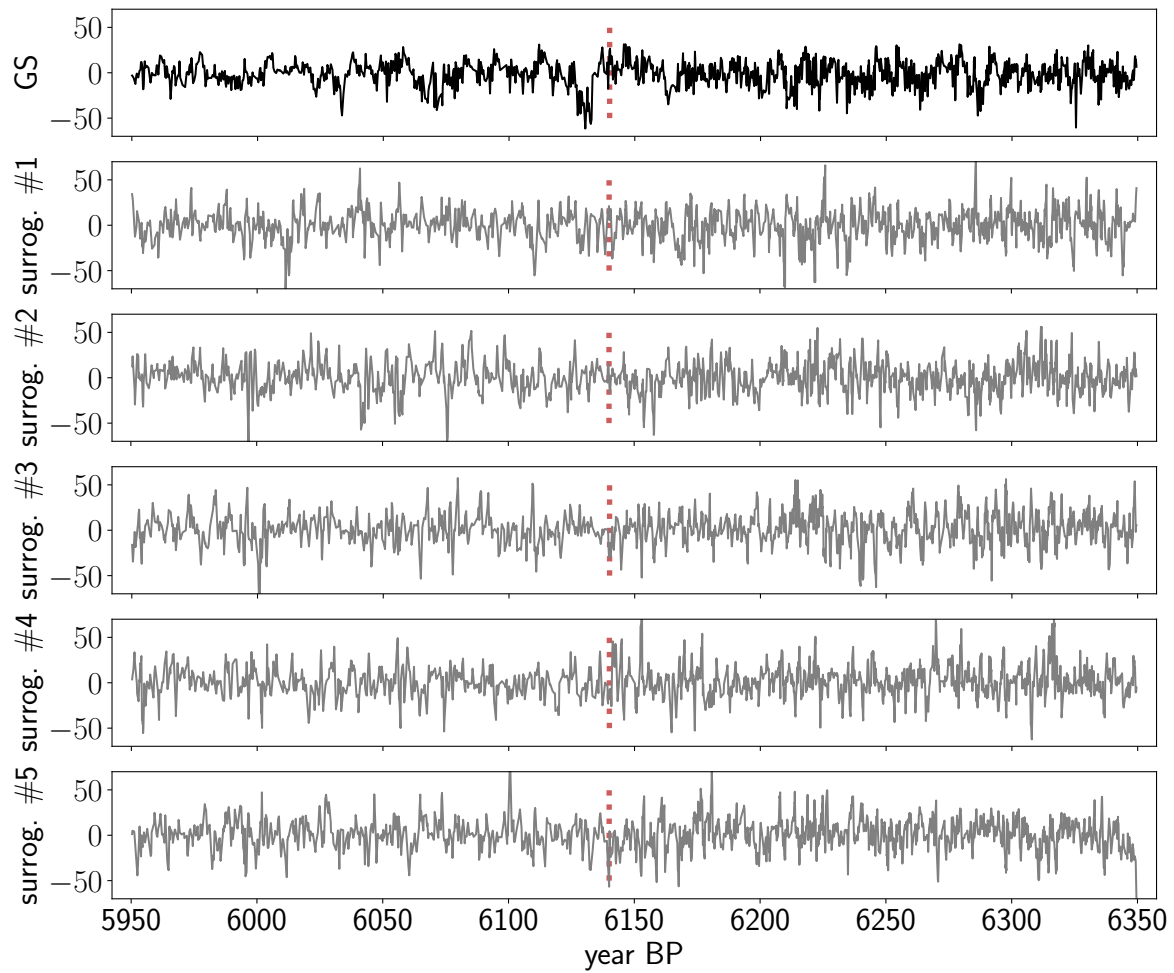


**Figure D.3:** Zoomed section of grayscale anomaly time series (black) and five exemplar SRC-surrogate realizations (gray). The red dotted line indicates the transition of the sampling rate towards more dense sampling.

## E | Supplementary material for Chapter 10: Mid-Holocene rainfall changes in the south- western Pacific

**Supplement 1:** Correlation of oxygen and carbon isotopes in stalagmite C132.

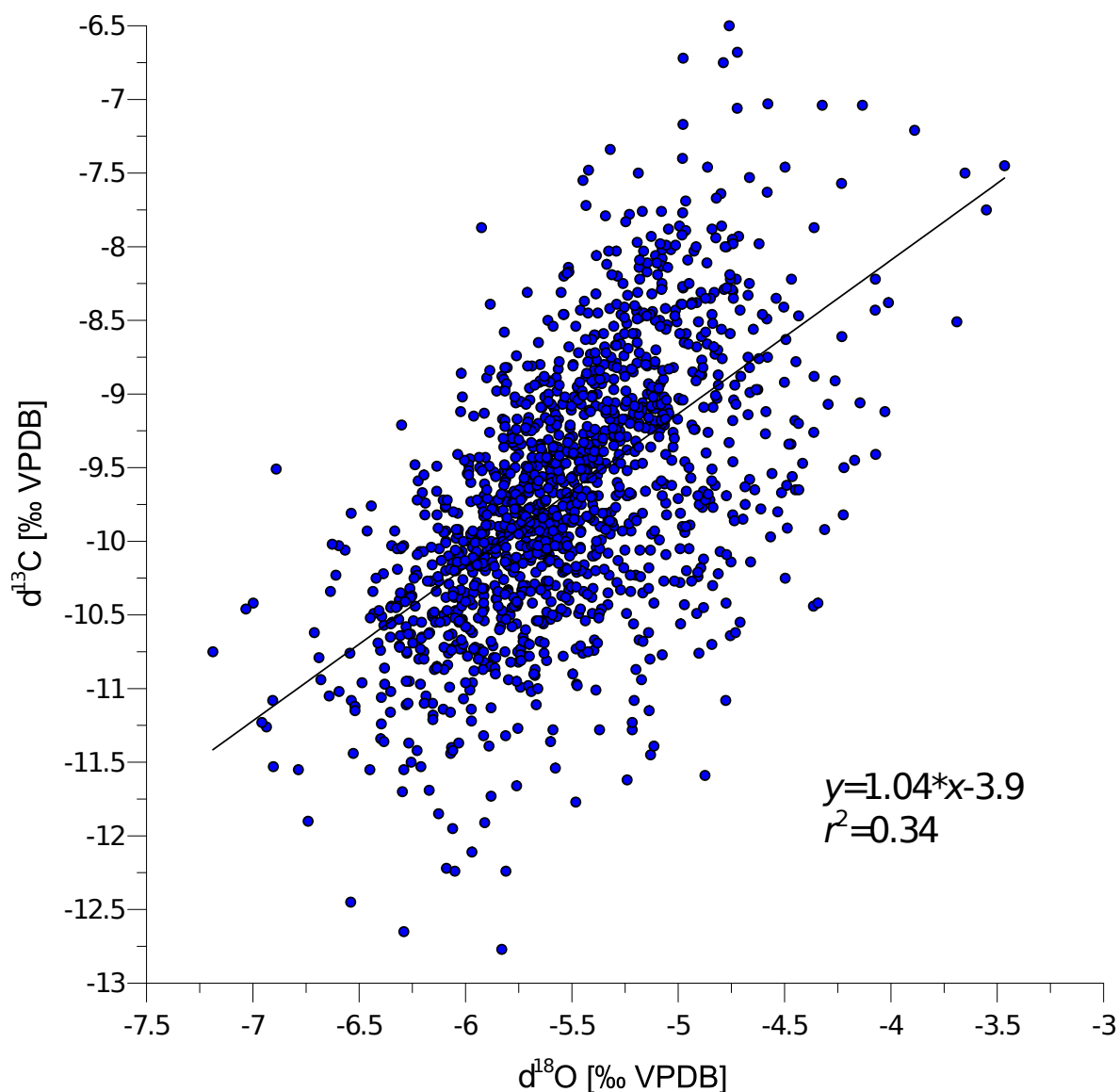


**Figure E.1:** Stalagmite C132 oxygen and carbon isotope ratios correlate in both, high and low resolution data sets.

**Supplement 2:** PCAs of the trace elements records at high resolution (30 $\mu$ m).

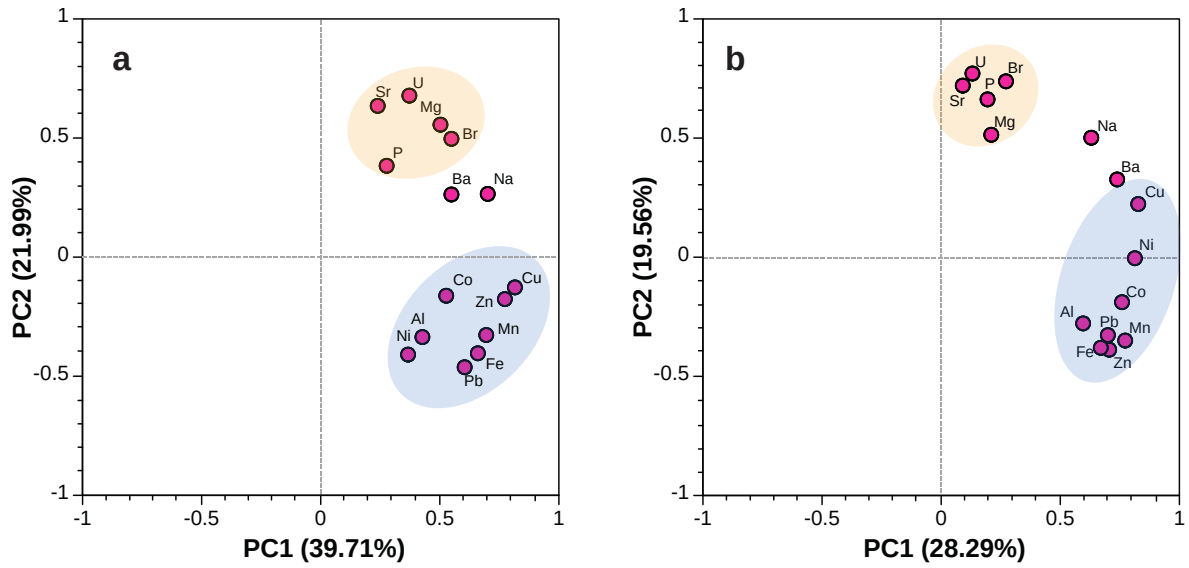


**Figure E.2:** Results of principal component analyses. a) PCA-3a, and b) PCA-3b. Two clusters are evident: group 1 is formed by Zn, Mn, Fe, Pb, and Al (blue shaded area), and group 2 comprises Sr, Mg, U and P (orange shaded area).

**Supplement 3:** Seasonality reconstruction.

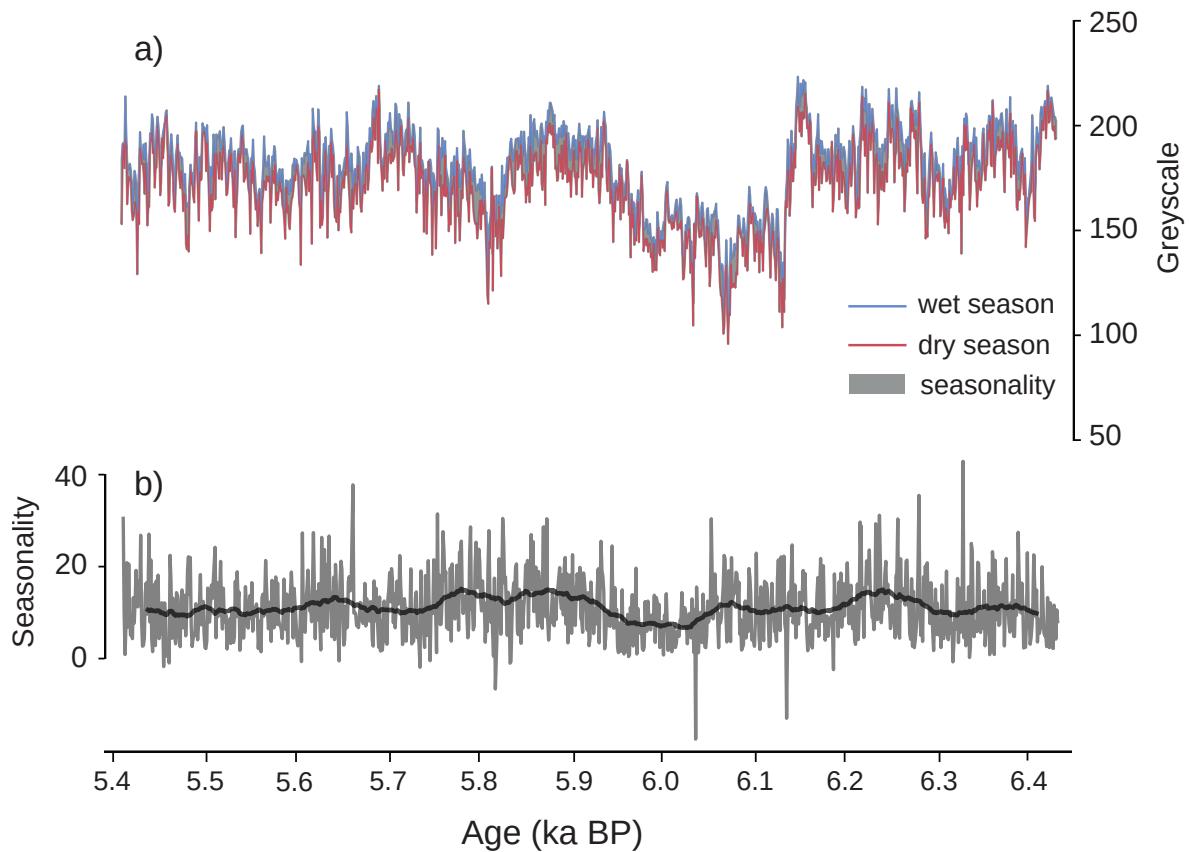


**Figure E.3:** a) seasonality (grey area) derived from the difference between the wet (blue line) and dry season (red line). b) seasonality record (grey line) and its running average (black line).

**Supplement 4:** Wavelet spectral analysis of the PCA-2.

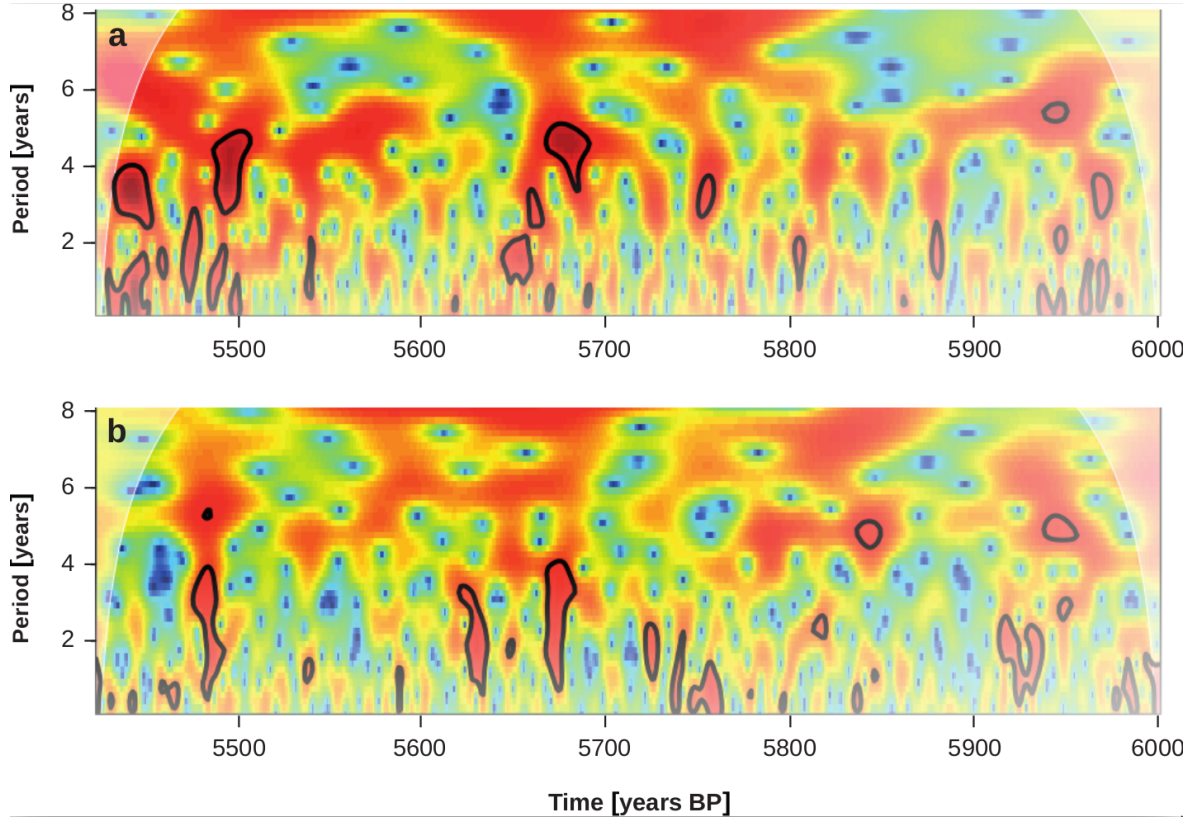


**Figure E.4:** Wavelet analysis of the principal components extracted from PCA-2 of the annually resolved C132 proxy records for the period of 5422 to 6002 y BP (a) PC1 and b) PC2). Significant periods are outlined in black.

#### Supplement 5: Recurrence plots.

Recurrence plots (RPs) are a powerful nonlinear time series analysis tool. In several applications, RPs have been effectively applied for the detection of abrupt transitions in palaeoclimate records [24]. An RP is represented by a symmetric 2-dimensional binary matrix in which each black dot denotes a recurrence between the states of the system at two times  $i$  and  $j$  while white dots mark no recurrences. The notion of recurrence is based on a distance measure (e.g., Euclidean distance) between the amplitudes of the studied time series at times  $i$  and  $j$ . In the study of nonlinear dynamical systems, a univariate time series often has to be regarded as a series of 1-dimensional observations of an underlying (but unknown) higher dimensional system, represented by a phase space trajectory. In order to obtain an RP that is based on this phase space representation of the system, time-delay embedding is the most common method to reconstruct the unknown phase space. To obtain RPs for the different segments of the seasonality time series, we estimated the embedding delay as the first zero-crossing of the autocorrelation ( $\tau = 2$ ) and the embedding dimension by the false nearest neighbour-algorithm ( $m = 3$ ) [526]. Using these embedding parameters, the time series was split into 200 yrs.-windows and an RP was computed for each embedded time series segment with a fixed recurrence rate of 15%. RPs exhibit different line structures that can be interpreted in context of the variability of the time series and which are often used to obtain quantitative measures of recurrence characteristics [42]. Diagonal lines reflect predictable dynamics whereas their length can be interpreted as a proxy for the predictability time of the system. To obtain an indicator of seasonal predictability, we analysed the occurrence of diagonal lines in each RP by the determinism measure DET which is defined as the fraction of diagonal lines exceeding a specified minimum length ( $l = 2$ ). Significance was assessed by bootstrap resampling of

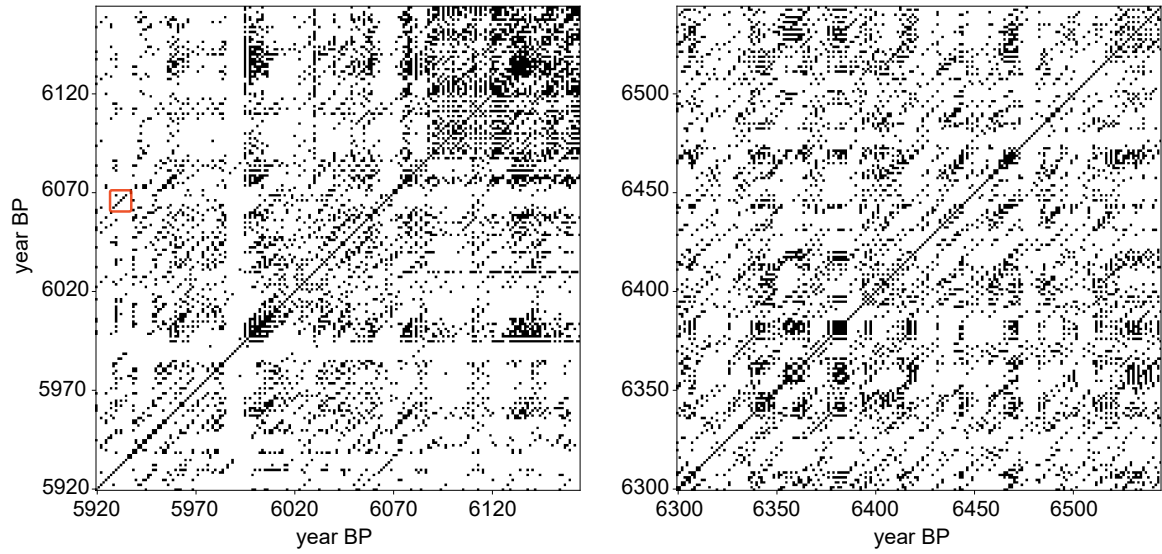


**Figure E.5:** Two exemplary recurrence plots that yield distinct determinism parameter DET values for the respective time periods, i.e.,  $DET = 0.28$  (left) and  $DET = 0.23$  (right). Both axes are time axes. Black dots mark recurrences between similar states. DET quantifies the number of diagonal lines that exceed a certain minimum line length ( $l_{\min} = 2$  years). An exemplary diagonal line of length  $l_{\min} = 6$  years is highlighted by a red box and reflects six years of predictable seasonal variations.

diagonal lines as described in [42]. Two exemplary RPs are shown in suppl. Fig. E.5.

**Supplement 6:** Correlation of rain and drip water oxygen and hydrogen isotope ratios.

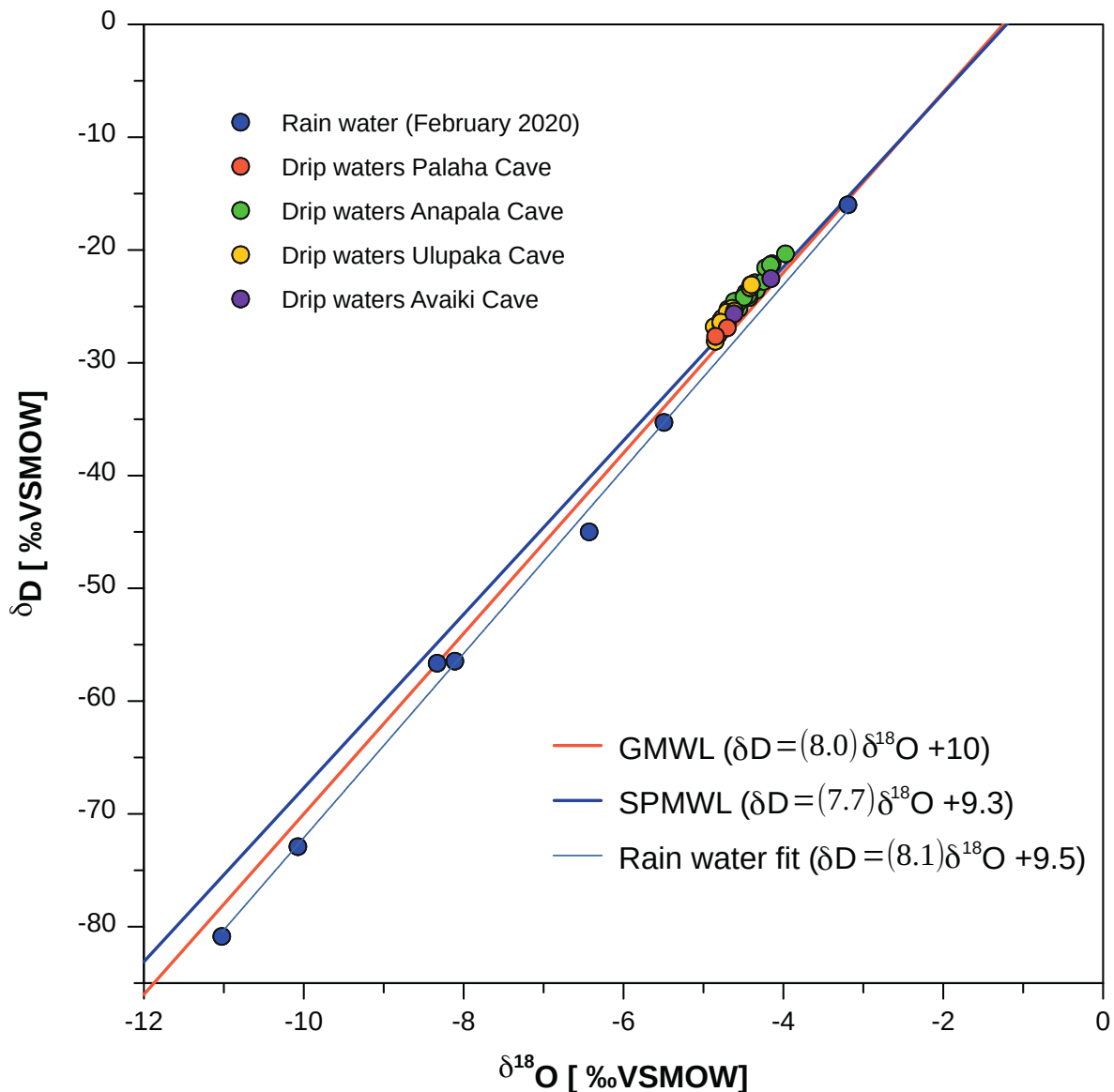


**Figure E.6:** Relationship between  $\delta^{18}\text{O}$  and  $\delta\text{D}$  of Niue rain and dripwater collected in February 2020. Dripwaters were collected from Anapala Cave (inland), Palaha Cave (sea cave), Ulupaka Cave (inland) and Avaiki Cave (sea cave). The collected samples plot along the SPMWL ( $\delta\text{D} = 7.7 \cdot \delta^{18}\text{O} + 9.3$ ) derived from rainfall data of neighboring Western Samoa and Rarotonga stations (IAEA/WMO, 2001) and show no signs of secondary evaporation.

## Technical details of the methods

### Speleothem stable isotope analyses at ETH Zurich

Between 90 and 140  $\mu\text{g}$  of sample powder was reacted with orthophosphoric at  $70^\circ\text{C}$  for 60 min. The resulting  $\text{CO}_2$  was then sampled and transported in a helium stream to the mass spectrometer. Details on the methods can be found in [527]. Reference materials include the international standards NBS19 and NBS18. The long-term  $1\sigma$  reproducibility of the internal standard is 0.05 ‰ for  $\delta^{13}\text{C}$  and 0.08‰ for  $\delta^{18}\text{O}$ .

## LA-ICP-MS device specifications

Analyses were conducted using a laser repetition rate of 20 Hz with a 60  $\mu\text{m}$  diameter ablation spot and scanning the sample at 29.55  $\mu\text{m}/\text{sec}$  with a beam energy density of 5  $\text{J}/\text{cm}^2$ , yielding a spatial resolution of 30  $\mu\text{m}$ . Signals for  $^{23}\text{Na}$ ,  $^{24}\text{Mg}$ ,  $^{27}\text{Al}$ ,  $^{29}\text{Si}$ ,  $^{31}\text{P}$ ,  $^{34}\text{S}$ ,  $^{44}\text{Ca}$ ,  $^{55}\text{Mn}$ ,  $^{56}\text{Fe}$ ,  $^{60}\text{Ni}$ ,  $^{63}\text{Cu}$ ,  $^{66}\text{Zn}$ ,  $^{88}\text{Sr}$ ,  $^{137}\text{Ba}$ ,  $^{208}\text{Pb}$ , and  $^{238}\text{U}$  were monitored during analysis in a single track. The ICP-MS was optimised daily for maximum sensitivity. The ICP-MS operating settings are: forward power of 1350 watts, plasma gas flow rate of 15 L/min (Ar), carrier gas flow of 0.99 mL/min (nebuliser), sampling depth of 4 mm, pulse counting detector and peak hopping sweep mode, 0.01-0.1 s dwell time and one point per peak. Calcium was used as internal standard, assuming a concentration of 40.04 wt%. Background counts (He gas background, measured with the laser off) were collected for 45 seconds between samples. NIST (National Institute of Standards and Technology) glass standards 612 and 610 were analysed after every sample track (ca. 3 cm long) to account for any drift. Raw data were processed using Iolite v3.32 [528]. Background counts were subtracted from the raw data and all data were standardised to NIST 612. NIST 610 was utilised as a secondary standard. The GeoReM database [529] was used for NIST glass reference values.

## Spectral analysis

The continuous wavelet analysis of the greyscale record (Fig.10.6a), utilised linear interpolation with a sampling time of one year. Irregular sampling in the time dimension results in variations in the number of samples per year, biasing estimates of mean season-specific rainfall, a problem that is not resolved by interpolation. Significance testing of wavelet power was thus based on Monte-Carlo sampling of AR(1)-realisations computed by the REDFIT algorithm [338] to obtain an individual 95% confidence level for each time instance and period. The same procedure was applied to the seasonality time series (Fig. 10.6b) by transforming each AR(1)-surrogate into a ‘seasonality-surrogate’.

## Recurrence analysis

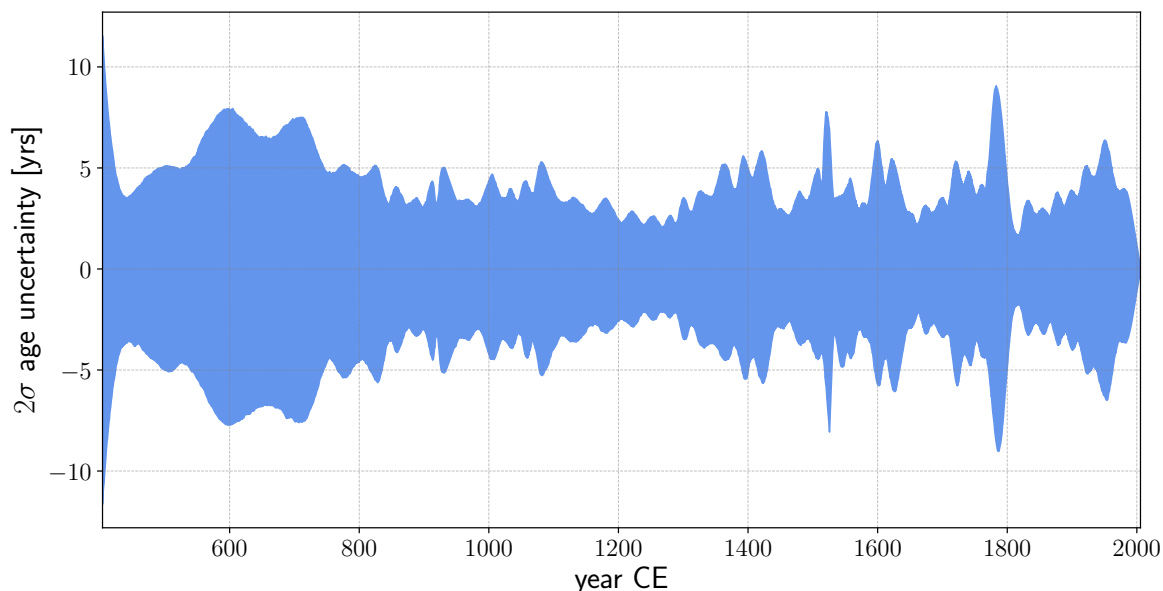
Diagonal lines in a RP reflect deterministic variations in a time series which can be characterised by the determinism parameter DET (see above). We characterised the seasonal-scale predictability by computing a DET value for each RP (Fig. 10.7g), and tested the hypothesis that no significant shift in DET has occurred over the covered period following the bootstrapping approach proposed by [42].



# F | Supplementary material for Chapter 12: Decline in seasonal predictability as potential trigger of Terminal Classic Maya Collapse

## Proxy records

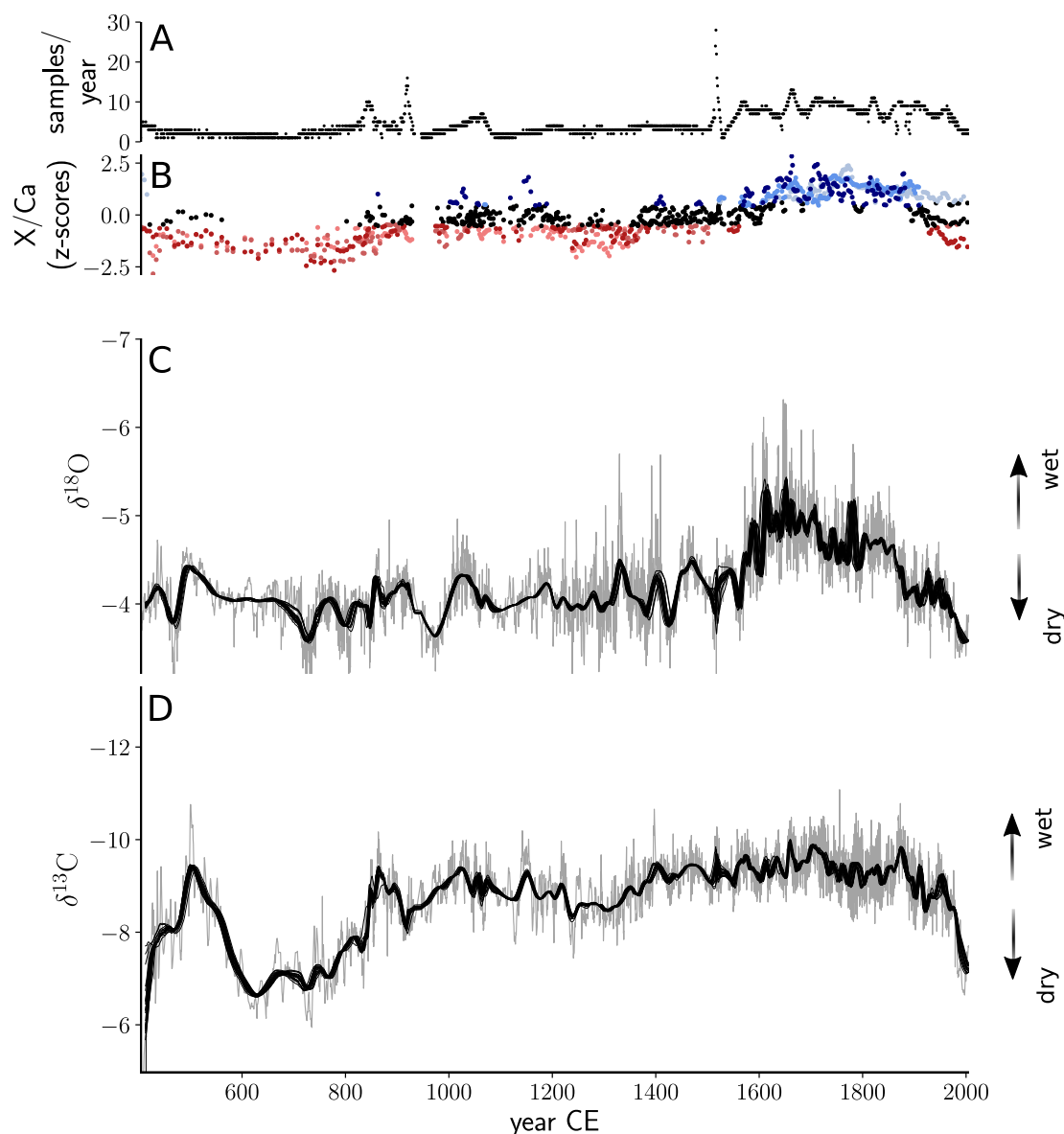
The age model of the studied record is shown in [362]. We use the  $2\sigma$  age uncertainty from the distribution of COPRA modelled ages given at each sampled depth as an estimate for the 95% confidence bounds (Fig. SF.1). Sampling resolution and long-term evolution of stable isotope records and trace element records (Ba/Ca, Sr/Ca, U/Ca) is shown in Fig. SF.2. Prior to spectral analysis, the computation of proxy correlations and the recurrence analysis, we apply a detrending based on Singular Spectrum analysis (SSA) [300] (Fig. SF.3.). Using SSA, a non-stationary time series can be decomposed into a sum of components that capture time scale-specific modes of variability, i.e., trends, periodic cycles and fast variations/noise. First, a trajectory matrix is generated from time-shifted copies of the time series by choosing a window length  $w$ . Next, a singular value decomposition of the trajectory matrix and grouping of eigenvalues yields the SSA components.



**Figure F.1:** Evolution of  $2\sigma$  age uncertainty after application of COPRA age model (50 U/Th-dated depths).

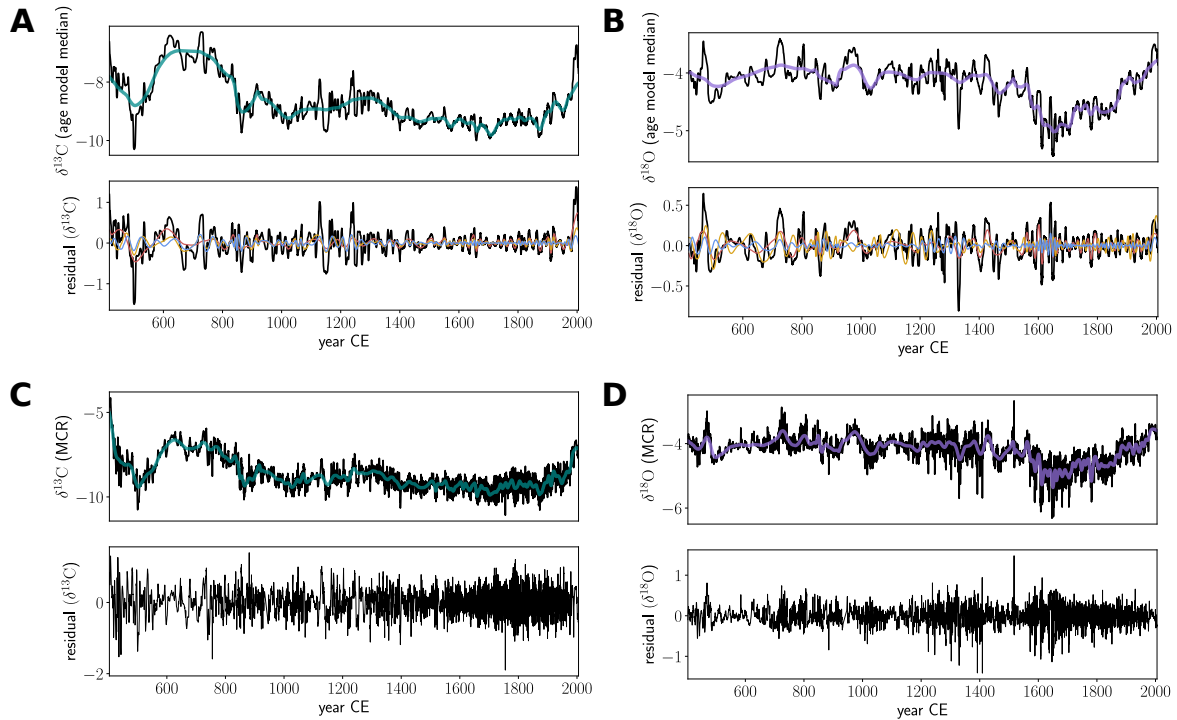
We only use the first component to detrend the age model medians and most central proxy realizations. Multi-decadal correlations between  $\delta^{13}\text{C}$  and  $\delta^{18}\text{O}$  (as discussed in Fig. 4 of the

main manuscript) are computed based on the residuals that result after extracting the first SSA component ( $w \approx 35\text{yr}$ ) (Fig. SF.3 A/B). Both the spectral and recurrence analysis are based on the full ensemble of age model realizations from which each is individually detrended with the first SSA component ( $w \approx 10\text{yr}$ , (Fig. SF.3 C/D).



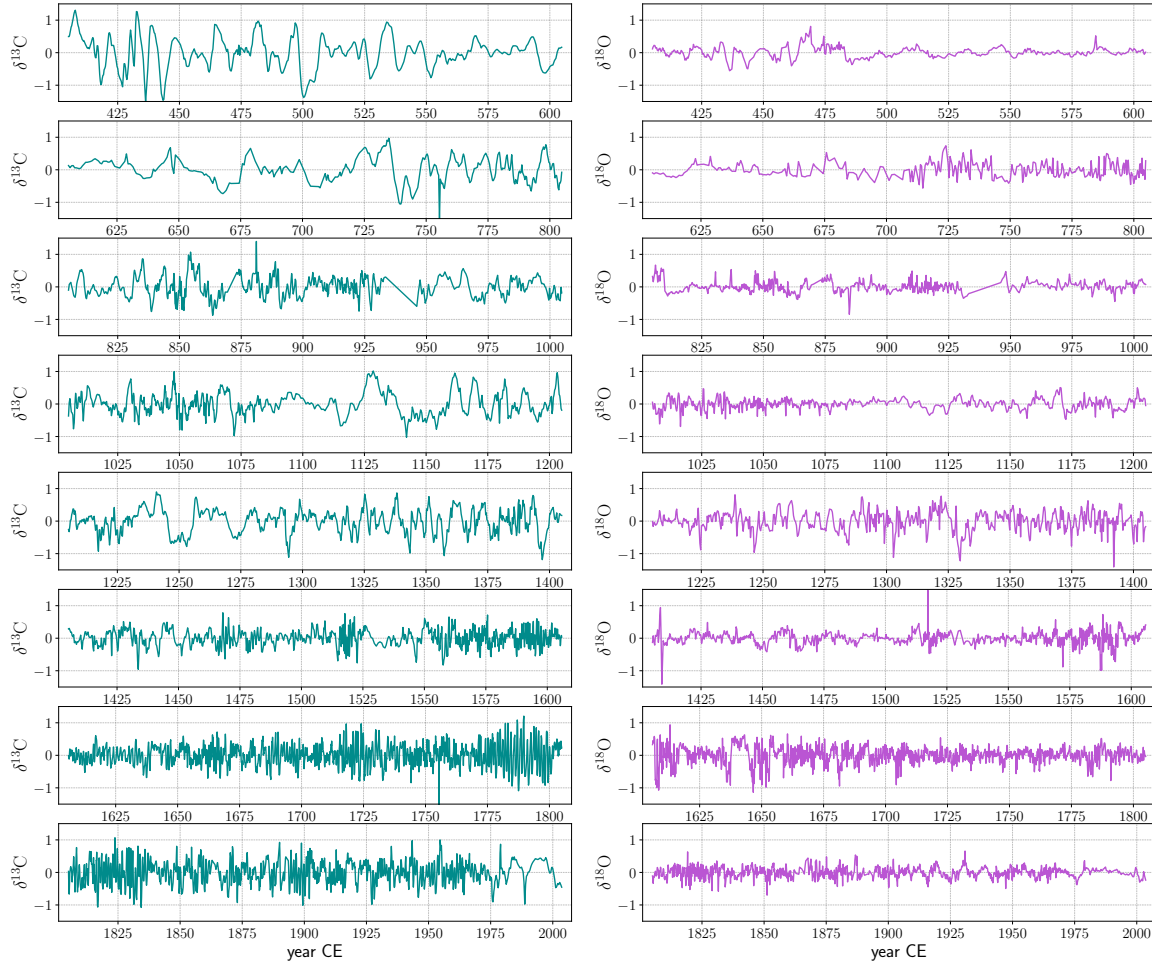
**Figure F.2:** Long-term variability of YOK-G proxy records. (A) Sampling resolution (samples/year) in the age-modelled stable isotope records. (B) z-scores of trace elements (Ba/Ca, Sr/Ca, U/Ca) to substantiate interpretation of stable isotope records.  $\delta^{18}\text{O}$  (C) and  $\delta^{13}\text{C}$  (D) long-term trends are individually estimated for all  $\delta^{18}\text{O}$  and  $\delta^{13}\text{C}$  proxy realizations as the first component of a Singular Spectrum Analysis ( $w \approx 10\text{yr}$ , trends for 50 realizations displayed). The maximum-correlated age model realizations for both isotope records (gray) additionally exhibit fluctuations at seasonal time scales.

Figure SF.4 allows a detailed inspection of variability at seasonal time scales as retrieved after detrending of both stable isotope record's most central realization (MCR, see methods in the main manuscript). Their correlation at seasonal time scales is continuously positive



**Figure F.3:** Detrending of age model medians and most central realizations using Singular Spectrum analysis (SSA). **(A)** Detrending of  $\delta^{13}\text{C}$  age model median with the first component returned by SSA (cyan). The residual is shown below, including the next three leading SSA components (red, yellow, blue). **(B)** same as (A), but for  $\delta^{18}\text{O}$ . **(C)** Detrending of  $\delta^{13}\text{C}$  most central realization with the first component returned by SSA (cyan). The residual is shown below, no additional components displayed for the sake of visibility. **(D)** same as (C), but for  $\delta^{18}\text{O}$ .

(and mostly significant tested against AR(1)-surrogates) throughout the Common Era (Fig. SF.5). At multi-decadal time scales, periods of insignificant and significantly negative proxy correlation stand out (Fig. SF.6).



**Figure F.4:** Most central realizations of  $\delta^{13}\text{C}$  (left) and  $\delta^{18}\text{O}$  (right) for the full covered time period (after detrending). They act as a representation for the full ensemble of age model realizations as they have the highest average correlation to all other realizations.

## Time-frequency analysis

We use Lomb-Scargle (LS) periodograms along with Continuous Wavelet Spectra (CWS) to examine the significance of the seasonal cycle and ENSO–multi-decadal-scale cycles throughout the Common Era for both stable isotope records. Both proxy records are split into five segments (430 - 650 CE, 650 - 950CE, 950 - 1400 CE, 1400 - 1800 CE and 1800 - 2005 CE) and Lomb–Scargle periodograms are computed for each segment separately. Welch spectra are computed to obtain robust estimates of spectral power with reduced noise intensity. We choose the number of sub-segments  $n_{\text{seg}}$  for each segment such that each sub-segment approximately covers 500 samples, corresponding to approximately 60 – 300 yrs. Each sub-segment is weighted with a Blackman-window to limit the effect of spectral leakage. We choose twice the average Nyquist frequency  $2f_{\text{Nyq}} = 1/\Delta\bar{t}$  as an upper limit for the frequency range. Each frequency is spaced with  $\Delta f = (n_{\text{seg}} + 1)/2\sigma T\Delta\bar{t}$  whereas  $T$  is the length of a time series segment,  $\Delta\bar{t}$  is the average sampling interval and  $\sigma = 2$  is the oversampling factor. We repeat the computation of LS-periodograms for a given time period for each MC-realization and averaged afterwards. Significance of spectral peaks is assessed by means of AR(1)-surrogates [530]. AR(1)-surrogates are frequently used for hypothesis testing in the paleoclimate literature [338]. The underlying idea is that in a low-order approximation, proxy time series

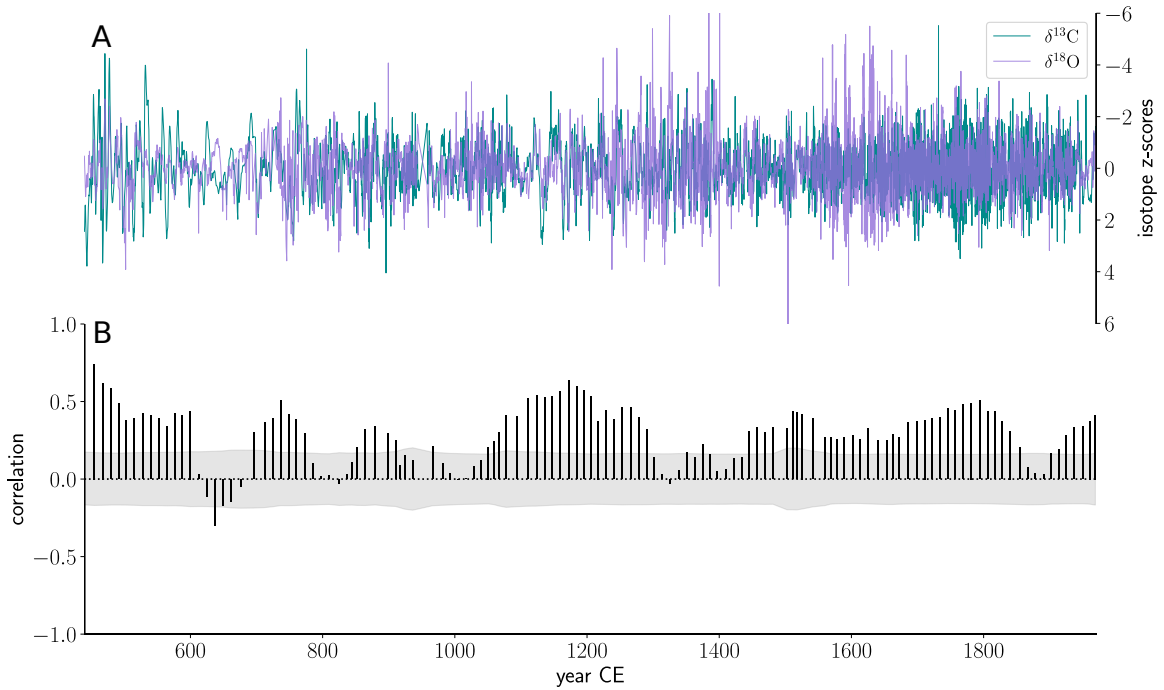


**Figure F.5:** (A) Most central realization z-scores of  $\delta^{13}\text{C}$  and  $\delta^{18}\text{O}$  after extraction of individual trends using SSA. (B) Averaged seasonal-scale correlation between 2000 pairs of  $\delta^{13}\text{C}$  and  $\delta^{18}\text{O}$  age model realization z-scores. Correlations are computed on 50 year-sliding windows and tested against 1000 (irregularly sampled) AR(1)-surrogates (gray shading).

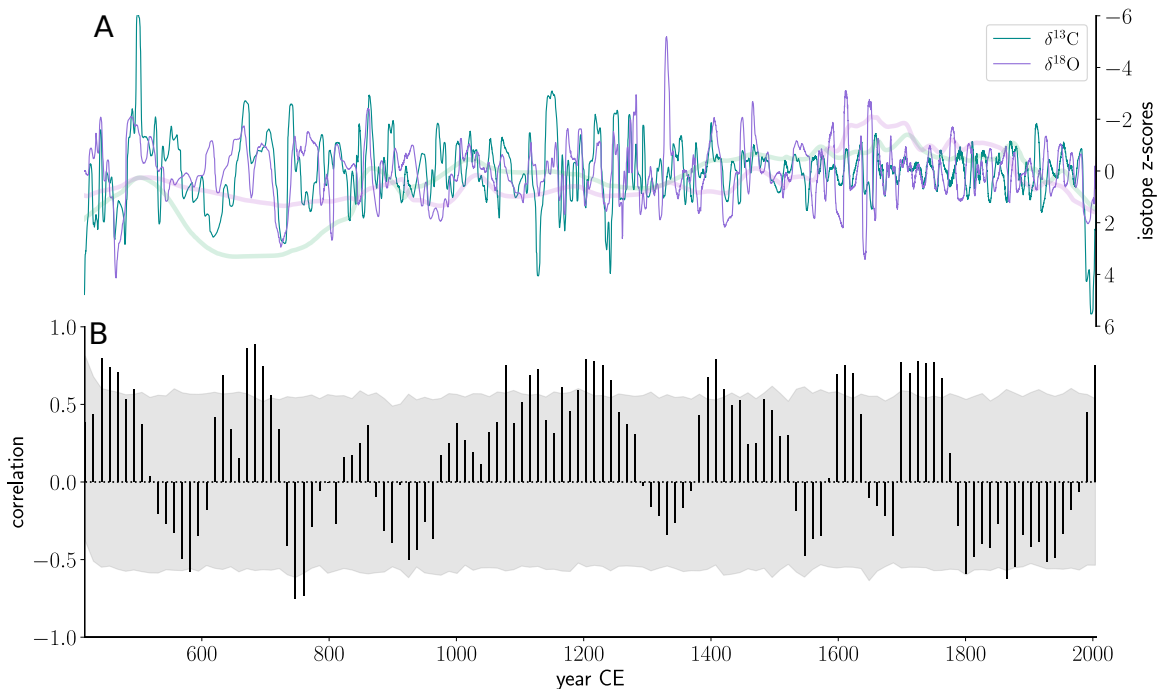


**Figure F.6:** (A) Age model median  $\delta^{13}\text{C}$  and  $\delta^{18}\text{O}$  z-scores after extraction of trends (shaded) using SSA. (B) Multidecadal correlations are computed on 50 year-sliding windows and tested against 1000 (irregularly sampled) AR(1)-surrogates (gray shading) (B).

exhibit deterministic (e.g. seasonal) variability superimposed on a background of correlated noise. By sampling  $N_s$  surrogate time series that resemble the correlated noise, it is tested whether the observed value for a statistic can occur just ‘by chance’ or if its occurrence is significantly different from the modelled noise time series. It is important to note that all AR(1)-surrogates are generated on the real unevenly spaced time axis and thus also recover the features which are affected by sampling biases. An  $\alpha$ -confidence level is obtained for each MC-realization separately and subsequently averaged.

For the computation of CWS for both stable isotope time series, we account for age-uncertainty following the scheme described in the methods to test whether the results obtained in [362] can be confirmed when uncertainties are included. In a first step, linear interpolation is applied to obtain a regular time axis with even spacing. The choice of the sampling interval  $\Delta t$  requires caution; if it is chosen too high, spurious serial dependence is imposed on the time series and will result in erroneous spectral peaks. In an attempt to limit the impact of spurious serial dependence, the root-mean-square error (RMSE) between the real LS-periodograms and LS-periodograms computed from interpolated time series is minimized. This optimization is displayed in Fig. SF.7 and yields a value of  $\Delta t = 0.30$ , averaged over the distinct optimal values obtained for  $\delta^{13}\text{C}$  and  $\delta^{18}\text{O}$ . This sampling interval is still low enough to assess seasonal variability ( $\Delta t < 0.50$ ). Continuous Wavelet transformation (as described in [356]) is carried out using the PyCWT package in Python with a Morlet mother Wavelet. Significance of spectral power is tested for each realization by generating 100 irregularly sampled AR(1)-surrogates, applying the same interpolation procedure to each and computing the resulting 90%-confidence level. The respective 90%-quantiles are computed for each time instance since variations in the sampling density entail variations in the significance of spectral peaks. A ‘MC-Wavelet spectrum’ is obtained by counting the number of realizations which indicate significant spectral power for a given period and time instance. If more than half of all realizations indicate significant spectral power, the corresponding cycle at a given time instance is considered significant within the given age uncertainty.

The resulting MC-Wavelet spectrum (Fig. SF.8) shows less spectral background noise than a regular Wavelet spectrum (see Fig. SF.9/SF.10 for comparison). Throughout some episodes, both proxy time series are not sufficiently resolved to reliably detect an annual cycle (see Fig. SF.2A, e.g. 700 CE) as the sampling frequency drops below the Nyquist frequency. It is well known that in such cases, aliasing can occur and may introduce spurious lower frequency cycles in spectral estimates. We perform a basic MC-sampling test to identify which aliased cycles might occur just due to a masked annual cycle. To this extent, a sinusoidal with annual periodicity is generated on the original irregular time axis and linear interpolation is applied as described above. Age uncertainty is mimicked by generating 2000 sinusoids with random phases which are drawn from a  $\mathcal{N}(0, \sigma_a)$ -distribution with the real standard deviation of ages  $\sigma_a$  obtained from COPRA. An example of the interpolated and non-interpolated sinusoidal time series is shown in Fig. SF.11 for a time period where aliasing effects can be observed. Ten MC-Wavelets are computed (with different random seeds for the phase distribution) and averaged, resulting in a single MC-Wavelet spectrum for the sinusoids. The white hatching in Fig. SF.8B/D indicates regions of masked seasonal variability caused by aliasing. Thus, any overlap between significant spectral power and the hatched spectral aliasing patches could actually reflect an annual cycle that can not be resolved rather than the indicated period.

Figure SF.9/SF.10 shows Wavelet spectra of the MCR of both stable isotope records. Comparing them to the MC-Wavelet spectra shown in Fig. SF.8B/D, it becomes clear that the latter recover most of the significant cycles that are found for the MCR, demonstrating that these cycles are significant also when age uncertainty is taken into account. This adds confidence to the findings from the LS-spectra and suggests that especially after 1400 CE, the seasonal cycle remains relatively stable. These observations align with the results in [362]

where the same  $\delta^{13}\text{C}$  record was studied but without computing MC-Wavelet spectra based on single proxy realizations. The finding of a strengthened, more pronounced seasonal cycle in the post-1400 CE period is further bolstered by the MC-Wavelet spectrum of all  $\delta^{18}\text{O}$  realizations in Fig. SF.8D where a high number of realizations indicate relatively high power in the annual band. These results complement and corroborate the transition in rainfall seasonality detected in the YOK-G  $\delta^{13}\text{C}$  record [362].

Between 435-950 CE, several years have less than two samples and do consequently not allow for reliable extraction of a seasonal cycle ( $f < f_{\text{Nyq}} = 2/\text{year}$ ). Some overlap of real spectral power and white hatched regions hints at the possibility that during these periods, a muted seasonal cycle could have also been present but can not be extracted reliably due to the low growth rate of the stalagmite during persistent drought conditions.

Beyond the observed variations in seasonal variability, distinctiveness of inter-annual and (multi-)decadal-scale cycles are also found to vary throughout the records. Both proxy records suggest that ENSO- (2-8 years) and (multi-)decadal-scale variability were more pronounced in the pre-1400 CE period. The presence of ENSO-scale variability is particularly strong in the  $\delta^{13}\text{C}$  record.

We show the LS spectra after averaging single-realization based spectra over all 2000 (detrended) realizations of  $\delta^{13}\text{C}$  and  $\delta^{18}\text{O}$  for the five time intervals in Fig. SF.8A/C. The (cyan and purple) triangles yield a less conservative estimate of significant cycles without accounting for age uncertainty and indicate that for the MCR, a seasonal cycle can be identified for each time interval and both proxies with 95% confidence. Yet, only between 950-2005 CE a robust seasonal cycle is identified in the  $\delta^{13}\text{C}$  record when accounting for age uncertainty (cyan shading).

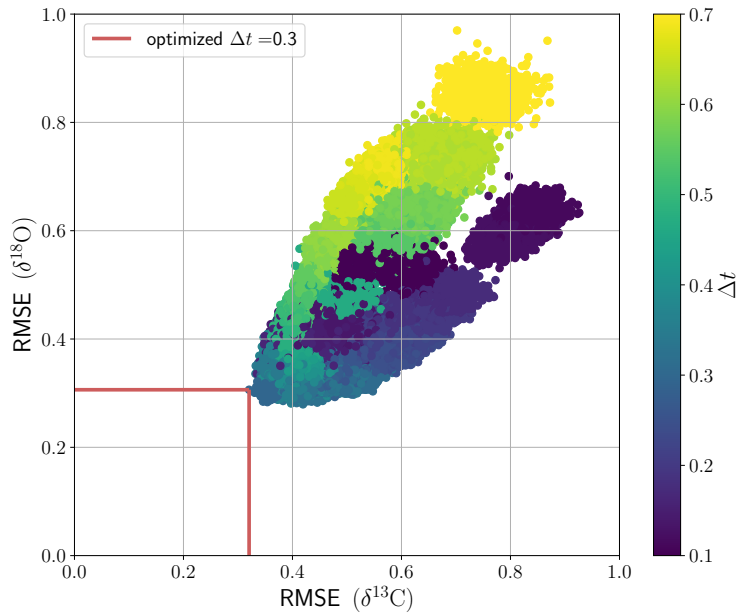


**Figure F.7:** Optimization of sampling interval  $\Delta t$  for linear interpolation (used exclusively in Wavelet analysis). Root-mean-square errors (RMSE) between Lomb-Scargle spectra for interpolated and non-interpolated time series are shown for all realizations of both stable isotope records. The trade-off value of  $\Delta t = 0.30$  years for which the sum of both RMSEs is minimized is indicated in red.

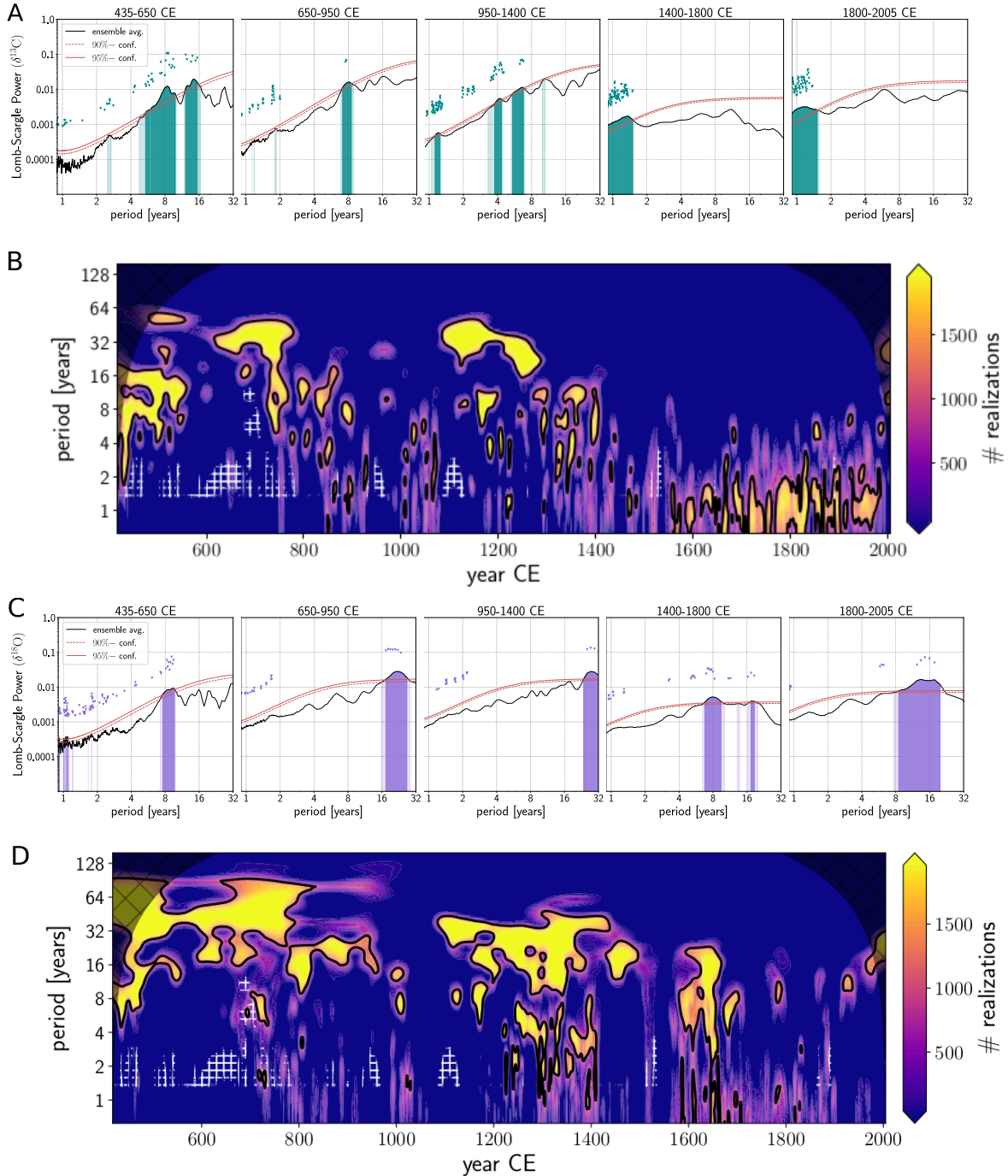


**Figure F.8:** Time-frequency analysis of stable isotope records: LS spectra for five segments of the  $\delta^{13}\text{C}$  (A) and  $\delta^{18}\text{O}$  (C) record respectively. Median spectral power, computed from 2000 detrended proxy realizations (black) is tested for significance using irregularly sampled AR(1)-surrogates (red). Significant cycles in the MCR are indicated by triangles. Computation of an individual continuous wavelet spectrum for each (linear interpolated & detrended) proxy realization results in a single MC-wavelet spectrum, shown for  $\delta^{13}\text{C}$  (B) and  $\delta^{18}\text{O}$  (D) respectively. Color coding denotes the number of proxy realizations that indicate a significant cycle. Black contours mark cycles for which more than half of all realizations indicate significant spectral power. White hatching marks regions of potential aliasing.



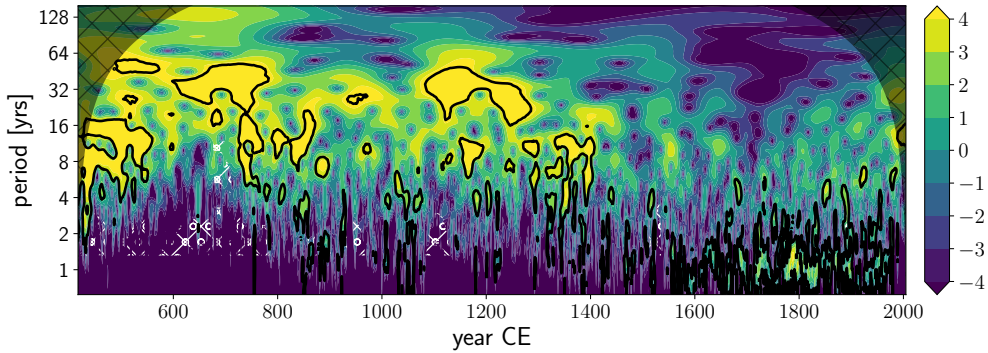


**Figure F.9:** Continuous wavelet spectra for most central realizations of  $\delta^{13}\text{C}$  age model ensembles. Spectral power is tested against a red noise background spectrum, generated from 2000 irregularly sampled and interpolated AR(1)-surrogates (90% confidence level).

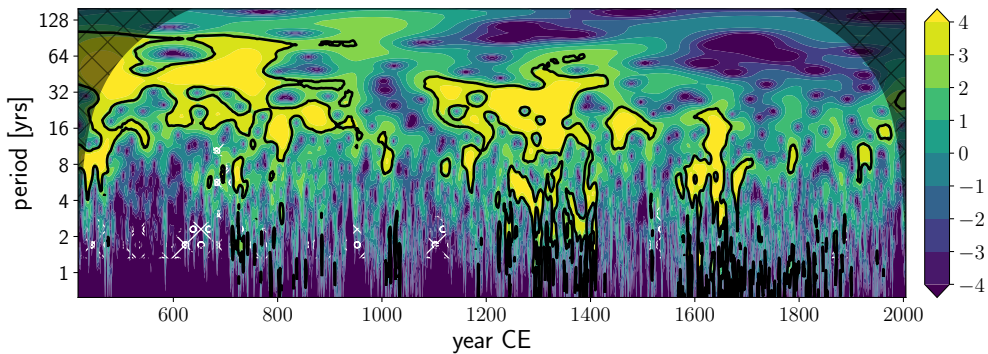


**Figure F.10:** Continuous wavelet spectra for most central realizations of  $\delta^{18}\text{O}$  age model ensembles. Spectral power is tested against a red noise background spectrum, generated from 2000 irregularly sampled and interpolated AR(1)-surrogates (90% confidence level).

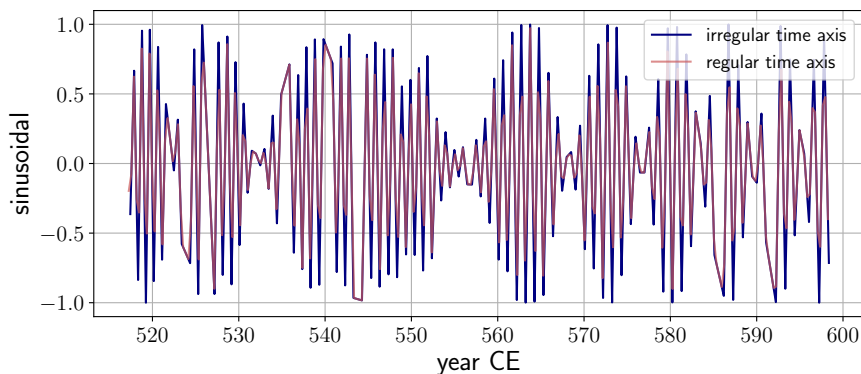


**Figure F.11:** Illustration of aliasing effect that occurs when sampling resolution falls below the Nyquist frequency of 2 samples/year based on a synthetic sinusoidal time series with a period of one year and the real proxy time axis (blue). Higher periods are appearing as an artefact due low sampling resolution and are not eliminated by linear interpolation (red). 1000 sinusoids with random phases are generated to inform about the resulting spurious but significant longer cycles in the Wavelet spectrum (suppl. fig. 8).

## Recurrence analysis

The recurrence analysis described in the methods of the main manuscript results in a total of 69 recurrence matrices on sliding windows for each proxy-realization. Six exemplary recurrence plots are shown in Fig. SF.12 for both stable isotope records. In the recurrence quantification analysis, the mean diagonal line length was used to describe changes in the predictability time of hydroclimate variability. In some of the examples (e.g. third row from top), striking block structures can be seen that solely arise from a finite-sampling effect of the (m)edit-distance discussed in [2]. Thus, sampling-rate constrained (SRC)-surrogates that reproduce this spurious effect and mimic the resulting recurrence properties are generated (displayed in the right columns). While the general structure (including the macroscopic block structures) are conserved by the surrogates, the microstructures (e.g. diagonal lines) differ between the real and the surrogate-based RPs.

In Fig. 2-4 of the main manuscript, the mean diagonal line length (denoted by  $T_{\text{pred}}$ ) is corrected for this effect based on the mean diagonal line lengths  $T_{\text{pred}}^{(\text{surr})}$  of the surrogate RPs for each window, yielding  $\tau_{\text{pred}}$ . We conduct the same analysis for the  $\delta^{18}\text{O}$  record (Fig. SF.13B/D). The mean predictability time  $\tau_{\text{pred}}$  computed from  $\delta^{18}\text{O}$  declines more rapidly but supports low seasonal rainfall predictability during the Terminal Classic period. After an increase towards 1200 CE that aligns well with the mean predictability time suggested by  $\delta^{13}\text{C}$ , seasonal rainfall amount appears well predictable during the LIA around 1600 CE (Fig. SF.13B). Both stable isotope records indicate declining seasonal predictability towards the modern period. Linking seasonal predictability to the hydroclimatic background state, both stable isotope records show significantly different relationships between seasonal predictability and long-term isotopic averages than expected from the random null model (gray dots, Fig. SF.13C/D). Furthermore, both stable isotope records showcase that a simple linear relationship in the sense ‘the drier, the less predictable’ would not suffice to capture the complexity of how seasonality and long term aridity are intertwined in the Maya lowlands.

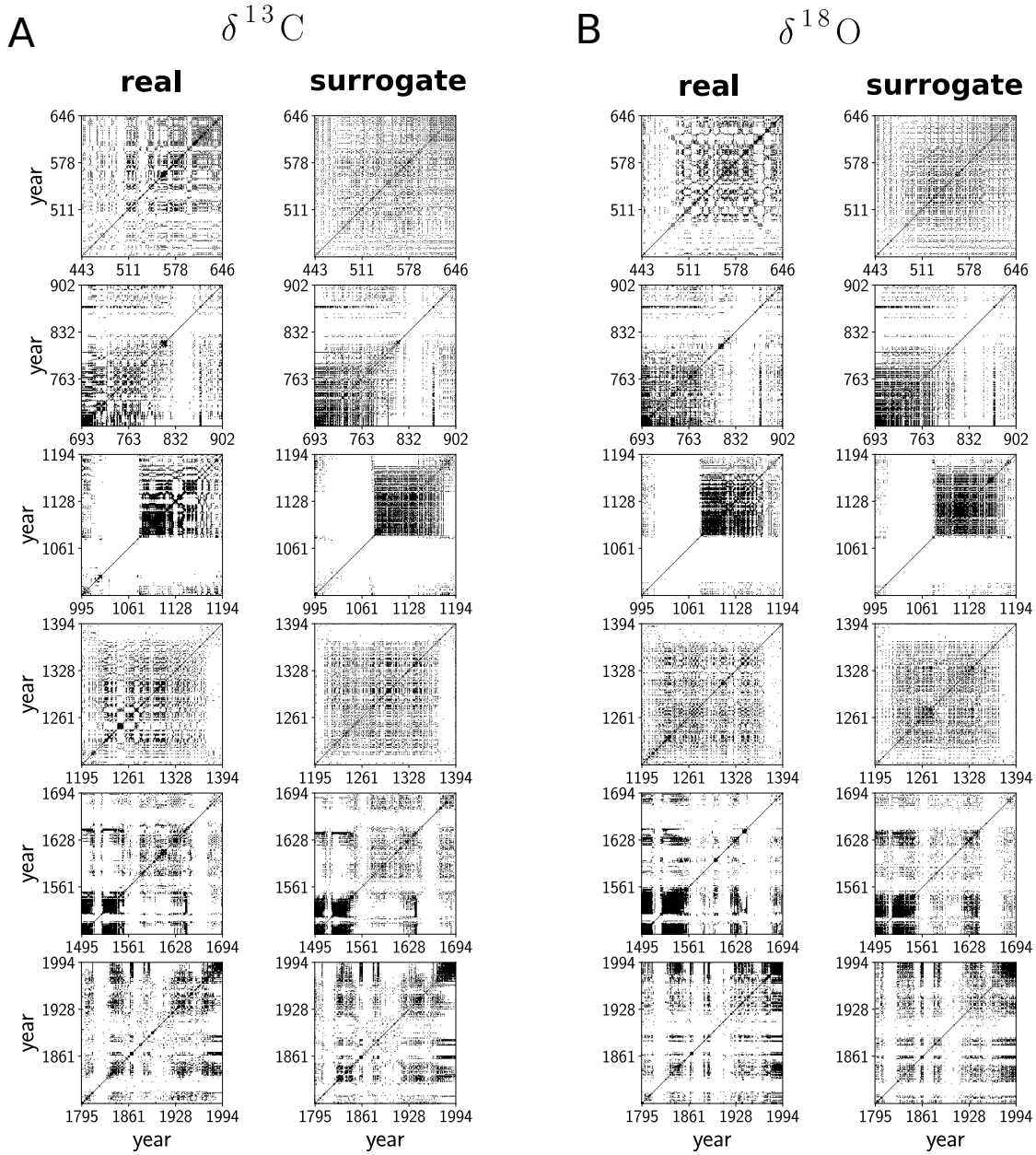


**Figure F.12:** Exemplary recurrence plots from the sliding window recurrence analysis (**A**:  $\delta^{13}\text{C}$ , **B**:  $\delta^{18}\text{O}$ ). Real RPs are shown in the left column and SRC-surrogate RPs are shown in the right column, respectively. Each RP covers a time window that correspond to 200 years and is computed with the (m)edit distance method.

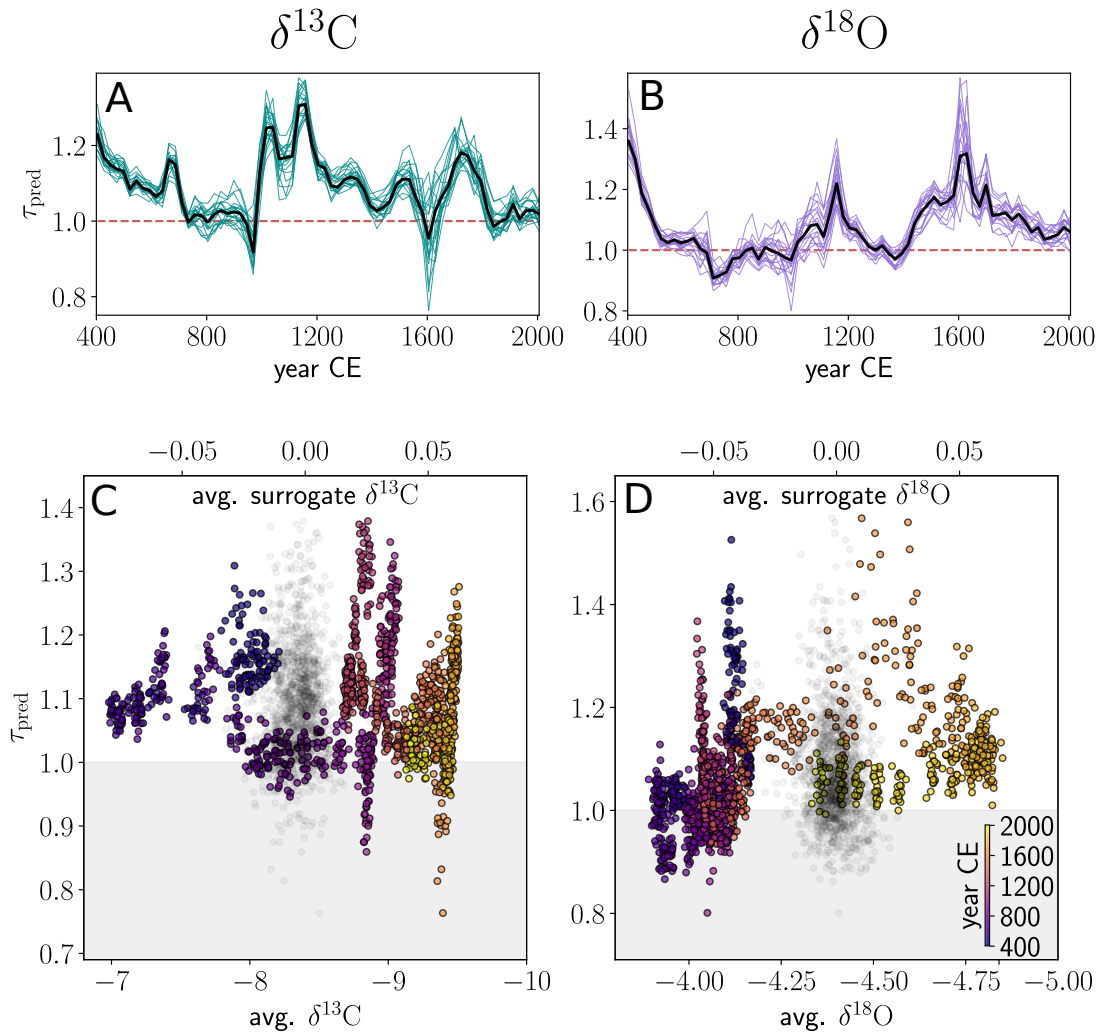


**Figure F.13:** (A/B) Predictability of sub-annual rainfall distribution, given by relative mean predictability times  $\tau_{\text{pred}}$  of 20 detrended proxy realizations for each stable isotope record.  $\tau_{\text{pred}}(t)$  with reference value of  $\tau_{\text{pred}}^{(\text{ref})} = 1$  (red dashed line) is displayed for  $\delta^{13}\text{C}$  (cyan) and  $\delta^{18}\text{O}$  (purple) to display transitions in time. (C/D) Scatter plots show relation between dry/wet episodes to predictability of the sub-annual rainfall distribution. Values on the  $x$ -axis indicate general hydroclimatic conditions during the respective period (average of non-detrended isotope values) while  $\tau_{\text{pred}}$  is computed from detrended proxy realizations. Gray shading(/dashed red line) indicates predictability times  $\tau_{\text{pred}} < 1$  that are not larger than expected from a random proxy-surrogate with the same sampling resolution. The dependency structure that results from the null model is indicated by gray dots.





---

## Bibliography





# Bibliography

- [1] Tobias Braun, Vishnu R. Unni, R.I. Sujith, Juergen Kurths, and Norbert Marwan. Detection of dynamical regime transitions with lacunarity as a multiscale recurrence quantification measure. *Nonlinear Dynamics*, pages 1–19, 2021.
- [2] Tobias Braun, Cinthya Nava-Fernandez, Deniz Eroglu, Adam Hartland, Sebastian F. M. Breitenbach, and Norbert Marwan. Sampling rate-corrected analysis of irregularly sampled time series. *Physical Review E*, 105:024206, Feb 2022.
- [3] Ola Kwiecien, Tobias Braun, Camilla Francesca Brunello, Patrick Faulkner, Niklas Hausmann, Gerd Helle, Julie A. Hoggarth, Monica Ionita, Christopher S. Jazwa, Saige Kelmelis, et al. What we talk about when we talk about seasonality—a transdisciplinary review. *Earth-Science Reviews*, 225:103843, 2022.
- [4] Cinthya Nava-Fernandez, Tobias Braun, Beth Fox, Adam Hartland, Ola Kwiecien, C. L. Pederson, S. N. Höpker, S. Bernasconi, M. Jaggi, J. Hellstrom, F. Gazquez, A. French, N. Marwan, A. Immenhauser, and S.F.M. Breitenbach. Mid-Holocene rainfall changes in the southwestern Pacific. *Submitted to Climate of the Past*, 2021.
- [5] Dagomar Degroot, Kevin Anchukaitis, Martin Bauch, Jakob Burnham, Fred Carnegy, Jianxin Cui, Kathryn de Luna, Piotr Guzowski, George Hambrecht, Heli Huhtamaa, et al. Towards a rigorous understanding of societal responses to climate change. *Nature*, 591(7851):539–550, 2021.
- [6] Will Steffen, Johan Rockström, Katherine Richardson, Timothy M. Lenton, Carl Folke, Diana Liverman, Colin P. Summerhayes, Anthony D. Barnosky, Sarah E. Cornell, Michel Crucifix, et al. Trajectories of the Earth System in the Anthropocene. *Proceedings of the National Academy of Sciences*, 115(33):8252–8259, 2018.
- [7] Erica A. Newman, Maureen C. Kennedy, Donald A. Falk, and Donald McKenzie. Scaling and complexity in landscape ecology. *Frontiers in Ecology and Evolution*, 7:293, 2019.
- [8] Tina Eliassi-Rad, Henry Farrell, David Garcia, Stephan Lewandowsky, Patricia Palacios, Don Ross, Didier Sornette, Karim Thébault, and Karoline Wiesner. What science can do for democracy: a complexity science approach. *Humanities and Social Sciences Communications*, 7(1):1–4, 2020.
- [9] Didier Sornette. A complex system view of why stock markets crash. *New Thesis*, 1(1):5–18, 2004.
- [10] Sandro Galea, Matthew Riddle, and George A. Kaplan. Causal thinking and complex system approaches in epidemiology. *International journal of epidemiology*, 39(1):97–106, 2010.

- [11] Shraddha Gupta, Nikolaos Mastrantonas, Cristina Masoller, and Jürgen Kurths. Perspectives on the importance of complex systems in understanding our climate and climate change—the nobel prize in physics 2021. *Chaos: An Interdisciplinary Journal of Nonlinear Science*, 32(5):052102, 2022.
- [12] John H Argyris, Gunter Faust, Maria Haase, and Rudolf Friedrich. *An exploration of dynamical systems and chaos: completely revised and enlarged second edition*. Springer, 2015.
- [13] Charles Spence. Multisensory flavour perception: Blending, mixing, fusion, and pairing within and between the senses. *Foods*, 9(4):407, 2020.
- [14] Philip W Anderson. More is different: broken symmetry and the nature of the hierarchical structure of science. *Science*, 177(4047):393–396, 1972.
- [15] Steven Strogatz, Sara Walker, Julia M. Yeomans, Corina Tarnita, Elsa Arcaute, Manlio De Domenico, Oriol Artime, and Kwang-II Goh. Fifty years of ‘more is different’. *Nature Reviews Physics*, pages 1–3, 2022.
- [16] Henri Poincaré. Sur le problème des trois corps et les équations de la dynamique. *Acta mathematica*, 13(1):A3–A270, 1890.
- [17] Miwa Fukino, Yoshito Hirata, and Kazuyuki Aihara. Coarse-graining time series data: Recurrence plot of recurrence plots and its application for music. *Chaos: An Interdisciplinary Journal of Nonlinear Science*, 26(2):023116, 2016.
- [18] Neil Sinhababu and Kuong Un Teng. Loving the Eternal Recurrence. *Journal of Nietzsche Studies*, 50(1):106–124, 2019.
- [19] J.-P. Eckmann, S. Oliffson Kamphorst, and D. Ruelle. Recurrence Plots of Dynamical Systems. *Europhysics Letters*, 4(9):973–977, 1987.
- [20] N. Marwan, M. C. Romano, M. Thiel, and J. Kurths. Recurrence Plots for the Analysis of Complex Systems. *Physics Reports*, 438(5–6):237–329, 2007.
- [21] N. Marwan, N. Wessel, U. Meyerfeldt, A. Schirdewan, and J. Kurths. Recurrence Plot Based Measures of Complexity and its Application to Heart Rate Variability Data. *Physical Review E*, 66(2):026702, 2002.
- [22] A. M. Nkomidio, E. K. Ngamga, B. R. N. Nbandjo, J. Kurths, and N Marwan. Recurrence-Based Synchronization Analysis of Weakly Coupled Bursting Neurons Under External ELF Fields. *Entropy*, 24(2):235, 2022.
- [23] Satoshi Suzuki, Yoshito Hirata, and Kazuyuki Aihara. Definition of distance for marked point process data and its application to recurrence plot-based analysis of exchange tick data of foreign currencies. *International Journal of Bifurcation and Chaos*, 20(11):3699–3708, 2010.
- [24] Thomas Westerhold, Norbert Marwan, Anna Joy Drury, Diederik Liebrand, Claudia Agnini, Eleni Anagnostou, James SK Barnet, Steven M Bohaty, David De Vleeschouwer, Fabio Florindo, et al. An astronomically dated record of Earth’s climate and its predictability over the last 66 million years. *Science*, 369(6509):1383–1387, 2020.
- [25] Benoît B. Mandelbrot. *The fractal geometry of nature*, volume 173. WH freeman New York, 1983.

- [26] Sid-Ali Ouadfeul. *Fractal analysis and chaos in geosciences*. BoD–Books on Demand, 2012.
- [27] Malcolm Gladwell. *The tipping point: How little things can make a big difference*. Little, Brown, 2006.
- [28] Timothy M. Lenton, Hermann Held, Elmar Kriegler, Jim W. Hall, Wolfgang Lucht, Stefan Rahmstorf, and Hans Joachim Schellnhuber. Tipping elements in the Earth’s climate system. *Proceedings of the national Academy of Sciences*, 105(6):1786–1793, 2008.
- [29] Norbert Marwan, Jonathan F. Donges, Reik V. Donner, and Deniz Eroglu. Nonlinear time series analysis of palaeoclimate proxy records. *Quaternary Science Reviews*, 274:107245, 2021.
- [30] K. Hauke Kraemer, Reik V. Donner, Jobst Heitzig, and Norbert Marwan. Recurrence threshold selection for obtaining robust recurrence characteristics in different embedding dimensions. *Chaos: An Interdisciplinary Journal of Nonlinear Science*, 28(8):085720, 2018.
- [31] Norman H. Packard, James P. Crutchfield, J. Doyne Farmer, and Robert S. Shaw. Geometry from a time series. *Physical review letters*, 45(9):712, 1980.
- [32] Christian Kuehn. A mathematical framework for critical transitions: Bifurcations, fast–slow systems and stochastic dynamics. *Physica D: Nonlinear Phenomena*, 240(12):1020–1035, 2011.
- [33] Manfred Mudelsee. *Climate time series analysis*. Springer, 2013.
- [34] Gemma Lancaster, Dmytro Iatsenko, Aleksandra Pidde, Valentina Ticcinelli, and Aneta Stefanovska. Surrogate data for hypothesis testing of physical systems. *Physics Reports*, 748:1–60, 2018.
- [35] Frank McDermott. Palaeo-climate reconstruction from stable isotope variations in speleothems: a review. *Quaternary Science Reviews*, 23(7-8):901–918, 2004.
- [36] Sebastian F.M. Breitenbach, Kira Rehfeld, Bedartha Goswami, James U.L. Baldini, Harriet E. Ridley, Douglas J. Kennett, Keith M. Prufer, Valorie V. Aquino, Yemane Asmerom, Victor J. Polyak, et al. Constructing proxy records from age models (CO-PRA). *Climate of the Past*, 8(5):1765–1779, 2012.
- [37] Ibrahim Ozken, Deniz Eroglu, Sebastian F.M. Breitenbach, Norbert Marwan, Liangcheng Tan, Ugur Tirnakli, and Jürgen Kurths. Recurrence plot analysis of irregularly sampled data. *Physical Review E*, 98(5):052215, 2018.
- [38] Tim Woollings, David Barriopedro, John Methven, Seok-Woo Son, Olivia Martius, Ben Harvey, Jana Sillmann, Anthony R Lupo, and Sonia Seneviratne. Blocking and its response to climate change. *Current climate change reports*, 4(3):287–300, 2018.
- [39] Small Michael. *Applied nonlinear time series analysis: applications in physics, physiology and finance*, volume 52. World Scientific, 2005.
- [40] Elizabeth Bradley and Holger Kantz. Nonlinear time-series analysis revisited. *Chaos: An Interdisciplinary Journal of Nonlinear Science*, 25(9):097610, 2015.

- [41] Marten Scheffer, Jordi Bascompte, William A. Brock, Victor Brovkin, Stephen R. Carpenter, Vasilis Dakos, Hermann Held, Egbert H. Van Nes, Max Rietkerk, and George Sugihara. Early-warning signals for critical transitions. *Nature*, 461(7260):53, 2009.
- [42] Norbert Marwan, Stefan Schinkel, and Jürgen Kurths. Significance for a recurrence based transition analysis. In *Proceedings of the 2008 International Symposium on Non-linear Theory and its Applications NOLTA08, Budapest, Hungary*, pages 412–415, 2008.
- [43] Jonathan F. Donges, Reik Donner, Norbert Marwan, Sebastian F.M. Breitenbach, Kira Rehfeld, and Jürgen Kurths. Non-linear regime shifts in holocene asian monsoon variability: potential impacts on cultural change and migratory patterns. *Climate of the Past*, 11(5):709–741, 2015.
- [44] Jonathan Friedmann Donges, Reik Volker Donner, K. Rehfeld, Norbert Marwan, Martin H. Trauth, and Jürgen Kurths. Identification of dynamical transitions in marine palaeoclimate records by recurrence network analysis. *Nonlinear Processes in Geophysics*, 18(5):545–562, 2011.
- [45] Nishant Malik, Y. Zou, Norbert Marwan, and Jürgen Kurths. Dynamical regimes and transitions in Plio-Pleistocene Asian monsoon. *EPL (Europhysics Letters)*, 97(4):40009, 2012.
- [46] D.A. Smirnov, S.F.M. Breitenbach, Georg Feulner, F.A. Lechleitner, K.M. Prufer, J.U.L. Baldini, Norbert Marwan, and Jürgen Kurths. A regime shift in the Sun-Climate connection with the end of the Medieval Climate Anomaly. *Scientific Reports*, 7(1):1–9, 2017.
- [47] Yun Chen and Hui Yang. Heterogeneous recurrence representation and quantification of dynamic transitions in continuous nonlinear processes. *The European Physical Journal B*, 89(6):155, 2016.
- [48] Vishnu R. Unni and R. I. Sujith. Multifractal characteristics of combustor dynamics close to lean blowout. *Journal of Fluid Mechanics*, 784:30–50, 2015.
- [49] V. Godavarthi, V. R. Unni, E.A. Gopalakrishnan, and R. I. Sujith. Recurrence networks to study dynamical transitions in a turbulent combustor. *Chaos: An Interdisciplinary Journal of Nonlinear Science*, 27(6):063113, 2017.
- [50] Norbert Marwan, Deniz Eroglu, Ibrahim Ozken, Thomas Stemler, Karl-Heinz Wyrwoll, and Jürgen Kurths. Regime change detection in irregularly sampled time series. In *Advances in Nonlinear Geosciences*, pages 357–368. Springer, 2018.
- [51] Bedartha Goswami, Niklas Boers, Aljoscha Rheinwald, Norbert Marwan, Jobst Heitzig, Sebastian F.M. Breitenbach, and Jürgen Kurths. Abrupt transitions in time series with uncertainties. *Nature communications*, 9(1):48, 2018.
- [52] Norbert Marwan, Niels Wessel, Udo Meyerfeldt, Alexander Schirdewan, and Jürgen Kurths. Recurrence-plot-based measures of complexity and their application to heart-rate-variability data. *Physical review E*, 66(2):026702, 2002.
- [53] T. de L. Prado, S.R. Lopes, C.A.S. Batista, J. Kurths, and R.L. Viana. Synchronization of bursting Hodgkin-Huxley-type neurons in clustered networks. *Physical Review E*, 90(3):032818, 2014.
- [54] Eugene M. Izhikevich. *Dynamical systems in neuroscience*. MIT press, 2007.

- [55] Jose G. Venegas, Tilo Winkler, Guido Musch, Marcos F. Vidal Melo, Dominick Layfield, Nora Tgavalekos, Alan J. Fischman, Ronald J. Callahan, Giacomo Bellani, and R. Scott Harris. Self-organized patchiness in asthma as a prelude to catastrophic shifts. *Nature*, 434(7034):777, 2005.
- [56] Rosario N. Mantegna and H. Eugene Stanley. *Introduction to econophysics: correlations and complexity in finance*. Cambridge university press, 1999.
- [57] Annalisa Fabretti and Marcel Ausloos. Recurrence plot and recurrence quantification analysis techniques for detecting a critical regime. examples from financial market indices. *International Journal of Modern Physics C*, 16(05):671–706, 2005.
- [58] Nishant Malik, Norbert Marwan, Yong Zou, Peter J. Mucha, and Jürgen Kurths. Fluctuation of similarity to detect transitions between distinct dynamical regimes in short time series. *Physical Review E*, 89(6):062908, 2014.
- [59] Abin Krishnan, R. I. Sujith, Norbert Marwan, and Jürgen Kurths. On the emergence of large clusters of acoustic power sources at the onset of thermoacoustic instability in a turbulent combustor. *Journal of Fluid Mechanics*, 874:455–482, 2019.
- [60] Jan W. Kantelhardt, Stephan A. Zschiegner, Eva Koscielny-Bunde, Shlomo Havlin, Armin Bunde, and H Eugene Stanley. Multifractal detrended fluctuation analysis of nonstationary time series. *Physica A: Statistical Mechanics and its Applications*, 316(1-4):87–114, 2002.
- [61] Christophe Letellier. Estimating the Shannon entropy: recurrence plots versus symbolic dynamics. *Physical review letters*, 96(25):254102, 2006.
- [62] Norbert Marwan. A historical review of recurrence plots. *The European Physical Journal Special Topics*, 164(1):3–12, 2008.
- [63] Gilberto Corso, Thiago de Lima Prado, Gustavo Zampier dos Santos Lima, Jürgen Kurths, and Sergio Roberto Lopes. Quantifying entropy using recurrence matrix microstates. *Chaos: An Interdisciplinary Journal of Nonlinear Science*, 28(8):083108, 2018.
- [64] Roy E. Plotnick, Robert H. Gardner, William W. Hargrove, Karen Prestegard, and Martin Perlmutter. Lacunarity analysis: a general technique for the analysis of spatial patterns. *Physical review E*, 53(5):5461, 1996.
- [65] Qiuming Cheng. Multifractal modeling and lacunarity analysis. *Mathematical Geology*, 29(7):919–932, 1997.
- [66] Rinku Jacob, K.P. Harikrishnan, R. Misra, and G. Ambika. Measure for degree heterogeneity in complex networks and its application to recurrence network analysis. *Royal Society open science*, 4(1):160757, 2017.
- [67] Yadvinder Malhi and Rosa María Román-Cuesta. Analysis of lacunarity and scales of spatial homogeneity in IKONOS images of Amazonian tropical forest canopies. *Remote Sensing of Environment*, 112(5):2074–2087, 2008.
- [68] Augusto Victor Martins Gomides, Lucas Josino de Paula Gonçalves, Lucas Ricciopo Silva, and André Ricardo Backes. Lacunarity as a tool for analyzing satellite images of urban areas. In *2018 7th Brazilian Conference on Intelligent Systems (BRACIS)*, pages 307–311. IEEE, 2018.

- [69] Norbert Marwan, Peter Saporin, and Jürgen Kurths. Measures of complexity for 3d image analysis of trabecular bone. *The European Physical Journal Special Topics*, 143(1):109–116, 2007.
- [70] José Gaité. Fractal analysis of the large-scale stellar mass distribution in the Sloan Digital Sky Survey. *Journal of Cosmology and Astroparticle Physics*, 2018(07):010, 2018.
- [71] Audrey Karperien, HF Jelinek, NT Milosevic, and Poland Cracow. Reviewing lacunarity analysis and classification of microglia in neuroscience. In *8th European Conference on Mathematical and Theoretical Biology*, 2011.
- [72] J. Tony, E.A. Gopalakrishnan, E. Sreelekha, and R. I. Sujith. Detecting deterministic nature of pressure measurements from a turbulent combustor. *Physical Review E*, 92(6):062902, 2015.
- [73] Floris Takens. Detecting strange attractors in turbulence. In *Dynamical systems and turbulence, Warwick 1980*, pages 366–381. Springer, 1981.
- [74] Liangyue Cao. Practical method for determining the minimum embedding dimension of a scalar time series. *Physica D: Nonlinear Phenomena*, 110(1-2):43–50, 1997.
- [75] Louis M. Pecora, Linda Moniz, Jonathan Nichols, and Thomas L Carroll. A unified approach to attractor reconstruction. *Chaos: An Interdisciplinary Journal of Nonlinear Science*, 17(1):013110, 2007.
- [76] Holger Kantz. A robust method to estimate the maximal lyapunov exponent of a time series. *Physics letters A*, 185(1):77–87, 1994.
- [77] Charles L. Webber Jr. and Norbert Marwan. Recurrence quantification analysis. *Theory and Best Practices*, 2015.
- [78] N. Marwan. How to avoid potential pitfalls in recurrence plot based data analysis. *International Journal of Bifurcation and Chaos*, 21(4):1003–1017, 2011.
- [79] K. Hauke Kraemer and Norbert Marwan. Border effect corrections for diagonal line based recurrence quantification analysis measures. *Physics Letters A*, 383(34):125977, 2019.
- [80] Yuhui Quan, Yong Xu, Yuping Sun, and Yu Luo. Lacunarity analysis on image patterns for texture classification. In *Proceedings of the IEEE conference on computer vision and pattern recognition*, pages 160–167, 2014.
- [81] Pinliang Dong. Test of a new lacunarity estimation method for image texture analysis. *International Journal of Remote Sensing*, 21(17):3369–3373, 2000.
- [82] M. Ivanovici, N. Richard, and H. Decean. Fractal dimension and lacunarity of psoriatic lesions—a colour approach. *medicine*, 6(4):7, 2009.
- [83] Cloitre Allain and M. Cloitre. Characterizing the lacunarity of random and deterministic fractal sets. *Physical review A*, 44(6):3552, 1991.
- [84] Markus Alber and Joachim Peinke. Improved multifractal box-counting algorithm, virtual phase transitions, and negative dimensions. *Physical Review E*, 57(5):5489, 1998.

- [85] R.A. Feagin, X.B. Wu, and T. Feagin. Edge effects in lacunarity analysis. *Ecological modelling*, 201(3-4):262–268, 2007.
- [86] N.A. Valous, W. Xiong, N. Halama, I. Zörnig, D. Cantre, Z. Wang, B. Nicolai, P. Verboven, and R. Rojas Moraleda. Multilacunarity as a spatial multiscale multi-mass morphometric of change in the meso-architecture of plant parenchyma tissue. *Chaos: An Interdisciplinary Journal of Nonlinear Science*, 28(9):093110, 2018.
- [87] Emmanuel Bacry, Jean Delour, and Jean-François Muzy. Multifractal random walk. *Physical Review E*, 64(2):026103, 2001.
- [88] P. Babinec, M. Kučera, and M. Babincová. Global characterization of time series using fractal dimension of corresponding recurrence plots: from dynamical systems to heart physiology. *Harmon Fractal Image Anal*, 1:87–93, 2005.
- [89] Bin Lin and ZR Yang. A suggested lacunarity expression for Sierpinski carpets. *Journal of Physics A: Mathematical and General*, 19(2):L49, 1986.
- [90] Charles Webber. Recurrence quantification of fractal structures. *Frontiers in physiology*, 3:382, 2012.
- [91] Reik V. Donner, Jobst Heitzig, Jonathan F. Donges, Yong Zou, Norbert Marwan, and Jürgen Kurths. The geometry of chaotic dynamics - a complex network perspective. *The European Physical Journal B*, 84(4):653–672, 2011.
- [92] Robert J. Tibshirani and Bradley Efron. An introduction to the bootstrap. *Monographs on statistics and applied probability*, 57:1–436, 1993.
- [93] Norbert Marwan, Stefan Schinkel, and Jürgen Kurths. Recurrence plots 25 years later – gaining confidence in dynamical transitions. *EPL (Europhysics Letters)*, 101(2):20007, 2013.
- [94] Edward Ott. *Chaos in dynamical systems*. Cambridge university press, 2002.
- [95] A. Aballe, M. Bethencourt, F.J. Botana, and M. Marcos. Using wavelets transform in the analysis of electrochemical noise data. *Electrochimica Acta*, 44(26):4805–4816, 1999.
- [96] Yu P. Kalmykov, W.T. Coffey, and S.V. Titov. On the Brownian motion in a double-well potential in the overdamped limit. *Physica A: Statistical Mechanics and its Applications*, 377(2):412–420, 2007.
- [97] L. Gammaitoni, P. Hänggi, P. Jung, and F. Marchesoni. Stochastic resonance. *Reviews of Modern Physics*, 70(1):223, 1998.
- [98] Peter Ashwin, Sebastian Wieczorek, Renato Vitolo, and Peter Cox. Tipping points in open systems: bifurcation, noise-induced and rate-dependent examples in the climate system. *Philosophical Transactions of the Royal Society A: Mathematical, Physical and Engineering Sciences*, 370(1962):1166–1184, 2012.
- [99] Praveen Kasthuri, Induja Pavithran, Samadhan A. Pawar, R. I. Sujith, Rohan Gejji, and William Anderson. Dynamical systems approach to study thermoacoustic transitions in a liquid rocket combustor. *Chaos: An Interdisciplinary Journal of Nonlinear Science*, 29(10):103115, 2019.

- [100] Vishnu R. Unni, Abin Krishnan, R. Manikandan, Nitin B. George, R. I. Sujith, Norbert Marwan, and Jürgen Kurths. On the emergence of critical regions at the onset of thermoacoustic instability in a turbulent combustor. *Chaos: An Interdisciplinary Journal of Nonlinear Science*, 28(6):063125, 2018.
- [101] Vineeth Nair, Gireeshkumaran Thampi, and R. I. Sujith. Intermittency route to thermoacoustic instability in turbulent combustors. *Journal of Fluid Mechanics*, 756:470–487, 2014.
- [102] Vedasri Godavarthi, Samadhan A. Pawar, Vishnu R. Unni, R. I. Sujith, Norbert Marwan, and Jürgen Kurths. Coupled interaction between unsteady flame dynamics and acoustic field in a turbulent combustor. *Chaos: An Interdisciplinary Journal of Nonlinear Science*, 28(11):113111, 2018.
- [103] R. I. Sujith and Vishnu R. Unni. Complex system approach to investigate and mitigate thermoacoustic instability in turbulent combustors. *Physics of Fluids*, 32(6):061401, 2020.
- [104] Qiang Ye, Yi Xia, and Zhiming Yao. Classification of gait patterns in patients with neurodegenerative disease using adaptive neuro-fuzzy inference system. *Computational and mathematical methods in medicine*, 2018, 2018.
- [105] Jarosław Kwapien, Paweł Oświęcimka, and Stanisław Drożdż. Detrended fluctuation analysis made flexible to detect range of cross-correlated fluctuations. *Physical Review E*, 92(5):052815, 2015.
- [106] Mark Newman. *Networks*. Oxford university press, 2018.
- [107] J. H. Feldhoff, R. V. Donner, J. F. Donges, N. Marwan, and J. Kurths. Geometric detection of coupling directions by means of inter-system recurrence networks. *Physics Letters A*, 376(46):3504–3513, 2012.
- [108] Jakob Runge, Vladimir Petoukhov, Jonathan F Donges, Jaroslav Hlinka, Nikola Jajcay, Martin Vejmelka, David Hartman, Norbert Marwan, Milan Paluš, and Jürgen Kurths. Identifying causal gateways and mediators in complex spatio-temporal systems. *Nature communications*, 6(1):1–10, 2015.
- [109] Jakob Runge, Peer Nowack, Marlene Kretschmer, Seth Flaxman, and Dino Sejdinovic. Detecting and quantifying causal associations in large nonlinear time series datasets. *Science advances*, 5(11):eaau4996, 2019.
- [110] A. M. T. Ramos, A. Builes-Jaramillo, G. Poveda, B. Goswami, E. E. N. Macau, J. Kurths, and N. Marwan. Recurrence measure of conditional dependence and applications. *Physical Review E*, 95:052206, 2017.
- [111] Vasilis Dakos, Marten Scheffer, Egbert H. van Nes, Victor Brovkin, Vladimir Petoukhov, and Hermann Held. Slowing down as an early warning signal for abrupt climate change. *Proceedings of the National Academy of Sciences*, 105(38):14308–14312, 2008.
- [112] Christopher Boettner, Georg Klinghammer, Niklas Boers, Thomas Westerhold, and Norbert Marwan. Early-warning signals for Cenozoic climate transitions. *Quaternary Science Reviews*, 270:107177, 2021.
- [113] Niklas Boers. Early-warning signals for Dansgaard-Oeschger events in a high-resolution ice core record. *Nature communications*, 9(1):1–8, 2018.



- [114] Georgios Balasis, Reik V. Donner, Stelios M Potirakis, Jakob Runge, Constantinos Papadimitriou, Ioannis A. Daglis, Konstantinos Eftaxias, and Jürgen Kurths. Statistical mechanics and information-theoretic perspectives on complexity in the Earth system. *Entropy*, 15(11):4844–4888, 2013.
- [115] Jie Sun, Carlo Cafaro, and Erik M. Bollt. Identifying the coupling structure in complex systems through the optimal causation entropy principle. *Entropy*, 16(6):3416–3433, 2014.
- [116] Maurizio Porfiri, Raghu Ram Sattanapalle, Shinnosuke Nakayama, James Macinko, and Rifat Sipahi. Media coverage and firearm acquisition in the aftermath of a mass shooting. *Nature human behaviour*, 3(9):913–921, 2019.
- [117] Bernd Pompe and Jakob Runge. Momentary information transfer as a coupling measure of time series. *Physical Review E*, 83(5):051122, 2011.
- [118] Alexander Kraskov, Harald Stögbauer, and Peter Grassberger. Estimating mutual information. *Physical review E*, 69(6):066138, 2004.
- [119] Andreas P. Nawroth and Joachim Peinke. Multiscale reconstruction of time series. *Physics Letters A*, 360(2):234–237, 2006.
- [120] Douglas Maraun and Jürgen Kurths. Cross wavelet analysis: significance testing and pitfalls. *Nonlinear Processes in Geophysics*, 11(4):505–514, 2004.
- [121] Ankit Agarwal, Rathinasamy Maheswaran, Norbert Marwan, Levke Caesar, and Jürgen Kurths. Wavelet-based multiscale similarity measure for complex networks. *The European Physical Journal B*, 91(11):296, 2018.
- [122] Ioannis Vlachos and Dimitris Kugiumtzis. Nonuniform state-space reconstruction and coupling detection. *Physical Review E*, 82(1):016207, 2010.
- [123] M. Thiel, M. C. Romano, P. L. Read, and J. Kurths. Estimation of dynamical invariants without embedding by recurrence plots. *Chaos*, 14(2):234–243, 2004.
- [124] S. Schinkel, O. Dimigen, and N. Marwan. Selection of recurrence threshold for signal detection. *European Physical Journal – Special Topics*, 164(1):45–53, 2008.
- [125] K. Klimaszcwska and J. J. Żebrowski. Detection of the type of intermittency using characteristic patterns in recurrence plots. *Physical Review E*, 80:026214, 2009.
- [126] Y. Hirata and K. Aihara. Devaney’s chaos on recurrence plots. *Physical Review E*, 82:036209, 2010.
- [127] M. Carmen Romano, Marco Thiel, Jürgen Kurths, and Celso Grebogi. Estimation of the direction of the coupling by conditional probabilities of recurrence. *Physical Review E*, 76(3):036211, 2007.
- [128] Joseph P. Zbilut and Norbert Marwan. The Wiener–Khinchin theorem and recurrence quantification. *Physics Letters A*, 372(44):6622–6626, 2008.
- [129] Elizabeth Bradley and Ricardo Mantilla. Recurrence plots and unstable periodic orbits. *Chaos: An Interdisciplinary Journal of Nonlinear Science*, 12(3):596–600, 2002.
- [130] Abhirup Banerjee, Bedartha Goswami, Yoshito Hirata, Deniz Eroglu, Bruno Merz, Jürgen Kurths, and Norbert Marwan. Recurrence analysis of extreme event-like data. *Nonlinear Processes in Geophysics*, 28(2):213–229, 2021.

- [131] Celik Ozdes and Deniz Eroglu. Transformation cost spectrum for irregularly sampled time series. *The European Physical Journal Special Topics*, pages 1–12, 2022.
- [132] M. C. Romano, M. Thiel, and J. Kurths. Generalized Synchronization Indices based on Recurrence in Phase Space. In *Generalized Synchronization Indices based on Recurrence in Phase Space*, volume 742, pages 330–336, 2004.
- [133] M. C. Romano, M. Thiel, J. Kurths, I. Z. Kiss, and J. L. Hudson. Detection of synchronization for non-phase-coherent and non-stationary data. *Europhysics Letters*, 71(3):466–472, 2005.
- [134] D. V. Senthilkumar, M. Lakshmanan, and J. Kurths. Transition from phase to generalized synchronization in time-delay systems. *Chaos*, 18(2):023118, 2008.
- [135] Yong Zou, M. Carmen Romano, Marco Thiel, Norbert Marwan, and Jürgen Kurths. Inferring indirect coupling by means of recurrences. *International Journal of Bifurcation and Chaos*, 21(04):1099–1111, 2011.
- [136] Bedartha Goswami, Norbert Marwan, Georg Feulner, and Jürgen Kurths. How do global temperature drivers influence each other? *The European Physical Journal Special Topics*, 222(3):861–873, 2013.
- [137] Maurizio Porfiri and Manuel Ruiz Marín. Transfer entropy on symbolic recurrences. *Chaos: An Interdisciplinary Journal of Nonlinear Science*, 29(6):063123, 2019.
- [138] Marco Thiel, M. Carmen Romano, and Jürgen Kurths. Analytical description of recurrence plots of white noise and chaotic processes. *arXiv preprint nlin/0301027*, 2003.
- [139] Marco Thiel, M. Carmen Romano, and Jürgen Kurths. Spurious structures in recurrence plots induced by embedding. *Nonlinear Dynamics*, 44(1):299–305, 2006.
- [140] N. Marwan and J. Kurths. Line structures in recurrence plots. *Physics Letters A*, 336(4–5):349–357, 2005.
- [141] K. Hauke Kraemer, Maximilian Gelbrecht, Induja Pavithran, R.I. Sujith, and Norbert Marwan. Optimal state space reconstruction via monte carlo decision tree search. *Nonlinear Dynamics*, pages 1–21, 2022.
- [142] Joseph P. Zbilut and Charles L. Webber Jr. Embeddings and delays as derived from quantification of recurrence plots. *Physics letters A*, 171(3-4):199–203, 1992.
- [143] Fatihcan M. Atay and Yiğit Altıntaş. Recovering smooth dynamics from time series with the aid of recurrence plots. *Physical Review E*, 59(6):6593, 1999.
- [144] Robin A.A. Ince, Bruno L. Giordano, Christoph Kayser, Guillaume A. Rousselet, Joachim Gross, and Philippe G. Schyns. A statistical framework for neuroimaging data analysis based on mutual information estimated via a gaussian copula. *Human brain mapping*, 38(3):1541–1573, 2017.
- [145] Kai Hauke Kraemer, George Datsoris, Jürgen Kurths, Istvan Z. Kiss, Jorge L. Ocampo-Espindola, and Norbert Marwan. A unified and automated approach to attractor reconstruction. *New Journal of Physics*, 2021.
- [146] Jacques Laskar, Philippe Robutel, Frédéric Joutel, Mickael Gastineau, A.C.M. Correia, and Benjamin Levrard. A long-term numerical solution for the insolation quantities of the Earth. *Astronomy & Astrophysics*, 428(1):261–285, 2004.

- [147] Michael Ghil, Ilya Zaliapin, and Sylvester Thompson. A delay differential model of ENSO variability: parametric instability and the distribution of extremes. *Nonlinear Processes in Geophysics*, 15(3):417–433, 2008.
- [148] A. Hannachi. *Patterns Identification and Data Mining in Weather and Climate*. Springer, Cham, 2021.
- [149] Philip Sura and Abdel Hannachi. Perspectives of Non-Gaussianity in Atmospheric Synoptic and Low-Frequency Variability. *Journal of Climate*, 28(13):5091 – 5114, 2015.
- [150] Abdel. Hannachi, David M. Straus, Christian L. E. Franzke, Susanna Corti, and Tim Woollings. Low-frequency nonlinearity and regime behavior in the northern hemisphere extratropical atmosphere. *Reviews of Geophysics*, 55(1):199–234, 2017.
- [151] John M. Wallace and David S. Gutzler. Teleconnections in the Geopotential Height Field during the Northern Hemisphere Winter. *Monthly Weather Review*, 109(4):784 – 812, 1981.
- [152] Anthony G. Barnston and Robert E. Livezey. Classification, seasonality and persistence of low-frequency atmospheric circulation patterns. *Monthly Weather Review*, 115(6):1083 – 1126, 1987.
- [153] Christophe Cassou. Intraseasonal interaction between the Madden–Julian Oscillation and the North Atlantic Oscillation. *Nature*, 455(7212):523–527, September 2008.
- [154] Michael Ghil and Andrew W. Robertson. “waves” vs. “particles” in the atmosphere’s phase space: A pathway to long-range forecasting? *Proceedings of the National Academy of Sciences*, 99:2493–2500, 2002.
- [155] Christian Franzke and Steven B. Feldstein. The continuum and dynamics of northern hemisphere teleconnection patterns. *Journal of the Atmospheric Sciences*, 62(9):3250–3267, 2005.
- [156] Stephen J. Colucci and David P. Baumhefner. Initial weather regimes as predictors of numerical 30-day mean forecast accuracy. *Journal of Atmospheric Sciences*, 49(17):1652 – 1671, 1992.
- [157] Randall M. Dole. Persistent anomalies of the extratropical northern hemisphere wintertime circulation: Structure. *Monthly Weather Review*, 114(1):178 – 207, 1986.
- [158] Lionel Pandolfo. Observational aspects of the low-frequency intraseasonal variability of the atmosphere in middle latitudes. In *Observational Aspects of the Low-Frequency Intraseasonal Variability of the Atmosphere in Middle Latitudes*, volume 34 of *Advances in Geophysics*, pages 93–174. Elsevier, 1993.
- [159] Tim Woollings, Abdel Hannachi, Brian Hoskins, and Andrew Turner. A regime view of the north atlantic oscillation and its response to anthropogenic forcing. *Journal of Climate*, 23(6):1291 – 1307, 2010.
- [160] Tim Woollings, Abdel Hannachi, and Brian Hoskins. Variability of the north atlantic eddy-driven jet stream. *Quarterly Journal of the Royal Meteorological Society*, 136(649):856–868, 2010.
- [161] A. Hannachi and W. Iqbal. Bimodality of hemispheric winter atmospheric variability via average flow tendencies and kernel EOFs. *Tellus A: Dynamic Meteorology and Oceanography*, 71(1):1633847, 2019.

- [162] A. Hannachi and W. Iqbal. On the Nonlinearity of Winter Northern Hemisphere Atmospheric Variability. *Journal of the Atmospheric Sciences*, 76(1):333–356, jan 2019.
- [163] Y. Zou, R. V. Donner, N. Marwan, J. F. Donges, and J. Kurths. Complex network approaches to nonlinear time series analysis. *Physics Reports*, 787:1–97, 2019.
- [164] Joshua B. Tenenbaum, Vin de Silva, and John C. Langford. A Global Geometric Framework for Nonlinear Dimensionality Reduction. *Science*, 290(5500):2319–2323, 2000.
- [165] A. Hannachi and A. G. Turner. 20th century intraseasonal Asian monsoon dynamics viewed from Isomap. *Nonlinear Processes in Geophysics*, 20(5):725–741, 2013.
- [166] M. E. J. Newman. Modularity and community structure in networks. *Proceedings of the National Academy of Sciences*, 103(23):8577–8582, 2006.
- [167] N. Marwan, J. F. Donges, Y. Zou, R. V. Donner, and J. Kurths. Complex network approach for recurrence analysis of time series. *Physics Letters A*, 373(46):4246–4254, 2009.
- [168] Bernhard Schölkopf, Alexander Smola, and Klaus-Robert Müller. Nonlinear Component Analysis as a Kernel Eigenvalue Problem. *Neural Computation*, 10(5):1299–1319, 07 1998.
- [169] Bernhard E. Boser, Isabelle M. Guyon, and Vladimir N. Vapnik. A training algorithm for optimal margin classifiers. In *Proceedings of the Fifth Annual Workshop on Computational Learning Theory, COLT '92*, page 144–152, New York, NY, USA, 1992. Association for Computing Machinery.
- [170] I. J. Schoenberg. Metric spaces and positive definite functions. *Transactions of the American Mathematical Society*, 44(3):522–522, March 1938.
- [171] Douglas Reynolds. *Gaussian Mixture Models*, pages 659–663. Springer US, Boston, MA, 2009.
- [172] B. W. Silverman. *Density Estimation for Statistics and Data Analysis*. Chapman & Hall, London, 1986.
- [173] M. E. J. Newman and M. Girvan. Finding and evaluating community structure in networks. *Phys. Rev. E*, 69:026113, Feb 2004.
- [174] John Marshall and Franco Molteni. Toward a dynamical understanding of planetary-scale flow regimes. *Journal of the Atmospheric Sciences*, 50(12):1792–1818, 1993.
- [175] S. Vannitsem and C. Nicolis. Lyapunov vectors and error growth patterns in a t2113 quasigeostrophic model. *Journal of the Atmospheric Sciences*, 54(2):347–361, 1997.
- [176] S. Corti, A. Giannini, S. Tibaldi, and F. Molteni. Patterns of low-frequency variability in a three-level quasi-geostrophic model. *Climate Dynamics*, 13(12):883–904, 1997.
- [177] D. Kondrashov, K. Ide, and M. Ghil. Weather regimes and preferred transition paths in a three-level quasigeostrophic model. *Journal of the Atmospheric Sciences*, 61(5):568–587, 2004.
- [178] Aleksei Seleznev, Dmitry Mukhin, Andrey Gavrilov, Evgeny Loskutov, and Alexander Feigin. Bayesian framework for simulation of dynamical systems from multidimensional data using recurrent neural network. *Chaos: An Interdisciplinary Journal of Nonlinear Science*, 29(12):123115, dec 2019.

- [179] E. Kalnay, M. Kanamitsu, R. Kistler, W. Collins, D. Deaven, L. Gandin, M. Iredell, S. Saha, G. White, J. Woollen, Y. Zhu, A. Leetmaa, R. Reynolds, M. Chelliah, W. Ebisuzaki, W. Higgins, J. Janowiak, K. C. Mo, C. Ropelewski, J. Wang, Roy Jenne, and Dennis Joseph. The NCEP/NCAR 40-year reanalysis project. *Bulletin of the American Meteorological Society*, 77(3):437–471, March 1996.
- [180] David W. J. Thompson and John M. Wallace. The Arctic oscillation signature in the wintertime geopotential height and temperature fields. *Geophysical Research Letters*, 25(9):1297–1300, 1998.
- [181] K. Haines and A. Hannachi. Weather Regimes in the Pacific from a GCM. *Journal of Atmospheric Sciences*, 52(13):2444 – 2462, 1995.
- [182] A. Hannachi. Low-frequency variability in a gcm: Three-dimensional flow regimes and their dynamics. *Journal of Climate*, 10(6):1357 – 1379, 1997.
- [183] Joseph Pedlosky. *Geophysical Fluid Dynamics*. Springer New York, 1987.
- [184] Dmitry Mukhin, Andrey Gavrilov, Alexander Feigin, Evgeny Loskutov, and Juergen Kurths. Principal nonlinear dynamical modes of climate variability. *Scientific Reports*, 5:15510, 2015.
- [185] Dmitry Mukhin, Andrey Gavrilov, Evgeny Loskutov, Alexander Feigin, and Juergen Kurths. Nonlinear reconstruction of global climate leading modes on decadal scales. *Climate Dynamics*, 51(5-6):2301–2310, sep 2018.
- [186] John M. Wallace. North Atlantic oscillation/annular mode: two paradigms – one phenomenon. *Quarterly Journal of the Royal Meteorological Society*, 126(564):791–805, 2000.
- [187] Steven B. Feldstein and Christian Franzke. Are the North Atlantic Oscillation and the northern annular mode distinguishable? *Journal of the Atmospheric Sciences*, 63(11):2915–2930, 2006.
- [188] Panxi Dai and Benkui Tan. The nature of the arctic oscillation and diversity of the extreme surface weather anomalies it generates. *Journal of Climate*, 30(14):5563–5584, 2017.
- [189] Thomas Önskog, Christian L.E. Franzke, and Abdel Hannachi. Nonlinear time series models for the North Atlantic Oscillation. *Advances in Statistical Climatology, Meteorology and Oceanography*, 6(2):141–157, 2020.
- [190] Ronald R. Coifman and Stéphane Lafon. Diffusion maps. *Applied and computational harmonic analysis*, 21(1):5–30, 2006.
- [191] Andrey Gavrilov, Aleksei Seleznev, Dmitry Mukhin, Evgeny Loskutov, Alexander Feigin, and Juergen Kurths. Linear dynamical modes as new variables for data-driven ENSO forecast. *Climate Dynamics*, 52(3-4):2199–2216, feb 2019.
- [192] D. Mukhin, A. Gavrilov, E. Loskutov, J. Kurths, and A. Feigin. Bayesian Data Analysis for Revealing Causes of the Middle Pleistocene Transition. *Scientific Reports*, 9(1), 2019.
- [193] Roberto Renò. A closer look at the Epps effect. *International Journal of theoretical and applied finance*, 6(01):87–102, 2003.

- [194] A.A. Fedotov, S.A. Akulov, and E.V. Timchenko. Methods of mathematical analysis of heart rate variability. *Biomedical Engineering*, 54(3):220–225, 2020.
- [195] Craig K. Enders. *Applied missing data analysis*. Guilford press, 2010.
- [196] Mourad Khayati, Alberto Lerner, Zakhar Tymchenko, and Philippe Cudré-Mauroux. Mind the gap: an experimental evaluation of imputation of missing values techniques in time series. *Proceedings of the VLDB Endowment*, 13(5):768–782, 2020.
- [197] Jeffrey D. Scargle. Studies in astronomical time series analysis. II-Statistical aspects of spectral analysis of unevenly spaced data. *The Astrophysical Journal*, 263:835–853, 1982.
- [198] Kira Rehfeld, Norbert Marwan, Jobst Heitzig, and Jürgen Kurths. Comparison of correlation analysis techniques for irregularly sampled time series. *Nonlinear Processes in Geophysics*, 18(3):389–404, 2011.
- [199] James U.L. Baldini. Detecting and Quantifying Paleoseasonality in Stalagmites using Geochemical and Modelling Approaches. *AGUFM*, 2017:PP54B–09, 2021.
- [200] Christian Mühlinghaus, Denis Scholz, and Augusto Mangini. Modelling stalagmite growth and  $\delta^{13}C$  as a function of drip interval and temperature. *Geochimica et Cosmochimica Acta*, 71(11):2780–2790, 2007.
- [201] Joshua Garland, Tyler R Jones, Michael Neuder, Valerie Morris, James WC White, and Elizabeth Bradley. Anomaly detection in paleoclimate records using permutation entropy. *Entropy*, 20(12):931, 2018.
- [202] Martin H Trauth. Spectral analysis in Quaternary sciences. *Quaternary Science Reviews*, 270:107157, 2021.
- [203] Kira Rehfeld, Norbert Marwan, Sebastian F.M. Breitenbach, and Jürgen Kurths. Late Holocene Asian summer monsoon dynamics from small but complex networks of paleoclimate data. *Climate dynamics*, 41(1):3–19, 2013.
- [204] Michael Schulz and Karl Stattegger. Spectrum: Spectral analysis of unevenly spaced paleoclimatic time series. *Computers & Geosciences*, 23(9):929–945, 1997.
- [205] Nitesh V. Chawla, Kevin W. Bowyer, Lawrence O. Hall, and W. Philip Kegelmeyer. SMOTE: synthetic minority over-sampling technique. *Journal of artificial intelligence research*, 16:321–357, 2002.
- [206] Sukarna Barua, Md Monirul Islam, Xin Yao, and Kazuyuki Murase. MWMOTE—majority weighted minority oversampling technique for imbalanced data set learning. *IEEE Transactions on knowledge and data engineering*, 26(2):405–425, 2012.
- [207] Timothy M Lenton, Johan Rockström, Owen Gaffney, Stefan Rahmstorf, Katherine Richardson, Will Steffen, and Hans Joachim Schellnhuber. Climate tipping points—too risky to bet against. *Nature*, 575, 2019.
- [208] Jaqueline Lekscha and Reik V. Donner. Phase space reconstruction for non-uniformly sampled noisy time series. *Chaos: An Interdisciplinary Journal of Nonlinear Science*, 28(8):085702, 2018.

- [209] Michael McCullough, Konstantinos Sakellariou, Thomas Stemler, and Michael Small. Counting forbidden patterns in irregularly sampled time series. i. the effects of under-sampling, random depletion, and timing jitter. *Chaos: An Interdisciplinary Journal of Nonlinear Science*, 26(12):123103, 2016.
- [210] Konstantinos Sakellariou, Michael McCullough, Thomas Stemler, and Michael Small. Counting forbidden patterns in irregularly sampled time series. ii. reliability in the presence of highly irregular sampling. *Chaos: An Interdisciplinary Journal of Nonlinear Science*, 26(12):123104, 2016.
- [211] Ibrahim Ozken, Deniz Eroglu, Thomas Stemler, Norbert Marwan, G. Baris Bagci, and Jürgen Kurths. Transformation-cost time-series method for analyzing irregularly sampled data. *Physical Review E*, 91(6):062911, 2015.
- [212] Esko Ukkonen. Algorithms for approximate string matching. *Information and control*, 64(1-3):100–118, 1985.
- [213] Enrique Garcia-Ceja, Md Zia Uddin, and Jim Torresen. Classification of recurrence plots’ distance matrices with a convolutional neural network for activity recognition. *Procedia computer science*, 130:157–163, 2018.
- [214] M. Carmen Romano, Marco Thiel, Jürgen Kurths, and Werner von Bloh. Multivariate recurrence plots. *Physics letters A*, 330(3-4):214–223, 2004.
- [215] Stefan Schinkel, Norbert Marwan, and Jürgen Kurths. Order patterns recurrence plots in the analysis of erp data. *Cognitive neurodynamics*, 1(4):317–325, 2007.
- [216] M. Allison Stegner, Zak Ratajczak, Stephen R Carpenter, and John W. Williams. Inferring critical transitions in paleoecological time series with irregular sampling and variable time-averaging. *Quaternary Science Reviews*, 207:49–63, 2019.
- [217] Kira Rehfeld and Jürgen Kurths. Similarity estimators for irregular and age-uncertain time series. *Climate of the Past*, 10(1):107–122, 2014.
- [218] William J. Masek and Michael S. Paterson. A faster algorithm computing string edit distances. *Journal of Computer and System sciences*, 20(1):18–31, 1980.
- [219] Lawrence Rabiner, A. Rosenberg, and S. Levinson. Considerations in dynamic time warping algorithms for discrete word recognition. *IEEE Transactions on Acoustics, Speech, and Signal Processing*, 26(6):575–582, 1978.
- [220] Jonathan D. Victor and Keith P. Purpura. Metric-space analysis of spike trains: theory, algorithms and application. *Network: computation in neural systems*, 8(2):127–164, 1997.
- [221] Yoshito Hirata. Recurrence plots for characterizing random dynamical systems. *Communications in Nonlinear Science and Numerical Simulation*, 94:105552, 2021.
- [222] Reik V. Donner and Susana M. Barbosa. Nonlinear time series analysis in the geosciences. *Lecture Notes in Earth Sciences*, 112, 2008.
- [223] Deniz Eroglu, Fiona H. McRobie, Ibrahim Ozken, Thomas Stemler, Karl-Heinz Wyrwoll, Sebastian F.M. Breitenbach, Norbert Marwan, and Jürgen Kurths. See-saw relationship of the Holocene East Asian–Australian summer monsoon. *Nature Communications*, 7:12929, 2016.

- [224] T.K. March, S.C. Chapman, and R.O. Dendy. Recurrence plot statistics and the effect of embedding. *Physica D: Nonlinear Phenomena*, 200(1-2):171–184, 2005.
- [225] Dennis C. Williams. Finite sample correction factors for several simple robust estimators of normal standard deviation. *Journal of Statistical Computation and Simulation*, 81(11):1697–1702, 2011.
- [226] Chanseok Park, Haewon Kim, and Min Wang. Investigation of finite-sample properties of robust location and scale estimators. *Communications in Statistics-Simulation and Computation*, pages 1–27, 2019.
- [227] Kevin E. Trenberth. Some effects of finite sample size and persistence on meteorological statistics. part i: Autocorrelations. *Monthly Weather Review*, 112(12):2359–2368, 1984.
- [228] Bedartha Goswami, Paul Schultz, Birte Heinze, Norbert Marwan, Benjamin Bodirsky, Hermann Lotze-Campen, and Jürgen Kurths. Inferring interdependencies from short time series. In *Indian Academy of Sciences Conference Series*, volume 1, pages 51–60, 2017.
- [229] Thomas Schreiber and Andreas Schmitz. Surrogate time series. *Physica D: Nonlinear Phenomena*, 142(3-4):346–382, 2000.
- [230] Xiaodong Luo, Tomomichi Nakamura, and Michael Small. Surrogate test to distinguish between chaotic and pseudoperiodic time series. *Physical Review E*, 71(2):026230, 2005.
- [231] Thomas Schreiber. Constrained randomization of time series data. *Physical Review Letters*, 80(10):2105, 1998.
- [232] Michael D. Abràmoff, Paulo J. Magalhães, and Sunanda J. Ram. Image processing with ImageJ. *Biophotonics international*, 11(7):36–42, 2004.
- [233] Paul Aharon, Michael Rasbury, and Valeriu Murgulet. Caves of Niue island, South Pacific: Speleothems and water geochemistry. *Geological Society of America Special Papers*, 404:283–295, 2006.
- [234] Benjamin D. Santer, Stephen Po-Chedley, Mark D. Zelinka, Ivana Cvijanovic, Céline Bonfils, Paul J. Durack, Qiang Fu, Jeffrey Kiehl, Carl Mears, Jeffrey Painter, Giuliana Pallotta, Susan Solomon, Frank J. Wentz, and Cheng-Zhi Zou. Human influence on the seasonal cycle of tropospheric temperature. *Science*, 361(6399), 2018.
- [235] Thomas J. Crowley, David A. Short, John G. Mengel, and Gerald R. North. Role of Seasonality in the Evolution of Climate During the Last 100 Million Years. *Science*, 231(4738):579–584, 1986.
- [236] George H. Denton, Richard B. Alley, Gary C. Comer, and Wallace S. Broecker. The role of seasonality in abrupt climate change. *Quaternary Science Reviews*, 24(10):1159–1182, 2005.
- [237] Jürg Luterbacher, Daniel Dietrich, Elena Xoplaki, Martin Grosjean, and Heinz Wanner. European seasonal and annual temperature variability, trends, and extremes since 1500. *Science*, 303(5663):1499–1503, 2004.
- [238] Thomas Felis, Gerrit Lohmann, Henning Kuhnert, Stephan J. Lorenz, Denis Scholz, Jürgen Pätzold, Saber A. Al-Rousan, and Salim M. Al-Moghrabi. Increased seasonality in Middle East temperatures during the last interglacial period. *Nature*, 429(6988):164–168, 2004.



- [239] Julie E. Ferguson, Gideon M. Henderson, Darren A. Fa, J. Clive Finlayson, and Norman R. Charnley. Increased seasonality in the Western Mediterranean during the last glacial from limpet shell geochemistry. *Earth and Planetary Science Letters*, 308(3):325–333, 2011.
- [240] Siim Veski, Heikki Seppä, Migle Stančikaitė, Valentina Zernitskaya, Triin Reitalu, Grażyna Gryguc, Atko Heinsalu, Normunds Stivrins, Leeli Amon, Jüri Vassiljev, and Oliver Heiri. Quantitative summer and winter temperature reconstructions from pollen and chironomid data between 15 and 8 ka BP in the Baltic–Belarus area. *Quaternary International*, 388:4–11, 2015.
- [241] William M. Brocas, Thomas Felis, Paul Gierz, Gerrit Lohmann, Martin Werner, J. Christina Obert, Denis Scholz, Martin Kölling, and Sander R. Scheffers. Last Interglacial Hydroclimate Seasonality Reconstructed From Tropical Atlantic Corals. *Paleoceanography and Paleoclimatology*, 33(2):198–213, 2018.
- [242] Florent Rivals, Kevin T. Uno, Faysal Bibi, Michael C. Pante, Jackson Njau, and Ignacio de la Torre. Dietary traits of the ungulates from the HWK EE site at Olduvai Gorge (Tanzania): Diachronic changes and seasonality. *Journal of Human Evolution*, 120:203–214, 2018.
- [243] Saúl Manzano, José S. Carrión, Lourdes López-Merino, Gonzalo Jiménez-Moreno, Jaime L. Toney, Hollie Armstrong, R. Scott Anderson, Antonio García-Alix, José Luis Guerrero Pérez, and Daniel Sánchez-Mata. A palaeoecological approach to understanding the past and present of Sierra Nevada, a Southwestern European biodiversity hotspot. *Global and Planetary Change*, 175:238–250, 2019.
- [244] Amy L. Prendergast, Alexander J.E. Pryor, Hazel Reade, and Rhiannon E. Stevens. Seasonal records of palaeoenvironmental change and resource use from archaeological assemblages. *Journal of Archaeological Science: Reports*, 21:1191–1197, 2018.
- [245] Dagomar Degroot, Kevin Anchukaitis, Martin Bauch, Jakob Burnham, Fred Carnegy, Jianxin Cui, Kathryn de Luna, Piotr Guzowski, George Hambrecht, Heli Huhtamaa, Adam Izdebski, Katrin Kleemann, Emma Moesswilde, Naresh Neupane, Timothy Newfield, Qing Pei, Elena Xoplaki, and Natale Zappia. Towards a rigorous understanding of societal responses to climate change. *Nature*, 591(7851):539–550, 2021.
- [246] Matthieu Carré and Rachid Cheddadi. Seasonality in long-term climate change. *Quaternaire*, 28:173–177, 2017.
- [247] S. Rutherford, M. E. Mann, T. J. Osborn, K. R. Briffa, P. D. Jones, R. S. Bradley, and M. K. Hughes. Proxy-Based Northern Hemisphere Surface Temperature Reconstructions: Sensitivity to Method, Predictor Network, Target Season, and Target Domain. *Journal of Climate*, 18(13):2308–2329, 2005.
- [248] S. Pezzulli, D. B. Stephenson, and A. Hannachi. The Variability of Seasonality. *Journal of Climate*, 18(1):71–88, 2005.
- [249] I. Colin Prentice, Joël Guiot, and Sandy P. Harrison. Mediterranean vegetation, lake levels and palaeoclimate at the Last Glacial Maximum. *Nature*, 360(6405):658–660, 1992.
- [250] M. Milankovitch. Mathematische Klimalehre und astronomische Theorie der Klimaschwankungen. In W. Köppen and R. Geiger, editors, *Handbuch der Klimatologie*. Gebrüder Borntraeger, Berlin, 1930.

- [251] J. D. Hays, John Imbrie, and N. J. Shackleton. Variations in the Earth’s Orbit: Pacesetter of the Ice Ages. *Science*, 194(4270):1121–1132, 1976.
- [252] D. Royer, R. Berner, I.P. Montanez, N.J. Tabor, and D.J. Beerling. CO<sub>2</sub> as a primary driver of phanerozoic climate. *GSA Today*, 14:4–10, 2004.
- [253] Laurent Augustin, Carlo Barbante, Piers R. F. Barnes, Jean Marc Barnola, Matthias Bigler, Emiliano Castellano, Olivier Cattani, Jerome Chappellaz, Dorte Dahl-Jensen, Barbara Delmonte, Gabrielle Dreyfus, Gael Durand, Sonia Falourd, Hubertus Fischer, Jacqueline Flückiger, Margareta E. Hansson, Philippe Huybrechts, Gérard Jugie, Sigfus J. Johnsen, Jean Jouzel, Patrik Kaufmann, Josef Kipfstuhl, Fabrice Lambert, Vladimir Y. Lipenkov, Geneviève C. Littot, Antonio Longinelli, Reginald Lorrain, Valter Maggi, Valerie Masson-Delmotte, Heinz Miller, Robert Mulvaney, Johannes Oerlemans, Hans Oerter, Giuseppe Orombelli, Frederic Parrenin, David A. Peel, Jean-Robert Petit, Dominique Raynaud, Catherine Ritz, Urs Ruth, Jakob Schwander, Urs Siegenthaler, Roland Souchez, Bernhard Stauffer, Jorgen Peder Steffensen, Barbara Stenni, Thomas F. Stocker, Ignazio E. Tabacco, Roberto Udisti, Roderik S. W. van de Wal, Michiel van den Broeke, Jerome Weiss, Frank Wilhelms, Jan-Gunnar Winther, Eric W. Wolff, and Mario (participants are listed alphabetically) Zucchelli. Eight glacial cycles from an Antarctic ice core. *Nature*, 429(6992):623–628, 2004.
- [254] Yi Ge Zhang, Mark Pagani, Zhonghui Liu, Steven M. Bohaty, and Robert DeConto. A 40-million-year history of atmospheric CO<sub>2</sub>. *Philosophical Transactions of the Royal Society A: Mathematical, Physical and Engineering Sciences*, 371(2001):20130096, 2013.
- [255] C. A. Petrie and J. Bates. ‘Multi-cropping’, Intercropping and Adaptation to Variable Environments in Indus South Asia. *Journal of World Prehistory*, 30(2):81–130, 2017.
- [256] W. Köppen. *Handbuch der Klimatologie*. Gebrüder Borntraeger, Berlin, 1936.
- [257] Samantha Bova, Yair Rosenthal, Zhengyu Liu, Shital P. Godad, and Mi Yan. Seasonal origin of the thermal maxima at the holocene and the last interglacial. *Nature*, 589(7843):548–553, 2021.
- [258] Niels J. de Winter, Inigo A. Müller, Ilja J. Kocken, Nicolas Thibault, Clemens V. Ullmann, Alex Farnsworth, Daniel J. Lunt, Philippe Claeys, and Martin Ziegler. Absolute seasonal temperature estimates from clumped isotopes in bivalve shells suggest warm and variable greenhouse climate. *Communications Earth & Environment*, 2(1):121, 2021.
- [259] N. J. de Winter, T. Agterhuis, and M. Ziegler. Optimizing sampling strategies in high-resolution paleoclimate records. *Climate of the Past*, 17(3):1315–1340, 2021.
- [260] Manuel Chevalier, Basil A.S. Davis, Oliver Heiri, Heikki Seppä, Brian M. Chase, Konrad Gajewski, Terri Lacourse, Richard J. Telford, Walter Finsinger, Joël Guiot, Norbert Köhl, S. Yoshi Maezumi, John R. Tipton, Vachel A. Carter, Thomas Brussel, Leanne N. Phelps, Andria Dawson, Marco Zanon, Francesca Vallé, Connor Nolan, Achille Mauri, Anne de Vernal, Kenji Izumi, Lasse Holmström, Jeremiah Marsicek, Simon Goring, Philipp S. Sommer, Michelle Chaput, and Dmitry Kupriyanov. Pollen-based climate reconstruction techniques for late quaternary studies. *Earth-Science Reviews*, 210:103384, 2020.
- [261] Harriet E. Ridley, Yemane Asmerom, James U. L. Baldini, Sebastian F. M. Breitenbach, Valorie V. Aquino, Keith M. Prufer, Brendan J. Culleton, Victor Polyak, Franziska A.

- Lechleitner, Douglas J. Kennett, Minghua Zhang, Norbert Marwan, Colin G. Macpherson, Lisa M. Baldini, Tingyin Xiao, Joanne L. Peterkin, Jaime Awe, and Gerald H. Haug. Aerosol forcing of the position of the Intertropical Convergence Zone since AD 1550. *Nature Geoscience*, 8(3):195–200, Mar 2015.
- [262] Thomas Felis, Cyril Giry, Denis Scholz, Gerrit Lohmann, Madlene Pfeiffer, Jürgen Pätzold, Martin Kölling, and Sander R Scheffers. Tropical Atlantic temperature seasonality at the end of the last interglacial. *Nature Communications*, 6:6159, 2015.
- [263] H. Meyer, T. Opel, T. Laepple, A. Y. Dereviagin, K. Hoffmann, and M. Werner. Long-term winter warming trend in the Siberian Arctic during the mid-to late Holocene. *Nature Geoscience*, 8(2):122–125, 2015.
- [264] Guoqiang Chu, Qing Sun, Xiaohua Wang, Meimei Liu, Yuan Lin, Manman Xie, Wenyu Shang, and Jiaqi Liu. Seasonal temperature variability during the past 1600 years recorded in historical documents and varved lake sediment profiles from northeastern China. *The Holocene*, 22(7):785–792, 2012.
- [265] Liang Yi, Hongjun Yu, Junyi Ge, Zhongping Lai, Xingyong Xu, Li Qin, and Shuzhen Peng. Reconstructions of annual summer precipitation and temperature in north-central China since 1470 AD based on drought/flood index and tree-ring records. *Climatic Change*, 110(1-2):469–498, 2012.
- [266] Jan Pawel Musial, Michael M. Verstraete, and Nadine Gobron. Comparing the effectiveness of recent algorithms to fill and smooth incomplete and noisy time series. *Atmospheric chemistry and physics*, 11(15):7905–7923, 2011.
- [267] Clive W.J. Granger. Investigating causal relations by econometric models and cross-spectral methods. *Econometrica: journal of the Econometric Society*, pages 424–438, 1969.
- [268] Julien Emile-Geay, Kim M. Cobb, Matthieu Carré, Pascale Braconnot, Julie Leloup, Y. Zhou, Sandy P. Harrison, T. Correge, Helen V. McGregor, Matthew Collins, et al. Links between tropical Pacific seasonal, interannual and orbital variability during the Holocene. *Nature Geoscience*, 9(2):168, 2016.
- [269] Marco Marozzi. Nonparametric simultaneous tests for location and scale testing: a comparison of several methods. *Communications in Statistics-Simulation and Computation*, 42(6):1298–1317, 2013.
- [270] T. Wang, D. Surge, and S. Mithen. Seasonal temperature variability of the Neoglacial (3300–2500 BP) and Roman Warm Period (2500–1600 BP) reconstructed from oxygen isotope ratios of limpet shells (*Patella vulgata*), Northwest Scotland. *Palaeogeography, Palaeoclimatology, Palaeoecology*, 317:104–113, 2012.
- [271] Stefanie B. Wirth, Adrian Gilli, Anaëlle Simonneau, Daniel Ariztegui, Boris Vannièrè, Lukas Glur, Emmanuel Chapron, Michel Magny, and Flavio S Anselmetti. A 2000 year long seasonal record of floods in the southern European Alps. *Geophysical Research Letters*, 40(15):4025–4029, 2013.
- [272] Robert S. Feranec, Elizabeth A. Hadly, and Adina Paytan. Stable isotopes reveal seasonal competition for resources between late Pleistocene bison (*Bison*) and horse (*Equus*) from Rancho La Brea, southern California. *Palaeogeography, Palaeoclimatology, Palaeoecology*, 271(1-2):153–160, 2009.

- [273] Xue Feng, Amilcare Porporato, and Ignacio Rodriguez-Iturbe. Changes in rainfall seasonality in the tropics. *Nature Climate Change*, 3(9):811–815, 2013.
- [274] O.C. De Jager, B.C. Raubenheimer, and J.W.H. Swanepoel. A powerful test for weak periodic signals with unknown light curve shape in sparse data. *Astronomy and Astrophysics*, 221:180–190, 1989.
- [275] Eleazar Chukwunye Nwogu, Iheanyi Sylvester Iwueze, and Valentine Uchenna Nlebedim. Some tests for seasonality in time series data. *Journal of Modern Applied Statistical Methods*, 15(2):24, 2016.
- [276] L.S. Freedman. The use of a Kolmogorov–Smirnov type statistic in testing hypotheses about seasonal variation. *Journal of Epidemiology & Community Health*, 33(3):223–228, 1979.
- [277] A.M. Davey and B.E. Flores. Identification of seasonality in time series: A note. *Mathematical and computer modelling*, 18(6):73–81, 1993.
- [278] Tobias Bischoff, Tapio Schneider, and Anna Nele Meckler. A conceptual model for the response of tropical rainfall to orbital variations. *Journal of Climate*, 30(20):8375–8391, 2017.
- [279] Edward R. Cook, Kevin J. Anchukaitis, Brendan M. Buckley, Rosanne D. D’Arrigo, Gordon C. Jacoby, and William E. Wright. Asian monsoon failure and megadrought during the last millennium. *Science*, 328(5977):486–489, 2010.
- [280] Birgit Schneider, Guillaume Leduc, and Wonsun Park. Disentangling seasonal signals in Holocene climate trends by satellite-model-proxy integration. *Paleoceanography*, 25(4), 2010.
- [281] R.P.D. Walsh and D.M. Lawler. Rainfall seasonality: description, spatial patterns and change through time. *Weather*, 36(7):201–208, 1981.
- [282] Salvatore Pascale, Valerio Lucarini, Xue Feng, Amilcare Porporato, et al. Projected changes of rainfall seasonality and dry spells in a high concentration pathway 21st century scenario. *arXiv preprint arXiv:1410.3116*, 2014.
- [283] J. Francis Thackeray and Jennifer M. Fitchett. Rainfall seasonality captured in micro-mammalian fauna in Late Quaternary contexts, South Africa. *Palaeontologia africana*, 51:1–9, 2016.
- [284] Antoine Nicault, S. Alleaume, S. Brewer, M. Carrer, P. Nola, and Joel Guiot. Mediterranean drought fluctuation during the last 500 years based on tree-ring data. *Climate Dynamics*, 31(2-3):227–245, 2008.
- [285] Laurens De Haan and Ana Ferreira. *Extreme value theory: an introduction*. Springer Science & Business Media, 2007.
- [286] P. Naveau and C.M. Ammann. Statistical distributions of ice core sulfate from climatically relevant volcanic eruptions. *Geophysical Research Letters*, 32(5), 2005.
- [287] Elizabeth Mannshardt, Peter F. Craigmile, and Martin P. Tingley. Statistical modeling of extreme value behavior in North American tree-ring density series. *Climatic Change*, 117(4):843–858, 2013.

- [288] Linyin Cheng, Amir AghaKouchak, Eric Gilleland, and Richard W Katz. Non-stationary extreme value analysis in a changing climate. *Climatic change*, 127(2):353–369, 2014.
- [289] William P. Patterson, Kristin A. Dietrich, Chris Holmden, and John T. Andrews. Two millennia of North Atlantic seasonality and implications for Norse colonies. *Proceedings of the National Academy of Sciences*, 107(12):5306–5310, 2010.
- [290] Elena Xoplaki, Jürg Luterbacher, Heiko Paeth, Daniel Dietrich, Niklaus Steiner, Martin Grosjean, and Heinz Wanner. European spring and autumn temperature variability and change of extremes over the last half millennium. *Geophysical Research Letters*, 32(15), 2005.
- [291] Juan P. Corella, Blas L. Valero-Garces, Sergio M. Vicente-Serrano, Achim Brauer, and Gerardo Benito. Three millennia of heavy rainfalls in Western Mediterranean: frequency, seasonality and atmospheric drivers. *Scientific reports*, 6:38206, 2016.
- [292] D. Peavoy and C. Franzke. Bayesian analysis of rapid climate change during the last glacial using Greenland  $\delta^{18}\text{O}$  data. *Climate of the Past*, 6(6):787, 2010.
- [293] Nishant Malik, Bodo Bookhagen, Norbert Marwan, and Jürgen Kurths. Analysis of spatial and temporal extreme monsoonal rainfall over south asia using complex networks. *Climate dynamics*, 39(3-4):971–987, 2012.
- [294] Fernando Domínguez-Castro, Juan I. Santisteban, Mariano Barriendos, and Rosa Mediavilla. Reconstruction of drought episodes for central Spain from rogation ceremonies recorded at the Toledo Cathedral from 1506 to 1900: A methodological approach. *Global and Planetary Change*, 63(2-3):230–242, 2008.
- [295] Zhaohua Wu, Norden E. Huang, Steven R. Long, and Chung-Kang Peng. On the trend, detrending, and variability of nonlinear and nonstationary time series. *Proceedings of the National Academy of Sciences*, 104(38):14889–14894, 2007.
- [296] Manfred Mudelsee, J. Fohlmeister, and D. Scholz. Effects of dating errors on nonparametric trend analyses of speleothem time series. *Climate of the Past*, 8(5):1637–1648, 2012.
- [297] Ben Hardt, Harold D. Rowe, Gregory S. Springer, Hai Cheng, and R. Lawrence Edwards. The seasonality of east central North American precipitation based on three coeval Holocene speleothems from southern West Virginia. *Earth and Planetary Science Letters*, 295(3):342 – 348, 2010.
- [298] Robert B. Cleveland, William S. Cleveland, Jean E. McRae, and Irma Terpenning. STL: A seasonal-trend decomposition. *Journal of Official Statistics*, 6(1):3–73, 1990.
- [299] Norden E. Huang and Zhaohua Wu. A review on Hilbert-Huang transform: Method and its applications to geophysical studies. *Reviews of geophysics*, 46(2), 2008.
- [300] Robert Vautard and Michael Ghil. Singular spectrum analysis in nonlinear dynamics, with applications to paleoclimatic time series. *Physica. D, Nonlinear Phenomena*, 35(3):395–424, 1989.
- [301] Michael Ghil, M.R. Allen, M.D. Dettinger, K. Ide, D. Kondrashov, M.E. Mann, Andrew W. Robertson, A. Saunders, Y. Tian, F. Varadi, et al. Advanced spectral methods for climatic time series. *Reviews of Geophysics*, 40(1):3–1, 2002.

- [302] D. Kondrashov and M. Ghil. Spatio-temporal filling of missing points in geophysical data sets. *Nonlinear Processes in Geophysics*, 13(2):151–159, May 2006.
- [303] Kristin B. Olafsdottir, Aslaug Geirsdottir, Gifford H Miller, and Darren J Larsen. Evolution of NAO and AMO strength and cyclicity derived from a 3-ka varve-thickness record from Iceland. *Quaternary Science Reviews*, 69:142–154, 2013.
- [304] Hai Cheng, P.Z. Zhang, C. Spötl, R.L. Edwards, Y.J. Cai, D.Z. Zhang, W.C. Sang, M. Tan, and Z.S. An. The climatic cyclicity in semiarid-arid central Asia over the past 500,000 years. *Geophysical Research Letters*, 39(1), 2012.
- [305] Martín Medina-Elizalde, Stephen J. Burns, David W Lea, Yemane Asmerom, Lucien von Gunten, Victor Polyak, Mathias Vuille, and Ambarish Karmalkar. High resolution stalagmite climate record from the Yucatán Peninsula spanning the Maya terminal classic period. *Earth and Planetary Science Letters*, 298(1-2):255–262, 2010.
- [306] Matthew S. Lachniet, Juan Pablo Bernal, Yemane Asmerom, Victor Polyak, and Dolores Piperno. A 2400 yr Mesoamerican rainfall reconstruction links climate and cultural change. *Geology*, 40(3):259–262, 2012.
- [307] Nicholas P. McKay and Darrell S. Kaufman. An extended Arctic proxy temperature database for the past 2,000 years. *Scientific Data*, 1:140026, 2014.
- [308] Ulf Büntgen, Paul J. Krusic, Anne Verstege, Gabriel Sangüesa-Barreda, Sebastian Wagner, J. Julio Camarero, Fredrik Charpentier Ljungqvist, Eduardo Zorita, Clive Oppenheimer, Oliver Konter, et al. New tree-ring evidence from the Pyrenees reveals Western Mediterranean climate variability since medieval times. *Journal of Climate*, 30(14):5295–5318, 2017.
- [309] Jun Hu, Julien Emile-Geay, and Judson Partin. Correlation-based interpretations of paleoclimate data—where statistics meet past climates. *Earth and Planetary Science Letters*, 459:362–371, 2017.
- [310] Eddie Haam and Peter Huybers. A test for the presence of covariance between time-uncertain series of data with application to the Dongge Cave speleothem and atmospheric radiocarbon records. *Paleoceanography*, 25(2), 2010.
- [311] Jason Roberts, Mark Curran, Samuel Poynter, Andrew Moy, Tas van Ommen, Tessa Vance, Carly Tozer, Felicity S Graham, Duncan A Young, Christopher Plummer, et al. Correlation confidence limits for unevenly sampled data. *Computers & Geosciences*, 104:120–124, 2017.
- [312] Dmitry A. Smirnov, Norbert Marwan, Sebastian F.M. Breitenbach, Franziska Lechleitner, and Jürgen Kurths. Coping with dating errors in causality estimation. *EPL (Europhysics Letters)*, 117(1):10004, 2017.
- [313] Nerilie J. Abram, Michael K. Gagan, Zhengyu Liu, Wahyoe S. Hantoro, Malcolm T. McCulloch, and Bambang W. Suwargadi. Seasonal characteristics of the Indian Ocean Dipole during the Holocene epoch. *Nature*, 445(7125):299, 2007.
- [314] Nadja Riedwyl, Marcel Küttel, Jürg Luterbacher, and Heinz Wanner. Comparison of climate field reconstruction techniques: Application to Europe. *Climate Dynamics*, 32(2-3):381–395, 2009.

- [315] Christo Buizert, Michael Sigl, Mirko Severi, Bradley R. Markle, Justin J. Wettstein, Joseph R. McConnell, Joel B. Pedro, Harald Sodemann, Kumiko Goto-Azuma, Kenji Kawamura, et al. Abrupt ice-age shifts in southern westerly winds and Antarctic climate forced from the north. *Nature*, 563(7733):681, 2018.
- [316] Michael Deininger and Frank McDermott. Coherency of European speleothem  $\delta^{18}\text{O}$  records linked to North Atlantic ocean circulation. *EGUGA*, pages EPSC2016–5031, 2016.
- [317] Raphael Neukom, Jürg Luterbacher, Ricardo Villalba, Marcel Küttel, David Frank, Phil D. Jones, Martin Grosjean, Heinz Wanner, J.-C. Aravena, David E. Black, et al. Multiproxy summer and winter surface air temperature field reconstructions for southern South America covering the past centuries. *Climate Dynamics*, 37(1-2):35–51, 2011.
- [318] Raphael Neukom, David J. Nash, Georgina H. Endfield, Stefan W. Grab, Craig A. Grove, Clare Kelso, Coleen H. Vogel, and Jens Zinke. Multi-proxy summer and winter precipitation reconstruction for southern Africa over the last 200 years. *Climate Dynamics*, 42(9-10):2713–2726, 2014.
- [319] Liangcheng Tan, Chuan-Chou Shen, Ludvig Löwemark, Sakonvan Chawchai, R. Lawrence Edwards, Yanjun Cai, Sebastian F.M. Breitenbach, Hai Cheng, Yu-Chen Chou, Helmut Duerrast, et al. Rainfall variations in central Indo-Pacific over the past 2,700 y. *Proceedings of the National Academy of Sciences*, 116(35):17201–17206, 2019.
- [320] Feng Shi, Zhengtang Guo, Hugues Goosse, Qiuzhen Yin, et al. Multi-proxy reconstructions of precipitation field in China over the past 500 years. *Climate of the Past*, 13, 2017.
- [321] Brandon R. Boldt, Darrell S. Kaufman, Nicholas P. McKay, and Jason P. Briner. Holocene summer temperature reconstruction from sedimentary chlorophyll content, with treatment of age uncertainties, Kurupa Lake, Arctic Alaska. *The Holocene*, 25(4):641–650, 2015.
- [322] Peter M. Franke, Brian Huntley, and Andrew C. Parnell. Frequency selection in paleoclimate time series: A model-based approach incorporating possible time uncertainty. *Environmetrics*, 29(2):e2492, 2018.
- [323] Niklas Boers, Bedartha Goswami, and Michael Ghil. A complete representation of uncertainties in layer-counted paleoclimatic archives. *Climate of the Past*, 13:1169–1180, 2019.
- [324] Andrew C. Parnell, Caitlin E. Buck, and Think K. Doan. A review of statistical chronology models for high-resolution, proxy-based Holocene palaeoenvironmental reconstruction. *Quaternary Science Reviews*, 30(21-22):2948–2960, 2011.
- [325] Bedartha Goswami, Jobst Heitzig, Kira Rehfeld, Norbert Marwan, Ambili Anoop, Sushma Prasad, and Jürgen Kurths. Estimation of sedimentary proxy records together with associated uncertainty. *Nonlinear Processes in Geophysics*, 21(6):1093–1111, 2014.
- [326] Denis Scholz and Dirk L Hoffmann. Stalage – an algorithm designed for construction of speleothem age models. *Quaternary Geochronology*, 6(3-4):369–382, 2011.
- [327] Walter Duesing, Nadine Berner, Alan L. Deino, Verena Foerster, K. Hauke Kraemer, Norbert Marwan, and Martin H. Trauth. Multiband wavelet age modeling for a  $\sim 293$  m ( $\sim 600$  kyr) sediment core from Chew Bahir Basin, Southern Ethiopian Rift. *Frontiers in Earth Science*, 9:35, 2021.

- [328] Bo Li, Douglas W. Nychka, and Caspar M. Ammann. The value of multiproxy reconstruction of past climate. *Journal of the American Statistical Association*, 105(491):883–895, 2010.
- [329] Rosemarie E. Came, Delia W. Oppo, and Jerry F. McManus. Amplitude and timing of temperature and salinity variability in the subpolar North Atlantic over the past 10 ky. *Geology*, 35(4):315–318, 2007.
- [330] Stacy A. Carolin, Kim M. Cobb, Jean Lynch-Stieglitz, Jessica W. Moerman, Judson W. Partin, Syria Lejau, Jenny Malang, Brian Clark, Andrew A. Tuen, and Jess F. Adkins. Northern Borneo stalagmite records reveal West Pacific hydroclimate across MIS 5 and 6. *Earth and Planetary Science Letters*, 439:182–193, 2016.
- [331] Jones, Matthew D. and Roberts, C. Neil and Leng, Melanie J. and Türkeş, Murat. A high-resolution late Holocene lake isotope record from Turkey and links to North Atlantic and monsoon climate. *Geology*, 34(5):361–364, 2006.
- [332] J. Bradford Hubeny, John W. King, and Antelmo Santos. Subdecadal to multidecadal cycles of Late Holocene North Atlantic climate variability preserved by estuarine fossil pigments. *Geology*, 34(7):569–572, 2006.
- [333] Yemane Asmerom, Victor Polyak, Stephen Burns, and Jessica Rasmussen. Solar forcing of Holocene climate: New insights from a speleothem record, southwestern United States. *Geology*, 35(1):1–4, 2007.
- [334] Ashish Sinha, Gayatri Kathayat, Hai Cheng, Sebastian F.M. Breitenbach, Max Berkelhammer, Manfred Mudelsee, Jayant Biswas, and RL Edwards. Trends and oscillations in the Indian summer monsoon rainfall over the last two millennia. *Nature Communications*, 6:6309, 2015.
- [335] Jacob T. VanderPlas. Understanding the lomb–scargle periodogram. *The Astrophysical Journal Supplement Series*, 236(1):16, 2018.
- [336] Prabhu Babu and Petre Stoica. Spectral analysis of nonuniformly sampled data—a review. *Digital Signal Processing*, 20(2):359–378, 2010.
- [337] Jeffrey D. Scargle. Studies in astronomical time series analysis. iii-fourier transforms, autocorrelation functions, and cross-correlation functions of unevenly spaced data. *The Astrophysical Journal*, 343:874–887, 1989.
- [338] Michael Schulz and Manfred Mudelsee. Redfit: estimating red-noise spectra directly from unevenly spaced paleoclimatic time series. *Computers & Geosciences*, 28(3):421–426, 2002.
- [339] Manfred Mudelsee, Dirk Scholz, Regine Röthlisberger, Dominik Fleitmann, A. Mangini, and Eric W. Wolff. Climate spectrum estimation in the presence of timescale errors. *Nonlinear Processes in Geophysics*, 16(1):43–56, 2009.
- [340] Chang Xu. Detection test for periodic signals revisited against various stochastic models. *IEEE Access*, 7:92203–92209, 2019.
- [341] Max Berkelhammer, Ashish Sinha, Manfred Mudelsee, Hai Cheng, R. Lawrence Edwards, and Kevin Cannariato. Persistent multidecadal power of the Indian Summer Monsoon. *Earth and Planetary Science Letters*, 290(1-2):166–172, 2010.



- [342] N. J. de Winter, S. Goderis, F. Dehairs, John W.M. Jagt, R.H.B. Fraaije, S.J.M. Van Malderen, F. Vanhaecke, and P. Claeys. Tropical seasonality in the late Campanian (late Cretaceous): Comparison between multiproxy records from three bivalve taxa from Oman. *Palaeogeography, Palaeoclimatology, Palaeoecology*, 485:740–760, 2017.
- [343] Dulce Oliveira, Maria Fernanda Sánchez Goñi, Filipa Naughton, J.M. Polanco-Martínez, Francisco J Jimenez-Espejo, Joan O. Grimalt, Belen Martrat, Antje H.L. Voelker, Ricardo Trigo, David Hodell, et al. Unexpected weak seasonal climate in the western Mediterranean region during MIS 31, a high-insolation forced interglacial. *Quaternary Science Reviews*, 161:1–17, 2017.
- [344] M. Zechmeister and M. Kürster. The generalised Lomb-Scargle periodogram—a new formalism for the floating-mean and Keplerian periodograms. *Astronomy & Astrophysics*, 496(2):577–584, 2009.
- [345] Guillaume Lenoir and Michel Crucifix. A general theory on frequency and time–frequency analysis of irregularly sampled time series based on projection methods—Part 1: Frequency analysis. *Nonlinear Processes in Geophysics*, 25(1):145, 2018.
- [346] Peter Welch. The use of fast Fourier transform for the estimation of power spectra: a method based on time averaging over short, modified periodograms. *IEEE Transactions on Audio and Electroacoustics*, 15(2):70–73, 1967.
- [347] Donald B. Percival, Andrew T. Walden, et al. *Spectral analysis for physical applications*. Cambridge University Press, 1993.
- [348] Alan D. Chave. A multitaper spectral estimator for time-series with missing data. *Geophysical Journal International*, 218(3):2165–2178, 2019.
- [349] Xueheng Shi and Colin Gallagher. Estimating Unknown Cycles in Geophysical Data. *Earth and Space Science*, 2019.
- [350] Petre Stoica and Niclas Sandgren. Spectral analysis of irregularly-sampled data: Paralleling the regularly-sampled data approaches. *Digital Signal Processing*, 16(6):712–734, 2006.
- [351] Matthew J. Graham, Andrew J. Drake, S.G. Djorgovski, Ashish A. Mahabal, Ciro Donalek, Victor Duan, and Allison Maker. A comparison of period finding algorithms. *Monthly Notices of the Royal Astronomical Society*, 434(4):3423–3444, 2013.
- [352] Kristín Björg Ólafsdóttir, Michael Schulz, and Manfred Mudelsee. REDFIT-X: Cross-spectral analysis of unevenly spaced paleoclimate time series. *Computers & Geosciences*, 91:11–18, 2016.
- [353] Zicheng Yu and Emi Ito. Possible solar forcing of century-scale drought frequency in the northern Great Plains. *Geology*, 27(3):263–266, 1999.
- [354] Wenfeng Deng, Gangjian Wei, Kefu Yu, and Jian-xin Zhao. Variations in the timing of the rainy season in the northern South China Sea during the middle to late Holocene. *Paleoceanography*, 29(2):115–125, 2014.
- [355] Jean Baptiste Tary, Roberto Henry Herrera, Jiajun Han, and Mirko van der Baan. Spectral estimation—what is new? what is next? *Reviews of Geophysics*, 52(4):723–749, 2014.

- [356] Christopher Torrence and Gilbert P Compo. A practical guide to wavelet analysis. *Bulletin of the American Meteorological Society*, 79(1):61–78, 1998.
- [357] Douglas Maraun, J. Kurths, and M. Holschneider. Nonstationary Gaussian processes in wavelet domain: synthesis, estimation, and significance testing. *Physical Review E*, 75(1):016707, 2007.
- [358] Aslak Grinsted, John C. Moore, and Svetlana Jevrejeva. Application of the cross wavelet transform and wavelet coherence to geophysical time series. *Nonlinear Processes in Geophysics*, 561–566:11, 2004.
- [359] K.-M. Lau and Hengyi Weng. Climate signal detection using wavelet transform: How to make a time series sing. *Bulletin of the American meteorological society*, 76(12):2391–2402, 1995.
- [360] A Rossi, Nicolas Massei, and Benoît Laignel. A synthesis of the time-scale variability of commonly used climate indices using continuous wavelet transform. *Global and Planetary Change*, 78(1-2):1–13, 2011.
- [361] Bernd R Schöne and Jens Fiebig. Seasonality in the North Sea during the Allerød and Late Medieval Climate Optimum using bivalve sclerochronology. *International Journal of Earth Sciences*, 98(1):83–98, 2009.
- [362] Yemane Asmerom, James U. L. Baldini, Keith M. Prufer, Victor J. Polyak, Harriet E. Ridley, Valorie V. Aquino, Lisa M. Baldini, Sebastian F. M. Breitenbach, Colin G. Macpherson, and Douglas J. Kennett. Intertropical convergence zone variability in the Neotropics during the Common Era. *Science Advances*, 6(7), 2020.
- [363] D.M. Labotka, H.D. Grissino-Mayer, C.I. Mora, and E.J. Johnson. Patterns of moisture source and climate variability in the southeastern United States: a four-century seasonally resolved tree-ring oxygen-isotope record. *Climate dynamics*, 46(7-8):2145–2154, 2016.
- [364] Elli R. Ronay, Sebastian F. M. Breitenbach, and Jessica L. Oster. Sensitivity of speleothem records in the Indian Summer Monsoon region to dry season infiltration. *Scientific Reports*, 9(1):5091, Mar 2019.
- [365] Grant Foster. Wavelets for period analysis of unevenly sampled time series. *The Astronomical Journal*, 112:1709, 1996.
- [366] Pietro Bazzicalupo, Patrizia Maiorano, Angela Girone, Maria Marino, Nathalie Combourieu-Nebout, Nicola Pelosi, Emília Salgueiro, and Alessandro Incarbona. Holocene climate variability of the Western Mediterranean: Surface water dynamics inferred from calcareous plankton assemblages. *The Holocene*, 30:691–708, 2020.
- [367] Annette Witt and A.Y. Schumann. Holocene climate variability on millennial scales recorded in Greenland ice cores. *Nonlinear Processes Geophysics*, 12:345–352, 2005.
- [368] Sushma Prasad, Annette Witt, Ulrike Kienel, Peter Dulski, Eva Bauer, and Gergana Yancheva. The 8.2 ka event: Evidence for seasonal differences and the rate of climate change in western Europe. *Global and Planetary Change*, 67(3-4):218–226, 2009.
- [369] Kai Wenzel Wirtz, Gerrit Lohmann, Knuth Bernhardt, and Carsten Lemmen. Mid-Holocene regional reorganization of climate variability: Analyses of proxy data in the frequency domain. *Palaeogeography, Palaeoclimatology, Palaeoecology*, 298(3-4):189–200, 2010.

- [370] Ebrahim Ghaderpour and Spiros D. Pagiatakis. Least-squares wavelet analysis of unequally spaced and non-stationary time series and its applications. *Mathematical Geosciences*, 49(7):819–844, 2017.
- [371] G. Lenoir and M. Crucifix. A general theory on frequency and time–frequency analysis of irregularly sampled time series based on projection methods – Part 2: Extension to time–frequency analysis. *Nonlinear Processes in Geophysics*, 25(1):175–200, 2018.
- [372] Gaurav Thakur, Eugene Brevdo, Neven S Fučkar, and Hau-Tieng Wu. The synchroqueezing algorithm for time-varying spectral analysis: Robustness properties and new paleoclimate applications. *Signal Processing*, 93(5):1079–1094, 2013.
- [373] Christopher J Keylock. A wavelet-based method for surrogate data generation. *Physica D: Nonlinear Phenomena*, 225(2):219–228, 2007.
- [374] Gabriel Rilling, Patrick Flandrin, Paulo Goncalves, et al. On empirical mode decomposition and its algorithms. In *IEEE-EURASIP workshop on nonlinear signal and image processing*, volume 3, pages 8–11. Citeseer, 2003.
- [375] Michael Ghil and Kingtse Mo. Intraseasonal oscillations in the global atmosphere. Part I: Northern Hemisphere and tropics. *Journal of the Atmospheric Sciences*, 48(5):752–779, 1991.
- [376] Michael Ghil and Kingtse Mo. Intraseasonal oscillations in the global atmosphere. Part II: Southern Hemisphere. *Journal of the Atmospheric Sciences*, 48(5):780–790, 1991.
- [377] Carla Taricco, Salvatore Mancuso, F.C. Ljungqvist, Silvia Alessio, and Michael Ghil. Multispectral analysis of Northern Hemisphere temperature records over the last five millennia. *Climate Dynamics*, 45(1-2):83–104, 2015.
- [378] George H. Denton, Richard B. Alley, Gary C. Comer, and Wallace S. Broecker. The role of seasonality in abrupt climate change. *Quaternary Science Reviews*, 24(10-11):1159–1182, 2005.
- [379] James Theiler, B. Galdrikian, Andr Longtin, S. Eubank, and J. Doyne Farmer. Testing for nonlinearity in time series: the method of surrogate data. Technical report, Los Alamos National Lab., NM (United States), 1991.
- [380] Martin Vejmelka and Milan Paluš. Detecting nonlinear oscillations in broadband signals. *Chaos: An Interdisciplinary Journal of Nonlinear Science*, 19(1):015114, 2009.
- [381] Victor Venema, Felix Ament, and Clemens Simmer. A stochastic iterative amplitude adjusted fourier transform algorithm with improved accuracy. *Nonlin. Processes Geophys.*, 13:321–328, 2006.
- [382] Milan Paluš. From nonlinearity to causality: statistical testing and inference of physical mechanisms underlying complex dynamics. *Contemporary Physics*, 48(6):307–348, 2007.
- [383] Niklas Boers, Aljoscha Rheinwalt, Bodo Bookhagen, Henrique MJ Barbosa, Norbert Marwan, José Marengo, and Jürgen Kurths. The South American rainfall dipole: a complex network analysis of extreme events. *Geophysical Research Letters*, 41(20):7397–7405, 2014.
- [384] Donald J. Berndt and James Clifford. Using dynamic time warping to find patterns in time series. In *KDD workshop*, volume 10, pages 359–370. Seattle, WA, 1994.

- [385] Niklas Hausmann, Amy L. Prendergast, A. Lemonis, Jana Zech, Patrick Roberts, Panayiotis Siozos, and Demetrios Anglos. Extensive elemental mapping unlocks Mg/Ca ratios as climate proxy in seasonal records of Mediterranean limpets. *Scientific Reports*, 9(1):3698, 2019.
- [386] Norbert Marwan, Marco Thiel, and Norbert R Nowaczyk. Cross recurrence plot based synchronization of time series. *Nonlinear processes in Geophysics*, 9(3/4):325–331, 2002.
- [387] Joshua Garland, Tyler R. Jones, Elizabeth Bradley, Michael Neuder, and James WC White. Climate entropy production recorded in a deep Antarctic ice core. *arXiv preprint arXiv:1806.10936*, 2018.
- [388] J. F. Donges, R. V. Donner, M. H. Trauth, N. Marwan, H. J. Schellnhuber, and J. Kurths. Nonlinear detection of paleoclimate-variability transitions possibly related to human evolution. *Proceedings of the National Academy of Sciences*, 108(51):20422–20427, 2011.
- [389] N. Marwan and J. Kurths. Complex network based techniques to identify extreme events and (sudden) transitions in spatio-temporal systems. *Chaos*, 25:097609, 2015.
- [390] Pablo M. Cincotta, Mariano Mendez, and Josue A. Nunez. Astronomical time series analysis. I. A search for periodicity using information entropy. *The Astrophysical Journal*, 449:231, 1995.
- [391] Pablo Huijse, Pablo A. Estévez, Pablo Zegers, José C. Príncipe, and Pavlos Protopapas. Period estimation in astronomical time series using slotted correntropy. *IEEE Signal Processing Letters*, 18(6):371–374, 2011.
- [392] Jessica L. Oster and Neil P. Kelley. Tracking regional and global teleconnections recorded by western North American speleothem records. *Quaternary Science Reviews*, 149:18–33, 2016.
- [393] Fiona H. McRobie, Thomas Stemler, and K.-H. Wyrwoll. Transient coupling relationships of the Holocene Australian monsoon. *Quaternary Science Reviews*, 121:120–131, 2015.
- [394] Odile Peyron, Simon Goring, Isabelle Dormoy, Ulrich Kotthoff, Jörg Pross, Jacques-Louis De Beaulieu, Ruth Drescher-Schneider, Boris Vannièrè, and Michel Magny. Holocene seasonality changes in the central Mediterranean region reconstructed from the pollen sequences of Lake Accesa (Italy) and Tenaghi Philippon (Greece). *The Holocene*, 21(1):131–146, 2011.
- [395] Josephine R Brown, Matthieu Lengaigne, Benjamin R Lintner, Matthew J Widlansky, Karin van der Wiel, Cyril Dutheil, Braddock K Linsley, Adrian J Matthews, and James Renwick. South Pacific Convergence Zone dynamics, variability and impacts in a changing climate. *Nature Reviews Earth & Environment*, 1(10):530–543, 2020.
- [396] Axel Timmermann, Soon-Il An, Jong-Seong Kug, Fei-Fei Jin, Wenju Cai, Antonietta Capotondi, Kim M. Cobb, Matthieu Lengaigne, Michael J. McPhaden, Malte F. Stuecker, Karl Stein, Andrew T. Wittenberg, Kyung-Sook Yun, Tobias Bayr, Han-Ching Chen, Yoshimitsu Chikamoto, Boris Dewitte, Dietmar Dommenges, Pamela Grothe, Eric Guilyardi, Yoo-Geun Ham, Michiya Hayashi, Sarah Ineson, Daehyun Kang, Sunyong Kim, WonMoo Kim, June-Yi Lee, Tim Li, Jing-Jia Luo, Shayne McGregor, Yann Planton, Scott Power, Harun Rashid, Hong-Li Ren, Agus Santoso, Ken Takahashi,

- Alexander Todd, Guomin Wang, Guojian Wang, Ruihuang Xie, Woo-Hyun Yang, Sang-Wook Yeh, Jinho Yoon, Elke Zeller, and Xuebin Zhang. El Niño–Southern Oscillation complexity. *Nature*, 559(7715):535–545, 2018.
- [397] Australian Bureau of Meteorology and CSIRO. Climate Change in the Pacific: Scientific Assessment and New Research. Volume 1: Regional Overview. Volume 2: Country Reports. Technical report, Australian Government, 2011.
- [398] Mark A. Cane. The evolution of El Niño, past and future. *Earth and Planetary Science Letters*, 230(3):227–240, 2005.
- [399] Antonietta Capotondi, Andrew T. Wittenberg, Matthew Newman, Emanuele Di Lorenzo, Jin-Yi Yu, Pascale Braconnot, Julia Cole, Boris Dewitte, Benjamin Giese, Eric Guilyardi, Fei-Fei Jin, Kristopher Karnauskas, Benjamin Kirtman, Tong Lee, Niklas Schneider, Yan Xue, and Sang-Wook Yeh. Understanding ENSO Diversity. *Bulletin of the American Meteorological Society*, 96(6):921 – 938, 2015.
- [400] Athanasios Koutavas, Peter B DeMenocal, George C Olive, and Jean Lynch-Stieglitz. Mid-Holocene El Niño–Southern Oscillation (ENSO) attenuation revealed by individual foraminifera in eastern tropical Pacific sediments. *Geology*, 34(12):993–996, dec 2006.
- [401] Kim M. Cobb, Niko Westphal, Hussein R. Sayani, Jordan T. Watson, Emanuele Di Lorenzo, H. Cheng, R. L. Edwards, and Christopher D. Charles. Highly Variable El Niño Southern Oscillation Throughout the Holocene. *Science*, 339(6115):67–70, 2013.
- [402] Alexander W. Tudhope, Colin P. Chilcott, Malcolm T. McCulloch, Edward R. Cook, John Chappell, Robert M. Ellam, David W. Lea, Janice M. Lough, and Graham B. Shimmield. Variability in the El Niño–Southern Oscillation Through a Glacial–Interglacial Cycle. *Science*, 291(5508):1511–1517, 2001.
- [403] Jessica L. Conroy, Jonathan T. Overpeck, Julia E. Cole, Timothy M. Shanahan, and Miriam Steinitz-Kannan. Holocene changes in eastern tropical Pacific climate inferred from a Galápagos lake sediment record. *Quaternary Science Reviews*, 27(11):1166–1180, 2008.
- [404] Christopher M. Moy, Geoffrey O. Seltzer, Donald T. Rodbell, and David M. Anderson. Variability of El Niño/Southern Oscillation activity at millennial timescales during the Holocene epoch. *Nature*, 420(6912):162–165, 2002.
- [405] Sang Chen, Sharon S. Hoffmann, David C. Lund, Kim M. Cobb, Julien Emile-Geay, and Jess F. Adkins. A high-resolution speleothem record of western equatorial Pacific rainfall: Implications for Holocene ENSO evolution. *Earth and Planetary Science Letters*, 442:61–71, 2016.
- [406] Donald T. Rodbell, Geoffrey O. Seltzer, David M. Anderson, Mark B. Abbott, David B. Enfield, and Jeremy H. Newman. An ~15,000-Year Record of El Niño–Driven Alluviation in Southwestern Ecuador. *Science*, 283(5401):516–520, 1999.
- [407] Athanasios Koutavas and Stephan Joanides. El Niño–Southern Oscillation extrema in the Holocene and Last Glacial Maximum. *Paleoceanography*, 27(4), 2012.
- [408] James Shulmeister and Brian G. Lees. Pollen evidence from tropical Australia for the onset of an ENSO-dominated climate at c. 4000 BP. *The Holocene*, 5(1):10–18, 1995.

- [409] Amy C. Clement, Richard Seager, and Mark A. Cane. Suppression of El Niño during the Mid-Holocene by changes in the Earth’s orbit. *Paleoceanography*, 15(6):731–737, 2000.
- [410] Sarah M. White, A. Christina Ravelo, and Pratigya J. Polissar. Dampened El Niño in the Early and Mid-Holocene Due To Insolation-Forced Warming/Deepening of the Thermocline. *Geophysical Research Letters*, 45(1):316–326, 2018.
- [411] Ian J. Fairchild and Pauline C. Treble. Trace elements in speleothems as recorders of environmental change. *Quaternary Science Reviews*, 28(5):449 – 468, 2009.
- [412] Hai Cheng, Christoph Spötl, Sebastian F.M. Breitenbach, Ashish Sinha, Jasper A. Wassenburg, Klaus Peter Jochum, Denis Scholz, Xianglei Li, Liang Yi, Youbing Peng, Yanbin Lv, Pingzhong Zhang, Antonina Votintseva, Vadim Loginov, Youfeng Ning, Gayatri Kathayat, and R. Lawrence Edwards. Climate variations of Central Asia on orbital to millennial timescales. *Scientific Reports*, 6(1):36975, 2016.
- [413] Sebastian F.M. Breitenbach, Jess F. Adkins, Hanno Meyer, Norbert Marwan, Kani-kicharla Krishna Kumar, and Gerald H. Haug. Strong influence of water vapor source dynamics on stable isotopes in precipitation observed in Southern Meghalaya, NE India. *Earth and Planetary Science Letters*, 292(1):212–220, 2010.
- [414] Matthew S. Lachniet. Climatic and environmental controls on speleothem oxygen-isotope values. *Quaternary Science Reviews*, 28(5):412 – 432, 2009.
- [415] Jens Fohlmeister, Ny Riavo G. Voarintsoa, Franziska A. Lechleitner, Meighan Boyd, Susanne Brandtstätter, Matthew J. Jacobson, and Jessica L. Oster. Main controls on the stable carbon isotope composition of speleothems. *Geochimica et Cosmochimica Acta*, 279:67 – 87, 2020.
- [416] D. Genty, D. Blamart, R. Ouahdi, M. Gilmour, A. Baker, J. Jouzel, and Sandra Van-Exter. Precise dating of Dansgaard–Oeschger climate oscillations in western Europe from stalagmite data. *Nature*, 421(6925):833–837, Feb 2003.
- [417] I.J. Fairchild and A Baker. *Speleothem Science: From Process to Past Environment*. Wiley-Blackwell, Chichester, UK,, 2012.
- [418] Mohammadali Faraji, Andrea Borsato, Silvia Frisia, John C. Hellstrom, Andrew Lorrey, Adam Hartland, Alan Greig, and David P. Matthey. Accurate dating of stalagmites from low seasonal contrast tropical Pacific climate using Sr 2D maps, fabrics and annual hydrological cycles. *Scientific Reports*, 11(1):2178, 2021.
- [419] Paul Aharon, Michael Rasbury, and Valeriu Murgulet. Caves of Niue Island, South Pacific: Speleothems and water geochemistry. In *Perspectives on Karst Geomorphology, Hydrology, and Geochemistry - A Tribute Volume to Derek C. Ford and William B. White*, pages 283–295. Geological Society of America, 01 2006.
- [420] M. C. Peel, B. L. Finlayson, and T. A. McMahon. Updated world map of the Köppen-Geiger climate classification. *Hydrology and Earth System Sciences*, 11(5):1633–1644, 2007.
- [421] Michael Rasbury and Paul Aharon. ENSO-controlled rainfall variability records archived in tropical stalagmites from the mid-ocean island of Niue, South Pacific. *Geochemistry, Geophysics, Geosystems*, 7(7), 2006.

- [422] Andrew Lorrey, Giovanni Dalu, James Renwick, Howard Diamond, and Marco Gaetani. Reconstructing the South Pacific Convergence Zone Position during the Presatellite Era: A La Niña Case Study. *Monthly Weather Review*, 140(11):3653 – 3668, 2012.
- [423] Emmanuel M. Vincent, Matthieu Lengaigne, Christophe E. Menkes, Nicolas C. Jourdain, Patrick Marchesiello, and Gurvan Madec. Interannual variability of the South Pacific Convergence Zone and implications for tropical cyclone genesis. *Climate Dynamics*, 36(9):1881–1896, 2011.
- [424] Adam Hartland, Ian J. Fairchild, Wolfgang Müller, and David Dominguez-Villar. Preservation of non-metal complexes in a modern hyperalkaline stalagmite: Implications for speleothem trace element geochemistry. *Geochimica et Cosmochimica Acta*, 128:29–43, 2014.
- [425] John Hellstrom. Rapid and accurate U/Th dating using parallel ion-counting multi-collector ICP-MS. *J. Anal. At. Spectrom.*, 18:1346–1351, 2003.
- [426] Caroline A. Schneider, Wayne S. Rasband, and Kevin W. Eliceiri. NIH Image to ImageJ: 25 years of image analysis. *Nature Methods*, 9(7):671–675, 2012.
- [427] E. J. Steig, V. Gkinis, A. J. Schauer, S. W. Schoenemann, K. Samek, J. Hoffnagle, K. J. Dennis, and S. M. Tan. Calibrated high-precision  $^{17}\text{O}$ -excess measurements using cavity ring-down spectroscopy with laser-current-tuned cavity resonance. *Atmospheric Measurement Techniques*, 7(8):2421–2435, 2014.
- [428] Valeriu Murgulet. *Paleoclimate reconstructions over the last century from a tropical speleothem on Niue Island, South Pacific*. PhD thesis, University of Alabama Libraries, 2010.
- [429] Andy Baker, Claire Smith, Catherine Jex, Ian Fairchild, Dominique Genty, and Lisa Fuller. Annually laminated speleothems: a review. *International Journal of Speleology*, 37(3):193–206, 2008.
- [430] Silvia Frisia. Microstratigraphic logging of calcite fabrics in speleothems as tool for palaeoclimate studies. *International Journal of Speleology*, 44(1), 2014.
- [431] Peter E. Carlson, Nathaniel R. Miller, Jay L. Banner, Daniel O. Breecker, and Richard C. Casteel. The potential of near-entrance stalagmites as high-resolution terrestrial paleoclimate proxies: Application of isotope and trace-element geochemistry to seasonally-resolved chronology. *Geochimica et Cosmochimica Acta*, 235:55–75, 2018.
- [432] Board of Governors. Annual report. Technical report, International Atomic Energy Agency, 2001.
- [433] Darrel M. Tremaine, Daniel J. Sinclair, Heather M. Stoll, Maria Lagerström, Carlos P. Carvajal, and Robert M. Sherrell. A two-year automated dripwater chemistry study in a remote cave in the tropical south pacific: Using [cl-] as a conservative tracer for seasalt contribution of major cations. *Geochimica et Cosmochimica Acta*, 184:289–310, 2016.
- [434] Francisco W. Cruz, Ivo Karmann, Oduvaldo Viana, Stephen J. Burns, José A. Ferrari, Mathias Vuille, Alcides N. Sial, and Marcelo Z. Moreira. Stable isotope study of cave percolation waters in subtropical brazil: Implications for paleoclimate inferences from speleothems. *Chemical Geology*, 220(3):245–262, 2005.

- [435] Frank McDermott. Palaeo-climate reconstruction from stable isotope variations in speleothems: a review. *Quaternary Science Reviews*, 23(7):901–918, 2004. Isotopes in Quaternary Palaeoenvironmental reconstruction.
- [436] Andrea Borsato, Silvia Frisia, Ian J. Fairchild, Andrea Somogyi, and Jean Susini. Trace element distribution in annual stalagmite laminae mapped by micrometer-resolution X-ray fluorescence: Implications for incorporation of environmentally significant species. *Geochimica et Cosmochimica Acta*, 71(6):1494 – 1512, 2007.
- [437] Adam Hartland, Ian J. Fairchild, Jamie R. Lead, Andrea Borsato, Andy Baker, Silvia Frisia, and Mohammed Baalousha. From soil to cave: Transport of trace metals by natural organic matter in karst dripwaters. *Chemical Geology*, 304-305:68–82, 2012.
- [438] Jessica L. Oster, Warren D. Sharp, Aaron K. Covey, Jansen Gibson, Bruce Rogers, and Hari Mix. Climate response to the 8.2 ka event in coastal California. *Scientific Reports*, 7(1):3886, Jun 2017.
- [439] Peter M. Wynn, Ian J. Fairchild, Andrea Borsato, Christoph Spötl, Adam Hartland, Andy Baker, Silvia Frisia, and James U.L. Baldini. Sulphate partitioning into calcite: Experimental verification of pH control and application to seasonality in speleothems. *Geochimica et Cosmochimica Acta*, 226:69–83, 2018.
- [440] Robert A. Jamieson, James U.L. Baldini, Marianne J. Brett, Jessica Taylor, Harriet E. Ridley, Chris J. Ottley, Keith M. Prufer, Jasper A. Wassenburg, Denis Scholz, and Sebastian F.M. Breitenbach. Intra- and inter-annual uranium concentration variability in a Belizean stalagmite controlled by prior aragonite precipitation: A new tool for reconstructing hydro-climate using aragonitic speleothems. *Geochimica et Cosmochimica Acta*, 190:332 – 346, 2016.
- [441] Fes A. de Scally. Historical Tropical Cyclone Activity and Impacts in the Cook Islands. *Pacific Science*, 62(4):443 – 459, 2008.
- [442] J. Emile-Geay and M. Tingley. Inferring climate variability from nonlinear proxies: application to palaeo-ENSO studies. *Climate of the Past*, 12(1):31–50, 2016.
- [443] William S. Kessler. Is ENSO a cycle or a series of events? *Geophysical Research Letters*, 29(23):40–1–40–4, 2002.
- [444] Jose Iriarte, Sarah Elliott, S. Yoshi Maezumi, Daiana Alves, Regina Gonda, Mark Robinson, Jonas Gregorio de Souza, Jennifer Watling, and Josephine Handley. The origins of Amazonian landscapes: Plant cultivation, domestication and the spread of food production in tropical South America. *Quaternary Science Reviews*, 248:106582, 2020.
- [445] Douglas J. Kennett and Norbert Marwan. Climatic volatility, agricultural uncertainty, and the formation, consolidation and breakdown of preindustrial agrarian states. *Philosophical Transactions of the Royal Society A: Mathematical, Physical and Engineering Sciences*, 373(2055):20140458, 2015.
- [446] Pradeep Kurukulasuriya and Shane Rosenthal. Climate Change and Agriculture : A Review of Impacts and Adaptations. Environment department papers;no. 91. Climate change series. Technical report, Environment department, 2013.
- [447] Salvatore Pascale, Valerio Lucarini, Xue Feng, Amilcare Porporato, and Shabeh ul Hassan. Projected changes of rainfall seasonality and dry spells in a high greenhouse gas emissions scenario. *Climate Dynamics*, 46(3-4):1331–1350, 2016.



- [448] Takeshi Inomata, Daniela Triadan, Verónica A Vázquez López, Juan Carlos Fernandez-Diaz, Takayuki Omori, María Belén Méndez Bauer, Melina García Hernández, Timothy Beach, Clarissa Cagnato, Kazuo Aoyama, et al. Monumental architecture at Aguada Fénix and the rise of Maya civilization. *Nature*, 582(7813):530–533, 2020.
- [449] Douglas J. Kennett, Keith M. Prufer, Brendan J. Culleton, Richard J. George, Mark Robinson, Willa R. Trask, Gina M. Buckley, Emily Moes, Emily J. Kate, Thomas K. Harper, et al. Early isotopic evidence for maize as a staple grain in the Americas. *Science Advances*, 6(23):eaba3245, 2020.
- [450] Claire E. Ebert, Keith M. Prufer, Martha J. Macri, Bruce Winterhalder, and Douglas J. Kennett. Terminal long count dates and the disintegration of Classic Period Maya polities. *Ancient Mesoamerica*, 25(2):337–356, 2014.
- [451] Martín Medina-Elizalde and Eelco J. Rohling. Collapse of Classic Maya civilization related to modest reduction in precipitation. *Science*, 335(6071):956–959, 2012.
- [452] Keith M. Prufer, Amy E. Thompson, Clayton R. Meredith, Brendan J. Culleton, Jilian M. Jordan, Claire E. Ebert, Bruce Winterhalder, and Douglas J. Kennett. The Classic Period Maya transition from an ideal free to an ideal despotic settlement system at the polity of Uxbenká. *Journal of Anthropological Archaeology*, 45:53–68, 2017.
- [453] Eva Jobbová, Christophe Helmke, and Andrew Bevan. Ritual responses to drought: An examination of ritual expressions in Classic Maya written sources. *Human Ecology*, 46(5):759–781, 2018.
- [454] Douglas J. Kennett, Sebastian F.M. Breitenbach, Valorie V. Aquino, Yemane Asmerom, Jaime Awe, James U.L. Baldini, Patrick Bartlein, Brendan J. Culleton, Claire Ebert, Christopher Jazwa, et al. Development and disintegration of Maya political systems in response to climate change. *Science*, 338(6108):788–791, 2012.
- [455] Marilyn A. Masson. Cultural transformation at the Maya Postclassic community of Laguna de On, Belize. *Latin American Antiquity*, 8(4):293–316, 1997.
- [456] K.M. Prufer, A.E. Thompson, A. Wickert, and D.J. Kennett. The development and disintegration of a Classic Maya center and its climate context. *Progress in Physical Geography*, in press.
- [457] Marilyn Masson and Carlos Peraza Lope. *Kukulcan’s realm: Urban life at Ancient Mayapán*. University Press of Colorado, 2014.
- [458] Julie A. Hoggarth, Sebastian F.M. Breitenbach, Brendan J. Culleton, Claire E. Ebert, Marilyn A. Masson, and Douglas J. Kennett. The political collapse of Chichén Itzá in climatic and cultural context. *Global and planetary change*, 138:25–42, 2016.
- [459] Amy Benoit Frappier, James Pyburn, Aurora D. Pinkey-Drobnis, Xianfeng Wang, D. Reide Corbett, and Bruce H. Dahlin. Two millennia of tropical cyclone-induced mud layers in a northern Yucatán stalagmite: Multiple overlapping climatic hazards during the Maya Terminal Classic “megadroughts”. *Geophysical Research Letters*, 41(14):5148–5157, 2014.
- [460] Julie A. Hoggarth, Matthew Restall, James W. Wood, Douglas J. Kennett, Victoria R. Bricker, John F. Chuchiak I.V., Mauricio Lima, Marilyn A. Masson, Richard R. Paine, Robert W. Patch, et al. Drought and its demographic effects in the Maya lowlands. *Current Anthropology*, 58(1):000–000, 2017.

- [461] Karen L. Kramer and Joseph Hackman. Scaling climate change to human behavior predicting good and bad years for Maya farmers. *American Journal of Human Biology*, 33(4):e23524, 2021.
- [462] Rico Kongsager. Barriers to the adoption of alley cropping as a climate-smart agriculture practice: Lessons from maize cultivation among the Maya in southern Belize. *Forests*, 8(7):260, 2017.
- [463] Claire E. Ebert, Julie A. Hoggarth, Jaime J. Awe, Brendan J. Culleton, and Douglas J. Kennett. The role of diet in resilience and vulnerability to climate change among early agricultural communities in the Maya Lowlands. *Current Anthropology*, 60(4):589–601, 2019.
- [464] Scott L. Fedick and Louis S. Santiago. Large variation in availability of Maya food plant sources during ancient droughts. *Proceedings of the National Academy of Sciences*, 119(1):e2115657118, 2022.
- [465] Douglas J. Kennett, Marilyn A. Masson, Stanley Serafin, Brendan J. Culleton, and Carlos Peraza Lope. War and food production at the Postclassic Maya City of Mayapán. In *The archaeology of food and warfare*, pages 161–192. Springer, 2016.
- [466] Harriet E. Ridley, James U.L. Baldini, Keith M. Prufer, Izabela W. Walczak, and Sebastian F.M. Breitenbach. High resolution monitoring of Yok Balum Cave, Belize: an investigation of seasonal ventilation regimes and the atmospheric and drip-flow response to a local earthquake. *Journal of Cave and Karst Studies.*, 77(3):183–199, 2015.
- [467] Franziska A. Lechleitner, James U.L. Baldini, Sebastian F.M. Breitenbach, Jens Fohlmeister, Cameron McIntyre, Bedartha Goswami, Robert A. Jamieson, Tessa S. van der Voort, Keith Prufer, Norbert Marwan, et al. Hydrological and climatological controls on radiocarbon concentrations in a tropical stalagmite. *Geochimica et Cosmochimica Acta*, 194:233–252, 2016.
- [468] Jens Fohlmeister, Ny Riavo G. Voarintsoa, Franziska A. Lechleitner, Meighan Boyd, Susanne Brandtstätter, Matthew J. Jacobson, and Jessica L. Oster. Main controls on the stable carbon isotope composition of speleothems. *Geochimica et Cosmochimica Acta*, 279:67–87, 2020.
- [469] Carlos Martinez, Lisa Goddard, Yochanan Kushnir, and Mingfang Ting. Seasonal climatology and dynamical mechanisms of rainfall in the Caribbean. *Climate Dynamics*, 53(1):825–846, 2019.
- [470] Michael P. Byrne and Tapio Schneider. Narrowing of the ITCZ in a warming climate: Physical mechanisms. *Geophysical Research Letters*, 43(21):11–350, 2016.
- [471] Michael P. Byrne, Angeline G. Pendergrass, Anita D. Rapp, and Kyle R. Wodzicki. Response of the intertropical convergence zone to climate change: Location, width, and strength. *Current Climate Change Reports*, 4(4):355–370, 2018.
- [472] Dominik Schmitt, Eberhard Gischler, Daniel Birgel, Jörn Peckmann, Flavio S Anselmetti, and Hendrik Vogel. Great Blue Hole (Lighthouse Reef, Belize): A continuous, annually-resolved record of Common Era sea surface temperature, Atlantic Multidecadal Oscillation and cyclone-controlled run-off. *Quaternary Science Reviews*, 247:106570, 2020.

- [473] Jiaying Wu, David F. Porinchu, and Sally P. Horn. Late Holocene hydroclimate variability in Costa Rica: Signature of the terminal classic drought and the Medieval Climate Anomaly in the northern tropical Americas. *Quaternary Science Reviews*, 215:144–159, 2019.
- [474] Tripti Bhattacharya, John C.H. Chiang, and Wei Cheng. Ocean-atmosphere dynamics linked to 800–1050 CE drying in Mesoamerica. *Quaternary Science Reviews*, 169:263–277, 2017.
- [475] Xiaojing Du, Ingrid Hendy, Linda Hinnov, Erik Brown, Arndt Schimmelmann, and Dorothy Pak. Interannual Southern California precipitation variability during the Common Era and the ENSO teleconnection. *Geophysical Research Letters*, 47(1):e2019GL085891, 2020.
- [476] Dominik Schmitt, Eberhard Gischler, Flavio S. Anselmetti, and Hendrik Vogel. Caribbean cyclone activity: an annually-resolved Common Era record. *Scientific Reports*, 10(1):1–17, 2020.
- [477] Lisa M. Baldini, James U.L. Baldini, Jim N. McElwaine, Amy Benoit Frappier, Yemane Asmerom, Kam-biu Liu, Keith M. Prufer, Harriet E. Ridley, Victor Polyak, Douglas J. Kennett, et al. Persistent northward North Atlantic tropical cyclone track migration over the past five centuries. *Scientific Reports*, 6(1):1–8, 2016.
- [478] Linda Kuil, Gemma Carr, Alberto Viglione, Alexia Prskawetz, and Günter Blöschl. Conceptualizing socio-hydrological drought processes: The case of the Maya collapse. *Water Resources Research*, 52(8):6222–6242, 2016.
- [479] Gerald H. Haug, Detlef Günther, Larry C. Peterson, Daniel M. Sigman, Konrad A. Hughen, and Beat Aeschlimann. Climate and the collapse of Maya civilization. *Science*, 299(5613):1731–1735, 2003.
- [480] Henry C. Wu, Thomas Felis, Denis Scholz, Cyril Giry, Martin Kölling, Klaus P. Jochum, and Sander R. Scheffers. Changes to Yucatán Peninsula precipitation associated with salinity and temperature extremes of the Caribbean Sea during the Maya civilization collapse. *Scientific Reports*, 7(1):1–12, 2017.
- [481] Marcello A. Canuto, Francisco Estrada-Belli, Thomas G. Garrison, Stephen D. Houston, Mary Jane Acuña, Milan Kováč, Damien Marken, Philippe Nondédéo, Luke Auld-Thomas, Cyril Castanet, et al. Ancient lowland Maya complexity as revealed by airborne laser scanning of northern Guatemala. *Science*, 361(6409):eaau0137, 2018.
- [482] Blanca Mendoza, Virginia García-Acosta, Victor Velasco, Ernesto Jáuregui, and Rosa Díaz-Sandoval. Frequency and duration of historical droughts from the 16th to the 19th centuries in the Mexican Maya lands, Yucatan Peninsula. *Climatic Change*, 83(1):151–168, 2007.
- [483] Sabin Roman, Erika Palmer, and Markus Brede. The dynamics of human-environment interactions in the collapse of the classic Maya. *Ecological economics*, 146:312–324, 2018.
- [484] Timothy Beach, Sheryl Luzzadder-Beach, Samantha Krause, Tom Guderjan, Fred Valdez Jr, Juan Carlos Fernandez-Diaz, Sara Eshleman, and Colin Doyle. Ancient Maya wetland fields revealed under tropical forest canopy from laser scanning and multiproxy evidence. *Proceedings of the National Academy of Sciences*, 116(43):21469–21477, 2019.

- [485] Arlen F. Chase and Diane Z. Chase. Scale and intensity in classic period Maya agriculture: Terracing and settlement at the "garden city" of Caracol, Belize. *Culture & Agriculture*, 20(2-3):60–77, 1998.
- [486] Jeremy D. Coltman and John M.D. Pohl. *Sorcery in Mesoamerica*. University Press of Colorado, 2020.
- [487] Tapio Schneider, Tobias Bischoff, and Gerald H. Haug. Migrations and dynamics of the intertropical convergence zone. *Nature*, 513(7516):45–53, 2014.
- [488] Kevin T. Wright, Kathleen R. Johnson, Tripti Bhattacharya, Gabriela Serrato Marks, David McGee, Dillon Elsbury, Yannick Peings, Jean-Louis Lacaille-Muzquiz, Gianna Lum, Laura Beramendi-Orosco, et al. Precipitation in Northeast Mexico Primarily Controlled by the Relative Warming of Atlantic SSTs. *Geophysical Research Letters*, 49(11):e2022GL098186, 2022.
- [489] Jennifer B. Wurtzel, David E. Black, Robert C. Thunell, Larry C. Peterson, Eric J. Tappa, and Shaily Rahman. Mechanisms of southern Caribbean SST variability over the last two millennia. *Geophysical Research Letters*, 40(22):5954–5958, 2013.
- [490] Eduardo Moreno-Chamarro, J. Marshall, and T.L. Delworth. Linking itcz migrations to the amoc and north atlantic/pacific sst decadal variability. *Journal of Climate*, 33(3):893–905, 2020.
- [491] Alyssa R. Atwood, D.S. Battisti, Elynn W.u., D.M.W. Frierson, and Julian P. Sachs. Data-Model Comparisons of Tropical Hydroclimate Changes Over the Common Era. *Paleoceanography and Paleoclimatology*, 36(7):e2020PA003934, 2021.
- [492] Byron A. Steinman, Nathan D. Stansell, Michael E. Mann, Colin A. Cooke, Mark B. Abbott, Mathias Vuille, Broxton W. Bird, Matthew S. Lachniet, and Alejandro Fernandez. Interhemispheric antiphasing of neotropical precipitation during the past millennium. *Proceedings of the National Academy of Sciences*, 119(17):e2120015119, 2022.
- [493] David A. Hodell, Jason H. Curtis, Glenn A. Jones, Antonia Higuera-Gundy, Mark Brenner, Michael W. Binford, and Kathleen T. Dorsey. Reconstruction of Caribbean climate change over the past 10,500 years. *Nature*, 352(6338):790–793, 1991.
- [494] Gerald H. Haug, Konrad A. Hughen, Daniel M. Sigman, Larry C. Peterson, and Ursula Rohl. Southward migration of the intertropical convergence zone through the Holocene. *Science*, 293(5533):1304–1308, 2001.
- [495] Franziska A. Lechleitner, Sebastian F.M. Breitenbach, Kira Rehfeld, Harriet E. Ridley, Yemane Asmerom, Keith M. Prufer, Norbert Marwan, Bedartha Goswami, Douglas J. Kennett, Valorie V. Aquino, et al. Tropical rainfall over the last two millennia: evidence for a low-latitude hydrologic seesaw. *Scientific Reports*, 7(1):1–9, 2017.
- [496] Peter J. van Hengstum, Jeffrey P. Donnelly, Patricia L. Fall, Michael R. Toomey, Nancy A. Albury, and Brian Kakuk. The intertropical convergence zone modulates intense hurricane strikes on the western North Atlantic margin. *Scientific Reports*, 6(1):1–10, 2016.
- [497] Billie L. Turner and Jeremy A. Sabloff. Classic Period collapse of the Central Maya Lowlands: Insights about human–environment relationships for sustainability. *Proceedings of the National Academy of Sciences*, 109(35):13908–13914, 2012.

- [498] Celia A. Harvey, Milagro Saborio-Rodríguez, M. Ruth Martínez-Rodríguez, Barbara Viguera, Adina Chain-Guadarrama, Raffaele Vignola, and Francisco Alpizar. Climate change impacts and adaptation among smallholder farmers in Central America. *Agriculture & Food Security*, 7(1):1–20, 2018.
- [499] Christopher P.O. Reyer, Sophie Adams, Torsten Albrecht, Florent Baarsch, Alice Boit, Nella Canales Trujillo, Matti Carlsburg, Dim Coumou, Alexander Eden, Erick Fernandes, et al. Climate change impacts in Latin America and the Caribbean and their implications for development. *Regional Environmental Change*, 17(6):1601–1621, 2017.
- [500] Stephen Shennan, Sean S. Downey, Adrian Timpson, Kevan Edinborough, Sue Colledge, Tim Kerig, Katie Manning, and Mark G. Thomas. Regional population collapse followed initial agriculture booms in mid-Holocene Europe. *Nature communications*, 4(1):1–8, 2013.
- [501] Alan N. Williams. The use of summed radiocarbon probability distributions in archaeology: a review of methods. *Journal of Archaeological Science*, 39(3):578–589, 2012.
- [502] Enrico R. Crema and Andrew Bevan. Inference from large sets of radiocarbon dates: software and methods. *Radiocarbon*, 63(1):23–39, 2021.
- [503] Julie A. Hoggarth, Brendan J. Culleton, Jaime J. Awe, Christophe Helmke, Sydney Lonaker, J. Britt Davis, and Douglas J. Kennett. Building high-precision AMS 14C Bayesian models for the formation of peri-abandonment deposits at Baking Pot, Belize. *Radiocarbon*, 63(3):977–1002, 2021.
- [504] Christopher Bronk Ramsey. Methods for summarizing radiocarbon datasets. *Radiocarbon*, 59(6):1809–1833, 2017.
- [505] Paula J. Reimer, William E.N. Austin, Edouard Bard, Alex Bayliss, Paul G. Blackwell, Christopher Bronk Ramsey, Martin Butzin, Hai Cheng, R. Lawrence Edwards, Michael Friedrich, et al. The IntCal20 Northern Hemisphere radiocarbon age calibration curve (0–55 cal kBP). *Radiocarbon*, 62(4):725–757, 2020.
- [506] Enrico R Crema. Statistical inference of prehistoric demography from frequency distributions of radiocarbon dates: a review and a guide for the perplexed. *Journal of Archaeological Method and Theory*, pages 1–32, 2022.
- [507] Peter Mathews. Classic Maya emblem glyphs. *Classic Maya political history: Hieroglyphic and archaeological evidence*, pages 19–29, 1991.
- [508] Viviana Amati, Jessica Munson, Jonathan Scholnick, et al. Applying event history analysis to explain the diffusion of innovations in archaeological networks. *Journal of Archaeological Science*, 104:1–9, 2019.
- [509] David Webster. The not so peaceful civilization: A review of Maya war. *Journal of World Prehistory*, 14(1):65–119, 2000.
- [510] Nicholas P. McKay, Julien Emile-Geay, and Deborah Khider. geoChronR – an R package to model, analyze, and visualize age-uncertain data. *Geochronology*, 3(1):149–169, 2021.
- [511] Shaun Lovejoy and Daniel Schertzer. *The weather and climate: emergent laws and multifractal cascades*. Cambridge University Press, 2018.
- [512] Rafael H.C. de Melo and Aura Conci. How succolarity could be used as another fractal measure in image analysis. *Telecommunication Systems*, 52(3):1643–1655, 2013.

- [513] Jie Zhang and Michael Small. Complex network from pseudoperiodic time series: Topology versus dynamics. *Physical review letters*, 96(23):238701, 2006.
- [514] Martin A. Reiss, Birgit Lemmerer, Arnold Hanslmeier, and Helmut Ahammer. Tug-of-war lacunarity – A novel approach for estimating lacunarity. *Chaos: An Interdisciplinary Journal of Nonlinear Science*, 26(11):113102, 2016.
- [515] Charles R. Tolle, Timothy R. McJunkin, and David J. Gorsich. An efficient implementation of the gliding box lacunarity algorithm. *Physica D: Nonlinear Phenomena*, 237(3):306–315, 2008.
- [516] K Hauke Kraemer, Frank Hellmann, Mehrnaz Anvari, Jürgen Kurths, and Norbert Marwan. Spike spectra for recurrences. *Entropy*, 24(11):1689, 2022.
- [517] Kai Hauke Krämer. *Towards a robust framework for recurrence analysis: automated state space reconstruction, optimal parameter selection and correction schemes*. PhD thesis, Universität Potsdam, 2021.
- [518] Ian R. Cleasby, Ewan D. Wakefield, Barbara J. Morrissey, Thomas W. Bodey, Steven C. Votier, Stuart Bearhop, and Keith C. Hamer. Using time-series similarity measures to compare animal movement trajectories in ecology. *Behavioral Ecology and Sociobiology*, 73(11):1–19, 2019.
- [519] Raphaël Hébert, Kira Rehfeld, and Thomas Laepple. Comparing estimation techniques for timescale-dependent scaling of climate variability in paleoclimate time series. *Non-linear Processes in Geophysics Discussions*, 2021:1–26, 2021.
- [520] Maria Reschke, Torben Kunz, and Thomas Laepple. Comparing methods for analysing time scale dependent correlations in irregularly sampled time series data. *Computers & Geosciences*, 123:65–72, 2019.
- [521] Torben Kunz, Andrew M. Dolman, and Thomas Laepple. A spectral approach to estimating the timescale-dependent uncertainty of paleoclimate records – Part 1: Theoretical concept. *Climate of the Past*, 16(4):1469–1492, 2020.
- [522] Johann H Jungclauss, Noel Keenlyside, Michael Botzet, H Haak, J-J Luo, Mojib Latif, J Marotzke, U Mikolajewicz, and Erich Roeckner. Ocean circulation and tropical variability in the coupled model echam5/mpi-om. *Journal of climate*, 19(16):3952–3972, 2006.
- [523] A. Hannachi and A. O’Neill. Atmospheric multiple equilibria and non-Gaussian behaviour in model simulations. *Quarterly Journal of the Royal Meteorological Society*, 127(573):939–958, 2001.
- [524] S. Kravtsov, D. Kondrashov, and M. Ghil. Multilevel Regression Modeling of Nonlinear Processes: Derivation and Applications to Climatic Variability. *Journal of Climate*, 18(21):4404 – 4424, 2005.
- [525] David R Cox. *Renewal theory*. Springer, 1967.
- [526] Holger Kantz and Thomas Schreiber. *Nonlinear time series analysis*, volume 7. Cambridge university press, 2004.
- [527] Sebastian F.M. Breitenbach and Stefano M. Bernasconi. Carbon and oxygen isotope analysis of small carbonate samples (20 to 100  $\mu\text{g}$ ) with a GasBench II preparation device. *Rapid Communications in Mass Spectrometry*, 25(13):1910–1914, 2011.

- [528] Chad Paton, John Hellstrom, Bence Paul, Jon Woodhead, and Janet Hergt. Iolite: Freeware for the visualisation and processing of mass spectrometric data. *Journal of Analytical Atomic Spectrometry*, 26(12):2508–2518, 2011.
- [529] Klaus Peter Jochum, Uwe Nohl, Kirstin Herwig, Esin Lammel, Brigitte Stoll, and Albrecht W Hofmann. GeoReM: a new geochemical database for reference materials and isotopic standards. *Geostandards and Geoanalytical Research*, 29(3):333–338, 2005.
- [530] Manfred Mudelsee. Tauest: A computer program for estimating persistence in unevenly spaced weather/climate time series. *Computers & Geosciences*, 28(1):69–72, 2002.

## Selbständigkeitserklärung

Über die Bedeutung einer zur Vorlage bei Gericht bestimmten eidesstattlichen Versicherung und über die Strafbarkeit einer falschen Versicherung belehrt, erkläre ich, Tobias Braun, geb. am 13.01.1993 in Dinslaken, folgendes an Eides statt:

Ich erkläre, dass ich die vorliegende Arbeit selbstständig und nur unter Verwendung der angegebenen Literatur und Hilfsmittel angefertigt habe. Ich habe mich nicht anderwärts um einen Doktorgrad im Promotionsfach Physik beworben und besitze keinen Doktorgrad im Promotionsfach Physik.

Die Promotionsordnung der Mathematisch-Naturwissenschaftlichen Fakultät, veröffentlicht in den Amtlichen Bekanntmachungen der Universität Potsdam Nr. 19/2013 am 19.12.2013 habe ich zur Kenntnis genommen.

Potsdam, den 27. September 2022, Tobias Braun